Characterization of Minerals, Metals, and Materials 2023

EDITED BY
Mingming Zhang
Zhiwei Peng
Bowen Li
Sergio Neves Monteiro
Rajiv Soman
Jiann-Yang Hwang
Yunus Eren Kalay
Juan P. Escobedo-Diaz
John S. Carpenter
Andrew D. Brown
Shadia Ikhmayies

TMS
Springer

The Minerals, Metals & Materials Series

Mingming Zhang · Zhiwei Peng · Bowen Li ·
Sergio Neves Monteiro · Rajiv Soman ·
Jiann-Yang Hwang · Yunus Eren Kalay ·
Juan P. Escobedo-Diaz · John S. Carpenter ·
Andrew D. Brown · Shadia Ikhmayies
Editors

Characterization of Minerals, Metals, and Materials 2023

TMS

Springer

Editors
Mingming Zhang
Baowu Ouyeel
Shanghai, China

Bowen Li
Michigan Technological University
Houghton, MI, USA

Rajiv Soman
Eurofins EAG Laboratories
Liverpool, NY, USA

Yunus Eren Kalay
Middle East Technical University
Ankara, Turkey

John S. Carpenter
Los Alamos National Laboratory
Los Alamos, NM, USA

Shadia Ikhmayies
Amman, Jordan

Zhiwei Peng
Central South University
Changsha, China

Sergio Neves Monteiro
Military Institute of Engineering
Rio de Janeiro, Brazil

Jiann-Yang Hwang
Michigan Technological University
Houghton, MI, USA

Juan P. Escobedo-Diaz
University of New South Wales
Canberra, ACT, Australia

Andrew D. Brown
United States Army Research Laboratory
Abingdon, MD, USA

ISSN 2367-1181 ISSN 2367-1696 (electronic)
The Minerals, Metals & Materials Series
ISBN 978-3-031-22575-8 ISBN 978-3-031-22576-5 (eBook)
https://doi.org/10.1007/978-3-031-22576-5

Cover Illustration: From Chapter "Structural Characterization of Europium-Doped $BaTiO_3$ Obtained by Solid-State Reaction Synthesis", J. P. Hernández-Lara et al., Figure 5: Micrograph of the sample x = 0.007% by weight Eu^{3+} sintered at 1300 °C. https://doi.org/10.1007/978-3-031-22576-5_56.

This Springer imprint is published by the registered company Springer Nature Switzerland AG
The registered company address is: Gewerbestrasse 11, 6330 Cham, Switzerland

Preface

Materials characterization is a vital part of all science and engineering practice, as it is a fundamental process to achieving a good understanding of the processing-microstructure-property relationship. Various advances in characterization techniques and instruments in recent years have contributed, in a significant way, to an in-depth knowledge of the material's properties and structure on different scales. This enhanced understanding has also profoundly impacted the efficiency of existing industrial processes and how minerals, metals, and materials are applied in many fields.

This year, the Characterization of Minerals, Metals, and Materials symposium received 146 abstract submissions, of which 62 papers were accepted in 8 technical sessions. This symposium is among one of the largest in the TMS Annual Meeting & Exhibition. The proceedings volume includes state-of-art techniques used in modern minerals, metals, and materials characterization and the latest research in materials engineering and technologies. This proceedings publication is a valuable reference for academic scholars and industry professionals interested in advanced characterization methods and instrumentations that cover a wide range of research subjects. Readers will enjoy the diversity of topics in this book with innovative approaches to process and characterize materials at various scales and levels.

The Characterization of Minerals, Metals, and Materials 2023 symposium is sponsored by the Materials Characterization Committee under the Extraction & Processing Division (EPD) of TMS. The main focuses of this symposium include but are not limited to advanced characterization of Extraction and processing of minerals, process-microstructure-property relation of metal alloys, ceramics, polymers, and composites. New characterization methods, techniques, and instrumentations are also emphasized.

As a lead organizer of this symposium, I would like to take this opportunity to express my sincere gratitude to all authors for their contribution and generosity to share their research work. On behalf of the organizing committee, I would like to thank TMS for providing us with the valuable opportunity to publish this standalone proceedings volume. Much appreciation is also extended to the EPD for sponsoring this symposium.

Most importantly, the success of this proceeding's publication would not be possible without the fabulous contribution and support from all members of the Materials Characterization Committee. I also would like to thank our publisher, Springer, for their timely and quality publication of this book.

Mingming Zhang
Lead Organizer

Contents

About the Editors

Mingming Zhang is currently a principal consultant at Wood Mackenzie. He has more than 20 years of experience in the field of mining, mineral processing, smelting and refining, and materials engineering. Before joining Wood Mackenzie, Dr. Zhang held lead engineer position at ArcelorMittal Global R&D in East Chicago, Indiana. He obtained his Ph.D. in Metallurgical Engineering from The University of Alabama and his master's degree in Mineral Processing from the General Research Institute for Non-ferrous Metals in China. Prior to joining ArcelorMittal, he worked with Nucor Steel in Tuscaloosa, Alabama where he was a metallurgical engineer leading the development of models for simulating slab solidification and secondary cooling process. Dr. Zhang has conducted a number of research projects involving mineral beneficiation, thermodynamics and kinetics of metallurgical reactions, electrochemical processing of light metals, metal recycling, and energy-efficient and environmentally cleaner technologies. He has published more than 50 peer-reviewed research papers and he is the recipient of several U.S. patents. Dr. Zhang also serves as editor and reviewer for a number of prestigious journals including *Metallurgical and Materials Transactions A* and *B*, *JOM*, *Journal of Phase Equilibria and Diffusion*, and *Mineral Processing and Extractive Metallurgy Review*. Dr. Zhang has made more than 30 research presentations at national and international conferences including more than 10 keynote presentations. He was the recipient of the 2015 TMS Young Leaders Professional Development Award. He has served as conference/symposium

organizer and technical committee chair in several international professional organizations including The Minerals, Metals &Materials Society (TMS), the Association for Iron & Steel Technology (AIST), and the Society for Mining Metallurgy & Exploration (SME).

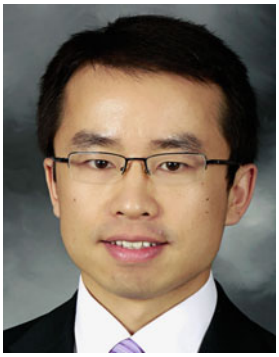

Zhiwei Peng is a professor in the School of Minerals Processing and Bioengineering at Central South University, China. He received his B.E. and M.S. degrees from Central South University in 2005 and 2008, respectively, and his Ph.D. degree in Materials Science and Engineering from Michigan Technological University, USA, in 2012. His research interests include dielectric characterization, ferrous metallurgy, microwave processing, comprehensive utilization of resources, waste valorization, powder agglomeration, low-carbon technology, process simulation, electromagnetic shielding, and synthesis of functional materials.

Dr. Peng has published over 190 papers, including more than 140 peer-reviewed articles in journals such as *International Materials Reviews*; *Journal of Hazardous Materials*; *ACS Sustainable Chemistry & Engineering*; *Resources, Conservation & Recycling*; *Journal of Cleaner Production*; *Waste Management*; *Metallurgical and Materials Transactions A*; *Metallurgical and Materials Transactions B*; *JOM*; *Journal of Power Sources*; *Fuel Processing Technology*; *Energy & Fuels*; *IEEE Transactions on Magnetics*; *IEEE Transactions on Instrumentation and Measurement*; *Ceramics International*; *Powder Technology*; and *Separation and Purification Technology*. He holds 65 Chinese patents and has served as an associate editor for *Mining, Metallurgy & Exploration*, as a guest editor for *JOM* and *Metals*, and as an editor for *PLOS ONE*. He has also been a member of editorial boards of *Scientific Reports*, *Journal of Central South University*, and *Journal of Iron and Steel Research International*, and has served as a reviewer for more than 70 journals.

Dr. Peng is an active member of The Minerals, Metals & Materials Society (TMS). He has co-organized 12 TMS symposia and co-chaired 24 symposia sessions since 2012. He is a member of the Pyrometallurgy Committee and the vice chair of the Materials Characterization Committee. He was a winner of the TMS EPD Young Leaders Professional Development Award

in 2014 and the TMS EPD Materials Characterization Award Best Paper—1st Place in 2020.

Bowen Li is a research professor in the Department of Materials Science and Engineering and Institute of Materials Processing at Michigan Technological University. His research interests include materials characterization and analysis, metals extraction, ceramic process, antimicrobial additives and surface treatment, porous materials, applied mineralogy, and solid waste reuse. He has published more than 140 technical papers in peer-reviewed journals and conference proceedings, authored/co-authored 3 books, and edited/co-edited 12 books. He also holds 16 patents and has delivered more than 30 invited technical talks. Dr. Li received a Ph.D. degree in Mineralogy and Petrology from China University of Geosciences Beijing in 1998 and a Ph.D. degree in Materials Science and Engineering from Michigan Technological University in 2008. He has been an active member in The Minerals, Metals & Materials Society (TMS), Society for Mining, Metallurgy & Exploration (SME), and China Ceramic Society. At TMS, he has served as the chair of the Materials Characterization Committee and as a member of TMS CDDC Committee, Powder Materials Committee, and the Biomaterials Committee. He has also served as an EPD Award committee member, *JOM* subject advisor, and key reader for *Metallurgical and Materials Transactions A*. He has been organizer/co-organizer of a number of international symposia and sessions. He also served as an editorial board member of the *Journal of Minerals and Materials Characterization and Engineering*, *Reviews on Advanced Materials Science*, and *FUTO Journal Series*. He is the recipient of AIME Hal W. Hardinge Award (2022).

Sergio Neves Monteiro graduated as a metallurgical engineer (1966) at the Federal University of Rio de Janeiro (UFRJ). He received his M.Sc. (1967) and Ph.D. (1972) from the University of Florida, followed by a 1975 course in energy at the Brazilian War College, and a post doctorate (1976) at the University of Stuttgart. In 1968, he joined the Metallurgy Department of UFRJ as full professor of the postgraduation program in engineering (COPPE). He was elected as head of department (1978), coordinator of COPPE (1982), Under-Rector for Research (1983), and was invited as Under-Secretary of Science for the State of Rio de Janeiro (1985) and Under-Secretary of the College Education for the Federal Government (1989). He retired in 1993 from the UFRJ and joined the State University of North Rio de Janeiro (UENF), where he retired in 2012. He is now a professor at the Military Institute of Engineering (IME), Rio de Janeiro. Dr. Monteiro has published more than 2,000 articles in journals and conference proceedings and has been honored with several awards including the ASM Fellowship and several TMS awards. He is the top researcher (1A) of the Brazilian Council for Scientific and Technological Development (CNPq) and Emeritus Scientist of State of Rio de Janeiro (FAPERJ). He was president of the Superior Council of the State of Rio de Janeiro Research Foundation, FAPERJ (2012), and currently is coordinator of the Engineering Area of this foundation. He has also served as president of the Brazilian Association for Metallurgy, Materials and Mining (ABM, 2017–2019), as a consultant for the main Brazilian R&D agencies, and as a member of the editorial board of five international journals as well as associate editor-in-chief of the *Journal of Materials Research and Technology*. He is the author of 130 patents and a top world researcher in “Natural Fiber Composites” and “Ballistic Armor”, Scopus 2020.

Rajiv S. Soman is currently with Purity Survey Analysis, Materials Sciences Division at Eurofins EAG Laboratories, USA, where he is responsible for developing new business opportunities, and expanding R&D initiatives. Prior to his current responsibilities, he served as Director, Purity Survey, Eurofins EAG Laboratories. He has over 33 years of professional experience in analytical chemistry and materials sciences. He earned a doctorate in Analytical Chemistry from Northeastern University, Boston, and M.Sc. in Applied Chemistry from the Faculty of Technology & Engineering, Maharaja Sayajirao University of Baroda, India. He commenced his professional career as an Advanced Analytical Chemist in the Engineering Materials Technology Laboratories of General Electric Aircraft Engines. Prior to joining EAG Laboratories, Dr. Soman served as Professor (Full) of Chemical Engineering, Chemistry, and Chemical Technology, and served as a faculty member for 21 years. He also served as Department Head and Associate Dean. He has received numerous awards for excellence in teaching and twice has been listed in *Who's Who Among America's Teachers*. Dr. Soman's research interests are in the areas of atomic and mass spectrometry, with an emphasis on trace element determination and chemical speciation in a wide range of complex sample matrices. He was an invited guest scientist at the prestigious research institute, Forschungszentrum Jülich, Germany, where he conducted research in elemental mass spectrometry. He has co-authored several peer-reviewed publications in international journals and has made numerous presentations at national and international conferences. He holds two U.S. patents. Dr. Soman has been a member of the Society for Applied Spectroscopy (SAS) and the American Chemical Society (ACS) since 1986 and has served in numerous leadership positions in the Professional Societies. He was an invited panel member for the American Chemical Society's National Initiative on *Preparing for the Workforce 2015*. He is a member of TMS, where he serves as a member of the Materials Characterization Committee and as Chair of the Poster Awards Committee. He has also served as co-organizer for several TMS Symposia and is a reviewer for the TMS proceedings volume *Characterization of Minerals, Metals, and Materials* and *JOM*.

Jiann-Yang Hwang is a professor in the Department of Materials Science and Engineering at Michigan Technological University. He is also the Chief Energy and Environment Advisor at the Wuhan Iron and Steel Group Company, a Fortune Global 500 company. He has been the editor-in-chief of the *Journal of Minerals and Materials Characterization and Engineering* since 2002. He has founded several enterprises in areas including water desalination and treatment equipment, microwave steel production, chemicals, fly ash processing, antimicrobial materials, and plating wastes treatment. Several universities have honored him as a guest professor, including the Central South University, University of Science and Technology Beijing, Chongqing University, Kunming University of Science and Technology, and Hebei United University. Dr. Hwang received his B.S. from National Cheng Kung University in 1974, M.S. in 1980 and Ph.D. in 1982, both from Purdue University. He joined Michigan Technological University in 1984 and served as its Director of the Institute of Materials Processing from 1992 to 2011 and the Chair of Mining Engineering Department in 1995. He has been a TMS member since 1985. His research interests include the characterization and processing of materials and their applications. He has been actively involved in the areas of separation technologies, pyrometallurgy, microwaves, hydrogen storage, ceramics, recycling, water treatment, environmental protection, biomaterials, and energy and fuels. He has more than 28 patents and has published more than 200 papers. He has chaired the Materials Characterization Committee and the Pyrometallurgy Committee in TMS and has organized several symposia. He is the recipient of the TMS Technology Award and of Michigan Tech's Bhakta Rath Research Award.

Yunus Eren Kalay is an associate professor in the Metallurgical and Materials Engineering Department and assistant to the president at Middle East Technical University (METU), Ankara, Turkey. Dr. Kalay received his Ph.D. degree with Research Excellence award from Iowa State University in 2009. His Ph.D. topic was related to the metallic glass formation in Al based metallic alloy systems. Following his Ph.D., he pursued postdoctoral research at Ames National Laboratory. In 2011, Dr. Kalay joined the Department of Metallurgical and Materials Engineering (METE) of METU as an assistant professor and in 2014 he was promoted to associate professor. His research interests span microstructural evolution in metallic alloys, rapid solidification of metallic alloys, nanostructured and amorphous alloys, high-entropy alloys, electronic packaging, and advanced characterization techniques such as scanning and transmission electron microscopy, electron and X-ray spectroscopy, atom probe tomography, and synchrotron X-ray scattering. Dr. Kalay was awarded the METU Prof. Dr. Mustafa Parlar Foundation Research Incentive Award, which is a very prestigious award that recognizes young scientists in Turkey with exceptional achievements and research productivity. He is also an active member of the TMS Materials Characterization Committee and served on organizing committees of three international and one national congress including IMMC, MS&T, and TMS. Dr. Kalay has also been involved in many synergistic activities such as being founding editor of Turkey's first undergraduate research journal, *MATTER*, and organizing the Materials Science Camps for K–12 students.

Juan P. Escobedo-Diaz is a senior lecturer in the School of Engineering and Information Technology (SEIT) at UNSW Canberra. He obtained his doctoral degree in Mechanical Engineering at Washington State University. Prior to taking up this academic appointment, he held research positions at the Institute for Shock Physics at Los Alamos National Laboratory. His main research interests center on the dynamic behavior of materials under extreme conditions, in particular high pressure and high strain rate. His focus has been on investigating the effects of microstructural features on the dynamic fracture behavior of metals and metallic

alloys. He has published primarily in the fields of shock physics and materials science. He has been a member of The Minerals, Metals & Materials Society (TMS) since 2011. During this time, he has co-organized more than five symposia at the Annual Meetings including the symposium on Characterization of Minerals, Metals, and Materials since 2014. He was awarded a 2014 SMD Young Leaders Professional Development Award.

John S. Carpenter is a scientist within the manufacturing and metallurgy division at Los Alamos National Laboratory. Dr. Carpenter received his Ph.D. in Materials Science and Engineering from The Ohio State University in 2010 after performing his undergraduate studies at Virginia Tech. Dr. Carpenter's research focus is on enabling advanced manufacturing concepts through experiments employing novel processing techniques, advanced characterization, and small-scale mechanical testing. Currently, he is working on projects related to the qualification of additively manufactured components, development of new materials for high field magnets using severe plastic deformation and using high energy X-rays to study phase transformations during solidification in MIG cladding. Throughout his career he has utilized many characterization techniques including neutron scattering, X-ray synchrotron, XCT, PED, TEM, EBSD, and SEM. He has more than 75 journal publications, one book chapter, and 45 invited technical talks to his credit. With regard to TMS service, Dr. Carpenter is a past chair for both the Materials Characterization and Advanced Characterization, Testing & Simulation Committees. He is current chair for the Joint Commission for *Metallurgical and Materials Transactions A* and the SMD representative on the Content Development and Dissemination Committee. He is also the Program Committee Representative for the MS&T Conference. He recently received the McKay-Helm Award from the American Welding Society and is the 2018 recipient of the Distinguished Mentor Award at Los Alamos National Laboratory.

Andrew D. Brown serves as Technical Core and Mission Support for the Science of Extreme Materials Competency Branch at DEVCOM ARL Army Research Office, Durham, NC. He obtained his B.S. in Mechanical Engineering at North Carolina State University (2009) and his doctoral degree in Mechanical Engineering at Arizona State University (2015). He spent three years (2015–2018) at UNSW Canberra as a postdoctoral researcher where he oversaw the daily operations of the Impact Dynamics Laboratory, mentored undergraduate and graduate student research projects, and performed teaching duties. His research expertise is understanding microstructural effects on the mechanical performance and damage processes of materials subjected to high dynamic pressures (shock) and high strain rates, high-rate injury biomechanics research to improve injury outcome prediction and protect the U.S. Warfighter. He has been an active member of TMS since 2011; was a co-organizer for the symposium on Characterization of Minerals, Metals, and Materials in 2018; and has been the symposium's EPD Award Representative from 2017–2022. Dr. Brown has published over 40 peer-reviewed articles in the fields of mechanical engineering, materials science, and biomechanics.

Shadia Ikhmayies received a B.Sc. and M.Sc. from the physics department at the University of Jordan in 1983 and 1987, respectively, and a Ph.D. in producing CdS/CdTe thin film solar cells from the same university in 2002. Her research is focused on producing and characterizing semiconductor thin films and thin film CdS/CdTe solar cells. She also works in characterizing quartz in Jordan for the extraction of silicon for solar cells and characterizing different materials by computation. She has published 59 research papers in international scientific journals, 85 research papers in conference proceedings, and 3 chapters in books. She is the founder and editor of the eBook series *Advances in Material Research and Technology* published by Springer, and the editor-in-chief/editor of several books. Dr. Ikhmayies is a member of The Minerals, Metals & Materials Society (TMS) where she was the chair of the TMS Materials Characterization Committee (2016–2017), and the leading organizer of three symposiums;

Solar Cell Silicon 2017–2020, Mechanical Characteristics and Application Properties of Metals and Nonmetals for Technology: An EPD Symposium in Honor of Donato Firrao, and Green Materials Engineering: An EPD Symposium in Honor of Sergio Monteiro. Dr. Ikhmayies is also a member of the World Renewable Energy Network/Congress (WREN/WREC) 2010–present. She is a member of the international organizing committee and the international scientific committee in the European Conference on Renewable Energy Systems (ECRES2015–ECRES2022). She is a guest editor and a member of the editorial board of several journals including *JOM* and the *Journal of Electronic Materials*. Dr. Ikhmayies is a reviewer of 24 international journals and several international conference proceedings. She has received several international awards including the TMS Frank Crossley Diversity Award 2018 and World Renewable Energy Congress 2018 Pioneering Award.

Part I
Advanced Characterization Methods I

Characterization of Lunar and Martian Meteorites Using a Scanning Electron Microscope (SEM)

Hussain Al Halwachi

Abstract Lunar and Martian meteorites are rare rocks found on Earth and classified by meteoritical experts depending on their physical and chemical features. Three different types of certified lunar rock samples and one Martian rock sample were tested and scanned by a scanning electron microscope (SEM) to obtain the chemical composition, explore the elemental mapping, and provide a statistical comparison between the different types. The SEM was able by EDS detector to provide accurate chemical compositions, in addition to microstructure images and elements mapping. The data provided by SEM were treated statistically by the principal component analysis (PCA) technique to obtain the relation between the elements and obtain a statistical model to help in differentiating similar rocks in the future.

Keywords SEM · Lunar · Martian · PCA

Introduction

The Moon and Martian meteorites are considered among the rarest space rocks available on Earth. They usually blast off from the surface of the Moon and Mars due to collisions occurring with possible asteroids and then are captured by Earth's gravity until they fall on Earth's surface after penetrating the atmosphere [1]. Meteorite classification and identification became a crucial step in the past decade since a lot of people are interested to own a genuine piece from space. The classification is carried out by international meteoritical societies and throughout the years an international database was generated for the certified meteorites [2]. The classification is carried out by experts in this field. The sorting and classification of meteorites are carried out by scientists depending on the meteorites' mineralogy and structures [2], using several analytical tools and isotope analysis [2]. In this study, I am exploring the chemical compositions of four certified meteorite samples that had been bought from Mr. Mendy Ouzillou, a trusted dealer in this field and recommended by the

H. Al Halwachi (✉)
Bahrain Society of Chemists, P.O. Box 21741, Manama, Bahrain
e-mail: h.halwachi@alba.com.bh

M. Zhang et al. (eds.), *Characterization of Minerals, Metals, and Materials 2023*, The Minerals, Metals & Materials Series
https://doi.org/10.1007/978-3-031-22576-5_1

Meteoritical Society in the United States. Since the moon is not a uniform, homogeneous planet, and consists of different rocks formed in different ways and times [3], I had selected three genuine lunar samples carefully from different kinds to have a variety of Moon meteorites, in addition to a sample for Mars meteorite. The four samples measured by scanning electron microscope (SEM) and the data provided were treated statistically by principal component analysis (PCA) to obtain a better comparison between the different types of Meteorites.

Four Meteorite Samples

The four certified meteorite samples were selected from different kinds of rocks, to allow me to study different rock natures and chemical compositions. The size and dimension of each sample were important criteria for selection. Smaller size samples will not be prepared and fit easily in SEM instrument. The price was also one of the selection criteria since the genuine certified meteorite samples are not cheap. I could not add more samples due to the high price of some rare pieces, i.e., Zagami Shergottite piece. The samples selected were big enough in size to take three SEM images for each sample with the flexibility to select the best position for mapping and measurements.

(1) **NWA 6963 Martian Shergottite**
Meteorite Northwest Africa (NWA) 6963 is a gabbroic Shergottite rock classified as a basaltic Martian meteorite [4]. The NWA 6963 was found in Guelmim Es-Semara, Morocco in 2011 [5], and based on its bulk chemistry and oxygen isotopes, it was classified as a Martian meteorite [4]. The mineralogical model of NWA was containing Pyroxene, Plagioclase, Opaques, and Melt pockets with no ferroan Olivine. The absence of olivine in Shergottite rocks indicates that they crystallized from fractionated magmas [6]. Shergottites are the most abundant of Martian rocks (50 out of 61), almost three-quarters of all Martian meteorites [7]. The name Shergottites is given after five Shergotties meteorites, which fell in India in 1965 in an area called Shergotty [2]. Figure1 shows the four meteorite samples.

(2) **Lahmada 020, Lunar rock**
Meteorite Lahmada 020 is a lunar meteorite that was found in Saguia el Hamra, Western Sahara in Morocco in November 2018 [5]. The rock was classified as feldspathic regolith melt breccia. The feldspathic lunar meteorites likely originated from the inner and outer regions of Fledspathic Highlands Terrane (FHT) on the Moon [8]. Furthermore, the lunar surface is covered by a layer of unconsolidated debris known as lunar regolith [3, 9]. Lunar regolith are rocks that were broken from underlying bedrock by collision with meteorites [1]. Lunar regolith meteorite is ejected from the Moon by the impact of the cratering process [1]. This type of meteorite reflects a broad range from different lunar lithological terraces [10], including FHT [1]. One type of lunar lithologies is

Fig. 1 The four samples involved in the study

known as lunar regolith melt, which is formed when a meteorite impact melts the material, and then ejected from a crater, then solidifies before they land on earth [3, 11]. The geochemistry of Lahmada 020 rock includes Olivine, Pigeonite, and anorthite [5].

(3) **NWA 11474 Lunar**
Meteorite (NWA) 11474 was found in Northwest Africa in 2017 and classified as lunar feldspathic breccia [5]. The geochemistry includes Olivine, Pigeonite, pyroxene, and Plagioclase [5].

(4) **Meteorite NWA 10203**
Meteorite (NWA) 10203 was found in Northwest Africa in 2015 and classified as Polymict lunar [5]. Polymict (or polylithologic) breccias are a mixture of many different types of rocks, which result from the mixing of different lithologies formed under different conditions [9]. The Geochemistry of NWA 10203 includes Olivine gabbro, clinopyroxene, and plagioclase [5].

Experimental Method

SEM is a non-destructive technique used to magnify images up to at least 1,000,000X times [12]. SEM was used to produce magnified images for the four meteorite samples. The samples were fitted with special clamps to avoid destruction during measurement under a vacuum medium. Micro-mapping of the sample was carried out to determine the microtopographic locations of each element. SEM is equipped with an EDS detector that can produce quantitative analysis. The measurements were carried out in Louvre Museum Laboratory in Abu Dhabi, using SEM instrument from Thermo Fisher company (Fig. 2 and 3).

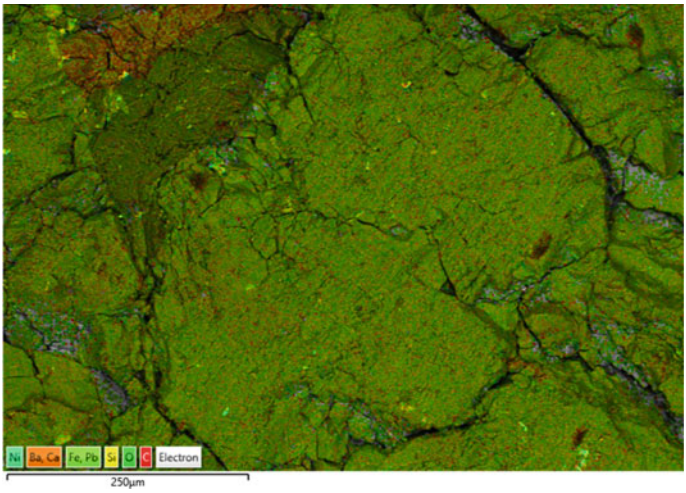

Fig. 2 SEM image for sample NWA 6369 overlapped with EDS maps, showing the microtopographic locations of the elements

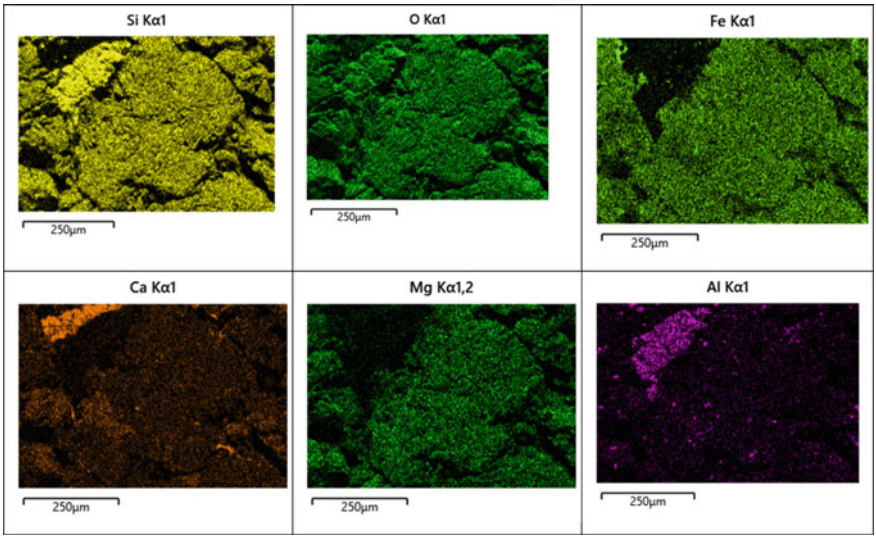

Fig. 3 EDS maps, the elementary micro-mapping of main elements for sample NWA 6369

Results

The main elements found in the four samples are oxygen, silicon, iron, carbon, calcium, magnesium, and aluminum, while other elements are found in the trace levels. The level of oxygen found in the four samples is from 40 to 45.9%, which is

Table 1 Semi-quantitative EDS analysis for NWA 6963 and Lahmada 20

NWA 6963- Martian				Lahmada 020			
Element	Image1	Image 2	Image3	Element	Image1	Image 2	Image3
	Weight %	Weight %	Weight %		Weight %	Weight %	Weight %
O	42.0	43.0	42.9	O	42.8	42.6	43.9
Si	18.3	18.6	17.3	Si	18.6	15.4	18.3
Fe	16.2	16.2	14.3	Fe	4.8	3.6	2.9
C	8.5	8.7	9.0	C	5.7	9.7	5.9
Ca	5.5	4.6	6.1	Ca	9.4	13.1	11.2
Mg	5.2	5.4	4.6	Mg	3.7	1.8	1.8
Al	1.9	1.0	2.7	Al	13.7	12.8	15.2
Na	0.7		1.0	Ba	0.6		
P	0.6	0.6	0.6				
Mn	0.5	0.5					

expected since minerals always occur in oxide form and exist in crystalline form. The level of silicon was almost around 18% in NWA6963, Lahmada 020, NWA10203, and lower than 18% in NWA11474. The level of iron was one of the characteristic elements for each sample. Iron was high in NWA 6963 at the level of 15%, and at the level of 10% in NWA10203, while it was lower in Lahmada 020 and NWA11474.Carbon: the level of Carbon differed from one sample to another. It was high in NWA11474 at around 20% and lower in NWA 6963 and Lahmada and no carbon was detected in NWA 10203. Lahmada 020 and NAW 10203 contained a high level of calcium (higher than 10%) compared with NWA 6963 and NWA 11474. The level of magnesium was almost lower than 4% in Lahmada 020 and NWA 11474, and slightly higher in NWA6963 and NWA 10203. The level of aluminum was characteristic for NWA 6963. The level in NWA 6963 was low compared with the other three samples (Tables 1 and 2).

PCA Multivariate Statistical Analysis

In order to identify the similarities and differences between the four meteorite samples, an unsupervised type of statistic was applied. It should be remembered that an unsupervised statistical technique allows a display of multivariate data (multiple variables) and allows for the identification of groups within the proposed data set. For our research, we have a data set consisting of 15 variables (O, Si, Fe, C, Ca, Mg, Al, Na, P, Mn, K, S, Ba, Ni, Sn). The samples consist of 3 Moon rocks and one Mars rock. The three Moon rocks are from different types of lunar rocks. Before starting the statistical treatment, the dataset was cleaned and the missing values were

Table 2 Semi-quantitative EDS analysis for NWA 11474 and NWA 10203

NWA 11474				NWA 10203			
Element	Image1	Image 2	Image3	Element	Image1	Image 2	Image3
	Weight %	Weight %	Weight %		Weight %	Weight %	Weight %
O	45.4	45.7	45.9	O	44.2	40.7	42.5
Si	13.2	15.7	13.7	Si	18.9	18.4	17.2
Fe	2.7	2.3	2.4	Fe	9.5	12.5	10.8
C	20.6	18.2	21.5	C			
Ca	5.1	3.9	4.1	Ca	7.5	9.4	11.0
Mg	3.3	1.8	1.8	Mg	7.1	4.3	4.5
Al	8.6	10.5	8.6	Al	8.9	12.0	10.9
K	0.5	1.3	1.2	Na			0.5
				S		0.8	
				Ni		0.6	
				Sn	2.1		1.2

replaced with the average value. The correlation between the variables is assessed and everything is highlighted in Fig. 4.

As can be seen in the graph, the blue dots outside the main diagonal show a positive correlation between the variables (e.g., Fe–P are positively correlated), while the red dots represent a negative correlation (e.g., Si–C are related negatively). The "*" in the graph represents the impossibility to evaluate the correlation because the variable values are constant in all samples. The PCA was therefore performed and the variance explained was obtained. Let's see how the data represented in the first two main components behave (score plot Fig. 5).

It is interesting to note from the graph how the data differ very well in groups, highlighting that the samples of rock from the Moon are different from each other (Red, green, blue) while the Martian rock samples (purple) form another group. The three samples per single collection that are displayed on the graph are the three sampling points that were measured by SEM. This leads to the assumption that the different measurements on a single sample do not affect the discrimination of the samples. The points on the graph that have a different size represent the centroids.

In order to understand which are the most discriminated variables for group separation, the biplot chart is shown below.

As can be seen from the biplot (Fig. 6), Iron and Magnesium have a high discriminant power in class separation in the Martian rock samples. Lahmada 020 samples are discriminated to calcium and aluminum, NWA 10203 are discriminated to silicon and NWA 11474 are discriminated to oxygen and carbon.

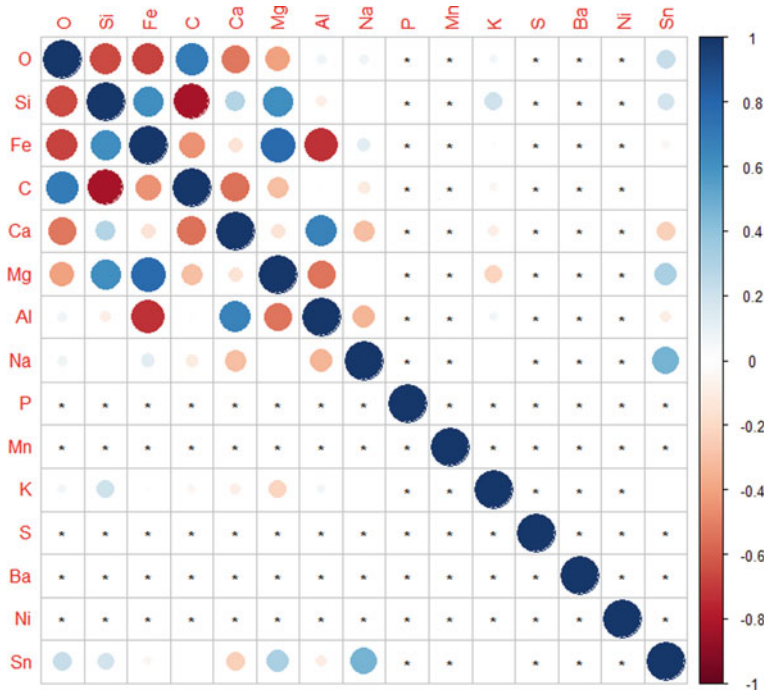

Fig. 4 Graph showing the correlation between the variables

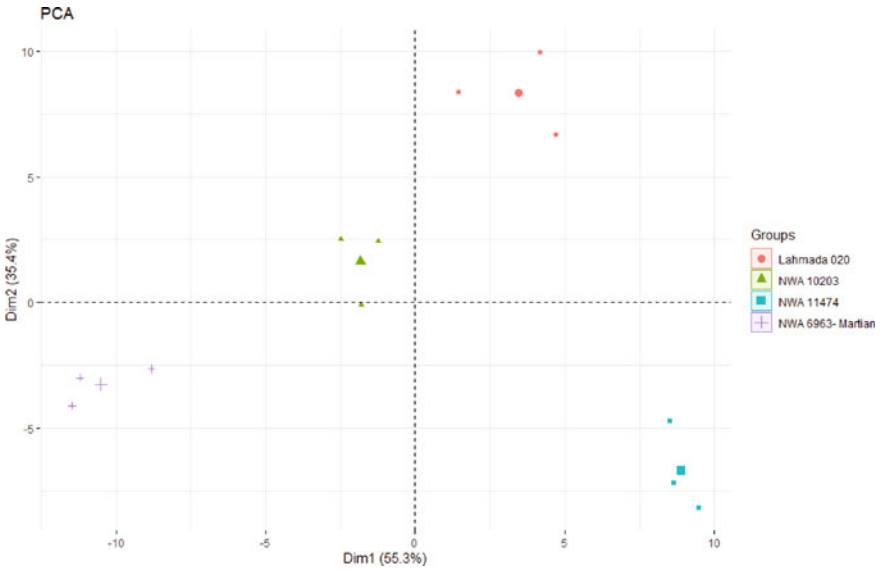

Fig. 5 Score plot, representation of data within the first 2 main components

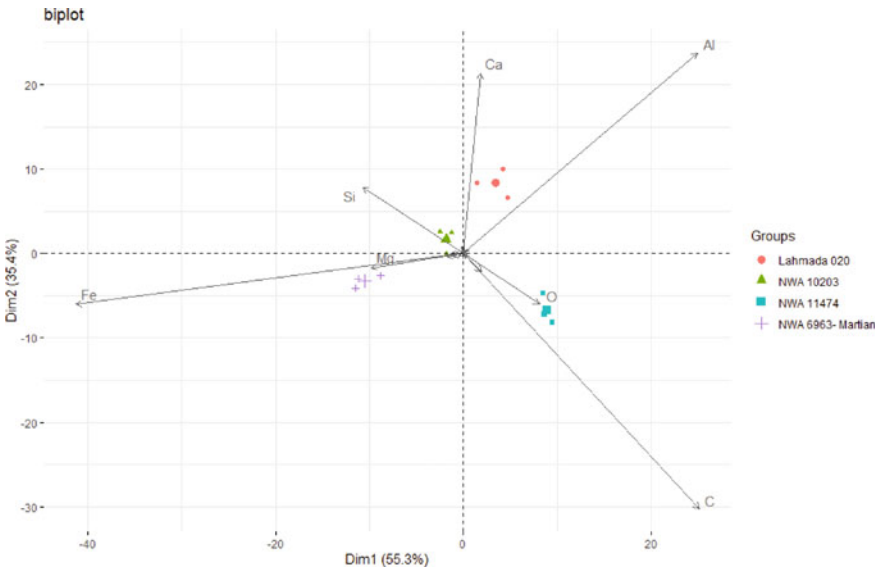

Fig. 6 Biplot graph for the four groups

Discussion

In this study, four different meteorite samples (three moon rocks and one Mars rock) were scanned by SEM in order to obtain the microtopographic locations of each element, while the qualitative analysis was carried out by the EDS channel in the SEM. Usual meteorite samples are available in very small sizes, the samples involved in this study were good enough in size to have the flexibility to measure in a different spot. The samples had a straight-cut surface, which allow me to produce the best possible images and results. The four samples were selected from different types of lunar rocks in addition to Martian rock in order to have a variety of space fall rocks. The analyses showed a characteristic difference between the four samples for some elements. For example, aluminum was low in NWA 6963, while carbon was very high in NWA 11474. For better differentiation and classification, multivariate statistical analysis was carried out. Principle component analysis (PCA) was able to provide the correlation between the elements and produce clusters for each group of analysis.

Conclusion

A SEM instrument was used successfully to micro-mapping images and obtain the microtopographic locations of each element in the four meteorites samples involved

in this study (NWA 6963- Martian rock, Lahmada 020 lunar rock, NWA 11474 lunar rock, and NWA 10203 lunar rock). The EDS in SEM was able to provide an accurate qualitative analysis of the existing elements in each sample. The data produced were treated statistically by multivariate statistical analysis (PCA). The PCA technique was able to differentiate the cluster of each group separately. The biplot graph was able to diatreme that iron and manganese had a high discriminant power in class separation for NWA 6963 Martian rock, calcium and aluminum had a high discriminant power for Lahmada 020 rock, calcium and aluminum had a high discriminant power for NWA 10203 lunar rock, while oxygen and carbon had a high discriminant power for NWA 11474. The statistical model obtained is useful guidance for any future comparisons to the same type of Moon and Martian rocks.

Acknowledgements I would like to thank Professor Tasha Dunn from the Meteoritical Society in the USA for all the support given. My thanks go to Menday Ouzillou (SkyFall Meteorites) for the support given. I am grateful to Dileep Hassan from Gulf Support Centre—Dubai for the analytical support given. Thanks are due to Dr. Pablo Londero at Louvre Museum Laboratory—Abu Dhabi. My thanks go to Prof. Sadiq Al Alawi for all the support given. My thanks go to Marco Ferrante from Trace Technologies. My thanks go to Professor Randy L. Korotev from Washington University for the support given. My thanks go to Professor Sadeq Al Alawi for all the analytical support given.

References

1. Joy K, Crawford I, Russell S, Kearsley A (2010) Lunar meteorite regolith breccias: an in situ study of impact melt composition using LA-ICP-MS with implications for the composition of the lunar crust. Meteorit Planet Sci 45(6):917–946
2. Norton O (2004) Rocks from space. Mountain Press Publishing, Missoula
3. Heiken G, Vaniman D, French B (2005). Lunar sourcebook. Cambridge University Press, Cambridge
4. Filiberto J, Gross J, Udry A, Trela J, Wittmann A, Cannon K, Penniston-Dorland S, Ash R, Hamilton V, Meado A, Carpenter P, Jolliff B, Ferré E (2018) Shergottite Northwest Africa 6963: a pyroxene-cumulate Martian Gabbro. J. Geophys. Res. Planets, 123(7):1823–1841
5. Grossman JN (2020) Meteoritical bulletin database. https://www.lpi.usra.edu/meteor/. Accessed January 1, 2020.
6. Stolper E, McSween HY (1979) Petrology and origin of The shergottite meteorites. Geochimica et Cosmochimica Acta 43(9):1475–1498. https://doi.org/10.1016/0016-7037(79)90142-x
7. Davis A (2014) Meteorites and cosmochemical processes, volume 1 of treatise on geochemistry (2nd edn). Elsevier
8. Nagaoka H, Karouji Y, Arai T, Ebihara M, Hasebe N (2022) Geochemistry and mineralogy of a feldspathic lunar meteorite (regolith breccia), Northwest Africa 2200
9. Meyer C (2022) Lunar petrographic thin section set study guide. [online] Available at https://curator.jsc.nasa.gov/education/lpetss/index.cfm. Accessed 21 May 2022
10. Korotev R, Irving A (2022) Compositions of three Lunar meteorites: meteorite Hills 01210, Northeast Africa 001, and Northwest Africa 3136. [online] NASA/ADS. Available at https://ui.adsabs.harvard.edu/abs/2005LPI....36.1220K/abstract. Accessed 8 May 2022.

11. Jolliff BL, Wieczorek MA, Shearer CK, Neal CR (2006) New views of the moon. De Gruyter, Berlin
12. FEI Company (2000) XL30 ESEM TMP, scanning electron microscope, technical manual. FEI Company, Hillsboro

Study on the Magnetocaloric Effect of Molten Mold Flux Under Low-Frequency Electromagnetic Field

Yijia Wang, Bo Bai, Yu Wang, Hongpo Wang, Mingxing Wang, and Fushen Li

Abstract Numerical simulation was used to study the magneto-Joule heating effect of molten mold flux under a low-frequency electromagnetic field in continuous casting. The effects of electromagnetic field parameters on the conductivity of molten mold flux were also investigated. The results showed that the induced current and magnetic induction in molten mold flux increased with its increasing conductivity and excitation current, and the magneto-induced Joule heat also increased. The magneto-Joule heat was found around 0.97×10^3 to 6.29×10^3 J m^{-3}. For every 10 mm decrease from the magnetic field action center, the Joule heat of molten mold flux increased 11.8% on average. A greater conductivity of the mold flux resulted in a more significant change in Joule heat.

Keywords Molten mold flux · Low-frequency electromagnetic field · Magnetocaloric Effect · Joule heat

Introduction

In recent years, the quality of steel has been significantly improved with the rapid development of continuous casting technology, among which mold flux plays an irreplaceable role [1]. The properties of mold flux under the action of the electromagnetic field have gradually attracted extensive attention. Relevant studies have found that electromagnetic force applied to the meniscus can widen the mold flux channel between the primary shell and the mold and reduce the dynamic pressure caused by mold vibration and reduce the depth of vibration marks [2–4]. The previous research on the thermal effect of the magnetic field mainly focuses on the induction heating of the mold and the solidified shell by the electromagnetic field, few attention was paid to its magnetocaloric effect on the molten mold flux, though. In this paper, numerical simulation was used to study the magneto-induced Joule heating effect of molten mold flux under a low-frequency electromagnetic field.

Y. Wang · B. Bai · Y. Wang (✉) · H. Wang · M. Wang · F. Li
College of Materials Science and Engineering, Chongqing University, Chongqing 400045, China
e-mail: wangyu@cqu.edu.cn

M. Zhang et al. (eds.), *Characterization of Minerals, Metals, and Materials 2023*, The Minerals, Metals & Materials Series
https://doi.org/10.1007/978-3-031-22576-5_2

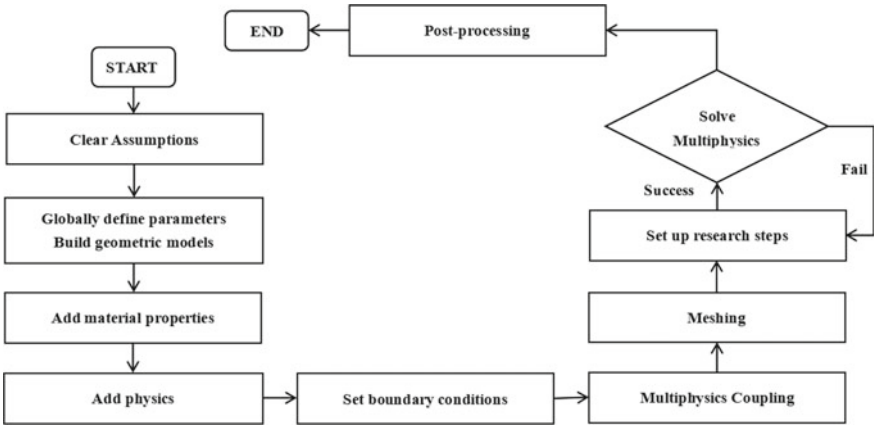

Fig. 1 Simulation analysis flow chart

Model Establishment

Process Analysis

Since multi-physical fields need to be coupled to solve, the secondary conditions are ignored. The actual workpiece is abstracted into a three-dimensional model, the global parameters and geometric parameters are defined, the material performance parameters related to mold flux are consulted, and the model is established using the set of parameters. The mesh is established based on the basic geometric model. To improve the calculation accuracy and speed, user-defined meshes and mesh sweeps are added to the geometric part (electromagnetic coil part) that needs to be analyzed carefully. Meantime, the appropriate boundary conditions and the coupling coefficient are added to the model. Moreover, the entire solution process is iterative, and the material property variables need to be added at the same time [5, 6]. The simulation flow is shown in Fig. 1.

Determination of the Parameters

A circular mold was used as the research object. The mold height is 800 mm, the radius is 100 mm, and the thickness of the mold wall is 15 mm. A 12 Hz rotating magnetic field was applied to generate the electromagnetic stirring. The current intensities of 400 A and 600 A were used as the power source excitation. Other specific parameters are shown in Table 1.

Table 1 Simulation parameters [4]

Object	Parameter value
Coil height	150 mm
Coil width	40 mm
Coil turns	100
Magnetic field frequency	12 Hz
Current intensity	6A、12A
Conductivity of copper coil	6.0×10^7 S/m
Magnetic permeability of vacuum	1
Copper relative permeability	1
The relative permeability of mold flux	1
Air relative permeability	1
Conductivity of mold flux	$\ln k = 10.173–1.689 \times 10^4/\mathrm{T}$ Ω^{-1} cm^{-1}
Copper relative permittivity	1

Basic Assumptions and Equations

When electromagnetic theory is applied to the electromagnetic stirring of mold, some reasonable simplifications and basic assumptions are involved, as follows [7]:

1. The molten mold flux is incompressible.
2. The electrode vector is parallel to the electric field, the magnetic pole vector is parallel to the magnetic field, and the applied magnetic field is a quasi-steady electromagnetic field.
3. The molten mold flux is electrically neutral, so only the conduction current is considered and the convection current is ignored.
4. The molten mold flux only has Joule heat without an internal heat source.
5. The influence of displacement current can be ignored in the calculation of low-frequency electromagnetic field.

Under the low-frequency alternating electromagnetic field, the electromagnetic environment is mainly determined by the electromagnetic stirring of the conductive coil because the flow rate of the mold flux is low. Passing an alternating current into the coil will form a time-varying electromagnetic field in space. The Maxwell equations have provided a comprehensive and overall description of the electromagnetic field, which is the basis for analyzing the electromagnetic field [8]**.** Therefore, when the medium is static, the specific expression is as follows:

$$\nabla \times \overrightarrow{E} = \mu \partial \overrightarrow{H} \Big/ \partial \mathrm{t} \tag{1}$$

$$\nabla \times \overrightarrow{H} = \overrightarrow{J} + \frac{\partial \overrightarrow{D}}{\partial \mathrm{t}} \tag{2}$$

$$\nabla \times \overrightarrow{D} = \rho \tag{3}$$

$$\nabla \cdot \overrightarrow{B} = 0 \tag{4}$$

In the formula, $\overrightarrow{E}$ is the electric field intensity vector (V/m), $\overrightarrow{H}$ is the magnetic field intensity vector (A/m), $\overrightarrow{J}$ is the current density vector (A/m^2), $\overrightarrow{D}$ is the electric displacement vector, $\overrightarrow{B}$ is the magnetic induction intensity vector (Wb/m^2).

Ohm's equation:

$$\overrightarrow{J} = \sigma(\overrightarrow{E} + \overrightarrow{V} + \mu \overrightarrow{H}) \tag{5}$$

Stokes's equation:

$$\rho[\partial \overrightarrow{V} / \partial t + (\overrightarrow{V} \cdot \nabla) \overrightarrow{V}] = \nabla P + \mu_f \nabla^2 \overrightarrow{V} + \overrightarrow{F} \tag{6}$$

Among them, $\vec{F}$ is:

$$\overrightarrow{F} = J \times \mu \overrightarrow{H} \tag{7}$$

The continuity equation:

$$\nabla \cdot \overrightarrow{V} = 0 \tag{8}$$

The energy conservation equation:

$$\nabla T / \partial t + \overrightarrow{V} \cdot \nabla T = \alpha \nabla^2 T + S + Q(\rho C_P)^{-1} \tag{9}$$

Among them, Q is

$$Q = J^2 \sigma^{-1} / 2 \tag{10}$$

where $\overrightarrow{F}$ is the electromagnetic force, Q is the Joule heat, J is the current density, S is the latent heat of fusion, C_p is the specific heat, σ is the conductivity, μ is the magnetic permeability, and α is the thermal conductivity.

It can be seen that the electromagnetic field acting on the molten mold flux will involve the mutual coupling and interaction of multiple-physical fields. In this paper, the influence of the electromagnetic field only be considered and the influence of the fluid flow on the electromagnetic field be ignored because the flow rate of the mold flux and the characteristic size of the system is small. It makes the relevant magnetic

Reynolds number ($Ra_m = \mu\sigma VL$ where V and L represent the characteristic volume and characteristic length, respectively) much smaller than 1.

According to Eqs. 1, 2, and 3, the charge density is the divergence source of the electric field, the time-varying magnetic field is the curling element of the electric field, the total current density is the curl source of the magnetic field, and the magnetic field is a non-scattering field. After vector operation, the electromagnetic force can be expressed as

$$\overrightarrow{F} = \mu(\overrightarrow{H} \cdot \nabla) - \mu\overrightarrow{H}^2/2 = \overrightarrow{F}_{\text{rot}} + \overrightarrow{F}_{\text{irrot}} \tag{11}$$

Among them, $\overrightarrow{F}_{\text{rot}}$ is the rotational force that causes the fluid motion, and $\overrightarrow{F}_{\text{irrot}}$ is the non-rotational force that does not affect the fluid motion. The relationship between them is as follows:

$$\left|\overrightarrow{F}_{\text{irrot}}/\overrightarrow{F}_{\text{rot}}\right| \propto L\delta^{-1} \tag{12}$$

Electromagnetism has a skin effect, and its skin depth can be expressed as $delta = (\pi\mu\sigma f)^{-1/2}$ where f is the frequency of the electromagnetic field. As the frequency increasing, the proportion of non-rotational force increases, which can control the shape of molten mold flux more effectively, while the lower frequency is more suitable to realize the driving of the fluid by rotational force (such as electromagnetic stirring). This is why a low-frequency electromagnetic field was chosen to analyze molten mold flux. The Joule heat intensity produced by the alternating frequency induced current is

$$q_v = \frac{\left|\overrightarrow{J}^2\right|}{\kappa} \tag{13}$$

where q_v is the density of the Joule heat body produced by the induced current, W/m3; $\overrightarrow{J}^2$ is the density vector of the induced current, A/m^2; $\kappa$is the resistivity of the slag, Ω^{-1} cm^{-1}.

Assuming that the material properties of the mold wall (the material is set to copper) and mold flux are isotropic, the Fourier heat conduction equation when the wall conductivity changes with temperature are considered as

$$\frac{\partial}{\partial \mathrm{x}}(k\frac{\partial T}{\partial \mathrm{x}}) + \frac{\partial}{\partial y}(k\frac{\partial T}{\partial y}) + \frac{\partial}{\partial z}(k\frac{\partial T}{\partial z}) + q_v = \rho_t c_{p-t}\frac{\partial T}{\partial t} \tag{14}$$

where T is the temperature, K; ρ_t is the density of the mold wall material, kg/m^3; $c_{p\text{-}t}$ is the specific heat capacity of the mold wall material, J/(kg K);$\kappa$is the thermal conductivity of the mold wall material, W/(m K).

Equation 15 can be obtained by substituting Eq. 13 into Eq. 14 and adding the convective heat transfer term of the mold flux at a steady state, which is the mathematical model for solving the induction heating temperature field. And the relevant

Table 2 Parameter values used in mathematical models of temperature fields [9]

Material	Parameter	Value
copper plate	Density, kg/m^3	8973
	specific heat capacity, J/(kg K)	390
mold flux	Density, kg/m^3	2500
	specific heat capacity, J/(kg K)	830

parameters used in the model are shown in Table 2.

$$frac\partial\partial \mathrm{x}(k\frac{\partial T}{\partial \mathrm{x}})+\frac{\partial}{\partial y}(k\frac{\partial T}{\partial y})+\frac{\partial}{\partial z}(k\frac{\partial T}{\partial z})+\frac{\left|\overrightarrow{J}^2\right|}{\kappa}=\rho_t c_{p-t}\frac{\partial T}{\partial t}+\rho_s c_{p-s}(\overrightarrow{U}\nabla T) \tag{15}$$

Electromagnetic Field Boundary Conditions and Meshing

When the Maxwell equations are used to solve the electromagnetic field, the steady-state solution is obtained at a certain time point in the frequency domain, which is a general solution [10]. Therefore, the electromagnetic field boundary conditions need to be established which is based on the following conditions:

The boundary needs to be included in the calculation range of the model and does not affect the boundary conditions.

The calculation part mainly includes the electromagnetic coil, mold wall, air layer, and molten mold flux area.

The outlet and inlet are calculated according to the law of conservation of energy, and the periodic sinusoidal vibration of the copper plate of the mold is simulated by a dynamic grid.

In the calculation area V, the electromagnetic field can be determined by analyzing the electromagnetic field vector and scalar, and specifying the initial value of the power excitation and the vector magnetic potential.

Given the following boundary conditions:

$$\overrightarrow{A}=\overrightarrow{A0} \tag{16}$$

$$n\times\frac{1}{\mu}\nabla\cdot\overrightarrow{A}=\overrightarrow{H_0} \tag{17}$$

Among them, the sum of $\overrightarrow{A0}$ and $\overrightarrow{H0}$ is zero or constant, and the magnetic potential $\overrightarrow{A}$ is uniquely determined.

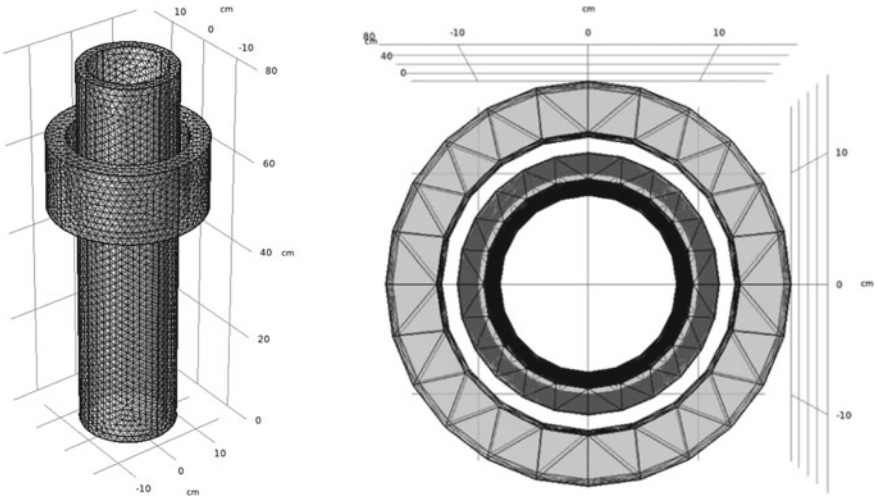

Fig. 2 Schematic diagram of 3D model

The current is the load current ($\overrightarrow{J0}$) of the load, the vector sum of the induced current produced by the alternating magnetic field and the induced current produced by the moving cutting magnetic field lines, which is expressed as follows:

$$\overrightarrow{J} = \vec{J}_0 + \sigma \frac{\partial \overrightarrow{A}}{\partial \mathrm{t}} + \mu\sigma(\overrightarrow{V} \times \overrightarrow{H}) \tag{18}$$

From Eq. 18, it can be seen that since the $\overrightarrow{J0}$ of flux is 0, the induced current in molten mold flux is completely generated by the alternating magnetic field under the premise of ignoring the induced current generated by the displacement. Therefore, the magnetic potential $\overrightarrow{A}$ can calculate the induced current in molten mold flux. The mesh of the model is divided as shown in Fig. 2.

Results

It can be seen from Eq. 13 that the Joule heat is proportional to the square of the current density in value. The change of the magnetic flux in the closed loop generates an induced electromotive force, and then an induced current is generated. The magnitude of the induced current increases with the increase of the excitation current. The principle can be expressed by Faraday's law of induction [11].

$$E = \frac{n\Delta\Phi}{\Delta t} \tag{19}$$

$$I = \frac{E}{R} = \frac{n\Delta\Phi}{R\Delta t} \tag{20}$$

where E is the induced electromotive force, V; I is the induced current, A; n is the number of turns of the coil; $\Delta\Phi/\Delta t$ is the rate of change of the magnetic flux.

In order to study the electromagnetic induction phenomenon of molten mold flux, the excitation electromagnetic field changes periodically, so the frequency domain analysis results of the electromagnetic field at the same phase section are intercepted. And the properties of molten mold flux are assumed to be isotropic. Meanwhile, the excitation current was set to 6 A and 12 A, and the frequency was 12 Hz.

At 1623 K, mold fluxes with different components were selected as the research object, and the specific components are shown in Table 3. And the conductivity of A1 and A2 is 0.360 Ω^{-1} cm^{-1} and 0.810 Ω^{-1} cm^{-1}, respectively.

Under the multiphysics module, the conductivity data is formed into a material scan, and the parametric scan is set in the research step. Finally, the average temperature difference of the Joule heat of the molten mold flux is calculated, and the simulation results are shown in Fig. 3.

Table 3 Chemical composition of mold fluxes for the experiment (*wt*%)

Number	CaO	SiO_2	Al_2O_3	MgO	Na_2O	CaF_2	Total
A1	35.630	29.680	2.720	3.230	11.810	16.930	100
A2	38.100	27.208	2.720	3.230	11.810	16.930	100

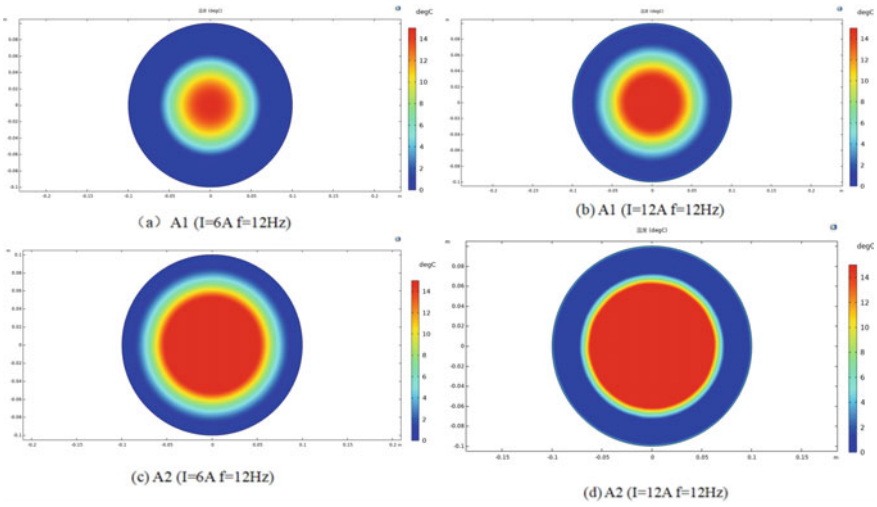

Fig. 3 Temperature difference cloud diagram of A1 and A2 slag

Table 4 The magnetic Joule temperature difference between A1 and A2 mold flux

Number	Conductivity(1623 K)/Ω^{-1} cm^{-1}	Temperature Rise/°C
A1	0.36	13
A2	0.81	15

Discussion

Effect of the Molten Mold Flux Conductivity on Magneto-Induced Joule Heat

In this study, the self-designed and developed low-frequency magnetic field molten mold flux performance testing system was used to test the temperature changes of the aforementioned A1 and A2 mold flux due to magneto-induced Joule heating under the low-frequency electromagnetic field. The experimental excitation current is 12 A, the frequency is 12 Hz, the initial temperature of mold flux in the crucible is 1350 °C, and the magnetic field action time is 5 min. The experimental results are shown in Table 4.

As we can see that the conductivity of A1 at 1623 K is lower than that of A2. Under the action of the low-frequency electromagnetic field and at the same time, the temperature rise of A2 with higher conductivity due to magneto-Joule heating is greater than that of A1 with low conductivity, which is consistent with the law obtained by simulation calculation, further indicating that the magneto-induced Joule heating of mold flux increasing with the increase of conductivity.

The Relationship Between Excitation Current and Magnetic Induction Intensity

Firstly, it can be seen in Fig. 3 that when the conductivity is the same, the excitation current increases, the high-temperature area in the center of the magnetic field expands, and the surrounding low-temperature area decreases. Therefore, it can be concluded that the excitation current is positively correlated with Joule heat.

Then the induction current density (ICD) and magnetic induction intensity (B) can be calculated while the coil current is 6 A and 12 A, and the frequency is 12 Hz. The result is shown in Fig. 4.

It can be found from Fig. 4 that the induced current density and the magnetic induction intensity increase with the increase of the coil current. And under the same coil current condition, the further away from the outer surface, the greater the current density and the stronger the magnetic induction intensity. Both values are maximized at the center. When the coil current is 6 A, the maximum values of induced currents of A1 and A2 are 1.161×10^2 A m^{-2} and 1.499×10^2 A m^{-2}, and

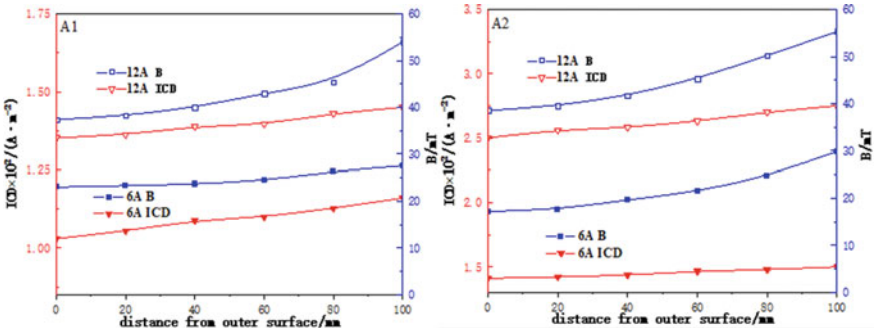

Fig. 4 Curve of induction current density and magnetic induction intensity with different coil current

the maximum values of magnetic induction intensity of A1 and A2 are 27.66 mT and 30.01 mT, respectively. When the coil current is 12 A, the maximum values of induced currents of A1 and A2 are 1.64×10^2 A m^{-2} and 2.75×10^2 A m^{-2}, and the maximum values of magnetic induction intensity of A1 and A2 are 54.01 mT and 55.34 mT, respectively. In brief, the induced current increasing with the increase of the conductivity under the same coil current, which is consistent with the previous conclusion. And the coil current is positively correlated with the magnetic induction intensity, which indicates that the conductivity of molten mold flux is enhanced, the magnetic flux per unit area of the loop increases, and the magnetic induction intensity increases.

The Effect of the Distance from the Center of Magnetic Field Action on Joule Heat

Based on the analysis in previous sections, the Joule heat in molten mold flux can be solved by combining the data in Fig. 4. The Joule heating change caused by the induced current in molten mold flux is calculated by adding the material property of conductivity for the multiphysics calculation module and then sweeping. And the calculation frequency is 12 Hz, the coil currents are 6 A and 12 A, respectively. The calculation results are shown in Fig. 5.

It can be seen from Fig. 5 that the area where the Joule heat rises rapidly in molten mold flux is between 25 and 60 mm away from the surface of the mold. The greater the coil current, the greater the Joule heat generated by the induction heating. But the change of Joule heat with distance is not linear. From Fig. 5, it can be found that when the coil current and the conductivity of molten mold flux change, the changing trend of Joule heat with the distance from the induction heating center does not change. The Joule heat of all molten mold flux increase slowly at first, and then the rising speed increases between 25 and 60 mm, and decreases between 60 and 100 mm.

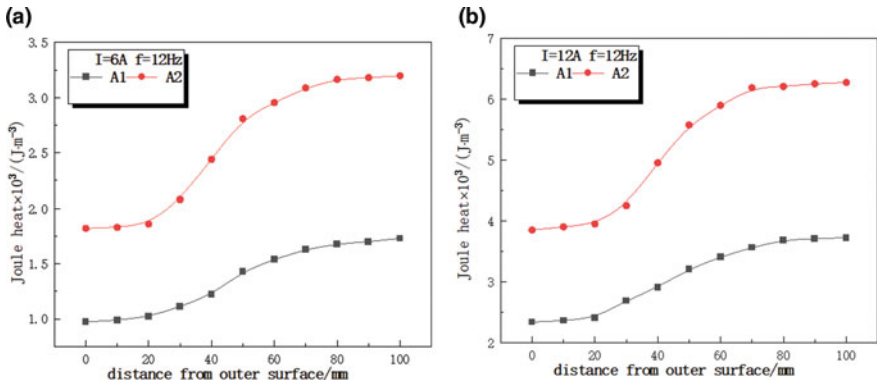

Fig. 5 Induced current produces Joule heat change curve under 400 A (**a**) and 600 A (**b**), 12 Hz power

Combined with the magnetic induction intensity in Fig. 4 for analysis, the change rate of the magnetic induction intensity in the middle area is slightly larger than that of the two sides, so the distribution of the magnetic induction lines in the middle is denser than the two sides. And it can be seen from Eq. 2 that in the case of the same coil current, the stronger the magnetic field strength is, the larger the current density vector is, which leads to the increase in the change rate of the electric displacement vector and the faster Joule heat rise rate. From the cloud map in Fig. 3, it also can be found that the temperature difference in the central region changes more obviously than on both sides, and the temperature gradient is larger.

When the current is 6A, the Joule heat range is approximately 0.974×10^3 J m^3 − 3.198×10^3 J m^{-3}, and when the current is 12 A, the Joule heat range is roughly 2.337×10^3 J m^{-3}–6.277×10^3 J m^{-3}. In the interval from 25 to 60 mm from the surface of the mold to the center, under the conditions of 6 A and 12 A for A1 and A2 mold flux, the increase rate of Joule heat per unit distance is 10.96% and 12.96%, respectively. Therefore, in the range from 25 to 60 mm in the center direction, for every 10 mm increase, the Joule heat increase about 11.8% on average. It can be seen that the greater the conductivity, the greater the variation of the Joule heat with the distance from the center of the magnetic field.

The main reason for the gradient change in the Joule heating is the change in the conductivity of mold flux. Under the same excitation current, the conductivity increases, the conductivity of mold flux ions is enhanced, the resistance performance is weakened, and the Joule heating effect is more significant. At the same time, the greater conductivity of the mold flux is, the more obvious the change of Joule heat in the area with the greater magnetic field strength will be.

Conclusion

Under the action of low-frequency electromagnetic field, the greater the change in distance from the heating center is, the greater the change in Joule heat will be, and the range is roughly 0.974×10^3 to 6.277×10^3 J m^{-3}. Along the inner surface of the mold towards the center from 25 to 60 mm, the average increase rate of Joule heat is about 11.8% for every 10 mm increase. Moreover, a higher conductivity of the mold flux results in a greater variation range of Joule heat with the change of the distance from the magnetic field center. The Joule heating effect of mold flux dramatically affects its performance.

References

1. Lechosław Trębacz, Katarzyna Miłkowska-Piszczek, Konopka K (2014) Numerical simulation of the continuous casting of steel on a grid platform. eScience on distributed computing infrastructure, pp 407–418
2. Li T, Sassa K, Asai S (2007) Surface quality improvement of continuously cast metals by imposing intermittent high frequency magnetic field and synchronizing the field with mold oscillation. ISIJ Int 36(4):410–416
3. Tingju, LI, Kensuke (1996) Improvement of surface quality of continuously cast metals by imposing intermittent high frequency magnetic field and synchronizing the field with mold oscillation. Tetsu-to-Hagane 82(3):197–202
4. Toh T, Takeuchi E, Hojo M (1997) Electromagnetic control of initial solidification in continuous casting of steel by low frequency alternating magnetic field. ISIJ Int 37(11):1112–1119
5. Jiang PG, Lai CB (2016) Numerical simulation of the flow field in a wide slab continuous casting mold. Chin J Eng 38(1):50–55
6. Huixiang YU, Zhang J, Wang W (2002) Numerical simulation of fluid flow in continuous slab-casting mold. J Univ Sci Technol Beijing 24(5):492–496
7. BE Launder, DB Spalding (1990) The numerical computation of turbulent flows. Elsevier Sequoia S. A
8. Yang H, Zhang X, Deng K (1998) Mathematical simulation on coupled flow, heat, and solute transport in slab continuous casting process. Metall Mater Trans B 29(6):1345–1356
9. Mills KC (2016) Structure and properties of slags used in the continuous casting of steel: Part 1 conventional mold powders. ISIJ Int 56(1):1–13
10. Sahib SS (2010) Numerical solutions of Maxwell's equations in 1D, 2D, and 3D via the finite element method. California State University, Long Beach
11. Gamo H (1979) A general formulation of Faraday's law of induction. Proc IEEE 67(4):676–677

The Power and Limitation of Ion Beam Imaging in Focused Ion Beam Microscopes

Pei Liu

Abstract In the past three decades, the focused ion beam microscope has evolved from a semiconductor production tool into an advanced microstructure characterization instrument. The FIB microscopes have changed from the first generation of single ion beam systems to multi-beam systems that often couple with various types of analytical instruments. However, the powerful FIB systems are often recognized as advanced TEM specimen preparation machines due to their superior capability of making high quality, site-specific thin foils from almost any types of materials and any geometry. This is a vast under usage of such powerful systems. Most users do not take advantage of the primary ion beam imaging capability that can provide high-quality images to reveal important microstructure features. In this paper, the author uses practical examples to demonstrate the power of ion beam imaging.

Keywords FIB · Secondary electrons · Backscattered electrons

Introduction

CanmetMATERIALS' research covers a wide range of topics on structural materials. The three different programs include materials for energy production, energy transportation, and energy end use. Research activities include materials from lightweight aluminum and magnesium alloys to various kind of steels and Nickle-based super alloys. Process development includes metal casting, forming, mechanical properties to corrosion assessment. CanmetMATERIALS technical staffs gained extensive experience with FIB technology in the past 10 years. In addition, the wide spectrum of materials development work at CanmetMATERIALS provided unique opportunities to explore new FIB techniques. Most FIB microscopes are recognized as high-resolution ion beam milling machines to produce TEM specimens. However, at CanmetMATERIALS, the FIB microscope goes much beyond a TEM expensive sample preparation tool.

P. Liu (✉)
CanmetMATERIALS, 183 Longwood Road South, Hamilton, ON L8P 0A5, Canada
e-mail: pei.liu@NRCan-RNCan.gc.ca

M. Zhang et al. (eds.), *Characterization of Minerals, Metals, and Materials 2023*, The Minerals, Metals & Materials Series
https://doi.org/10.1007/978-3-031-22576-5_3

A typical focused ion beam (FIB) microscope includes a Ga ion beam and an electron beam. Main function of Ga ion beam is to provide milling power to remove materials from bulk specimens, while the electron beam is used to provide images and other analytical functions (e.g., EDS and EBSD). Sputtered atoms are not always neutrals. A good percentage of sputtered materials are ionized and carry a positive charge that is associated with secondary electrons (SE) emission. These secondary electrons can be collected by the same Everhart Thornley type of secondary electron detectors. Though there are no differences in nature and the energy between secondary electrons excited by a high energy primary electron beam and Ga ion beam, their contrast mechanisms are very different. SE from primary electron source (here after named as eSE) are not sensitive to crystallographic information, while the SE from Ga ion beam (here after named as iSE) are extremely sensitive to crystallography orientation. Although backscattered electrons (BSE) images in SEM can be used to reveal grains structure from polished surfaces, the image resolution is relatively poor due to very large electron beam–specimen interaction volume. In contrast, iSE from Ga ion source are generated from much smaller volume due to the extremely limited penetration depth of Ga ion beam. Thus the iSE images provide images with much higher sensitivity to surface structure [1, 2]. In this paper, the author uses practical examples to demonstrate the advantages of ion beam imaging.

The Crystallographic Orientation Contrast

In many metallurgical applications, samples are mounted and mechanically polished for microstructure investigations. A typical SEM study would require metallographic etching to reveal grain boundaries. However using FIB, such etching is not necessary. Careful metallographic polishing is needed to obtain high-quality iSE images. Apart from potential surface/subsurface mechanical damages introduced during sample polishing, any surface oxidation or contamination will also have a negative impact on FIB imaging. However, under certain circumstances, gallium ions can also be used to sputter off minor surface oxide (and contaminants) prior to imaging. The interaction between the gallium ion beam and the metal surface depends on many factors. These include beam acceleration voltage, beam raster parameters, and materials properties (including crystallographic orientation). Figure 1 shows a typical microstructure of cold drawn steel wire. The heavily deformed ferritic grains are shown clearly at relatively high magnification.

Figure 2 shows the microstructure of coarse-grained Ni-based superalloy. The iSE image clearly reveal the fully recrystallized grain structure with significant amount of micro twins.

Focused ion beam microscopes are mainly used to cross-sectional materials in microscopic scale. Microscopic features on sample surfaces can be cross sectioned using the primary Ga ion beam. High-resolution images of the cross sections can be obtained by either tilting the sample in single beam FIB systems or using the electron beam in modern dual-beam systems. Typical width of cross sections ranges

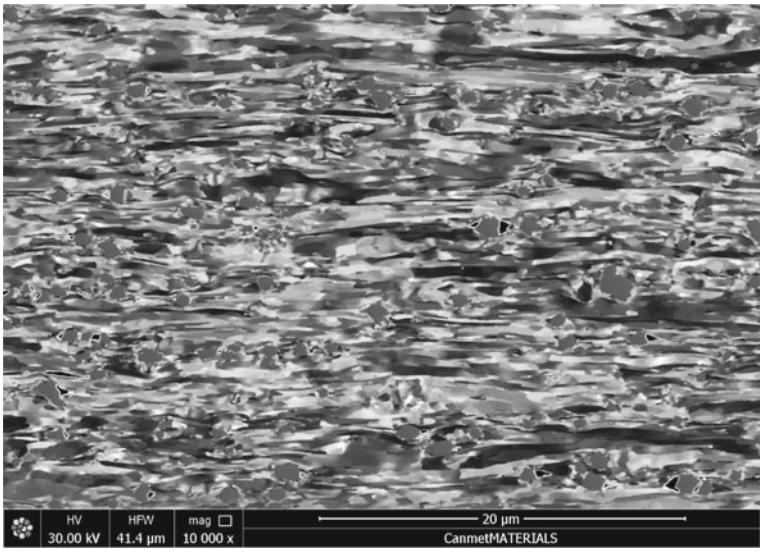

Fig. 1 FIB iSE image showing the microstructure of a cold drawn steel wire

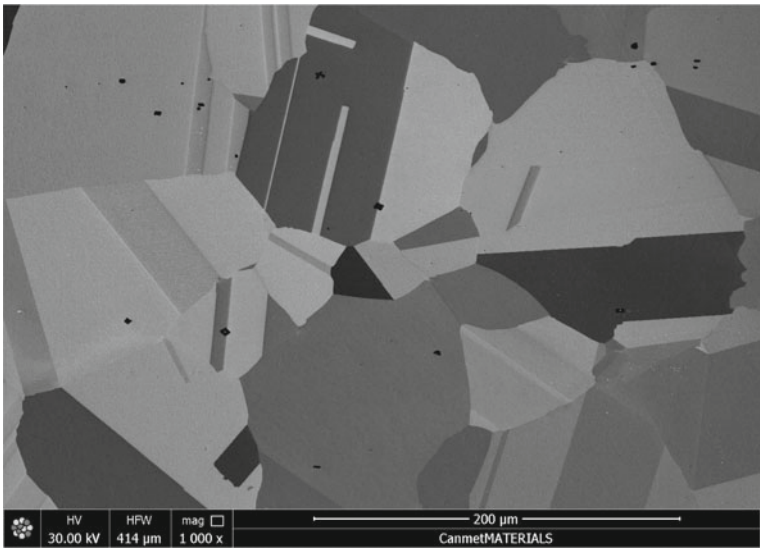

Fig. 2 FIB iSE image showing the microstructure of a typical Ni-based superalloy

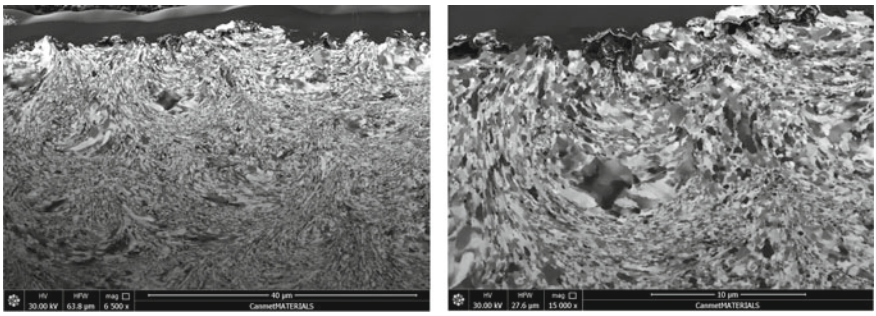

Fig. 3 FIB iSE images showing the microstructure of a severely deformed Cu alloy

from 10-100 μm in FIBs with liquid metal ion source (LMIS). With a plasma FIB, cross sections as wide as 1–2 mm can be prepared rapidly.

FIB sectioning and imaging not only reveals surface and subsurface features, but also provides microstructure details without stress and potential damage from metallurgical cross sections. Again, iSE from primary ion beam can produce enhanced crystallographic orientation contrast. Figure 3 shows iSE images of FIB cross section of severely deformed copper alloy. Copper alloys have FCC structure that has 12 active slip systems. There is no "hard" orientation to resist deformation. The relatively un-deformed and near equiaxed grains in the higher magnification images suggest the deformation process could have resulted in dynamic recrystallization (or recovery).

Thermally grown oxide (TGO) process is frequently used to provide a continuous and dense surface oxide layer on stainless steel surfaces to improve their corrosion resistance in harsh environment. TGO layers are usually very thin and brittle, and metallurgical cross section can easily damage the layer prior to investigation. In addition, imaging with SEM does not provide enough resolution due to large beam-specimen interaction volume of backscattered electrons.

Figure 4 shows an iSE image of FIB cross section of a ferritic-matensitic (FM) alloy. A thin TGO layer, on the order of 600 nm in thickness, was grown on the surface prior to the corrosion experiment in supercritical water (SCW) condition at 625 °C. In this case, the TGO layer failed to protect the substrate alloy from corrosion attack. Although the TGO layer stayed intact, a uniform layer of magnetite are formed above the TGO. This is attributed to the thin TGO layer failed to stop the outwards diffusion of Fe at high temperature that led to surface oxidation.

Stress corrosion cracking is one of the most important failure mechanism for austenitic stainless steels in aggressive chemical environment. The iSE image in the FIB cross section indicated this intergranular crack arrested at the triple junction (Fig. 5). The large number of shear bands and corrosion products on the crack side walls in the iSE image confirmed the cracking is attributed to significant local stress/strain and oxidizing environment.

Secondary electron from primary Ga ion sources in FIB microscopes can provide high-resolution images with enhanced crystallographic orientation contrast for most

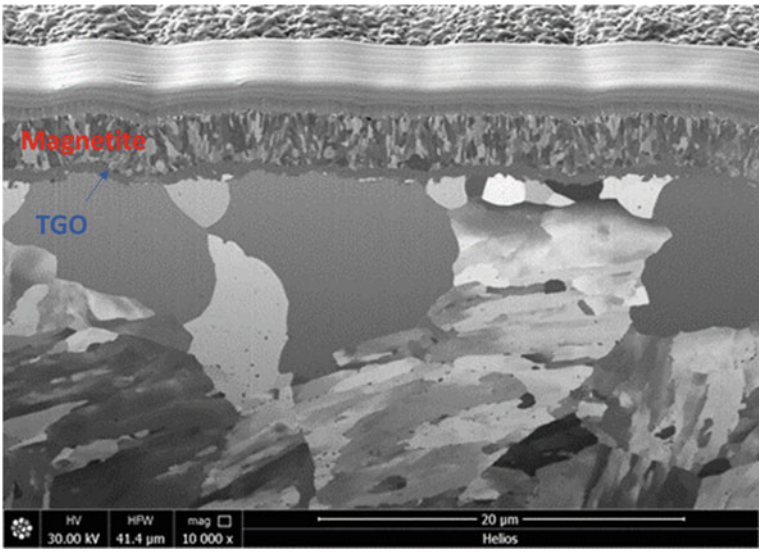

Fig. 4 FIB iSE image of thin TGO layer and surface oxide formation on a stainless steel after SCW exposure

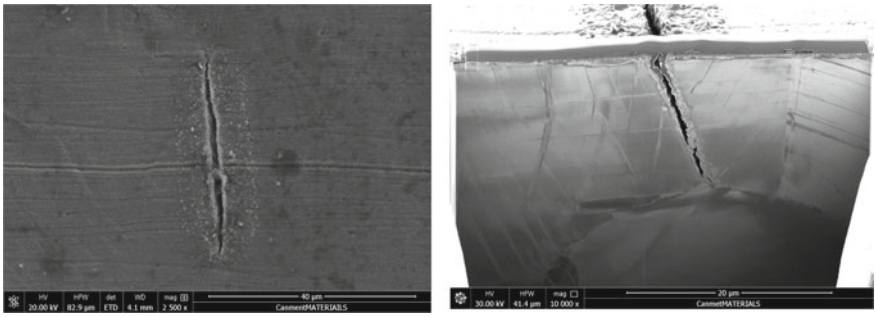

Fig. 5 FIB cross section of an SCC formed on an SS310 steel

types of metal alloys. The contrast is more pronounced for materials with FCC and BCC structure. Although the BSE images in SEMs also show crystallographic contrast, their resolution is far inferior. This is due to the backscattered electrons have much larger interaction volume (on the order of micrometers under a 20 keV electron beam). Although the interaction volume does shrink significantly under lower kV, the image intensity also reduces dramatically that results in poor S/N ratio. In contrast, the interaction volumes of Ga ion beam with specimens are on the order of a few nanometers. The iSE provides much higher imaging resolution. Figure 6 shows a dramatically different contrast of the iSE image and BSE image. These two images were taken from the same area on a traditional X65 pipeline steel sample. In addition

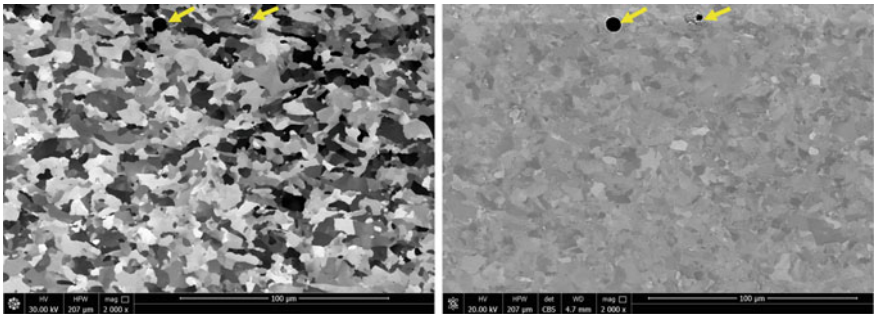

Fig. 6 Comparison of SE (left) and BSE (right) images. The voids are used as markers on both images (arrows)

to the much enhanced contrast, the iSE image shows much more of microstructure details.

Summary

The iSE imaging in FIB microscopes can provide high crystallographic orientation contrast to reveal microstructure details in metallurgical specimens. However, care should also be taken when using Ga ion beams for imaging purpose. One should always keep in mind that while imaging, the Ga beam is also sputtering specimen surfaces at the same time. Not only target materials being investigated is milling away at the same time, the Ga ion beam can also introduce unwanted artifacts if not controlled properly [3].

Acknowledgements This work is supported by research programs at CanmetMATERIALS funded by Natural Resources Canada.

References

1. Phaneuf MW (1999) Micron 30:277–288
2. Li J (2008) New material science research. In: Olivante LV (ed) Nova Science Publisher. ISBN-13: 978-1-60021-654-1
3. Li J (2011) Advanced techniques in TEM specimen preparation. In: Khan M (ed) The transmission electron microscope. ISBN 979-953-307-311-7

Part II
Advanced Microstructural Characterization Methods

Optical Parameters of ZnO Thin Films

Shadia J. Ikhmayies

Abstract Zinc oxide (ZnO) is a very important material with diverse uses in solar cells, optoelectronic devices, and other applications. Optimizing the optical properties is required in such applications. In this work the influence of annealing in nitrogen atmosphere and aluminum doping on the optical properties was investigated. Undoped (ZnO) and aluminum doped (ZnO:Al) thin films were deposited using spray pyrolysis (SP) method on glass substrates, and some of these films were annealed in nitrogen atmosphere. The microstructure of the films was explored using X-ray diffraction, and it is found that the films are polycrystalline. Transmittance of the films was recorded as a function of wavelength in the range of 300–1100 nm. Transmittance was used to calculate the absorption coefficient, extinction coefficient, reflectance, refractive index, real and imaginary parts of the dielectric constant, and optical conductivity. All these parameters are found to be affected by Al-doping and annealing. It is found that optical parameters were influenced by Al-doping and annealing.

Keywords Characterization · Electronic materials · Energy conversion and storage · Transparent conducting oxides · Zinc oxide · Spray pyrolysis

Introduction

Zinc oxide (ZnO) is a wide band gap, II-VI compound semiconductor that has attracted the attention of the scientific community. It has three phases; the cubic (zinc blend) phase of space group $F\overline{4}3m$ or T_d^2, which is a metastable phase that can be stabilized when it is grown on cubic substrates, rocksalt which can be obtained at relatively high pressures, and hexagonal (wurtzite) phase of space group P63mc or C6v4, which is the thermodynamically stable phase under ambient conditions. The lattice constants of the hexagonal phase are $c = 5.025$ Å and $a = 3.249$ Å

S. J. Ikhmayies (✉)
Jabal El-Hussain, Amman 11121, Jordan
e-mail: shadia_ikhmayies@yahoo.com

M. Zhang et al. (eds.), *Characterization of Minerals, Metals, and Materials 2023*, The Minerals, Metals & Materials Series
https://doi.org/10.1007/978-3-031-22576-5_4

[1, 2]. ZnO has several applications including solar cells, optoelectronic devices, gas sensors, piezo-electric transducers, and phosphors. It is a transparent conducting oxide (TCO) of transparency comparable to that of tin oxide (SnO_2) and indium tin oxide (ITO), so it is an alternative to both of them. Naturally, ZnO is an n-type semiconductor due to intrinsic defects such as oxygen vacancies and/or zinc interstitials. The n-conductivity can be enhanced by intentional doping. Aluminum doping was found to be effective in improving the electrical and optical properties of ZnO, and aluminuim doped zinc oxide (ZnO:Al) is commonly used as a front contact in thin film solar cells such as CdTe-based and Cu(In,Ga)Se_2 (CIGS)-based solar cells.

There are different physical and chemical methods to prepare ZnO thin films such as chemical solution deposition (CSD) [3], DC magnetron sputtering [4], spin coating [5], and spray pyrolysis technique (SP) [6–10]. The spray pyrolysis (SP) method was chosen because it is cost effective and simple method. The film's microstructure was checked using X-ray diffraction, and the transmittance was recorded at room temperature. The transmittance was used to deduce the reflectance, absorption coefficient, refractive index, extinction coefficient real and imaginary parts of the dielectric function, and optical conductivity of the films. The results were analyzed and discussed in the light of using the films in solar cells' applications.

Experimental Procedure

ZnO thin films were deposited on ultrasonically cleaned glass substrates using the spray pyrolysis technique. A precursor solution was prepared from 7.61×10^{-3} mol of zinc chloride ($ZnCl_2$), and 1.33×10^{-5} mol of Al_2O_3, in 300 ml of distilled water, and about 1 ml of hydrochloric acid (HCl). The solution was intermittently sprayed on the hot substrates of temperature $T_s = 450$ °C. Nitrogen (N_2) was used as the carrier gas, where the optimum carrier gas pressure was around 5 kg/cm^3. The microstructure of the films was explored by X-ray diffraction (XRD) using XRD-7000 X-Ray diffractometer with Cu K_α radiation ($\lambda = 1.54$ A°). Transmittance was measured at room temperature using a double beam Shimadzu UV 1601 (PC) spectrophotometer in the wavelength range $\lambda = 290-1100nm$ with respect to a piece of glass similar to the substrates. Annealing was performed in nitrogen atmosphere at 250 °C for 45 min.

Results and Discussion

Figure 1 displays the X-ray diffractograms of two films of the set under study. The films are polycrystalline with a hexagonal (wurtzite) structure. The peaks were assigned to their corresponding Miller indices (hkl). The (100), (101), and (002) diffraction peaks are observed, with the highest intensity is that of the (002) peak. So, the preferential orientation is the one perpendicular to the surface (002), or in

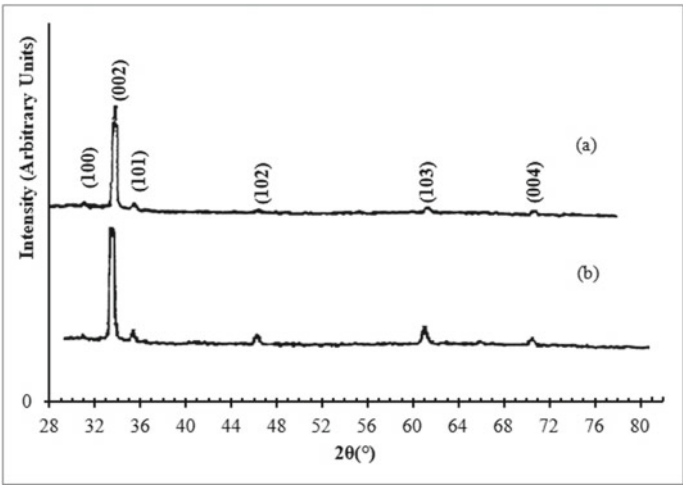

Fig. 1 X-Ray diffractograms of ZnO thin films. **a** As deposited. **b** Annealed at 250˚C for 45 min

other words along the optical c-axis, which is perpendicular to the substrate [11]. This is because the c-axis has the lowest energy of the hexagonal crystalline structure [12].

Figure 2 shows the transmittance $T\%$ of as-deposited, annealed, undoped, and Al-doped ZnO thin films plotted against the wavelength λ. . All the films showed high transmittance (60%-92%) in the visible and near infrared spectral regions. The figure shows that the maximum transmittance of the films reaches as high as more than 91% for the ZnO:Al as-deposited and annealed film in the red and near infrared regions, which means the films can be used as forecontacts, windows, or antireflection coatings in solar cells. It is observed that the transmittance increased when the films were doped with Al, and when the films were annealed. The highest transmittance was obtained for the Al-doped annealed film. The increase of transmittance after annealing is due to the increase of films crystallinity, and decrease of film defects especially surface defects, in addition to the decrease of surface roughness. The increase of transmittance with Al-doping is due to the decrease of the absorption coefficient in the visible region [13]. A slight shift of the band edge towards lower wavelengths was observed, where the annealed ZnO:Al has the shortest cut-off wavelength, while as-deposited ZnO has the longest one.

Figure 3 displays the reflectance ($R = 1 - T$) of the same films deduced from the transmittance and plotted against wavelength λ. As the figure shows, the reflectance decreases rapidly near the absorption edge of ZnO, then it decreases slowly and becomes approximately constant in the visible and near infrared region, where the films become highly transparent. The reflectance is smallest for the Al-doped and annealed film due to the increase in the density of free charge carriers, which are the electrons. The greatest reflectance is that for the as-deposited ZnO in most of the wavelength range.

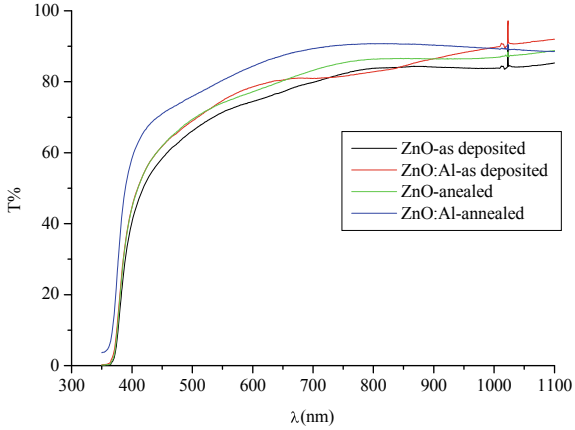

Fig. 2 Transmittance of ZnO thin films

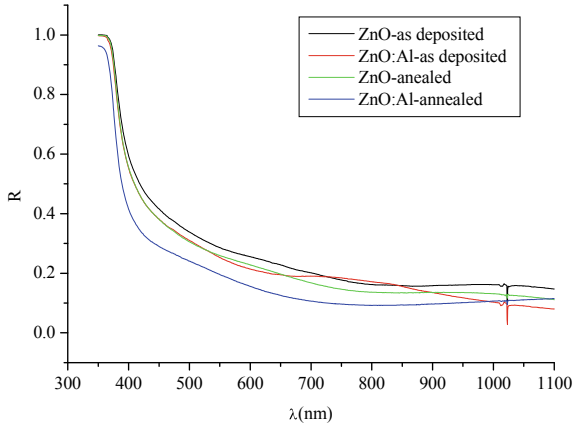

Fig. 3 Reflectance of ZnO thin films

ZnO has a direct band gap, and for a direct transition, the optical absorption edge is analyzed by the following equation [14],

$$(\alpha h\nu)^2 = C\left(h\nu - E_g\right) \tag{1}$$

where α is the absorption coefficient, $h\nu$ is the photon's energy, C is a constant, and E_g is the direct band gap energy. The absorption coefficient α was deduced from the transmittance T using the following formula

$$\alpha = \frac{\ln(1/T)}{t} \tag{2}$$

where T is the transmittance and t is the film thickness. To estimate the band gap energy of the films, a plot of $(\alpha h\nu)^2$ versus $(E = h\nu)$ was performed and displayed

in Fig. 4. A linear fit was performed in the linear parts of the curves as shown in the figure, and the direct band gap energy was estimated and displayed in the figures. The obtained values of the annealed and doped films are all the same (3.28 eV), while that of the as-deposited undoped film is 3.27 eV. The reason why, the films have approximately the same value of band gap energy is that, they were deposited at high temperature (450 °C), which means the crystal growth was approximately complete, the grains have a large size as can be deduced from the sharp (002) peak, hence doping and annealing have unobservable influence on the band gap energy.

The extinction coefficient k was calculated from the following formula

$$k = \frac{\alpha\lambda}{4\pi} \tag{3}$$

Figure 5a shows the extinction coefficient, and Fig. 5b shows the refractive index for as-deposited, and annealed ZnO and ZnO:Al thin films, both as functions of wavelength in the range $\lambda = 300 - 1100$ nm. As Fig. 5a shows the extinction coefficient k decreases abruptly at the absorption edge, then it becomes approximately

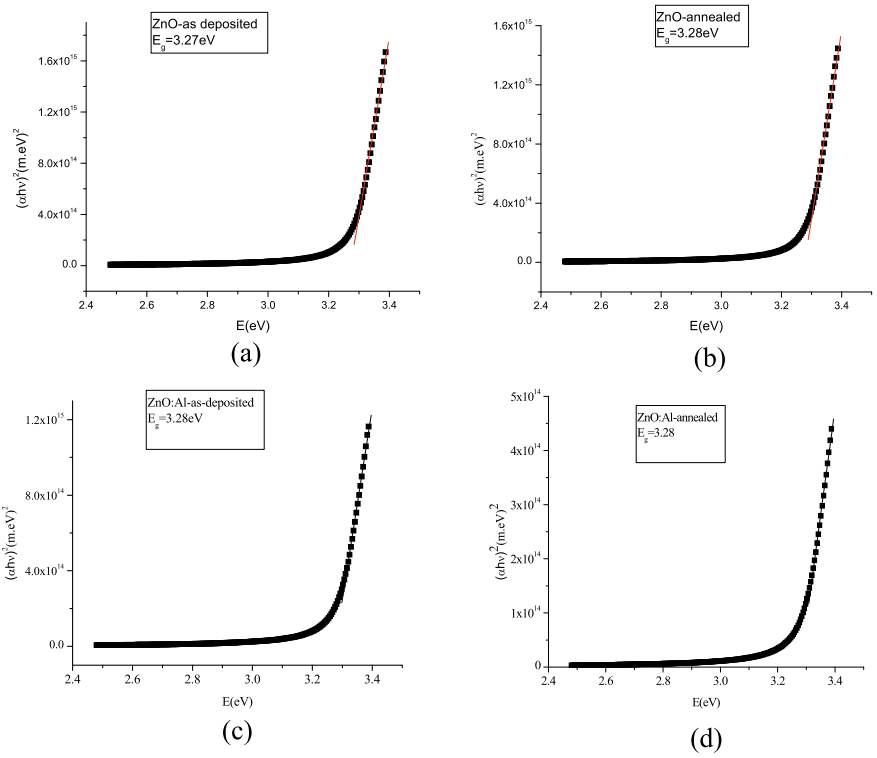

Fig. 4 The plots of $(\alpha h\nu)^2$ versus $(E = h\nu)$, and linear fits for: **a** as deposited ZnO thin films. **b** Annealed ZnO thin films. **c** As deposited ZnO:Al thin films. **d** Annealed ZnO:Al thin films

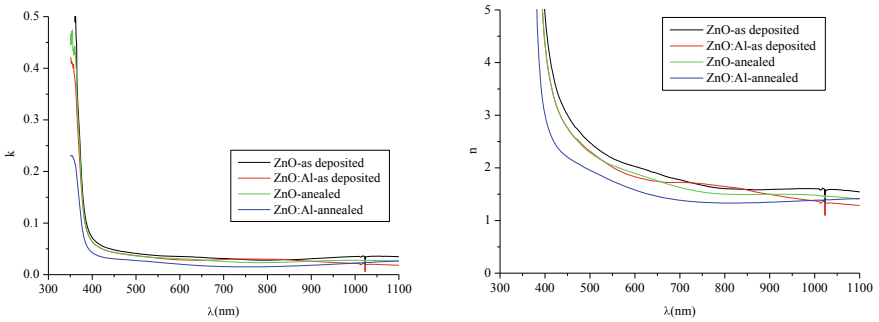

(a) (b)

Fig. 5 The extinction k coefficient (**a**), and refractive index n (**b**) for as-deposited, and annealed ZnO and ZnO:Al thin films as a function of wavelength λ

constant. Its value for all films at $\lambda = 550$ nm is in the range 0.022–0.034, where the smallest value is for the annealed ZnO:Al films and the greatest value is for the as-deposited ZnO thin films. The small value of k is preferred for use of the thin film in solar cells.

Reflectance is related with the refractive index n and the extinction coefficient k by the following relationship [15]

$$R = \frac{(n^* - 1)^2}{(n^* + 1)^2} = \frac{(n-1)^2 + k^2}{(n+1)^2 + k^2} \tag{4}$$

and the complex refractive index of the film is given by

$$n^* = n + ik \tag{5}$$

Solving Eq. (4) for the refractive index n gives

$$n = \frac{(1+R) + \left[(1+R)^2 - (1-R)^2\left(1+k^2\right)\right]^{1/2}}{1-R} \tag{6}$$

The refractive index decreases with wavelength λ as shown in Fig. 5b, where this decrease is strong in the region of the band edge, but becomes slower after that. Then the refractive index becomes constant in the visible and near infrared regions (1.35–3.5), and n_∞ can be estimated as 1.33 for annealed ZnO:Al, 1.41 for both annealed ZnO and as-deposited ZnO:Al, and 1.57 for as-deposited ZnO. These results are consistent with those obtained by Tüzemen et al. [16] for ZnO thin films prepared at room temperature using pulsed filtered cathodic vacuum arc deposition (PFCVAD), where the value of refractive index in the visible and near infrared spectral regions is in the range 1.5–2.4. Also from Fig. 5b it can be noticed that at $\lambda = 550$ nm, n is restricted in the range in the range 1.75- 2.17 for all films, where the smallest value is

for the annealed ZnO:Al films, and the greatest value is for the as-deposited ZnO thin films. It is well known that the refractive index is mainly determined by the crystal quality, and it is correlated with crystallinity, surface roughness, and resistivity of the films.

The complex dielectric function is given as

$$\varepsilon^* = \varepsilon_1 + i\varepsilon_2 \tag{7}$$

where ε_1 is the real part which is associated to the refractive index, and the imaginary part ε_2 which is related to the absorption coefficient or extinction coefficient. The real and imaginary parts of the dielectric function are given by the following equations [15]

$$\varepsilon_1 = n^2 - k^2 \tag{8}$$

$$\varepsilon_2 = 2nk \tag{9}$$

Figure 6 displays the real and imaginary parts of the dielectric function ε_1, and ε_2 respectively as functions of wavelength of light λ. Both of ε_1, and ε_2 decrease with λ, but the decrease of ε_2 is faster, and in both cases the decrease is fast around the band edge, after which both of them become approximately constant, where ε_1 for long wavelengths denoted as ε_∞ is 1.68 for annealed ZnO:Al, 2.00 for both annealed ZnO and as-deposited ZnO:Al, and 2.43 for as-deposited ZnO. These values are consistent with the relationship $\varepsilon_\infty = n_\infty^2$. Figure 6 shows that at $\lambda = 550nm$ the real dielectric function is in the range of 3.06–4.76, and ε_2 is in the range of 0.083–0.161 for all films, where the smallest values are for annealed ZnO:Al and largest ones are for as-deposited ZnO. The values of ε_1 are always larger than those of ε_2. That is ε_1 is related to the refractive index, while ε_2 is related to the extinction coefficient.

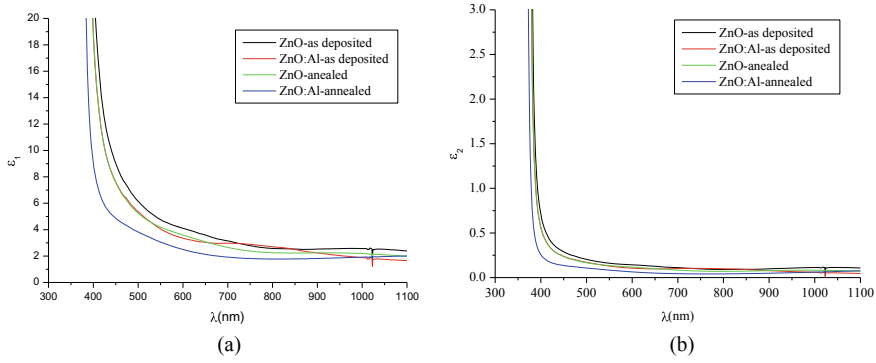

Fig. 6 The dielectric function against wavelength λ. **a** Real part ε_1. **b** Imaginary part ε_2

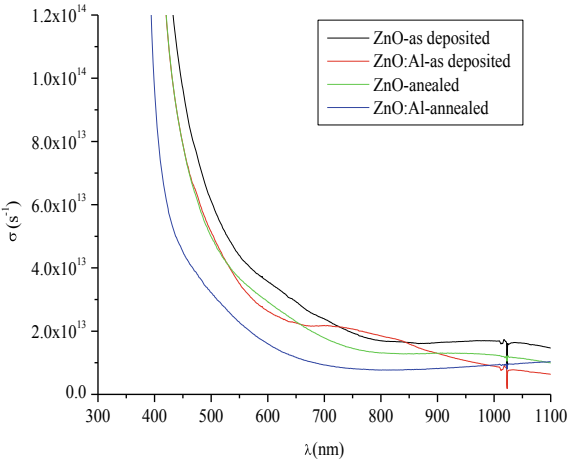

Fig. 7 Optical conductivity σ of ZnO films under study against wavelength of radiation λ

The optical conductivity of the ZnO thin films can be determined by the formula [17];

$$\sigma = \frac{\alpha n c}{4\pi} \tag{10}$$

where c is the speed of light. Figure 7 depicts the optical conductivity σ against wavelength of incident radiation λ. It is observed that σ shows the same behavior as the other optical constants discussed before. That is it decreases with wavelength λ, and the decrease is fast in the region of the absorption edge, then it becomes slow, and then constant in the visible and near infrared regions. The smallest σ is that of annealed ZnO:Al film and the largest one is for the as-deposited ZnO film.

Conclusions

Undoped and aluminum doped ZnO thin films were deposited on glass substrates by the spray pyrolysis method at substrate temperature $T_s = 450$ °C. X-ray diffraction was used to explore the microstructure of the films, where all films showed hexagonal (wurtzite) structure, with preferential orientation along the c-optical axis perpendicular to the substrate. UV–VIS spectroscopy was used to investigate the optical properties of the films. The transmittance was measured at room temperature and used to deduce reflectance, band gap energy, extinction coefficient, refractive index, real and imaginary parts of the dielectric function, and optical conductivity.

The maximum transmittance exceeds 91%, and transmittance for all films is in the range of 60–91% in the visible and infrared regions. The optical energy band gap E_g is 3.27 for as-deposited ZnO thin films, but 3.28 for annealed ZnO thin film, annealed, and as-deposited ZnO:Al. The extinction coefficient k and refractive index

n decrease with wavelength, and the values of k are small which reflects the high quality of the films. Real and imaginary parts of the complex dielectric function decrease with radiation wavelength and go to a constant value. The behavior of ε_1 follows the refractive index, while the behavior of ε_2 follows that of the extinction coefficient. These results demonstrate that good quality of the prepared ZnO thin films and their potential use in solar cells and the optoelectronic industry.

References

1. Shakti N, Gupta PS (2010) Structural and optical properties of sol-gel prepared ZnO thin film. Appl Phys Res 2(1):19–28
2. Morkoç H, Özgür Ü (2008) Zinc Oxide: fundamentals, materials and device technology. Wiley-VCH. pp1–76. https://doi.org/10.1002/9783527623945
3. Rakhshani AE (2005) Thin ZnO films prepared by chemical solution deposition on glass and flexible conducting substrate. Appl Phys A 81:1497–1502
4. Abduev AK, Akhmedov AK, Asvarov AS, Abdullaev AA, Sulyanov SN (2010) Effect of growth temperature on properties of transparent conducting gallium_doped ZnO films. Semiconductors 44(1):32–36
5. Kumar SA, Jitendra K (2011) Effect of aluminum addition on the optical, morphology and electrical behavior of spin coated zinc oxide thin films. AIP Adv 1:032153
6. Studenikin SA, Golego N, Cocivera M (1998) Optical and electrical properties of undoped ZnO films grown by spray pyrolysis of zinc nitrate solution. J Appl Phys 83(4):2104–2111
7. Ikhmayies SJ, Abu El-Haija NM, Ahmad-Bitar RN (2010) Electrical and optical properties of ZnO:Al thin films prepared by the spray pyrolysis technique. Phys Scr 81:015703 (5pp)
8. Ikhmayies SJ, Abu El-Haija NM, Ahmad-Bitar RN (2010) Characterization of undoped spray-deposited ZnO thin films of photovoltaic applications. FDMP. 6(2):165–177
9. Ikhmayies SJ, Abu El-Haija NM, Ahmad-Bitar RN (2015) A comparison between different ohmic contacts for ZnO thin films. J Semicond 36(3):033005(5 pp)
10. Ikhmayies SJ, Abu El-Haija NM, Ahmad-Bitar RN (2010) The Influence of annealing in nitrogen atmosphere on the electrical, optical and structural properties of spray-deposited ZnO thin films. FDMP. 6(2):219–232
11. Kadi Allah F, Cattin L, Morsli M, Khelil A, Langlois N, Bernéde JC (2010) Microstructural properties of ZnO: Sn thin films deposited by intermittent spray pyrolysis process. J Mater Sci Mater Electron 21:179–184
12. Ekthammathat N, Phuruangrat A, Thongtem S, Thongtem T (2015) Hydrothermal-assisted synthesis and photoluminescence of ZnO microds. Dig J Nanomater Biostruct 10(1):149–153
13. Alrefaee M, Singh UP, Das SK (2021) Growth of aluminum doped zinc oxide nanostructure thin films by nonconventional sol-gel method. In: Macromolecular symposia 402(1) special issue: international conference on science and engineering of materials—ICSEM 2021 Part II. 2100350. https://doi.org/10.1002/masy.202100350
14. Benhaliliba M, Benouis CE, Aida MS, Yakuphanoglu F, Sanchez Juarez A (2010) Indium and aluminium-doped ZnO thin films deposited onto FTO substrates: nanostructure, optical, photoluminescence and electrical properties. J Sol-Gel Sci Technol 55:335–342. https://doi.org/10.1007/s10971-010-2258-x
15. Alnajjar AA, Al-Shaikley FY, Alias MFA (2012) Optical properties and photoconductivity of undoped and In-doped CdTe thin films. J Electron Devices 16:1306–1314
16. Tüzemen EŞ, Eker S, Kavak H, Esen R (2009) Dependence of film thickness on the structural and optical properties of ZnO thin films. Appl Surf Sci 255:6195–6200
17. Mishra RL, Mishra SK, Prakash SG (2009) Optical and gas sensing characteristics of tin oxide nano-crystalline thin film. J Ovonic Res 5(4):77–85

Investigation of Interdendritic Fluidity in Steel Billets: Based on Three-Dimensional Characterization of Solidification Structure at the Millimeter Scale

Zibing Hou, Kunhui Guo, Dongwei Guo, Fuli Zhang, and Jianghai Cao

Abstract During the solidification process, interdendritic liquid flow at the millimeter scale in the mushy zone can finally result in the macro/semi-macro segregation. In this paper, a new method (abbreviated as MSS) for the three-dimensional structure morphology of different dendrites at the millimeter scale was proposed based on the serial-sectioning and hot pickling experiments, which allows interdendritic liquid flow behavior in opaque steel billets to be analyzed. By using the three-dimensional computational fluid dynamics simulation of interdendritic liquid flow, it's found that the fractal dimension is smaller and the permeability is larger in the equiaxed crystal zone than that of the columnar crystal zone, leading to larger liquid flow velocity and smaller pressure loss in the equiaxed dendrites zone. The above results indicate that the liquid flow resistance in the equiaxed crystal zone is less, thus is more likely to lead to the formation of macro/semi-macro segregation.

Keywords Continuous casting · Segregation · Serial-sectioning · Interdendritic liquid flow · Permeability

Z. Hou (✉) · K. Guo · D. Guo · F. Zhang · J. Cao
College of Materials Science and Engineering, Chongqing University, No. 174 Shazhengjie, Shapingba, Chongqing 400044, China
e-mail: houzibing@cqu.edu.cn

K. Guo
e-mail: guokunhui@cqu.edu.cn

D. Guo
e-mail: guodongwei@cqu.edu.cn

F. Zhang
e-mail: cqzhangfuli@163.com

J. Cao
e-mail: caojhai@cqu.edu.cn

Chongqing Key Laboratory of Vanadium-Titanium Metallurgy and New Materials, Chongqing University, Chongqing 400044, China

M. Zhang et al. (eds.), *Characterization of Minerals, Metals, and Materials 2023*, The Minerals, Metals & Materials Series
https://doi.org/10.1007/978-3-031-22576-5_5

Introduction

The steel material is opaque, so the growth of the solidification structure during continuous casting cannot be observed directly. Generally, the two-dimensional cross-section and longitudinal section of the billets are used to analyze and speculate on the growth process of the three-dimensional microstructure during the solidification process. However, the use of two-dimensional images to investigate the three-dimensional solidification structure characteristics of materials is limited and may lead to erroneous results to some extent [1]. In addition, the flow of solute-enriched liquid phase between three-dimensional dendrites is an important reason for the formation of macro/semi-macro segregation.

During the process of three-dimensional reconstruction of materials, based on multiple continuous two-dimensional images of materials, the geometric and topological information of adjacent two-dimensional images can be obtained through specific algorithms, which can be used to reconstruct the three-dimensional structure of materials. At present, there are many methods for the three-dimensional reconstruction of material structure, such as industrial computerized tomography (ICT) [2], magnetic resonance imaging (MRI) [3], ultrasonic testing [4], and other non-destructive testing methods. However, these methods cannot be widely used due to the resolution, scope of application, and other factors. The destructive method represented by serial-sectioning [5, 6] is still one of the main methods to construct the three-dimensional structure of metal materials.

In this work, the millimeter serial-sectioning (MSS) method for three-dimensional reconstruction of millimeter-scale solidification structure was proposed based on the principle of serial-sectioning method and optimized hot pickling experiments. Subsequently, the MSS method was used to analyze the three-dimensional morphology of the solidification structure and the flow of the solute-enriched liquid phase between dendrites, which can provide theoretical support for the precise control of segregation defects.

Experiment Method

During the serial-sectioning method, a series of two-dimensional images of the research object are obtained by destructive methods such as grinding and cutting, and the three-dimensional structure of the research object is reconstructed by image processing. In this work, 70 steel was selected as the research object. The main chemical composition and process parameters are shown in Table 1, and the main steps of reconstructing a three-dimensional structure by the serial-sectioning method are shown in Fig. 1.

On the cross-section (170 mm $\times$ 170 mm) of the selected billet, three cube samples at 40 mm (No. 1), 50 mm (No. 2), and 60 mm (No. 3) from the surface were selected for three-dimensional reconstruction. The four corners of the selected

Table 1 Specification of studied alloys in the present work

Liquidus temperature, °C	Solidus temperature, °C	Main chemical compositions, mass%					
		C	Si	Mn	P	S	Fe
1475	1388	0.7000	0.2000	0.6500	0.0110	0.0023	Bal

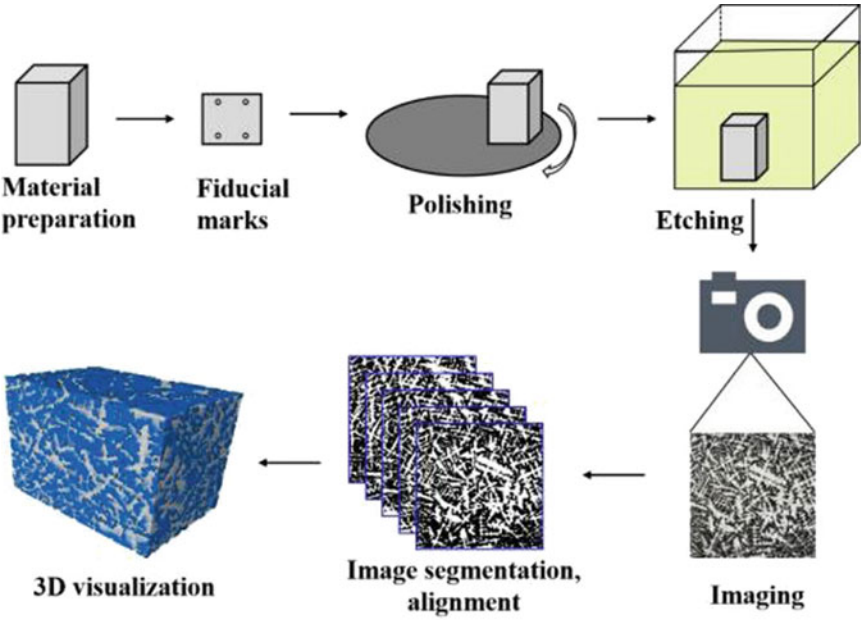

Fig. 1 Flow chart of serial-sectioning and 3D reconstruction process

cube samples are marked to align the subsequent two-dimensional slice positions. The two-dimensional solidification structure of selected cube samples can be obtained by the hot pickling experiment. Subsequently, the cube samples were polished, corroded, and repeated the above steps to obtain a series of two-dimensional images. During the hot pickling experiment, the samples were etched with 1:1 warm hydrochloric acid–water solution for revealing the solidification structure more clearly. The temperature of the hydrochloric acid–water solution was 60–80°C, and the pickling time was 25 min.

During the serial-sectioning process, the distance between adjacent two-dimensional images was measured by a micrometer. Figure 2 shows the relationship between the number of two-dimensional images and the distance between adjacent two-dimensional images. It can be seen that the distance between adjacent two-dimensional images is 108 ± 11 μm. After obtaining a series of two-dimensional images, the reconstruction and visualization of the three-dimensional structure were carried out through preprocessing, registration and segmentation. The whole process

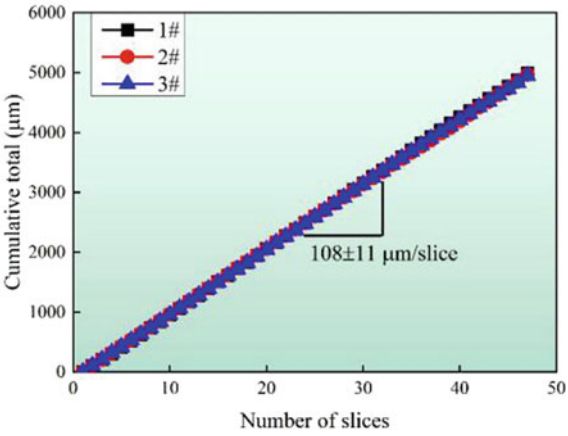

Fig. 2 The recession rates for serial-sectioning of 70 steel

is realized by Image J [7] and Avizo [8] software. Image J software is mainly used to preprocess the pictures, and Avizo software is used to perform three-dimensional visualization of organizational structure and subsequent qualitative and quantitative analysis for the interdendritic fluidity.

Results and Discussion

Three-Dimensional Morphology of Solidification Structure

Figure 3 shows the three-dimensional morphology of the actual solidification structure of the continuous casting billet obtained by the serial-sectioning method. The size of each three-dimensional structure is 5000 μm (length) × 5000 μm (width) × 4950 μm (height). **a**–**c** represent the three-dimensional structure of cube samples No. 1–No. 3, respectively. The left side of Fig. 3 is the three-dimensional structure of macrostructure, and the right side is the three-dimensional structure of dendrites and segregation, respectively. It can be seen that the solidification structure of cube sample No. 1 is mainly columnar crystal, the solidification structure of cube sample No. 2 is the coexistence of columnar crystal and equiaxed crystal, and the solidification structure of cube sample No. 3 is mainly equiaxed crystal. To compare the difference between the two-dimensional and three-dimensional solidification structures in the selected billet, the secondary dendrite arm spacing (SDAS) of the two-dimensional and three-dimensional solidification structures was measured, respectively.

Figure 4 shows the two-dimensional image and three-dimensional structure of typical dendrites inside the selected billet. The SDAS of typical dendrites can be measured and used to compare the two-dimensional and three-dimensional characteristics of the solidification structure. Figure 5 shows the SDAS of typical dendrites in two-dimensional images and three-dimensional structures of cube samples No.

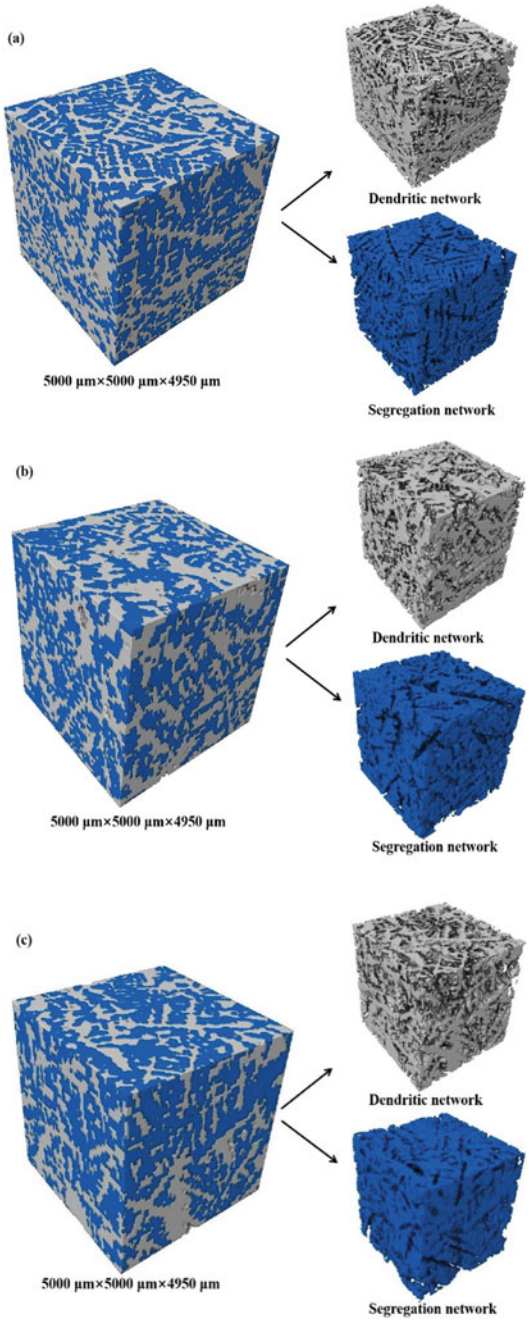

Fig. 3 The 3D reconstruction of the macrostructure in the billet: **a** sample No. 1 (40 mm from the billet surface); **b** sample No. 2 (50 mm from the billet surface); **c** sample No. 3 (50 mm from the billet surface)

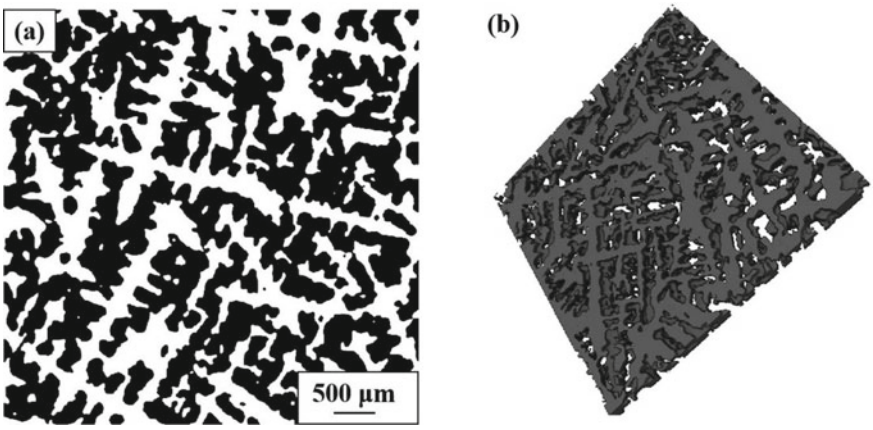

Fig. 4 Solidification structure image with typical secondary dendritic arms for SDAS measurement: **a** 2D; **b** 3D

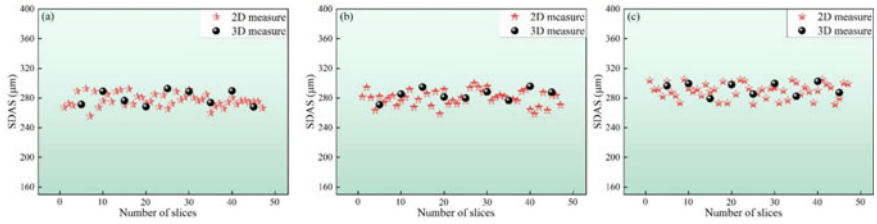

Fig. 5 A comparison of 2D and 3D measures for SDAS: **a** sample No. 1; **b** sample No. 2; **c** sample No. 3

1–No. 3. It can be seen that the SDAS in the two-dimensional image and the three-dimensional structure are basically the same. This is because the cube samples No. 1–No. 3 are obtained along the columnar crystal growth direction on the cross-section of the selected billet. If the cube samples are obtained on the inclined section of the billet, the two-dimensional and three-dimensional SDAS will be different. Meanwhile, the consistent results of two-dimensional and three-dimensional SDAS in Fig. 5 can verify the accuracy of three-dimensional reconstruction results to some extent.

Liquid Flow Between Three-Dimensional Solidification Structures

The research results of Flemings [9] show that the macrosegregation defect in the billets is caused by the flow of the solute-enriched liquid phase between dendrites.

Therefore, the investigation of the flow behavior of the solute-enriched liquid phase between dendrites can provide guidance for the control of macro/semi-macro segregation. Based on the obtained three-dimensional solidification structure, the flow behavior of the liquid phase in the three-dimensional structure was simulated by the absolute permeability experiment simulate module of Avizo software. During the simulation process, the Navier–Stokes equation of the flow process was solved, and the molten steel is assumed to be incompressible Newtonian fluid. The pressure of molten steel at the inlet (upper surface of the sample) is set to be 1.3×10^5 Pa, the pressure at the outlet (lower surface of the sample) is 1.0×10^5 Pa, and the viscosity of molten steel is set to 0.0025 Pa s.

Figure 6 shows the calculated flow velocity and pressure distribution of molten steel in three-dimensional structures No. 1–No. 3. It can be seen that the molten steel flows from the upper surface to the lower surface between the dendrites. Qualitatively, the flow velocity of molten steel in three-dimensional structure No. 1 is lower, while the flow velocities in three-dimensional structures No. 2 and No. 3 are larger. From the pressure distribution, it is known that the pressure from the inlet to the outlet gradually decreases, and the pressure loss of the three-dimensional structure No. 1 is significantly greater than that of No. 2 and No. 3. Combined with the flow velocity and pressure distribution of molten steel, the flow resistance of three-dimensional structure No. 1 to molten steel is larger. At the same time, according to the flow velocity and pressure distribution, the permeability of the solidification structure can be calculated based on Darcy's law. The calculated permeability of three-dimensional structures No. 1–No. 3 are 1.47×10^{-10} m^2, 3.75×10^{-10} m^2, and 3.77×10^{-10} m^2, respectively. The calculation results show that the permeability of three-dimensional structure No. 1 is the smallest and that of three-dimensional structure No. 3 is the largest. From Fig. 3, it can be seen that the three-dimensional structure No. 1 is mainly columnar crystal, while the three-dimensional structure No. 3 is mainly equiaxed crystal, which indicates that the flow resistance of the solute-enriched liquid phase in the columnar crystal is larger, and the flow resistance in the equiaxed crystal is smaller. This result also reflects that the equiaxed crystal morphology is more likely to lead to the formation of macro/semi-macro segregation. During the actual continuous casting process, the macrosegregation defect of the billets is usually controlled by increasing the equiaxed crystal ratio. Based on the results in this paper, the three-dimensional morphology of the solidification structure and the flow behavior of the solute-enriched liquid phase should be considered simultaneously during the actual continuous casting process. For example, while increasing the equiaxed crystal ratio, the cooling rate should also be increased to reduce the SDAS of the equiaxed crystal, thereby increasing the flow resistance of the liquid phase.

At the same time, the calculated fractal dimensions of three-dimensional structures No. 1–No. 3 are 2.6556, 2.6521, and 2.6416, respectively, which is opposite to the trend of permeability. This is because the fractal dimension is mainly used to describe the complexity and compact degree of three-dimensional structures. As the fractal dimension increases, the three-dimensional solidification structure becomes more complex and compact. At this time, the flow resistance of the solute-enriched liquid phase in the three-dimensional structure increases, and the permeability decreases.

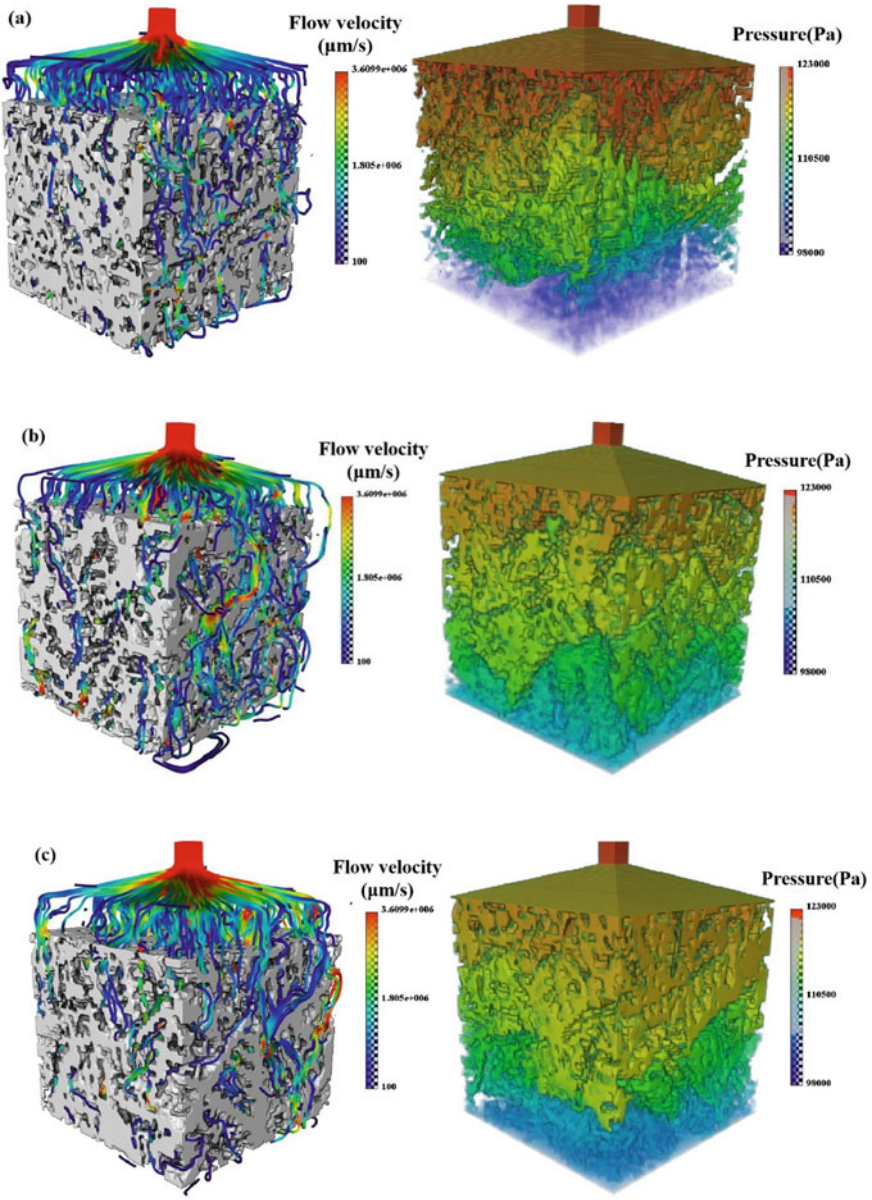

Fig. 6 Simulated flow velocity and pressure contour for 3D reconstructed structures: **a** sample No. 1 (40 mm from the billet surface); **b** sample No. 2 (50 mm from the billet surface); **c** sample No. 3 (50 mm from the billet surface)

The MSS method proposed in this work provides a new way for the reconstruction of the three-dimensional solidification structure at the millimeter scale and the investigation of liquid flow behavior between dendrites.

Conclusions

(1) Based on the principle of the serial-sectioning method and optimized hot pickling experiments, a new method for reconstructing the three-dimensional morphology of solidification structures at the millimeter scale is proposed in this paper.
(2) According to the reconstructed three-dimensional solidification structure, it is found that the flow resistance of the solute-enriched liquid phase in the columnar crystal zone is larger, and the flow resistance in the equiaxed crystal zone is smaller, so the macro/semi-macrosegregation is more likely to form in the equiaxed crystal zone of the continuous casting billets.

Acknowledgements The authors are very grateful for Image J software corporation, Avizo software corporation, and the support from the National Natural Science Foundation of China (52274318).

References

1. Holm EA, Duxbury PM (2006) Three-dimensional materials science. Scr Mater 54(6):1035–1040
2. Maire E, Fazekas A, Salvo L, Dendievel R, Youssef S, Cloetens P, Letang JM (2003) X-ray tomography applied to the characterization of cellular materials. Related finite element modeling problems. Compos Sci Technol 63(16):2431–2443
3. Stannarius R (2017) Magnetic resonance imaging of granular materials. Rev Sci Instrum 88(5):051806
4. Ding H, Li X, Wang Z, Wei GY, Liu HQ, Li M (2019) Ultrasonic nondestructive and characterization for internal defects in the slab. Steelmaking 35(3):47–61
5. Kammer D, Voorhees PW (2008) Analysis of complex microstructures: serial sectioning and phase-field simulations. MRS Bull 33(6):603–610
6. Dudek MA, Chawla N (2008) Three-dimensional (3D) microstructure visualization of LaSn3 intermetallics in a novel Sn-rich rare-earth-containing solder. Mater Charact 59(9):1364–1368
7. ImageJ. https://imagej.nih.gov/ij/
8. Avizo. http://www.fei.com/software/avizo3d/
9. Flemings MC (2000) Our understanding of macrosegregation: past and present. ISIJ Int 40(9):838–841

Part III
Characterization of Mechanical Properties

Dynamic and Quasi-Static Mechanical Response and Associated Microstructural Evolution of Damascus Steels

A. M. W. Wackwitz, A. A. H. Ameri, J. Wang, P. Hazell, H. Wang, H. Timmers, and J. P. Escobedo-Diaz

Abstract This study examines the mechanical response and microstructural evolution of modern manufactured high carbon pattern welded Damascus steels. The characterisation consists of quasi-static and dynamic compression testing, optical microscopy, ultrasonic sound speed measurements, and Vickers hardness. The results from the quasi-static compression testing at a strain rate of 10^{-3}/s show that the yield strength of the materials is approximately 500 MPa, which is comparable to that of plain carbon steel (~450 MPa) and display similar strain hardening properties. The compression results also display a slightly higher Young's Modulus for samples with layer orientation perpendicular to the uniaxial load than those with layer orientation of approximately 45° to the uniaxial load. Dynamic testing using a Split-Hopkinson Bar results showed a similar yield strength of ~ 1150 MPa for the samples with 45° layer orientation, whereas samples with perpendicular orientation showed a slight increase in the yield stress with increasing the strain rate.

Keywords Iron and steel · Mechanical properties · Characterization

Introduction

Damascus steel has long held a reverence because of its excellent performance characteristics and has been shrouded in mystery since its discovery by Europeans. A contributing factor to this has been the controversial and conflicting literature published based on the origins of the steel. The performance of Damascus steel, or Wootz steel, is entwined with the history of the steel and the legends of its performance [1]. This fame caused the spread of Damascus steel through the Middle East after the Christian Crusades. Due to the somewhat legendary status of this steel,

A. M. W. Wackwitz (✉) · A. A. H. Ameri · J. Wang · P. Hazell · H. Wang · H. Timmers · J. P. Escobedo-Diaz
University of New South Wales at the Australian Defence Force Academy, Canberra, ACT 2600, Australia

J. P. Escobedo-Diaz
e-mail: j.escobedo-diaz@unsw.edu.au

M. Zhang et al. (eds.), *Characterization of Minerals, Metals, and Materials 2023*, The Minerals, Metals & Materials Series
https://doi.org/10.1007/978-3-031-22576-5_6

and the weapons created utilising it, it can be hard to distinguish fact from fiction regarding its performance characteristics. Despite this, there are numerous reports of the quality of Damascus steel being far higher than that of European steel in the early nineteenth century [2].

Genuine Damascus steel has a long and rather confusing history, which dates to the thirteenth century in India. The first time Europeans met Damascus steel, was in Persia, hence the name of Damascus steel. Similar process and material methodologies are known to have been in use across many different cultures. One of these was in Russia under the name of Bulat steel [3]. Another culture that embraced the process of using Damascus steel processes was traditional Japanese blade making, where the lower carbon steel, hocho-tetsu, was forged in with the higher carbon steel, tamahagane, in order to retain the edge hardness and retention of the tamahagane on the cutting edge, whilst also leveraging the shock absorption of the hocho-tetsu in the spine [4].

The original Damascus in India was produced via smelting iron which resulted in an inhomogeneous microstructure throughout the hypereutectoid steel [5]. It is commonly accepted that during the cooling phase, the damascene patterns are features of semi-uniform bands of cementite that formed parallel to the forging surface [6]. This is also known as carbide-banding phenomenon [2]. The patterns then emerged on the blades as the Bladesmith manipulated the blade plane to intercept that of the cementite bands and as such reveal the pattern so often associated with Damascus. In addition, some interesting performance characteristics emerged caused by the differing strength throughout the blade. The formation of these bands within genuine Damascus is still under investigation but is known to be directly related to the heat treatment process and the unique combination of impurities as a result of the manufacturing process [2].

Modern Damascus steel, or fire welded pattern steel, is primarily designed for the aesthetic appeal over performance, however, there is very limited research investigating the performance of this material under dynamic testing conditions or uniaxial stress. It is important to note that modern Damascus is different from genuine Damascus, the damascene pattern of the genuine version was a function of the microstructure, whereas the pattern of the modern version is a function of the difference between the fire welded alloys used to create it [7].

In this paper, we present our results of the characterization of modern Damascus steel, with particular interest in the response of the samples under quasi-static and dynamic loading conditions. These results include optical and electron microscopy imaging, hardness testing, and compression testing at different strain rates.

Material and Experimental Methods

Two Damascus steels were used in this study, they were made out of 1095 and 15N20 steels. Two plates (50 mm wide, 150 mm long, and 10 mm thick) consist of

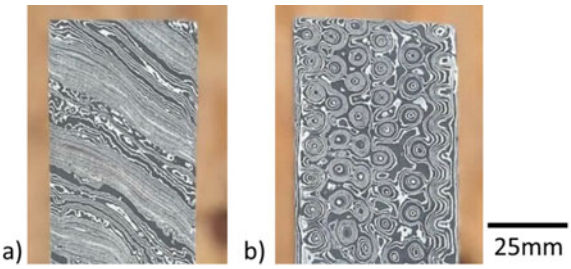

Fig. 1 Image of **a** Twist pattern sample; **b** Raindrop pattern sample

Table 1 Chemical composition of the parent materials 1095 and 15N20

Elements	Fe	C	S	P	Mn	Ni	Cr	Si
1095	98.40	0.95	0.05	0.04	0.4	0.00	0.00	0.00
15N20	96.40	0.75	0.00	0.00	0.4	2.00	0.11	0.30

250 layers were used with different patterns: a twist pattern (Fig. 1a) and a raindrop pattern (Fig. 1b). Table 1 lists the chemical compositions of the materials.

The twist pattern material is made by fire welding the two steels together, drawing them out and then refolding them until the required layer count is obtained. Then, the material is forged into a square bar and twisted to a high degree. Once completed, the newly twisted bar is then reforged into flat bar stock, from which the sample acquired for these experiments was cut. The rain drop pattern follows a similar process to the twist pattern by stacking and refolding the dissimilar steels until the required layer count is obtained. Next, small holes were drilled in the steel and then the bar was reforged flat, allowing the layers to flow into the small gaps created by the drill.

These two different patterns were chosen primarily because the orientation of the layer boundaries will be significantly different. The orientation of the layer boundaries in reference to the loading axis will be approximately 90° for the rain drop pattern, while the twist pattern will be approximately 45°. Figure 1 shows the face of the material that was compressed.

Once the samples were rough forged, with the internal folds and twists completed for each pattern, the material was then finish forged into a flat bar with dimensions approximately 120 mm × 60 mm × 12 mm. This flat bar was then ground into the final dimensions of the sample, 100 mm × 50 mm × 10 mm, plus or minus 1.5 mm. The samples were then rough polished using a belt grinder using a 600-grit belt and etched with Ferric Chloride in order to show the pattern and contrast between the two steels. This etching will be polished off during experimentation, however, some samples will be re-etched for imaging and microscopy purposes, after further polishing and mounting.

The hardness testing of the material was completed for the as-received material. This testing was done on the Shimadzu Micro Hardness Tester HMV-G21 which enabled the individual testing of the different materials within the Damascus samples. The procedure for mounting and polishing resulted in a surface finish that visually

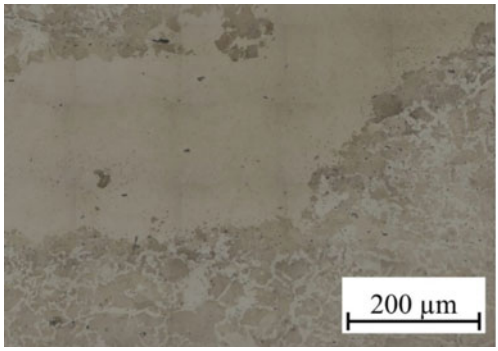

Fig. 2 Optical image of Damascus sample showing distinction between layers

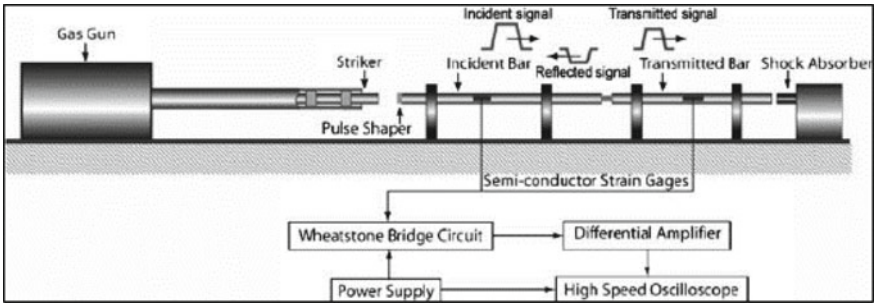

Fig. 3 Split-Hopkinson pressure bar set-up [8]

displayed the pattern of the Damascus, and a Nital etching solution was used to expose the grain boundaries. This resulted in a surface finish distinct enough to accurately test both materials separately (Fig. 2). Hardness tests were conducted in several different positions within each individual layer in order to verify the results and increase experimental accuracy.

Quasi-static compression testing was conducted on a Shimadzu Universal Testing Machine, with a strain rate of 10^{-3}/s. The operating parameters of the SHPB tests (Fig. 3) were set such that strain rate of 1000–2000/s was imposed on each material.

Imaging has been conducted on conventional bright-field, differential interference contrast on a Zeiss Axio Optical Microscope. Scanning electron and electron backscatter microscopy were also conducted on the specimens.

Results and Discussion

The hardness of the 1095 specimen was measured as 225 HV while the 15N20 material was measured to be 430 HV. The difference in hardness of the materials was not expected given their similar chemical composition, specifically of carbon

content, which is of primary concern in regard to the hardness of steel. This difference in hardness of the materials could be caused by the alloying elements in the 15N20 material, being primarily nickel. It should also be noted that it is commonly known that both materials have a similar carbon content and as such, it is standard in the blacksmithing industry to treat 15N20 with the same process as basic high carbon knife making steels, 1095. It is then therefore safe to state that the annealing procedure followed in the production of the material has been optimised for 1095, rather than the more chemically complex 15N20.

The difference in hardness of the materials could mean that the initial deformation of the material will happen within the softer material, the 1095, and then transition into the 15N20 material. This could extend the time of the compression of the material and as such increase the spread of the load throughout the material. This also means that a majority of the damage will occur within the 1095 material, to a certain threshold, in which damage or deformation will occur in the 15N20 material.

The quasi-static stress–strain responses are shown in Fig. 4. Both materials, Raindrop and Twist pattern, display very similar response, with the Raindrop pattern sample having a slightly higher Youngs modulus. Compliance correction was completed on the Shimadzu Universal Testing Machine by running the quasi-static compression cycle with no sample present, in order to track the degree of movement of the machine under loading. This data was then zeroed in order to exclude the machine movement from the future testing. It was found that both materials have an approximate yield strength of 500–550 MPa and the strain hardening of the materials is also very similar.

The dynamic stress–strain responses are shown in Fig. 5. Once again, the response of the different pattern materials is very similar. Both twist and raindrop patterns display a yield strength in the 1100–1200 MPa

A pulse shaper was not used in these experiments but it can be seen from the force equilibrium graph, Fig. 6, that though there is a marked oscillation in the elastic

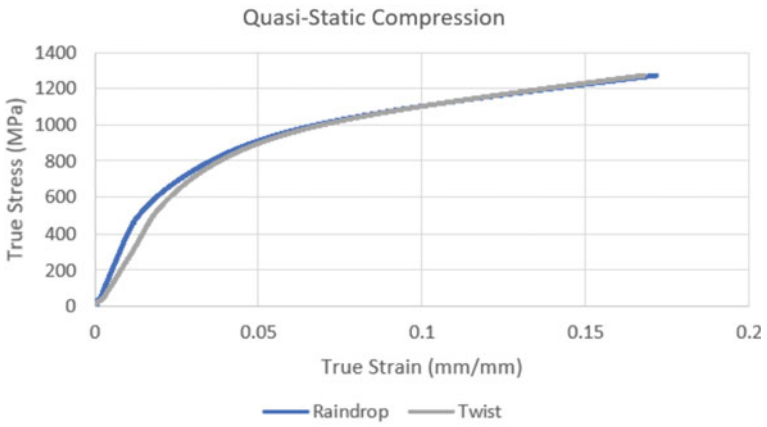

Fig. 4 True stress–strain curves from the quasi-static testing of Damascus samples

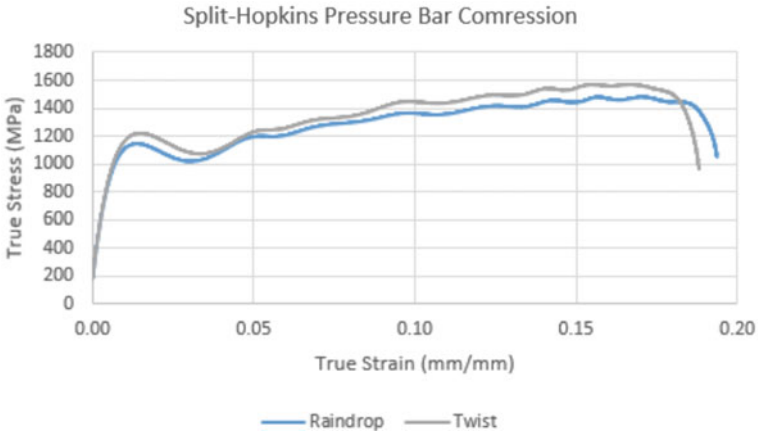

Fig. 5 True stress–strain compression curves from the dynamic deformation of Damascus samples

portion of the graph, the oscillations decrease in the plastic region. Furthermore, the front and rear force waves follow a similar gradient.

Optical and SEM images in Fig. 7 show that most defects and imperfections within the material occur in the 1095 layer of the samples. This might primarily occur in the production stage of the materials and it is a function of the high degree of deformation in this process. This could also be due to the difference in hardness of the two base materials, meaning that more of the deformation in the manufacturing process occurs in the softer material, thereby leaving the 15N20 with less deformation and as such a lower chance of inclusions or imperfections occurring. It should be noted that both materials show effects of porosity, signified by the small round imperfections in the

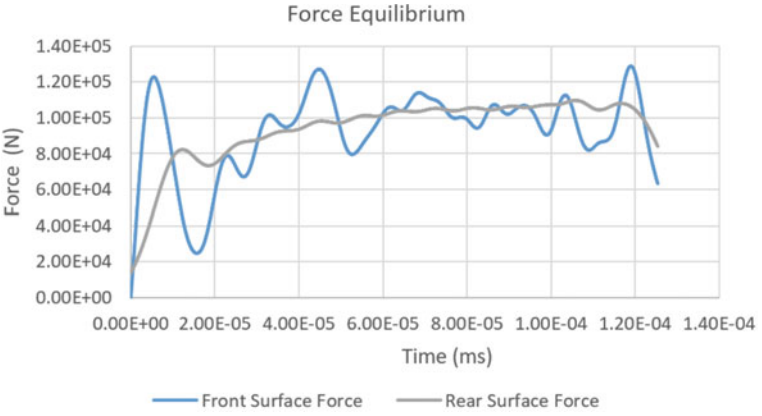

Fig. 6 Force equilibrium graph for SHPB compressive deformation of Damascus samples

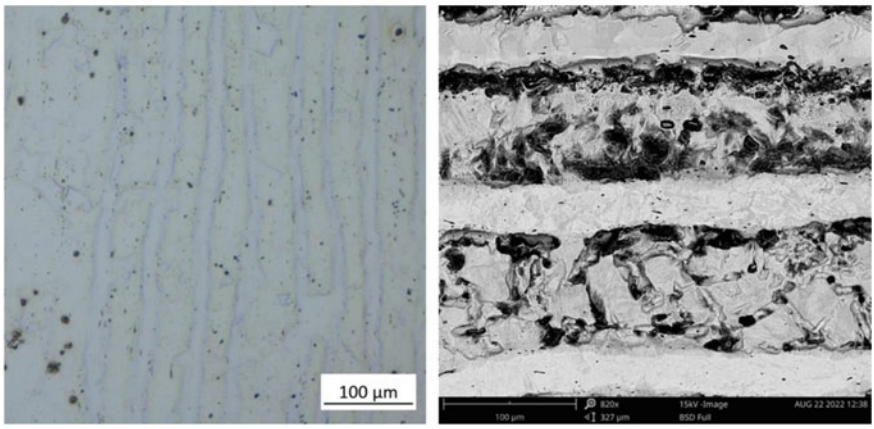

Fig. 7 Images of a Damascus steel sample **a** Optical; **b** SEM

material, and this is a function of the as-received base material the Damascus pattern samples are made from, rather than that of the manufacturing process.

Figure 7 shows a clear and distinct layer boundary formed at the interface of the 1095 and 15N20 materials, with a clear difference in the microstructure of each material evident. Within the 1095 material, a relatively clear grain structure can be seen, with a relatively large size difference present. The chemical makeup of this material can be seen in Fig. 8, which shows an EDS overlay of carbon, iron, and nickel. No nickel is present the 1095 bands but has a relatively even distribution throughout.

Due to the difference in hardness of the two materials, there is a relief between them, in which the softer 1095 has been polished to beneath that of the 15N20.

It should also be noted that a majority of the visible imperfections within the materials appear within the 1095 material, Fig. 7. Once again this could be due to the manufacturing process, where more of the deformation occurs within this material, and as such it increases its likelihood of inclusion and other imperfections within the material. This could lead to failure occurring within this material first when under higher loading.

The composition of the 15N20 material is more difficult to understand, as its microstructure wasn't visible under bright-field microscope and is only partially evident under SEM. The distinction between microstructure within the material can be seen by the slight variation within the colour of the material. The heavier materials, primarily nickel and manganese are shown as lighter whilst the lighter elements are darker within Fig. 8.

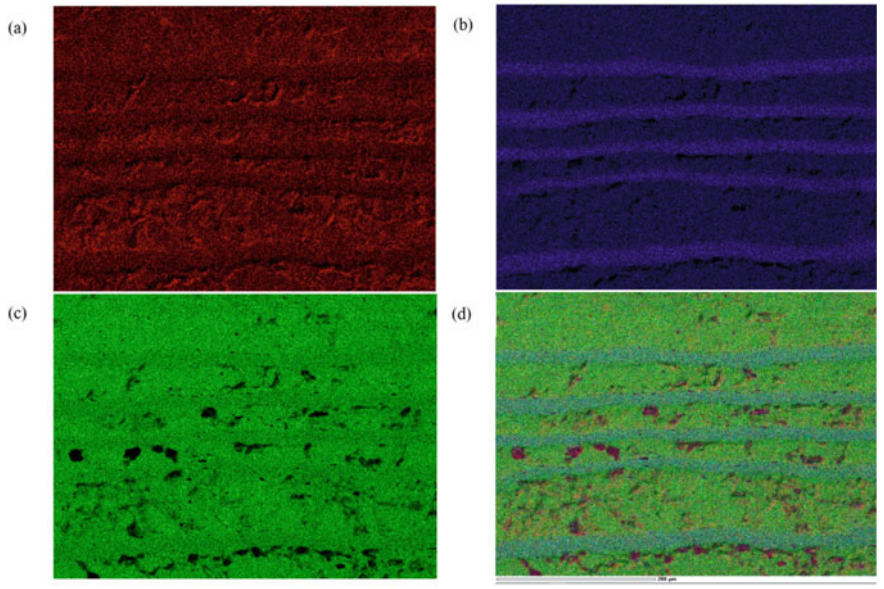

Fig. 8 EDS image of 10 **a** Carbon; **b** Nickel; **c** Iron; **d** element overlay

Conclusions

Through imaging, compression, and hardness testing, the characterisation of a couple of Damascus steel materials has been conducted. It has been shown that there is a difference in the hardness of the materials, likely caused by the alloying elements in the 15N20 material, paired with the optimisation of annealing for the 1095 material. The difference in hardness also results in a majority of manufacturing deformation occurring within the 1095 material, which also leads to a higher percentage of imperfections occurring within this material.

The grain size of the materials appears to be relatively similar, with the structure of the 15N20 being more consistent, while the 1095 structure appears to have a larger variety, possibly caused by the higher level of manufacturing deformation.

The stress–strain response in quasi-static and SHPB experiments show that there are only slight differences in the response of the material as a function of the pattern of the sample, with the twist pattern returning a very slightly higher yield strength than the raindrop pattern under dynamic loading.

References

1. Verhoeven J, Pendray A, Gibson E (1996) Wootz Damascus steel blades. Mater Charact 37(1):9–22
2. Sukhanov D, Arkhangel'skii L (2016) Damascus steel microstructure. Metallurgist 59(9–10):818–822
3. Verhoeven J (2002) Genuine Damascus steel: a type of banded microstructure in hypereutectoid steels. Steel Res 73(8):356–365
4. Peterson D, Baker H, Verhoeven J (1990) Damascus steel, characterization of one Damascus steel sword. Mater Charact 24(4):355–374
5. Verhoeven J, Pendray A (2001) Origin of the Damask pattern in Damascus steel blades. Mater Charact 47(5):423–424
6. Pendray A, Dauksch W (1998) The key role of impurities in ancient Damascus steel blades. JOM 50(9):58–64
7. Wadsworth J, Sherby O (1980) On the Bulat—Damascus steels revisited. Prog Mater Sci 25(1):35–68
8. Sunny G, Yuan F, Prakash V, Lewandowski J (2009) Design of inserts for split-Hopkinson pressure bar testing of low strain-to-failure materials. Exp Mech 49(4):479

High Strain-Rate Testing of Brittle Materials Using Miniature Beryllium Split-Hopkinson Pressure Bars

Bryan Zuanetti, Kyle Ramos, Carl Cady, Adam Golder, Chris Meredith, Dan Casem, and Cynthia Bolme

Abstract Split-Hopkinson Pressure Bars (SHPB) or "Kolsky" bars are often employed for determining the high-rate compressive failure strength of high-strength brittle materials. However, experiments generating very high strain-rates demand miniaturization of the setup for appropriately measuring decreasingly short loading events. Miniature aluminum and steel bars are often sufficient for this. However, for high enough strain-rates, miniaturization of these bars may require prohibitively small test specimens that can be inappropriate for inferring representative properties of materials with large grain size relative to the specimen size. The low Poisson's ratio of beryllium relative to aluminum and steel is expected to minimize the effect of elastic wave dispersion on the measurable strain-rates in Kolsky bar experiments. For these reasons, we have developed a Be Kolsky bar apparatus, and, in this paper, we experimentally determine the dispersion characteristics of these bars and compare the results with those of similarly size setups made from aluminum and steel. The

B. Zuanetti (✉) · K. Ramos · C. Cady · C. Bolme
Los Alamos National Laboratory, Los Alamos, NM 87545, USA
e-mail: bzuanetti@lanl.gov

K. Ramos
e-mail: Kramos@lanl.gov

C. Cady
e-mail: Cady@lanl.gov

C. Bolme
e-mail: Cbolme@lanl.gov

C. Meredith · D. Casem
DEVCOM Army Research Laboratory, Aberdeen Proving Ground, Edgewood, MD 21005, USA
e-mail: Christopher.s.meredith3.civ@army.mil

D. Casem
e-mail: daniel.t.casem.civ@army.mil

A. Golder
Intuitive Surgical Instruments, Sunnyvale, CA 94086, USA
e-mail: Adam.Golder@intusurg.com

M. Zhang et al. (eds.), *Characterization of Minerals, Metals, and Materials 2023*, The Minerals, Metals & Materials Series
https://doi.org/10.1007/978-3-031-22576-5_7

results show no appreciable dispersion in the data from the beryllium Kolsky bar setup, demonstrating its advantage over aluminum and steel.

Keywords Kolsky bar · Dispersion · High strain-rate · Dynamic

Introduction

Split-Hopkinson Pressure bars are often used for determining the dynamic failure strength of high-strength brittle materials. However, the measurement of the failure strength of brittle materials at exceedingly high strain-rates (>10^4/s) with Kolsky bars require careful design considerations for maintaining the validity of the underlying assumptions that allow for unambiguous interpretation of the experimental data. Two important assumptions [1] are that (1) the stress/strain equilibrium in the specimen must be achieved, and (2) the measured stress pulses must undergo minimal distortion by dispersion (i.e., the signals must be corrected for dispersion) for the SHPB analysis to maintain a high temporal resolution. The first assumption is influenced by the design of the specimen geometry, while the second assumption is a characteristic of the bar setup (i.e., geometry and material of the bars).

The distortion of the traveling signals is a result of the frequency dependence of the wavespeed of the discrete frequencies that make up the signal. The characteristic speed associated with these frequencies has been found to be proportional to the elastic wavespeed of the bar, C_{bar} and can be expressed as a function of the ratio d_{bar}/λ (i.e., $c_n/c_{bar} = f(d_{bar}/\lambda)$) where λ is the characteristic wavelength for each particular frequency. For small values of d_{bar}/λ, the Raleigh approximation [2] can be used to demonstrate the relationship of the phase velocity to the uniaxial stress wavespeed

$$f(d_{\text{bar}}/\lambda) = 1 - \frac{\upsilon^2\pi^2}{4}\left(\frac{d_{\text{bar}}}{\lambda}\right)^2 \tag{1}$$

where υ is Poisson's ratio of the bar material. From Eq. (1), it can be seen that this function becomes approximately unity as the bar diameter approaches zero, showing that the effect of elastic wave dispersion reduces with the miniaturization of Kolsky bars. However, for testing at exceedingly high strain-rates, (>$10^{\wedge 6}$/s) the dispersion characteristics of typical Kolsky bar materials like aluminum and steel, require prohibitively small diameter bars that become inappropriate for testing representative volume elements (RVE) of materials with large grain sizes relative to the test specimen size. The extremely low Poisson's ratio of beryllium (Be) relative to aluminum and steel is expected to minimize the effect of elastic wave dispersion [3–5]. Hence, the use of Be building Kolsky bar apparatus is expected to extend the range of measurable strain-rates for larger diameter bars and specimen sizes. This advantage will be especially usefully for testing RVE of low strength brittle materials (e.g., polymer bonded explosives), as required, due to their large grains relative to the

finite test specimen size [6–8]. Ascertaining the statistical response of the minimum RVE is important for developing constitutive models that bridge scales.[7]

For these reasons, we have developed a Be Kolsky bar apparatus, and, in this paper, we experimentally measure the dispersion characteristics of one of the setups using the approach outlined by Bacon [9] and compare the data with aluminum and steel bars of the same size. These measurements, which agree well with the numerical solution of the Pochhammer-Chree equations [10, 11], reveal the frequency dependence of the elastic wavespeed of the different Kolsky bar setups. The results show no appreciable dispersion in the data from the beryllium Kolsky bar setup, demonstrating its advantage over aluminum and steel.

Experimental Method

A schematic of the Kolsky bar setup employed in the present study is shown in Fig. 1.

The main components of a Kolsky bar apparatus include a simple firing mechanism and three bars (i.e., the striker, incident, and transmitted bars) that are held within a tight tolerance support fixture for maintaining good alignment between the components of the system. In the present experiments, the incident and transmitted bars have a diameter and length of 4.8 mm (0.189 in) and 457.2 mm (18.0 in), respectively, and are made from 7075-T6 aluminum, C350 maraging steel and S200F beryllium. The striker bars are made from the same materials as the incident and transmitted bars for the steel and aluminum setups but are made from Ti6Al4V in the beryllium setup. The length of the striker bar is 50.8 mm (2.0 in).

The striker bar is accelerated down the steel barrel using the firing mechanisms and is made to impact the incident bar. The impact between the striker and incident bar generates a stress pulse that travels from the incident bar to the transmitted bar. For all the experiments presented herein, photonic doppler velocimetry (PDV) with probes inclined relative to the bar axis is used for monitoring the traveling pulses. The schematic of our PDV system and the placement of the PDV probes relative to the Kolsky bar apparatus is shown schematically in Fig. 2.

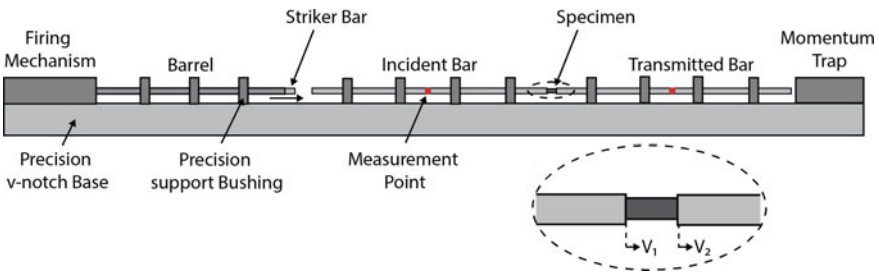

Fig. 1 A general layout of the Split-Hopkinson pressure bar setup

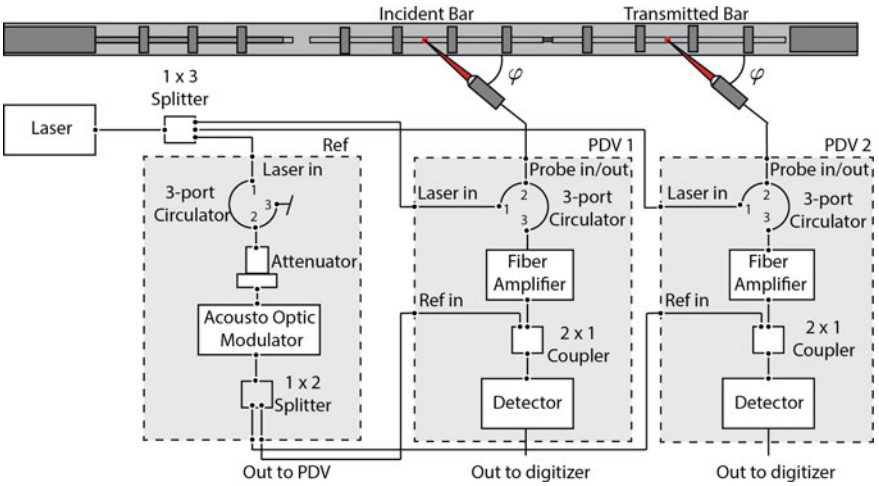

Fig. 2 Shows the placement of the probes and schematic of the present PDV setup. The components of the PDV are boxed by a dashed line, and the components of the reference leg are boxed by a dotted line

Our present PDV setup (boxed by dashed line) has five main components: a three-port circulator (Thorlabs 6015–3-APC), an Erbium-Doped fiber amplifier (Thorlabs EDFA100S), a single mode 50:50 fused coupler (TW1550R5A1), a 20 GHz detector (DXM20AF), and the illuminating source is a 1550 nm 40 mW Koheras Mikro E15 laser. The source of reference light (boxed by dotted line) light is split from the illuminating source using a single mode 90:10 fused coupler (TW1550R2A1), for probe-to-reference, respectively, and can be frequency upshifted. The source of doppler-shifted light is from diffuse reflection from a roughed region of the bar, rather than a holographic grating [12–14].

The experimental approach for determining the dispersion characteristics of the bars is similar to the approach detailed in [9] for Hopkinson bars, however, for the present Kolsky bars we use either a "bars apart" or "bars together" to measure the traveling wave. Briefly summarized, let $\tilde{\varepsilon}(\omega)$ be the Fourier transform of the strain pulse $\varepsilon(t)$. It is possible to relate the former pulses to the later pulses, e.g.,

$$\tilde{\varepsilon}_1(\omega) = \tilde{\varepsilon}_2(\omega)\mathrm{e}^{i(-\phi_2(\omega))} \tag{2}$$

where the phase difference between the two pulses, $\phi_2(\omega) = k(\omega)2L_2$, accounts for the distance that the pulse has propagated and contains a frequency dependent wave number, $k(\omega)$ representing the different wave numbers for each discrete frequency making up the traveling pulse. The wave number can be written as

$$k(\omega) = \frac{\omega}{C_n(\omega)} \tag{3}$$

From determining the frequency dependent wavenumber, it is trivial to also determine the characteristic speed as a function of frequency. The frequency dependent wavenumber can be computed from the measured pulses using

$$k(\omega) = -\frac{IM\left\{ln\left(\frac{\tilde{\varepsilon}_1(\omega)}{\tilde{\varepsilon}_3(\omega)}\right)\right\}}{2L_2}. \tag{4}$$

Results and Discussion

For experimentally determining the elastic wave dispersion characteristics of the Be, Al, and steel bars, we have performed a series of "bars apart" and "bars together" experiments. A summary of the experimental conditions for each designated experiment in the series is provided in Table 1, which includes the experiment number, projectile velocity, bar material, experiment type, and the pulse travel distance. These experiments are designed to reveal the effects of wave dispersion. A total of three experiments are conducted, one for each of the materials of interest.

Figure 3 shows the velocity versus time after the arrival of the incident pulse at the PDV monitoring locations for all experiments. In experiments (A) and (B) (bars together experiments) the solid black curve is the pulse measured at the incident bar (incident pulse) and the red dashed curve is the pulse measured at the transmitted bar (transmitted pulse), the pulse travel distance references to the spatial distance between the two measurement locations. In (C) (bars apart), the measurement point is at the same location on the incident bar, however, the black curve shows the pulse as it first arrives at the measurement location and the red dashed curve shows the same pulse after it reflects off a free surface at the end of the bar and returns to the same measurement location, in this case, the pulse travel distance is twice the distance of the measurement location from the end of the bar.

In a typical Kolsky bar experiment, the propagation of a compressive wave along the bar axis results in a radial motion of the bar due to the Poisson's effect, moreover, the radial inertia of the bars results in a two-dimensional state of stress. These effects manifest in elastic wave dispersion and cause local fluctuations that can be observed on the plateau region of the traveling pulses. These oscillations due to elastic wave dispersion can be readily seen in Fig. 3a and b, however, due to the low Poisson's

Table 1 A summary of the experimental conditions for all Kolsky bar experiments conducted in the present investigation

Experiment #	Bar material	Striker velocity (m/s)	Pulse travel distance (mm), (in)
00415502BT	7075-T6 Al	30.0	457.2,18.0
00305502BT	C350 Steel	14.9	464.8,18.3
00219102BA	S200F Beryllium	10.8	477.5,18.8

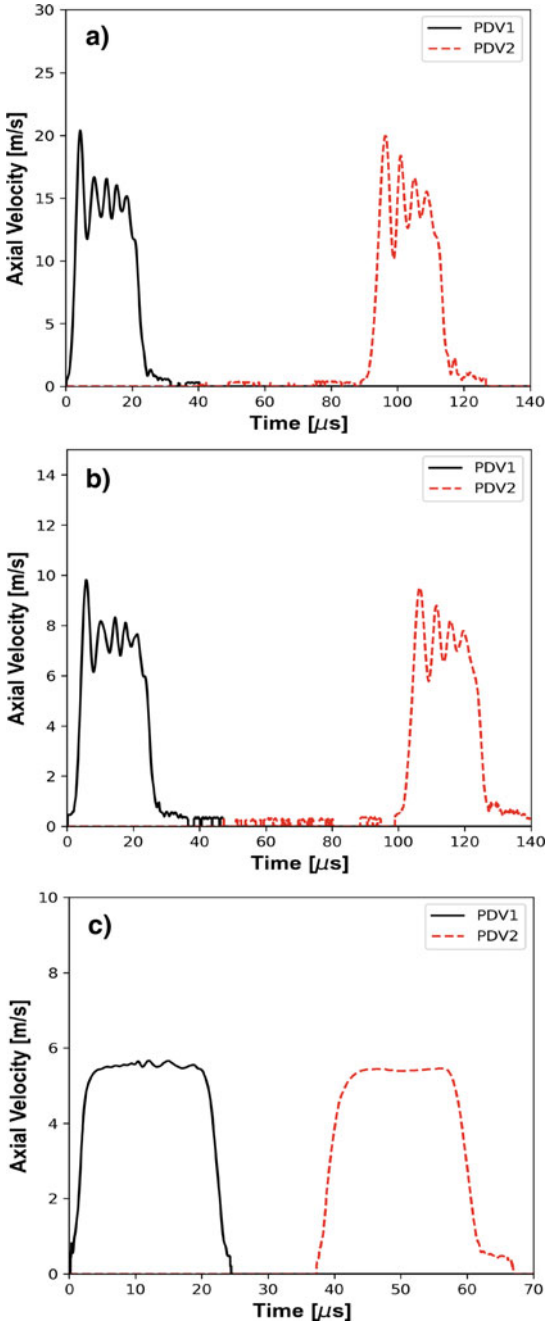

Fig. 3 Shows the velocity versus time after the arrival of the incident pulse at the PDV monitoring location for experiments employing setup 4 and **a** 7075-T6 aluminum, **b** C350 maraging steel and **c** S200F beryllium. The oscillations on the plateau of the traveling pulses manifest due to the elastic wave dispersion. These effects are minimized in the Beryllium setup in comparison to aluminum and steel

ratio of beryllium, these effects are virtually eliminated for beryllium bars, which can be observed in Fig. 3c. These observations qualitatively show the reduced elastic wave dispersion in beryllium Kolsky bars in comparison to aluminum and steel.

To quantitatively assess the differences in the dispersion characteristics of this Kolsky bar setup for different materials, we use the analysis procedure described in Eqs. (2)–(4). In Eq. (4), L_2 is the pulse travel distance. In these experiments, the traveling wave pulses generated by the impact of the striker on the incident bar are composed of a spectrum of frequencies. There exists a characteristic speed associated with each of these frequency components. Typically, the higher frequency components have a slower characteristic speed in comparison to lower frequency components, which results in the distortion (local fluctuations on the plateau) of the traveling pulses. We have found that we are able to resolve frequency components of up to about 300–400 kHz, however, the amplitude associated with the frequency spectrum above this range was too small to be noticeable. The characteristic wavespeed versus frequency and ratio of wavespeed by the speed of the fundamental frequency (C_n/C_o) versus the ratio of bar diameter by wavelength (d/λ) for all experiments is shown in Fig. 4.

The plots show the frequency dependence of the wavespeed, on the left, and a comparison between the present experiments and the numerical solution of the Pochhammer-Chree equations on the right. The plots reveal an initial wavespeed equal to the extensional wavespeed (i.e., $\sqrt{E/\rho}$) of the material, however, for (A) and (B) (7075-T6 aluminum and C350 maraging steel, respectively) the wavespeed decreases with increasing frequency for the range of resolvable frequencies (up to 300 kHz). Within this range, there is excellent agreement between the present experiments and theory, however, beyond this limit there is an abrupt deviation from the theoretical solution marking the limit of validity of the present analysis. (C) shows the results for beryllium Kolsky bars, which reveals no appreciable dependence of the wavespeed with frequency for the range of resolvable frequencies. This significant advantage over aluminum and steel can be exploited in order to conduct experiments at exceedingly high strain-rates with large Kolsky bars. The same size bars would be limited by elastic dispersion if made from aluminum and steel. This result is of particular importance for testing RVE of low strength brittle materials (e.g., polymer bonded explosives), as required, due to their large grains relative to the finite test specimen size.

Summary

In summary, we have built beryllium Kolsky bars, and experimentally measured the dispersion characteristics of these bars using “bars together” experiments. We compare the data from beryllium with typical Kolksy bar materials (aluminum and steel) of the same size. The results, which agreed well with the numerical solution of the Pochhammer–Chree equations, revealed the frequency dependence of the elastic wavespeed of the different Kolsky bar setups. The results showed no appreciable

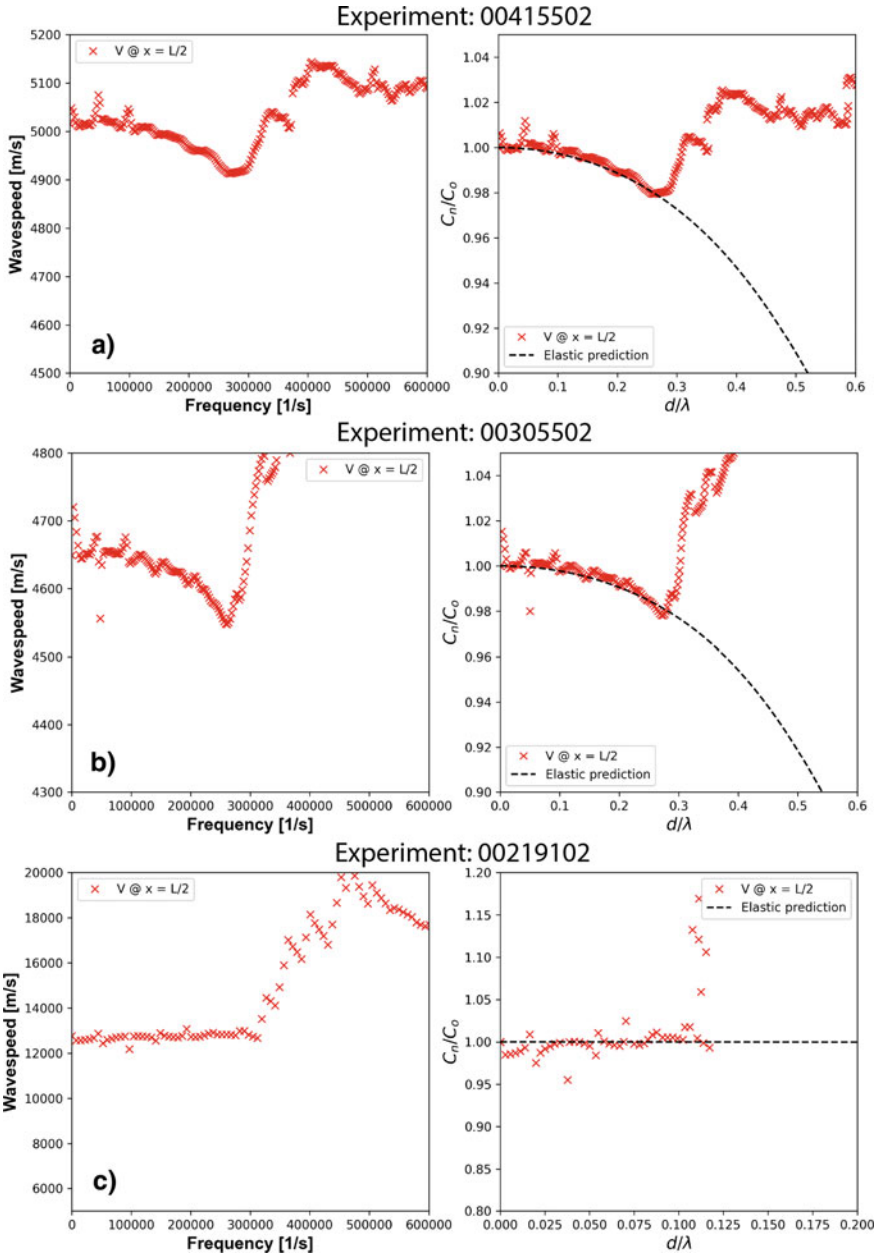

Fig. 4 Shows the characteristic wavespeed versus frequency, and ratio of wavespeed by the speed of the fundamental frequency (C_n/C_o) versus the ratio of bar diameter by wavelength (d/λ) for **a** 7075-T6 aluminum, **b** C350 maraging steel, **c** S200F beryllium. The plot shows no frequency dependence of the wavespeed for the range of resolvable frequencies for the beryllium Kolsky bar

frequency dependence of the elastic wavespeed for the range of resolvable frequencies in Be Kolsky bar experiments, demonstrating the significant advantage of the use of Be for Koksy bars in comparison to Al and steel. From these results, it was concluded that the new Be Kolsky bars are not limited by dispersion for the range of frequencies of the current investigation, showing that they can be used to extend the range of measurable strain-rates for larger bars and specimen volumes in comparison to miniature Al and steel Kolsky bars. This advantage will be especially useful for testing low strength brittle materials (e.g., polymer bonded explosives).

References

1. Ravichandran G, Subhash G (1994) Critical appraisal of limiting strain rates for compression testing of ceramics in a split Hopkinson pressure bar. J Am Ceram Soc 77(1):263–267
2. Kolsky H (1949) An investigation of the mechanical properties of materials at very high rates of loading. Proc Phys Soc Sect B **62**(11):676
3. Bateman V, Brown F, Davie N (1996) Use of a beryllium Hopkinson bar to characterize a piezoresistive accelerometer in shock environments. J IES 39(6):33–39
4. Cady CM et al (2012) Characterization of shocked beryllium. In: EPJ web of conferences. EDP Sciences
5. Jones IR (1966) Beryllium pressure bar having submicrosecond risetime. Rev Sci Instrum 37(8):1059–1061
6. Liu C (2005) On the minimum size of representative volume element: an experimental investigation. Exp Mech 45(3):238–243
7. Zuanetti B et al (2021) Unraveling the implications of finite specimen size on the interpretation of dynamic experiments for polycrystalline aluminum through direct numerical simulations. Int J Plast 145:103080
8. Zuanetti B et al (2020) Dynamic flow stress of pure polycrystalline aluminum: pressure-shear plate impact experiments and extension of dislocation-based modeling to large strains. J Mech Phys Solids 104185
9. Bacon C (1998) An experimental method for considering dispersion and attenuation in a viscoelastic Hopkinson bar. Exp Mech 38(4):242–249
10. Bragov AM et al. (2019) Dispersion correction in split-Hopkinson pressure bar: theoretical and experimental analysis. Continuum Mech Thermodyn 1–13
11. Bancroft D (1941) The velocity of longitudinal waves in cylindrical bars. Phys Rev 59(7):588
12. Zuanetti B, Wang T, Prakash V (2017) A compact fiber optics-based heterodyne combined normal and transverse displacement interferometer. Rev Sci Instrum 88(3):033108
13. Casem DT, Grunschel SE, Schuster BE (2012) Normal and transverse displacement interferometers applied to small diameter Kolsky bars. Exp Mech 52(2):173–184
14. Zuanetti B et al (2018) Measurement of elastic precursor decay in pre-heated aluminum films under ultra-fast laser generated shocks. J Appl Phys 123(19):195104

Evaluation of Feature Engineering Methods for the Prediction of Sheet Metal Properties from Punching Force Curves by an Artificial Neural Network

M. Görz, A. Schenek, M. Liewald, and K. R. Riedmüller

Abstract The part quality that can be achieved in forming and stamping processes strongly depends on the properties of the sheet metal material to be processed. However, since these material properties may fluctuate considerably and thus lead to the production of scrap, it is important to monitor such material fluctuations during part production. For this, the ongoing digitization of production processes provides new possibilities for part or quality monitoring. In this context, a novel AI-based method for the direct determination of material parameters from punching force curves measured in production was presented in a past study by the authors. This paper deals with the investigation of three further methods for extracting features from these recorded measuring data. In addition to domain knowledge-based feature engineering, statistical feature extraction (PCA) as well as a derivative-based method are analyzed and compared with each other and with the previously used AI (ANN) regarding their prediction accuracy of sheet metal properties.

Keywords Machine learning · Material characterization · Punching force · Tensile properties

M. Görz (✉) · A. Schenek · M. Liewald · K. R. Riedmüller
Institute for Metal Forming Technology, University of Stuttgart, Holzgartenstr. 17, 70174 Stuttgart, Germany
e-mail: marcel.goerz@ifu.uni-stuttgart.de

A. Schenek
e-mail: adrian.schenek@ifu.uni-stuttgart.de

M. Liewald
e-mail: mathias.liewald@ifu.uni-stuttgart.de

K. R. Riedmüller
e-mail: kim.riedmueller@ifu.uni-stuttgart.de

M. Zhang et al. (eds.), *Characterization of Minerals, Metals, and Materials 2023*, The Minerals, Metals & Materials Series
https://doi.org/10.1007/978-3-031-22576-5_8

Introduction and State of the Art

A combination of several shearing and forming operations is generally used to produce sheet metal components. The achievable resultant quality of the finished parts is thereby strongly dependent on the material parameters of the processed semi-finished products. Characteristic failures such as tearing at the bottom [1] of the parts during deep drawing or a change in the springback behaviour of the final part [2] can be directly connected to fluctuating material parameters and are therefore still one of the main causes for quality losses and failures during the production of sheet metal components [3]. Hereby, fluctuations in the material parameters can occur not only from batch to batch, but also within a single coil in the longitudinal [4] and transverse [5] direction of the coil.

Since classical methods for material characterization cannot characterize an entire coil in a production-relevant time frame, various novel methods for inline material characterization have been developed. Ruzovic uses the correlation between the microstructure of the material with its electromagnetic and mechanical properties to determine material parameters [6]. Wisenmayer et al. determined the material parameters by using simple linear correlations of process data determined during shear cutting with the material parameters. However, the investigations were only carried out for one class of material (DP600) [7].

Through the use of artificial neural network ANNs, a novel method for inline material characterization based on machine learning methods has been developed at the Institute for Metal Forming Technology (IFU) [8]. Figure 1 shows the underlying principle. By means of a pre-trained ANN, the relation between the cutting force curve and the stress–strain diagram is used to predict the material parameters. The authors were able to show that for a large number of different steel materials (DC03, DP600, DP800, DP1000, DP1200, HX380) this pre-trained ANN allowed a precise prediction of the material parameters on the basis of force curves measured during the shear cutting of sheet metal materials. In addition, Schenek et al. showed that even for unseen but similar materials (DX54) a prediction is possible by using this ANN The research reported in this paper was conducted without targeted feature engineering or hyperparameter tuning.

Various studies have shown that the prediction quality of an AI model is strongly dependent on the quality and preparation of the training data. The process of systematic preparation of the training data is also referred to as feature engineering. Feature engineering can be based on domain-specific expert knowledge or on algorithms for the statistical analysis of the data. To classify the wear of tool active parts by analysing measured force path curves, Hoppe et al. [9] employed both types of feature engineering. Hoppe et al. [9] compared features based on expert knowledge (cutting length, the maximum cutting force, and the work integral) with features determined by Principal Component Analysis (PCA). It was shown that both methods lead to good results.

Asahi et al. [10] showed, on the contrary, that with a similar data set and prediction goal, no feature engineering is necessary and the force–displacement curves recorded

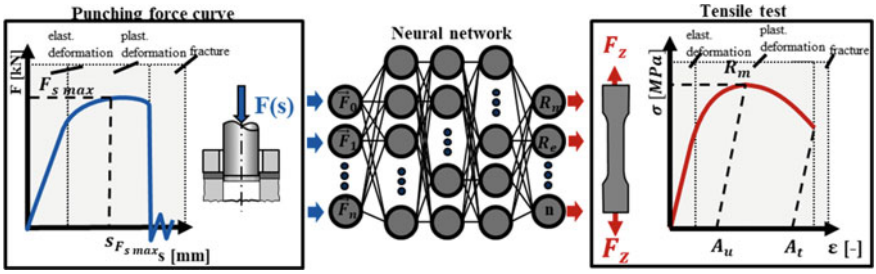

Fig. 1 Neural network-based approach to predict mechanical sheet metal parameters from experimentally measured punching force curves [8]

as time-series data can be directly given to the neural network without any kind of feature engineering.

From the analysis of the state of the art, no clear recommendations can be drawn as to whether feature engineering should be carried out in order to improve the prediction results of machine learning models. Therefore, the research question to be addressed by this contribution is: *Is it possible to increase the prediction quality of ANNs for the prediction of material parameters based on cutting force–displacement curves by using feature engineering?*

To address this scientific question, three different ANNs were trained with differently prepared training data in the course of the research work described in the present paper and their prediction performances were compared with each other and against a reference ANN based on the ANN presented in [8]. Three different strategies were used to prepare the training data. The training data for Model 1 ("Derivative") was generated on the basis of the derivatives of the force–displacement curves. The training data for Model 2 ("Domain Knowledge") was generated by feature engineering using specific domain knowledge. The training data for Model 3 ("PCA") was obtained by statistical feature engineering by use of PCA.

Experimental Setup

The basis for the training of the ANNs was punching force curves and the mechanical properties of the considered sheet metal materials DC03, DP600, DP800, DP1000, DP1200, HX380, and DX54, which have been determined in experimental investigations. The experimental investigations for recording the punching force curves were performed using a modular test tool equipped with a load cell for direct force measurement. The measuring frequency was set to 10 kHz, ensuring a high resolution (60 data points) of the measured punching force curves. The basic design of the tool is shown in a schematic sectional view in Fig. 2. During the experimental investigations, all punches were firmly clamped over a length of 22 mm in the shank area. The shank diameter of the punches was 13 mm according to the ISO8020 standard

in all tests. The punching parameters used during the experiments are listed in Table 1. The measured punching force curves are shown in Fig. 3 (left).

For determining the mechanical properties of the different sheet metal materials, tensile tests were carried out on a Roell + Korthaus RKM 100 Material Testing

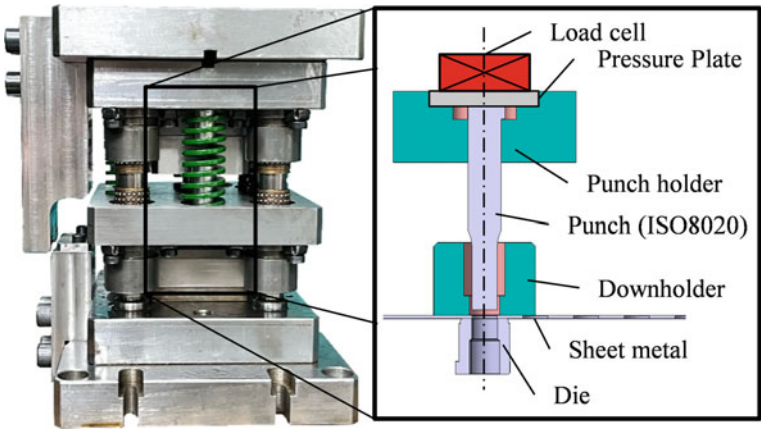

Fig. 2 Punching tool with schematic sectional view

Table 1 Punching parameters [8]

Parameter	Value
Length of punch	80 mm
Cutting clearence	15%
Sheet thickness	1 mm
Punch diameter	10 mm

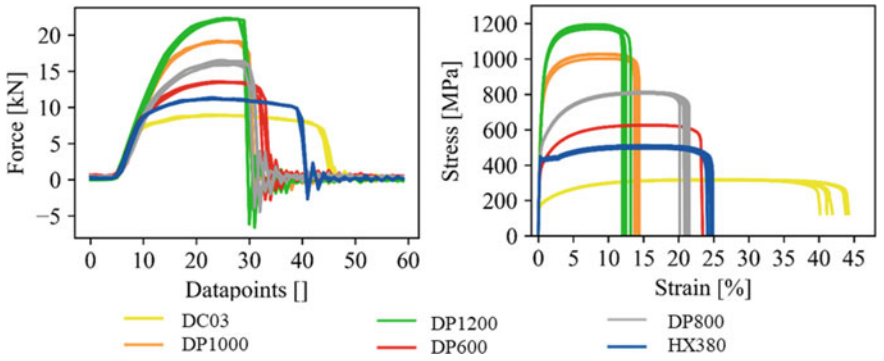

Fig. 3 Experimentally determined punching force curves (left side) and stress–strain curves (right side) [8]

Machine according to DIN EN ISO 6892–1. The tensile test specimens for the test series were manufactured according to DIN 50,125 (H20 × 80). The stress–strain curves determined by the tensile tests are depicted in Fig. 3 (right).

Feature Engineering, Model Design, and Training

For the investigations described in this scientific research the programming language Python was used. To correlate punching force curves or features with mechanical sheet metal parameters, the deep-learning library TensorFlow (TF) was used. TF was developed by researchers from Google dedicated to artificial intelligence. Further Python libraries used for the presented investigations are Numpy for data preparation purposes, Matplotlib for plotting, pandas for reading data from measuring protocols, and Scikit-learn to perform PCA.

For a presentation of the basic steps for measurement data preparation, the authors refer to the publication [8]. In the following section, only the subsequent data processing steps and the feature engineering performed will be discussed. A plot of the training data to be used with the reference model "Standard" is shown in the upper left corner of Fig. 4. The derivative-based training data was created using the python library Numpy and is depicted in the upper right corner of Fig. 4.

To identify suitable features based on domain knowledge of the shear cutting process, the cutting force–displacement curve was analysed in more detail. The process of shear cutting sheet metal materials can be divided into three typical phases (see Fig. 5) [11]. Phase 1 predominately consists of the elastic deformation of the sheet metal material, but also the elastic deformation of the punch, the cutting tool and the press. After this initial phase, phase 2 contains the plastic flow of the sheet metal material. During this phase the cutting force reaches its maximum $F_{s\,max}$. At the beginning of phase 3, the slug and the remaining sheet metal grid are split from each other due to the punch movement. Thus, the beginning of phase 3 is characterised by a sudden decrease in the cutting force–displacement curve due to the material separation.

Because of its prominent position in the Force–Stroke diagram, $F_{s\,max}$ can also be used as a feature for characterization. Furthermore, as described by Lange [1], there is a direct connection between the maximum force during shear cutting and the tensile strength of the sheared material. An additional feature to detect the moment of material separation from punching force curves is the cutting length l_s. In addition to the maximum cutting force ($F_{s\,max}$) and the cutting length (l_s), the cutting work (W) was identified as a suitable feature. The cutting work (W) summarizes information on all three phases by integrating the punch force over the punch stroke (S). The training data based on these three features determined on the basis of domain knowledge are depicted in Fig. 4 on the lower left-hand side.

PCA is performed on the initial training data to identify a reduced data set based on features that still represents the original training data in a lower dimensional subspace but with a minimal loss of information. PCA provides therefore a method to summarize the training data and extract features that describe the individual differences of

the process [12]. The PCA was performed ensuring that the calculated features will describe 95% of the variance of the initial dataset. This condition can be achieved with four features that are determined by the PCA algorithm. The diagram depicted on the bottom right side of Fig. 4 ("PCA") shows a plot of the new reduced training data generated through PCA.

In order to determine optimal hyperparameters for the models used in this investigation a comprehensive hyperparameter optimization is done for all four models. The "Hyperband" tuner integrated in Keras was used to optimize the hyperparameters [13]. The goal of the optimization was to minimize the validation accuracy of the model. Table 2 presents an overview of the variation parameters as well as the corresponding parameter range varied during hyperparameter tuning. The results of the tuning process are summarized in Table 3.

Figure 6 depicts the characteristic structure of a feed-forward neural network (FFNN) made up of an input, a hidden, and an output layer. The inputs for the different ANNs consist of the measured force vectors during the shearing process

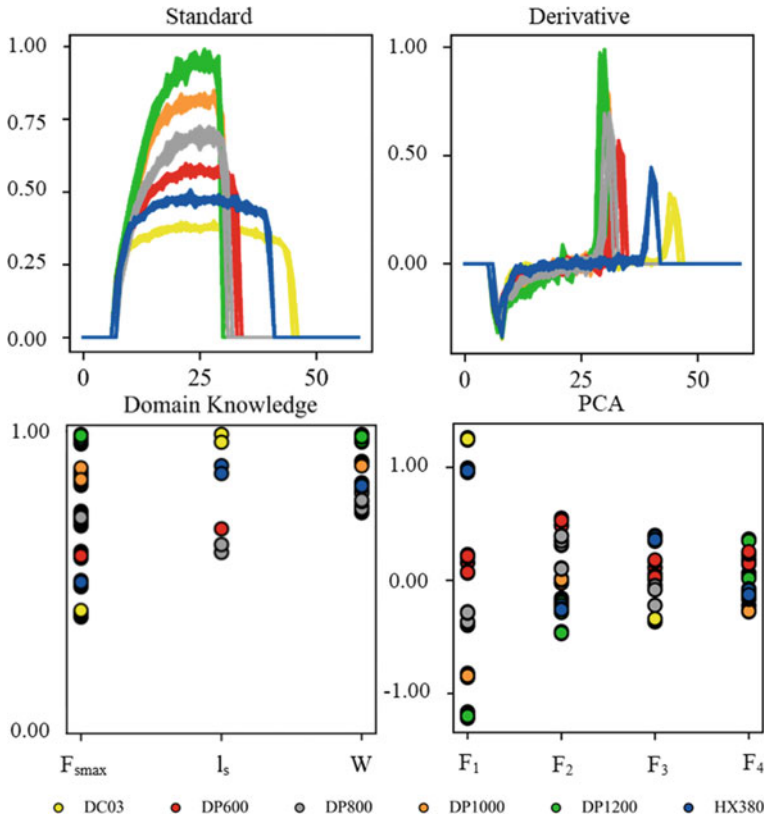

Fig. 4 Normalized training data for the four different ANNs

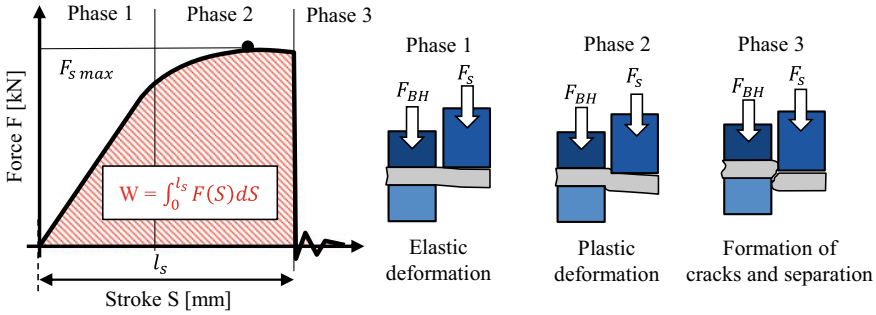

Fig. 5 Features extracted from punching force curves (left) [11]; different phases of the shear cutting process

Table 2 Parameters hyperparameter tuning

Parameter	Parameter range
Number of hidden layers	1–20
Neurons per hidden layer	5–50 (steps of 5)
Activation function	Sigmoid, relu

Table 3 Parameters of the ANNs after hyperparameter tuning

Model	Inputs	Hidden Layers	Neurons per Layer	Activation function
Standard	60	7	40,20,45,40,35,20,35	Relu
Derivative	60	5	25,30,20,45	Relu
Domain Knowledge	3	15	30,30,10,15,30,10,35,30, 5,50,45,15,10,15,20	Relu
PCA	5	8	15,15,5,10,15,5,15,10	Relu

or the identified features. The output layer of the ANNs represents the five different sheet metal material parameters R_m, $R_{p0.2}$/ R_e, A_g, A_t, and n in the given order.

For the training cycles of the designed FFNN, 85% of the datasets were used as training data. 10% of the datasets were used as validation data, in order to improve the model training throughout the training. In order to determine the convergence point, a convergence study was performed. The training was conducted with 100, 150, 200, 250, and 300 epochs. After 200 training epochs, convergence was detected and the training was subsequently discontinued.

The remaining 5% finally were used to evaluate the trained neural networks on unseen data. The errors calculated during the training cycles (loss function: mean squared error) were used to incrementally improve the initially randomly initialized weights of the ANNs by using the Adam optimization algorithm.

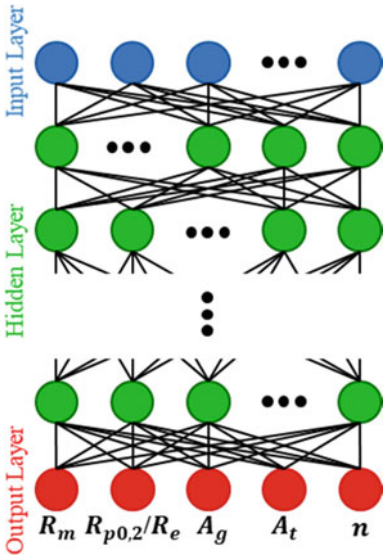

Fig. 6 Schematic architecture of an ANN

Results and Discussion

The objective of the presented study was to evaluate the effects of different data preparation methods on the regression capability of an artificial neural network in order to obtain mechanical sheet metal parameters from punching force curves. Table 4 summarizes the training metrics for the four created models after 200 training epochs. Loss (mean squared error (MSE)) and Accuracy (mean absolute error (MAE))) are presented for all four trained models and each separate dataset. Especially the low metrics (MAE) after model evaluation shows, that, principally, the output of all neural networks (predicted values for R_m, $R_{p0.2}$/ R_e, A_t, A_G, and n) precisely matches to the target values derived from the uniaxial tensile test. By comparing the accuracy (MAE) of the models for the evaluation data, a significant improvement in the prediction performance can be observed due to the decrease of the MAE for the evaluation data. Feature engineering based on domain knowledge or statistical methods leads to a 50% reduction of the MAE for data unseen by the ANN in comparison to the reference model ("Standard").

Figure 7 shows the prediction of the four trained models for the unseen evaluation datasets. All models show good agreement between values predicted by the ANNs and the actual sheet metal material parameters determined in tensile tests. However, when examined closely, the reference model shows visible deviations above values of 0.9. These deviations cannot be observed in the predictions of the models "Gradient", "Domain Knowledge" and "PCA". The majority of the deviating values can be allocated to the material HX380. It can therefore be stated that the prediction quality for this material in particular could be increased. Moreover, the use of models based on features created by domain knowledge offers further advantages. Thus, these

Table 4 Summary of the ANNs metrics after 200 training epochs

	Model	Training Data	Validation Data	Evaluation data
Loss (MSE)	Standard	1.49×10^{-5}	1.76×10^{-5}	
Accuracy (MAE)		1.40×10^{-3}	1.75×10^{-3}	3.20×10^{-3}
Loss (MSE)	Derivative	4.29×10^{-5}	3.74×10^{-6}	
Accuracy (MAE)		1.60×10^{-3}	1.75×10^{-3}	2.50×10^{-3}
Loss (MSE)	Domain knowledge	4.93×10^{-5}	2.1×10^{-6}	
Accuracy (MAE)		1.20×10^{-3}	1.3×10^{-3}	1.70×10^{-3}
Loss (MSE)	PCA	4.49×10^{-5}	3.76×10^{-3}	
Accuracy (MAE)		1.15×10^{-3}	1.35×10^{-3}	1.50×10^{-3}

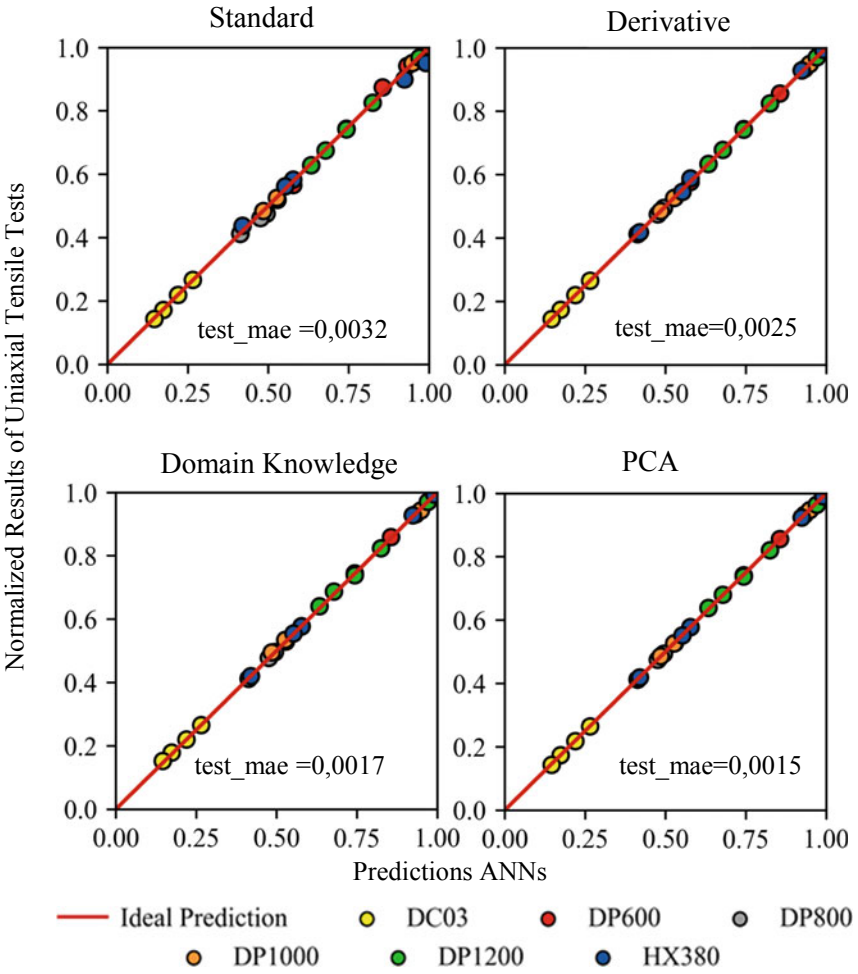

Fig. 7 Comparison between the predicted mechanical sheet metal parameters and the targeted values from tensile tests for the different data preparation methods

models are expected to be more transferable to other tools or presses, because only the associated features are needed for a correct prediction. In addition, these models are also more robust to variations in the measurement frequency during data collection; the measurement frequency just has to be sufficiently large to reliably detect the features.

Summary and Outlook

Material parameters of sheet metal materials have a strong influence on the achievable quality of punched and formed parts. Due to the strong fluctuation of these sheet metal parameters, a novel machine learning based method for inline process monitoring was developed at IFU. In particular, the data preparation and training process have a substantial influence on the prediction accuracy of these machine learning based systems. In this contribution, different data preparation methods have been compared in order to investigate their influence on the prediction accuracy of material parameters from cutting force–displacement curves. It has been shown that by using feature engineering based on domain knowledge or statistical methods, a significant improvement (50%) in the prediction accuracy of a neural network can be achieved.

To advance the research presented in this publication, further investigations will be undertaken at IFU. In addition to the transferability of the models used to other presses and sensors, these future investigations will also investigate the transferability to other material classes (copper or aluminium). Furthermore, the influence of wear of the tool parts on the prediction quality of the models will be investigated through endurance tests. Finally, a transfer to open cutting lines will be investigated.

References

1. Lange, K (Hrsg) (1990) Umformtechnik Handbuch für Industrie und Wissenschaft Band 3: Blechbearbeitung. Springer, Berlin
2. de Souza T, Rolfe BF (2010) Characterising material and process variation effects on springback robustness for a semi-cylindrical sheet metal forming process. Int J Mech Sci Bd. 52(12):1756–1766
3. Maier SJ (2018) Inline-Qualitätsprüfung im Presswerk durch intelligente Nachfolgewerkzeuge, Technische Universität München, Dissertation
4. Faaß I (2009) Prozessregelung für die Fertigung von Karosserieteilen in Presswerken, Technische Universität München, Dissertation
5. Held C, Liewald M, Sindel M (2009) Untersuchungen zum Einfluss werkstofflicher Schwankungen innerhalb eines Coils auf die Umformbarkeit *. In: wt Werkstattstechnik online, vol 99, issue no. 10, pp 732–739
6. Ružovič M (2004) Die zerstörungsfreie Ermittlung von genauen Zugversuchsdaten mit dem Wirbelstromverfahren, Eidgenössiche Technische Hochschule, Dissertation

7. Wiesenmayer S, Frey P, Lechner M, Merklein M (2020) Determination of the properties of semi-finished parts in blanking processes. In: IOP conference series: materials science and engineering, vol 967, issue no. 1
8. Schenek A, Görz M, Liewald M, Riedmüller KR (2022) Data-driven derivation of sheet metal properties gained from punching forces using an artificial neural network. In: Vincze G, Barlat F (Hrsg.) Key engineering materials, vol 926, pp 2174–2182
9. Hoppe F, Hohmann J, Knoll M, Kubik C, Groche P (2019) Feature-based supervision of shear cutting processes on the basis of force measurements: evaluation of feature engineering and feature extraction. In: Procedia manufacturing, vol 34, Elsevier B.V., pp 847–856
10. Asahi S, Karadogan C, Tamura S, Hayamizu S, Liewald M (2021) Process data based estimation of tool wear on punching machines using TCN-Autoencoder from raw time-series information. In: IOP conference series: materials science and engineering, vol 1157 issue no 1
11. Hoffmann H, Neugebauer R, Spur G (Hrsg.) (2012) Handbuch Umformen. Carl Hanser Verlag GmbH Co. KG, München. ISBN 978-3-446-42778-5
12. Jolliffe IT (2002) Principal component analysis. Springer, New York
13. Li L, Jamieson K, DeSalvo G, Rostamizadeh A, Talwalkar A (2018) Hyperband: a novel bandit-based approach to hyperparameter optimization. J Mach Learn Res 18:1–52

Part IV
Characterization of Polymers, Composites, Coatings and Ceramics

Performance Study of 3D Printed Continuous Fiber Reinforced Composites

Xiaofang Liu, Anil Saigal, and Michael Zimmerman

Abstract Additive manufacturing (3D Printing) has made tremendous progress in the past two decades and the success of continuous fiber fabrication (CFR) technology has made it conceivable to print continuous carbon fiber reinforced composites. In this paper, the tensile strength, Young's modulus, flexure strength, and flexural modulus of 3D printed continuous carbon fiber reinforced composites were investigated using test specimens based on the standards ASTM D3039/D3039M and ASTM D790, respectively. A proportional increase in tensile strength, Young's modulus, flexural strength, and flexural modulus were measured with increasing carbon fiber volume fractions for a given fiber orientation. The test results indicate that except for the flexure strength of the highest (0.767) volume fraction fiber composites, the other measured values are much lower and are about half the values listed in the given datasheet.

Keywords Additive manufacturing · Carbon fiber volume fraction · Tensile strength · Flexure strength

Introduction

Compared to metals and alloys, continuous carbon fiber reinforced composites (CCFR) are extensively applied in automobiles, aircrafts, ships and bridges, railway vehicles, and aerospace areas for their light weight and high specific strength [1, 2]. With the superior properties of continuous carbon fiber reinforced composites, the weight of structures used is greatly reduced and they are resistant to corrosion and high temperatures, as well as offering significant savings in energy consumption while working towards the goal of global carbon neutrality. The advent of 3D printing technology for continuous carbon fiber reinforced composites has made it feasible to combine advanced materials with complex geometries in various fields including architectural, medical, and biological fields, etc. 3D printing technology has made

X. Liu · A. Saigal (✉) · M. Zimmerman
Department of Mechanical Engineering, Tufts University, Medford, MA 02155, USA
e-mail: anil.saigal@tufts.edu

M. Zhang et al. (eds.), *Characterization of Minerals, Metals, and Materials 2023*, The Minerals, Metals & Materials Series
https://doi.org/10.1007/978-3-031-22576-5_9

tremendous advances over the past two decades, facilitating the emergence of fiber reinforced composites as a powerful development paradigm, and sustained research into the characterization of 3D printed continuous fiber reinforced composites also greatly contributed to the innovation and advancement of 3D printing technology.

The most common types of additive manufacturing (also termed as AM) techniques include continuous filament fabrication (CFR), fused filament fabrication (FFF), also termed as fused deposition modeling (FDM), stereolithography (SLA), atomic diffusion additive manufacturing (ADAM, also termed as DMLS for metal), direct light processing (DLP), binder jetting and LOM (Laminated Object Manufacturing). Among them, CFR, FFF, SLA, and LOM techniques are applied to print continuous fiber reinforced composites [2, 3].

Markforged company has made significant development in CFR technology since 2014 with the launch of the Desktop Composite 3D Printer, the first printer to print continuous carbon fibers. CFR is an enhanced FFF process used in conjunction with an FFF printer to deploy continuous fibers in the part. In this process, the printer uses a specific nozzle to deposit a continuous stream of composite fibers in a conventional FFF thermoplastic part. The strength and stiffness of parts made with CFR are attributed to its reinforced fibers. In Markforged Printers, type of layers, the number of layers, infill density, layer thickness, fiber orientation, infill pattern, and fiber locations can all be edited by employing Eiger, the slicing software dedicated to 3D printers [3]. In recent research, the most common printers used are Markforged Onyx One, Markforged Two, and Markforged X7.

The matrix materials utilized in the CFR process are thermoplastic polymers in the form of filaments. The most common matrix materials that can be used in FFF and CFR processes include acrylonitrile–butadiene–styrene (ABS), nylon (PA), polylactic acid (PLA), and new novel material polyether ether ketone (PEEK) [1, 2]. Shape memory polymers (SMP) and liquid crystal elastomers (LCE) have also been used to make multifunctional smart composites [1].

In recent years, many papers have characterized continuous carbon fiber reinforced composites (CCFR) manufactured using CFR method. Multiple factors have been found to influence the tensile and flexure strength and their stiffness, including voids, notches, temperature, pressure, stacking sequence, and printing process parameters [2]. Printing process parameters like printing speed, printing temperature, fiber orientation, fiber types, infill angle, infill density, infill pattern, fiber volume fractions, and layer thickness contribute significantly to the characterization of the samples manufactured through CFR technique [4–6]. It was also discovered that printing speed and printing temperature of Markforged Onyx One and Markforged Two could not be varied.

Most of the published literatures on 3D printed continuous fiber reinforced composites have concentrated on the microstructure and tensile strength. Strength and modulus studies in creep [6], compression [7–10], shear [8, 11, 12], fatigue [6, 13], and Charpy impact [14, 15] have also been reported, but data are very limited. Many authors have found significant effects of voids, pressure, and temperature on mechanical properties. High temperature and pressure can reduce voids and increase

interlaminar bonding, thus improving the performance of continuous fiber reinforced composites. It was found that voids existed within fibers and matrix filaments, between layers and between fiber bundles deployed within a layer [1, 2, 4, 5].

The influences of fiber orientation, temperature and pressure on tensile properties were investigated by Saeed et al. It was reported that a large 3D printed continuous carbon fiber reinforced composite plate was prepared and compressed according to the ASTM standards. Subsequently the plate was cut into rectangular tensile samples by water jetting and all four nylon layers at the top and bottom respectively were removed to obtain the maximum fiber volume fraction. The results showed that the fibers could resist tension along the longitudinal direction (at 0 degree) and withstand the highest load. The hot-pressed samples with unidirectional fiber orientation had the highest tensile strength and tensile modulus. The values for the hot-pressed samples were significantly larger (768 MPa, 80.4 GPa) compared to those of the non-hot-pressed samples (604 MPa, 73.1 GPa). The test specimens for bending strength were fabricated without hot pressing. The bending strength also exhibited an increase with increasing number of fiber layers. It was also found that the voids of the pressed samples were reduced and all samples included cracks with an average of void content of 3.96% for the uniaxial samples fabricated without any compression applied [4].

Lupone et al. and Saeed et al. investigated the microstructure and tensile behaviors of 3D printed carbon fiber reinforced nylon composites with different fiber layups. It was concluded that the maximum strength and stiffness were obtained in test samples with fibers distributed along the longitudinal direction (at 0 degree). A significant decrease in tensile properties was found for test samples with cross-ply and quasi-isotropic laminates [11, 16]. It is worth noting that they utilized tensile test samples of different sizes and different laminate layups. The maximum strength is 597.8 MPa and 524.66 MPa, while the elastic modulus is 48.3 GPa and 73.2 GPa, respectively [11, 16].

Saeed et al. and Peng et al. demonstrated the synergistic effect of short and continuous carbon fiber reinforcement on the tensile behaviors of 3D printed carbon fiber reinforced composites. The strength of short and continuous carbon fiber reinforced composites proved to be superior to their respective reinforced composites while the elastic modulus was not the case [4, 17]. It was noted that the stacking sequence of fibers had a significant role on the tensile properties of short and continuous carbon fiber reinforced composites. It was reported that better strength and elastic modulus were obtained with separated continuous carbon fiber layups [17].

Geometry and carbon fiber filling patterns have been reported to influence the tensile and compressive behaviors of 3D printed specimens by Li et al. Two types of specimens (longitudinal 0° and cross-ply (0°/90°) were used for flexure testing and the flexure strength were 235.06 MPa and 148.04 MPa, respectively [14]. The studies conducted by Chen et al. focused on tensile properties and flexure properties by using test samples with cross-ply laminates. The average ultimate flexure strength obtained by 3D printed specimens was 89.46 MPa, which is lower than the value (178.7 MPa) for hand-layup specimens [18]. The flexure test conducted by Yu et al. was four-point bending test to analyze the effects of carbon fiber concentration and

filling pattern on bending properties. The specimens containing 48.72% carbon fiber exhibited maximum flexural strength of 270.63 MPa [19].

It is particularly of significance to investigate various categories of the performances of 3D printed continuous fiber reinforced composites. Hundreds of previous papers have been published to study the properties of 3D printed continuous carbon fiber reinforced composites. However, there are some significant discrepancies in the data obtained from different sets of experiments, which may be due to different test samples in geometries, different fiber volume fractions, different test setups, and printing process parameters. In this work, a series of nylon carbon fiber samples and pure nylon samples were fabricated by a Markforged Two printer to study the tensile strength, flexure strength, Young's modulus, flexure modulus, and test responses. The test data are compared with that obtained from previous research and Markforged datasheet [20].

Materials and Testing Setup

Materials and Fabrication Process

Markforged Two is used to print test samples through CFR method. There are two printing heads, one for printing matrices and the other for printing enhanced filaments. The two nozzles cannot work simultaneously. If two identical samples are printed at the same time, the distance between them needs to be noted. The printing process is divided into two steps. Step one is to deploy matrix material with a plastic dispensing nozzle at 270 °C. Step two is to apply the fiber reinforcement to the matrix on an unheated print bed at the temperature of 250 °C. During the printing process, we found some limitations of the Markforged Two printer, such as the printing speed cannot be programmed which is inherent of the 3D printer; the test sample needs to have an upper and a bottom thickness matrix and a wall thickness matrix as well, and those settings cannot be changed; the carbon fibers are set with a fixed layer thickness of 0.125 mm; no monitoring devices to check printing quality.

A sketch view of Markforged Two with the CFR technique is shown in Fig. 1.

Sample Fabrication

Tensile Test Samples

Rectangular geometry following the dimensions in ASTM standard D3039 [21] was utilized to fabricate the test samples. Even though dog bone test samples have been used in other research papers, we believe that using this rectangular geometry is ideal to reduce the discontinuity of the test samples. The sizes of the tensile test sample

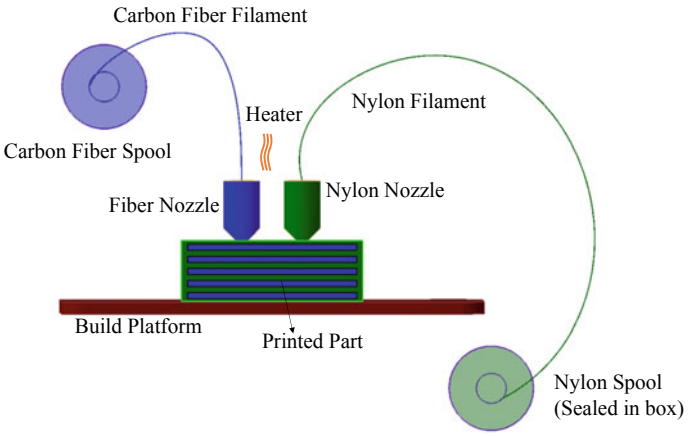

Fig. 1 Sketch view of Markforged Two with CFR technique

are 1 mm (thickness) × 15 mm (width) × 250 mm (length). Given that the clamping section might be damaged since the thickness was too small, taps were used during the tensile testing. However, glued taps might not be able to bear the shear loads from the tensile test, thus test samples and taps were printed together with clamping thickness up to 4 mm. Figure 2 shows a tensile test sample with printed taps.

In this paper, the printing parameters including infill density, layer thickness, infill pattern, and fiber fill type were determined except the carbon fiber volume fracture. Carbon fiber volume fraction was defined by modifying the number of fiber layers in the test sample, which can be figured out in Table 1. Test samples with carbon fiber volume percentages of 0%, 21%, 42.3%, 63.6%, and 68.7% were fabricated for tensile testing.

The tensile test samples were fabricated with a fixed layer thickness of 0.125 mm. From the previous literatures, we learned that the tensile properties of nylon carbon fiber test samples would not change significantly as a function of filling density [5]. Thus, we chose the default value of Markforged Two, which was 37%. It was also found that the fibers along the longitudinal direction (at 0 degree) were able to withstand stretching and bear the highest loads [4]. The type of fiber filling used for the nylon carbon fiber samples was isotropic. Isotropic fibers have demonstrated a

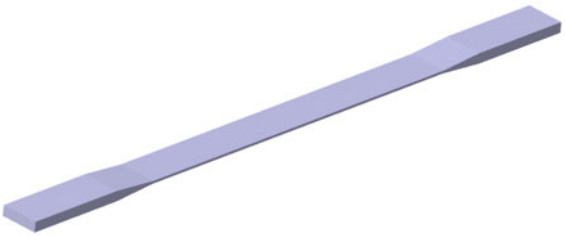

Fig. 2 Tensile test sample created by 3D software CATIA

Table 1 Printing process parameters for tensile test samples

Para-meters	Nylon	Nylon-21%CF	Nylon-42.3% CF	Nylon-63.6% CF	Nylon-68.7% CF
Fiber fill type	Isotropic	Isotropic	Isotropic	Isotropic	Isotropic
Fill density	37%	37%	37%	37%	37%
Fill pattern	Solid fill	Rectili-near	Rectili-near	Rectili-near	Rectili-near
Fiber layers	0	2	4	6	8
Wall layers	1	1	1	1	1
Roof layers	–	3	2	1	1
Bottom layers	–	3	2	1	1
Concentric fiber rings	2	2	2	2	2
Fiber orientation (angle)	0	0	0	0	0
Total layers	8	8	8	8	10
Fiber volume fraction	0	21%	42.3%	63.6%	68.7%

higher capacity to resist fatigue damage compared to concentric filling patterns [13]. Figure 3 shows the filling pattern and fiber orientation for the nylon and nylon carbon fiber tensile test samples.

The nylon and nylon carbon fiber tensile test samples are referred to as Nylon, Nylon-21%CF, Nylon-42.3%CF, Nylon-63.6%, and Nylon-68.7%CF samples based on the carbon fiber volume fractions. Five samples were printed for each volume fraction of fibers.

To compare with Markforged datasheet [20], the thickness of 68.7%CF samples was increased to 1.25 mm while the width and length were kept constant.

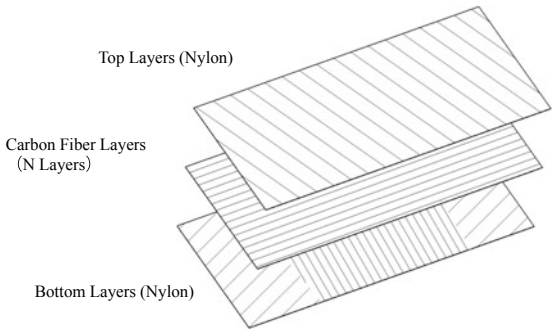

Fig. 3 Fill pattern and fiber orientation of nylon and nylon carbon fiber tensile test samples

Flexure Test Samples

The flexure test samples were printed in rectangular geometry following the requirements in ASTM standard D790 [22]. The dimensions of the flexure test samples are 3.2 mm (thickness) × 12.7 mm (width) x 125 mm (length). Figure 4 shows a flexure test sample created by 3D software CATIA.

The flexure test specimens were also fabricated with those parameters fixed including infill pattern, fiber fill type, layer thickness, and infill density. Test specimens with carbon fiber volume percentages of 0%, 20.5%, 40.7%, 57.8%, and 76.7% were printed, which are addressed in Table 2. All of them were fabricated with a layer thickness of 0.125 mm. Figure 5 shows the fill pattern and fiber orientation of nylon and nylon carbon fiber flexure test samples.

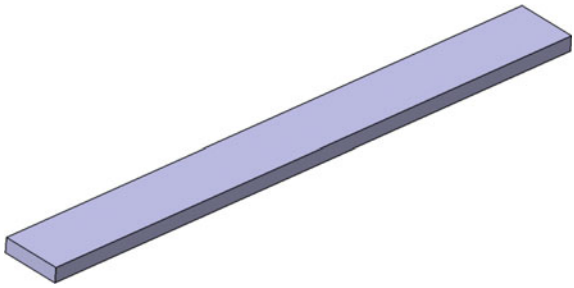

Fig. 4 Flexure test sample created by 3D software CATIA

Table 2 Printing process parameters for flexure test samples

Para-meters	Nylon	Nylon-20.5% CF	Nylon-40.7% CF	Nylon-57.8% CF	Nylon-76.7% CF
Fiber fill type	Iso-tropic	Iso-tropic	Iso-tropic	Iso-tropic	Iso-tropic
Fill density	37%	37%	37%	37%	37%
Fill pattern	Solid fill	Rectili-near	Rectili-near	Rectili-near	Rectili-near
Fiber layers	0	6	12	18	24
Wall layers	1	1	1	1	1
Roof layers	–	10	8	4	1
Bottom layers	–	10	8	4	1
Concentric fiber rings	2	2	2	2	2
Fiber orientation (angle)	0	0	0	0	0
Total layers	26	26	26	26	26
Fiber volume fraction	0	20.5%	40.7%	57.8%	76.7%

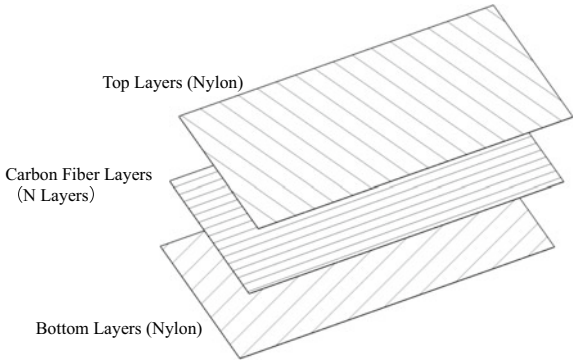

Fig. 5 Fill pattern and fiber orientation of nylon and nylon carbon fiber flexure test samples

The nylon and nylon carbon fiber flexure test samples are referred to as Nylon(F), Nylon-20.5%CF, Nylon-40.7%CF, Nylon-57.8%, and Nylon-76.7%CF samples based on the carbon fiber volume fractions. Three samples were printed for each volume fraction of fibers.

Sample Testing

Tensile testing was performed as per ASTM standard D3039/3039 M [21]. An Instron 5800 Series Universal Testing System was used for the tensile testing with a strain rate of 2 mm/min. Twenty-five samples consisting of different carbon fiber volume fractions (Pure Nylon, 21%CF, 42.3%CF, 63.6%CF, and 68.7%CF) were printed. The test repeats five times for each type of sample.

Flexure testing was performed as per ASTM standard D790 [22]. Fifteen samples (Pure Nylon, 20.5%CF, 40.7%CF, 57.8%CF, and 76.7%CF) were printed. A 16:1 span-to-thickness setup was conducted for the flexure testing. The Instron 5800 Series Universal Testing System was also used for the flexure testing with a speed of 1.365 mm/min. The test was repeated three times for each type of sample.

Results and Discussion

Tensile Testing Results

The nylon and nylon carbon fiber tensile test samples were tested as per ASTM standard 3039/3039 M [21]. After testing, the raw data were analyzed and transformed into strength (modulus)-carbon fiber volume fraction diagrams, from which many properties of the composites can be observed.

Figure 6 shows the tensile properties of pure nylon and nylon carbon fiber samples. Table 3 lists the average tensile testing results for each type of sample. From Table 3, the average strength of 68.7% carbon fiber volume fraction is close to 700 MPa, which is about 92% of the value listed in the datasheet [20]. The average strength of pure nylon is 18.77 MPa, which is only half of the value listed in the datasheet [20]. For the average young's modulus, the measured values are all lower than half the values given in the datasheet [20].

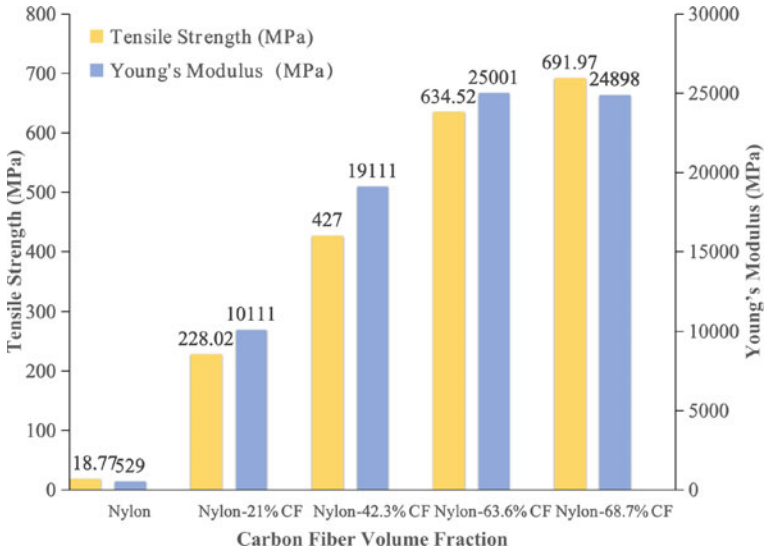

Fig. 6 Tensile properties of pure nylon and nylon carbon fiber samples

Table 3 Tensile strength and Young's modulus for nylon and nylon carbon fiber samples

Tensile strength (MPa)	Nylon	Nylon-21%CF	Nylon-42.3% CF	Nylon-63.6% CF	Nylon-68.7% CF
Average	18.77	228.02	427.00	634.52	691.97
St.dev	0.17	14.18	17.58	23.65	25.28
Datasheet [20]	36	–	–	–	760
Young's Modulus (MPa)	Nylon	Nylon-21%CF	Nylon-42.3% CF	Nylon-63.6% CF	Nylon-68.7% CF
Average	529	10,111	19,111	25,001	24,898
St.dev	33	354	324	1649	2001
Datasheet [20]	1700	–	–	–	57,000

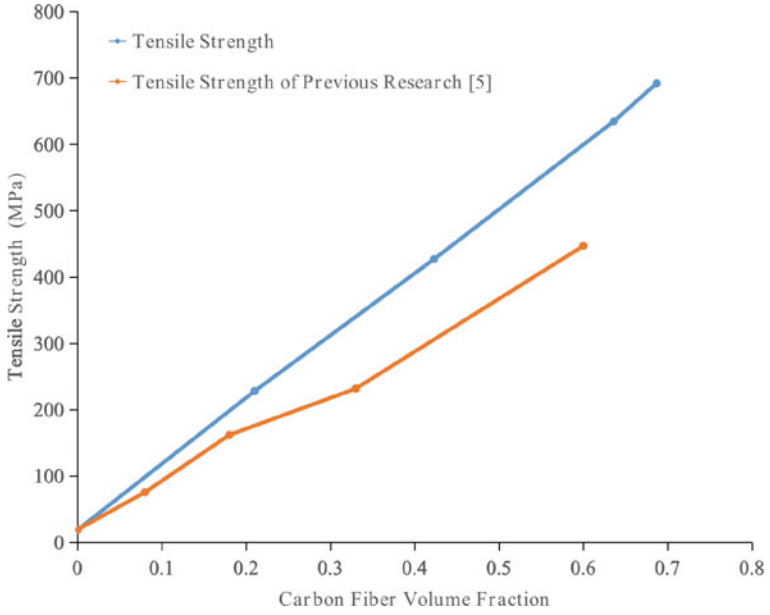

Fig. 7 Comparison with previous research [5] on tensile testing results of CCFR

Figure 7 shows the relationship of carbon fiber volume fraction and the tensile strength of 3D printed continuous carbon fiber reinforced composites. It demonstrates a linear relationship between the carbon fiber volume fraction and the average tensile strength, and the blue slope is almost a straight line.

Tensile Testing Discussion

The highest carbon fiber volume fraction of the tensile test samples is only 68.7%, which demonstrates the test samples have a relatively weak capacity to resist stretching. Therefore, Young's modulus values are relatively low compared to the datasheet [20].

The test results were also compared to previous studies [5] on tensile strength in Fig. 7. From Fig. 7, it can be found that when the carbon fiber volume fraction is less than 20%, they match very well. It is also found that the tensile testing results of pure nylon samples are consistent. However, both are only half of the value listed in the datasheet [20]. With the increasing of carbon fiber volume (more than 20%), the stresses are different due to the different dimensions of tensile test samples and printing process parameters. Previous studies on tensile strength used dog bone test samples conforming to ASTM D638 [5]. The dog bone test samples had some discontinuities in the 3D printing which would lead to the reduction of stresses.

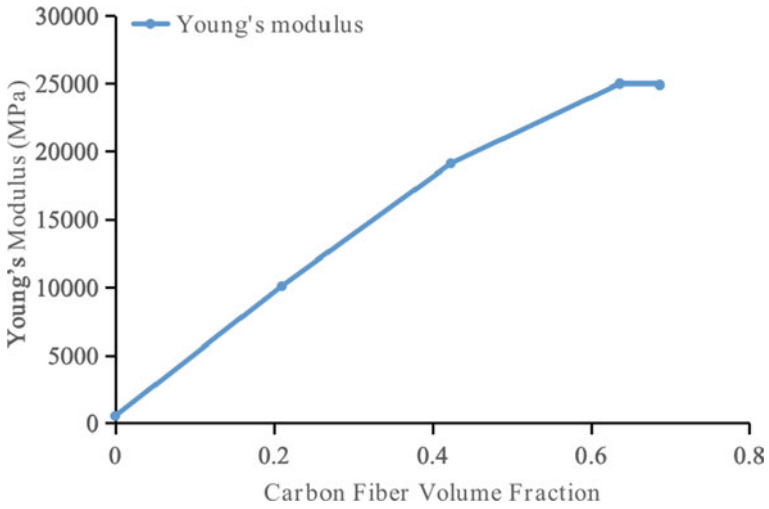

Fig. 8 Relationship of carbon fiber volume fraction and Young's modulus

Figure 8 shows the relationship of carbon fiber volume fraction and Young's modulus of 3D printed continuous carbon fiber reinforced composites. It was observed that Young's modulus increased significantly with the increase of carbon fiber volume fraction as well.

In tensile tests, it was also noted that all the samples failed close to the tabs where the samples were clamped. This is because the cross-sectional area varies, which is where the samples were expected to fail [23]. The other type of failure was along the longitudinal direction. Figure 9 presents the failures of the nylon 42.3% CF tensile testing samples. For nylon-68.7%CF tensile testing samples, several drop-off points were discovered in the stress–strain curve close to ultimate failure, which is shown in Fig. 10. Tensile failure and fracture patterns need to be further analyzed and investigated.

Flexure Testing Results and Discussion

Flexure testing is commonly performed in research and engineering analysis to assess the behaviors of materials. The nylon and nylon carbon fiber flexure test samples were tested as per ASTM standard D790 [22]. Figure 11 shows the flexure properties of nylon and nylon carbon fiber samples. Table 4 lists the average tensile testing results for each type of sample.

Other flexure test results found that the concentric infill pattern exhibited a better flexural strength with 43.5% weight carbon fiber [19]. The observed premature failures were due to interlayer delamination associated with the manufacturing process of 3D printing [9]. Since most 3D printers do not have monitoring devices, such as

Fig. 9 The failures of Nylon-42.3%CF tensile test samples (50% represents half carbon fiber layers and half nylon layers, and for this type of test samples, the carbon fiber volume fraction is 42.3%)

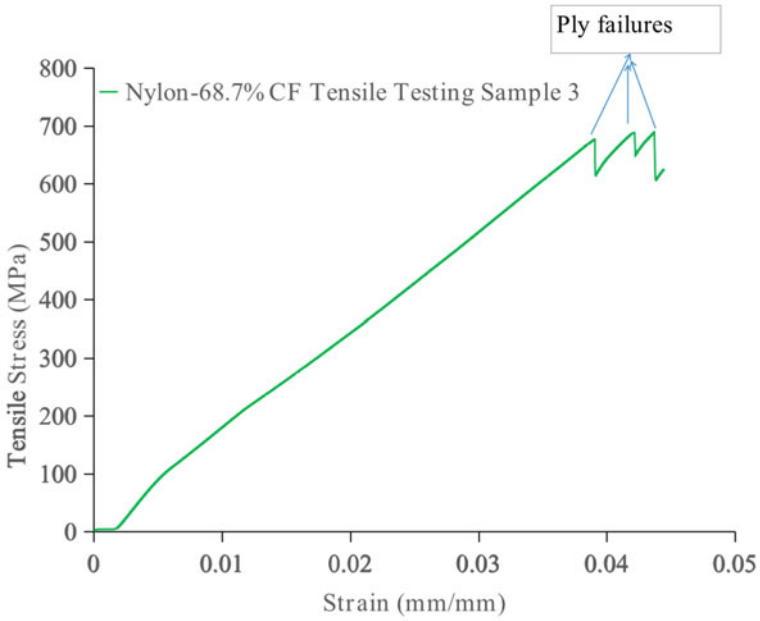

Fig. 10 Failure behavior of Nylon-68.7%CF tensile test samples

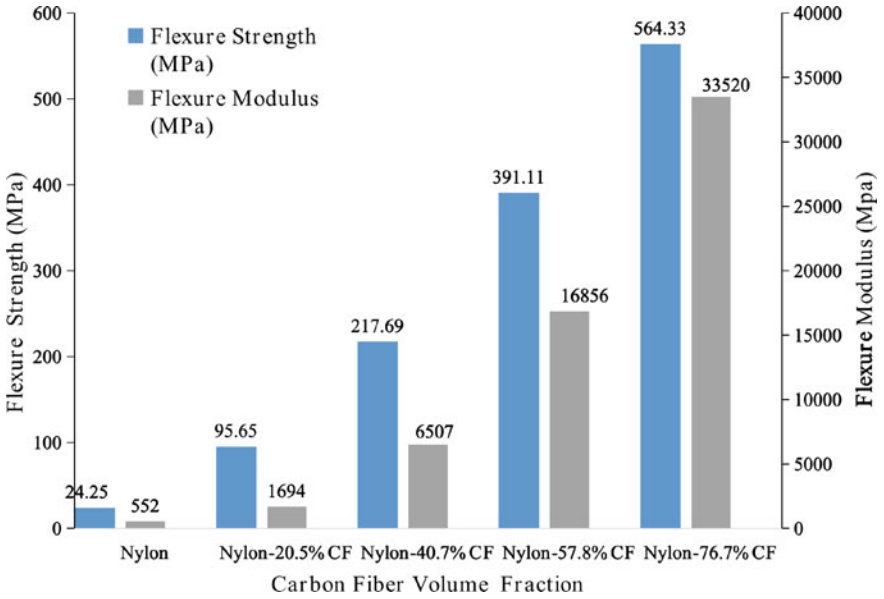

Fig. 11 Flexure properties of nylon and nylon carbon fiber samples

Table 4 Flexure test results for nylon and nylon carbon fiber samples

Flexure strength (MPa)	Nylon	Nylon-20.5% CF	Nylon-40.7% CF	Nylon-57.8% CF	Nylon-76.7% CF
Average	24.25	95.65	217.69	391.11	564.33
St. dev	3.60	4.06	7.35	3.97	8.84
Datasheet [20]	50	–	–	–	540
Flexure strength (MPa)	Nylon	Nylon-20.5% CF	Nylon-40.7% CF	Nylon-57.8% CF	Nylon-76.7% CF
Average	552	1694	6507	16,856	33,520
St. dev	94	110	220	138	713
Datasheet [20]	1400	–	–	–	50,000

high-definition cameras, it is difficult to determine the quality of the internal printing of test samples. In this study, it was also observed that failure occurred layer by layer especially in Nylon-76.7% CF samples, which is shown in Fig. 12. There are some drop-off points observed in the flexure stress–strain curve close to the ultimate failure. Figure 13 demonstrates the effect of carbon fiber volume fraction on flexure strength and flexure modulus. It is found that with an increment of carbon fiber volume fraction, the flexure strength and modulus increase proportionally.

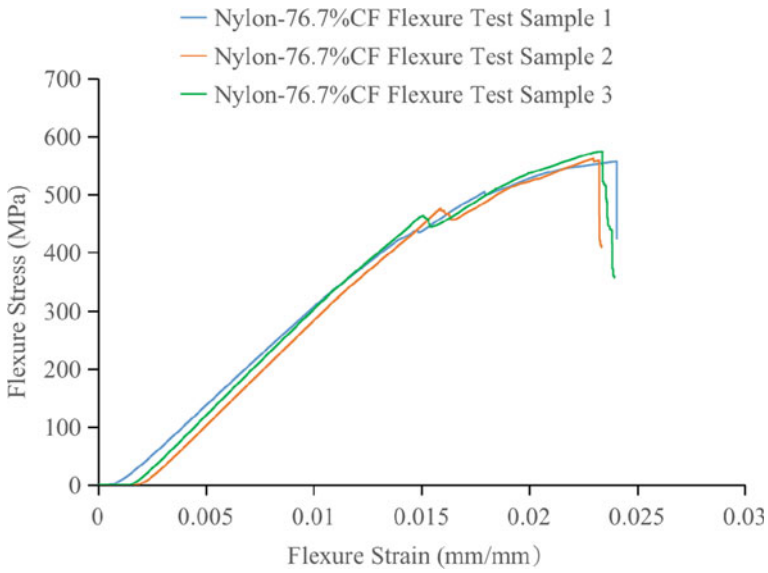

Fig. 12 Stress strain diagram for Nylon-76.7CF flexure test samples

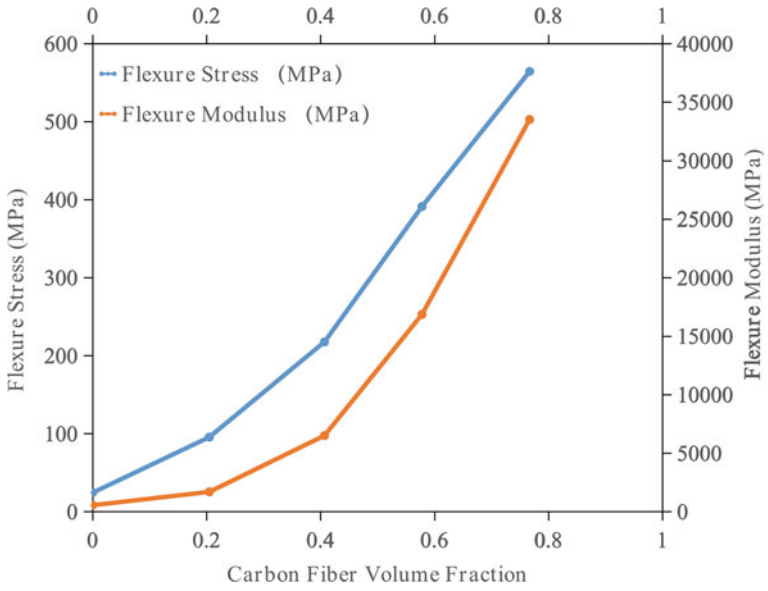

Fig. 13 The effect of carbon fiber volume fraction on flexure strength and flexure modulus

The flexure strength of Nylon-76.7%CF samples agrees very well with the value in the datasheet while the other measured values in Table 4 are about half the values listed in the datasheet [20].

Conclusion

The main goal of this paper was to investigate the tensile and flexural properties of 3D printed continuous carbon fiber reinforced composites and compare the test data with previous literatures and datasheet provided by the Markforged company. Several limitations and influencing factors in the fabrication and testing of the specimens were also presented in this paper. By conducting this investigation, the following conclusions can be drawn:

- The maximum average tensile strength obtained in this paper is 691.97 MPa and the average Young's modulus is 24.898 GPa; the maximum average bending strength is 564.33 MPa and the flexure modulus is 33.52 GPa.
- The average tensile strength of Nylon-68.7%CF samples is 92% of the value in datasheet [20]. The flexure strength of Nylon-76.7%CF samples agrees very well with the value in the datasheet while the other measured values are only about half the values listed in the datasheet.
- There is a linear relationship between the carbon fiber volume fraction and the average tensile strength. With the increment of carbon fiber volume fraction, the flexure strength and flexure modulus increase proportionally as well as Young's modulus.
- Some failure phenomena were observed in the tensile and bending tests, and it was confirmed that as the volume fraction of carbon fibers increased, some fiber layers were successively pulled off and the failure phenomena became more pronounced. However, the failure and fracture modes still need to be further analyzed and investigated.

Several reasons might explain the measured values in this paper are only about half the values listed in the datasheet [20] and they are addressed briefly as below:

- Different shapes and sizes of test specimens,
- Different specimen processing, such as if nylon layers were removed prior to datasheet testing to ensure the maximum fiber volume fraction,
- Different 3D printer parameter settings,
- Different printing times and ambient temperatures

Nowadays, in view of the widespread application of 3D printed fiber reinforced composites, it becomes more crucial to explore various behaviors and properties of them. This work provides some experience and insights for further research and potential applications of 3D printed continuous carbon fiber reinforced nylon composites.

References

1. Tian XY et al (2022) 3D printing of continuous fiber reinforced polymer Composites: development, application, and prospective. Chinese J Mech Eng Addi Manuf Front 1(1):100016. https://doi.org/10.1016/j.cjmeam.2022.100016
2. Li JH et al (2022) Additively manufactured fiber-reinforced composites: a review of mechanical behavior and opportunities. J Mater Sci Technol 119:219–244. https://doi.org/10.1016/j.jmst.2021.11.063
3. Markforged 3D Printer Types & Technologies https://markforged.com/resources/learn/3d-printing-basics
4. Saeed K et al (2022) Characterization of continuous carbon fiber reinforced 3D printed polymer composites with varying fiber volume fractions. Compos Struct 282:115033. https://doi.org/10.1016/j.compstruct.2021.115033
5. Mohammadizadeh M et al (2021) Tensile performance of 3D-printed continuous fiber-reinforced nylon composites. J Manuf Mater Process 5(3):68. https://doi.org/10.3390/jmmp5030068
6. Mohammadizadeh M et al (2019) 3D Printed fiber reinforced polymer composites—structural analysis. Compos Part B Eng 175:107112. https://doi.org/10.1016/j.compositesb.2019.107112
7. Chen Y et al (2021) Compression behaviours of 3D-printed CF/PA metamaterials: experiment and modelling. Int J Mech Sci 206:106634. https://doi.org/10.1016/j.ijmecsci.2021.106634
8. Iragi M et al (2019) Ply and interlaminar behaviours of 3D printed continuous carbon fibre-reinforced thermoplastic laminates; effects of processing conditions and microstructure. Addi Manuf 30:100884. https://doi.org/10.1016/j.addma.2019.100884
9. Araya-Calvo M et al (2018) Evaluation of compressive and flexural properties of continuous fiber fabrication additive manufacturing technology. Addit Manuf 22:157–164. https://doi.org/10.1016/j.addma.2018.05.007
10. Tang HB et al (2021) Longitudinal compression failure of 3D printed continuous carbon fiber reinforced composites: an experimental and computational study. Compos Part A Appl Sci Manuf 146:106416. https://doi.org/10.1016/j.compositesa.2021.106416
11. Saeed K et al (2021) Predication of the in-plane mechanical properties of continuous carbon fibre reinforced 3D printed polymer composites using classical laminated-plate theory. Compos Struc 259:113226, https://doi.org/10.1016/j.compstruct.2020.113226
12. Caminero M et al (2018) Interlaminar bonding performance of 3D printed continuous fibre reinforced thermoplastic composites using fused deposition modelling. Polym Test 68:415–423. https://doi.org/10.1016/j.polymertesting.2018.04.038
13. Imeri A et al (2018) Fatigue analysis of the fiber reinforced additively manufactured objects. Int J Adv Manuf Technol 98(9–12):2717–2724. https://doi.org/10.1007/s00170-018-2398-7
14. Li LJ et al (2022) Mechanical characterization of 3D printed continuous carbon fiber reinforced thermoplastic composites. Compos Sci Technol 227. https://doi.org/10.1016/j.compscitech.2022.109618
15. Caminero M et al (2018) Impact damage resistance of 3D printed continuous fibre reinforced thermoplastic composites using fused deposition modelling. Compos Part B Eng 148:93–103. https://doi.org/10.1016/j.compositesb.2018.04.054
16. Lupone F, Padovano E et al (2022) Experimental characterization and modeling of 3D printed continuous carbon fibers composites with different fiber orientation produced by FFF process. Polymers 14(3):426. https://doi.org/10.3390/polym14030426
17. Peng Y et al (2019) Synergistic reinforcement of polyamide-based composites by combination of short and continuous carbon fibers via fused filament fabrication. Compos Struct 207:232–239. https://doi.org/10.1016/j.compstruct.2018.09.014
18. Chen AY et al (2021) Carbon-fiber reinforced polymer composites: a comparison of manufacturing methods on mechanical properties. Int J Lightweight Mater Manuf 4(4):468–79. https://doi.org/10.1016/j.ijlmm.2021.04.001

19. Yu TY et al (2019) Tensile and flexural behaviors of additively manufactured continuous carbon fiber-reinforced polymer composites. Compos Struct 225: 111147. https://doi.org/10.1016/j.compstruct.2019.111147
20. Markforged data sheet available online: https://markforged.com/materials/data-sheet/
21. ASTM D3039/D3039M-17 (2017) Standard test method for tensile properties of polymer matrix composite materials, ASTM International, West Conshohocken
22. ASTM D790-17 (2017) Standard test methods for flexural properties of unreinforced and reinforced plastics and electrical insulating materials, ASTM International, West Conshohocken
23. Van Der Klift F et al (2016) 3D printing of continuous carbon fibre reinforced thermo-plastic (CFRTP) tensile test specimens. Open J Compos Mater 6:18–27. https://doi.org/10.4236/ojcm.2016.61003

Part V
Metallurgical Processing Analysis and Characterization

Physico-Chemical Characteristics of Deselenized Copper Anode Slime

Jhumki Hait and Navneet Singh Randhawa

Abstract During copper extraction from copper concentrate, the slime generated in a copper electrorefining tank contains many valuable elements like Cu, Ni, Se, Te, Au, Ag, Pt, Pd, Bi, Sb, along with As, Pb, Fe, Ba, etc. The conventional process for the treatment of the slime includes initial copper extraction by sulphuric acid leaching and extraction of tellurium by the cementation process. After copper and most of the tellurium extraction, the residue is treated for selenium recovery. The slime after selenium extraction is called deselenized slime, mainly containing Au, Ag, Pt, Pd, Pb, As, Te, Bi, Sb, and Ba. The complex nature of the deselenized slime makes further processing of the slime more complicated. This paper illustrates the detailed characterization, including physical, chemical, and mineralogical studies of the deselenized anode slime that can provide valuable information, including the morphology, which can help in process development for further metals recovery from the slime.

Keywords Deselenized slime · Copper slime · Anode slime · Characterization · Mineralogy

Introduction

Copper is mainly extracted by pyro or hydrometallurgical methods based on the type of ore [1]. Anode slime is the byproduct generated during the electrorefining of impure copper anode produced in the pyrometallurgical extraction of copper. Copper anode slime generated at the bottom of the electrolytic cell contains many valuable metals, including precious metals and some rare elements. Though the elements present in the anode slime are more or less the same all over the world, their compositions may vary from refinery to refinery based on the composition of the copper ore and the processing steps followed for extraction of copper from the ore. The slime primarily consists of copper, nickel, selenium, tellurium, lead,

J. Hait (✉) · N. S. Randhawa
CSIR-National Metallurgical Laboratory, Jamshedpur, India
e-mail: jhumki@nmlindia.org

M. Zhang et al. (eds.), *Characterization of Minerals, Metals, and Materials 2023*, The Minerals, Metals & Materials Series
https://doi.org/10.1007/978-3-031-22576-5_10

bismuth, arsenic, antimony, barium, gold, silver, and platinum group metals (PGM), mainly in compound form along with some other minor elements [2]. Based on the composition of anode slime, various methods have been adopted at different refineries to recover valuable metals [3]. The conventional method of treating the anode slime is the initial de-copperization of the slime by sulphuric acid leaching in the presence of air/oxygen at atmospheric/elevated pressure conditions. During the de-copperization process, some amount of tellurium (35–60%) is also dissolved in the leach solution along with copper, which is recovered as copper telluride with the addition of copper chips in the solution [4–7]. The de-copperized slime is then subjected to deselenization for the recovery of selenium as selenium oxide. After removing selenium from the slime, the deselenized slime, which is still complex, is further treated for the recovery of precious metals from the slime. The precious metals recovery process again depends upon the composition and the mineralogical phases present in deselenized slime [8, 9].

Recent investigations have shown that mineralogical methods can provide valuable information for hydrometallurgical processes by studying the reaction products and inferring chemical reactions that occur in the process. The information obtained can also help the process development or improve the existing process technologies [10]. However, products like copper refinery anode slimes are challenging to characterize because they are very fine-grained (mostly below 10 μm) and heterogeneous in nature. The fine grain sizes make phase identification by scanning electron microscopy SEM- EDX and microbeam techniques difficult because the analytical resolution of the instrument frequently exceeds the size of the particles being analyzed [11]. The products' heterogeneity significantly reduces the capability of X-ray powder diffraction (XRD) to identify the important phases/constituents. Consequently, it becomes necessary to resort to various mineralogical techniques with different sample preparation methods for characterizing copper anode slime. The present work examined the deselenized anode slime sample with various characterization techniques. Each method provided complementary information about the products that may help in processing the sample for further extraction of valuable/precious metals.

Experimental

The deselenized anode slime sample was obtained from an Indian copper electrorefining plant. Representative samples of the slime were used for characterization studies. Characterization studies include physical properties, chemical analysis, TG–DTA, XRD, SEM-EDX, and EPMA. The particle size analysis and the thermal analysis were carried out respectively by Particle Size Analyzer [Model: Malvern-Master Size, Make-UK] and Thermo Gravimetric Analyzer [Model: Linseis STAPT

1600, Make-Germany]. The chemical composition of the slime sample was determined using two different instrumental techniques: Inductively Coupled Plasma—Optical Emission Spectrometer (ICP-OES) [Model: VISTA-PMX, CCD simultaneous, Make-Australia] and X-ray Fluorescence spectrometer. The XRD analysis of the sample was performed using a diffractometer [Model: Bruker AXS D8, Make-Germany] to determine the significant phases. The slime sample was investigated by imaging both secondary and backscattered electrons. The sample was investigated using a scanning electron microscope (SEM) equipped with EDS [Model: Thermo Noran NSS-300, Make-USA] to identify the mineral species and their morphologies. The as-received powdery slime sample coated with carbon was examined directly using SEM. Quantitative electron microprobe analysis (EPMA) [by Model: JXA-8230 Electron Probe Micro Analyzer (JEOL, Japan)] was also conducted to determine the exact compositions of the various species.

Results and Discussion

Physical Characterization

Physical Properties

The physical properties of the deselenized anode slime are given in Table 1. The table shows the form, color, odor, and density of the deselenized slime.

Particle Size Analysis

The particle size of the as-received sample was analyzed and depicted in Fig. 1, representing the size distribution of the deselenized anode slime particles. The result shows that the particle size in the sample, which was less than a 10 μm size fraction, accounted for about 25%, the size ranging from 10 to 75 μm accounted for about 55%, and that of more than 75 μm accounted for 20%. It was also found that none of the particles was more than 330 μm in size. The mean particle size of the sample was determined to be 27.54 μm.

Table 1 Physical properties of deselenized anode slime

Feature	Property
Form	Solid powder
Color	Gray
Odor	Odorless
Density	2.1

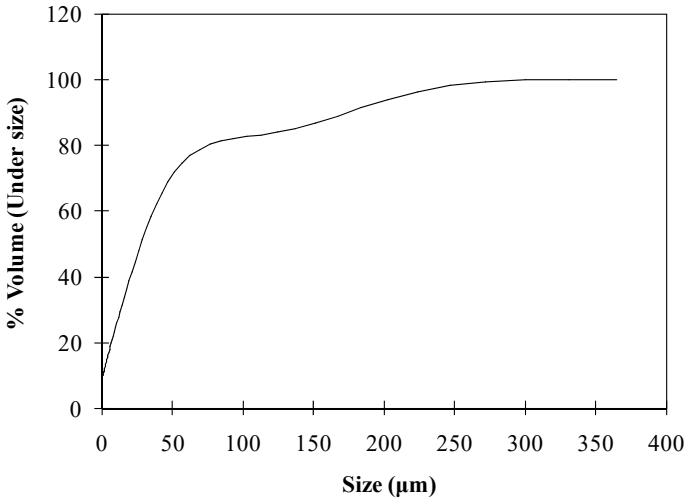

Fig. 1 Particle size analysis of deselenized anode slime

Thermal Analysis

The thermo-gravimetric (TG) and differential thermal analysis (DTA) of the deselenized anode slime sample were carried out at the heating rate of 10 °C/min in the presence of air and depicted in Fig. 2. In the TG curve, gradual loss of mass can be seen over the entire temperature range. Change in mass starts from 200 °C falling steadily up to the endpoint, i.e., 1000 °C. This curve is often attributed to decomposition reactions occurring throughout the heating path. The deselenized anode slime contained several phases that might undergo decomposition at different temperatures giving rise to a steady loss in mass.

Apart from the significant drift spread over the entire temperature range in the DTA curve, an exothermic peak at 400 °C and an endothermic peak at ~ 950 °C are observed. An exothermic peak at 400 °C (spanning from 300 to 490 °C) mainly represents the oxidation reaction of selenium to selenium dioxide. However, an endothermic peak at around 950 °C indicates the decomposition of some metallic compounds (tellurides, etc.) present in deselenized anode slime.

Chemical Characterization

Chemical Analysis

Table 2 represents the elemental analysis of the slime by ICP-OES and XRF methods. Both techniques show lead, silver, bismuth, tellurium, arsenic, and barium as major constituents with a significant amount of gold. Platinum and palladium were also

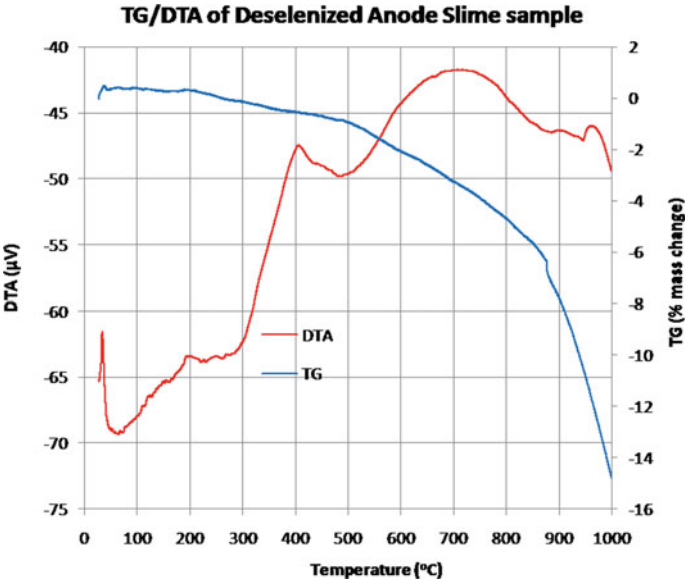

Fig. 2 TG–DTA curves of deselenized anode slime

found at trace levels. The table also shows the presence of about 0.60–0.75% Se which accounts for selenium unrecovered during the deselenization process. XRF analysis also determined sulfur and chlorine in appreciable quantities. Other elements quantified by XRF are silicon, iron, strontium, aluminum, etc.

Mineralogical Characterization

X-ray Powder Diffraction

The X-ray powder diffraction method conclusively identifies crystalline phases and is found to be effective even for fine-grained material such as anode slime. Some indication of non-stoichiometry or solid solution species can also be inferred with the help of the XRD technique. The XRD data of the deselenized anode slime sample (Fig. 3) indicates the presence of $BaSO_4$, (Ba, Pb)SO_4, Ag_2SO_4, and $Bi_{3.73}Sb_{0.27}O_{6.0+x}$ as the major phases and AgCl, Ag_3AuTe_2, and Ag_2O as the minor phases. The XRD method is advantageous with analytical techniques such as SEM-EDX or electron microprobe analysis.

Table 2 Chemical composition of deselenized anode slime

ICP-OES method		XRF method	
Constituent	Wt.-%	Constituent	Wt.-%
Cu	0.61	Cu	0.75
Pb	12.02	Pb	12.32
Sb	0.76	Sb	1.09
Bi	6.80	Bi	6.12
Se	0.60	Se	0.75
Te	2.22	Te	2.45
As	1.82	As	1.62
Ba	22.41	Ba	23.59
Pt	0.01	Pt	–
Pd	0.02	Pd	–
Au	1.62	Au	0.81
Ag	22.36	Ag	23.11
		S	6.98
		Cl	2.54
		Si	0.78
		Fe	0.19
		Sr	0.16
		Al	0.14

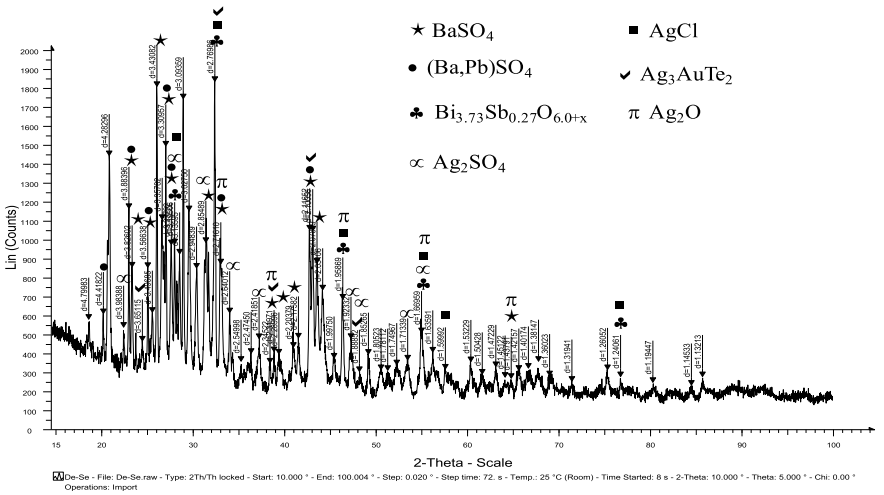

Fig. 3 X-ray diffractogram of deselenized anode slime

Scanning Electron Microscopy

Because of their high magnification-high resolution capabilities, scanning electron microscopy and EDX are probably the most effective single technique for studying the reaction products during hydrometallurgical processing. Figures 4 and 5 represent the secondary electron micrograph of the bulk deselenized slime sample with corresponding EDX analyses. Both figures show the general morphology of the slime particles with the composition.

SEM-EDX analysis of the as-received deselenized anode slime sample indicates the presence of various phases in a variety of morphologies. Figure 5 presents the secondary electron image of the deselenized slime. In this figure, the spot analyses

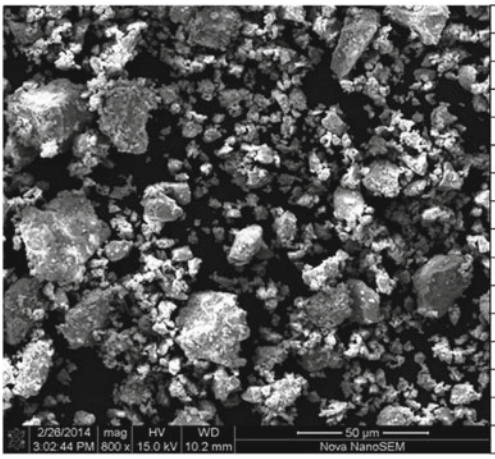

Element	Wt %
O K	05.07
AsL	01.10
SeL	00.62
SiK	00.38
PtM	01.00
AuM	01.32
S K	07.54
PbM	17.56
BiM	00.00
PdL	01.80
AgL	11.63
SbL	02.25
TeL	03.60
BaL	34.03
CuK	12.09

Fig. 4 SEM image of deselenized anode slime (Bulk analysis determined by EDX is shown in adjoining table)

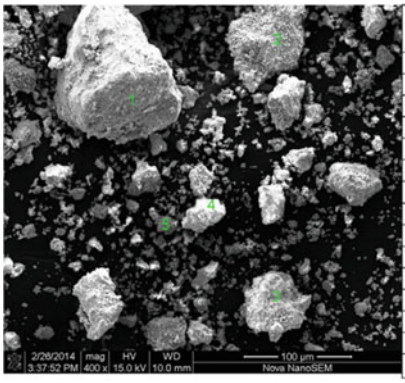

Element	Pt. 1 (wt. %)	Pt. 2 (wt. %)	Pt. 3 (wt. %)	Pt. 4 (wt. %)	Pt. 5 (wt. %)
O K	10.94	08.84	05.75	09.91	11.43
AsL	02.49	00.98	02.07	00.74	00.91
SeL	00.52	00.00	00.78	00.38	00.42
SiK	00.36	00.54	00.35	00.20	00.17
PtM	00.00	00.32	00.35	00.00	00.00
AuM	00.22	01.07	01.24	00.78	00.43
S K	09.24	12.10	05.78	09.53	10.22
PbM	10.71	31.56	12.24	25.81	04.79
BiM	08.02	00.83	17.18	01.96	04.54
PdL	00.38	00.00	01.11	00.47	00.29
AgL	31.66	11.65	24.10	18.51	13.12
SbL	00.88	00.00	05.78	08.61	02.59
TeL	02.98	00.00	06.68	02.65	02.08
BaL	16.13	28.70	09.28	16.45	44.85
CuK	05.49	03.40	07.31	03.99	-

Fig. 5 SEM-EDX point analysis of deselenized anode slime

at five points are included, along with the general morphology of the slime. The elemental analyses of all the points (1–5) clearly show the presence of PGMs and precious metals, with silver being the major metal, varying from 11.65–31.66%. Though the analyses at points 2, 3 and 5 show the absence of platinum, a good amount of silver associated with other elements is noticed. SEM-EDX studies also reveal a significant amount of barium (44.85%) present at point 5 with other elements.

Microbeam Analysis

Microbeam technique such as electron microprobe analysis (EPMA) is one of the most useful methods for determining phase composition. For detailed characterization, EPMA was conducted for mineralogical study of the deselenized slime sample, and the details are discussed below. Figure 6 illustrates the general morphology of the deselenized slime sample. The corresponding table summarizes the compositional data for the slime sample at two locations. The data indicate the average composition for various elements. Both the figures show the presence of barium, lead, silver, arsenic, sulfur, and oxygen in considerable amounts, along with the presence of minor amount of chlorine, antimony, tellurium, and precious metals. The data also confirm the heterogeneity for PGM and gold in the deselenized sample.

Figures 7 and 8 depict the backscattered electron image showing the presence of various elements in the deselenized slime sample. The corresponding tables present the compositions at various spots in the slime.

The electron microbeam analysis shows that the slime sample predominantly contains barium, lead, Sulphur, and oxygen at various spots. The presence of silver is also observed at some spots, along with other elements. This confirms the presence

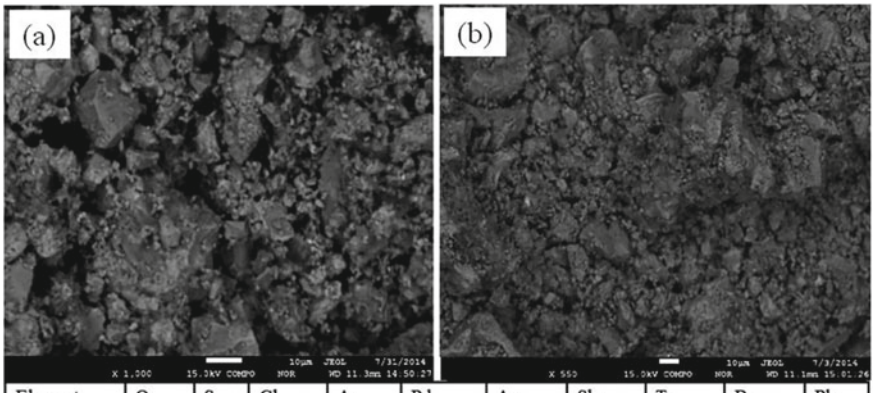

Element	O	S	Cl	As	Pd	Ag	Sb	Te	Ba	Pb
6(a), ms%	16.68	7.16	1.04	4.98	1.60	20.35	1.57	3.18	23.82	19.62
6(b), ms%	16.40	7.17	1.25	10.08	2.11	18.51	1.89	2.32	20.23	19.79

Fig. 6 **a**, **b** EPMA images and bulk analyses of deselenized anode slime sample

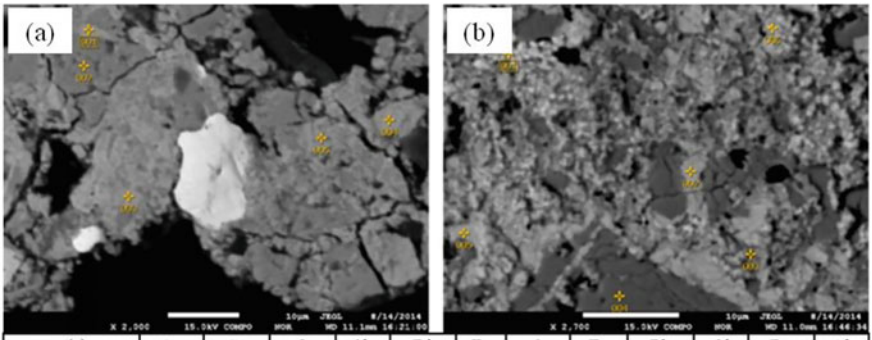

(a)	Ag	As	O	Sb	Bi	Te	S	Fe	Pb	Cl	Ba	Al
Spot 1(wt. %)	-	-	11.19	-	-	-	8.2	-	62.91	-	17.70	-
Spot 2(wt. %)	-	-	22.91	-	-	-	14.94	-	-	-	62.15	-
Spot 3(wt. %)	-	-	12.61	-	-	-	8.40	-	60.49	-	18.49	-
Spot 4(wt. %)	-	-	11.16	-	-	-	8.39	-	62.99	-	17.49	-
Spot 5(wt. %)	41.94	8.17	10.06	-	-	-	3.19	-	15.55	-	9.30	-
(b)												
Spot 1(wt. %)	10.31	43.02	12.49	-	34.18	-	-	-	-	-	-	-
Spot 2(wt. %)	33.89	19.96	11.94	2.51	-	5.5	0.93	2.20	15.54	4	-	-
Spot 3(wt. %)	-	-	10.93	-	-	-	8.05	-	67.33	-	13.69	-
Spot 4(wt. %)	-	-	20.03	-	-	-	11.92	-	13.85	-	54.20	-
Spot 5(wt. %)	3.99	4.55	13.89	-	-	-	7.89	-	54.18	-	15.5	-
Spot 6(wt. %)	84.32	-	2.70	-	-	-	-	-	-	12.2	-	0.79

Fig. 7 **a**, **b** EPMA images and spot analyses of deselenized anode slime sample

of various sulfates in varied proportions. The compositions at other spots are also indicated in the tables.

A few particles comprising Au, Ag & Pb, and Au & Ag with some oxygen inclusion have also been observed in spot analyses. The presence of minor/trace amounts of other elements like Sb, Bi, and Te at some spots as inclusion in the major phases in varied amounts depicts their association in the slime particles (Figs. 7b and 8b). Some spots with high arsenic content have also been found during analysis. Arsenic is mainly associated with silver, antimony, bismuth, and oxygen (Figs. 7b and 10a). Sometimes a significant amount of lead is also observed in arsenic-containing particles (Figs. 9a and 10b). The elemental composition in the point analyses of each spot shown in Figs. 6–11 is appended with the respective images/plots.

In terms of bulk sample EPMA, the presence of gold is not reflected (Fig. 6). However, in the preceding discussion, it emerges that some amount of gold is present in alloy/compound form in the bulk sample (observed at high magnification × 1500), as can be seen in (Figs. 8b, 9, and 11). The deselenized slime sample contains a significant amount of silver, mainly present with oxygen (Figs. 7, 8, and 9b) or in association with tellurium, arsenic, and bismuth (Figs. 7b and 10). The observation also shows some silver in alloy form with gold (Fig. 9a).

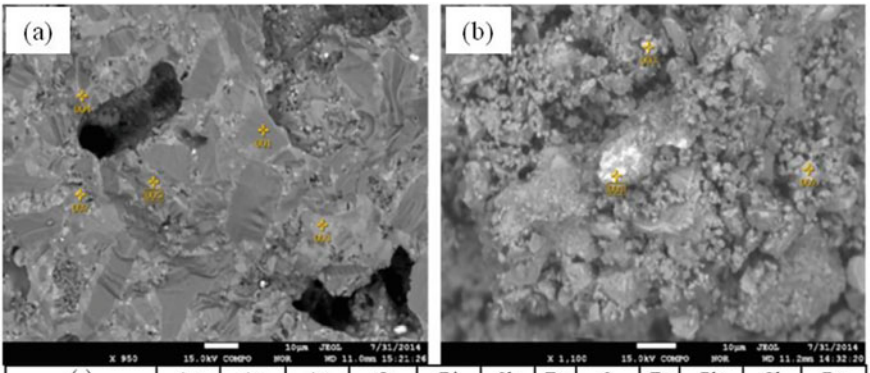

(a)	Ag	Au	As	O	Bi	Sb	Te	S	Fe	Pb	Cl	Ba
Spot 1(wt. %)	-	-	-	15.15	--	-	-	10.06	-	46.01	-	28.78
Spot 2(wt. %)	-	-	-	7.46	-	-	-	10.32	-	55.23	-	26.99
Spot 3(wt. %)	9.92	-	-	18.13	-	-	-	8.80	-	41.72	-	21.44
Spot 4(wt. %)	7.16	-	0.08	15.44	-	-	-	10.59	-	10.27	-	45.65
Spot 5(wt. %)	4.46	-	46.69	9.16	39.68	-	-	-	-	-	-	-
(b)												
Spot 1(wt. %)	16.10	11.42		17.63		6.21	-	5.03	-	23.14	1.17	19.28
Spot 2(wt. %)	16.29	80.43		3.29		-	-	-	-	-	-	-
Spot 3(wt. %)	8.57	-		15.66		-	-	8.21	-	48.90	-	18.66

Fig. 8 **a**, **b** EPMA images and spot analyses of deselenized anode slime sample

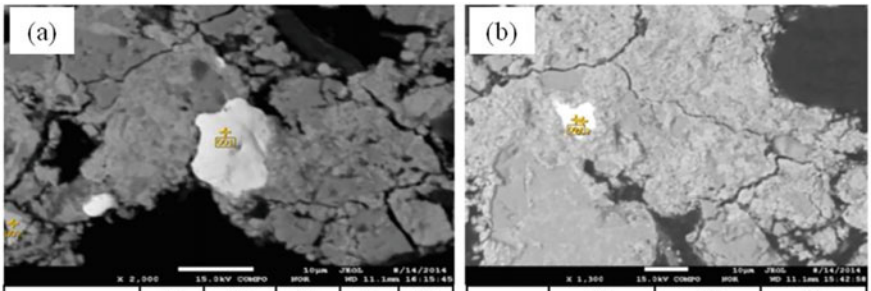

	Au	Ag	Pb	As	O
Spot 1 (wt. %)	88.95	11.05	-	-	-
Spot 2 (wt. %)	-	-	56.34	38.0	5.63

	Au	Ag	O
Wt. %	89.6	8.25	2.07

Fig. 9 **a**, **b** EPMA images and spot analyses of deselenized anode slime sample showing Ag and Au abundant particles

Conclusion

The deselenized anode slime sample received from an Indian copper electrorefining plant was characterized in detail. The characterization studies revealed the chemical composition and various mineralogical phases present in the slime. About 23% Ag,

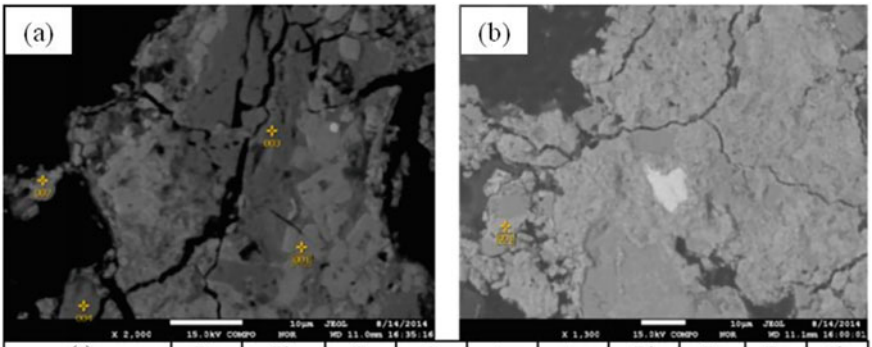

(a)	Ba	Pb	S	O	Ag	As	Bi	Te	Fe	Sb
Spot 1 (wt. %)	13.72	59.79	6.99	11.17	8.33	-	-	-	-	-
Spot 2 (wt. %)	-	-	-	11.0	16.27	38.35	27.19	4.93	-	2.26
Spot 3 (wt. %)	55.96	14.97	12.03	17.04	-	-	-	-	-	-
Spot 4 (wt. %)	55.52	16.53	11.53	16.42	-	-	-	-	-	-
(b)										
	-	9.16	-	15.58	17.45	41.21	-	10.04	2.22	-

Fig. 10 **a**, **b** EPMA images and spot analyses of deselenized anode sime sample showing **a** Ba and Pb rich, and **b** tellurium-rich particles

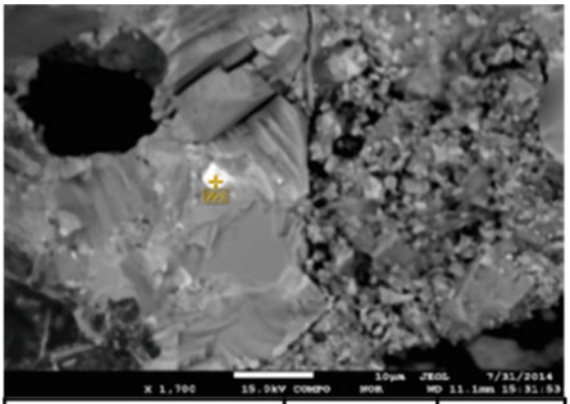

	Au	O
Spot 1 (wt. %)	97.89	2.11

Fig. 11 EPMA image and spot analysis of deselenized anode slime sample showing Au particle

0.8–1.6% Au, 0.01% Pt, and 0.02% Pd, along with high amount of Ba (23%), Pb (12%), and other elements, is observed in chemical analysis. XRD studies also reveal the presence of an abundant quantity of Ba, Pb, and Ag, where Ba is mainly present as $BaSO_4$ and also frequently associated with Pb. Ag is mainly found to be present as oxide and sometimes present as an alloy with Au and Te. Preferential association of various elements has also been observed by EPMA analysis. The association

of various elements present in a complex material like the slime sample may help investigate further processing the sample to extract precious /valuable metals.

Acknowledgements The authors are thankful to the Director, CSIR-National Metallurgical Laboratory, Jamshedpur, India, for kind permission to publish the paper.

References

1. Mark ES, King MJ, Kathryn CS, Davenport WG (2011) Extractive Metallurgy of Copper, 5th Edn, Elsevier Ltd. Amsterdam, Netherland
2. Randhawa NS, Hait J (2019) Characteristics and processing of copper Refinery anode slime. In: Hossain Md. Anawar, Valdimir S, Abhilash (Eds) Sustainable and economic waste management: resource recovery techniques. CRC Press, pp 263–287
3. Hait J, Jana RK, Sanyal SK (2009) Processing of copper electrorefining anode slime : a review. Miner Process Extr Metall 118(4):240–252
4. Mokmeli M, Dreisinger D, Wassink B (2014) Thermodynamics and kinetics study of tellurium removal with cuprous ion. Hydrometallurgy 147–148:20–29
5. Liang G, Shu W, Cai Y, Zheng W (1997) New technology of recovering selenium and tellurium from copper anodic slimes. Rare Met. (English Edition) 16(2):117–121
6. Amer AM (2003) Processing of copper anodic-slimes for extraction of valuable metals. Waste Manage 23(8):763–770
7. Wang C, Li S, Wang H, Fu J (2016) Selenium minerals and the recovery of selenium from copper refinery anode slimes. J South Afr Inst Min Metall 116(6):593–600
8. Makuei FM, Senanayake G (2018) Extraction of tellurium from lead and copper bearing feed materials and interim metallurgical products—A short review. Miner Eng 115:79–87
9. Kilic Y, Kartal G, Timur S (2013) An investigation of copper and selenium recovery from copper anode slimes. Inter J Miner Proc 124:75–82
10. Chen TT, Dutrizac JE (2005) Mineralogical characterization of copper anode and the anode slime from La Caridad Copper Refinery of Mexicana de Caobre. Metall Mater Trans B (36B):229–240
11. Hait J, Jana RK, Sanyal SK (2004) Mineralogical characterization of copper electrorefining Anode Slime and its Leached Residues. Ind Eng Chem Res 43(9):2079–2087

Transformation of Desulfurization Performance of Activated Carbon During Multiple Cycles of Adsorption and Regeneration and Its Mechanism

Rongguang Xu, Yong Zhang, Manxiang Zhao, and Huaiying Ma

Abstract Transformation of desulfurization performance of activated carbon during multiple cycles of adsorption and regeneration was investigated and the causes were analysed. Results showed that the desulphurization performance of activated carbon descended gradually with cycle times of adsorption and regeneration increasing. The properties of activated carbon were characterized by using XRD, XPS, TGA, and FT-IR. Results showed that the acidic functional groups contents on activated carbon surface increased with multiple cycles, which would affect its desulfurization performance. Besides, the content of calcium sulfate in activated carbon increased with multiple cycles, which would be another reason for that. Furtherly, the formation process of calcium sulfate was analysed.

Keywords Activated carbon · Desulfurization · Acidic functional group · Calcium sulfate

Introduction

With the continuous progress of environmental governance, air pollutants emitted by industry have become the key issue of environmental protection, and the treatment of pollutants in the steel industry has become the most important. Flue gas emissions of sintering and pelletizing, which are important steps in iron and steel smelting, are so huge, accounting for more than 50% of total flue gas emissions in the process [1]. In recent years, China has paid special attention to energy conservation and emission reduction in the steel industry and has issued a number of targeted policies. Such as sulfur dioxide and nitrogen oxides emission thresholds are lower than 35 mg/m^3 and 50 mg/m^3, respectively. Furtherly, some local governments have even

R. Xu (✉) · Y. Zhang · M. Zhao · H. Ma
Beijing Key Laboratory of Green Recyclable Process for Iron & Steel Production Technology, Beijing 100043, P. R. China
e-mail: xrg1220@163.com

Research Institute of Technology, Shougang Group Co. Ltd, Beijing 100043, P. R. China

M. Zhang et al. (eds.), *Characterization of Minerals, Metals, and Materials 2023*, The Minerals, Metals & Materials Series
https://doi.org/10.1007/978-3-031-22576-5_11

put forward stricter emission requirements, for instance, sulfur dioxide and nitrogen oxides emission thresholds were reduced to 20 mg/m^3 and 30 mg/m^3, respectively.

Activated carbon (AC) has significant advantages in the purification of industrial flue gas and can remove multiple pollutants at the same time, such as sulfur dioxide, nitrogen oxides, and dioxins. Besides, it does not produce waste water in the process and can be recycled for many times. Therefore, it is widely recommended to purify flue gases in the steel industry.

In industrial application, moving bed is often used for the removal of pollutants by AC, mainly including countercurrent flow and cross flow. AC flows downward through the reactor under the action of gravity. The flue gas flows transversely through AC bed of the reactor when the cross flow bed is used, while the flue gas flows upward through the reactor from below when the counter flow bed is used. After a certain period of desulfurization reaction, different forms of sulfur will be adsorbed in the pores of AC, and the pores and active sites will be covered. Therefore, AC needs to be sent to the regenerator for treatment to recover its activity. After multiple cycles of adsorption and regeneration, the performances of AC may change, which would affect the removal effect of pollutants.

In this work, transformation of desulfurization performance of AC during multiple cycles of adsorption and regeneration was investigated. Variation of surface properties and chemical compositions of AC were studied, and the influences of which on desulfurization performance were analyzed.

Experiment Results and Discussion

Influence of Cycles of Adsorption and Regeneration on Desulfurization Performance of AC

The experiments were carried out in a fixed-bed reactor at 120 °C, and the inner diameter of which is 25 mm. The loading volume of AC was 10 mL in every tests, and the mass is about 6.5 g. The simulated gas consisted of 6% O_2 and 8% water vapor and $1000*10^{-6}$ SO_2, and balanced by N_2, and the space velocity is 400 h^{-1}. When the penetration concentration of SO_2 reached 10% of its entrance concentration, then stopped the experiments. The penetration adsorption capability of SO_2 was calculated by penetration curve integration. Furtherly, AC was regenerated in N_2 atmosphere for 2 h. Until then, a cycle of adsorption and regeneration of AC was completed.

The effect of cycle times of adsorption and regeneration on desulfurization performance of AC were shown in Fig. 1. Results showed that the desulphurization performance of AC descended gradually with cycle times of adsorption and regeneration increasing, which is consistent with the result of PI et al. [2].

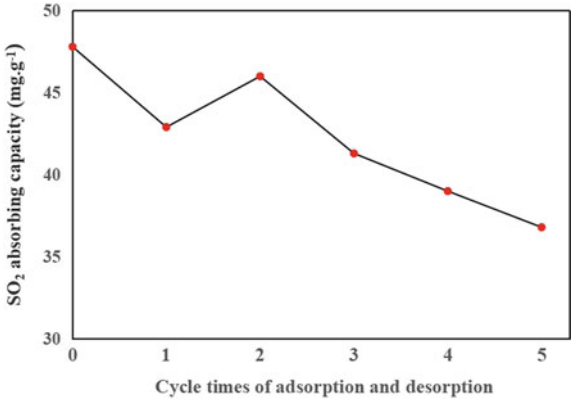

Fig. 1 Effect of cycle times of adsorption and regeneration on SO_2 absorbing capacity of AC

Transformation of Functional Groups of AC

To study the transformation of functional groups of AC, Fourier transform infrared spectroscopy (FT-IR) of AC with different cycle times of adsorption and regeneration was analyzed.

As is seen in Fig. 2, the strong absorption peak in the region of 3100 cm^{-1} ~ 3600 cm^{-1} of the sample is caused by the O–H bond of chemisorbed water and the stretching vibration of the surface hydroxyl-COOH bond in the hydrogen bond region. Spectrum peak at 1632 cm^{-1} is due to the stretching vibration of C = C bond and C = O in carboxylic acid. Spectrum peak at 1583 cm^{-1} has no significant change, which is attributed to the stretching vibration of C = C bond and of C = O bond of polyaromatics. The spectral peak at 1385 cm^{-1} is caused by the stretching

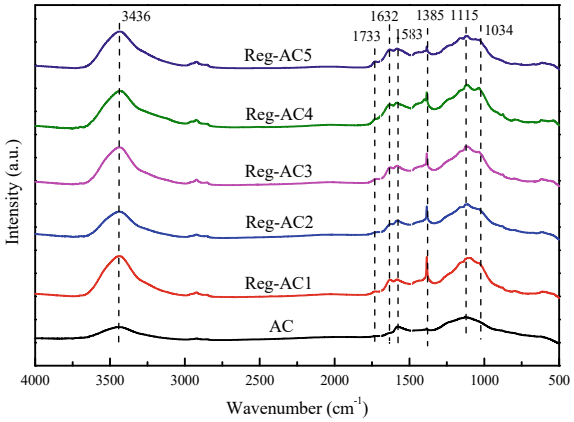

Fig. 2 FTIR spectra of fresh and regenerated AC

vibration of the carboxyl group. After multiple cycles of adsorption and regeneration, the intensity of the peak gradually increases, indicating that more esters, anhydrides, and carboxyl groups are formed during the cycle of adsorption and regeneration [3].

After recycling, the content of carboxyl functional groups increases, and hydrogen bonds (O = C-O–H·· = O = S = O) are formed between O = C–OH and SO_2 [3]. Therefore, the enhanced broad peak at 1385 cm^{-1} may be due to the high sulfur capacity in the regenerated AC, which indicates that it is conducive to the adsorption of SO_2. Besides, the stretching vibration of C-O corresponds to the gradual enhancement of spectral peaks in the range of 1000 cm^{-1} ~ 1300 cm^{-1}, indicating the formation of lactones, phenols, and ethers during regeneration [3].

Therefore, acidic functional groups on AC surface are generated during multiple cycles of adsorption and regeneration.

Transformation of Chemical Composition of AC

In this section, AC which was used to purify industrial sintering and pelletizing flue gas was investigated.

Chemical compositions of AC and its ash residues before and after regeneration are shown in Table 1 and Table 2, respectively. Comparing with fresh AC, chemical compositions of AC after multiple cycles have changed significantly, including volatile matter, carbon, oxygen, nitrogen, and sulfur content. Among those above indexes, oxygen content increased evidently, which is consistent with the increase of oxygen-containing functional group of AC after multiple cycles. There were no obvious differences between ash residues compositions of fresh AC and those of ACs used in sintering and pelleting, which underwent multiple cycles of adsorption and regeneration. In addition, all ACs contain a certain amount of calcium.

X-ray diffraction (XRD) spectrums of ACs were shown in Fig. 3. The characteristic peaks of calcium sulfate in the XRD spectrum of fresh AC ($2\theta = 25.4°$ and $2\theta = 31.4°$) are not obvious, indicating that the calcium sulfate content in fresh AC is low. The characteristic peaks of calcium sulfate in the XRD spectrum of AC for pelleting began to appear, indicating that AC for pellets contains a small amount of calcium sulfate. The characteristic peaks of calcium sulfate in the XRD spectrum of AC for

Table 1 Chemical composition of AC before and after regeneration

Sample	A_d	V_d	C_d	H_d	O_d	N_d	$S_{t,d}$
Fresh AC	12.6	5.16	83.28	0.65	2.18	0.66	0.63
AC for pelletizing before regeneration	11.09	17.33	74.49	0.35	9.96	1.51	2.60
AC for pelletizing after regeneration	11.93	11.09	80.18	0.29	5.43	1.31	0.86
AC for sintering before regeneration	10.91	16.54	74.73	0.40	9.44	1.68	2.84
AC for sintering after regeneration	11.53	10.00	78.66	0.41	6.24	1.90	1.26

Table 2 Chemical compositions of ash residues of AC before and after regeneration

Sample	SiO_2	Al_2O_3	CaO	Fe_2O_3	MgO	Na_2O	K_2O	TiO_2	P_2O_5	MnO	Cl
Fresh AC	38.76	24.7	11.46	9.25	4.01	1.1	0.6	0.71	0.45	0.15	0.002
AC for pelletizing before regeneration	41.02	26.51	12.13	8.92	3.75	0.91	0.68	0.87	0.45	0.13	0.004
AC for pelletizing after regeneration	40.75	26.60	11.56	8.51	3.82	1.02	0.64	0.76	0.42	0.14	0.004
AC for sintering before regeneration	39.22	24.98	11.66	9.17	3.93	0.95	1.26	0.79	0.44	0.13	0.001
AC for sintering after regeneration	38.39	24.44	12.60	9.98	3.93	0.94	1.15	0.84	0.43	0.15	0.005

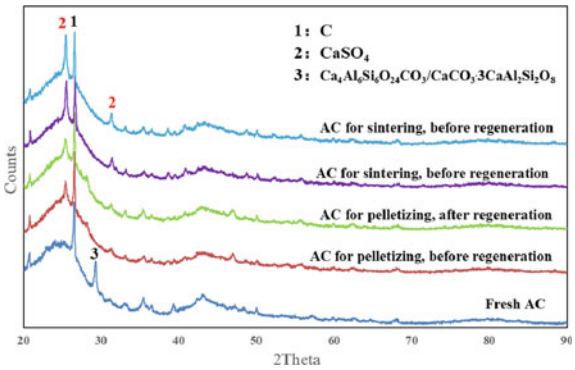

Fig. 3 XRD spectrums of ACs

sintering are more distinct prominent, indicating that AC for pelletizing contains a considerable amount of calcium sulfate.

Therefore, calcium sulfate content in the AC for sintering is the most, and that of fresh AC is the least.

In addition, the peak intensity of calcium sulfate in the XRD spectrum of AC before and after regeneration hardly changed, no matter whether it was used for sintering or pelletizing, indicating that sulfur in the form of calcium sulfate has not been largely resolved under the current regeneration conditions.

X-ray photoelectron spectroscopy (XPS) spectrums of ACs are shown in Fig. 4. The characteristic peak of S2p in XPS spectrum of fresh AC is 162.8 eV, indicating that fresh AC only contains sulfur in the form of thiophene. While characteristic peaks of S2p in the XPS spectrum of ACs for sintering and pelletizing, which had undergone multiple cycles of adsorption and regeneration, are in the range of 168.56 eV ~ 168.74 eV, indicating that those ACs mainly contain sulfur in the form of sulfate [4].

The characteristic peak intensity of sulfur in the XPS spectrum of AC after regeneration significantly weakened, indicating that most of the sulfur in AC was decomposed. However, combining with XRD results, there is sulfur in the form of calcium sulfate still in the AC after regeneration, which would affect its desulfurization performance [2].

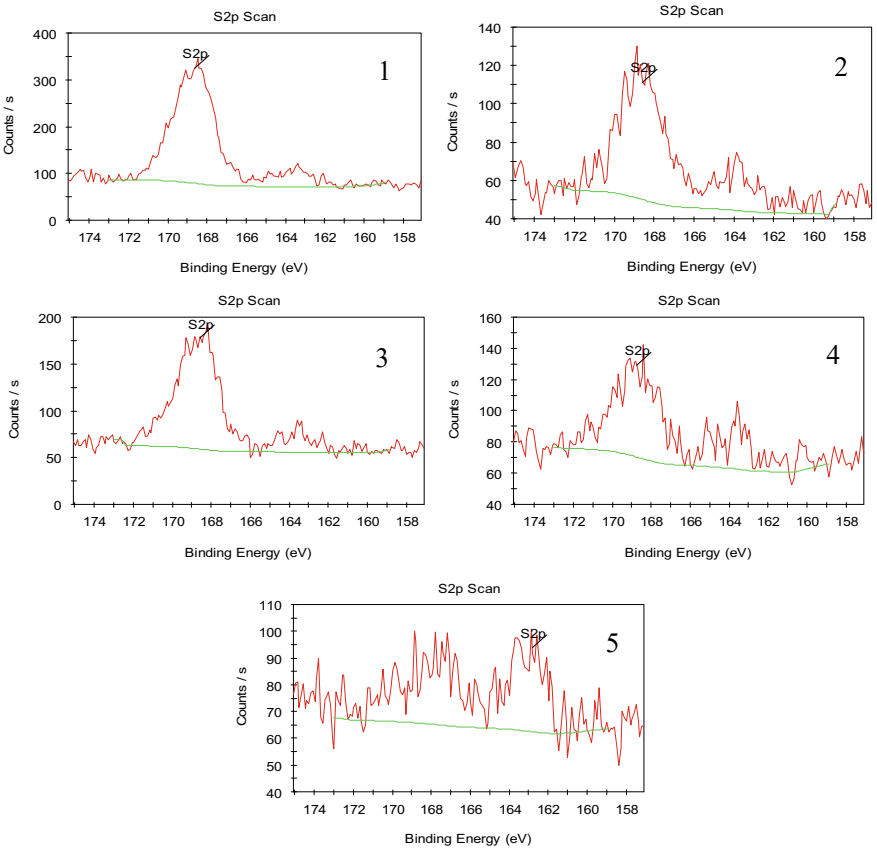

Fig. 4 XPS spectrums of ACs, (1-AC for sintering before regeneration; 2-AC for sintering after regeneration; 3-AC for pelletizing before regeneration; 4-AC for pelletizing after regeneration; 5-fresh AC)

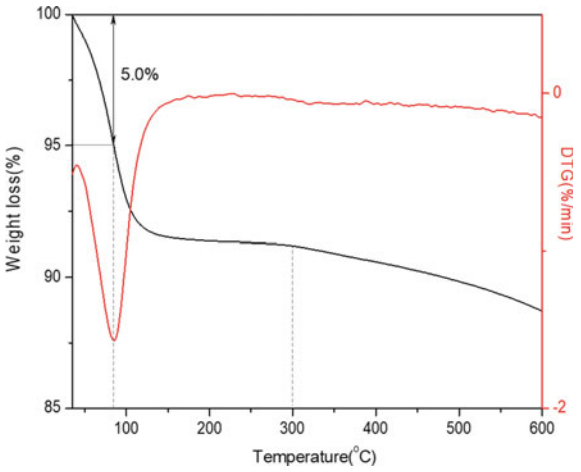

Fig. 5 TG and DTG curves of ACs

The AC after regeneration, which was used to purify sintering flue gas with multiple cycles of adsorption and regeneration, was taken to carry out thermal gravimetric analysis (TGA). Heating system: from room temperature to final temperature of 600°C with a heating rate is 10°C/min.

The thermal gravimetry (TG) and differential thermal gravimetry (DTG) curves of ACs are shown in Fig. 5. There is a peak within 100 °C corresponding to the weight loss of adsorbed water/lattice water, and no weight loss peak of sulfur dioxide. Even if the temperature rose to 600 °C sulfur in the form of calcium sulfate was still not decomposed, which is related to the high decomposition temperature of calcium sulfate.

Sources of Calcium Sulfate

There are two sources of calcium sulfate.

(1) Sulfur dioxide is chemically adsorbed from flue gas, and sulfuric acid is generated with water. Sulfuric acid reacted with calcium in AC to generate calcium sulfate.

(2) Ash in flue gas contained some soluble sulfate, which can react with the calcium in AC to form calcium sulfate. As is shown in Table 1, sulfur content in AC for sintering after regeneration is more than that for pelletizing. As is shown in Fig. 6, soluble sulfate was found in ash in sintering flue gas, but not found in ash in pelletizing flue gas. It is supposed that soluble sulfate may react with the calcium in AC to form calcium sulfate.

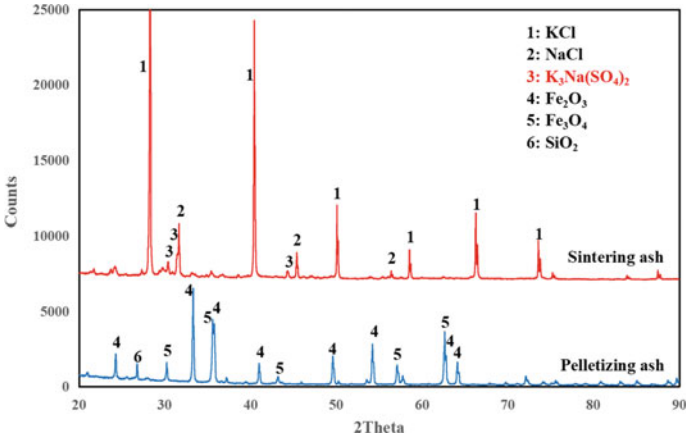

Fig. 6 XRD of ash in sintering and pelletizing flue gas

Conclusions

Desulphurization performance of AC descended gradually with cycle times of adsorption and regeneration increasing. Formation of acidic functional groups on AC surface and calcium sulfate in AC would be the two reasons for desulfurization performance degradation.

References

1. Zhang HL, Shi Q, Long HM, et al (2017) Analysis on the removal of nitrogen oxides from sintering flue gas//The Chinese society for metals. In: Proceedings of the 2017 sintering flue gas denitrification and comprehensive treatment technology exchange symposium, pp 63–67
2. Pi XX, Sun F, Gao JH et al (2017) Microwave irradiation induced high-efficiency regeneration for desulfurized activated coke: a comparative study with conventional thermal regeneration. Energy Fuels 31(9):9693–9702
3. Zhou JH, Sui ZJ, Zhu J, et al (2007) Characterization of surface oxygen complexes on carbon nanofibers by TPD, XPS and FT-IR. Carbon 45(4):785–796
4. Li C, Zhang HR, Guo YX et al (2021) Effects of inherent pyrite on AC for SO_2 and NO removal and its mechanism. Coal Convers 44(2):9–17
5. Chen P (1996) The application of XPS to studying the forms of organic sulfur in coal desulfurization. Clean Coal Technol 3(2):17–20

Effect of TiO_2 on Slag Fluidity Under Different Atmospheres

Buxin Chen, Jian Hou, Bo Yang, Chenguang Bai, Jian Han, Shengfu Zhang, and Meilong Hu

Abstract In this study, we determined the influence of different TiO_2 contents in high-alumina slag under a neutral atmosphere, N_2 atmosphere (without carbon), and reductive atmosphere on blast furnace (BF) slag considering the phase changes, viscosity, melting temperature, and slag structure. The results show that the viscosity and melting temperature of the slag first increase and then decrease in a neutral atmosphere, and the turning point is 5wt%. The slag structure is somewhat complex and then simple. Under an N_2 atmosphere (without carbon), slag viscosity and melting temperature decrease first and then increase, and the turning point is 10wt%. This is because when the TiO_2 content reaches10wt%, the slag begins to appear high melting point phase (TiN). The structure of slag tends to be complicated under a reducing atmosphere. The high melting point phases Ti (C, N) and TiN appear, which makes the slag viscosity and melting property.

Keywords Viscosity · TiO_2 · Atmosphere

Introduction

China's iron ore resources depend on imports; 80% of imported iron ores come from Australia, India, and Brazil. Due to the increase of Al_2O_3 content in the imported ore, the Al_2O_3 content in the slag increases, affecting the slag's metallurgical properties. Many studies examined the effect of the Al_2O_3 content on the viscosity of $CaO–SiO_2–Al_2O_3–(MgO–TiO_2)$ slag, Most researchers point out that, the addition of Al_2O_3 would result in a decrease in the slag temperature and an increase in the slag viscosity, for a fixed heat quantity of the slag [1–4]. In contrast, some studies

B. Chen · B. Yang · C. Bai · S. Zhang · M. Hu (✉)
College of Materials Science and Engineering, Chongqing University, Chongqing 400044, China
e-mail: hml@cqu.edu.cn

J. Hou (✉) · J. Han
Ironmaking R&D Center, Produce and Manufacture Department, HBIS Hansteel, No. 232, Fuxing Road, Handan 056015, Hebei, China
e-mail: houjian1021@163.com

M. Zhang et al. (eds.), *Characterization of Minerals, Metals, and Materials 2023*, The Minerals, Metals & Materials Series
https://doi.org/10.1007/978-3-031-22576-5_12

reported that Al_2O_3 acted as an amphoteric oxide in the CaO–SiO_2–Al_2O_3–(MgO–TiO_2) slag. As the Al_2O_3 content increased, the slag viscosity initially increased and subsequently decreased [5, 6]. According to the literature [7–12], TiO_2 as an alkaline oxide in high-alumina slag reduces slag viscosity. For the CaO-SiO_2-MgO-TiO_2 slag system, Nakamoto et al. [13] found that the viscosity of slag decreased with the increase of TiO_2 concentration. When studying the influence of adding TiO_2 on the structural change of slag, it is generally believed that TiO_2 plays the role of network modifier in the slag, which reduces the viscosity of slag. Chang et al. [14] found that TiO_2 will change the network structure of silicate, breaking the link between silicate and aluminate, depolymerizing slag, and reducing slag viscosity. Zhang et al. [15] studied the effect of the CaO/TiO_2 ratio on the structure of CaO-SiO_2-14wt% Al_2O_3-TiO_2 slag at 1500 °C by molecular dynamics simulation and FT-IR spectroscopy. The results show that replacing CaO with TiO_2 only slightly changes the degree of polymerization, which indicates that TiO_2 has a similar function to Cao, and is a basic oxide. Cheng-bin Shi et al. [16] conducted a Raman spectrum analysis for CaF_2-CaO-Al_2O_3-MgO- (TiO_2) five-element titanium-containing steel electroslag. It was found that the viscosity of the slag decreases with the increase of TiO_2 content in the slag. With the increase of TiO_2 content in the slag, the structural units of Al–O–Al and Q^4 were destroyed, and the structural units of simple Q^2 and $Ti_2O_6^{4-}$ chains increased. Therefore, with the increase of TiO_2 content, the polymerization degree of slag decreases, and the change in slag structure is consistent with the evolution of measured viscosity. Kutuzov [17], Zhao [18], Zhao Guohong [19], and others pointed out that in a reducing atmosphere, Ti can form high melting point compounds TiC and Ti (C, N) with C and N, which makes the slag fluidity worse.

To sum up, at present, the research on the influence of TiO_2 on the structure and properties of slag under different atmospheres is not uniform, and there is no systematic conclusion to guide blast furnace smelting high-alumina raw materials. In this work, experimental tests combined with theoretical were used to research the influence of different TiO_2 content on the performance and structure of slag under different atmospheres, including neutral atmosphere, N_2 atmosphere, and reducing atmosphere.

Methods

Experimental Procedure

According to the composition of slag in Table 1, ~ 180 g slag sample used in the experiment was made of pure analytical reagent. Here, R_2 is binary basicity, defined as the mass percentage ratio of CaO to SiO_2. Before configuration, put the analytical reagent in a muffle furnace at a temperature of 800 °C for 2 h to remove the water in the reagent. After that, the viscosity furnace was heated to 1500 °C for two hours to ensure the complete melting of slag, and the molybdenum bar was stirred every

Table 1 Main chemical composition of the raw materials (wt.%)

Item	R_2	*w*/%				
		CaO	SiO_2	MgO	TiO_2	Al_2O_3
A1	1.25	40.00	32.00	8	3	17
A2	1.25	38.89	31.11	8	5	17
A3	1.25	36.11	28.89	8	10	17
A4	1.25	30.56	24.44	8	20	17
A5	1.25	27.78	22.22	8	25	17
B1	1.25	40.00	32.00	8	3	17
B2	1.25	38.89	31.11	8	5	17
B3	1.25	36.11	28.89	8	10	17
B4	1.25	30.56	24.44	8	20	17
C1	1.25	40.00	32.00	8	3	17
C2	1.25	38.90	31.10	8	5	17
C3	1.25	36.10	28.90	8	10	17
C4	1.25	30.60	24.40	8	20	17

15 min to ensure the mixing of slag. Then, the slag viscosity at this temperature was measured, and the slag viscosity at 1500 °C is obtained. Then, the temperature is reduced to 1300 °C at a cooling rate of 3 °C/min, and the viscosity of slag at each temperature point is measured to obtain the viscosity-temperature curve of slag. At last, the furnace slag was heated to 1500 °C again and kept at a constant temperature for 0.5 h, then the furnace slag was taken out for water quenching, which was convenient for subsequent furnace slag structure analysis. A series of components are protected by argon, B is changed into nitrogen, C is changed into nitrogen and carbon. Before the experiment, the viscometer was corrected with 100 centipoise silicone oil.

Experimental Equipment

The constant temperature viscosity (1500 °C) and viscosity-temperature curve of slag were measured by the rotary drum method. The viscometer is composed of four parts: control cabinet, high-temperature heating furnace, software system, and viscometer. The highest temperature can be heated to 1650 °C, and the heating element and the crucible are separated by a corundum furnace tube to achieve a uniform temperature field. The probe and crucible used in the experiment are made of molybdenum. The molybdenum probe on the viscometer is immersed in the center of the slag and rotates at a certain speed. The internal friction generated by the slag acts on the demand for torque generation. The torque in the test range is related to the viscosity of slag and the rotation speed of the probe.

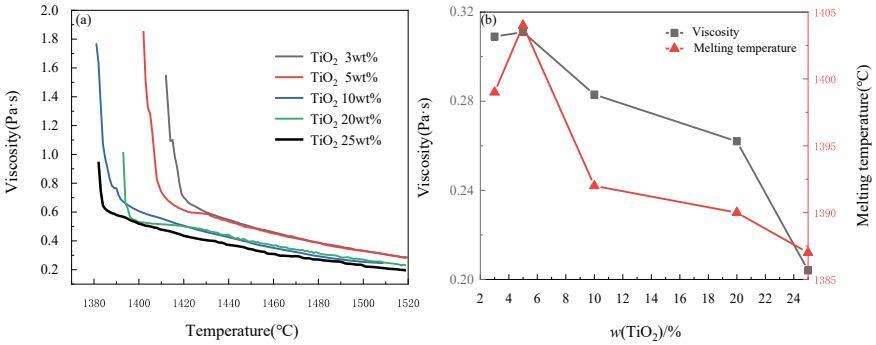

Fig. 1 Changes in the viscosity and melting temperature with varying TiO_2 content in the CaO-SiO_2-17wt%Al_2O_3-8.0wt%MgO-TiO_2 slag in the neutral atmosphere (**a** η–T curves changes with increasing TiO_2 content, **b** the viscosity, melting temperature change with increasing TiO_2 content)

Results and Discussion

Neutral Atmosphere

In the neutral atmosphere, Fig. 1(a) depicts the effects of TiO_2 concentration on the η–T curves of the CaO–SiO_2–MgO–TiO_2–Al_2O_3 slag. The viscosity and the melting temperature dependence of viscosity are shown in Fig. 1(b). Figure 2 depicts the changes in the slag structure units with increasing TiO_2 content (a. single structure units, b. ratio of sum both of $Q^2 + Q^3$and $Q^0 + Q^1$). When the content of TiO_2 increased from 3wt.% to 25wt.%, the viscosity and melting temperature of slag increased first and then decreased. The ratio of complex structure content to simple structure content is expressed by the ratio of $(Q^2 + Q^3)/(Q^0 + Q^1)$, the ratio of $(Q^2 + Q^3)/(Q^0 + Q^1)$ first increases and then decreases, and the structure of slag is complicated first and then simplified. It's the turning point, 5wt.%. When the content of TiO_2 is 25wt.%, the viscosity and melting temperatures of slag are the lowest, which are 0.204 Pa·s and 1387 °C, respectively. This may be because when the content of TiO_2 is 5wt.%, the slag has a high melting point phase (calcium titanate), but in the neutral atmosphere, TiO_2 is mostly Ti hexacoordinate ions, which dilutes the slag.

N_2 Atmosphere

In the N_2 atmosphere, Fig. 1(a) depicts the effects of TiO_2 concentration on the η–T curves of the CaO–SiO_2–MgO–TiO_2–Al_2O_3 slag. The viscosity and the melting temperature dependence of TiO_2 concentration are shown in Fig. 1(b). With the

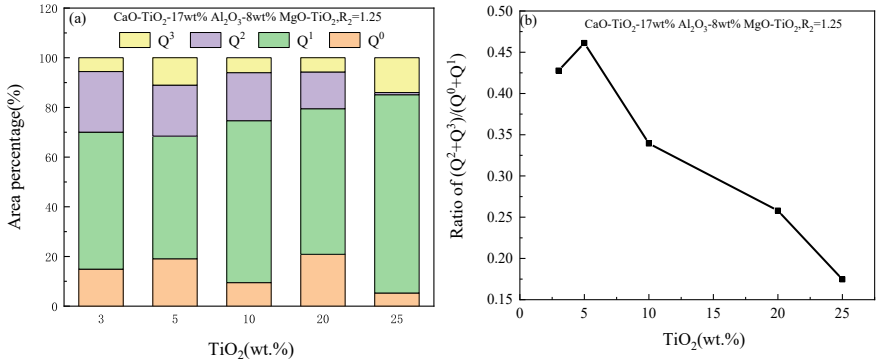

Fig. 2 Changes in the slag structure units with increasing TiO_2 content (**a** single structure units, **b** ratio of sum both of $Q^2 + Q^3$ and $Q^0 + Q^1$)

increase of TiO_2 content from 3wt.% to 20wt.%, the viscosity and melting temperature of slag first decrease and then increase, and the turning point is 10wt.%. When the content of TiO_2 is 10wt.%, the viscosity and melting temperature of slag are the lowest, which are 0.287 Pa·s and 1351 °C respectively. This may be due to a high melting point phase (TiC) in the slag when the content of TiO_2 is 10wt.%. When the content of TiO_2 is less than 10wt.%, TiO_2 is used as a basic oxide to dilute the slag (Fig. 3).

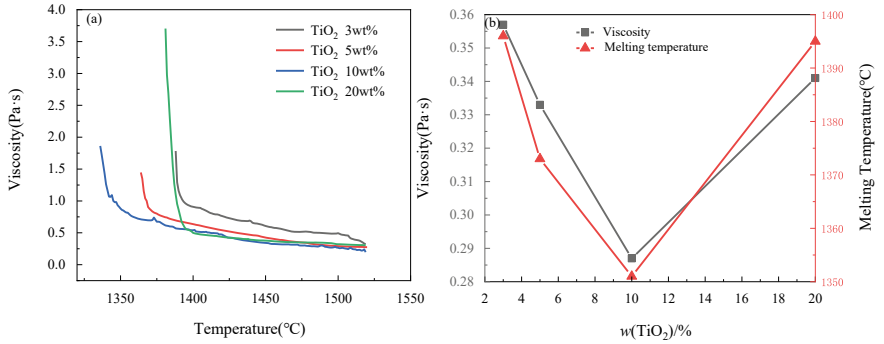

Fig. 3 Changes in the viscosity and melting temperature with varying TiO_2 content in the CaO-SiO_2-17wt%Al_2O_3-8.0wt%MgO-TiO_2 slag in the N_2 atmosphere (**a** η–T curves changes with increasing TiO_2 content, **b** the viscosity, melting temperature change with increasing TiO_2 content)

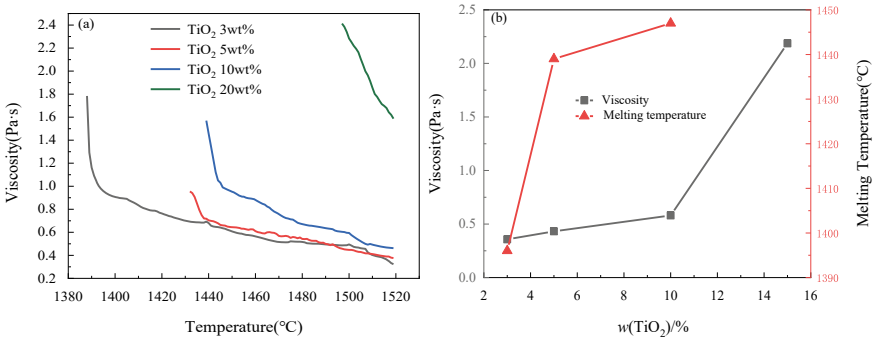

Fig. 4 Changes in the viscosity and melting temperature with varying TiO_2 content in the CaO-SiO_2-17wt%Al_2O_3-8.0wt%MgO-TiO_2 slag in the reducing atmosphere (**a** η–T curves changes with increasing TiO_2 content, **b** the viscosity, melting temperature change with increasing TiO_2 content)

Reducing Atmosphere

Figure 4 depicts the effects of TiO_2 content on the viscosity and melting temperature of the CaO-SiO_2-17wt%Al_2O_3-8.0wt%MgO-TiO_2 slag in the reducing atmosphere. It can be seen that the viscosity and melting temperature of slag both increase with the increase of TiO_2 content from 3wt.% to 20wt.%.

Figure 5 is the XRD curve of the water-quenched slag sample. It can be seen from the figure that when the TiO_2 concentration is 3wt.%, 5wt.%, and 10wt.%, there is no obvious characteristic peak in the slag sample, and the FT-IR spectrum results can reflect the structure of the slag well. However, when the concentration of TiO_2 is 20wt.%, (TiNa), (TiO_3), Ti (C,N), and TiN phases appear. When the concentration of bound TiO_2 is 20wt.%, the viscosity becomes higher in Fig. 4, which shows that Ti (C, N) and TiN with high melting points increase the viscosity of slag.

Figure 6 (a) shows the changes of TiO_4^{4-}, $Ti_2O_6^{4-}$, and Qn structural units, indicating the effect of TiO_2 addition on TiO_4^{4-}, $Ti_2O_6^{4-}$, and Q^n structural units. The results showed that with the increase of TiO_2 content, the content of monomer TiO_4^{4-} first increases and then decreases. With the increase of TiO_2 content from 3wt% to 20wt%, the area percentage of the band at 850 cm^{-1} first increased and then decreased. The reason is that the increase of TiO_2 content increases the mole fraction of the $Ti_2O_6^{4-}$ structural unit in the melt, while the decrease of SiO_2 content decreases the mole fraction of the SiO_4^{4-} structural unit. With the increase of TiO_2 content, the area percentage of Q^0 and Q^1 increased, and the area percentage of Q^2 and Q^3 increased, indicating that the degree of polymerization of the skeleton increased with the increase of TiO_2 content. As can be seen from Fig. 6 (b) with the increase of TiO_2 content, the ratio of $(Q^2 + Q^3)/(Q^0 + Q^1)$ increases, indicating that the slag structure is complex and the slag viscosity increases.

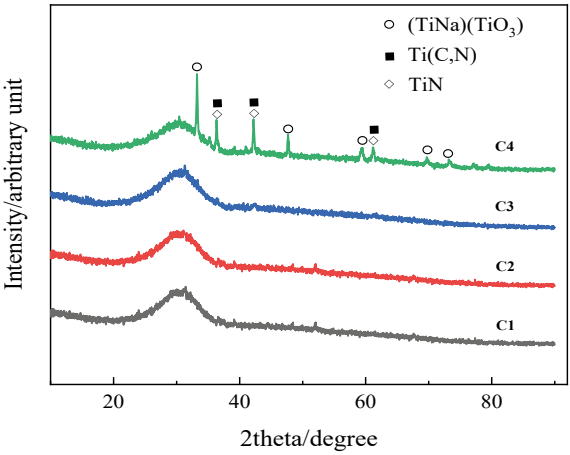

Fig. 5 The XRD curve of the water-quenched slag sample

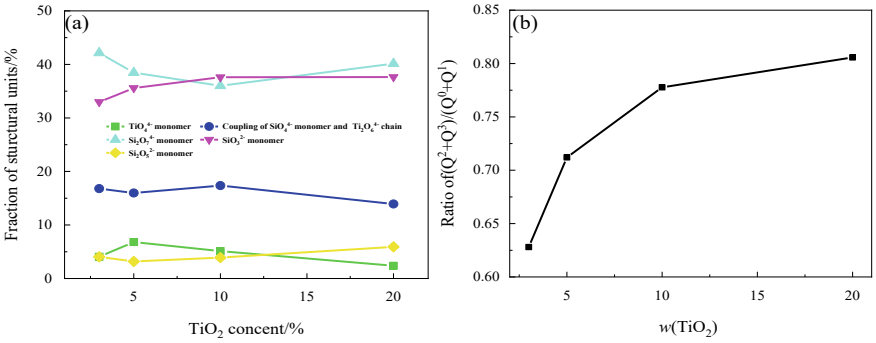

Fig. 6 Changes in the slag structure units with increasing TiO_2 content in the reducing atmosphere (**a** single structure units, **b** ratio of sum both of $Q^2 + Q^3$and $Q^0 + Q^1$)

Conclusion

1. In neutral atmosphere, with the increase of TiO_2 content from 3wt% to 25wt%, the viscosity and melting temperature of slag first increased and then decreased, and the ratio of $(Q^2 + Q^3)/(Q^0 + Q^1)$ first increased and then decreased. The turning point was 5wt%. When the content of TiO_2 is 5wt%, there is a high melting point phase (calcium titanate) in the slag, and TiO_2 is mostly Ti hexacoordinate ions, diluting the slag in the neutral atmosphere.
2. In the N_2 atmosphere, with the increase of TiO_2 content from 3wt% to 20wt%, the viscosity and melting temperature of slag first decrease and then increase, and the turning point is at 10wt%. A high melting point phase (TiC) was generated in the slag when the TiO_2 content was 10wt%. When the content of TiO_2 is lower than 10wt%, TiO_2 is used as an alkaline oxide to dilute the slag.

3. In a reducing atmosphere, the viscosity decreases with the increase in temperature, and with the increase of TiO_2 content from 3wt% to 20wt%, the viscosity and melting temperature of the slag also increase. The increase of the $(Q^2 + Q^3)/(Q^0 + Q^1)$ ratio indicates that the slag structure is complex and the slag viscosity is increased. When the concentration of TiO2 is 20wt%, (TiNa) (TiO_3), Ti (C, N), and TiN phases appear.

References

1. Sunahara K, Nakano K, Hoshi M, Inada T, Komatsu S, Yamamoto T (2008) Effect of high Al_2O_3 slag on the blast furnace operations. ISIJ Int 48(4):420–429
2. Kim GH, Sohn I (2012) Effect of Al_2O_3 on the viscosity and structure of calcium silicate-based melts containing Na_2O and CaF_2. J Non-Cryst Solids 358(12–13):1530–1537
3. Machin JS, Yee TB, Hanna DL (2012) Viscosity studies of system CaO-MgO-Al_2O_3-SiO_2: III, 35, 45, and 50wt% SiO_2. J Am Ceram Soc 35(12):322–325
4. Suzuki M, Jak E (2013) Quasi-Chemical viscosity model for fully liquid slag in the Al_2O_3-CaO-MgO-SiO_2 system—part I: revision of the model. Metall Mater Trans B 44(6):1451–1465
5. Park JH, Min DJ, Song HS (2004) Amphoteric behavior of alumina in viscous flow and structure of CaO-SiO_2 (-MgO)-Al_2O_3 slags. Metall Mater Trans B 35(2):269–275
6. Yan ZM, Lv XW, Liang D, Zhang J, Bai CG (2017) Transition of blast furnace slag from silicates-based to aluminates-based: viscosity. Metall Mater Trans B 48(2):1092–1099
7. Zhang SF, Zhang X, Liu W, Lv XW, Bai CG, Wang L (2014) Relationship between structure and viscosity of CaO–SiO_2–Al_2O_3–MgO–TiO_2 slag. J Non-Cryst Solids 402:214–222
8. Chang ZY, Jiao KX, Zhang JL, Ning XJ, Liu ZQ (2018) Effect of TiO_2 and MnO on viscosity of blast furnace slag and thermodynamic analysis. ISIJ Int 58(12):2173–2179
9. Yan Z, Pang Z, Lv XW, et al (2018) Effect of TiO_2 on the viscous behavior of high alumina blast furnace slag. In: 9th international symposium on high-temperature metallurgical processing, pp 725–733
10. Wang Z, Shu QF, Chou K (2013) Viscosity of fluoride-free mold fluxes containing B_2O_3 and TiO. Steel Res Int 84(8):766–776
11. Park H, Park JY, Kim JH et al (2012) Effect of TiO_2 on the viscosity and slag structure in blast furnace type slag. Steel Res Int 83(2):150–156
12. Xu RZ, Zhang JL, Zhang HS et al (2017) Effect of TiO_2 on properties of Jingtang blast furnace slag and thermodynamic analysis. Iron steel 52(9):104–109
13. Nakamoto M, Tsugawa Y, Kiyose A et al (2007) Effect of TiO_2 on the viscosity of molten slag in SiO_2CaO-MgO system. J High Temp Soc 32(1):74–77
14. Chang ZY, Jiao KX, Zhang JL et al (2018) Effect of TiO_2 and MnO on viscosity of blast furnace slag and thermodynamic analysis. ISIJ Int 58(12):2173–2179
15. Zhang S, Zhang X, Peng H et al (2014) Structure analysis of CaO-SiO_2-Al_2O_3-TiO_2 slag by molecular dynamics simulation and FT-IR spectroscop. Trans Iron Steel Inst Jpn 54(4):734–742
16. Shi CB, Zheng DL, Shin SG et al (2017) Effect of TiO_2 on the viscosity and structure of low-fluoride slag used for electro slag remelting of Ti-containing steels. Int J Miner Metall Mater 24(1):18–24
17. Kurunov IF, Loginov VN, Lyapin SS et al (2007) New technological solutions to protect the lining of blast-furnace hearths. Metallurgist 51:425–433
18. Zhao Y (2014) The impact of titanium on skull formation in the blast furnace hearth. In: AIST.org,editor. AISTech-2013.Pittsburgh, Pa, USA, pp 95–103
19. Zhao GH, Zhang SH, Lan CC (2015) Effects of titanium compounds on the flow properties of medium titanium blast furnace slag. Steel Vanadium Titanium 36(06):74–78

Melting and Solidification Behaviors of the Copper Slags with Different CaO Content at Various Oxygen Partial Pressures

Yannan Wang, Shuigen Huang, Bart Blanpain, and Muxing Guo

Abstract The solidification behavior of slag plays a vital role in its recycling. In this study, Confocal Laser Scanning Microscope (CLSM) experiments were performed under various oxygen partial pressure (pO_2) for FeO-SiO_2-Al_2O_3-CaO slags with around 4 wt.% and 26 wt% CaO to study their melting and solidification behaviors. Samples after the CLSM tests were analyzed by EPMA. Analysis indicated that the start melting temperature of the high CaO slag decreased with decreasing pO_2 from 10^{-4} atm to 10^{-12} atm, and the CaO concentration in the slag had a significant influence on its solidification behavior at pO_2 of 10^{-8} atm. Under pO_2 of 10^{-8} atm with a cooling rate over 1 °C/s, wustite crystal precipitated in the CaO-rich slag at temperatures over 1200 °C, while spinel precipitated in the low CaO slag at temperatures between 1100 and 1250 °C. When the cooling rate was below 1 °C/s, the spinel precipitated firstly at temperatures over 1277 °C in both slag systems. In addition, other minerals, such as melilite and fayalite, were observed, respectively, in the CaO-rich slag and low CaO slag.

Keywords Slag solidification · Melting · CaO content · Copper slag · Oxygen partial pressure (pO_2)

Introduction

It has been reported that secondary copper smelter slag with 12 to 16 wt.% ZnO can be fumed via a submerged plasma fumer to recover Zn [1, 2]. For added value applications of the slag after Zn recovery, a CaO-rich material was added into the fuming slag to generate CaO-rich slag [3]. The water granulated CaO modified copper slag exhibited an improved pozzolanic activity and better strength [4, 5].

Y. Wang (✉) · S. Huang · B. Blanpain · M. Guo
Department of Materials Engineering, KU Leuven, Kasteelpark Arenberg 44, 3001 Leuven, Belgium
e-mail: yannan.wang@kuleuven.be

M. Zhang et al. (eds.), *Characterization of Minerals, Metals, and Materials 2023*, The Minerals, Metals & Materials Series
https://doi.org/10.1007/978-3-031-22576-5_13

After fuming, the main components are FeO_t, SiO_2, and CaO and considerable lower ZnO content [6, 7]. In the FeO-Fe_2O_3-SiO_2-CaO slag system, the slag crystallization ability decreased with decreasing pO_2 at 1175 °C [8]. A. Semykina et. al. measured the time-temperature-transformation (TTT) curve of 28 wt.% FeO_t-SiO_2-CaO-11.5 wt% MnO ($CaO/SiO_2 = 0.59 \sim 1.05$) slag under air atmosphere in the temperature range of 1000–1600 °C. It was found that the size of precipitated calcium silicate ($CaSiO_3$) and spinel (the magnetite ferrite crystal) was increased with temperatures, and the crystallization ability of the slag at the gas/liquid interface enhanced with the slag basicity [9]. The crystallization of 28 wt.% FeO_t-SiO_2-CaO-5 wt% MnO ($CaO/SiO_2 = 0.96–1.41$) slags, i.e., the TTT and CCT (continuous cooling transformation) diagrams, was observed in-situ by Li et al. using CLSM in the temperature range of 900–1600 °C [10]. The nose temperature was found to increase from 1200 to 1425 °C with increasing basicity from 0.96 to 1.41. Besides, the onset precipitation temperature of calcium silicate ($CaSiO_3$) and spinel (solid solution of Fe_3O_4 and $FeMn_2O_4$) was also increased with basicity. However, most of the slags studied were from steelmaking processes [11–13], whereas the crystallization behavior of Zn fuming slag with a high FeO_t and SiO_2 content has not been reported. In this study, the melting and solidification behaviors of a Zn fuming slag with and without CaO-rich material addition, i.e., the slag with high and low CaO content, were studied under various pO_2 and cooling rates by CLSM. The CCT curves of two slags were constructed. The influence of CaO content on slag solidification behaviors was discussed.

Experimental Methods

Industrial Slag Sampling

Industrial slag samples were used to study the crystallization behavior. As shown in Fig. 1a, a steel rod was immersed into the Zn fuming bath to take industrial slag samples. Detailed microstructures of the cross-sectional slag are shown in Fig. 1b, indicating a clear gradient microstructure. Close to the steel rod surface, the layer experienced a high cooling rate and generated an amorphous structure. On the other hand, multiple crystals were formed at the other side of the sample due to a lower cooling rate. The chemical compositions of the amorphous matrix obtained from the standard fuming and the CaO modified fuming processes were measured by Electron Probe Micro Analysis (EPMA, JEOL JXA-8530F). The results are shown in Table 1. The standard deviation of the analysis is 1% and all the Fe was considered to be FeO since the fuming slag was in equilibrium with the bright metallic Fe particles, as shown in Fig. 1b.

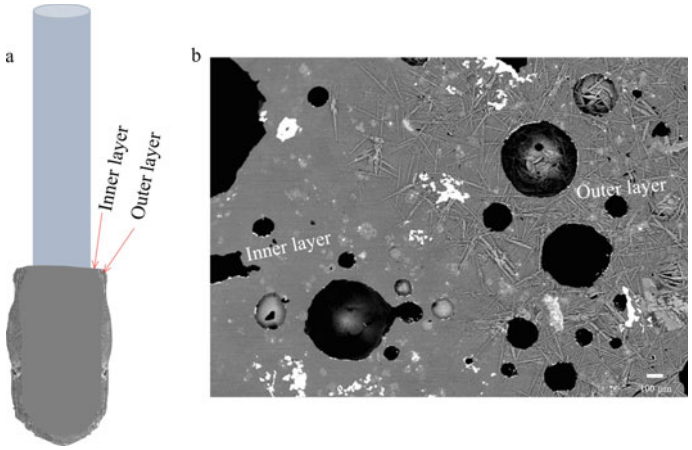

Fig. 1 **a** The sampling system in the industry and **b** the double layers microstructure of the sample

Table 1 The chemical composition of the amorphous matrix in the modified fuming and standard fuming slags

Sample	Chemical composition (wt%)						FeO/SiO_2
	MgO	Al_2O_3	SiO_2	CaO	FeO	ZnO	
S1	2.30	7.67	33.04	26.67	28.12	2.20	0.85
S2	1.36	12.87	40.25	4.36	39.24	1.92	0.97

CLSM Observation of Slag Behaviours

The in-situ observation of the melting and crystallization behaviors of slags was carried out by using a confocal scanning laser microscope with a high temperature cell (CLSM, Lasertec, 1LM21H-SVF17SP). Figure 2a shows a schematic diagram of the CLSM setup. The sample temperature was measured by a B-type thermocouple, which is connected to the Pt holder. The temperature accuracy (11 °C) was calibrated by a melting experiment of CaF_2 (melting point 1418 °C).

Before the thermal cycle, around 20 mg of the slag was loaded on a pre-formed Pt foil. The chamber was flushed by Ar gas. The gas flow was then stopped when the target atmosphere (pO_2 of 10^{-4} atm, 10^{-8} atm, and 10^{-12} atm) was reached. The sample was then heated up to the maximum temperature at a rate of 3.5 °C/s and hold for 3 min to homogenize the sample. Afterward, the sample was cooled down at different cooling rates for constructing the CCT curve. Figure 2b shows the thermal history of the CCT measurement. During cooling, a fixed surface area of the sample was continuously imaged by the CLSM device. Results of the in-situ CLSM observations were used to construct the CCT diagrams. In the diagrams, the temperatures at which the first precipitate appeared (T_{start1}) and the secondary precipitate appeared (T_{start2}) are plotted for the different cooling rates. When the

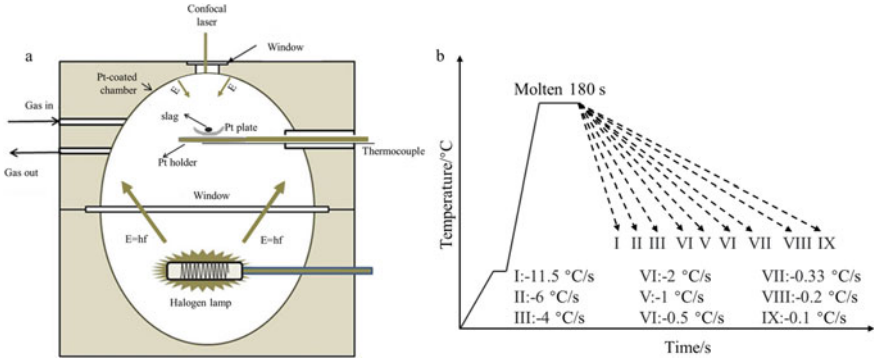

Fig. 2 **a** The schematic diagram of CLSM set-up and **b** thermal history of the CCT measurement

slag was completely solid, the sample was quenched to room temperature for later microscopy analysis. The samples were embedded in resin, grinded, polished, and coated with carbon and then analysed by EPMA at an operating voltage of 15 kV.

The "equilib" module with databse "FactPS" and "FToxide" of FactSage 8.1 was applied for phase equilibrium calculation. All the solutions in "FToxide" database were chosen and the gas phase was provided by "FactPS" database during the computation.

Results and Discussion

Slag Melting Behaviors

Under the pO_2 of 10^{-4} atm, the CaO modified slag S1 was still in a solid state at 1350 °C, as shown in Fig. 3a. After holding at 1600 °C for 3 min, the solid sample turned into mainly liquid and some fine particles, as seen in Fig. 3b. The BSE images of the sample, furnace cooled from 1600 °C, are shown in Fig. 3c and d. The observed particles were confirmed to be a spinel phase, enriched in Fe-Al-Zn–O. The FeO content in the liquid slag phase (22.0 wt.% FeO-34.9 wt.% SiO_2-31.6 wt.% CaO) decreased significantly, compared to the original slag composition (in Table 1), due to the formation of iron oxide rich spinel phase (86.2 wt% FeO-4.2 wt% ZnO-7.5 wt% Al_2O_3).

When the sample 1 was treated under pO_2 of 10^{-12} atm, melting of the slag seemed to start at about 900 °C, as seen in Fig. 4a. Metallic Fe droplet (see Fig. 4b) and Zn gas bubble (Fig. 4c) were observed at 1099 and 1217 °C, respectively. This phenomina was confirmed through the composition analysis of the quenched slag sample after the CLSM melting test as shown in Fig. 4e and f, where a number of round pores and Fe metal particles were observed in the sample centre area, and some large Fe particles were attached on the bubbles surface. The former confirms the reduction of

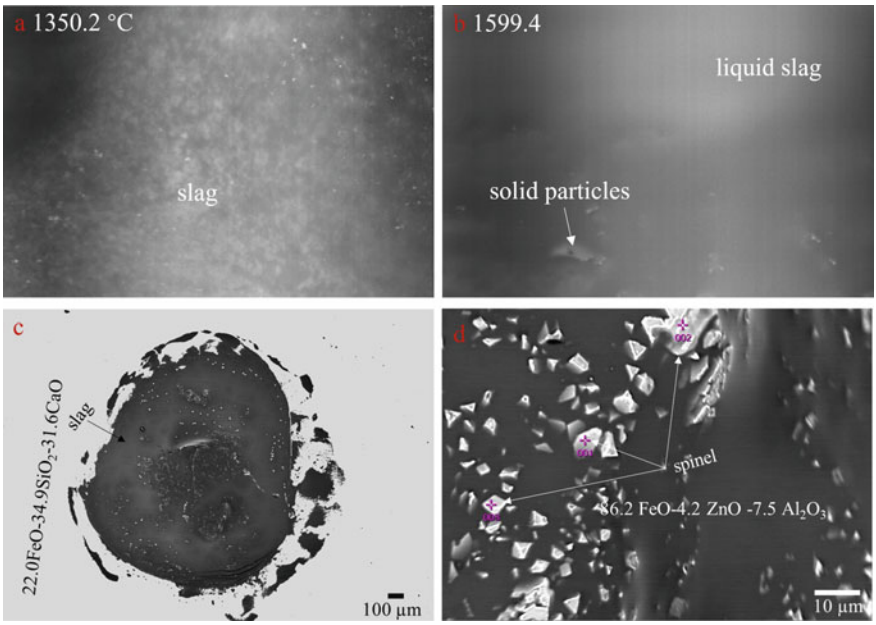

Fig. 3 The CLSM image of slag sample 1 (S1) under pO_2 of 10^{-4} atm at **a** 1350 °C, **b** 1600 °C and the BSE images of S1 after the CLSM test: **c** overview of slag sample and **d** enlarged view of an area in the overview image

ZnO into metallic Zn, while the latter indicates FeO in the slag can be also reduced by the in-situ formed Zn gas bubble. With increasing temperature and time, the in-situ formed Fe particles merged together, as shown in Fig. 4d. The amorphous matrix was measured to only contain Al_2O_3, SiO_2, and CaO (14.4 wt.% Al_2O_3-54.1 wt.% SiO_2-31.5 wt.% CaO) due to the complete reduction of iron and zinc oxides.

In order to avoid the reduction of iron and zinc oxides during the slag melting, the slag was treated under pO_2 of 10^{-8} atm. As seen in Fig. 5a, the slag started melting at approximately 933 °C and it became nearly full liquid at 1350 °C (Fig. 5b) except for some spinel particles on the surface. The Fe droplets and/or Zn gas bubbles were not observed during the melting process when using pO_2 of 10^{-8} atm.

Based on CLSM tests, it can be concluded that (1) the start melting temperature of the high CaO content slag decreases with decreasing pO_2 level, and (2) zinc and iron oxides reduction occurs during the melting at pO_2 of 10^{-12} atm.

Slag Crystallization Behaviors

The crystallization of the slag with and without CaO modification was investigated under pO_2 of 10^{-8} atm. As shown in Fig. 2b, the slags were heated up to 1350 °C

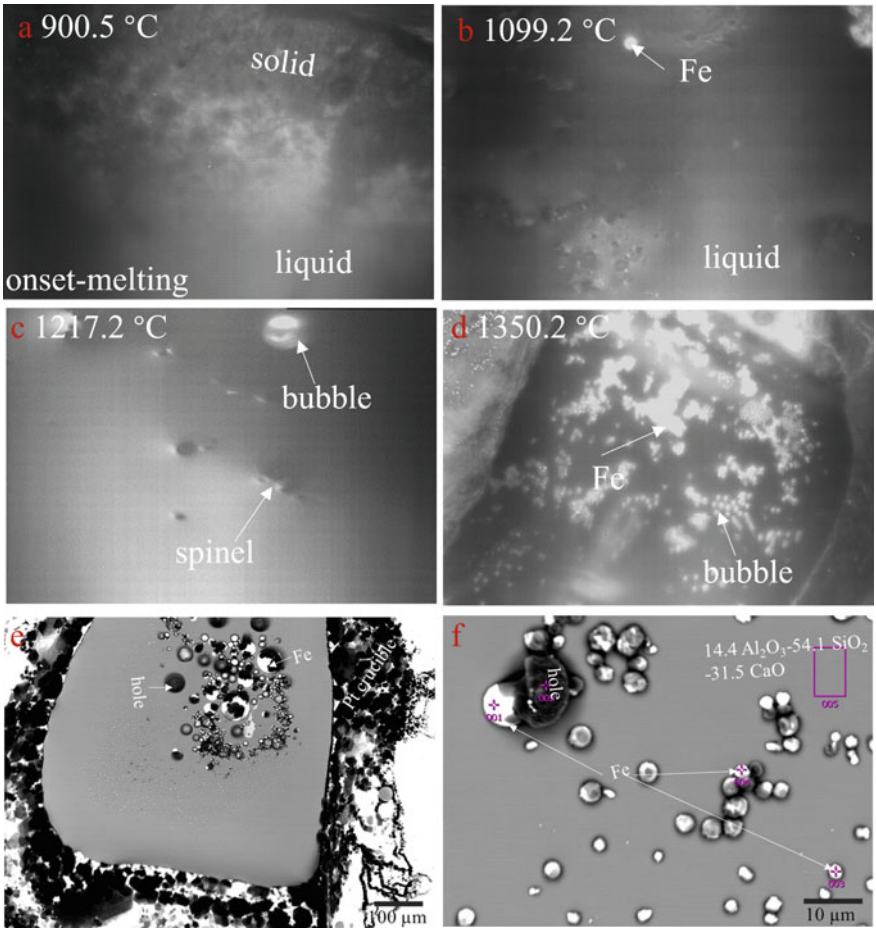

Fig. 4 **a**–**d** The melting process of slag sample 1 under pO_2 of 10^{-12} atm and images of S1 after the CLSM test **e** general view **f** enlarged view

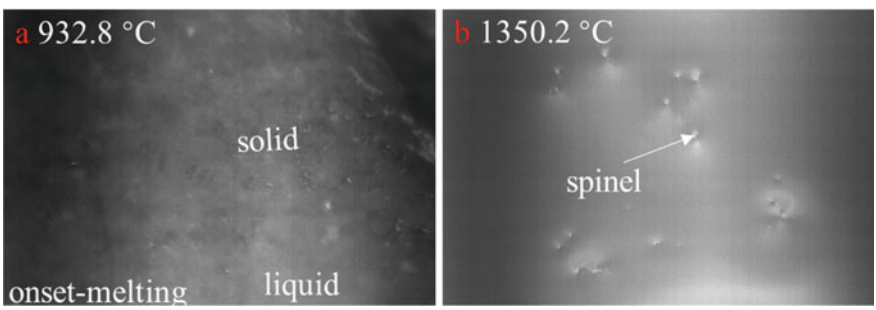

Fig. 5 The CLSM images of the slag sample 1 melting under pO_2 of 10^{-8} atm: **a** started melting at 933 °C and **b** completely melted at 1350 °C

at a rate of 3.5 °C/s and then hold for 3 min. Afterwards, the slags were cooled down at various cooling rates for measuring the CCT curves of the slags. Figure 6 demonstrates the CCT curves of the S1 and S2 with cooling rates ranging from 1 to 11.5 °C/s. The open circles present the onset crystallization temperature of the slags and the data points are connected with a dashed line. According to the post Morten analysis, the onset crystallization temperature of wustite precipitation was over 1200 °C for the high CaO slag, as shown in Fig. 6a. The onset temperature was found to decrease with increasing cooling rates till 6 °C/s, and then levelled off. With regards to the low CaO slag (S2), the onset crystallization temperature of spinel was in the range of 1100 and 1250 °C, and it decreased first with increasing cooling rate to 4 °C/s and then slightly increased with further increasing the cooling rate. Apparently, CaO addition into the slag enhanced the wustite precipitation, which on the other hand prevented the spinel formation at higher cooling rates (over 1 °C/s) since both the wustite and spinel are FeO-rich phases. Figure 7 shows the CLSM images at the onset crystallization temperature and the BSE images of S1 and S2 after the CLSM test under a cooling rate of 4 °C/s. Based on the BSE images, the primary crystals for the slag 1 and 2 were, respectively, the round shape wustite (Fig. 7c) and the spinel with sharp edges (Fig. 7d), which are in agreement with the CLSM observations of slag 1 (Fig. 7a) and salg 2 (Fig. 7b). The primary wustite and spinel contain 90 wt.% and 60 wt.% FeO, respectively.

Figure 8 shows the measured CCT curves of S1 and S2 under the cooling rate below 1 °C/s. In the diagrams, the temperatures at which the first precipitate (open circles) and the second precipitate appeared (solid circles) are plotted for the different cooling rates. Under these low cooling conditions, the spinel phase precipitated firstly in both slags. The spinel onset crystallization temperature of the S1 was between 1323 and 1346 °C, whereas the precipitation temperature of spinel in the S2 was around 1277–1322 °C. With further cooling, melilite precipitated from the S1 in the temperature range of 1258–1311 °C and fayalite crystallized from the S2 between 1220 and 1289 °C. Apparently insteading of fayalite, melilite crystallized with increasing CaO

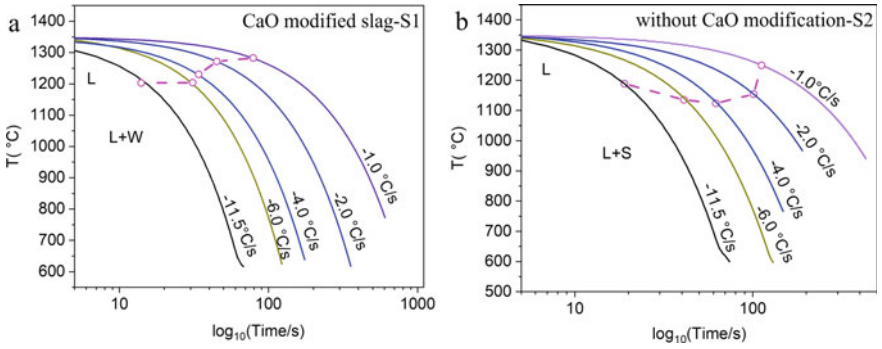

Fig. 6 The CCT curve of **a** S1 and **b** S2 with a cooling rate over 1 °C/s. L: liquid, S: spinel

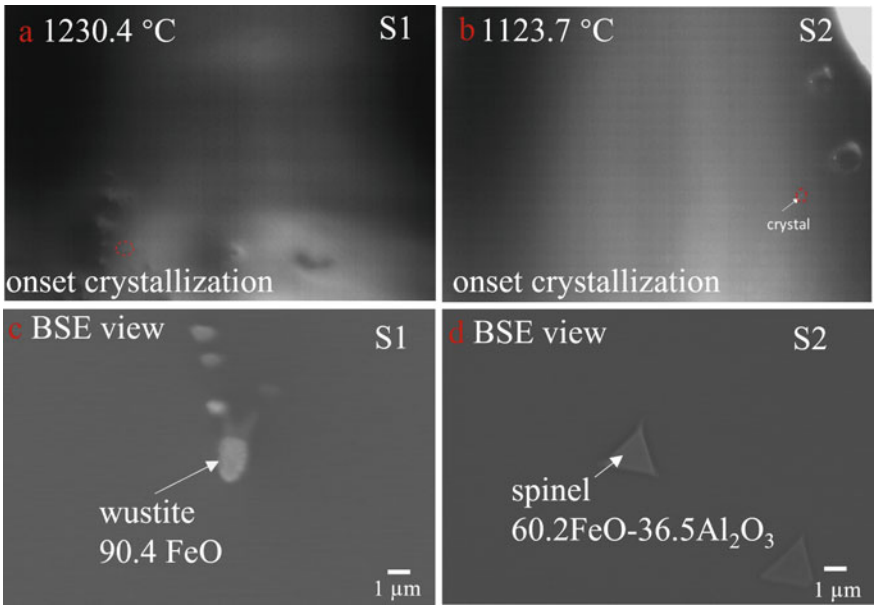

Fig.7 The onset crystallization image of **a** S1 and **b** S2 observed in CLSM tests, and the BSE images of **c** S1 and **d** S2 after the CLSM tests under a cooling rate of 4 °C/s

content in copper slag under slow cooling conditions. Besides, both melilite and fayalite crystallized at lower temperature with increasing cooling rate.

The calculated equilibrated phases of CaO modified slag and the slag without CaO modification at temperatures from 1050 to 1350 °C are shown in Fig. 9. Compared with the experimental results (Fig. 8), the solid phase generated at a lower temperature in computed results, which indicates the unmelted spinel particles at the maximum temperature enhanced the precipitation of solid particles during the

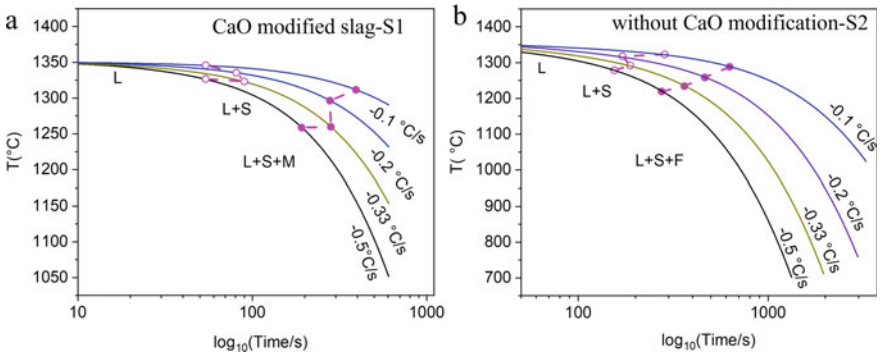

Fig. 8 The CCT curve of **a** S1 and **b** S2. M: melilite, F: fayalite

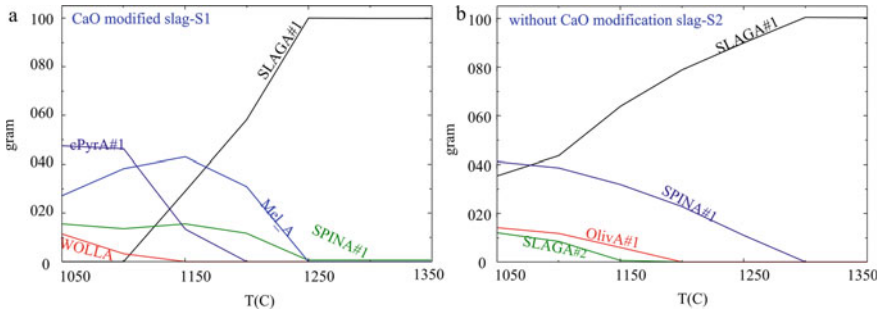

Fig. 9 The computed equilibrated phases of **a** S1 and **b** S2 by FactSage 8.1

cooling process. However, the first two precipitates of S1 and S2 are consistent with the experimental results at a cooling rate below 1 °C/s, i.e., spinel/melilite from the S1 and spinel/olivine (fayalite) from the S2.

Conclusions

The melting and crystallization of the FeO_t-SiO_2-Al_2O_3-CaO slags with 4 wt.% and 26 wt.% CaO content were investigated under various oxygen partial pressure (pO_2) by using CLSM technique. The main conclusions can be summarized as.

(1) The copper slag with 26 wt.% CaO can be hardly melted even at 1600 °C under $pO_2 = 10^{-4}$ atm. However, the start melting temperature of the slag decreases with decreasing oxygen partial pressure.
(2) Zinc and iron oxides reduction occurred during the melting process under $pO_2 = 10^{-12}$ atm, and metallic Fe grew on the gas bubble surface.
(3) To avoid zinc and iron oxides reduction at low pO_2, the slag solidification behavior was investigated under $pO_2 = 10^{-8}$ atm using the in-situ CLSM observation. CCT curves of the slags with 4 wt% and 26 wt% CaO content were constructed.
(4) The wustite precipitated in the CaO-rich slag at a cooling rate of over 1 °C/s with an onset precipitation temperature of over 1200 °C. While the spinel phase precipitated in the low CaO slag with an onset precipitation temperature range of 1100–1250 °C. When the cooling rate is below 1 °C/s, the spinel phase precipitated firstly at approximately 1300 °C in both CaO-rich slag and low CaO slag. With further cooling, melilite precipitated from the CaO-rich slag in the temperature range of 1258–1311 °C and fayalite from the low CaO slag between 1220 and 1289 °C. The increasing CaO content enhanced the precipitation of melilite and prevented the generation of fayalite under slow cooling conditions.

Acknowledgements The research is supported by the "TOGETHER" project. Yannan Wang acknowledges the support of the KU Leuven Hitemp Centre and the China Scholarship Council (CSC, Grant no. 202007650005).

References

1. Nagraj S, Chintinne M, Guo M, Blanpain B (2020) Miner Met Mater Ser 237
2. Nagraj S, Chintinne M, Guo M, Blanpain B (2022) JOM 74:274
3. S. Kumar, Leuven NK, Huang S, Leuven KU, Nagraj S, Chintinne M, Guo M, Blanpain B, Coletti B (2021)
4. Shi C, Qian J (2000) Resour Conserv Recycl 29:195
5. Feng Y, Yang Q, Chen Q, Kero J, Andersson A, Ahmed H, Engström F, Samuelsson C (2019) J Clean Prod 232:1112
6. Chen L, Guo M, Shi H, Huang S, Jones PT, Blanpain B, Malfliet A (2016) J Eur Ceram Soc 36:1821
7. Shi H, Chen L, Jones TP, Blanpain B, Guo M (2016) TMS Annu Meet 0:583
8. Kongoli F, Yazawa A (2003) Mater Trans 44:2130
9. Semykina A, Nakano J, Sridhar S, Shatokha V, Seetharaman S (2010) Metall Mater Trans B 41:940
10. Li J, Bhattacharjee D, Hu X, Zhang D, Sridhar S, Li Z (2019) Metall Mater Trans B 50:1931
11. Fredericci C, Zanotto ED, Ziemath EC (2000) J Non Cryst Solids 273:64
12. Wang ZJ, Ni W, Jia Y, Zhu LP, Huang XY (2010) J Non Cryst Solids 356:1554
13. Lin B, Wang H, Zhu X, Liao Q, Ding B (2016) Appl Therm Eng 96:432

Test Method of Mold Powder Melting Rate Based on Copper Bath and Its Application

Fuhang Chen, Guanghua Wen, Ping Tang, and Qu Fu

Abstract Given the deficiencies of the present test methods of mold powder melting rate, a method based on the copper bath was established in this study. The correctness and reproducibility of this method were verified. The relative standard error was less than 5%. The effect of carbonaceous materials and powder granule size on the melting rate was investigated by this method. The results show that: (1) The melting rate of mold powder decreased with increasing carbonaceous materials content. (2) Besides carbonaceous materials, the powder granule size also affected the melting rate. The melting rate of the mold powder for high-nitrogen stainless steel increased with increasing granule powder size. The use of powders in the steel plant was consistent with the experimental results. The larger the proportion of larger than 0.5 mm granules in the powder, the thicker the liquid slag layer, and the higher the qualified rate of slab quality.

Keywords Continuous casting · Mold powder · Carbonaceous materials · Granule size · Melting behavior

F. Chen · G. Wen (✉) · P. Tang · Q. Fu
College of Materials Science and Engineering, Chongqing University, Chongqing 400044, China
e-mail: wengh@cqu.edu.cn

F. Chen
e-mail: 20152625@cqu.edu.cn

P. Tang
e-mail: tping@cqu.edu.cn

Q. Fu
e-mail: 202009131260@cqu.edu.cn

F. Chen · G. Wen · G. Wen · P. Tang · Q. Fu
Chongqing Key Laboratory of Vanadium-Titanium Metallurgy and New Materials, Chongqing University, Chongqing 400044, China

M. Zhang et al. (eds.), *Characterization of Minerals, Metals, and Materials 2023*, The Minerals, Metals & Materials Series
https://doi.org/10.1007/978-3-031-22576-5_14

Introduction

Mold powder is a functional material commonly used in continuous casting processes to ensure smooth continuous casting process and improve surface quality of the slab [1, 2]. Due to the longitudinal heat transfer of liquid steel, the mold powder forms a granular powder layer, sintered layer, and liquid slag layer from top to bottom in the mold. These layers have functions of preventing secondary oxidation of liquid steel, heat preservation, and absorption of inclusions in liquid steel. After the liquid slag is formed, it infiltrates into the gap between the mold copper plate and the slab shell to form a liquid slag film and a solid slag film, which have the effects of controlling horizontal heat transfer and lubrication. The realization of the above functions of mold powder is almost related to liquid slag. In this view, the speed of liquid slag formation, that is, the melting rate of the mold powder has an important influence on the continuous casting process. Therefore, the accurate test of the melting rate of mold powder is particularly important.

However, there is no uniform method for testing the melting rate of mold powder. Several scholars have proposed some test methods, which can be divided into the following categories. The first is the softening method [3]. In this method, the granule powder is ground into powder less than 74 μm, and the cylinder or triangular cone sample is made by mold. The time of melting to a certain height is observed by a hot stage microscope. The sample pretreatment of this method destroys the granule structure of the powder and is not suitable for the test of the melting rate of the hollow granule mold powder. Some scholars have found that the melting rate measured by this method is contrary to the actual use. To accurately reflect the actual use of mold powder, the melting rate test conditions should be similar to the actual use conditions of mold powder. The second is the meltage method [4–6]. This method is to add a certain quality of the mold powder into the preheated crucible, test the melting amount of the powder within a certain time or the complete melting time of a certain amount of powder. This method does not need to pretreat the mold powder and maintains the initial shape of the mold powder. Scholars have tried to use different ways to provide heat for powder melting. Koyama [6] used a thermocouple to heat the crucible and provided heat for the mold powder through the heat conduction of the crucible. Kromhout [3] and Kamaraj [7] use induction heating of liquid steel in a quartz crucible to provide heat to the mold powder. Kromhout found that the flow of liquid steel caused by induction heating increases the heat transfer between liquid steel and liquid slag and increases the melting rate of the mold powder. The surface of the liquid steel in the mold is also in motion, so this heating method is more similar to the actual use of mold powder. However, the experimental conditions of the meltage method are still different from the actual conditions of the mold. As mentioned above, the actual use of mold powder continuous melting, and consumption, is a continuous process. The meltage method can only analyze the overall melting of the mold powder over a while, rather than continuous melting. Some scholars use the drip method to simulate the continuous melting of mold powders. Wei [8] heated a graphite crucible with a hole at the bottom by induction heating. After reaching the set temperature,

the mold powder was added. The liquid slag flowed from the hole to the collecting device after melting. The melting rate ($g.cm^{-2}.s^{-1}$) was calculated from the liquid slag collected over some time. In this method, the unsintered granule powder was easy to drip directly during the experiment, which affected the accuracy of the results. Däcker [9] improved this method and redesigned the crucible according to the siphon principle. The liquid slag only drips after forming at a certain height to prevent the unsintered slag from falling. Münch [10] used a Cu-Ni plate (melting point 1100 °C) to block the slag discharge hole and prevent the unsintered granule powder from dripping. Compared with the meltage method, although the drip method realizes to simulate the continuous melting and consumption of the mold powder, there is no flow behavior of the interface between the liquid steel and slag. Therefore, the test conditions of the drip method and the meltage method are similar and different from the actual use conditions of the mold powder.

Given the above background, this study developed a test method based on a copper bath for mold powder melting rate. The reproducibility of the method was verified, and the correctness of the method was verified by the influence of carbonaceous materials on the melting rate of mold powder. In addition, the melting rate of three batches of high-nitrogen stainless steel mold powder used in a steel plant was tested by this method. The influence of powder granule size on the melting rate was explored, and the reasons for the fluctuation of the actual use effect of mold powders in the steel plant were analyzed.

Experimental

Methodology and Equipment

To simulate the actual use conditions of mold powder and accurately test the melting rate, the method based on a copper bath established in this study is shown in Fig. 1. The equipment is mainly composed of a medium frequency induction furnace, graphite crucible, copper bath, and weight system. Copper is used as the heat transfer medium between the crucible and the mold powder. There are two main considerations: First, the surface of liquid copper will also flow under the action of induced current. Second, copper can achieve rapid heat transfer because of its large thermal conductivity. Third, there is no reaction between copper and graphite crucible, which is conducive to the reuse of graphite crucible. At the beginning of the experiment, the graphite crucible was heated to 1500 ± 20 °C by controlling the current of the medium frequency induction furnace. A 120 g copper was added to the crucible and heat preservation for a period of time so that the copper is completely melted. The surface of copper liquid was tested by infrared temperature measurement, and the mold powder was added after the temperature was no longer increased. Mold powder was heated by the liquid copper in one direction, forming the powder layer, sintered layer, and liquid slag layer from top to bottom. The liquid slag flowed out from the slag discharge

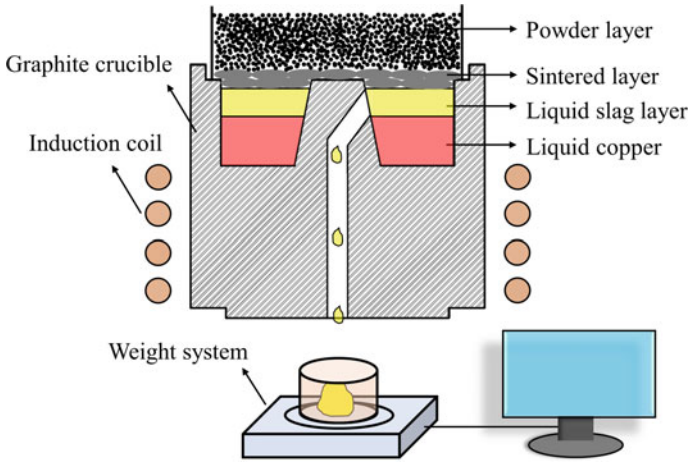

Fig. 1 Test method of mold powder melting rate based on copper bath

hole after formation. The slag discharge hole is designed to be inclined to prevent the unsintered powder from flowing directly through the slag discharge hole at the beginning of the experiment. The diameter of the slag discharge hole is 4.5 mm. Under the action of interfacial tension, the newly formed liquid slag will not flow out directly. When the thickness of the liquid slag layer reaches 5 mm, the gravity and static pressure of the droplet exceed the interfacial tension, and the droplet flows out from the slag discharge hole to the weight system. The time and quality of each liquid slag drop were automatically recorded by the weight system. The experiment lasted for 15 min from the dripping of the second liquid slag. The mass of liquid slag collected in 15 min was linearly regressed with time, and the ratio of the slope to the surface area of the copper bath (16.6 cm^2) was the melting rate of mold powder $g{\cdot}cm^{-2}{\cdot}min^{-1}$.

Experimental Materials

The components of mold powders involved in this study are shown in Table 1. To verify the reproducibility of the equipment, four repeated experiments were carried out using the stainless steel mold powder MP1 from a steel plant. MPA, MPB, MPC, and MPD are four mold powders with different contents of carbonaceous materials. The method's correctness is verified by the influence of carbonaceous materials on the mold powder melting rate. Among them, MPC is a high-nitrogen stainless steel mold powder used in a steel plant. According to the production date, it is divided into three batches MPC-1, MPC-2, and MPC-3, and their components are the same.

Table 1 Components of mold powders/wt.%

	C_{free}	CaO	SiO_2	F-	Na_2O	Al_2O_3	MgO
MPA	0.61	32.66	30.49	7.22	8.69	6.71	1.67
MPB	1.09	28.05	35.47	4.80	12.13	6.89	1.35
MPC-1	1.55	26.07	34.79	4.00	10.44	7.58	2.10
MPC-2	1.62	26.17	34.83	4.28	10.97	7.44	2.18
MPC-3	1.51	26.19	34.85	4.64	10.94	7.41	3.13
MPD	2.57	32.60	27.24	8.35	9.24	5.40	3.97

Results and Discussion

Reproducibility of the Test Method for Mold Powder Melting Rate Based on a Copper Bath

Four melting rate tests were performed using MPA. The results are shown in Fig. 2 and Table 2. The four test liquid slag drops were 118.02 g, 125.22 g, 117.58 g, and 122.52 g, respectively, and the relative standard error was 3.04%. After linear regression, the melting rates were 0.472 $g{\cdot}cm^{-2}{\cdot}min^{-1}$, 0.507 $g{\cdot}cm^{-2}{\cdot}min^{-1}$, 0.466 $g{\cdot}cm^{-2}{\cdot}min^{-1}$ and 0.527 $g{\cdot}cm^{-2}{\cdot}min^{-1}$, respectively. The relative standard error was 5.88%. It can be seen that the melting rate test method based on a copper bath has good experimental reproducibility.

Effect of Carbonaceous Material Content on Melting Rate of Mold Powder

Several scholars have studied the effect of carbonaceous materials on the melting rate of mold powder [3–5]. The results show that the melting rate of mold powder decreases with the increase of carbonaceous material content. Carbonaceous materials play an isolation and skeleton role in mold powder, hindering the contact sintering of raw materials and preventing droplet aggregation, reducing the melting rate of mold powder. Therefore, the method's correctness was verified by the influence of carbonaceous material content on the melting rate of mold powder. Figure 3 and Table 3 show the test results for the melting rates of MPA, MPB, MPC-1, and MPD. With the increase of carbonaceous material content, the melting rate of mold powder decreases, which is consistent with the existing research. Therefore, the test method based on a copper bath can accurately reflect the change rule of mold powder melting rate, which is suitable for testing the melting rate of mold powder.

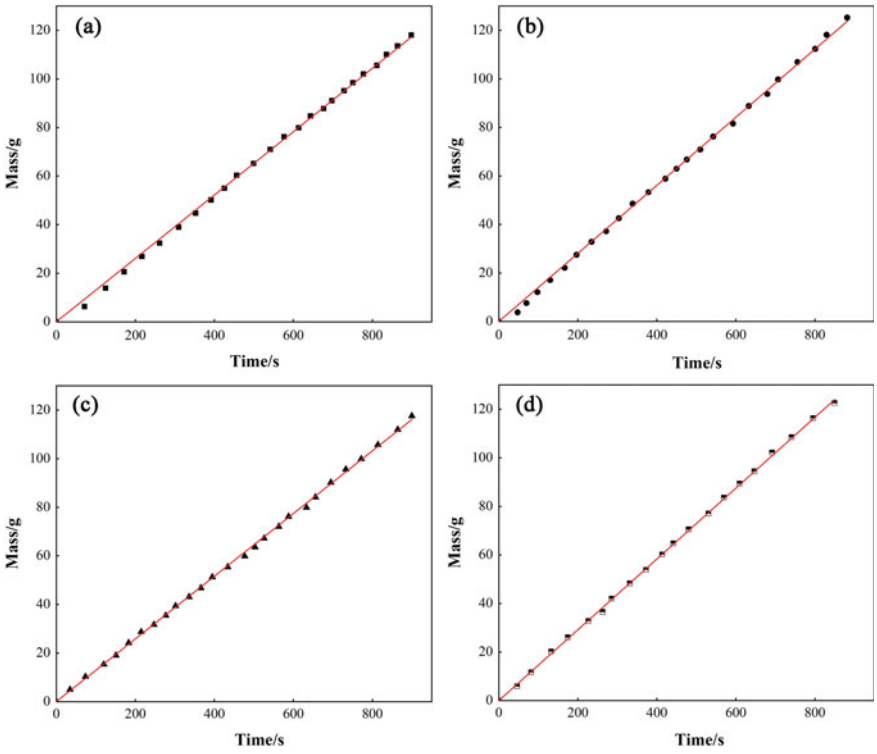

Fig. 2 Liquid slag dropping curve of MPA repeated experiments

Table 2 Repeat test results of MPA melting rate

	Mass/g	Regression equation	Peasons'r	Melting rate/g.cm^{-2}.min^{-1}
a	118.02	y = 0.13046x	0.99987	0.472
b	125.22	y = 0.14030x	0.99986	0.507
c	117.58	y = 0.12904x	0.99993	0.466
d	122.52	y = 0.14584x	0.99995	0.527

Application of the Test Method for Mold Powder Melting Rate Based on a Copper Bath

MPC is a high-nitrogen stainless steel mold powder used in a steel plant. According to the production date, it is divided into three batches MPC-1, MPC-2, and MPC-3. According to the statistics on the quality of slabs, the use effect of different batches of MPC is significantly different under the conditions of the constant casting process, steel grade, and mold dimensions. When using MPC-1, MPC-2, and MPC-3, the qualified rates of the slab were respectively 36.57%, 61.36%, and 44.88%. The main

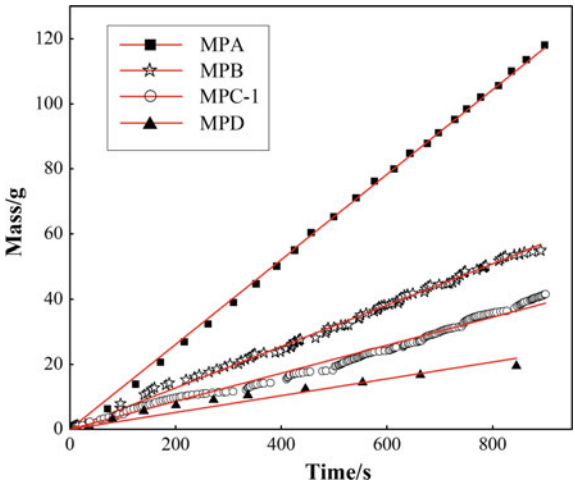

Fig. 3 Liquid slag dropping curve of mold powders with different carbonaceous material contents

Table 3 Test results of powders with different carbonaceous material contents

	Mass/g	Regression equation	Peasons'r	Melting rate /g.cm^{-2}.min^{-1}
MPA	118.02	y = 0.13046x	0.99987	0.472
MPB	54.96	y = 0.06366x	0.99936	0.230
MPC-1	41.60	y = 0.04312x	0.99667	0.156
MPD	19.48	y = 0.02587x	0.98059	0.094

defect of slabs was surface depression. The conventional test results show that there is almost no difference in physical and chemical indexes such as components, melting point, and viscosity of MPC-1, MPC-2, and MPC-3. Existing researches [11, 12] show that the formation of slab surface depression may be related to the fluctuation of liquid level, slag rim, and thin liquid slag layer. According to the field test, the thickness of the liquid slag layer is 12 mm when using MPC-2. When using MPC-1 and MPC-3, the liquid slag thickness is 9–10 mm. The thickness of the liquid slag layer is controlled by the melting rate of mold powder. The melting rates of MPC-1, MPC-2, and MPC-3 were tested by the test method based on a copper bath. The results are shown in Fig. 4 and Table 4. It can be seen that the melting rate of MPC-2 is higher than that of MPC-1 and MPC-3. According to the above statistical results, the qualified rate of slab surface quality is the highest when using MPC-2. The fluctuation of the qualified rate of slab surface quality is related to the fluctuation of the melting rates of different batches of mold powder. Current research shows that the main factors affecting the melting rate of mold powders are carbonaceous materials and carbonate content [3–5, 13, 14]. However, according to Table 1, the carbonaceous materials and carbonate contents of MPC-1, MPC-2, and MPC-3 are almost unchanged. Therefore, in addition to carbonaceous materials and carbonate content, the melting rate of mold powder may also be affected by other factors.

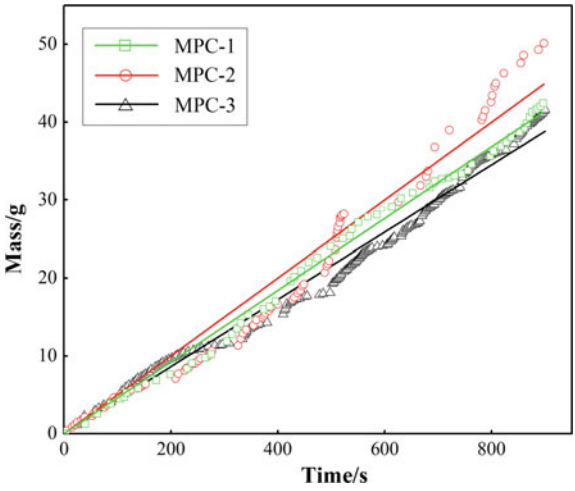

Fig. 4 Liquid slag dropping curves of different batches of MPC

Table 4 Test results of the melting rates of different batches of MPC

	Mass/g	Regression equation	Peasons'r	Melting rate /g.cm^{-2}.min^{-1}
MPC-1	41.60	y = 0.04312x	0.99667	0.156
MPC-2	50.16	y = 0.04998x	0.98554	0.185
MPC-3	42.40	y = 0.04604x	0.99836	0.166

In addition to the component, the hollow granule mold powder product also has an obvious feature, namely granule size. The size of the hollow granule mold powder product is controlled at 0.15 ~ 1.00 mm, and the fluctuation range is large. To explore the reason for the fluctuation of the melting rate of different batches of MPC, the granule size of MPC-1, MPC-2 and MPC-3 were tested by standard sieves. The results are shown in Table 5. In MPC-2, the granules with granule size > 0.5 mm account for a large proportion, while in MPC-1 and MPC-3, the granule size distribution is mainly concentrated in 0.2 ~ 0.5 mm. Combined with the melting rate test results, it can be seen that the mold powder melting rate increases with the proportion of granules with granule size > 0.5 mm in the mold powder. The effect of granule size on the melting rate of mold powder may be related to the heat transfer of the powder layer. The heat transfer in the mold powder layer mainly depends on the convection heat transfer of gas [5, 12], so the permeability of the powder layer will affect the heat transfer efficiency. The larger the granule size of the mold powder, the larger the porosity in the powder layer and the better the permeability, which is beneficial to the convection heat transfer of the gas and promotes the melting of the mold powder. The experimental results show that, in addition to the carbonaceous material and carbonate content, the granule size of the mold powder also affects the melting rate. Therefore, the difference in the use effect of different batches of high-nitrogen stainless steel mold powder MPC is attributed to the fluctuation of the granule size

Table 5 Granule size of different batches of MPC

	<0.2 mm	0.2 ~ 0.5 mm	>0.5 mm
MPC-1	10.89	80.26	8.85
MPC-2	1.75	30.56	67.69
MPC-3	1.90	65.40	32.70

of the mold powder. This may be related to the production process of mold powder, including parameters such as slurry viscosity, orifice diameter, and pressure during spray granulation, which are worthy of attention in the future production of mold powder.

Conclusions

(1) The test method of mold powder melting rate based on a copper bath has good reproducibility, and the relative standard error of the repeat experiments is 5.88%. The melting rate test results of mold powders with different carbonaceous material contents show that the melting rate decreases with the increase of carbonaceous material content. This rule is consistent with the existing research, which verifies the correctness of the test method based on a copper bath. Therefore, the test method based on a copper bath is suitable for testing the melting rate of hollow granule mold powder.

(2) In addition to the carbonaceous material and carbonate content, the granule size also affects the melting rate of the hollow granule mold powder. The difference in the use effect of different batches of high-nitrogen stainless steel mold powder MPC in a steel plant is related to this phenomenon. Compared with MPC-1 and MPC-3, the proportion of granules with a size > 0.5 mm in MPC-2 is large, the melting rate is high, the liquid slag layer is thick in actual use, and the qualified rate of the slab is high.

References

1. Mills KC, Fox AB (2003) The role of mould fluxes in continuous casting-so simple yet so complex. ISIJ Int 43(10):1479–1486
2. Kromhout JA (2013) Mould powder development for continuous casting of steel. Trans Indian Inst Met 66(5–6):587–596
3. Kromhout JA, van der Plas DW (2013) Melting speed of mould powders: determination and application in casting practice. Ironmaking Steelmaking 29(4):303–307
4. Pradhan N, Ghosh M, Basu DS, Mazumdar S (1999) Prediction of slag pool thickness in continuous casting mould. ISIJ Int 39(8):804–808
5. Kawamoto M, Nakajima K, Kanazawa T, Nakai K (1994) Design principles of mold powder for high-speed continuous casting. ISIJ Int 34(7):593–598

6. Koyama K, Nagano Y, Nagano K, Nagano T (1987) Design for chemical and phyisical properties of continuous casting powders. Nippon Steel Tech Rep 34:41–47
7. Kamaraj A, Ansuman D, Murugaiyan P, Misra S (2020) Investigation on mold flux melting and consumption during continuous casting of liquid steel. Metall Mater Trans B 51(5):2159–2170
8. Wei E, Yang Y, Feng C, Sommerville ID, McLean A (2006) Effect of carbon properties on melting behavior of mold fluxes for continuous casting of steels. J Iron Steel Res Int 13(2):22–26
9. Däcker C-Å, Eggertsson C, Lönnqvist J (2009) Development of a laboratory method for characterization of mould powder melting rate. In: Conference paper presented at the 8th conference on Molten Slags, Fluxes and Salts, Santiago, Chile
10. Münch S (2019) Investigation of the melting behaviour of mold powders and of the slag-steel-interaction close to the meniscus of the mold. Ph.D. thesis, RWTH Aachen University
11. Thomas BG, Jenkins MS, Mahapatra RB (2004) Investigation of strand surface defects using mould instrumentation and modelling. Ironmaking Steelmaking 31(6):485–494
12. Mills KC, Däcker C-Å (2017) The casting powders book. Springer International Publishing, Cham
13. Kim JW, Lee YD and Lee HG (2001) Decomposition of Na_2CO_3 by interaction with SiO_2 in mold flux of steel continuous casting. ISIJ Int 41(2):116–123
14. Kim JW, Lee YD, Lee HG (2004) Decomposition of Li_2CO_3 by interaction with SiO_2 in mold flux of steel continuous casting. ISIJ Int 44(2):334–341

Part VI
Mineralogical Analysis and Process Improvement

Evaluating the Morphology of Crystalline Glass Developed from Corn Cob Ash

Bidemi Omowumi Elesho, Andrew Ojonugwa Adejo, and Adele Dzikwi Garkida

Abstract Samples of Corn cob (Sammaz 40) was collected, beneficiated and pulverized into 10 mm particle size, carbonized at 400 °C for 3 h and activated at 600 °C for 6 h in a furnace, using the approximation method, Sodium-aluminosilicate based glass batch was designed. Adopting the petrurgic method, 5% of the designed batch was melted at 1200 °C for 5 h, cooled to room temperature at 1 °C and 5 °C respectively for every 60 s and a crystallized glass was formed. The glass was analyzed using Scanning Electron Microscopy (ASTM E-986), X-ray diffraction (ASTM E-975) and compressive strength evaluation (ASTM C-773). The results showed the presence of an amorphous and a crystalline phase within a ratio of 70:30 range, sharp Bragg's peak zone near $2\theta = 27$ °C indicates Nepheline (NaAlSiO4) crystalline phase and a compressive strength ranging between 11,000–12000psi which implies that crystalline glass developed from agro-waste (Corn cob) is advantageous in areas where strength is of high essence.

Keywords Morphology · Crystalline glass · Corn cob ash

Introduction

The crystallization or devitrification of glass to form a glass ceramic is usually a heterogeneous transformation that consists of two stages, namely a nucleation stage and a growth stage. In the nucleation stage, small, stable volumes of the product (crystalline) phase are formed mostly at preferred sites in the parent glass. This conversion of glass to glass ceramics undergoes nuclei formation to crystal growth as the

B. O. Elesho (✉)
Department of Glass and Ceramic Technology, The Federal Polytechnic, Ado-Ekiti, Nigeria
e-mail: bidemiadigun91@yahoo.com

A. O. Adejo
Department of Glass and Silicate Technology, Federal University of Lafia, Nasarawa, Nigeria

A. D. Garkida
Department of Glass and Silicate Technology, Ahmadu Bello University, Zaria, Nigeria

M. Zhang et al. (eds.), *Characterization of Minerals, Metals, and Materials 2023*, The Minerals, Metals & Materials Series
https://doi.org/10.1007/978-3-031-22576-5_15

preferred sites are interfaces within the parent glass or the free surface [1]. The latter is usually undesirable as the resulting glass ceramic microstructure often consists of large oriented crystals that are detrimental to mechanical properties. However, in a few instances, an oriented structure is beneficial e.g., glass ceramics for piezoelectric and pyroelectric devices and machinable glass ceramics. Once a stable nucleus has been formed the crystal growth stage commences which involves the movement of atoms/molecules from the glass across the glass-crystal interface and into the crystal. The driving force for this process is the difference in volume or chemical free energy between the glass and crystalline states. The transport of atoms/molecules across the interface is thermally activated with associated activation energy [2].

Glass ceramics from waste can be produced by a method, known as the "Petrurgic method" Rincón and Romero, (1999) [3] named it this way because of the similarity with the process of crystallization of natural rocks. This method has actually been applied since the 1970s, with the development of "Silceram" ceramics from metallurgical slags [4]. It was found with "Silceram" that it made little difference whether the glass was heated up to nucleation and maximum crystallization temperature (T_{NG}) from room temperature or the molten glass was cooled to T_{NG}. This led to the development of the production of certain glass ceramics by a controlled, usually very slow cooling of the parent glass from the molten state without a hold at an intermediate temperature. With this method, both nucleation and crystal growth can take place during the cooling [5].

In recent years glass ceramics have been produced by the synthesis of materials from ash gotten from agricultural waste such as rice husk, corn cob etc. [6, 7]. Numerous silicate based wastes, such as blast furnace slag [5, 8] fly ash, [2, 8] and different types of sludge as well as glass cullet [3, 8] have been considered for the production of glass ceramics. Magnetic glass ceramics have been obtained from mixtures of coal ash and 20–60wt% soda-lime glass by the petrurgic method [4]. This study explores the use of corn cob ash in developing glass ceramic materials that are suitable for high strength applications.

Materials and Methods

Materials

The raw materials used in the course of this work for the preparation of sodium aluminosilicate glass ceramics are corn cobs (agro waste), alumina and soda ash. The corn cobs were obtained from agro-processing plants while as-received alumina and soda ash are highly pure analytical grade and are used as supplementary sources of alumina and sodium oxide. The as-received corn cobs were initially beneficiated by washing to remove adherence of dirt and unwanted particles and air-dried for 7 days. The corn cobs were then ground to smaller particle sizes of about 10 mm to enhance adequate combustion and reduce carbon content [9]. The ground corn cobs

Table 1 Heating schedules for glass ceramic production

Samples	Cooling rate	Duration
A	1 °C/minute	5 h (melting) and 20 h (cooling)
B	5 °C/minute	5 h (melting) and 4 h (cooling)

were placed in an incinerator for combustion into ash. The ash obtained was poured into crucibles and placed in a muffle furnace and heated at a temperature of 600 °C for 6 h to reduce the carbonaceous matter and increase the percentage of active silica content. The obtained whitish corn cob ash was then sieved through a 0.25 mm sieve with mesh number 60. The determination of the chemical composition of the corn cob ash was carried out by X-ray fluorescence spectrometry which identified each of the oxides contained in the ash.

Batch Formulation

The standard composition of sodium aluminosilicate glass [10] was utilized for the batch formulation of the base glass which was converted to glass ceramics. The corn cob ash was used as the major glass former (silica precursor) while alumina and soda ash was used to provide other supplementary oxides required in the batch. The approximation method was used in calculating the batch based on the percentage yield of the major oxides introduced by the various raw materials. A total of 127.56% of batch raw materials was needed for 100% of glass.

Glass Ceramics Production by Petrurgic Method

The Petrurgic method [4] was employed for the development of glass ceramics. The formulated batch was melted in ceramic moulds at 1200 °C for 5 h and cooled to room temperature at the rates of 1 °C and 5 °C per minute to produce a total of 24 samples A, B and C (8 samples each) in a temperature controlled electric muffle furnace. The glass ceramics production was carried out at Dana Steel Limited, Nigeria. Table 1 shows the heating schedules utilized to obtain the glass ceramics.

Characterization

According to ASTM E-986, [11] scanning electron microscopy (SEM) which involves the microstructural morphology of selected spots on each glass ceramic sample was analyzed. X-ray diffraction (XRD) according to ASTM E-975 [12] was carried out on the glass ceramic sample where the sample was finely ground

Table 2 Result of XRF of CCA

Oxides	SiO_2	P_2O_5	K_2O	CaO	Na_2O	MgO	TiO_2	MnO	Fe_2O_3	others
Composition (%)	68.70	1.61	4.56	9.50	4.60	5.20	0.26	0.14	3.44	0.11

and homogenized and mounted on a goniometer and gradually rotated while being bombarded with X-rays, producing a diffraction pattern of regularly spaced spots known as reflections which determined its atomic and molecular structure.

Compressive Strength Test

According to ASTM C-773, [13] compressive (crushing) strength is a mechanical test measuring the maximum amount of compressive load the glass ceramic can bear before fracturing. The sample glass ceramic piece of up to 20 mm square and 5 mm thick was placed on a solid surface and a force was applied with the testing apparatus (Instron 3400 universal testing machine) until the sample failed. Upon failure, the failure force in units of lbf (pound-force) was recorded.

The cross-section area, A of the specimen was calculated. The specimen is four-sided, so the formula $A = LW$, where L is the length and W is the width was used. The area is in units of in^2 or square inches. The compressive strength was calculated using the formula $S = P/A$, where S is the compressive strength, P is the maximum load applied to the specimen and A is the area. The final compressive strength value was in units of psi (lbf/in^2). This was carried out at Dana Steel Limited, Katsina.

Results and Discussion

Chemical Composition (Corn Cob Ash)

The result of XRF analysis of the corn cob ash (CCA) as shown in Table 2 reveals that it contains 68.70% SiO_2 and the rest constituted 29.416%, making the corn cob ash a good source of SiO_2 for glass and glass ceramic production. Also, the Fe_2O_3 content of 3.44% is high enough to serve as a nucleating agent for glass ceramic production.

Visual Observation

Figures 1 (a) and 1 (b) showed the resultant glass ceramics cooled at varying temperature ranges from the molten state. They were characterized by a rough surface which

Fig. 1 **a** Glass ceramics obtained from cooling at 1 °C/minute. **b** Glass ceramics obtained from cooling at 5 °C/minute

is a result of inhomogeneity of the melt which is due to the fact that the alumina contained in the batch requires a higher temperature of 1500 °C to melt. Therefore complete melting of alumina failed to occur at 1200 °C. The batch melted at 1200 °C due to the particle size of the batch which was 0.25 mm. Also, the sodium oxide (Na_2O) contained in the corn cob ash and the addition of soda ash to supplement the required amount of Na_2O required for the development of sodium aluminosilicate glass facilitated the melting process by bringing down the melting point of the batch.

Microstructure and Phase Characterization

Figures 2 (a) and (b) showed the representative morphology of glass ceramics obtained from cooling at 1 °C/min and 5 °C/min respectively. The morphology of the glass ceramic sample obtained from cooling at 1 °C/min showed an irregularly-shaped structure which was due to the precipitation of ceramics in the glassy matrix. So, the grains and clusters shown by this surface are attributed to the formation of nepheline phases. The morphology of the crystalline phase from glass ceramics obtained from cooling at 5 °C/min was characterized by a rough texture also with irregular shapes on it.

Figures 3 (a) and (b) showed the phase composition by XRD patterns of glass ceramic samples obtained from cooling at 1 °C/min and 5 °C/min respectively. Both indicated sharp Bragg's peak zones near $2\theta = 27^0$C which signified that nepheline ($NaAlSiO_4$) was the major crystalline phase present.

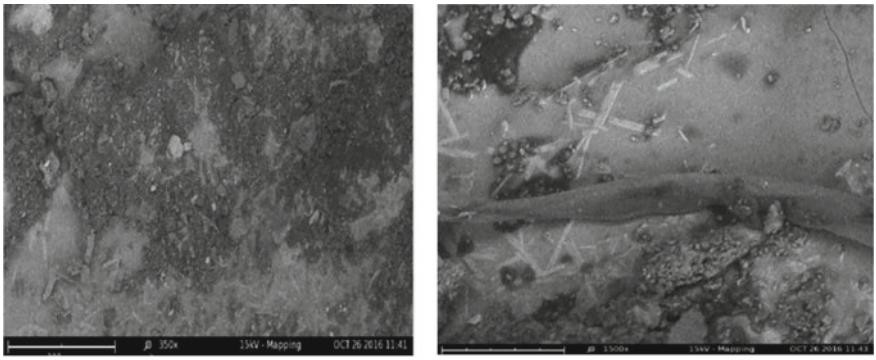

Fig. 2 **a** SEM images of glass ceramics obtained from cooling at 1 °C/minute. **b** SEM images of glass ceramics obtained from cooling at 5 °C/minute

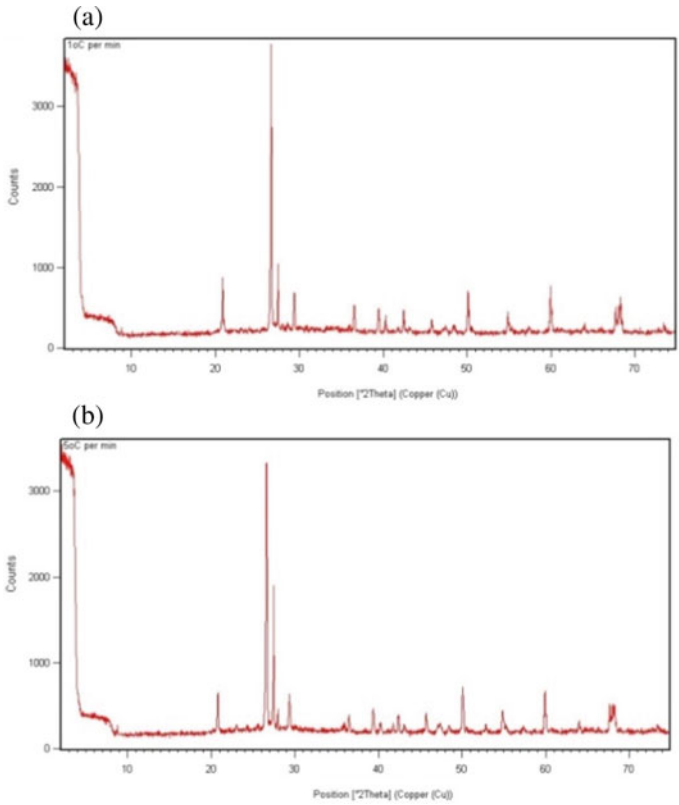

Fig. 3 **a** XRD pattern of glass ceramics cooled at 1 °C/minute. **b** XRD pattern of glass ceramics cooled at 5 °C/min

Compressive Strength

The results of the compressive strength test showed that the samples, A and B requires a load of 4800000lbf and 4400000lbf respectively to fail. Therefore, their compressive strengths of 12000psi and 11000psi conform to the standard of compressive strength of advanced ceramics which is between 8000-20000psi [14].

Conclusion

In this study, investigation was carried out on the crystallization of sodium aluminosilicate glass ceramics using agro waste as silica precursor by the Petrurgic method. From the results and discussions of this study, the following conclusions were drawn;

1. By analyzing the CCA it was found that it contained compounds such as 68.70% SiO_2 and the rest 29.42% which can be used for glass and glass ceramics production.
2. The particle size of the batch which is 0.25 mm and the addition of soda ash as a supplementary raw material for Na_2O served as a flux which made it possible for the batch to melt at 1200 °C for 5 h.
3. The samples exhibited rough surfaces with visible particles of unmelted alumina powder which was added as a supplementary source of Al_2O_3, this was difficult to melt and homogenize with the other raw materials due to its high melting temperature [15].
4. The examination by XRD and the morphology shown by SEM confirmed both crystalline and amorphous phases which identified the material obtained from test-melting the batch as that of glass ceramics.
5. The glass ceramic samples developed possess high strength from compressive strength test carried out and the morphology shown by SEM; therefore they are suitable for commercial applications like floor tiles and wall claddings, building bricks, etc.

References

1. Holand W, Beall G (2002) Glass-ceramic technology, 2nd edn. The American Ceramic Society, Westerville, OH, pp 231–236
2. Rincón JM, Romero M, Boccaccini AR (1999) Microstructural characterization of a glass and a glass ceramic obtained from municipal incinerator fly ash. J Mater Sci 34:4413–4423
3. Ponsot IM (2015) Glasses and glass-ceramic components from inorganic waste and novel processing. PhD. Thesis, University of Padova, Department of Industrial Engineering, pp 47–58
4. Francis AA, Rawlings RD, Boccaccini AR (2002) Glass ceramics from mixtures of coal ash and soda lime glass by the petrurgic method. J Mater Sci 21:975–978

5. Saad MS, Hussein D (2006) Development of glass-ceramic based on blast furnace slag and granite. Ceram Silik 50:88–97
6. Dávalos J, Bonillaa A, Villaquirán-Caicedo MA, Mejía de Gutiérrez R, Rincón JM (2020) Preparation of glass–ceramic materials from coal ash and rice husk ash: microstructural, physical and l mechanical properties. Boletín de la Sociedad Española de Cerámica y Vidrio. https://doi.org/10.1016/j.bsecv.2020.02.002
7. Odewole PO (2022) Properties of glass-ceramics foam based on granite dust-clay-maize cob composite as a sustainable building material. J Sustain Constr Mater Technol. https://doi.org/10.14744/jscmt.2022.07
8. Montoya-Quesada E, Villaquirán-Caicedo MA, Mejía de Gutiérrez R (2022) New glass-ceramic from ternary–quaternary mixtures based on Colombian industrial wastes: blast furnace slag, cupper slag, fly ash and glass cullet. Boletín de la Sociedad Española de Cerámica y Vidrio 61(4):284–299. https://doi.org/10.1016/j.bsecv.2020.11.009
9. Adesanya DA, Raheem AA (2009) Development of corn cob ash blended cement. Constr Build Mater 23:347–352
10. David MZ, Stephen HG (2005) Structure of sodium aluminosilicate glass surfaces. J Am Ceram Soc
11. ASTM E986–04 (2010) Standard practice for scanning electron microscope of glass and glass ceramic materials. ASTM International, West Conshohocken, PA. http://www.astm.org. Accessed 26 May 2016
12. ASTM E975–13 (2015) Standard practice for X-ray crystallography of glass and glass ceramic materials. ASTM International, West Conshohocken, PA. http://www.astm.org. Accessed 26 May 2016
13. ASTM C-773–88 (2016) Standard test method for compressive strength of glass, glass ceramic and fired white-ware. ASTM International, West Conshohocken, PA. http://www.astm.org. Accessed 16 August 2016
14. Jenkins MG, Salem JA (2019) ASTM committee C28: international standards for properties and performance of advanced ceramics. https://core.ac.uk/download/pdf/76422385.pdf. Accessed 6 September 2021
15. Patnaik P (2002) Handbook of inorganic chemicals. McGraw-Hill

Investigation of the Effect of Cr_2O_3 Content on the Surface Tension of Chromium-Containing High-Titanium Blast Furnace Slag

Yaoran Cui, Liangbin Chen, Ying Deng, Jiachang Hao, Zhenyun Tian, Jialong Kang, Ding Yang, and Guibao Qiu

Abstract The influence of the Cr_2O_3 content on the surface tension of $CaO–SiO_2$–9.25 wt.%MgO–14.7wt.%Al_2O_3–22wt.%TiO_2–Cr_2O_3 slag system was investigated in the temperature range of 1450–1550 °C using the ring method. The mechanism of the changes in surface tension with different Cr_2O_3 content in slag was analyzed from the perspective of the model and ion theory in the melts. Increasing the Cr_2O_3 content from 0 to 3 wt.% caused an increase in the surface tension for the reason that the surface tension of Cr_2O_3 is the largest and that of SiO_2 is the smallest in the components of the slag. Another reason is that the anions are repelled to the surface layer of the slag and adsorbed. The surface tension decreased with increasing temperature. This is because of the decrease of interaction force between the ions and the reduction of the bulk phase density between the two phases adjacent to the surface layer.

Keywords Cr_2O_3 · Surface tension · Interaction force · Temperature

Introduction

With the acceleration of consumption of high-grade iron ores, the iron ore resources tend to be depleted gradually [1–3]. The ore raw materials available to iron and steel enterprises are gradually transformed to medium and low–grade raw materials. China has a huge reservoir of vanadium-titanium magnetite (VTM), which mainly exists in Panzhihua, Chengde and Maanshan areas [4–8]. According to the content of Cr_2O_3 in the ore, VTM is divided into ordinary VTM and high-chromium vanadium-titanium magnetite (HCVTM) [9]. In Panzhihua Iron & Steel Co. Ltd., China, the utilization of VTM mostly adopts blast furnace (BF) ironmaking process. The ordinary

Y. Cui · L. Chen · Y. Deng · J. Hao · Z. Tian · J. Kang · D. Yang · G. Qiu (✉)
Chongqing Key Laboratory of Vanadium-Titanium Metallurgy and Advanced Materials, Chongqing University, Chongqing 400044, China
e-mail: qiuguibao@cqu.edu.cn

College of Materials Science and Engineering, Chongqing University, Chongqing 400044, China

M. Zhang et al. (eds.), *Characterization of Minerals, Metals, and Materials 2023*, The Minerals, Metals & Materials Series
https://doi.org/10.1007/978-3-031-22576-5_16

VTM has been consumed a lot with the smelting over the years. HCVTM is bound to be used in the future. In blast furnace ironmaking process. Cr from HCVTM enters into slag in the form of Cr_2O_3, which affects the slagging and smelting-reduction process [10, 11]. The great change in the composition of the slag has a dramatic impact on its physics character (e.g. slag viscosity and surface tension). In our previous work [11, 12], the effect of Cr_2O_3 content on viscosity of chromium-containing high-titanium blast furnace slag has been investigated. Subsequently, this work systematically studied the effect of Cr_2O_3 on surface tension of CaO–SiO_2–9.25 wt.%MgO–14.7 wt.%Al_2O_3–22 wt.%TiO_2–Cr_2O_3 system.

The effect of slag composition on surface tension of BF slag has been studied by several researchers. Tian et al. [13] studied the surface tension of SiO_2–Al_2O_3–RO–R_2O glass system and found that the surface tension of high alkali aluminosilicate glass increases continuously with the increase of Al_2O_3 content. Appropriately increasing the content of Al_2O_3 can make the network structure of glass more compact, so that the energy required to break the network structure of glass becomes greater, and the surface tension of glass becomes greater macroscopically. Dong et al. [14] investigated the effect of MgO and SiO_2 content on surface tension of fluoride containing slag. The surface tension of slag decreases with increasing MgO content when the MgO content is less than 8% but increases when the MgO content is from 8–30%. SiO_2 can reduce the surface tension of the slag when it is in the range from 2 to 8%. However, few researchers have studied the effect of Cr_2O_3 content on CaO–SiO_2–MgO–Al_2O_3–TiO_2–Cr_2O_3 senary slag.

In the present work, the influence of the content of Cr_2O_3 (0 to 3 wt.%) on the surface tension of CaO–SiO_2–MgO–Al_2O_3–TiO_2–Cr_2O_3 slags were studied systematically using ring method. The mechanism of the changes in surface tension with Cr_2O_3 content was considered from the viewpoint of the model and ion theory in the melts.

Experimental

Sample Preparation

In the experimental, CaO–SiO_2–9.25 wt.%MgO–14.7 wt.%Al_2O_3–22 wt.%TiO_2–Cr_2O_3 slags were employed for surface tension measurements and the influence of the content of Cr_2O_3 on slag surface tension were investigated. Through a composition analysis of the on–site slag of Panzhihua steel, the chemical composition of the on–site slag was presented in Table 1. The slag samples were all prepared from pure grade reagents (CaO, MgO, Al_2O_3, SiO_2, TiO_2, Cr_2O_3) according to the on–site slag. Before preparation, CaO was placed in a 950 °C muffle furnace and heated for 10 h to remove impurities and moisture and other reagents were placed in a 100 °C oven and heated for 3 h to remove excess moisture. Then these high–temperature treated reagents were weighed with precision to form given compositions, as shown

Table 1 Chemical composition of blast furnace slag from Pan Steel

CaO	SiO_2	MgO	Al_2O_3	TiO_2	Cr_2O_3
25.88	24.91	9.25	14.69	21.58	*

Table 2 Chemical composition of experimental slag, wt.%

Number	CaO	SiO_2	MgO	Al_2O_3	TiO_2	Cr_2O_3	(CaO + MgO)/SiO_2
1#	27.78	26.27	9.25	14.7	22	0	1.41
2#	27.20	25.85	9.25	14.7	22	1	1.41
3#	26.61	25.44	9.25	14.7	22	2	1.41
4#	26.05	25.12	9.25	14.7	22	3	1.41

in Table 2. The weighed powders (total 200 g) were thoroughly mixed and pressed into cylindrical pellets and placed into a Mo crucible. Mo crucible (I.D: 46 mm, O.D: 48 mm, H: 120 mm) was used in the experiment, which was coated with graphite crucible and filled with 99.999% high purity Ar to prevent molybdenum crucible and ring from being oxidized. The slag samples were heated to 1500 °C and kept for 3 h to homogenize the slag. The dimensions of molybdenum crucible and ring are shown in Figure 1.

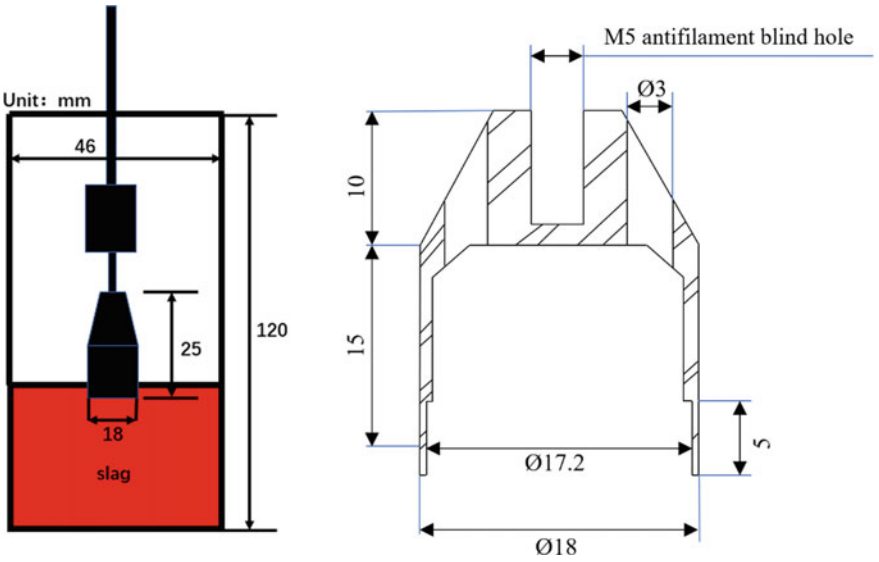

Fig. 1 Dimensions of the molybdenum crucible and ring

Surface Tension Measurements

The ring method has been shown to be a common method for the measurement of the surface tension of the melts [15]. Figure 2 shows the schematic illustrations of the apparatus for slag heating and surface tension measurements. The heating system is mainly composed of Si-Mo furnace, Brookfield viscometer, temperature control cabinet and a computer. $MoSi_2$ rod was used as the heating element and the furnace tube was made of corundum tubes. During measurement, the molybdenum ring was connected to the molybdenum rod with a graphite joint, and the molybdenum rod was placed under the electronic scale. The molybdenum ring was lowered to 5 mm below the slag liquid level by computer. The ring was then slowly pulled out of the slag, and when the ring was about to leave the slag surface, the slag formed a film on the metal ring. As the ring was withdrawn from the surface of the liquid level, the surface tension of the solution will prevent the ring from being pulled out. When the film broke, the tension of the ring reached the maximum. The maximum force was measured 3 times at each of the examined temperatures and take the average. Determination of the surface tension, γ, is based on measurements of the maximum force, W_{max}, exerted on a ring body as the ring is withdrawn from the surface of the liquid [16]. γ is expressed by Eq. (1):

$$\gamma = \frac{W_{\max} \cdot g}{4\pi R_0(1 + \alpha \Delta T)} \cdot S \tag{1}$$

where R_0 is the radius of the ring. S is an empirical correction factor known as Harkins and Jordan's correction factor.

Results and Discussion

Effect of Cr_2O_3 Content on the Surface Tension

Table 3 shows the measured results of surface tension of experimental slag samples under different Cr_2O_3 content. In order to study the influence of Cr_2O_3 content on the surface tension of CaO–SiO_2–9.25 wt.%MgO–14.7 wt.%Al_2O_3–22 wt.%TiO_2–Cr_2O_3 melts, the surface tension values measured under each Cr_2O_3 content and each temperature were plotted as surface tension (γ) –Cr_2O_3 (wt.%) diagram, as shown in Fig. 3 The surface tension increased with increasing Cr_2O_3 content. Lin[17] investigated the surface tension of the CaO-SiO_2-FeO system using pull-tube method under an Ar atmosphere and found a similar trend. With the increase of Cr_2O_3 content, the slag viscosity increased and the surface tension increased. Cr_2O_3 made the greatest influence on the surface tension of slag, as in the tests conducted by Zhang et al. [18] using pull-tube method.

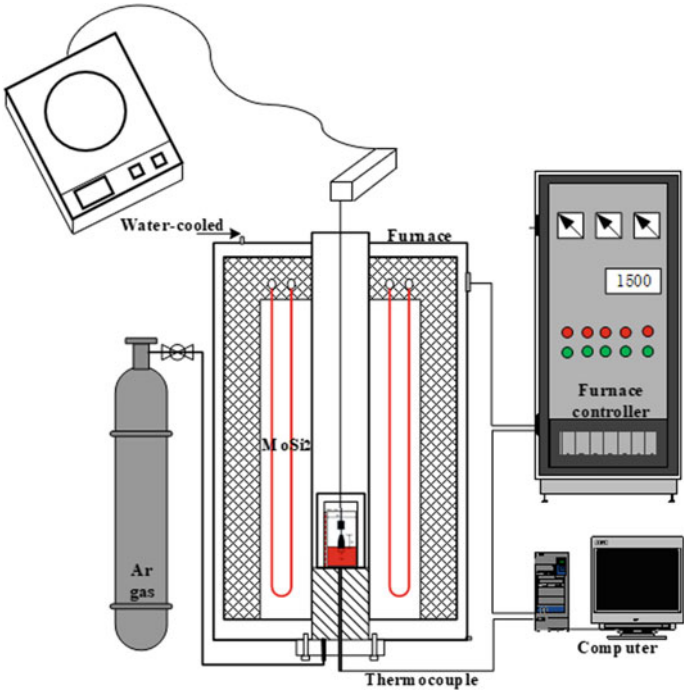

Fig. 2 Schematic illustrations of the apparatus for slag heating and surface tension measurements

Table 3 Measured surface tension values at fixed temperature

Number	Cr_2O_3 (wt.%)	(CaO + MgO)/SiO_2	Surface tension, N/m		
			1450 °C	1500 °C	1550 °C
1#	0	1.41	479.4	473.8	466.5
2#	1	1.41	510.2	505.1	490.1
3#	2	1.41	528.5	521.3	506.2
4#	3	1.41	551.9	540.0	535.4

The surface tensions of some pure oxides at 1773 K (1500 °C) have been given by Mills [19], as shown in Table 4. Based on the ionic solution model, the slag is a kind of ionic structure melt containing oxides, that is to say, the surface tension of the slag can be viewed as infinitely close to the surface tension of the oxide component of the slag, as shown in following equation (Eq. 2). Since the surface tension of Cr_2O_3 (800 mN/m) is more than that of other oxides and the surface tension of SiO_2 (260 mN/m) is the lowest of all the oxides, it follows that surface tension of the slag increases with increasing Cr_2O_3 content and decreasing SiO_2 content.

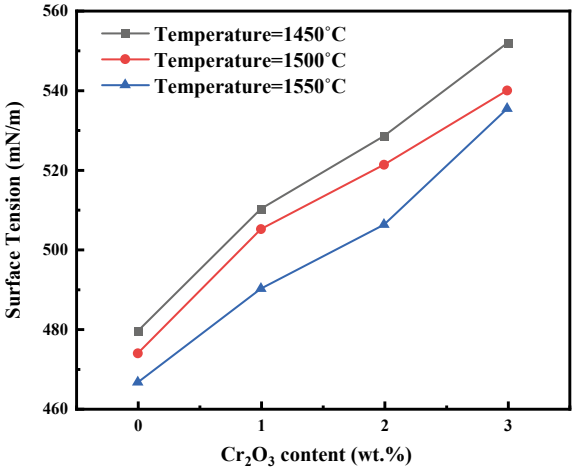

Fig. 3 Effect of Cr_2O_3 content on surface tension of slag

Table 4 Surface tensions of pure slag components at 1500 °C

Oxides	SiO_2	BaO	CaO	MgO	Al_2O_3	MnO	FeO	SrO
Surface tensions (mN/m)	260	560	625	635	655	645	645	600
Oxides	Na_2O	ZrO_2	K_2O	TiO_2	Cr_2O_3	B_2O_3	CaF_2	Fe_2O_3
Surface tensions (mN/m)	295	400	160	360	800	110	290	300

$$\gamma_s = \sum \gamma_i \cdot \chi_i \tag{2}$$

where, γ_s is the surface tension of slag sample (mN/m), γ_i represents the surface tension of the oxides that compose the slag (mN/m), χ_i represents the mole fraction of each component of slag.

From a mechanical point of view, the surface tension of the slag is that the particles (ions or ion groups) in the surface layer of the slag are attracted by the particles in the slag more than the molecules in the gas, and the resultant force is along the tangent direction of the surface of the slag. Therefore, there exists a tendency for slag to reduce its surface area under the action of surface tension. The interaction force between ions is the electrostatic force and the molecular force, but the molecular force is many orders of magnitude smaller than the electrostatic force, and we will only discuss the effect of the electrostatic force. There are a large number of simple cations and complex anions in the slag, and the surface of the slag is mainly occupied by oxygen ions (O^{2-}). Because the ionic radius of O^{2-} is larger than that of other cations, the change of the surface tension of the slag is mainly affected by the interaction between O^{2-} located on the slag surface and adjacent cations. With the increasing Cr_2O_3 content in the slag, Cr is oxidized to form CrO_4^{2-}, and the electrostatic potential of the generated CrO_4^{2-} is much smaller than that of O^{2-}, hence the bond energy between the anion and the metal cation in the slag is small, which leads to the anion

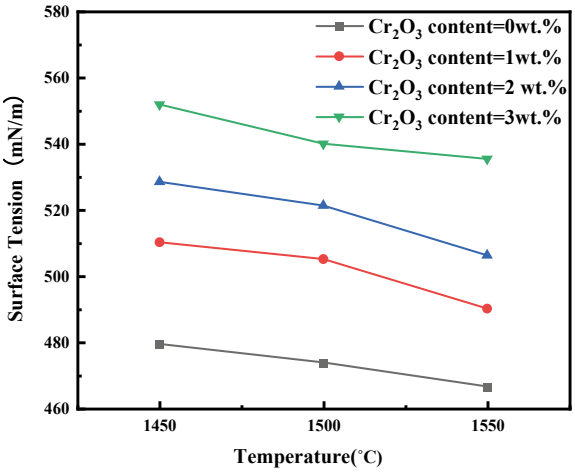

Fig. 4 Effect of temperature on surface tension of slag

being repelled and free to the surface layer of the slag, followed by adsorption, which leads to the increase of the surface tension of the slag. Another reason is that the anions are repelled to the surface layer of the slag and adsorbed. The surface tension decreased with the increasing temperature,

Temperature Dependence of Surface Tension

Figure 4 shows the temperature dependences of the surface tension for the CaO–SiO_2–9.25wt.%MgO–14.7wt.%Al_2O_3–22wt.%TiO_2–Cr_2O_3 slag system. As shown in Fig. 4, the obtained values of the surface tension decreased but changed slightly with the increasing temperature.

One is the effect of temperature on the interaction force between ions in liquid. With the increase of temperature, the thermal motion of the ions increases, and the interaction force between ions decreases, so that the attraction of particles in slag to surface ions or ion clusters weakens, resulting in a decrease of surface tension. The other is the effect of temperature change on the bulk phase density on both sides of the surface. With the increase of temperature, the bulk phase density difference between the two phases adjacent to the surface layer becomes smaller, resulting in the decrease of surface tension.

Conclusions

In the present study, the effect of the Cr_2O_3 addition on the surface tension of the CaO–SiO_2–9.25 wt.%MgO–14.7 wt.%Al_2O_3–22 wt.%TiO_2–Cr_2O_3 melt have been explored.

(1) With the increase of Cr_2O_3 content in slag, the surface tension of the CaO–SiO_2–9.25 wt.%MgO–14.7 wt.%Al_2O_3–22wt.%TiO_2–Cr_2O_3 system gradually increased. This is because the surface tension of Cr_2O_3 at 1500 °C is the maximum while that of SiO_2 is the minimum, so the surface tension of the slag increased with the addition of Cr_2O_3 and reduction of SiO_2. The other reason is that CrO_4^{2-} anion formed by oxidation of Cr are repulsed to the surface of the slag, resulting in an increase in surface tension.
(2) The surface tension of the slag decreased with the increasing temperature. This is because of the decrease of interaction force between the ions and the reduction of the bulk phase density between the two phases adjacent to the surface layer.

Acknowledgements We appreciate the National Natural Science Foundation of China (project no. 52074052) for the financial support.

References

1. Demir O, Eric RH (2013) Rate and mechanism of reduction-dissolution of chromite in liquid slags. High Temp Mat Processes 32:255–63
2. Morita K, Shibuya T, Sano N (1988) The solubility of the chromite in MgO-Al_2O_3-SiO_2-CaO melts at 1 600-degrees-c in air. Tetsu to Hagane 74:632–9
3. Fan G Q, Wang M, Dang J (2020) A novel recycling approach for efficient extraction of titanium from high-titanium-bearing blast furnace slag. Waste Manage 120:626–34
4. Sunahara K, Nakano K, Hoshi M (2008) Effect of high Al_2O_3 slag on the blast furnace operations ISIJ Int 48:420–9
5. Qiu KH, Gong YC, Zhang PC (2009) Scientific and sustainable development of vanadium and titanium industry in Panzhihua. Steel Vanadium Titanium 3:21–4
6. Yang LL (2015) Effect of boron mud and CaF_2 on surface tension and density of CaO-SiO_2-B_2O_3 ternary slag systems J Iron Steel Res Int 21:745–8
7. Hanao M, Tanaka T, Kawamoto M (2007) Evaluation of surface tension of molten slag in multi-component systems ISIJ Int 47:935–9
8. Sukenaga S, Haruki S, Nomoto Y (2011) Density and surface tension of CaO-SiO_2-Al_2O_3-R_2O (R=Li, Na, K) melts ISIJ Int 51:1285–9
9. Yang D, Zhou HH, Wang J (2021) Influence of TiO_2 on viscosity, phase composition and structure of chromium-containing high-titanium blast furnace slag. J Mater Res Technol 12:1615–1622
10. Wang J (2019) Study on Phase and Structure and Viscous Flow Characteristics of Chromium-Containing High Titanium Blast Furnace (in Chinese) (ChongQing University)
11. Qiu GB, Chen L, Zhu JY (2015) Effect of Cr_2O_3 Addition on viscosity and structure of Ti-bearing blast furnace slag ISIJ Int 55:1367–1376
12. Yang D, Zhang F, Wang J (2020) Effect of Cr_2O_3 content on viscosity and phase structure of chromium-containing high-titanium blast furnace slag. J. Mater Res Technol 9:14673–14681

13. Tian YL, Guo SG, Sun SB (2014) Effect of Al_2O_3 on Surface tension of the SiO_2-Al_2O_3-RO-R_2O glass system.Key Engineering Materials 633 322–5.
14. Dong YW, Jiang ZH, Cao YL (2014) Effect of MgO and SiO_2 on surface tension of fluoride containing slag. J Cent South Univ 21:4104–4108
15. Sasaki H, Anzai Y, Huan X (1995) Surface tension variation of molten silicon measured by the ring method Jpn J Appl Phys 34:414
16. Sukenaga S, Higo T, Shibata H (2015) Effect of CaO/SiO_2 ratio on surface tension of CaO–SiO_2–Al_2O_3–MgO Melts ISIJ Int 55:1299–304
17. Lin TC (2016) Study on physicochemical properties and rheological properties of converter slag containing chromium (in Chinese) (ChongQing University)
18. Zhang KH, Wang Y, Zou CD (2020) Calculation model of viscosity and surface tension of converter slag containing chromium. Chin Metall 30:38–43
19. Mills KC (1993) The influence of structure on the physico-chemical properties of slags[J]. ISIJ Int 33:148–155

Research and Practice on the Effect of Different Calcium-Containing Fluxes on the Production of Fluxed Pellets

Xiangjuan Dong, Yu Cao, Jixiang Huo, Shengli Wu, Gang An, Dawei Sun, Yan Zhang, Xiangfeng Cheng, Chengwei Ma, Yunqing Tian, and Wei Wu

Abstract In this paper, five kinds of calcium-containing fluxes (calcium-containing flux A, calcium-containing flux B, calcium-containing flux C, calcium-containing flux D, and calcium-containing flux E) were selected to improve the basicity of pellets, at the same time, their physicochemical properties and microstructure were analyzed and compared. A new production process and technical route of using calcium-containing flux C to produce fluxed pellets were proposed, which has been well applied in Shougang Jingtang Company. The fluxed pellets possessed good quality with basicity at 1.1, SiO_2 at 2.1%, and reduction swelling index at 16.5%. A good application effect was demonstrated that the pellet ratio in the charge of Shougang Jingtang Company increased from 28 to 55%, while the blast furnace slag reduced from 280 to 215 kg/tHM, and the fuel rate is reduced from 500 to 483 kg/tHM.

Keywords Fluxed pellets · Calcium-containing fluxes · Falling numbers · Compressive strength · Reduction swelling index

X. Dong (✉) · W. Wu
Iron and Steel Research Institute, Beijing 100094, People's Republic of China
e-mail: dongxiangjuan715@163.com

X. Dong · Y. Cao · J. Huo · G. An · D. Sun · C. Ma
Shougang Jingtang United Iron and Steel Co. Ltd, Tangshan 063200, Hebei, People's Republic of China

S. Wu
School of Metallurgical and Ecological Engineering, University of Science and Technology Beijing, Beijing 100083, China

Y. Zhang · X. Cheng · Y. Tian
Research Institute of Technology, Shougang Group Co. Ltd., Beijing 100043, People's Republic of China

M. Zhang et al. (eds.), *Characterization of Minerals, Metals, and Materials 2023*, The Minerals, Metals & Materials Series
https://doi.org/10.1007/978-3-031-22576-5_17

Introduction

The blast furnace process dominates the iron-making industry in terms of the production scale and production efficiency with sinter + pellet + lump ore as the main raw material structure [1–3]. Due to historical reasons, sinter has been used in China as the main charging structure, while the proportion of pellets is less than 20% on average. However, compared with sintering, pelletizing has obvious advantages, i.e. low process energy consumption, dust, sulfur dioxide, NOx and other pollutant emissions, and thus increasing pellet proportion in the blast furnace has become a trend. In 2017, the United States still used pellets as the main charge. The average charge was 92% pellets +7% sinter +1% lump ore with 14 of 19 blast furnaces using 100% pellets [4].

To achieve green development and reduce pollutant emissions, Shougang Jingtang Company Phase II increased the pellet production line to increase the proportion of pellets from 28 to 55%. The completed iron-making facilities include three large blast furnaces of 5500 m^3, two sintering machines of 500 m^2 and three roasters of 504 m^2. At present, the proportion of pellets fed into the three blast furnaces in Shougang Jingtang Company is basically stable at about 55%, and the production continues to be stable. After the blast furnace ball ratio was increased, the basicity of the pellets was correspondingly increased to satisfy the basicity balance of the slag, and the research on the production technology of fluxed pellets was carried out. In this paper, the basic study was conducted on five kinds of calcium-containing fluxes needed to increase the alkalinity of pellets, and a new technological route for producing molten pellets using calcium-containing flux C was proposed. It also has been applied in Shougang Jingtang Company and good application results were obtained.

Experimental Materials

There were five kinds of calcium-containing fluxes used in the test, including calcium-containing flux A, calcium-containing flux B, calcium-containing flux C, calcium-containing flux D and calcium-containing flux E. The chemical composition of the five kinds of calcium-containing fluxes were shown in Table 1. Calcium-containing flux B had the highest CaO content, whose CaO content was 90.52%, followed by calcium-containing flux C, which was 72.26%. Calcium-containing flux A, calcium-containing flux B, calcium-containing flux D and calcium-containing flux E were all lumpy, so the flux was finely ground to a particle size of 98% or more below 200 mesh with a ball mill before the experiment.

The chemical composition and particle size composition of iron ore concentrate powder and bentonite were shown in Table 2. The bentonite expansion multiplier, water absorption and particle size index were better, and the specific indicators were shown in Table 3.

Table 1 Chemical composition index of experimental calcium-containing fluxes

Content (%)	SiO_2	CaO	Al_2O_3	MgO	K_2O	Na_2O	S	Burn damage	<200 mesh
Calcium-containing flux B	1.34	90.52	0.28	1.87	0.071	0.075	0.027	10.76	99.23
Calcium-containing flux C	1.19	72.26	0.36	1.22	0.034	0.008	0.037	22.26	98.35
Calcium-containing flux D	0.82	30.23	0.23	19.28	0.11	0.067	0.021	45.37	98.38
Calcium-containing flux E	0.59	36.24	0.11	25.43	0.047	0.10	0.010	36.84	98.52

Experimental Methods and Analysis

The experimental process was based on Shougang Jingtang's 504 m^2 large belt roaster production line, including batching, drying, mixing, disc pelletizing, green pellet roasting and finished product screening, and testing green and roasted pellets for strength, composition and reduction swelling index.

Effect of Different Calcium-Containing Fluxes on Green Pellets Index

To study the balling performance of different calcium-containing fluxes, balling tests of iron ore concentrate powder with five different calcium-containing fluxes of different proportions (1%, 2%, 3%, 4%, 5%) were conducted, and the experimental schemes were shown in Table 4, with the same bentonite ratio of 1.0%.

Balling test methods were shown as follows. Firstly, raw materials were mixed well according to the ratio, and mixed materials were balled. After the ball-making test, the green pellets of 10–12.5 mm were sieved for the analysis test of falling numbers and drop strength.

The variation of the falling numbers of green pellets with the ratio of calcium-containing flux was shown in Fig. 1, and calcium-containing flux C has the most obvious effect on increasing the falling numbers, followed by calcium-containing flux B and calcium-containing flux E. Calcium-containing flux A and calcium-containing flux D have little effect on reducing the falling numbers. In the basic experiment, the falling numbers were 3.5 times/0.5 m, and the falling numbers were 3.5 times/0.5 m, 4 times/0.5 m, 5.5 times/0.5 m, 6.8 times/0.5 m and 7.6 times/0.5 m with the addition of 1%, 2%, 3%, 4% and 5% of calcium-containing flux C.

The drop strength of green pellets varies with the ratio of calcium-containing fluxes as shown in Fig. 2, and the drop strength of green pellets with calcium-containing fluxes was improved. The increase ranges from large to small were

Table 2 Chemical composition indexes of iron ore concentrate powder and bentonite for experiments

Content (%)	TFe	FeO	SiO_2	CaO	MgO	Al_2O_3	P	S	Burn damage	<200 mesh
Iron ore concentrate powder	69.76	29.6	1.8	0.30	0.35	0.29	0.008	0.13	−2.56	89.5
Bentonite	–	–	60.4	2.13	1.89	15.21	0.008	0.013	9.31	98.5

Table 3 Experimental bentonite physical property indexes

Indexes	Colloid price ml/15 g	Blue absorption amount g/100 g	Expansion index ml/2 g	2 h water absorption %
Bentonite	375	29.3	13	350

calcium-containing flux E, calcium-containing flux C, calcium-containing flux B, calcium-containing flux A, and calcium-containing flux D. The drop strength of the green pellets in the basic experiment was 8.35 N/P. With 1%, 2%, 3%, 4%, and 5% of calcium-containing flux E added, the drop strength of the green pellets increased to 8.83 N/P, 9.23 N/P, 10.98 N/P, 11.25 N/P, 12.06 N/P, respectively. When the added amounts of calcium-containing flux C was 5%, the maximum drop strength of green pellets was 11.69 N/P.

The microscopic particle profile of calcium-containing flux A, B, C, D, and E were shown in Fig. 3. The microscopic particle morphology shows that the particles of calcium-containing flux C were the finest and flocculent, followed by the particles of calcium-containing flux B and calcium-containing flux E, which were also flocculent. The particles of calcium-containing flux A and calcium-containing flux D were gravelly, with smooth surface and no flocculation. So, in terms of the particle morphology, calcium-containing flux C, calcium-containing flux B and calcium-containing flux E have relatively good ball-making performance.

Based on the index data of falling numbers, drop strength and microscopic analysis, calcium-containing flux B, calcium-containing flux C, and calcium-containing flux E ball had better balling performance. Therefore, the bentonite ratio was reduced from 1.0 to 0.5% for these three types of calcium-containing fluxes, and the variation of falling numbers with the change of calcium-containing flux was shown in Fig. 4 after the reduction of bentonite. When the bentonite ratio was reduced to 0.5%, the falling numbers were 5.2 times/0.5 m with 3% calcium-containing flux C, 5.8 times/0.5 m with 4.0% calcium-containing flux C, and 6.3 times/0.5 m with 5.0% calcium-containing flux C, which could meet the production requirements. The falling numbers were relatively low for calcium-containing flux B and calcium-containing flux E. In the experimental range, calcium-containing flux B with 5% had the highest falling numbers, with 3.1 times/0.5 m, and calcium-containing flux E with 5% had the highest falling numbers, with 3.3 times/0.5 m. The main reason was that calcium-containing flux C has finer particle shape, higher dispersion, better water absorption, stronger bonding and better ball formation; and calcium-containing flux C itself contains a large amount of $Ca(OH)_2$. During the pellet formation process, it has hydrogel properties, which can improve the plasticity of the mixed powder and thus increase the strength of the raw pellet [5, 6].

Table 4 Experimental proportioning scheme(%)

Serial number	Iron ore concentrate powder proportion	Bentonite proportion	Calcium-containing flux A ratio	Calcium-containing flux B ratio	Calcium-containing flux C ratio	Calcium-containing flux D ratio	Calcium-containing flux E ratio
Baseline	100	1					
1	100	1	1				
2	100	1	2				
3	100	1	3				
4	100	1	4				
5	100	1	5				
6	100	1		1			
7	100	1		2			
8	100	1		3			
9	100	1		4			
10	100	1		5			
11	100	1			1		
12	100	1			2		
13	100	1			3		
14	100	1			4		
15	100	1			5		
16	100	1				1	
17	100	1				2	
18	100	1				3	

(continued)

Table 4 (continued)

Serial number	Iron ore concentrate powder proportion	Bentonite proportion	Calcium-containing flux A ratio	Calcium-containing flux B ratio	Calcium-containing flux C ratio	Calcium-containing flux D ratio	Calcium-containing flux E ratio
19	100	1				4	
20	100	1				5	
21	100	1					1
22	100	1					2
23	100	1					3
24	100	1					4
25	100	1					5

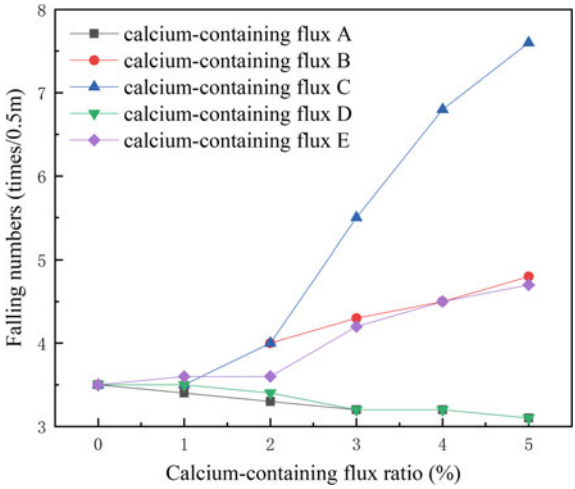

Fig. 1 Trend of the falling numbers with the ratio of calcium-containing flux

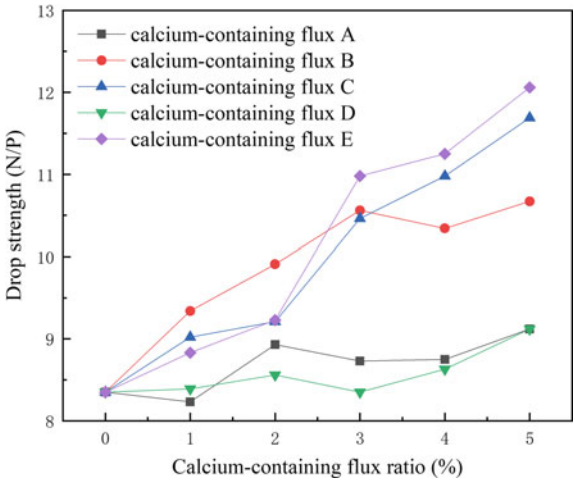

Fig. 2 Trend of drop strength with the ratio of calcium-containing flux

Effects of Different Calcium-Containing Fluxes on the Index of Pellets

The compressive strength of preheated pellets with the ratio of calcium-containing fluxes was shown in Fig. 5. The results show that the compressive strength of preheated pellets without fluxes was 560 N/P when preheated at 950 °C for 15 min, and the compressive strength of preheated pellets with calcium-containing fluxes has a decreasing trend. Calcium-containing flux A and calcium-containing flux D had the greatest effects on the compressive strength of preheated pellets.

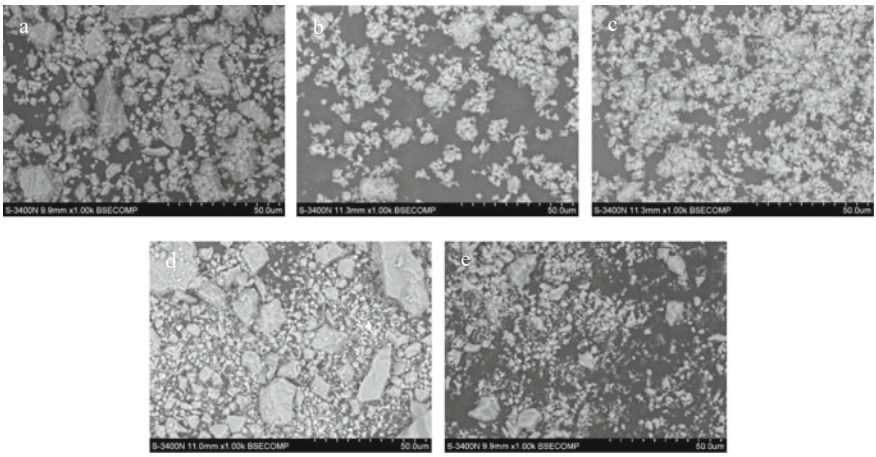

Fig. 3 Particle morphology of calcium-containing flux A, B, C, D, and E

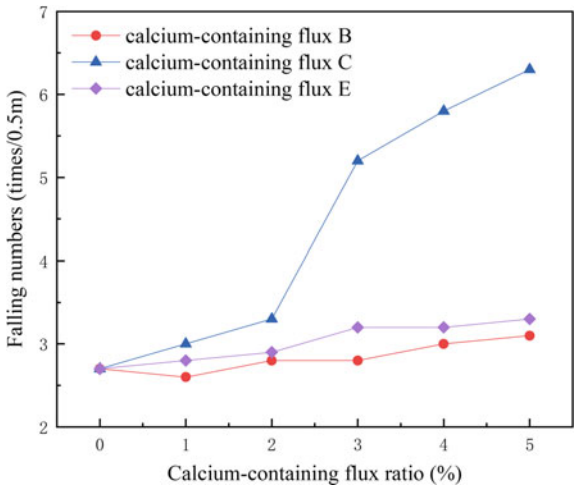

Fig. 4 Variation trend of falling numbers with calcium-containing flux ratio after bentonite lowers

The compressive strength of pellets with the ratio of calcium-containing fluxes was shown in Fig. 6. The results show that the compressive strength of pellets without fluxes was 2835 N/P when pellets were roasted at 1260 °C for 15 min, and the compressive strength of all pellets with calcium-containing fluxes have a decreasing trend. It is mainly because the addition of calcium-containing flux into the fluxed pellets results in the occurrence of calcium iron-acid system which will influence the pellet formation mechanism, leading to the decreasing pellet strength [7]. Calcium-containing flux A, calcium-containing flux D and calcium-containing flux E had the greatest effects on decreasing the compressive strength of pellets. The compressive strength of pellets decreased to 2359 N/P, 2314 N/P, and 2234 N/P when 3%, 4%, and

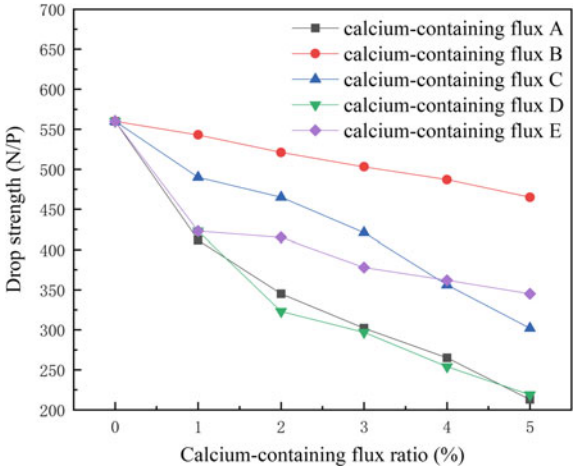

Fig. 5 Trend of compressive strength of preheated pellets with the ratio of calcium-containing flux

5% of calcium-containing flux A were added. However, when 3%, 4%, and 5% of calcium-containing flux D were added, the compressive strength of pellets decreased to 2325 N/P, 2268 N/P, and 2243 N/P, respectively.

The effect of different calcium-containing fluxes on the reduction swelling index of pellets were investigated, and analytical tests on the reduction swelling index of pellets with different proportions of fluxes were carried out. The reduction swelling index analysis test was carried out according to the national standard GB/T 13240–2010. The variation of reduction swelling index of pellet ore with flux was shown in Fig. 7. The experimental results showed that the reduction swelling index of pellets increased and then decreased after the addition of five different calcium-containing fluxes. In the test range, the reduction swelling index of calcium-containing flux B with 4% and 5% pellets reduced to 17.2% and 14.3%, respectively. The reduction

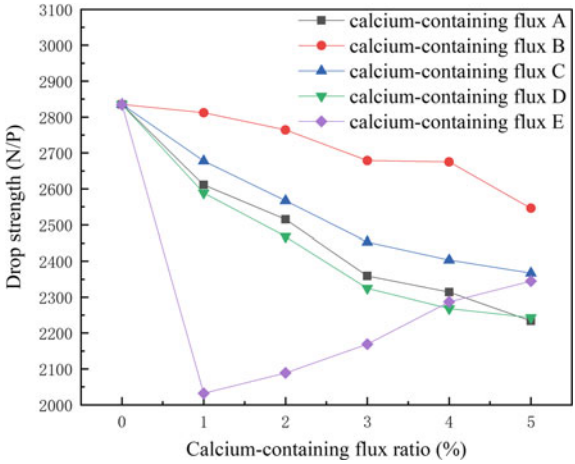

Fig. 6 Trend of compressive strength of pellets with the ratio of calcium-containing flux

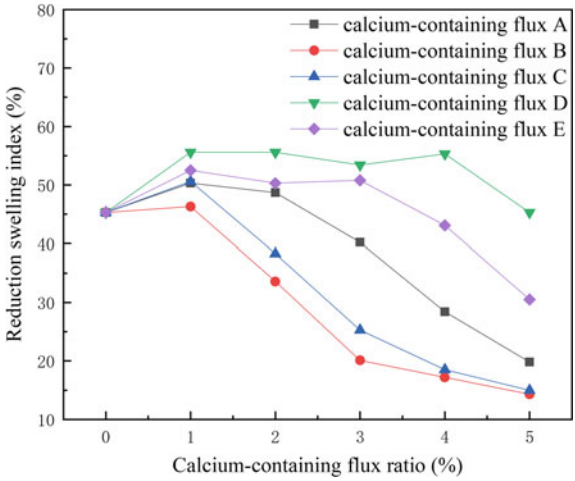

Fig. 7 Trend of pellet reduction swelling index with calcium-containing flux ratio

swelling index of pellets containing calcium-containing flux C with 4% and 5% were reduced to 18.5% and 15.0%, respectively. The reduction swelling index of pellet containing calcium-containing flux A with 5% reduced to 19.5%, which can meet the requirements of blast furnace charging.

Application

A new production process and technical route of using calcium-containing flux C to produce fluxed pellets were proposed by Shougang Jingtang Company according to the experimental results. At the same time, good application results were obtained. Specifically, the fluxed pellets possessed a good quality with basicity at 1.1, SiO_2 at 2.1%, and reduction swelling index at 16.5%. The pellet ratio in the furnace charge of Shougang Jingtang Company was increased from 28 to 55%, while the blast furnace slag was reduced from 280 to 215 kg/tHM, and the fuel rate was reduced from 505 to 483 kg/tHM (Tables 5 and 6).

Table 5 Shougang Jingtang pellets

%	TFe	SiO_2	CaO	MgO	Al_2O_3	Reduction swelling rate
Indicators	65.55	2.10	2.31	0.65	0.52	16.5

Table 6 Shougang Jingtang blast furnace feed structure

	Fluxed pellet ore	Sintered ore	Raw ore
Feeding ratio %	55	42	3

Conclusions

(1) Calcium-containing flux C has the most obvious effect on increasing falling numbers, followed by calcium-containing flux B and calcium-containing flux E. Calcium-containing flux A and calcium-containing flux D have little effect on reducing the falling numbers.
(2) The addition of calcium-containing fluxes increased the drop strength with the increasing range from large to small in the order of calcium-containing flux E, calcium-containing flux C, calcium-containing flux B, calcium-containing flux A, calcium-containing flux D. When the bentonite ratio was reduced to 0.5%, at the 3.0%, 4.0%, and 5.0% calcium-containing flux C, the falling numbers were 5.2 times/0.5 m, 5.8 times/0.5 m, and 6.3 times/0.5 m, which can meet the production requirements. The falling numbers of calcium-containing flux B and calcium-containing flux E were relatively low and could not meet the production requirements.
(3) The compressive strength of preheated pellets with five kinds of calcium-containing fluxes has a decreasing trend.
(4) After the addition of five different calcium-containing fluxes, the reduction swelling index of pellets showed an increasing and then decreasing trend. In the test range, the reduction swelling index of calcium-containing flux B with 4% and 5% pellets decreased to 17.2% and 14.3%, respectively. The reduction swelling index of pellets containing calcium-containing flux C with 4% and 5% decreased to 18.5% and 15.0%, respectively. The reduction swelling index of pellets containing calcium-containing flux A with 5% was reduced to 19.5%, which meets the requirements of blast furnace charging.
(5) Shougang Jingtang Company proposed a new production process technology route of using calcium-containing flux C to produce molten pellets, which has been well applied.

References

1. Zhang FM (2016) Future-oriented development direction of low-carbon green blast furnace ironmaking technology. Ironmaking 35(1):1–6
2. Mao QW, Zhang QF, Li X, Liu GY, Chen J (2020) Research and application of high proportion pellet ore technology for very large blast furnaces. Ironmaking 39(6):1–6
3. Xu MX, Feng GS, Qi CL (2019) On the future of blast furnace charge structure and high quality pellet ore production in China. World Met 2019-12-06(B16)
4. Liu WQ, Su BX, Zhang M (2019) Comparative analysis and innovative development of ironmaking technology in China and the United States. World Met 2019-01-2-03(B02)
5. Jiang T, Fan XH, Li GH (2014) Theory and technology of fusible pellet ore production. In: 2014 National ironmaking production technology conference and annual ironmaking academic conference. Zhengzhou, 13-16 May 2014

6. Xu JX (2014) Experimental research of alkaline pellets of Chengchao iron mine. Master thesis, Wuhan University of Science and Technology
7. Zhang YM (1997) Theory and process of pellets. Metallurgical Industry Press, Beijing

Characterization of Rayfield-Jos Columbite Deposit for Efficient Beneficiation and Recovery of Niobium and Tantalum

Nnaemeka S. Nzeh, Patricia Popoola, Samson Adeosun, and Abraham Adeleke

Abstract The study primarily focuses on the characterization and physicochemical investigations of columbite samples from Rayfield-Jos, Plateau state, Nigeria. Samples were prepared and characterized by particle size, microstructural, physical and chemical analyses. Further, density/specific gravity, pH, moisture content and water absorption were determined. Chemical analyses showed reasonable compositions of Nb/Ta penta-oxides with certain degree of impurities/gangue minerals including radioactive materials. Results of analyses conducted strongly depict the columbite deposit as a somewhat promising mineral source of Nb and Ta but however of low-grade, and with the potential in developing appropriate, (cost) effective beneficiation routes for the metal(s) recovery. Thus, the study will create baseline information on choice selection as well as designing suitable, feasible extraction process routes/techniques to efficiently harness the refractory metals and other value metals from the study area. This will also serve as a tool in the advancement of mineral upgrade/beneficiation routes prior to hydrometallurgical and thermal treatments.

Keywords Columbite mineral · Rayfield-Jos · Niobium · Tantalum · Physicochemical · Characterization · Beneficiation

N. S. Nzeh (✉) · P. Popoola
Department of Chemical, Metallurgical and Materials Engineering, Tshwane University of Technology, Pretoria West 0183, South Africa
e-mail: 220056104@tut4life.ac.za

S. Adeosun
Department of Metallurgical and Materials Engineering, University of Lagos, Akoka 100213, Nigeria

A. Adeleke
Department of Materials Science and Engineering, Obafemi Awolowo University, Ile-Ife 220002, Nigeria

M. Zhang et al. (eds.), *Characterization of Minerals, Metals, and Materials 2023*, The Minerals, Metals & Materials Series
https://doi.org/10.1007/978-3-031-22576-5_18

Introduction

Columbite is generally described as a low-grade complex oxide ore of majorly metal oxide compounds like niobium penta-oxide (Nb_2O_5) of ~ 55–78% content and ~ 5–30% tantalum penta-oxide (Ta_2O_5) as its main constituents in the ore composition with significantly associated oxide gangue minerals/elemental impurities [1–6]. Its composition is proportional to its specific gravity (SG) with high values of ~ 5.0 to about 8.0. The SG increases with increase in Nb and Ta contents and decreases with the presence of gangue/elemental impurities like Fe_2O_3, Mn_3O_4, MgO, TiO_2, SnO_2, Al_2O_3, SiO_2, ZrO_2, CaO, WO_3, Sc_2O_3, Y_2O_3, ThO_2 and UO_2 contained in the ore [6–10]. Columbite ore is regarded as the most important primary source of Nb and/or sometimes Ta [10]. It is often time referred to as tantalite [$(Fe,Mn)(Ta,Nb)_2O_6$] when Ta_2O_5 content in the mineral ore is significantly greater than Nb_2O_5 [4]; and at times, referred to as columbite-tantalite (coltan) when it has almost equal percentage content of Nb_2O_5 and Ta_2O_5. Columbite generally has a composition of about 40–75% Nb_2O_5 and 1–40% Ta_2O_5; Tantalite with a composition of about 2–40% Nb_2O_5 and 42–84% Ta_2O_5; Coltan with about 25–60% Nb_2O_5 and 20–50% Ta_2O_5; and a composition of about 10–20% Fe_2O_3, 2–6% MgO, 0.5–3% TiO_2, 2% SnO_2 for columbite, tantalite and coltan respectively [11, 12].

There is generally a lack of Nb and Ta processing plants in the mineral processing industries, especially in the separation/purification of Nb from Ta. Howbeit, the Nb and Ta mineral ores are usually processed after being mined through rigorous process steps applying several various process techniques for the production of high purity Nb and Ta metals. The successful and efficient mineral processing in order to obtain certain essential mineral products or value minerals is usually on the basis of the knowledge and complete understanding of the minerals' physicochemical property differences of the different various mineral species contained in the mineral ore deposit. Thus, a complete comprehension of the physical and chemical properties as well as the mineralogical characteristics of the Nb and Ta mineral deposits is imperative in order to achieve efficient/effective, environmentally friendly beneficiation and separation techniques. However, mineralogy which includes: occurrence, physical appearance and chemical composition of mineral deposits, may vary significantly with their geographical locations [11–14]. Table 1 depicts some economically essential Nb and Ta minerals, their major characteristics and locations.

Rayfield-Jos is a popular area in Nigeria, known for the mining and production of several distinctive minerals such as cassiterite, columbite, tantalite or coltan deposits. However, there has not been any significant study carried out for the purpose of characterizing and analyzing the physical properties of the low-grade columbite mineral deposited in this area. This study is therefore imperative as it focuses on the characterization and physicochemical analyses of the columbite mineral sample collected from the Rayfield-Jos deposit. In addition, certain mineral characterization methods which include the X-ray diffraction (XRD), X-ray fluorescence (XRF), scanning electron microscopy (SEM) coupled with the energy dispersive spectroscopy (EDS) as well as some other physical characterization techniques were performed on the

Table 1 General characteristics of some important Nb/Ta minerals

Minerals/chemical content	Locations	Major characteristics/properties				
		Colour	SG	Structure	Host/occurrence/deposition	Mag/electrostatic response
Columbite-tantalite (Coltan) $(Fe,Mn)(Nb,Ta)_2O_6$	Australia, Brazil, DRC, Ethiopia, Finland, France, Japan, Madagascar, Nigeria, Norway, Russia, USA	Black to reddish-brown	5.2–8.2	Orthorhombic	Carbonatites, Beryl pegmatites (granitic and syenitic), Peraluminous granites, Peralkalines	P; C
Pyrochlore $(Na,Ca)Nb_2O_6(O,OH,F)$	Brazil, Canada, DRC, Norway	Dark black to pale yellow	4.2–5.8	Isometric; Octahedral	Carbonatites, Peralkalines, Pegmatites	D; C
Microlite $(Na,Ca)_2Ta_2O_6(O,OH,F)$	Australia, Brazil, Madagascar, Norway, Sweden, USA, Zimbabwe	Pale yellow to brown	5.5–6.4	Isometric; Cubic isomorphic	Carbonatites, Peralkalines, Pegmatites	D; NC
Fergusonite $(REE)(Ba,Nb,Ta)O_4$	Australia, Madagascar, Norway, Rhodesia, Russia, Srilanka, Sweden, USA	Brown to yellow	4.3–5.8	Tetragonal; Monoclinic	Granitic pegmatites	P; C
Samarskite $(Fe,Ca,U,Y,Ce)_2(Nb,Ta)_2O_6$	Canada, DRC, India, USA	Reddish-brown to black	4.2–6.2	Orthorhombic	Granitic pegmatites	P-F; C
Mossite-tapiolite $(Fe,Mn)(Nb,Ta,Ti)_2O_6$	Morocco	Black to brownish-black	7.3–7.9	Tetragonal	Granitic pegmatites	P; C

Adopted from Nzeh et al. [5]

Key: *SG* Specific gravity, *Mag* Magnetic, *F* Ferromagnetic, *P* Paramagnetic, *D* Diamagnetic, *C* Conductive, *NC* Non-conductive

Rayfield-Jos columbite mineral sample. Since the nature and composition of the associated minerals in the ore deposit are usually explained via proper characterization analyses, this study was carried out in order to ascertain the general characteristics of the columbite mineral from Rayfield-Jos and to also have an in-depth understanding/knowledge of the mineral's physicochemical properties. This will therefore serve as a tool in dictating and selecting the most appropriate and efficient mineral processing routes for the columbite mineral. It will also provide baseline information or data for selecting and designing the proper technique for (cost) effective mineral beneficiation and processing/harnessing of high purity level or degree recoveries of columbite mineral as well as Nb/Ta metal from this mineral deposit for industrial purposes.

Experimental

Collection and Preparation of Sample

A representative columbite deposit of about 50 kg was obtained for this study. Figure 1 shows the Rayfield-Jos mine area and the as-received columbite sample, respectively. Samples were thoroughly washed off clay, dirt/debris and dust coatings in situ, sun dried then homogenized and re-weighed subsequently. In order to achieve a true representation of the sample, it was taken for coning, quartering and splitting (10-way riffle splitter) processes [15, 16] before being subjected to characterization by physical, chemical, morphological and particle size distribution analyses. Hitherto, the coning and quartering technique was done by pouring the samples into a conical heap, which was then flattened and made into four sample sections that were identical. Samples on the opposite sides were chosen and selected as representative samples [17]. This process was repeated further until about 1 kg of the homogenized sample was got, split further and taken for microstructural, chemical composition and PSD analyses. Hence, this study adopted the following methodology to achieve the physicochemical characteristics of the mineral.

Fig. 1 **a–c** Rayfield-Jos mine area. **d** As-received (washed and dried) columbite sample

Sample Characterization

Particle Size Distribution

PSD was carried out in this study in order to indicate the size range by which the mineral particles with commercial or industrial value are likely to be beneficiated. As represented in Table 2 and graphically illustrated in the PSD curve in Fig. 2, the columbite sample particles of 15.38% oversize particles were retained on the 425 μm sieve (which was regarded as the coarsest sieve). This is as a result of the presence of little rocky particles in the sample. Howbeit, about 84.61% of the sample undersized particles passed through the sieve. Similarly, the 355 μm sieve retained sample particles of about 10.66% with undersize particles of about 73.95% passing. Also, 31.31% was retained on the 250 μm sieve with about 42.64% passing of undersized particles. In the same way, 150, 90 and 53 μm sieves retained oversized sample particles of 17.07, 1.75 and 0.27% respectively; having about 11.06, 2.16 and 0.27% undersize particles passing accordingly. It was observed further that 0.2% particles of the columbite sample were retained on the 38 μm sieve which was considered the finest sieve. However, about 0.07% of finer particles passed through the sieve and were received on the pan.

The PSD results in Table 1 indicated that the crude columbite particulate is defined generally within a variety of particle size fractions from 38 to 500 μm (− 500 + 38 μm). The PSD graphical representation or curve in Fig. 2 shows the cumulative weight % undersize and oversize of the columbite particles plotted against the sieve sizes. From the PSD analysis carried out, it can be seen that the cumulative wt % undersize decreased proportionally as the particle size decreased while that of the

Table 2 PSD of the Rayfield-Jos columbite sample

Sieve size (μm)	Weight (g)	Weight (%)	Norminal aperture (μm)	Cumm. oversize (%)	Cumm. undersize (%)
+ 425	45.6	15.38	425	15.38	84.61
− 425 + 355	31.6	10.66	355	26.04	73.95
− 355 + 250	92.8	31.31	250	57.35	42.64
− 250 + 212	43.0	14.51	212	71.86	28.13
− 212 + 150	50.6	17.07	150	88.93	11.06
− 150 + 106	21.2	7.15	106	96.08	3.91
− 106 + 90	5.2	1.75	90	97.83	2.16
− 90 + 63	4.8	1.62	63	99.45	0.54
− 63 + 53	0.8	0.27	53	99.72	0.27
− 53 + 38	0.6	0.2	38	99.92	0.07
− 38 (Pan)	0.2	0.07	–	–	–
Total	296.4	99.99			

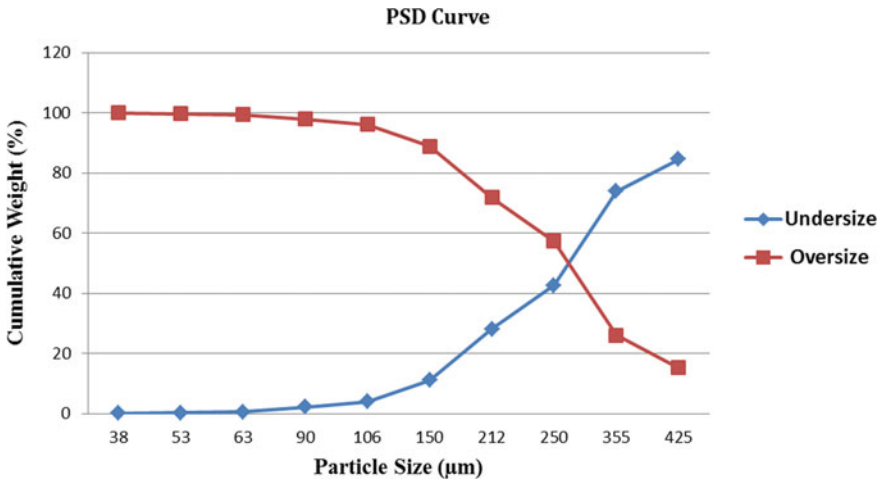

Fig. 2 Graphical representation of the PSD curve

oversize increased significantly as the particle size decreased. However, particle sizes from 90 to 38 µm (− 90 + 38 µm) had no significant change in cumulative wt% for both undersize and oversize cumulative wt %. This indicates and also confirms that the 80 and 60% passing of the columbite samples have particle size fractions of approximately 395 and 308 microns respectively which are in the range of − 425 + 355 and − 355 + 250 µm sieve sizes. This observation explains that the columbite sample particles are mainly of moderately sized particles (ranging from medium or moderately fine to fairly coarse particle sizes); indicating more columbite particulates of about 88.93% falling within the range of 150 to about 500 microns (− 500 + 150 µm) size fractions for the coarser particles, about 8.9% particles within 90–150 µm (− 150 + 90 µm) for medium particles and about 2.16% columbite particles falling within 38–90 µm (− 90 + 38 µm) for the finer particles. A particle size range of − 355 + 250 µm was determined to have the highest retained particle fraction of about 31.31% which corresponds with literature [5]. As the particle size decreased, especially at ≤ 150 microns, there was a drastic change or difference in colour and texture of the mineral particles from lighter to darker or black particles. This practically explains that silica and zirconia are more deposited in coarser particle sizes while the hematite and columbite particles are in finer sizes. Therefore, adoption of physical pre/primary concentration techniques such as mineral processing applications like magnetic and gravity concentration for columbite upgrade is encouraged prior to hydrometallurgical extraction of Nb and/or Ta.

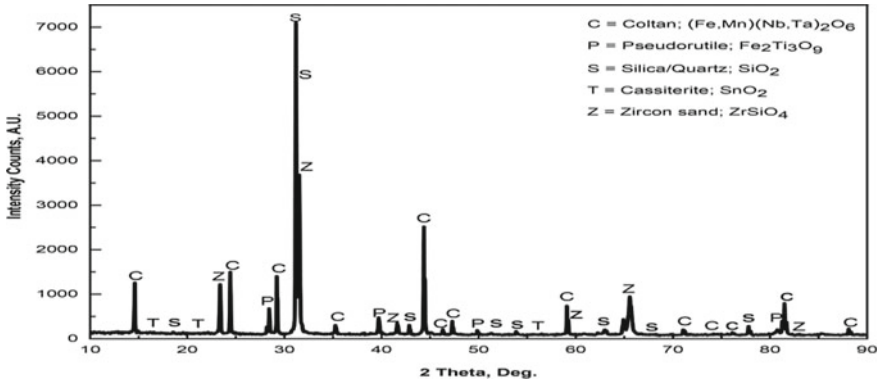

Fig. 3 XRD phase pattern of the columbite mineral sample

Phase Analysis

The analytical test for identifying and quantifying the mineral phases was carried out as can be seen in Fig. 3. The XRD analysis conducted produced scattered X-ray peaks indicating crystalline materials. Each mineral in the ore produced a specific X-ray fingerprint of different intensities against a scattering angle. This is regarded as the characteristic of the columbite mineral crystalline atomic structure as well as the presence of quartz and zirconia. The intensity of the various peaks indicated different compositions of different minerals ranging from ferro-columbite, zirconia to quartz. The mineral sample showed high intensity peaks of quartz compared to the other mineral compositions. This indicates that the ferro-columbite mineral's major impurity is silica. Cassiterite and pseudo-rutile minerals are also present in somewhat lower quantities. However, it also showed the presence of ferro-columbite and zirconia in almost similar increased proportions.

Chemical Analysis

The associated elements with Nb/Ta contained in a columbite-tantalite (coltan) mineral deposit have been reported to be the major factors contributing to the physicochemical properties/characteristics of the mineral sample [12, 13]. Hence, proper characterization analyses in order to determine these associated elemental compositions in the columbite mineral sample brings about the feasible selection of suitable, appropriate beneficiation method. From results of the ED-XRF chemical composition analysis conducted, it can be seen that the columbite deposit from Rayfield-Jos is a promising mineral deposit for the extraction of Nb. However, the mineral deposit is of low-grade, as it has been reported that any Nb–Ta deposit with Nb_2O_5 and/or Ta_2O_5 composition < 25% is a low-grade deposit [12, 18]. The

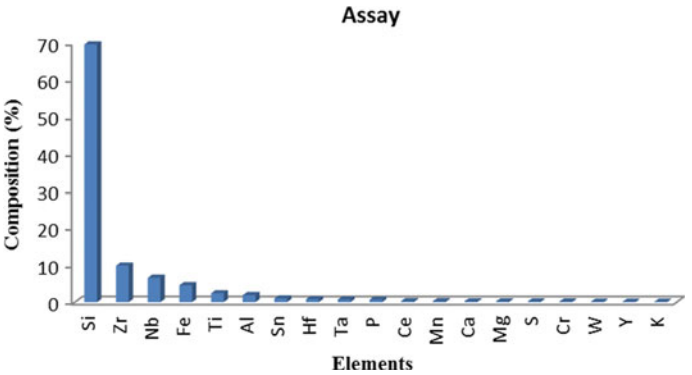

Fig. 4 Assay of Rayfield-Jos columbite sample

sample however contains mainly silicon dioxide (SiO_2), zirconium dioxide (ZrO_2), niobium penta-oxide (Nb_2O_5), iron III oxide (Fe_2O_3), titanium dioxide (TiO_2), and oxides of aluminum (Al_2O_3), tin (SnO_2), hafnium (HfO_2) and tantalum pent-oxide (Ta_2O_5) as major constituents with large percentage compositions of 69.60, 9.88, 6.60, 4.58, 2.39, 1.90, 0.99, 0.80 and 0.70% respectively. However, P_2O_5, CeO_5, MnO, CaO, MgO, SO_3, Cr_2O_3, WO_3, Y_2O_3, K_2O are in somewhat minute compositions. Howbeit, the radioactive property (uranium) of the mineral deposit was detected in trace and somewhat negligible amounts of ~0.0686%. Figures 3 and 4 respectively depicts the graphical distribution of the XRD pattern/phases and assay of the Rayfield-Jos columbite.

The ED-XRF result gave the percentage quantity of Fe_2O_3 and MnO to be 4.58% and 0.23%; Nb_2O_5 and Ta_2O_5, 6.60% and 0.70% respectively. As regards the general chemical formula of columbite mineral ore, $(Fe,Mn)(Nb,Ta)_2O_6$, this simply confirms that the columbite sample is a ferro-columbite mineral. Thus, it explains the possibility of a relatively high magnetic field. Hence, the presence of Fe_2O_3 and other ferromagnetic and strong paramagnetic responses such as TiO_2 and NiO compounds. Weak paramagnetic responses such as MnO, Nb_2O_5 and Ta_2O_5 were also present indicating significant difference in magnetism and the utilization of such material response differences for separation [7, 19–21]. The sample chemical composition analysis also showed the difference in density and specific gravity of the particles present in the columbite deposit. Hence, significant presence of heavy materials such as stannic oxide (SnO_2), haematite (Fe_2O_3), titania (TiO_2), zirconia (ZrO_2) and Nb/Ta_2O_5 amidst lighter materials such as silica (SiO_2) and aluminum (Al_2O_3), etc. were indicated, which however can be utilized in separating each other [19, 22–27]. The knowledge of the difference in their electrical conductive/electrostatic responses can also be utilized [19–21, 24, 26]. Thus, the material particles with varying density and specific gravity, magnetic, electrical and conductive responses however explains the possibility of exploiting their characteristics, upgrading and processing the columbite adopting certain physical separation techniques such as

gravity, magnetic and electrostatic separations respectively for subsequent extraction and recovery of Nb. More so, the radioactive properties (U and/or Th elements) were negligible or detected in very trace quantities. This was however < 0.5 wt% critical value. This therefore is a key factor by which its absence enables better handling and transportation, and reduces the process complexity and cost during Nb/Ta extraction/recovery [28].

Morphological/Microstructural Analysis

The microstructural of the columbite from Rayfield-Jos using a scanning electron microscope is represented in Fig. 5. The SEM-EDS was carried out in order to investigate the mineral's surface morphological characteristics as well as determining the elemental composition of the columbite mineral. The examined SEM microstructure of magnifications 300× and 100×, respectively; indicated significant amount of aggregate mineral particulates in particle sizes ranging mainly between 150 up to 500 μm, and of shapes varying from sub-hedral, sub-angular, spherical to sub-angular. Thus, in line with literature [1, 22] and also confirmed by the chemical composition analysis carried out, it is evident that the major constituents are suspected to be silica, zirconia and columbite, respectively. In addition, the peaks from the semi-quantitative EDS analysis shown in Fig. 6 explained the presence of different elements, ranging from Nb, O, Si, Sn, Zr, Fe, Al, Ta, and Mn, with significant compositions. From the EDS analysis in Fig. 6, it is however evident that the major elemental composition associated and dominating the columbite mineral includes Nb, Fe, as well as Si, which explains the mineral to be a silica-based ferro-columbite (Fe-columbite), and thus corresponds to the mineral phases, such as: columbite-tantalite (coltan), silica/quartz, zircon sand as well as pseudo-rutile, obtained from ED-XRF analysis conducted on the mineral.

Moisture Content and Water Absorption Determination

The MC of the columbite mineral was gotten as a percentage (MC%) of the dry sample weight. Table 3 represents different weight values obtained in the course of determining the MC of the columbite sample and its percentage mean value of ~0.56% MC%. WA of the columbite was calculated as a percentage (WA%) in Table 4. The results show that the columbite has an average WA% of ~0.02%. The low WA can be attributed to the high presence of Si in the mineral deposit. This explains that the mineral has a high degree of porosity and large amount of pores thereby allowing poor absorption and retention of liquid. This characteristic however may act as a limitation in dissolving the columbite mineral in solvents during dissolution and hydrometallurgical treatments of the value metals.

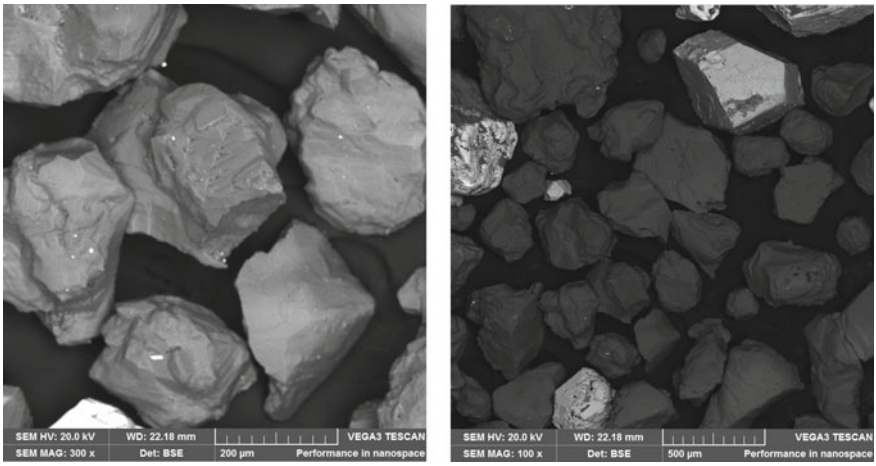

Fig. 5 SEM microstructural view of the Rayfield-Jos columbite sample

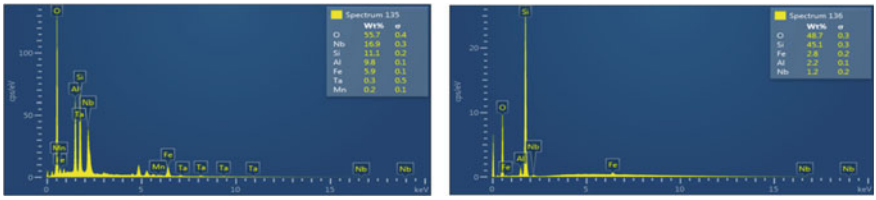

Fig. 6 EDS spectra of the columbite mineral sample

Table 3 Moisture content determination

MC tests	Sample (g)	MC% 1	MC% 2	MC% 3	Mean MC%	Mean % MC
A	50	0.60	0.60	0.20	0.47	**0.56%**
B	50	0.81	0.60	0.40	0.60	
C	50	0.40	0.60	0.81	0.60	

Table 4 Water absorption determination

WA tests	Sample (g)	WA%	Mean % WA
A	10	0.0204	**0.02%**
B	10	0.0228	
C	10	0.0234	
D	10	0.0179	

Table 5 Effect of sieve size on SG and pH parameters

Sieve size (μm)	Nominal aperture (μm)	SG	Ph
− 500 + 38	Crude	1.50	8.58
+ 425	425	1.18	7.61
− 425 + 355	355	1.25	7.51
− 355 + 250	250	1.43	7.73
− 250 + 212	212	1.67	7.58
− 212 + 150	150	1.82	7.71
− 150 + 106	106	1.43	7.54
− 106 + 90	90	0.65	8.18
− 90 + 63	63	0.61	7.86
− 63 + 53	53	0.55	7.85
− 53	–	0.55	7.85

Specific Gravity (SG) and pH Level Determination

The SG and pH values of the crude columbite sample were determined by a densimeter and a potentiometer, respectively, to be averagely about 1.50 and 8.58 respectively. Thus, indicating that the columbite deposit from Rayfield-Jos is a slightly dense basic mineral. Furthermore, the mean SG and pH of the columbite sample were determined for different sample particle sieve sizes as illustrated in Table 5 and the effect of the different sample sizes on the parameters were obtained.

From Fig. 7, it can be seen that the columbite sample of particle sizes between 53 and 425 μm, has a range of SG of 0.55–1.82. The SG of the sample increased rapidly with increasing particle size from 53 up to 150 μm. However, as the particle size increased from 150 up to 425 μm, there was a gradual reduction in the SG. This is due to the separation of less dense mineral particles of silica and zirconia from the denser particles of ferro-columbite and haematite. This does not only explain that the columbite sample composed, of different mineral particles (value and gangue) is of different sizes, but also they vary in density/SG. In this regard, it is safe to say that a physical mineral beneficiation process which involves the separation of particles using their sizes and specific gravities as its separation medium can be utilized effectively, as a pre/primary concentration process for the upgrade and enrichment of low and high-grade Nb/Ta minerals, respectively. This technique could either be a dry or wet gravity separation or a centrifugal assisted gravity concentration process, accordingly. This is also in line with the reports by various researchers [4, 6, 10, 18, 29–34]. Figure 8 shows the pH levels of the columbite at different size fractions, with indications that the mineral is slightly alkaline. This paves way to the mineral chemistry and reaction considerations, as well as the selection of suitable chemical reagents, decomposition solvents, leaching and hydrometallurgical reagents. Table 6 depicts a summary of the physicochemical characteristics of the Rayfield-Jos columbite deposit. Table 7 represents the associated minerals of the

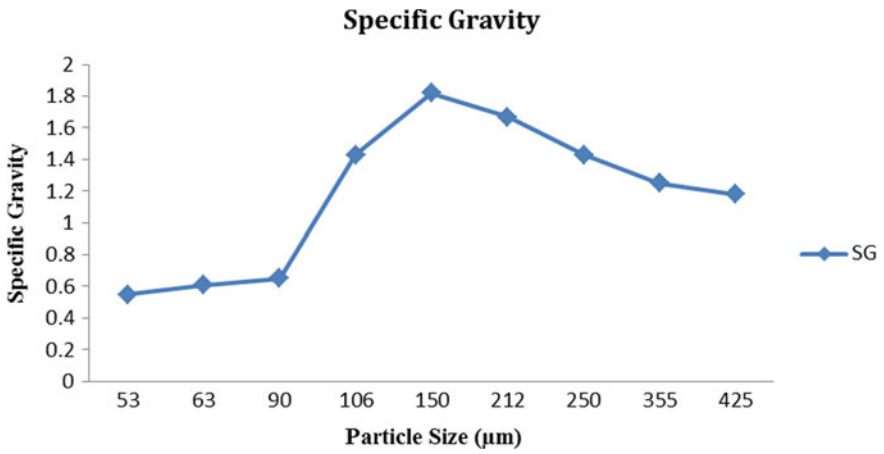

Fig. 7 Graphical representation of SG against particle size

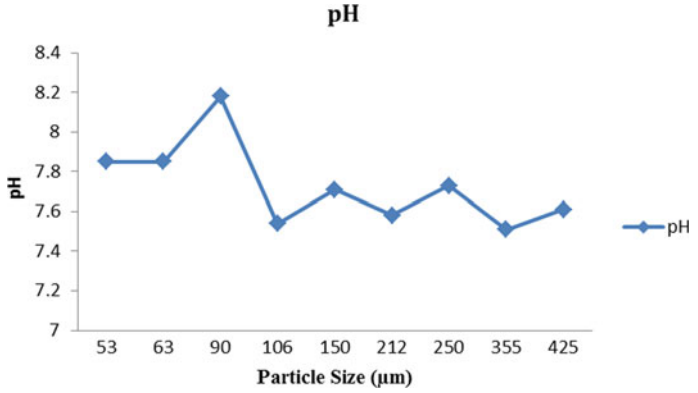

Fig. 8 Graphical representation of pH against particle size

Rayfield-Jos columbite deposit along with some of their magnetic and electrostatic responses.

Conclusion

It has been established very essential to explore and exploit untapped reserves and imperative to undergo proper and effective characterization of the mineral deposits for future exploitations. The characterization of these minerals with regards to their chemical composition, percentage content of the value and associated minerals or gangue, morphology, particle/grain size, texture, habit, and other physicochemical

Table 6 Characteristics of Rayfield-Jos columbite mineral

Properties	Mineral responses
60% passing (μm)	308.22
80% passing (μm)	394.73
Mean particle size (μm)	250
Mesh of grind (μm)	250
Median mesh size (%)	50
Bulk density (g/cm^3)	2.86
Specific gravity	1.50
pH level	8.58
Moisture content (%)	0.56
Water absorption (%)	0.02
Nb content (wt%)	6.60% Nb_2O_5
Ta content (wt%)	0.70% Ta_2O_5
Fe content (wt%)	4.58% Fe_2O_3
Mn content (wt%)	0.23% MnO
Radioactive content (wt%)	< 0.1

Table 7 Major minerals associated with Rayfield-Jos columbite and their physical responses

Mineral	Chemical formula	Responses
Columbite	$(Fe,Mn)(Nb,Ta)_2O_6$	PM; C
Tantalite	$(Fe,Mn)(Ta,Nb)_2O_6$	PM; C
Hematite	Fe_2O_3	PM; C
Magnetite	Fe_3O_4	FM; C
Rutile	TiO_2	NC; C
Ilmenite	$FeTiO_3$	PM; C
Ilmeno-rutile	$(Nb_2O_5,Ta_2O_5)_xTiO_2$	PM; C
Zircon	$(Zr,REE)SiO_4$	NM; NC
Silica/Quartz	SiO_2	NM; NC
Cassiterite	SnO_2	NM; C

Key: *FM* Ferromagnetic, *PM* Paramagnetic, *NM* Non-magnetic (diamagnetic), *C* Conductive, *NC* Non-conductive

properties or information concerning the mineral deposit, are key factors essential in obtaining detailed mineralogical data for a proper, comprehensive study; and also an integral part of the investigation in developing beneficiation/extraction process routes. In this study, columbite samples sourced from the localities of Rayfield, Jos South, Plateau in Nigeria, have been characterized. Various physicochemical responses of the columbite mineral were investigated. These investigations explain the physical, chemical, microstructural and particle properties of the mineral. PSD

analysis indicated that the crude columbite contains particulates generally of moderately fine and in particle size fraction range of $-500+38$ μm, with particle sizes mainly of $-425+150$ μm for the coarser particles, $-150+90$ μm for medium and $-90+38$ μm for the finer particles. Morphological analysis showed that the particulates are mainly irregularly shaped, sub-hedral, sub-angular and spherically shaped respectively; indicating the presence of mostly columbite, zirconia and silica. Chemical analysis carried out indicated the presence of metallic oxides, showing 6.60 wt% of Nb_2O_5 as the value mineral, as well as 0.70 wt% Ta_2O_5, 4.58 wt% Fe_2O_3, 0.23 wt% MnO, 2.39 wt% TiO_2, and 0.99 wt% SnO_2 along with certain gangue minerals such as silica and zirconia and other elements in trace quantities. Thus, the results of the analyses carried out strongly showed that the Rayfield-Jos columbite mineral deposit is: a low-grade deposit and a non-radioactive mineral, as it is contained < 25% Nb_2O_5 and Ta_2O_5 and possess negligible amounts of (U and Th) radioactive elements in composition of < 0.5% critical value, as an alkaline ferro-columbite and a fine, promising but however a low-grade source of Nb as well as Ta. In this regard, it is imperative to develop and carry out a pre-concentration or mineral upgrade process on the columbite, such as: conventional gravity concentration (CGC) and/or magnetic separation techniques; and also developing and adopting physical beneficiation routes, such as: magnetic and/or electrostatic concentrations, froth flotation or enhanced gravity concentration (EGC) techniques. This is prior to the subsequent hydrometallurgical or chemical treatment, such as: leaching/dissolution process as well as solvent extraction or chemical precipitation, for efficient value metal recovery. This study thus creates a baseline information/data on the choice, selection as well as the designing of feasible, cost effective, appropriate and suitable extraction techniques or process routes in order to harness successfully and (cost) effectively/efficiently the Nb, Ta and other value metals from the study area. This will also serve as a tool in the advancement of mineral upgrade/beneficiation routes prior to hydrometallurgical and thermal treatments, for Nb and/or Ta recovery. Therefore, for future trends in the exploration and exploitation of the ferro-columbite mineral deposit, there is a need for further investigations on the complete mineralogy and surface chemistry, as well as a comprehensive geological survey of the Rayfield-Jos mine field. This is to achieve proper statistics regarding the type, nature and quantity of the deposit and hence, develop proper concentration, beneficiation and extraction routes for Nb or Ta metal recovery.

Acknowledgements We appreciate the Faculty of Engineering and the Built Environment, Tshwane University of Technology, Pretoria, South Africa.

References

1. Agulyansky A (2004) The chemistry of tantalum and niobium fluoride compounds, 1st edn. Elsevier.

2. Baba AA, Jacob SO, Olaoluwa DT, Abubakar A, Womiloju AA, Olasinde FT, Abdulkareem AY (2018) Processing of a Nigerian columbite-rich ilmenite ore for improved industrial application by sulphuric acid solution. Indonesian Min J 21(1):9–19
3. Bamalli US, Moumouni A, Chaanda MS (2011) A review of Nigerian metallic minerals for technological development. Nat Resour 2:87–91
4. Ayeni FA, Ibitoye SA, Adeleke AA (2012A) Development of a wet magnetic-gravity processing route to recover columbite from Jos minefield tailings dump, Nigeria. J Min Metal 48A(1):63–72
5. Nzeh NS, Adeosun S, Popoola AP, Adeleke A, Okanigbe D (2021) Process applications and challenges in mineral beneficiation and recovery of niobium from ore deposits—a review. Miner Process Extr Metall Rev. https://doi.org/10.1080/08827508.2021.1964965
6. Berhe GG, Velazquez DRA, Abubeker Y, Girma W, Bogale T (2017) Alternative beneficiation of tantalite and removal of radioactive oxides from Ethiopian Kenticha pegmatite-spodumene ores. Int J Miner Metall Mater 24(7):727–735
7. Nete M, Purcell W, Snyders E, Nel JT, Beukes G (2012) Characterization and alternative dissolution of tantalite mineral samples from Mozambique. J Southern Afr Inst Min Metall 112:1079–1086
8. Finelib (2017) Columbite mineral resources information and its deposits in Nigeria. [Online]. Available from: https://www.finelib.com/about/nigeria-natural-resources/columbite-mineral-resources-information-and-its-deposits-in-nigeria/136. Accessed on: 27th June 2020
9. Britannica (2020) Columbite mineral. [Online]. Available from: https://www.britannica.com/science/columbite. Accessed on: 26 June 2020
10. Cheru MS, Del Rosario AV, Ali AY, Berhe GG, Tadesse B (2018) Separation of radioactive elements from Ethiopian Kenticha pegmatite ore by hydrometallurgical methods. JOM 70(12):2807–2812
11. Knorring OV, Fadipe A (1981) On the mineralogy and geochemistry of niobium and tantalum in some granite pegmatites and alkali granites of Africa. Bull Mineral 104:496–507
12. Adetunji AR, Siyanbola WO, Funtua II, Olusunle SOO, Afonja AA, Adewoye OO (2005) Assessment of beneficiation routes of tantalite ores from key locations in Nigeria. J Min Mater Charact Eng 4(2):85–93
13. Habinshuti JB, Munganyinka JP, Adetunji AR, Mishra B, Ofori-Sarpong G, Komadja GC, Tanvar H, Mukiza J, Onwualu AP (2021) Mineralogical and physical studies of low-grade tantalum-tin ores from selected areas of Rwanda. Result Eng 11:1–11
14. Shergold HL (1984) In: Ives KJ (ed) Flotation in mineral processing. Cambridge, 5–16 Jul 1982, pp 229–287. https://doi.org/10.1007/978-94-009-6926-1_7. ISBN 90-247-2907-6
15. Okanigbe DO, Popoola API, Adeleke AA (2017) Characterization of copper smelter dust for recovery. In: International conference on sustainable materials processing and manufacturing (SMPM), Kruger National Park. Procedia Manufacturing. Elsevier, vol 7, pp 121–126
16. Okanigbe DO, Ayomoh MK, Popoola OM, Popoola PA, Aigbodion VS (2020) Oxidative roasting experimentation and optimum predictive model development for copper and iron recovery from a copper smelter dust. Result Eng 7:1–11
17. Ayeni FA, Madugu IA, Sukop P, Ibitoye SA, Adeleke AA, Abdulwahab M (2012B) Secondary recovery of Columbite from tailing dump in Nigerian Jos mines field. J Min Mater Charact Eng 11:587–595
18. Alabi OO, Yaro SA, Dungka GT, Asuke F, Hassan B (2016) Comparative beneficiation study gyel columbite ore using double stage (magnetic-to-magnetic and magnetic-to-gravity) separation techniques. J Miner Mater Charact Eng 4:181–193
19. Nete M (2009) Dissolution and analytical characterization of tantalite ore, niobium metal and other niobium compounds. Published Dissertation. University of the Free State, Bloemfontein, pp 1–22
20. Ayeni FA, Alabi OO, Ola SO (1999) Beneficiation of tailings. In: Proceedings of the 16th Nigerian metallurgical society annual conference, Abuja, 3–5 Nov 1999, pp 67–75
21. Kimmel JL, Kitchell RW (2003) Oxygen reduced niobium oxides. United States Patent, US6576099B2, pp 1–30

22. Ryan (2018) Facts about niobium: production, properties, applications, and availability. ADMAT refractory metals. [Online]. Available from: https://www.admatinc.com/facts-about-niobium-production-properties-applications-and-availability. Accessed on: 27th June 2020
23. Deblonde GJP, Chagnes A, Weigel V, Cote G (2016A) Direct precipitation of niobium and tantalum from alkaline solutions using calcium-bearing reagents. Hydrometallurgy 165:345–350
24. Deblonde GJP, Weigel V, Bellier Q, Houdard R, Delvallée F, Bélair S, Beltrami D (2016B) Selective recovery of niobium and tantalum from low-grade concentrates using a simple and fluoride-free process. Sep Purif Technol 162:180–187
25. Cook NJ (2000) Mineral characterization of industrial mineral deposits at the geological survey of Norway: a short introduction. NGU-BULL 436:189–192
26. Everistus N (2010) Niobium ore mining and processing in Nigeria: the opportunities. Nigeria Business Place, Abuja, pp 1–3
27. Ogbonna AI, Nwakaudu SM, Onyemobi OO (1999) Strategic mineral deposits in Nigeria (the neglected case of niobotantalites). In: Proceedings of 16th Nigerian Metallurgical Society annual conference, Abuja, pp 67–75
28. Zhang Y, Du M, Liu B, Su Z, Li G, Jiang T (2017) Separation and recovery of iron and manganese from high-iron manganese oxide ores by reduction roasting and magnetic separation technique. Sep Sci Technol 52(7):1321–1332
29. Abaka-Wood GB, Addai-Mensah J, Skinner W (2016) Review of flotation and physical separation of rare earth element minerals. In: 4th UMaT biennial international mining and mineral conference, pp 55–62
30. Nete M, Purcell W, Nel JT (2014A) Separation and isolation of tantalum and niobium from tantalite using solvent extraction and ion exchange. Hydrometallurgy 149:31–40
31. Nete M, Koko F, Theron T, Purcell W, Nel JT (2014B) Primary beneficiation of tantalite using magnetic separation and acid leaching. Int J Miner Metall Mater 21(12):1153–1159
32. Wills BA, Napier-Munn TJ (2016) Will's mineral processing technology—an introduction to the practical aspects of ore treatment and mineral recovery, 7th edn. Elsevier Science and Technology Books
33. Maurice CF, Kenneth N (2003) Principle of mineral processing. Society of Mining, Metallurgy, and Exploration, Inc. (SME), Georgia, pp 245–299
34. Rejith RG, Sundararajan M (2018) Combined magnetic, electrostatic, and gravity separation techniques for recovering strategic heavy minerals from beach sands. Mar Georesour Geotechnol 36(8):959–965

Investigating the Morphology, Hardness, and Porosity of Spherical and Dendritic Copper Powder Filters Produced via Cold Isostatic Pressing

Hasan Ayub, Lehar Asip Khan, Eanna McCarthy, Inam Ul Ahad, Sithara Sreenilayam, Karsten Fleischer, and Dermot Brabazon

Abstract Porosity in copper filters is sensitive to powder type and space holder material in addition to fabrication processing conditions. This study is focused on the use of two different copper powder types (spherical and dendritic) to produce air flow filters. The hydraulic pressing method was used to produce copper filters under varying pressure with different spacer (polyvinyl alcohol (PVA)) concentrations. Following compaction, the samples were thermally sintered in two segments at 200 °C and 750 °C. The morphology, porosity, and mechanical properties of the sintered samples were characterized. The morphological analysis demonstrated better consolidation and overlapping of copper powder particles in samples with a higher weight percentage of the spacer material (PVA). The highest porosity was achieved in the sample produced using dendritic copper powder mixed with the highest weight percentage of PVA (3%). As a porous structure, the (Vickers) hardness of the samples greatly varied within the samples. Samples prepared with spherical powders at comparatively high pressures demonstrated the highest hardness. The results achieved in this study demonstrated that copper filters with 14% to 26% porosity can be produced using spherical and dendritic copper powders by controlling the compaction pressure from 635 to 793 MPa.

Keywords Copper powder · Air flow filtration · Mechanical properties · Microstructure SEM · Porosity

Introduction

Powder metallurgy is one of the widely utilized techniques on the commercial level due to its advantages such as sustainability and neat net-shaped product. Commonly,

H. Ayub (✉) · L. A. Khan · E. McCarthy · I. U. Ahad · S. Sreenilayam · K. Fleischer · D. Brabazon
I-Form, Advanced Manufacturing Research Centre, and Advanced Processing Technology Research Centre, School of Mechanical and Manufacturing Engineering, Dublin City University, Glasnevin Dublin-9, Ireland
e-mail: hasan.ayub@dcu.ie

M. Zhang et al. (eds.), *Characterization of Minerals, Metals, and Materials 2023*, The Minerals, Metals & Materials Series
https://doi.org/10.1007/978-3-031-22576-5_19

at the industrial and fundamental research level, metal powders used are copper, magnesium, aluminum, and titanium [1–5]. Powder metallurgy is performed by different techniques such as hot/cold isostatic pressing (HIP/CIP), spark plasma sintering, and laser-based additive manufacturing. Powder metallurgy has extensive contributions in different engineering fields such as the automotive industry [6] and aerospace industry [7, 8]. In literature, considerable work is still under investigation exploring different aspects of powder metallurgy.

Amiunl et al. [9] studied the effect of porosity on the tribological properties of the Al–Si alloys. The Al–Si samples were prepared via hot isostatic pressing and sintering for performing analysis on hardness-porosity relationship and material integrity under different porosities. Kabeer et al. [10] experimentally analyzed the cold isostatically pressed and sintered copper-diamond composite. Sintering was performed in the vacuum furnace and operating parameters such as compaction pressure, sintering time, and holding time were optimized for achieving maximum densification. Moreover, different percentages of the diamond particles were also used in the copper powder. Dixit et al. [11] prepared the copper samples using cold isostatic pressing at different compaction pressures. In their work, the effects of different compaction pressures and sintering parameters on densification were investigated. Abu-Qail et al. [12] Fabricated copper-tungsten composites using the cold compaction techniques under pressures ranging from 300–1200 MPa. The investigation was performed on variation in the densities for different compaction pressures and sintering time. They found out an increase in density as higher pressures and copper content. Moreover, homogeneity in the structure was observed for longer sintering times. Wilbert et al. [13] performed numerical and experimental investigations on different copper alloys fabricated using powder metallurgy. Metal powders in different percentages were blended and compacted into the copper powder and sintered using the furnace. Different mechanical parts were prepared with alloys, and their mechanical properties were analyzed. The presence of voids and high porosity in metals is widely utilized in various industrial applications. The porous metals a durable bearing compressive loads and copper is one of the good candidates in structural applications [14, 15]. In literature, a considerable work is performed on an intentional generation of porosity in different metals and alloys for different applications. Vincent et al. [16] Investigated experimentally the effect of porosity on the overall thermal conductivity of copper processed via powder metallurgy. The copper powder was compacted and sintered by hot-pressing at 650 °C. The relationship of pressing time and pressure was studied presenting the volume percentage of porosity. Application of pressure for 20 min lead to approximately 3% porosity while sintering up to 20 resulted in 3% of porosity.

In the present work, the cold isostatic pressing (CIP) metallurgical technique is used for Cu-PVA compaction, and sintering is performed in an inert environment to avoid contamination. For comparison copper powder of spherical and dendritic type is used. Porosity is intentionally induced by including PVA into the copper powder and evaporated via sintering leaving pores into sintered copper. The practical integrity of the porous copper produced in this work is gauged via mechanical and morphological analysis of the porous sintered material. Scanning electron microscopy (SEM) is

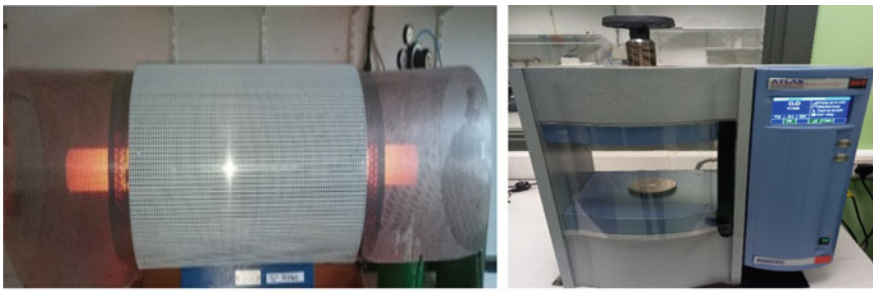

Fig. 1 Lenten tube furnace and autotouch 40 ton hydraulic press

used to investigate the microstructure of sintered samples for morphology analysis. Further, the investigations on resistance to deformation are also performed. Moreover, changes in physical properties linked with porosity are also calculated and discussed in detail.

Experimental Details

Experimental Procedure and Setup

The complete experimental setup for fabricating Cu-PVA compacted-sintered consisted of powder compaction machine of autotouch 40 ton hydraulic press automatic presented in Fig. 1a and programmable and Lenten tube furnace with Argon Environment presented in Fig. 1b. Firstly, the hydraulic press is set up for compacting the Cu-PVA mixtures. The machine was programmed to the desired pressure and the hold time for different samples. During the sintering process, each set of the sample parameters were kept the same. Secondly, the compacted Cu-PVA samples were sintered into the Lenten tube furnace raising the temperature to less than 80% of the melting temperature of copper. Argon gas was used in the tube environment to avoid contamination.

Powder Composition and Operating Parameters

The copper powder and PVA are mixed and compacted using the hydraulic press. Experimental investigations are performed for samples prepared with different mixing ratios. Copper powder with particle geometry of dendritic and spherical was received from Sigma Aldrich. For each type of powder different weight percentage ratios of PVA were added in order to achieve porosity later. Operating parameters

related to mixing and compaction were weight percentage of PVA, total mixture weight, applied pressure and pressure holding time. Compaction parameters was varied for three different sets of experiments. The compaction die of 20 mm diameter is used during the compaction process therefore, for each of the prepared sample diameter is constant.

Table 2 presents the preparation parameters used for the mixing of PVA into copper powder. For consistency and comparability of two different copper powders, the operating parameters were kept same.

Powder Compaction

In the present work, the cold isostatic pressing of Cu-PVA mixtures is achieved using hydraulic press technology. Spherical and dendritic type copper powder is received from Sigma-Aldrich with the purity of 98% and 99.7% respectively while particle size of 10–793 μm and < 45 μm respectively. The microscopic images of powders (spherical&dendritic) taken via SEM are presented in Fig. 2a and b. Further technical and physical properties of both types of copper powders are listed in Table 1. The detailed process of powder compaction is shown in Fig. 3.

The hydraulics presses technology is a well-known technique for compaction of powder. This method is preferred by the industry and widely used for forming pellets.

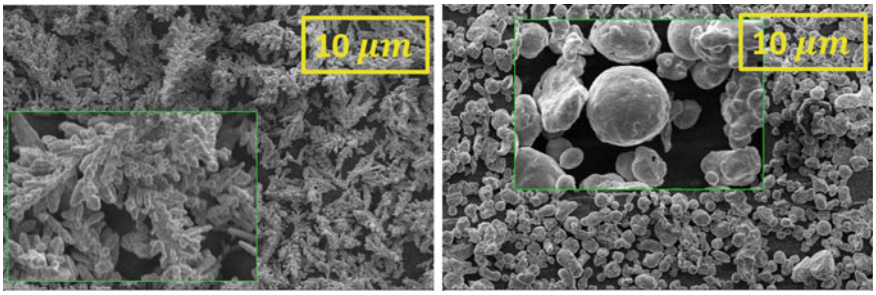

Fig. 2 SEM images, **a** dendritic powder, **b** spherical powder

Table 1 Technical and physical properties of materials

Product form	ID	Particle size (μm)	Purity (%)	Melting/boiling (C)	Density (g/mL)
Powder (spheroidal)	24,859,588	10–793	98	1083.4/79367	8.94
Powder (dendritic)	24,861,916	< 45	99.7	1083.4/79367	8.94

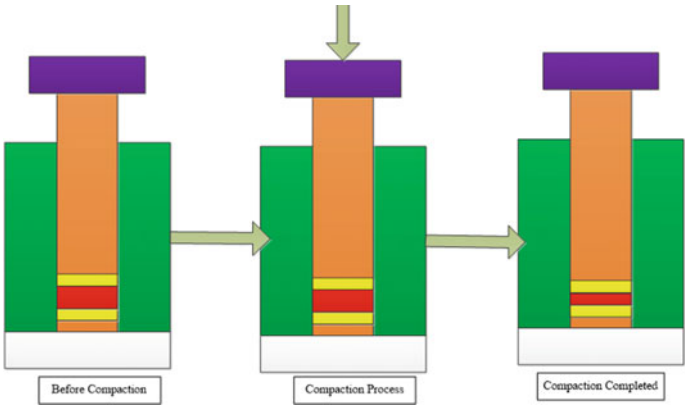

Fig. 3 The schematic diagram of autotouch hydraulic press compaction process

A hydraulic press is especially suited for the preparation of solid sample discs and pellets of different diameters. The commercially available copper in powder form (spheroidal (10–793 μm, 98%), dendritic (< 45 μm, 99.7%) and PVA (polyvinyl alcohol)) from Sigma Aldrich were used in the current studies. Eighteen samples were prepared with different percentages of PVA into the copper powder for investigations (Table 2).

Sintering of Copper Pellets

For the sintering of the copper pellets in a controlled environment Lenton tube furnace 1500° LTF 16 is used and to avoid any contamination of air Argon gas is used with a pressure rate of > 1 ml/min [17]. The sintered samples from S1–S18 are presented in Fig. 4a and b.

Results and Discussion

Spherical Powder

The mechanical properties are influenced by the distribution of the microstructure in copper compacts. The targeted surface of the pellets was analysed by using Zeiss EVO LS-15 scanning electron microscopy (SEM) without any polishing. The porosity can be seen in Fig. 5a and b. The microscopic images contain the sintered sample with 1% of the PVA at the same powder size of 10–793 μm, spherical shape. Compaction (holding time 9 min and pressure 635 Ton) and sintering temperature was kept at 200

Table 2 Operating parameters for copper samples (Spherical(S1–S9)/Dendritic(S10–S18)) with different mixing ratios of PVA

Sample #	PVA (%)	Composition (g)	Pressure (MPa)
S1	1	3	635
S2	2	3	635
S3	3	3	635
S4	1	3	714
S5	2	3	714
S6	3	3	714
S7	1	3	793
S8	2	3	793
S9	3	3	793
S10	1	3	635
S11	2	3	635
S12	3	3	635
S13	1	3	714
S14	2	3	714
S15	3	3	714
S16	1	3	793
S17	2	3	793
S18	3	3	793

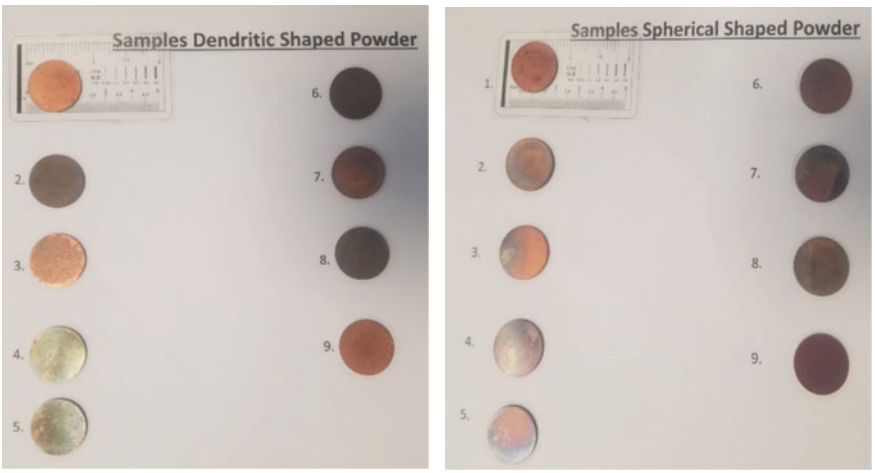

(a) (b)

Fig. 4 Sintered samples **a** spherical Cu-PVA samples **b** dendritic Cu-PVA samples

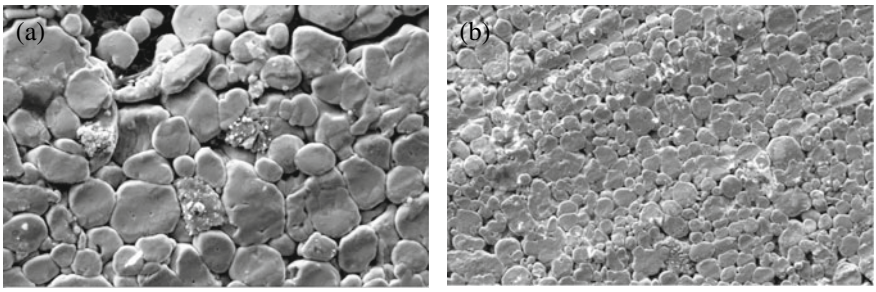

Fig. 5 SEM images for sintered samples spherical powder with 1% PVA at 10 μm scale

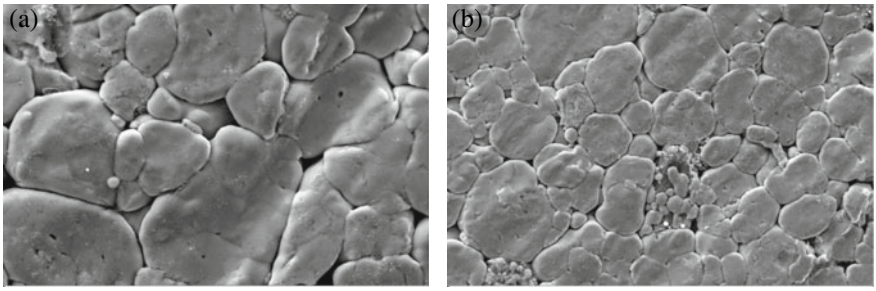

Fig. 6 SEM images for sintered samples spherical powder with 3% PVA at 10 μm scale

°C and 750 °C for 30 min and 60 min respectively. In Fig. 5a and b it can be observed that the lowest percentage of PVA leaves small pores on the upper surface of the pallets and some small cracks as well. The melting and expansion of the powder are also visible but the overlapping phenomenon of the powder particles is not observed.

To increase the mechanical bonding of the powder, pressure is increased during the compaction of the powder, compacted at maximum dye holding pressure of 793 MPa and to investigate the mechanical structure of the pellets. Figure 6 shows microscopic image of sintered samples with 3% induced PVA mixed with copper compacted at the pressure of 793 T. The surface and size of the pellets remain the same after sintering. The parameters of the sintering remain the same for all the pallets. With the increase in the concentration of the PVA in copper powder particles greater melting and expansion with particle overlapping is observed.

Dendritic Shaped Powder

In comparison to the spherical-shaped powder, dendritic-shaped powder shows a slight but noticeable difference in pore size. Figure 7a and b presents microscopic images of 1% PVA mixed in dendritic type copper powder. After compaction and

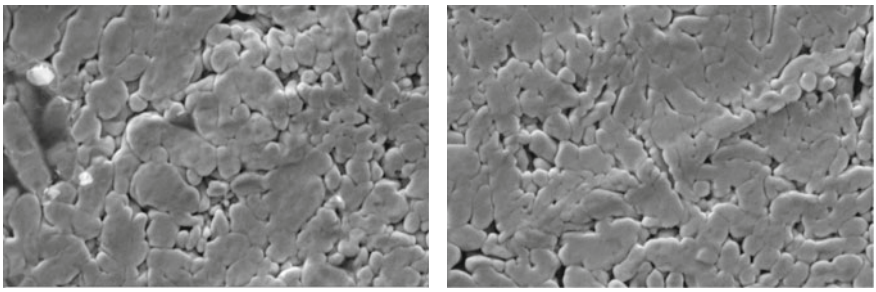

Fig. 7 SEM images for sintered samples dendritic powder with 1% PVA at 10 μm scale

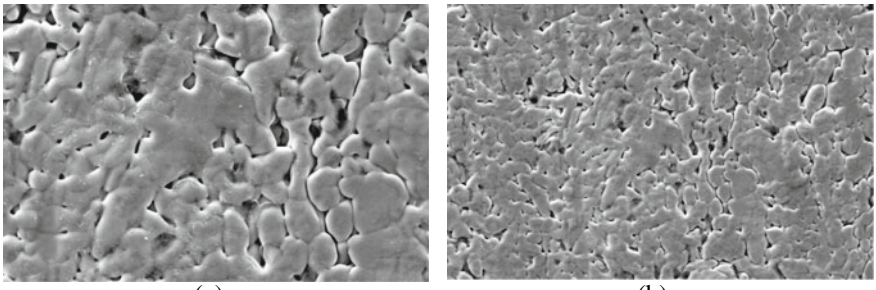

(a) (b)

Fig. 8 SEM images for sintered samples of dendritic powder with 3% PVA at 10 μm scale

sintering, these dendritic-shaped powder particles show less number of small pores but most of them are uniform. Powder particles expansion is seen but with no considerable overlapping leaving small pores on the surface.

Figure 8 shows the SEM images of the dendritic shape copper pellets compacting under 793 T of pressure. Figure 8 is 3% PVA mixed copper pellet compact at maximum dye holding pressure. The increase in pressure causes the high density in the pellet. With the addition of PVA to copper, there was more porosity as anticipated; however, there was no effective bonding between particles.

Porosity Measurements

PVA was added in different weight percentages in order to induce porosity in the compacted pallets. Figure 9 shows the diagram of the experimental setup which was used for measuring the porosity of the sintered samples. Archimedes principle was utilized for measuring the porosity of the samples and difference between densities were used to calculate the percentage difference in the porosities. Figure 9 shows the percentage of porosities for different weight percentages of PVA which show an

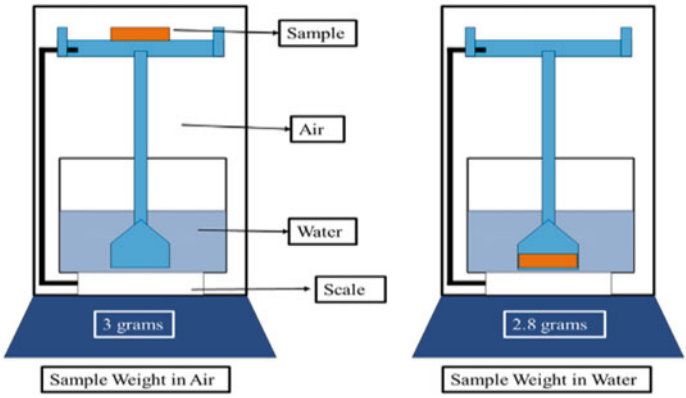

Fig. 9 Schematic diagram of experimental setup for density measurements of samples

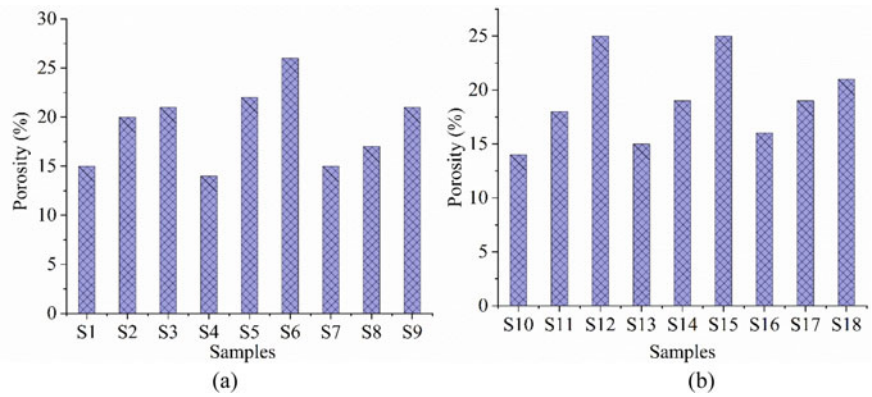

Fig. 10 Percentage porosities **a** Cu-PVA samples produced with spheroidal powder **b** Cu-PVA samples produced with dendritic powder

increase in the porosity by increasing PVA. The lowest porosity noted in the study was 15.96% while the highest porosity was 26.793% referred from Fig. 10a and b.

Hardness and Yield Strength

The geometrical integrity is one of the important aspects of designing the porous material which can be measured by some mechanical testing such as hardness. The Cu-PVA sintered samples were measured by Vickers hardness, which is a non-invasive method. Five different hardness values were taken from the samples. The results of hardness for each of the samples at the respective location with standard

deviation are shown in Table 3. The experimental results of the hardness on the samples interestingly depicted the porosity by variation in the hardness values. In five different locations shown in Fig. 11, the hardness values irregularly dipped which was important to analyse. Important aspect here from the SEM analysis is that the porosity is randomly distributed in all the samples. Due to this randomness in the porosity, a sudden decrease in the hardness values was observed. For spheroidal samples (i.e., S1–S9) referring to Table 3 the hardness values for samples S1 are except 70–89 except the location L3 which depicts that the indenter was placed where the surface has porosity. Similarly, for S2 the L2–L4 locations were porous where the indenter was placed during the experiments. Similar dips in the hardness were noted and are reported in the table for spheroidal samples. Moreover, an interesting aspect raised when the compaction pressure was increased which was the maximum hardness value. For compaction pressure of 635 MPa maximum hardness was 89.6 HV while for 714 MPa and 793 MPa the values were 116 HV and 118 HV respectively. Similarly, for dendritic type samples, the phenomenon observed was the same. Due to the random distribution of the porosity, the dips in the hardness values were observed.

Table 3 Vickers hardness results taken at five location on each samples with STDEV values

Samples		Measurement location					STDEV
		L1	L2	L3	L4	L5	
S1	Spherical	75.4	68.3	49.8	70.2	89.6	12.82
S2		71.9	57.1	55.1	53.1	116	23.63
S3		62	89.2	84.3	67	61	11.75
S4		68	74	71.3	68	67.8	2.46
S5		111	123	51.5	95.8	116	25.59
S6		84.3	90	98.5	90.8	83.9	5.32
S7		68.8	57	51.5	70.5	67.3	7.44
S8		68.3	52.4	98	133	61.3	29.49
S9		46.3	71.3	116	46.7	46.7	27.05
S10	Dendritic	95.8	86.9	68.6	95.3	86.1	9.85
S11		83.9	74.2	71	96.2	98.9	11.25
S12		95.8	100	29	102	94.9	27.79
S13		61.3	53.3	118	57.1	66	23.81
S14		100	74.2	128	116	111	18.20
S15		49.8	61.3	114	59.3	47.6	24.38
S16		46.7	53.3	98	52.4	49	19.21
S17		102	95.8	74.2	87.6	42	21.30
S18		66	55.1	80.2	54.2	61.3	9.45

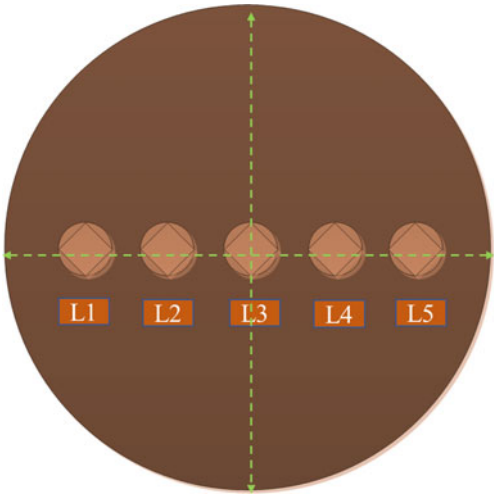

Fig. 11 Locations on the surface of sample selected for measurement of Vickers hardness

Conclusions

In conclusion, copper filters were produced using spherical and dendritic copper powders using the CIP and thermal sintering processing. Filters with different porosity levels and morphological characteristics were produced by changing the weight percentage of the porogen PVA and using different compaction pressures. It was found that PVA was useful for achieving a definable level of porosity within disk filters made from CIP'd copper compacts. A change from 1 to 3% in PVA weight percentage led to interesting results because of this dual role. As the concentration of PVA increased, the powders became more consolidated, and the copper particles overlapping on the filter surface increased. When two percent PVA was used to prepare the copper pellets, fine particles were observed compared to coarse particles in the samples prepared with one weight of PVA. Same as copper filters produced with 3 wt. % shows pores were well distributed and overlapping across the pellets. An interesting observation is that the compaction pressure did not have an impact on the porosity of the samples or had only a very minor effect. However, the 714 MPa pressure and the 3 wt. % PVA produces the pellet with the maximum level of porosity among all sets. Based on the processing conditions used in this study, copper air flow filters can be designed using copper powders with different powder morphologies.

Acknowledgements This work is supported in part by a research grant from Science Foundation Ireland (SFI) under Grant Numbers 16/RC/3872, 19/US-C2C/3579, and is co-funded under the European Regional Development Fund.

References

1. Liu B, Liu Y, He XY, Tang HP, Chen LF, Huang BY (2007) Preparation and mechanical properties of particulate-reinforced powder metallurgy titanium matrix composites. Metall Mater Trans A 38A(11):28793–2831. https://doi.org/10.1007/s11661-007-9329-9
2. Čapek J, Vojtěch D (2013) Properties of porous magnesium prepared by powder metallurgy. Mater Sci Eng C 33(1):564–569. https://doi.org/10.1016/j.msec.2012.10.002
3. Zhang ZW, Liu ZY, Xiao BL, Ni DR, Ma ZY (2018) High efficiency dispersal and strengthening of graphene reinforced aluminum alloy composites fabricated by powder metallurgy combined with friction stir processing. Carbon N Y 135:215–223. https://doi.org/10.1016/j.carbon.2018.04.029
4. Bolzoni L, Ruiz-Navas EM, Gordo E (2017) Quantifying the properties of low-cost powder metallurgy titanium alloys. Mater Sci Eng A 687:47–53. https://doi.org/10.1016/j.msea.2017.01.049
5. Fang ZZ et al (2018) Powder metallurgy of titanium–past, present, and future. Int Mater Rev 63(7):407–459. https://doi.org/10.1080/09506608.2017.1366003
6. Kianian B (2019) Comparing acquisition and operation life cycle costs of powder metallurgy and conventional wrought steel gear manufacturing techniques. Proc CIRP 81:1101–1106. https://doi.org/10.1016/j.procir.2019.03.260
7. Qiang Tan Z, Zhang Q, Yi Guo X, Jiang Zhao W, Shang Zhou C, Liu Y (2020) Recent developments in powder metallurgy based aluminium alloy composite for aerospace applications. J Cent South Univ 27(6):1611–1623. https://doi.org/10.1007/s11771-020-4394-y
8. Vasanthakumar P, Sekar K, Venkatesh K (2019) Recent developments in powder metallurgy based aluminium alloy composite for aerospace applications. Mater Today Proc 18:5400–5409. https://doi.org/10.1016/j.matpr.2019.07.568
9. Islam MA, Farhat ZN (2011) The influence of porosity and hot isostatic pressing treatment on wear characteristics of cast and P/M aluminum alloys. Wear 271(9–10):1594–1601. https://doi.org/10.1016/j.wear.2011.01.037
10. Raza K, Khalid FA (2014) Optimization of sintering parameters for diamond-copper composites in conventional sintering and their thermal conductivity. J Alloys Compd 615:111–118. https://doi.org/10.1016/j.jallcom.2014.06.139
11. Dixit M, Srivastava RK (2018) Effect of compaction pressure on microstructure, density and hardness of copper prepared by powder metallurgy route. IOP Conf Ser Mater Sci Eng 377(1). https://doi.org/10.1088/1757-899X/377/1/012209
12. Abu-Oqail A, Ghanim M, El-Sheikh M, El-Nikhaily A (2012) Effects of processing parameters of tungsten-copper composites. Int J Refract Met Hard Mater 35:207–212. https://doi.org/10.1016/j.ijrmhm.2012.02.015
13. Wong-Ángel WD, Téllez-Jurado L, Chávez-Alcalá JF, Chavira-Martínez E, Verduzco-Cedeño VF (2014) Effect of copper on the mechanical properties of alloys formed by powder metallurgy. Mater Des 58:12–18. https://doi.org/10.1016/j.matdes.2014.02.002
14. Uğuz H et al (2020) Compressive behavior of porous materials fabricated by laser melting deposition using AlSi12 powder and foaming agent. J Phys Energy 2(1):0–31
15. Wang B, Zhang E (2008) On the compressive behavior of sintered porous coppers with low-to-medium porosities-part II: preparation and microstructure. Int J Mech Sci 50(3):550–558. https://doi.org/10.1016/j.ijmecsci.2007.08.003
16. Vincent C, Silvain JF, Heintz JM, Chandra N (2012) Effect of porosity on the thermal conductivity of copper processed by powder metallurgy. J Phys Chem Solids 73(3):499–504. https://doi.org/10.1016/j.jpcs.2011.11.033
17. Ayub H, Khan LA, McCarthy E, Ahad IU, Fleischer K, Brabazon D (2022) Investigating the morphology, hardness, and porosity of copper filters produced via hydraulic pressing. J Mater Res Technol 19:208–219. https://doi.org/10.1016/j.jmrt.2022.05.012

Conversion of Ferronickel Slag to Thermal Insulation Materials by Microwave Sintering: Effect of Fly Ash Cenosphere Addition

Xiaolei Fang, Zhiwei Peng, Lei Yang, Guangyan Zhu, and Mingjun Rao

Abstract The conversion of ferronickel slag (FS) to thermal insulation materials by microwave sintering in the presence of different additions of fly ash cenosphere (FAC) was studied. The results showed that adding proper amount of FAC could promote the generation of cordierite with low thermal conductivity during the sintering process, while the hollow spherical FAC facilitated the pore development and reduced the bulk density of thermal insulation materials. The thermal conductivity, bulk density, compressive strength, water absorption and linear shrinkage of the thermal insulation material were 0.328 W/(m·K), 1.45 g/cm^3, 27.09 MPa, 23.48% and 7.74%, respectively, under the conditions of the mass ratio of FAC to FS of 1/3, sintering temperature of 890 °C, and sintering time of 20 min. This study represents a good example of clean and efficient value-added utilization of FS and other solid wastes.

Keywords Microwave sintering · Ferronickel slag · Fly ash cenosphere · Thermal insulation materials

Introduction

Ferronickel slag (FS) is an industrial waste produced by water quenching of molten slag from the rotary kiln-electric arc furnace (RKEF) process for ferronickel production [1–3], with an annual discharge of 0.3 billion tons [1, 3]. In order to eliminate the environmental problems caused by the accumulation of FS and to enhance the sustainable development of ferronickel production, FS has been used for the production of cement [4, 5], concrete [4], and refractory materials [3, 6, 7], and recovery of valuable metals [8, 9]. Because FS has the main phase of olivine, $(Mg,Fe)_2[SiO_2]$ [10], it has low chemical activity. For this reason, FS has a pretty low utilization percentage (< 15%) [4]. According to the characteristics of FS with high contents of silicon and magnesium [8], it is feasible to induce and promote the transformation of FS

X. Fang · Z. Peng (✉) · L. Yang · G. Zhu · M. Rao
School of Minerals Processing and Bioengineering, Central South University, Changsha 410083, Hunan, China
e-mail: zwpeng@csu.edu.cn

M. Zhang et al. (eds.), *Characterization of Minerals, Metals, and Materials 2023*, The Minerals, Metals & Materials Series
https://doi.org/10.1007/978-3-031-22576-5_20

components into thermal insulation phases with small thermal expansion coefficient and low thermal conductivity, such as cordierite and enstatite, at high temperatures. However, FS has a high density and some phases, such as cordierite and enstatite, with relatively high thermal conductivity (>1 W/(m·K)) [11, 12], making it ineligible for producing thermal insulation materials (bulk density less than 1.5 g/cm^3, thermal conductivity less than 1.0 W/(m·K), and compressive strength greater than 1.0 MPa) [13].

According to the above characteristics, the sintering technology has been used to induce the reactions of silicon, magnesium, aluminum and other components in FS with the use of additives to form corresponding thermal insulation phases (cordierite, enstatite, etc. [14, 15]) to improve the thermal insulation performance of the material. At the same time, light pore-forming agents (e.g., fly ash cenosphere (FAC)) and organic binders are often added to strengthen the comprehensive performance of thermal insulation materials. Specifically, the former can construct porous structures to extend the heat conduction path, reducing the thermal conductivity [16] and bulk density of FS, with increase of the porosity of materials. The latter has the advantages of low dosage, good dispersion, and easy volatilization [17]. It can optimize the micropore structure and increase the micropores of the material without affecting the phase transformation in the process of high-temperature processing. In our recent research [18, 19], a route was developed to prepare thermal insulation materials by co-sintering of FS and FAC, focusing on the effects of the addition of FAC and sintering temperature on the properties of thermal insulation materials.

The purpose of this study was to examine the feasibility of rapid preparation of lightweight thermal insulation materials by microwave sintering of FS and FAC at low temperatures. The changes in phases, microstructures, and properties of thermal insulation materials due to addition of FAC during the process were investigated systematically.

Experimental

Raw Materials and Experimental Procedure

The FS and FAC samples were obtained from a ferronickel smelting plant and coal-fired power plant, respectively, in China. The main phases of FS and FAC were olivine and mullite and quartz, respectively. The addition of FAC was represented by the mass ratio of FAC to FS (i.e., m(FAC)/m(FS)). Its values were specified as 0, 1/5, 1/4, 1/3, and 1/2, respectively. The mixtures of FS and FAC were then blended with 0.5 wt% carboxymethyl cellulose (CMC) and 10 wt% water before they were pressed into briquetted samples under the pressure of 6 MPa. The samples were dried in an oven at 105 °C for 0.5 h and then placed in a microwave furnace for sintering at 890 °C for 20 min with the ramp rate of 40 °C/min. The sintered samples were

used as the thermal insulation materials for characterizations after cooling to room temperature.

Characterizations

The phase and microstructural changes of samples were determined using an X-ray diffraction spectrometer (XRD, BRUKER D8 Advance, Bruker Co., Ltd., Germany) and electron scanning electron microscope (SEM, JSM-7900F, JEOL Co., Ltd., Japan), respectively. The thermal conductivities of the samples were measured using a hot disk thermal constants analyzer (TPS 2500S, Sweden). The porosities of the samples were determined by the Archimedes method and the pore sizes were measured using the software ImageJ 1.49 (National Institutes of Health, Bethesda, MD, USA) after binarization of corresponding SEM images [20].

Testing Standards

The values of bulk density, water absorption, and compressive strength of the resulting thermal insulation materials were determined according to the Chinese National Standard Test Methods GB/T 7322-2007, GB/T 2997-2000, and GB/T 1966-1996, respectively.

Results and Discussion

Mechanisms of Phase Transformation and Microstructural Evolution of Ferronickel Slag with the Addition of FAC

Phase Transformation Analysis

The phase changes after microwave sintering were studied by analyzing the XRD patterns of ferronickel slag mixed with different proportions of FAC. As shown in Fig. 1, the addition of FAC could induce the formation of cordierite. When the addition of FAC was 0 wt%, the main phases of thermal insulation materials were forsterite phase (*F*), enstatite (*E*), and magnesium iron chromate spinel (*D*). Forsterite and enstatite were produced due to the oxidation and decomposition of olivine in ferronickel slag and the two spinel phases were formed by the reactions of MgO in ferronickel slag with Fe_2O_3, Cr_2O_3, and trace Al_2O_3 with strong microwave absorption capabilities [21, 22].

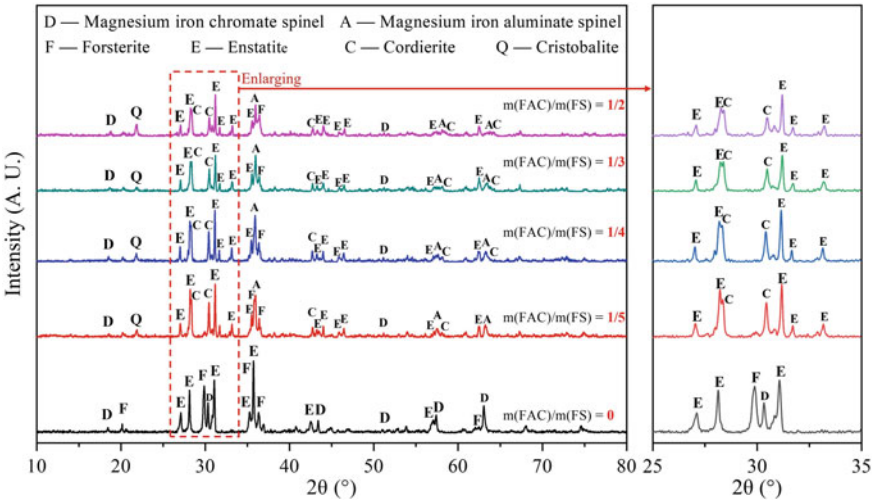

Fig. 1 XRD patterns of the thermal insulation materials prepared by sintering of ferronickel slag with different additions of FAC

When the value of m(FAC)/m(FS) was 1/5, the main phases of thermal insulation materials were forsterite (*F*), enstatite (*E*), spinel (*D*, *A*), cristobalite (*Q*), and cordierite (*C*). Cristobalite and enstatite were a result of further decomposition and oxidation of forsterite in ferronickel slag, while the other part was produced by the reaction of forsterite and SiO_2 [18]. The increase of Al_2O_3 promoted the generation of spinel. In addition, a small amount of magnesium iron aluminate spinel was newly formed and the increase of Al_2O_3 and SiO_2 promoted the transformation of enstatite into cordierite [19]. When the value of m(FAC)/m(FS) was 1/3, the diffraction peaks of cordierite became obvious, with the slowly weakened diffraction peaks of enstatite. It indicated that further increase of Al_2O_3 and SiO_2 promoted the transformation of more enstatite into cordierite. When the value of m(FAC)/m(FS) increased to 1/2, there were many Al_2O_3 and SiO_2. However, due to the limited content and diffusion of MgO, the diffraction peaks of enstatite and cordierite decreased.

As shown in Fig. 2, in the absence of FAC, the material after sintering was primarily composed of forsterite and enstatite and magnesium iron chromate spinel which was evenly distributed. With the addition of FAC, the amount of forsterite decreased, while that of enstatite increased. Meanwhile, cristobalite, magnesium iron aluminate spinel, and cordierite appeared. As shown in Fig. 2d (m(FAC)/m(FS) = 1/3), the FAC shell reacted with ferronickel slag, forming enstatite and magnesium iron aluminate spinel. With the decomposition of mullite, enstatite around FAC turned into cordierite in the area enriching Al_2O_3 and SiO_2. Therefore, the area around the FAC shell was mainly amorphous SiO_2. The magnesium iron chromate spinel in the slag reaction area did not change obviously, while the continuous decomposition of olivine and forsterite led to higher content of enstatite in the regions closer to the FAC area. Finally, forsterite was distributed in an island shape, with decreasing

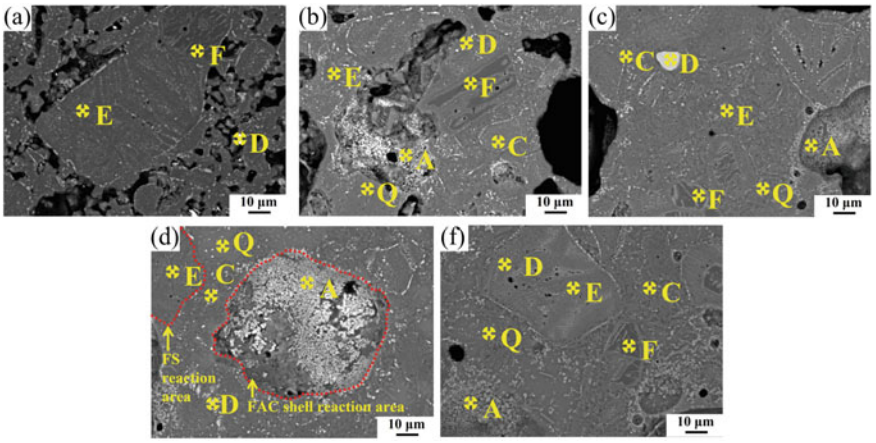

Fig. 2 SEM-EDS analysis of the thermal insulation materials prepared by sintering of FS with different additions of FAC (*E*–enstatite, *F*–forsterite, *C*–cordierite, *Q*–cristobalite, *D*–magnesium iron chromate spinel, and *A*–magnesium iron aluminate spinel): **a** sample 1 (m(FAC)/m(FS) = 0), **b** sample 2 (m(FAC)/m(FS) = 1/5), **c** sample 3 (m(FAC)/m(FS) = 1/4), **d** sample 4 (m(FAC)/m(FS) = 1/3), and **e** sample 5 (m(FAC)/m(FS) = 1/2)

quantity. Meanwhile, enstatite and cordierite became dominant. It was expected that the thermal conductivity could be lower than that in the initial state with forsterite as the main phase [23], due to the above phase transformations.

Microstructural Evolution Analysis

As shown in Figs. 3 and 4, the average pore size of the material obtained by sintering without the FAC addition was 16.13 μm and the apparent porosity was 33.04%. When the value of m(FAC)/m(FS) increased from 1/5 to 1/3, the apparent porosity increased from 27.63% to 42.01% and the average pore size significantly increased from 104.9 μm to 162.22 μm. When the value of m(FAC)/m(FS) increased from 1/3 to 1/2, the apparent porosity decreased to 37.48% and the average pore size increased to 200.46 μm. Because the pressing pressure of the material in the experimental process was small (6 MPa), water and CMC evaporated rapidly during microwave sintering, forming channels and pores. The addition of FAC as the pore-forming agent would increase the pore size of the material despite its small addition. In addition, the channels and open pores formed initially would be filled by the micro-area liquid phase in the sintering process, producing closed pores. As a result, the overall apparent porosity declined. After FAC was added, as shown in Fig. 4b, a small number of connected pores appeared in the material and most of them were isolated closed pores, as shown in Fig. 4b–d. When the value of m(FAC)/m(FS) increased from 1/5 to 1/3, the quantity of connected pores and isolated pores increased. The proportion of connected pores increased significantly. The average pore size and

apparent porosity of the material increased to 162.22 μm and 42.01%, respectively [24]. When the value of m(FAC)/m(FS) was 1/2, excessive liquid phase caused the evolution of connected pores to form large isolated pores. For this reason, the average pore size reached a maximum of 200.46 μm. Along with more evident shrinkage of the material, the apparent porosity decreased to 37.48%.

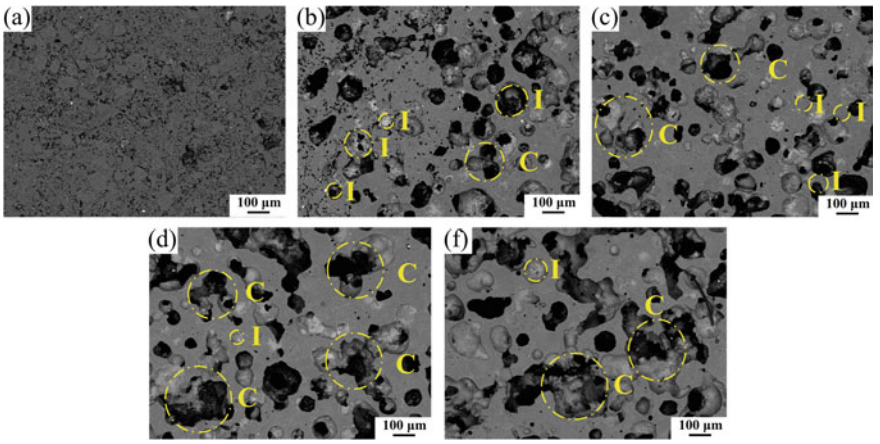

Fig. 3 Pore structures of the thermal insulation materials prepared by sintering of FS with different additions of FAC (*I*–isolated pore, *C*–connected pore) **a** sample 1 (m(FAC)/m(FS) = 0), **b** sample 2 (m(FAC)/m(FS) = 1/5), **c** sample 3 (m(FAC)/m(FS) = 1/4), **d** sample 4 (m(FAC)/m(FS) = 1/3), and **e** sample 5 (m(FAC)/m(FS) = 1/2)

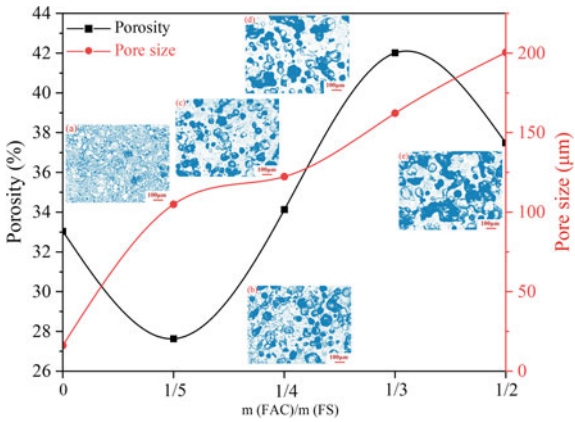

Fig. 4 Effects of FAC addition on the porosity and pore size of thermal insulation material: **a** sample 1 (m(FAC)/m(FS) = 0), **b** sample 2 (m(FAC)/m(FS) = 1/5), **c** sample 3 (m(FAC)/m(FS) = 1/4), **d** sample 4 (m(FAC)/m(FS) = 1/3), and **e** sample 5 (m(FAC)/m(FS) = 1/2)

Properties of Thermal Insulation Materials

Basic Properties

The values of bulk density, compressive strength, water absorption, and linear shrinkage of the thermal insulation material obtained by microwave sintering of ferronickel slag at 890 °C for 20 min with different FAC additions are shown in Fig. 5.

When the value of m(FAC)/m(FS) increased from 0 to 1/5 (stage 1), the bulk density of the material decreased from 2.21 g/cm^3 to 1.59 g/cm^3 and the compressive strength decreased from 49.43 MPa to 18.51 MPa. Meanwhile, the water absorption increased slightly from 11.56% to 13.93% and the linear shrinkage increased from 2.67% to 6.97%. These changes were closely associated with the addition of FAC which caused the formation of pores. As the value of m(FAC)/m(FS) increased from 1/5 to 1/3 (stage 2), the bulk density of the material continued to decline to 1.45 g/cm^3 and the compressive strength increased to 27.09 MPa. This was because of stronger sintering of the components at elevated temperatures in spite of the porous structure [25]. Moreover, the water absorption and linear shrinkage continued to rise to 23.48% and 7.74%, respectively. The higher water absorption was caused by increases of pore size and porosity. When the value of m(FAC)/m(FS) increased from 1/3 to 1/2 (stage 3), the bulk density of the material decreased sharply to 1.34 g/cm^3 and the compressive strength and water absorption decreased to 18.31 MPa and 21.62%, respectively. On the other hand, the linear shrinkage continued to rise to 10.22%. This was due to the further increase of FAC addition, which made the connected pores aggregate and grow again to form large and closed pores, producing more shrinkage.

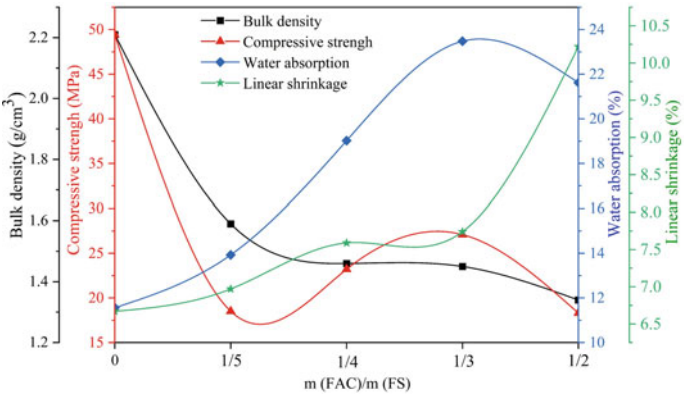

Fig. 5 Effects of FAC addition on the bulk density, compressive strength, water absorption, and linear shrinkage of thermal insulation material

Thermal Conductivity

Thermal conductivity is an important parameter to characterize the thermal insulation performance of the materials. As shown in Fig. 6, when the value of m(FAC)/m(FS) varied from 0 to 1/3, the thermal conductivity decreased from 0.61 W/(m·K) to 0.32 W/(m·K). As it increased from 1/3 to 1/2, the thermal conductivity increased from 0.32 W/(m·K) to 0.38 W/(m·K). The variation of thermal conductivity could be divided into three stages.

When the value of m(FAC)/m(FS) was less than 1/5 (stage 1), the main phases were forsterite and enstatite, with small pore size and high thermal conductivity. When it grew from 1/5 to 1/3 (stage 2), the continuous decomposition of forsterite in the material and the reaction between forsterite and silica caused an increase of enstatite and produced cordierite with low thermal conductivity [26]. At the same time, the addition of FAC significantly increased the pore number of the thermal insulation material and reduced the thermal conductivity [25]. With the increase of FAC addition, enstatite and cordierite kept forming with more pores, which reduced the thermal conductivity continuously. When the value of m(FAC)/m(FS) increased from 1/3 to 1/2 (stage 3), due to the excessive amount of silica and the fixed amount of magnesium oxide, the growth of cordierite slowed down and the quantity of enstatite and cristobalite increased. Note that the thermal conductivities of enstatite (4.52 W/(m·K)) and cristobalite (7.69 W/(m·K)) were higher than that of cordierite (1.2 W/(m·K)) [18]. The decreased proportion of thermal insulation phase in the material and the sharp increase in average pore size led to the formation of connected pores. It promoted the heat transfer process and increased the thermal conductivity. When the bulk density

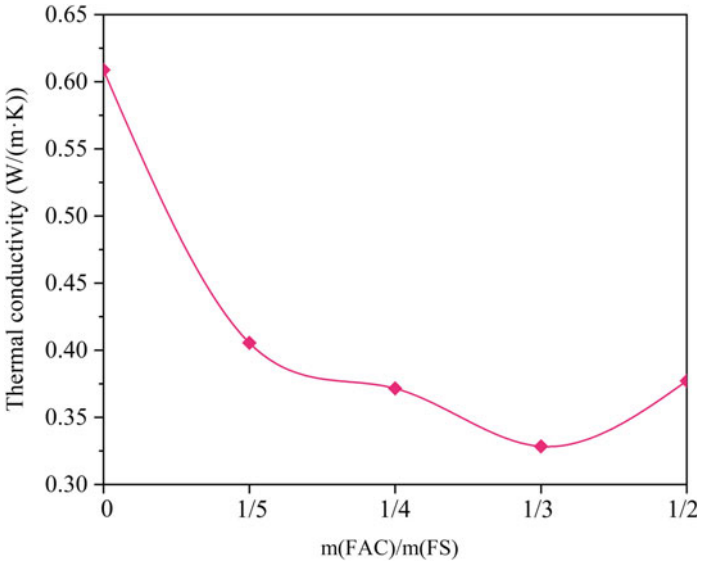

Fig. 6 Effect of FAC addition on the thermal conductivity of thermal insulation material

changed slightly (reduced by 0.11 g/cm^3), the porosity decreased by 4.53% and most of the isolated pores of the material changed into connected closed pores (the average pore size increased by 38.24 μm), which would increase the thermal conductivity [23].

Conclusion

A method of rapid preparation of high-performance thermal insulation materials by microwave sintering of ferronickel slag and FAC at low temperatures was proposed. The influence of FAC addition on the properties of the prepared thermal insulation material was examined. It was found that with the increase of FAC addition, Al_2O_3 and SiO_2 would induce the generation of cordierite, thus decreasing the thermal conductivity of the material. Water and CMC would evaporate rapidly, forming a structure with high apparent porosity and reducing the bulk density of the material. However, when FAC was excessive, less cordierite and more enstatite and cristobalite were found. On the other hand, the formation of excessive liquid phase caused the connected pores to evolve into large isolated pores in the material, leading to an increase in the thermal conductivity of the material. The results showed that under the conditions of the mass ratio of FAC to FS (m(FAC)/m(FS)) of 1/3, sintering temperature of 890 °C, and sintering time of 20 min, the thermal insulation material with thermal conductivity of 0.328 W/(m·K), bulk density of 1.45 g/cm^3, compressive strength of 27.09 MPa, water absorption of 23.48%, and linear shrinkage of 7.74% was prepared.

Acknowledgements This work was partially supported by the Science and Technology Planning Project of Hunan Province, China, under Grant 2019RS2008.

References

1. Trinh HB, Lee JC, Suh YJ, Lee J (2020) A review on the recycling processes of spent auto-catalysts: towards the development of sustainable metallurgy. Waste Manage 114:148–165
2. Nguyen QD, Castel A, Kim T, Khan MS (2021) Performance of fly ash concrete with ferronickel slag fine aggregate against alkali-silica reaction and chloride diffusion. Cem Concr Res 139:106265
3. Tang HM, Peng ZW, Gu FQ, Ye L, Hwang JY, Rao MJ, Li GH, Jiang T (2020) Alumina-enhanced valorization of ferronickel slag into refractory materials under microwave irradiation. Ceram Int 46(5):6828–6837
4. Li B, Huo B, Cao R, Wang S, Zhang Y (2019) Sulfate resistance of steam cured ferronickel slag blended cement mortar. Cement Concr Compos 96:204–211
5. Zhang Z, Zhu Y, Yang T, Li L, Zhu H, Wang H (2017) Conversion of local industrial wastes into greener cement through geopolymer technology: a case study of high-magnesium nickel slag. J Clean Prod 141:463–471

6. Peng ZW, Tang HM, Augustine R, Lee J, Tian WG, Chen YH, Gu FQ, Zhang YB, Li GH, Jiang T (2019) From ferronickel slag to value-added refractory materials: a microwave sintering strategy. Resour Conserv Recycl 149:521–531
7. Gu FQ, Peng ZW, Zhang YB, Tang HM, Ye L, Tian WG, Liang GS, Rao MJ, Li GH, Jiang T (2018) Facile route for preparing refractory materials from ferronickel slag with addition of magnesia. ACS Sustain Chem Eng 6(4):4880–4889
8. Ettler V, Kvapil J, Šebek O, Johan Z, Mihaljevič M, Ratié G, Jérémie G, Quantin C (2016) Leaching behaviour of slag and fly ash from laterite nickel ore smelting (Niquelândia, Brazil). Appl Geochem 64:118–127
9. Shen H, Forssberg E (2003) An overview of recovery of metals from slags. Waste Manage 23(10):933–949
10. Gu FQ, Zhang YB, Peng ZW, Su ZJ, Tang HM, Tian WG, Liang GS, Lee J, Rao MJ, Li GH, Jiang T (2019) Selective recovery of chromium from ferronickel slag via alkaline roasting followed by water leaching. J Hazard Mater 374:83–91
11. You N, Li B, Cao R, Shi J, Chen C, Zhang Y (2019) The influence of steel slag and ferronickel slag on the properties of alkali-activated slag mortar. Constr Build Mater 227:116614
12. Xi B, Li R, Zhao X, Dang Q, Zhang D, Tan W (2018) Constraints and opportunities for the recycling of growing ferronickel slag in China. Resour Conserv Recycl 139:15–16
13. Abu-Jdayil B, Mourad AH, Hittini W, Hassan M, Hameedi S (2019) Traditional, state-of-the-art and renewable thermal building insulation materials: an overview. Constr Build Mater 214:709–735
14. Liu H, Xiong X, Li M, Wang Z, Wang X, Ma Y, Yuan L (2020) Fabrication and properties of mullite thermal insulation materials with in-situ synthesized mullite hollow whiskers. Ceram Int 46(10):14474–14480
15. Sembiring S, Simanjuntak W, Situmeang R, Riyanto A, Sebayang K (2016) Preparation of refractory cordierite using amorphous rice husk silica for thermal insulation purposes. Ceram Int 42(7):8431–8437
16. Schlegel E, Haeussler K, Seifert H (1999) Microporosity and its use in highly efficient thermal insulating materials. Forum Technol 76(8):7–9
17. Capitani D, Porro F, Segre AL (2000) High field NMR analysis of the degree of substitution in carboxymethyl cellulose sodium salt. Carbohyd Polym 42(3):283–286
18. Yang L, Peng ZW, Huang YW, Wang LC, Zheng LX, Rao MJ, Li GH, Jiang T (2021) Co-utilization of ferronickel slag and fly ash cenosphere for production of superior thermal insulation materials. Ceram Int 47(7):10019–10026
19. Yang L, Peng ZW, Huang YW, Wang LC, Zheng LX, Rao MJ, Li GH, Jiang T (2020) Preparation of thermal insulation materials from ferronickel slag with addition of fly ash cenosphere. Charact Miner Met Mater 2020:217–226
20. Liu J, Li Y, Li Y, Sang S, Li S (2016) Effects of pore structure on thermal conductivity and strength of alumina porous ceramics using carbon black as pore-forming agent. Ceram Int 42(7):8221–8228
21. Haque KE (1999) Microwave energy for mineral treatment processes—a brief review. Int J Miner Process 57(1):1–24
22. Aksel C, Rand B, Riley FL, Warren PD (2002) Mechanical properties of magnesia-spinel composites. J Eur Ceram Soc 22(5):745–754
23. Ten JG, Orts MJ, Saburit A, Silva G (2010) Thermal conductivity of traditional ceramics. Part I: Influence of bulk density and firing temperature. Ceram Int 36(6):1951–1959
24. Liu B, Zhang Y, Su Z, Lu M, Peng Z, Li G, Jiang T (2017) Formation mechanism of $MnxFe_{3-x}O_4$ by solid-state reaction of MnO_2 and Fe_2O_3 in air atmosphere: morphologies and properties evolution. Powder Technol 313:201–209
25. Seyama H, Soma M (1987) Fe 2p spectra of silicate minerals. J Electron Spectrosc Relat Phenom 42:97–101
26. Allen GC, Curtis MT, Hooper AJ, Tucker PM (1973) X-ray photoelectron spectroscopy of chromium-oxygen systems. J Chem Soc Dalton Trans 16:1675–1683

Part VII
Poster Session

Activating Components in Activated Alkali Paste of Metakaolin and Ceramic Waste

A. L. Marques Junior, L. R. Cruz, L. U. D. Tambara Júnior, M. T. Marvila, C. M. F. Vieira, S. N. Monteiro, and A. R. G. Azevedo

Abstract The use of Portland cement occurs on a large scale in civil construction. However, its use causes a great environmental impact by emitting a high level of carbon dioxide in the atmosphere. An eco-friendly alternative is the development of alkali activated materials (AAM), as it is not necessary to calcine the precursor materials for use and because they have a high gain of initial mechanical strength. Furthermore, it is possible to value industrial wastes rich in silica and alumina in the compositions of AAM such as ceramic waste (CW), in addition to making use of reactive materials such as metakaolin (MK). This work shows the results achieved in microstructural and compressive strength tests. The aim was to optimize the dosage in pastes with different compositions between precursor materials and activator solution. Research results indicate the effectiveness of replacing 30% MK with CW when compared to a paste composed of 100% MK.

Keywords Alkaline activation · Ceramic waste · Metakaolin

Introduction

The use of Portland cement (OPC) occurs on a large scale in civil construction [1]. Its inferior application is leveraged from its wide use, from the characteristics of higher and relatively higher difficulty, allied to the resistance of shapes and speed

A. L. Marques Junior · L. R. Cruz · A. R. G. Azevedo (✉)
LECIV—Civil Engineering Laboratory, UENF—State University of Northern Rio de Janeiro, Av. Alberto Lamego, 2000, Campos Dos Goytacazes, Rio de Janeiro 28013-602, Brazil
e-mail: afonso.garcez91@gmail.com

L. U. D. Tambara Júnior · M. T. Marvila · C. M. F. Vieira
LAMAV—Advanced Materials Laboratory, UENF—State University of Northern Rio de Janeiro, Av. Alberto Lamego, 2000, Campos Dos Goytacazes, Rio de Janeiro 28013-602, Brazil
e-mail: vieira@uenf.br

S. N. Monteiro
Department of Materials Science, IME—Military Institute of Engineering, Square General Tibúrcio, 80, Rio de Janeiro 22290-270, Brazil

M. Zhang et al. (eds.), *Characterization of Minerals, Metals, and Materials 2023*, The Minerals, Metals & Materials Series
https://doi.org/10.1007/978-3-031-22576-5_21

of execution. The use of high Portland cement results in an environmental impact, being one of the biggest consumers of natural materials and an emitter of carbon dioxide in the atmosphere.

An alternative that has been proven to be eco-friendly is the development of activated alkali materials (AAM), since prior calcination of the precursors is not necessary and because they are elements with a high gain of initial mechanical strength, great resistance to fire and little absorption of water [2–5]. In addition, it is possible to value industrial waste rich in silica and alumina in the compositions of activated alkali materials, such as ceramic waste (CW), in addition to making use of reactive materials such as metakaolin (MK).

The municipality of Campos dos Goytacazes is known for its great wealth of ceramic artifacts, having a large ceramic sector with more than one hundred industries in operation. However, the number of non-organic solid waste emissions from these industries increases exponentially due to the processes of biomass burning [6].

Among the most used raw materials from biomass are firewood, charcoal and seasonal agricultural and forestry wastes. Resulting in a large amount of waste from the ceramic industry, which in turn, can present a great technological advantage in the application in alkali activated materials [7], in addition to being economically advantageous for the industry in question.

The objective of this work was to perform a dosage optimization in pastes with different compositions between precursor materials and activator solution of activated alkali materials composed of metakaolin and ceramic waste from Cerâmica Sardinha, a red ceramic industry located in Campos dos Goytacazes, with a view to a possible application of this material in tiles for civil construction.

Materials and Methods

For the development of the research, the following materials were used: commercial metakaolin of the HP Ultra brand, in 20 kg bags. The ceramic waste was extracted from the kiln of a red ceramic industry, called Cerâmica Sardinha, located in the municipality of Campos dos Goytacazes, which was collected in the form of ash and transported to the university laboratory for use. The preparation of the alkaline solution was made using sodium hydroxide (NaOH) and commercial sodium silicate in solid and liquid form. Figure 1a shows the firewood used by Cerâmica Sardinha for the burning procedure to take place. The oven of the red ceramic industry has a circular shape and is filled with about 45 thousand pieces inside and these steps are illustrated, respectively, in Fig. 1b and c. After all this process is completed, the oven is turned on and remains in activity for approximately 5 days. Its temperature is controlled throughout the time it is in the oven and can reach up to 900 °C. Only after completing the entire procedure is, it possible to visualize and collect the waste resulting from the burning. In Fig. 1d it is possible to see the waste resulting from the burning.

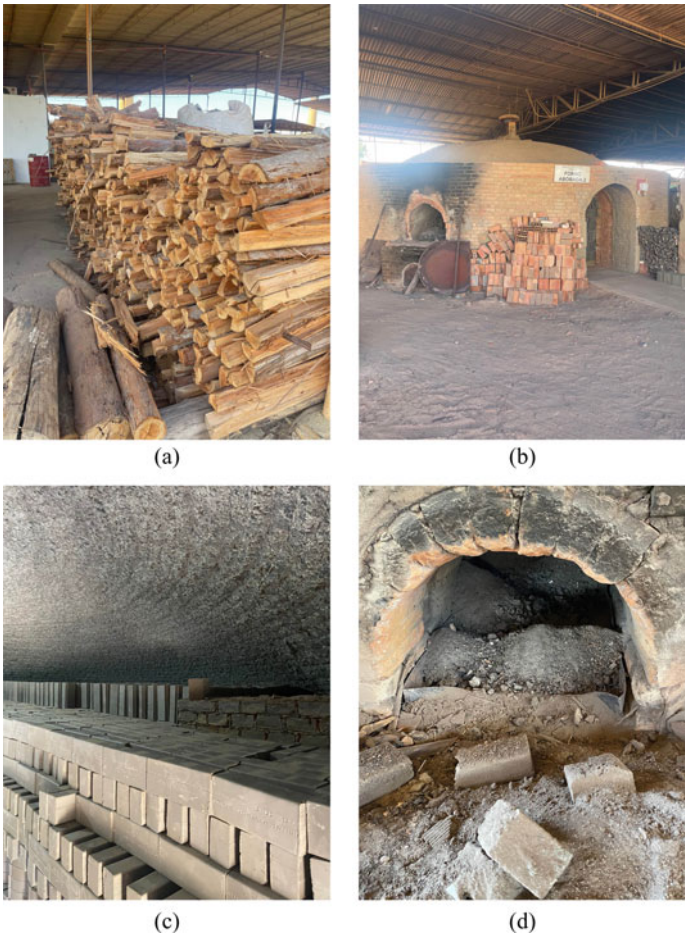

Fig. 1 Waste collection process: **a** firewood used for firing in the ceramic industry. **b** Kiln where a burning of the industry takes place. **c** Kiln being filled with ceramic artifacts. **d** Waste resulting from burning

After the stage of collection and characterization of the waste, the process of making the compositions of activated alkali pastes of metakaolin and ceramic waste began. The alkaline solution to be used in the synthesis of the activated alkali material was an 8 M solution of sodium hydroxide (NaOH) together with two sources of sodium silicate, one solid and the other liquid. Geopolymers are synthesized under different conditions by the alkaline activation of aluminosilicates derived from some industrial solid waste, as in this research, the activation mechanism being based on geopolymerization reactions with the presence of a sodium silicate solution.

To evaluate the influence of ceramic waste on the physical and mechanical properties of the activated alkali material [8], different combinations of metakaolin and

Fig. 2 Specimens of the 9 mixtures compositions

waste were tested for this research. The specimens used had a dimension of 2 × 1 cm. 9 compositions of mixtures with different proportions of MK/RC (100/0, 90/10, 70/30, 50/50 and 0/100) were performed (Fig. 2).

Finally, to verify the mechanical and microstructural behavior of the activations, compressive strength tests were performed (2, 7 and 28 days) and microstructural tests, such as X-ray diffraction (XRD) at 2 days, and kinetics of hydration by isothermal conduction calorimetry.

Results and Discussion

Figures 3 and 4 show the results obtained for the compressive strength tests for the samples with solid silicate and with liquid silicate, respectively.

The Figures show the results of compressive strength of samples with different percentages of MK/RC with 2, 7 and 28 days of curing for pastes produced with solid and liquid silicate. It is possible to observe, in Fig. 3, that the sample with the best mechanical performance was at 70/30 with solid silicate, reaching approximately 13 MPa at 7 days of hydration. On the other hand, at 28 days, the behavior of samples that have a higher percentage of metakaolin obtained a better result [9]. Furthermore, in Fig. 4, the liquid silicate was not effective in activating [10].

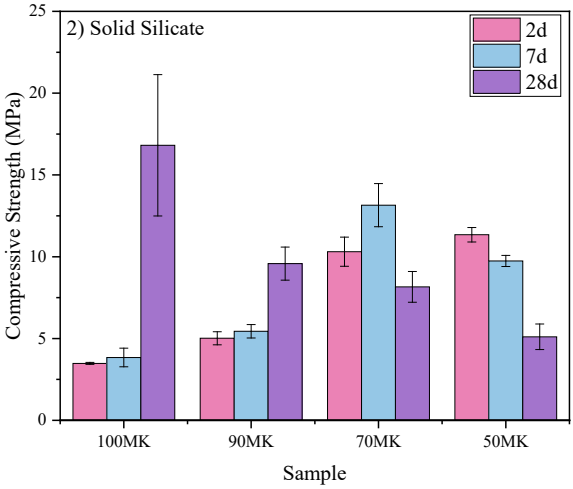

Fig. 3 Compressive strength 2, 7 and 28 days (solid silicate)

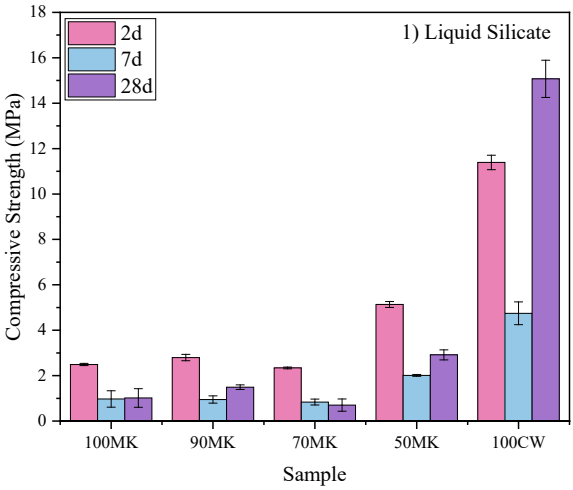

Fig. 4 Compressive strength 2, 7 and 28 days (liquid silicate)

Figures 5 and 6 show the hydration kinetics assay by isothermal conduction calorimetry. The graph of Fig. 8 reveals the formation of a peak for both samples in the initial reaction time; this peak is associated with the process of dissolution of the aluminosilicates. This process involves the dissolution of the precursor material by the activation solution, this occurs quickly due to the high alkaline concentration [11].

Figures 7 and 8 show the results of X-ray diffraction tests. It is possible to observe the formation of an amorphous halo in the XRD of the samples hydrated between 20° and 30°, corresponding to the formation of N–A–S–H gel and responsible for the resistance gain in the samples [12, 13].

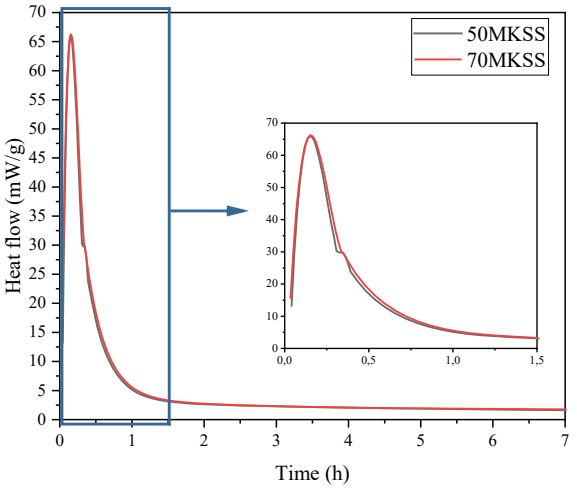

Fig. 5 Heat flow graph

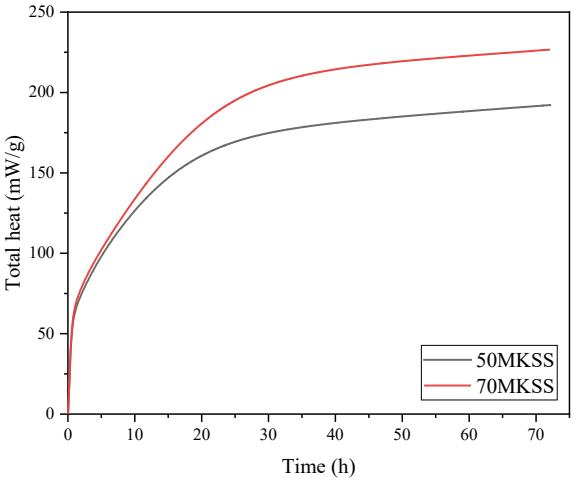

Fig. 6 Total heat of the samples

Conclusion

After the results, it can be concluded that the replacement of 30% of metakaolin by ceramic waste at 7 days of hydration improves the mechanical strength when compared to a paste composed only of metakaolin.

On the other hand, it is important to emphasize that complementary durability tests will be carried out to obtain more information about the physical–mechanical behavior of the specimens referring to the addition of ceramic waste and to investigate possible solutions for the samples with liquid silicate.

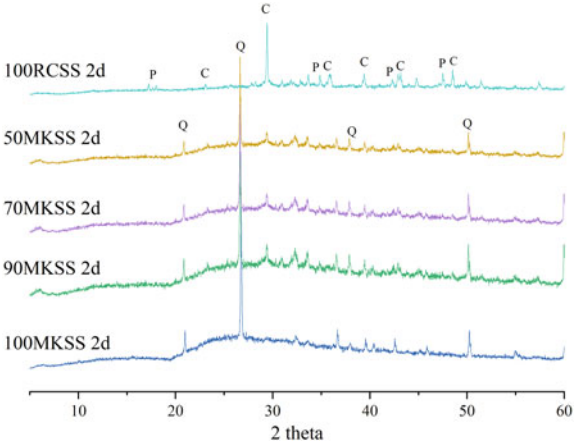

Fig. 7 X-ray diffraction (solid silicate)

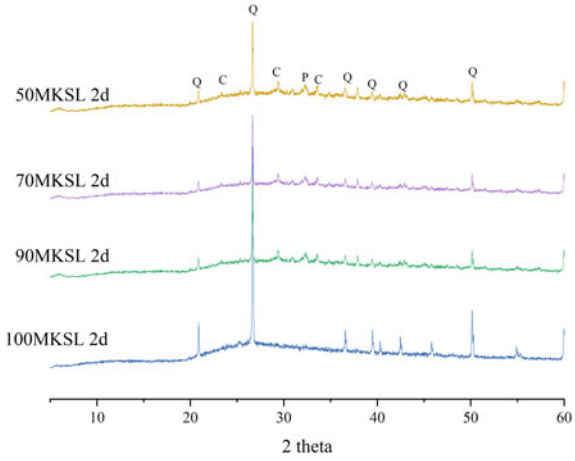

Fig. 8 X-ray diffraction (liquid silicate)

Finally, it is concluded that the use of ceramic waste gives value to a useless material and the addition of a non-noble material to the mixture generates positive impacts economically and ecologically.

Acknowledgements This research was funded by the State University of the Northern Fluminense (UENF), partially financed by CAPES (Coordenação de Aperfeiçoamento de Pessoal de Nível Superior—Brazil), CNPq (Coordenação Nacional de Pesquisa) and FAPERJ (Fundação de Apoio a Pesquisa do Estado do Rio de Janeiro). The participation of A.R.G.A. was sponsored by FAPERJ through the research fellowships proc.no: E-26/210.150/2019, E-26/211.194/2021, E-26/211.293/2021, E-26/201.310/2021 and by CNPq PQ2 307592/2021-9.

References

1. Chaves GLD, Siman RR, Ribeiro GM, Chang NB (2021) Synergizing environmental, social, and economic sustainability factors for refuse derived fuel use in cement industry: a case study in Espírito Santo, Brazil. J Environ Manag. https://doi.org/10.1016/j.jenvman.2021.112401
2. Pinto AT (2006) Introduction to the study of geopolymers. Vila Real
3. Khieng TK, Debnath S, Ting Chaw Liang E, Anwar M, Pramanik A, Basak AK (2021) A review on mechanical properties of natural fibre reinforced polymer composites under various strain rates. J Compos Sci 5(5):130. https://doi.org/10.3390/jcs5050130
4. Robayo-Salazar RA, Valencia-Saavedra W, Ramírez-Benavides S, Gutiérrez RM, Orobio A (2021) Eco-house prototype constructed with alkali-activated blocks: material production, characterization, design, construction, and environmental impact. Materials 14(5). https://doi.org/10.3390/ma14051275
5. Marvila MT, De Azevedo ARG, Vieira CMF (2021) Reaction mechanisms of alkali-activated materials. https://doi.org/10.1590/S1983-41952021000300009
6. Monteiro SN, Vieira CMF (2004) Solid state sintering of red ceramincs at lower temperatures. https://doi.org/10.1016/S0272-8842(03)00120-2
7. Beltrão SLD, Severo CGS, Bezerra IMT, Lira BS, Ferreira HC, Neves GA (2014) Kaolin waste as an alternative binder for grout seat and revetment. https://doi.org/10.4028/www.scientific.net/MSF.775-776.653
8. De Oliveira LB, De Azevedo ARG, Marvila MT, Pereira EC, Fediuk R, Vieira CMF (2022) Durability of geopolymers with industrial waste. Case Stud Constr Mater 16. https://doi.org/10.1016/j.cscm.2021.e00839
9. Marvila MT, De Azevedo ARG, De Matos PR, Monteiro SN, Vieira CM (2021) Materials for production of high and ultra-high-performance concrete: review and perspective of possible novel materials. Materials 14(15).https://doi.org/10.3390/ma14154304
10. Azevedo ARG, Marvila MT, Zanelato EB, Alexandre J, Xavier GC, Cecchin D (2020) Development of mortar for laying and coating with pineapple fiber. Revista Brasileira De Engenharia Agricola e Ambiental 24(3):187–193. https://doi.org/10.1590/1807-1929/agriambi.v24n3p187-193 (In Portuguese)
11. Carvalho A, Xavier GC, Alexandre J, Pedroti LG, de Azevedo ARG, Vieira CMF, Monteiro SN (2014) Environmental durability of soil-cement block incorporated with ornamental stone waste. https://doi.org/10.4028/www.scientific.net/MSF.798-799.548
12. Marvila MT, de Azevedo ARG, de Oliveira LB, Xavier GC, Vieira CMF (2021) Mechanical, physical and durability properties of activated alkali cement based on blast furnace slag as a function of $\%Na_2O$. Case Stud Constr Mater 15. https://doi.org/10.1016/j.cscm.2021.e00723
13. Zeyad AM, Magbool HM, Tayeh BA, Azevedo ARG, Abutaleb A, Hussain Q (2022) Production of geopolymer concrete by utilizing volcanic pumice dust. Case Stud Constr Mater 16. https://doi.org/10.1016/j.cscm.2

Analysis of the Performance of Cementitious Mortars Reinforced with Pineapple Crown Leaf Fiber and Coconut Fiber

I. S. A. Pereira, J. A. T. Linhares Júnior, I. D. Batista, K. M. S. Tavares, M. M. D. Pereira, S. N. Monteiro, and A. R. G. Azevedo

Abstract Natural fibers are renewable materials with high potential for reuse, being a possibility with low environmental impact for application in numerous environments. Pineapple and coconut are fruits consumed and produced in several countries. The peels of both fruits and the leaves of the pineapple crown are normally discarded by industries, generating waste, and negatively impacting the environment. The present work seeks to discuss about cementitious mortars made from these fibers and their effects, in which pineapple crown leaf fiber and coconut fiber were used in the proportions of 1.5% and 3.0% and mortar of reference, in this way, its characteristics were analyzed and compared through tests of consistency, viscosity, compressive and flexural strength, density and capillarity absorption. The results showed the feasibility of using natural fibers in cement mortar, making it more sustainable.

Keywords Building materials · Mortar · Pineapple leaf fiber · Sustainability

Introduction

Natural fibers are a sustainable alternative, from a renewable source, in order to seek certain technological properties, with low environmental impact, as opposed to materials used on a large scale in various industrial segments. The construction and

I. S. A. Pereira · J. A. T. Linhares Júnior · I. D. Batista · K. M. S. Tavares · M. M. D. Pereira
LAMAV—Advanced Materials Laboratory, UENF—State University of Northern Rio de Janeiro, Av. Alberto Lamego, 2000, Campos Dos Goytacazes, Rio de Janeiro 28013-602, Brazil

S. N. Monteiro
Department of Materials Science, IME—Military Institute of Engineering, Square General Tibúrcio, 80, Rio de Janeiro 22290-270, Brazil

A. R. G. Azevedo (✉)
LECIV—Civil Engineering Laboratory, UENF—State University of Northern Rio de Janeiro, Av. Alberto Lamego, 2000, Campos Dos Goytacazes, Rio de Janeiro 28013-602, Brazil
e-mail: afonso.garcez91@gmail.com

M. Zhang et al. (eds.), *Characterization of Minerals, Metals, and Materials 2023*, The Minerals, Metals & Materials Series
https://doi.org/10.1007/978-3-031-22576-5_22

agricultural industry continuously generate different types of waste that are harmful to the environment. [1–3]

Brazil is a notable producer and exporter of pineapple (*Ananas Comosus*), however, the fruit that is widely produced generates negative consequences on the environmental factor by discarding the crown, part not consumed and rejected by the industry [2], similar to pineapple, coconut (*Cocos Nucifera*) is also a fruit widely consumed and produced in several countries, mainly tropical, in which the pulp is used for final consumption and its husk is discarded, causing a similar problem.

Several cementitious composites have already been produced with the structure of natural fibers, however, their use has been reduced as the technology has developed, however, nowadays these fibers stand out as a material that can be more ecologically and economically viable than the popular synthetic fibers, consequently, these materials are studied in order to seek better utility through their characteristics, since natural fibers are largely composed of lignin, cellulose and hemicellulose in their composition [4] which may be a non-beneficial effect on cementitious matrices [3, 5, 6].

The objective of this work was the study of the viability and comparison of the natural fibers of each respective fruit in order to analyze related properties seeking better applicability in its use, in this way, fruits from production regions in the north of the state of Rio de Janeiro were used, being the pineapple from the municipality of São Francisco de Itabapoana, a major producer of the fruit in the state and the coconut from the locality of São Fidélis, which has high production in the manufacture of pulp.

To evaluate the parameters, consistency tests, material viscosity, mass density of the hardened state, flexural tensile strength, compressive strength, and capillary absorption tests were carried out, in the proportions of 1.5% and 3.0% to evaluate the effects caused by the incorporation of fibers in cementitious mortars.

Materials and Methods

At first, the fibers of the leaves of the pineapple crown and those of the coconut were prepared according to the method presented by (Motaleb et al. 2018) [7] in which, after removing the leaves from the pineapple crown and the threads from the external part of the coconut, they were sanitized and placed in an oven at 105 °C for 48 h in each cycle performed, then processed in a 900 W equipment, presenting a fibrous texture, after the completion of processing, as shown in Fig. 1. In addition, Portland cement CPII-E-32 was used, widely used in coating and laying mortars in the region, washed natural sand from the Paraíba do Sul River, $D_{MÁX}$: 2.4 mm, quartz type and water from the Águas do Paraíba concessionaire, located in the municipality of Campos dos Goytacazes, Brazil.

The cementitious mortars were prepared in a 1:4 ratio (cement: sand), referring to cement and sand, respectively. In this circumstance, 1.5 and 3.0% of fibers of each fruit were incorporated in relation to the cement mass and 0% for reference, without

Fig. 1 On the left the coconut fiber and on the right the fibers of the pineapple crown leaf (PALF)

Table 1 Determination of proportions of cementitious mortars

Mortar				
	Cement (g)	Sand (g)	Water (g)	Fiber (g)
REF	300	1200	270	–
PALF—1.5%	300	1200	270	4.5
PALF—3.0%	300	1200	270	9
Coconut—1.5%	300	1200	270	4.5
Coconut—3.0%	300	1200	270	9

addition of fibers, as shown in Table 1. The water/cement ratio determined for the 0% mortar was 0.9, being applied to all proposed proportions. The established parameters are in accordance with the consistency test, following NBR 13,276 (ABNT, 2016) [2], which indicates the level of workability required and the preparation of the mixture.

The consistency index determination test, established by NBR 13,276 [8], indicates that the mixture must present an interval of 260 ± 5 mm, therefore, it was adopted as a model for this study. Mixture preparation started [8] soon after, the mortar was placed on the Flow Table, and molded into a conical throne container.

After modeling, according to the standard, the mold was removed and the mortar was subjected to 30 successive blows, spreading the mass over the circular table, then the diameter measurement was carried out in three different directions of the formed circle. Thus, the reference consistency index was found, together with the water/cement ratio. From this result, the process was repeated in all percentages proposed to study the workability in relation to the incorporation of the fibers in the cement mortar.

The viscosity test was carried out, after the success of the result of the consistency index, using the mixtures in each proportion to carry out the test in the equipment, titled Digital Viscometer MVD-8, each prepared mortar was subjected to a temperature of 23 °C, with 60 RPM for 1 min per test.

The hardened state tests established as indicators for this study were performed on specimens of the prismatic model, with the following measurements: 40 × 40 ×

160 mm, based on current Brazilian standards, each test used three samples for each percentage, to enable statistical calculations relevant to this study.

The following properties were evaluated: mass density of the hardened state, calculated through the samples, mass per volume of each specimen performed at 28 days, in the curing process at room temperature 23 ± 2 °C, with the aid of NBR 13,280 [9], the tests of tensile strength in bending and compressive strength, in the standard of NBR 13,279 [10], performed using the Instron 5582 Universal Tester, finally, the capillary water absorption test, performed using the method of NBR 15,259 [11], had the procedure to arrange the specimens in a flat container, on permeable material, elevating the samples to avoid contact with the base surface, then water was added at a constant height of 5 mm and the masses measured in the periods between 10 and 90 min, to obtain the capillarity coefficient.

Results and Discussion

In the consistency index determination test, it was seen as a result, the workability with high parameters for the values established by the standard, NBR 13,276 [8], for the fibers of the leaves of the pineapple crown (PALF), since, when incorporating 1.5% of PALF in the mixture, it increases approximately 23% of fluidity of the mass in relation to the reference 0%, without addition of fibers, in the proportion of putty 1:4:0.9 (cement: sand: water) in cementitious mortar.

As shown in Fig. 2, the addition of 3.0% of pineapple crown fibers increases by 30% in relation to the reference sample, such results show inconsistency with previous studies that demonstrate reduced workability, regarding the incorporation of PALF, given that the fibers tend to absorb water, being a hygroscopic material, however, the coconut fiber maintains the trend of previous studies and reduces the workability, with the incorporation in 1.5%, decreasing around 10% in relation to the reference mortar and the consistency results with the addition of 3.0%, reduce approximately 19.50%.

In viscosity, the use of natural fibers, behaves in different proportions according to the fiber, as shown in Fig. 3, the coconut fiber maintains or subtly adds viscosity indices in relation to the reference mortar, while the addition of PALF, in the mortar mixture, increases significantly around 4 times, with the incorporation of 3.0% of fibers and when added 1.5% doubles the viscosity results according to 0%, endorsing discussions from previous work that natural fibers have a higher water absorption content.

Figure 4, shows the values of the results of the mass density in the hardened state in the specimens that were evaluated, emphasizing results of works already carried out that present the incorporation of natural fibers in the cementitious mortar, decreasing the density, checked according to the absorption of water caused by the fibers, as they are hygroscopic, in addition, this characteristic has the potential to increase the volume of fiber area, however, the decrease in density can promote benefits in the

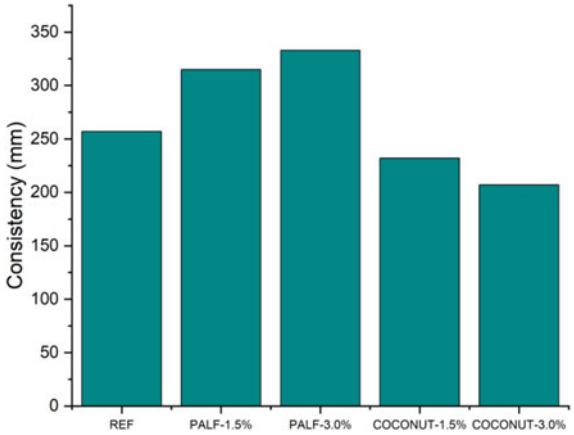

Fig. 2 Consistency results graph

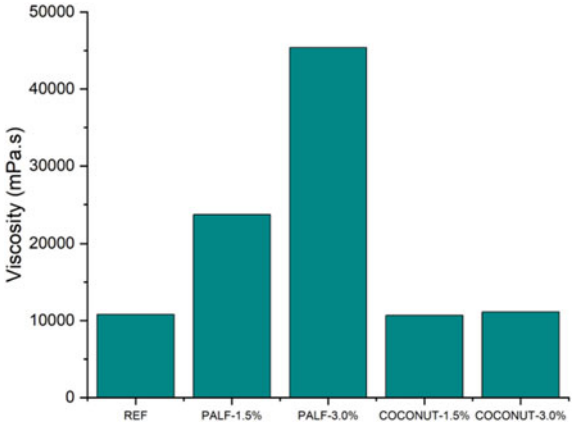

Fig. 3 Viscosity results graph

structural relationship, reducing self-weight loads [2] both incorporations with PALF and coconut fibers have similarity in the proportion of density reduction.

It can be seen that the tensile strength in bending, according to Fig. 5 obtained a decrease in relation to the 0% mortar, it can be observed that the addition of coconut fiber in both proportions maintains similar patterns of flexural strength, and that the fiber from the leaves of the pineapple crown significantly reduces the strength, in relation to previous studies [12] it is possible to verify that the specimens made with PALF, didn't demonstrate a rigid structure when removing them from the molds and the proportion of 3.0% did not obtain data in the hardened state, only 1.5%, which reached a performance of around 60% lower than the reference mortar.

For compressive strength, Fig. 6 shows results that the incorporation of natural fibers in cementitious mortars reduces the resistance, according to authors of previous works, the decrease of this property happens by the excess of water present inside the fiber, caused by the absorption of water, in this way the material tends to become

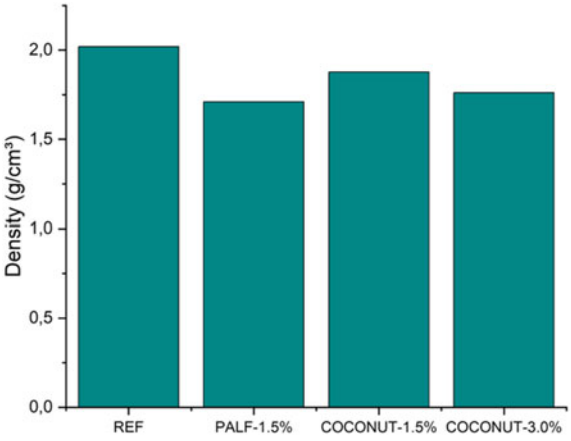

Fig. 4 Graph of density results

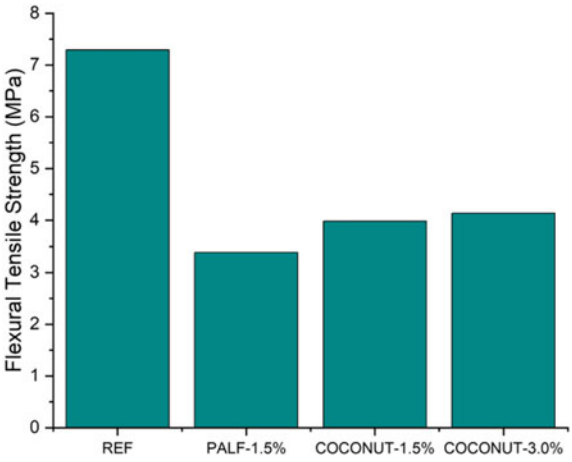

Fig. 5 Graph of flexural tensile strength results

more porous [3], the coconut fiber obtained better results in its addition, in the proportion of 3.0%, increasing approximately 4.0% of resistance in relation to 1.5%, the addition in the mixture with the proportion of PALF in 1.5% reduces about half of the resistance in comparison to the reference mortar.

The absorption of water by capillarity results as shown in Fig. 7 in incorporating natural fibers into the mortar mixture, the increase in water absorption over time, and for each percentage of fiber addition [1] the samples show even higher levels of absorption if compared to the reference value. When comparing PALF with coconut fiber pineapple crown leaf fiber offers a higher water absorption index compared to coconut fiber, when compared to 1.5%. It is not possible to compare the fibers to 3.0%, as the samples with PALF did not become solid after molding.

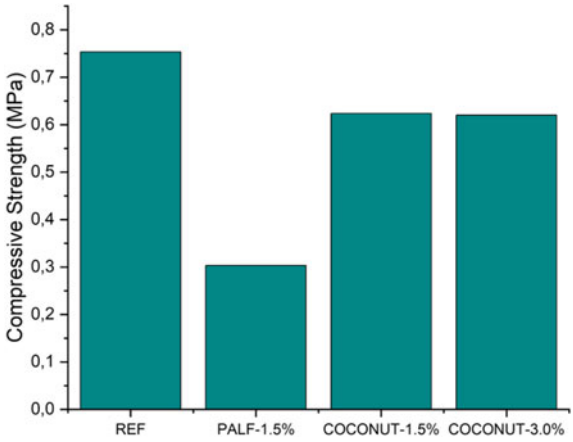

Fig. 6 Compressive strength results graph

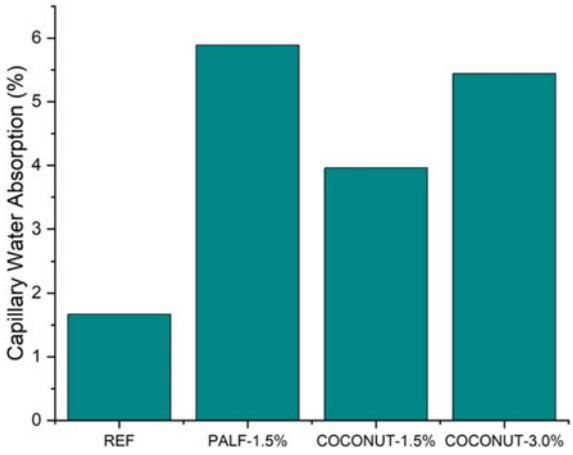

Fig. 7 Graph of capillary water absorption results

Conclusion

According to the results obtained through the tests carried out, it is concluded that the addition of natural fibers in cementitious mortars significantly impacts the workability of the material, since the fibers have hygroscopic properties, not meeting the current standard of determination of consistency index. It can be highlighted that the fibers of the leaves of the pineapple crown (PALF) presented an atypical result to previous studies of workability reduction, by this type of material, however, the coconut fiber reduces this property.

The use of the 0% mortar water/cement ratio as a reference for the other proportions showed that it may be necessary to carry out other studies, with a higher ratio to obtain results closer to what the standard requires.

In the present work, it is found that both natural fibers studied to reduce the mass density of the hardened state of the mortar, referring to 1.5% incorporation of PALF, obtaining the best result in relation to density and the coconut fibers reached responses similar, however, emphasizing that the content of 1.5% performs better results in the study.

It is concluded that both fibers that were used in cementitious mortar, did not achieve good results in compressive strength and flexural tensile strength, decreasing considerably in relation to the reference mortar, however, it is emphasized that the coconut fibers in the evaluated percentages achieved results better than PALF.

Acknowledgements This research was funded by the State University of the Northern Fluminense (UENF), partially financed by CAPES, CNPq, and FAPERJ. The participation of A.R.G.A. was sponsored by FAPERJ through the research fellowships proc.no: E-26/210.150/2019, E-26/211.194/2021, E-26/211.293/2021, E-26/201.310/2021, and by CNPq PQ2 307592/2021-9.

References

1. Hwang CL, Tran VA, Hong JW, Hsieh YC (2016) Effects of short coconut fiber on the mechanical properties, plastic cracking behavior, and impact resistance of cementitious composites. Constr Build Mater 127:984–992. https://doi.org/10.1016/J.CONBUILDMAT.2016.09.118
2. Azevedo AR, Marvila MT, Zanelato EB, Alexandre J, Xavier GC, Cecchin D (2020) Development of mortar for laying and coating with pineapple fibers. Revista Brasileira de Engenharia Agrícola e Ambiental 24(3):187–193. https://doi.org/10.1590/1807-1929/agriambi.v24n3p187-193
3. Kesikidou F, Stefanidou M (2019) Natural fiber-reinforced mortars. J Build Eng 25:100–124. https://doi.org/10.1016/J.JOBE.2019.100786
4. Nashiruddin NI, Mansor AF, Rahman RA, Ilias RM, Yussof HW (2020) Process parameter optimization of pretreated pineapple leaves fiber for enhancement of sugar recovery. Ind Crops Prod 152:112514. https://doi.org/10.1016/J.INDCROP.2020.112514
5. de Azevedo ARG, Marvila MT, Tayeh BA, Cecchin D, Pereira AC, Monteiro SN (2021) Technological performance of açaí natural fibre reinforced cement-based mortars. J Build Eng 33:101–135. https://doi.org/10.1016/J.JOBE.2020.101675
6. Ozerkan NG, Ahsan B, Mansour S, Iyengar SR (2013) Mechanical performance and durability of treated palm fiber reinforced mortars. Int J Sustain Built Environ 2(2):131–142. https://doi.org/10.1016/J.IJSBE.2014.04.002
7. Motaleb KZMA, Islam MS, Hoque MB (2018) Improvement of physicomechanical properties of pineapple leaf fiber reinforced composite. Int J Biomater. https://doi.org/10.1155/2018/7384360
8. ABNT (2016) NBR 13276: Mortar for laying and covering walls and ceilings—determination of consistency index (In Portuguese)
9. ABNT (2005b) NBR 13280: Mortar for laying walls and covering walls and ceilings—determination of the apparent mass density in the hardened state (In Portuguese)
10. ABNT (2005a) NBR 13279—Mortar for laying walls and coating walls and ceilings—determination of tensile strength in bending and compression (In Portuguese)
11. ABNT (2005c) NBR 15259: Mortar capillary absorption (In Portuguese)
12. Danso H, Manu D (2020) Influence of coconut fibers and lime on the properties of soil-cement mortar. Case Stud Constr Mater 12:e00316. https://doi.org/10.1016/J.CSCM.2019.E00316

Analysis of the Properties in the Fresh State of Alkali-Activated Paste of Metakaolin and Flue Gas Desulfurization Waste

D. V. A. Júnior, L. B. Oliveira, L. U. D. T. Júnior, M. T. Marvila, C. M. F. Vieira, S. N. Monteiro, and A. R. G. Azevedo

Abstract Activated alkali materials (AAMs) have been increasingly studied as a substitute for Portland cement, one of the most used materials in civil construction, which, during its manufacture, emits a large amount of carbon dioxide, one of the most harmful gases to the environment and responsible for the global warming. Activated alkali materials originate from one or more precursors, containing mainly alumina and silica, in addition to an activator with a high alkaline content. This work aims to analyze the properties in the fresh state of three pastes of AAMs with different proportions of metakaolin (MK) and flue gas desulfurization waste (FGD). The proportions are 100% MK, 90% MK, and 10% FGD, and 80% MK and 20% FGD. For each dosage, consistency index tests, viscosity tests, and mass density in the fresh state will be carried out. The research results show that as the FGD content is increased, there is a reduction in the workability of the material. However, the specific mass decreased with the addition of the waste.

Keywords Activated alkali materials · Metakaolin · Flue gas desulfurization waste

Introduction

The growing world population, in addition to industrialization, makes it increasingly necessary to build buildings, industries, and paving, for example. And for that, the

D. V. A. Júnior · L. B. Oliveira · L. U. D. T. Júnior · M. T. Marvila · C. M. F. Vieira
LAMAV—Advanced Materials Laboratory, UENF—State University of Northern Rio de Janeiro, Av. Alberto Lamego, 2000, Campos Dos Goytacazes, Rio de Janeiro 28013-602, Brazil
e-mail: vieira@uenf.br

S. N. Monteiro
Department of Materials Science, IME—Military Institute of Engineering, Square General Tibúrcio, 80, Rio de Janeiro 22290-270, Brazil

A. R. G. Azevedo (✉)
LECIV—Civil Engineering Laboratory, UENF—State University of Northern Rio de Janeiro, Av. Alberto Lamego, 2000, Campos Dos Goytacazes, Rio de Janeiro 28013-602, Brazil
e-mail: afonso.garcez91@gmail.com

M. Zhang et al. (eds.), *Characterization of Minerals, Metals, and Materials 2023*, The Minerals, Metals & Materials Series
https://doi.org/10.1007/978-3-031-22576-5_23

use of Portland cement tends to increase over time, since it is one of the most used materials in civil construction [1].

However, to reach the final product of Portland cement, industrial steps are necessary, in addition to the extraction of the raw material itself, which generates severe environmental impacts and health problems for the population, caused, for example, by the emission of carbon dioxide, one of the gases that potentiate the greenhouse effect [2].

With this problem, in addition to the massive need for raw material, it is necessary to search for new materials capable of replacing Portland cement [3]. An alternative that is increasingly being disseminated among researchers is products derived from alkaline activation, which have less environmental impact [4].

Geopolymers can be classified as inorganic polymeric materials, resulting from the chemical reaction of minerals containing aluminum, silica, and oxygen, known as aluminosilicates, with an alkaline solution [5].

For the geopolymerization reaction, the precursors can be, for example, metakaolin (MK), which is a pozzolanic material rich in silica and alumina in its amorphous phase, formed from the activation by the temperature increase of kaolin.

A potential and important precursor to be adopted is also flue gas desulfurization (FGD) waste. It is the result of a technique used in the coal and steel industry to remove toxic gases from the environment. Therefore, this work aims to analyze the properties in the fresh state of alkali-activated pastes partially replacing metakaolin with FGD waste.

Materials and Methods

For the execution of the tests, three Mixtures of alkali-activated material were made, changing the percentage of FGD. The first Mixture was the so-called control, without any incorporation of the waste, in the second Mixture, the MK was replaced with 10% FGD, and the third Mixture with 20% FGD. For all of them, the amount of activators as well as the amount of water remained constant, being 120 g of sodium hydroxide, 45 g of sodium silicate, and 315 g of water. Table 1 specifies the Mixtures, with reference being FGD10% and FGD20%.

For sample preparation, the activators were added to water, where they were diluted by a magnetic stirrer until the solution was colorless, and then the fluid was

Table 1 Mixtures used

Proportions	Metakaolin (g)	FGD (g)	NaOH (g)	Na_2SiO_3 (g)	H_2O (g)
Reference	600	0	120	45	315
FGD10%	540	60	120	45	315
FGD20%	480	120	120	45	315

Fig. 1 Consistency index test

homogenized with the precursor in a VELP Scientifica OHS 200 Advance stirrer for 5 min.

For all tests, Brazilian standards for cementitious materials were used, since there is no standard relating to alkali-activated materials. The first test performed was the consistency index. Following the procedures described in NBR 13276 (ABNT, 2016) [6], the paste was inserted in three layers, applying blows in each of them, 15, 10, and 5, respectively, in the frustoconical mold. Scraping was done and the mold removed. After this process, the equipment crank was activated 30 times and the average of 3 parts of the material was spread. In Fig. 1, it is possible to see the consistency index test performed.

The second test was the density test in the fresh state, performed according to NBR 13278 (ABNT, 2005) [7]. The test consists of inserting the paste into a cylindrical container in three layers, and for each layer, 20 blows are given finally, the cylinder is released three times at a height of 3 cm. After carrying out all these procedures, the mass density in the fresh state is calculated from Eq. (1).

$$d = \frac{m_c - m_v}{V_r} \times 100 \tag{1}$$

where d = specific mass of the mortar in the fresh state (g/cm^3);

m_c = mass of beaker + mortar (g);

m_v = mass of empty beaker (g);

V_r = volume of the beaker (cm^3).

Below, in Fig. 2 is shown the cylindrical container during the mass density test in the fresh state.

Finally, the Digital Rotational Viscometer MVD-8 from Marte Científica was used to measure the viscosity of the three Mixtures. The paste after being made and inserted into a beaker, which is positioned below the device, has a rotating spindler with a rotation of 60 rpm for 1 min. Within the quoted time, an average of the values

Fig. 2 Dough density test in the fresh state

measured by the equipment was made. In Fig. 3, it is possible to see the viscometer during the test.

Results and Discussion

The consistency index results are shown in Fig. 4. According to the results shown in the figure, a reduction in the spread of the paste can be observed as the FGD content increases. This reduction was 23 mm from the control paste to the one with 10% FGD and 73 mm from the control paste to the material with 20% FGD.

According to Zhong et al. [8], an explanation for the reduction in workability would be the morphology of the waste. Therefore, the possible fact that the waste has a lamellar shape requires a greater amount of water to obtain a high workability.

Figure 5 shows the results related to the mass density in the fresh state of the three Mixtures. Despite the very close results, it was possible to verify a slight decrease in the mass density in the fresh state as the FGD waste was increasing, where the reference paste obtained a mass density of 2.01 g/cm^3, for the paste with 10%, a mass density of 1.81 g/cm^3 was found, that is, 9.95% less than the reference, and finally,

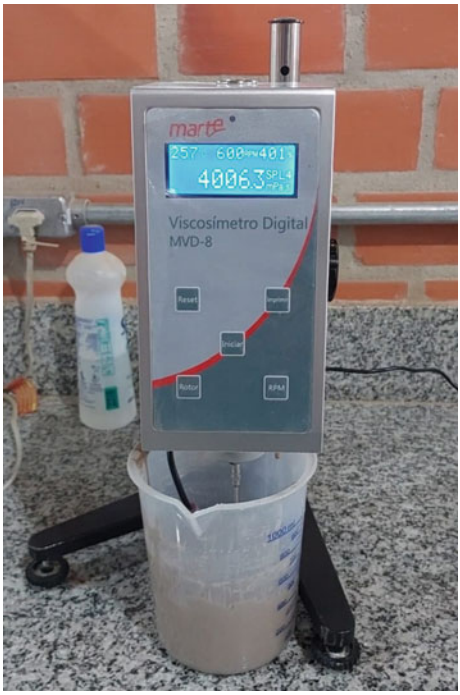

Fig. 3 Viscosity test

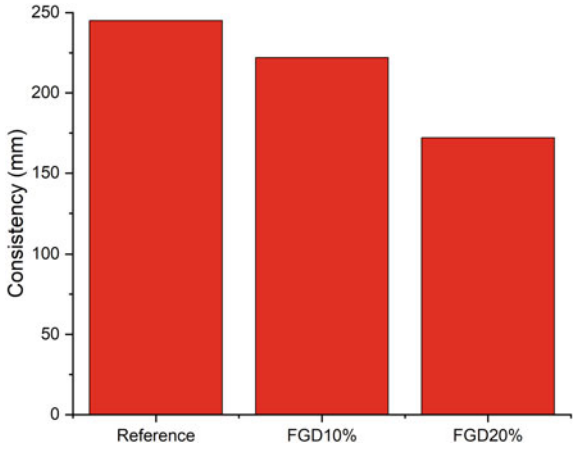

Fig. 4 Consistency test results

the paste with 20% of FGD had a drop of 13.43%, with a value of 1.74 g/cm^3. This decrease may also be related to the morphology of the waste, as lamellar grains have a lower degree of compaction, increasing the void index in the paste and contributing to a lower specific mass [8–10].

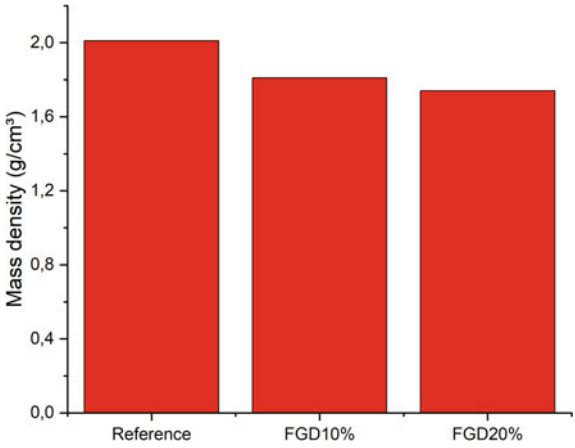

Fig. 5 Mass density test results

Figure 6, on the other hand, relates the viscosity of the studied traits. It is possible to analyze the averages of the measured values and the standard deviation. As can be analyzed, the viscosity of the material increased as the FGD content increased. The reference mix had a viscosity of 3420.58 mPa.s, as for the paste with 10% FGD, the viscosity was 4679.38 mPa.s, 36.80% more than the reference, and the paste with 20% of FGD presented a viscosity of 11,066.70 mPa.s, showing an increase of 223.53% in relation to the reference paste. This fact was reported by Doleželová et al. [9], where they attributed the lower workability to the specific area of the FGD waste, due to its morphology [11, 12]. Therefore, to maintain workability, it would be necessary to increase the water content [13, 14].

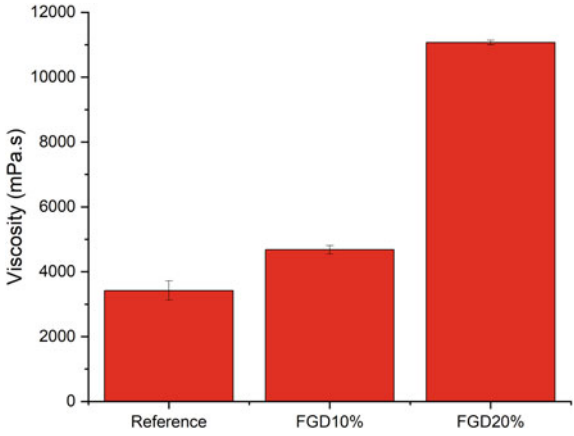

Fig. 6 Average of viscosity test results

Conclusion

After analyzing the results of the tests in the fresh state, it was possible to verify that the workability decreases as the replacement content of metakaolin by FGD increases. The consistency test, despite the decrease in values, did not have a very significant difference. For the material with 20% FGD, the reduction was 9%, and for the material with the highest percentage of FGD, the drop was 30%.

The mass density decreased with increasing FGD; however, there was not much difference in the results with increasing waste. The decrease was 9.95% and 13.43% in relation to the reference material.

And the viscosity showed the greatest discrepancy, increasing by 223.53% when 20% of metakaolin was replaced by FGD. However, when the replacement was 10%, the difference was much smaller, at 36%.

Thus, in order to reduce the production and consumption of cement and consequently the polluting gases released during its manufacture, alkali-activated materials show promise when using lower levels of FGD, preserving their workability characteristics.

Acknowledgements This research was funded by the State University of the Northern Fluminense (UENF), partially financed by CAPES (Coordenação de Aperfeiçoamento de Pessoal de Nível Superior—Brazil), CNPq (Coordenação Nacional de Pesquisa), and FAPERJ (Fundação de Apoio à Pesquisa do Estado do Rio de Janeiro). The participation of A.R.G.A. was sponsored by FAPERJ through the research fellowships proc. no: E-26/210.150/2019, E-26/211.194/2021, E-26/211.293/2021, E-26/201.310/2021, and by CNPq PQ2 307592/2021-9.

References

1. Van den Heede P, De Belie N (2012) Environmental impact and life cycle assessment (LCA) of traditional and 'green' concretes: literature review and theoretical calculations. Cement Concr Compos 34:431–444
2. Maury MB, Blumenschein RN (2012) Produção de cimento: impactos à saúde e ao meio ambiente. Sustentabilidade em Debate 3:75–96
3. Ayeni O, Onwualu AP, Boakye E (2021) Characterization and mechanical performance of metakaolin-based geopolymer for sustainable building applications. Constr Build Mater 272:121938
4. Palomo A, Krivenko P, Garcia-Lodeira I, Kavalerova E, Maltseva O, Fernandez Jimenez A (2014) A review on alkaline activation: new analytical perspectives. Mater Constr 64:315
5. Boonserm K, Sata V, Pimraksa K, Chindaprasirt (2012) Improved geopolymerization of bottom ash by incorporating fly ash and using waste gypsum as aditive. Cement Concr Compos 34:819–884
6. NBR 13276, 2016 NBR 13276 Brazilian Association of Technical Standards mortars applied to walls and ceilings—determination of the consistency index (In Portuguese)
7. NBR 13278, 2005 NBR 13278 Brazilian Association of Technical Standards—mortars applied to walls and ceilings—determination of specific gravity and content of air trapped in the fresh stage (In Portuguese)

8. Zhong E, Okwor E, Guo F, Smits AJ (2012) Testing and modelling of a biomimetric swimmer. Paper presented at the biomedical robotics and biomechatronics (BioRob), pp 24–27
9. Magdaléna D, Jitka K, Alena V (2021) Adhesive strength of gypsum composites with lightweight fillers. U. Porto J Eng 7(2):52–59
10. Marvila MT, De Azevedo ARG, De Matos PR, Monteiro SN, Vieira CM (2021) Materials for production of high and ultra-high-performance concrete: review and perspective of possible novel materials. Materials 14(15). https://doi.org/10.3390/ma14154304
11. Azevedo ARG, Marvila MT, Zanelato EB, Alexandre J, Xavier GC, Cecchin D (2020) Development of mortar for laying and coating with pineapple fiber. Revista Brasileira De Engenharia Agricola e Ambiental 24(3):187–193. https://doi.org/10.1590/1807-1929/agriambi.v24n3p187-193 (In Portuguese)
12. Carvalho A, Xavier GC, Alexandre J, Pedroti LG, de Azevedo ARG, Vieira CMF, Monteiro SN (2014) Environmental durability of soil-cement block incorporated with ornamental stone waste. https://doi.org/10.4028/www.scientific.net/MSF.798-799.548
13. Marvila MT, de Azevedo ARG, de Oliveira LB, Xavier GC, Vieira CMF (2021) Mechanical, physical and durability properties of activated alkali cement based on blast furnace slag as a function of $\%Na_2O$. Case Stud Constr Mater 15. https://doi.org/10.1016/j.cscm.2021.e00723
14. Zeyad AM, Magbool HM, Tayeh BA, Azevedo ARG, Abutaleb A, Hussain Q (2022) Production of geopolymer concrete by utilizing volcanic pumice dust. Case Stud Constr Mater 16. https://doi.org/10.1016/j.cscm.2021.e00802

Analysis of the Properties in the Hardened State of an Alkali Activated Paste of Metakaolin and Flue Gas Desulfurization (FGD) Residue

L. B. Oliveira, M. T. Marvila, D. V. André Júnior, L. U. D. Tambara Júnior, C. M. Vieira, S. N. Monteiro, and A. R. G. Azevedo

Abstract Alkali activated materials (AAMs) have been studied as an alternative to replace the high demand for common ordinary Portland cement (OPC) in civil construction, with the use of industrial by-products in order to reduce and recycle waste instead of disposal in landfills. The aim of the research is to analyze the properties in the hardened state of an alkali activated paste of metakaolin (MK) and residue from flue gas desulfurization (FGD). Samples of AAMs, with dosages of 100% MK and 0% FGD, 90% MK and 10% FGD, and 80% MK and 20% FGD, were produced with a thermal cure of 6 days at 65 °C in the oven. Subsequently, the specimens were submitted to compressive strength tests, apparent density in the hardened state, water absorption, and void ratio at 7 and 28 days.

Keywords Alkali activated materials · Paste · Metakaolin · FGD

Introduction

Portland cement is the main binder used in the production of materials in the construction industry and has recognized quality, with good resistance and durability properties [1]. However, its production is responsible for a considerable amount of CO_2 emission and energy consumption throughout its process [2]. Thus, researchers have sought alternatives for the production of sustainable materials [3].

L. B. Oliveira · M. T. Marvila · D. V. André Júnior · L. U. D. Tambara Júnior · C. M. Vieira
LAMAV—Advanced Materials Laboratory, UENF—State University of Northern Rio de Janeiro, Av. Alberto Lamego, 2000, Campos Dos Goytacazes, Rio de Janeiro 28013-602, Brazil
e-mail: vieira@uenf.br

S. N. Monteiro
Department of Materials Science, IME—Military Institute of Engineering, Square General Tibúrcio, 80, Rio de Janeiro 22290-270, Brazil

A. R. G. Azevedo (✉)
LECIV—Civil Engineering Laboratory, UENF—State University of Northern Rio de Janeiro, Av. Alberto Lamego, 2000, Campos Dos Goytacazes, Rio de Janeiro 28013-602, Brazil
e-mail: afonso.garcez91@gmail.com

M. Zhang et al. (eds.), *Characterization of Minerals, Metals, and Materials 2023*, The Minerals, Metals & Materials Series
https://doi.org/10.1007/978-3-031-22576-5_24

In recent years, several alternatives to OPC have been studied, with an emphasis on geopolymers or alkali activated materials (AAMs) [4]. This material is formed by the dissolution and polymerization of minerals rich in silica and alumina, under sufficient alkaline concentration [5]. The products formed will depend on the alkaline activation concentration and the type of precursor. Sources rich in Si, Al, and Ca will form amorphous N–A–S–H (sodium aluminosilicate hydrate) gels, while those rich in Ca will form C–A–S–H (calcium aluminosilicate hydrate) gels. These formed structures are responsible for the hardening and final properties of the material [6, 7].

Initially, natural minerals were the main raw material for AAMs, such as metakaolin, a source rich in aluminosilicate and produced by the calcination of kaolin at temperatures around 600–700 °C [8]. However, it was found that many residues have the potential to be applied as precursors in AAMs, due to their reactivity and chemical composition, with emphasis on blast furnace slag and fly ash, which present several researches [9, 10].

In addition to those mentioned, a by-product that has been the object of initial studies applied as a material in civil construction is FGD gypsum. This material is generated in the flue gas desulfurization process, where SO_2 gases are removed by adsorption in alkaline media, forming a product rich in gypsum [11]. This high amount of sulfur dioxide is formed from steel mills and thermoelectric plants in the process of burning coal. In this way, this material is produced on a large scale, and when not used, it is discarded in landfills, generating land occupation, environmental pollution, and high costs for its disposal [12].

Thus, the aim of this work is to analyze some properties in the hardened state of an alkali activated paste of metakaolin (MK) and partially substituted by gypsum residue from flue gas desulfurization (FGD).

Materials and Methods

The materials used in this research were metakaolin and FGD gypsum residue as precursors and sodium hydroxide and silicate as activators of the alkaline solution with the addition of water to produce the pastes. According to the chemical analysis, the metakaolin presents a composition of 61.85% of SiO_2 and 32.81 of Al_2O_3. While FGD presents 82.20% of CaO and 17.49% of SO_3 as main elements. The dosage of the pastes was performed from initial laboratory tests. The amount of mixtures of each of the compositions is in Table 1.

Table 1 Mixtures of alkali activated paste

Proportions	Metakaolin (g)	FGD (g)	NaOH (g)	Na_2SiO_3 (g)	H_2O (g)
0% FGD	130	0	10	40	75
10% FGD	117	13	10	40	75
20% FGD	104	26	10	40	75

The production of alkali activated pastes was carried out according to the following procedure: the alkaline activator solution, composed of sodium silicate, sodium hydroxide, and water, was mixed for 10 min in a magnetic stirrer, at least 6 h before entering in contact with precursors. After this process, the precursors were manually mixed. Then the activator solution was mixed with the precursors manually for 1 min and then placed in the electric mixer for 1 min and 30 s. Then, the electric mixer was turned off to remove the solids trapped in the walls of the container and it was turned on again for another 1 min and 30 s for homogenization.

Then, 4 specimens were molded for each of the three compositions of 0% FGD, 10% FGD, and 20% FGD, totaling 12 specimens for 7 days and 12 specimens for 28 days, performing thermal curing by 6 days at 65 °C. Thus, these compressive strength tests were carried out, adapting NBR 7215 [13].

Subsequently, the same quantity of specimens was produced under the same conditions for the tests at 7 and 28 days of apparent density in the hardened state, adapted from NBR 13,280 [14], and water absorption and void index from NBR 9778 [15].

Results and Discussion

Figure 1 shows the result of the compressive strength test of alkaline pastes activated at 7 and 28 days with 6 days of thermal curing in the oven at 65 °C. The pastes were made of metakaolin and partially replaced by 0, 10, and 20% FGD gypsum residue.

There is a high compressive strength of the reference paste containing only metakaolin, reaching an average of 40.4 MPa at 7 days. These values were expected by the literature. According to Chen et al. [16], curing values around 60 °C present the best compressive strength results for metakaolin AAMs. This optimal result was also achieved by other authors [17, 18].

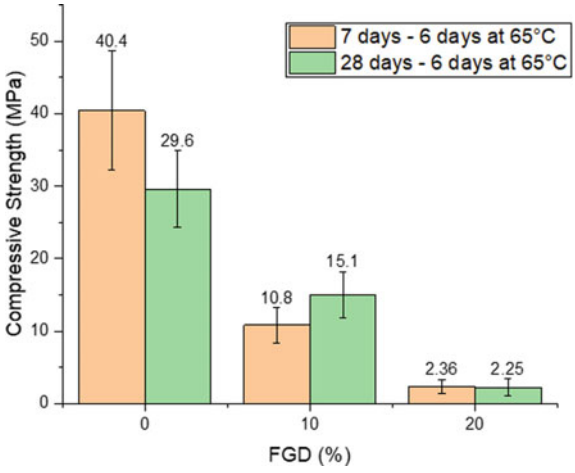

Fig. 1 Results of the compressive strength test of the AAMs at 7 and 28 days and thermal curing in the oven at 65 °C

This is because thermal curing accelerates the alkali activation process and favors hardening, improving the physical properties of the AAMs samples. However, at higher temperatures, above 80 °C, AAMs materials harden quickly, restricting their transformation into a less compact and resistant structure [19].

Some results had unexpected values. The compressive strength at 28 days of 29.6 MPa was lower than at 7 days for the reference paste with an average of 40.4 MPa. Some results had unexpected values such as the compressive strength at 28 days of 29.6 MPa was lower than at 7 days for the reference paste with an average of 40.4 MPa.

In addition, the decrease in strength is noticeable when replacing metakaolin with FGD gypsum residue, reaching low averages of 2.25 MPa at 28 days with 20% FGD. A possible explanation for this drop in strength may be associated with the presence of sulfates and the formation of ettringite, which causes expansion and consequently cracks and fissures in the samples [20].

Other tests served to validate the result of the compressive strength test. Figure 2 shows the result of the density test in the hardened state at 7 and 28 days with a curing temperature of 6 days at 65 °C of the alkali activated pastes.

The results show that the density maintains practically the same average values for 0 and 10% of FGD, between 1.40 and 1.46 g/cm^3 at 7 days and 1.65 and 1.52 g/cm^3 at 28 days. While with 20%, a lower density is observed, with average values of 1.26 g/cm^3 and 1.18 g/cm^3 at 7 and 28 days, respectively. This fact may be related to the difficulty of densifying and compacting the samples, because they have low workability with increasing FGD content. Thus, a lower apparent density is observed in the hardened state.

Figures 3 and 4 present the results of the water absorption and void index tests of the alkali activated pastes at 7 and 28 days with a curing temperature of 6 days at 65 °C.

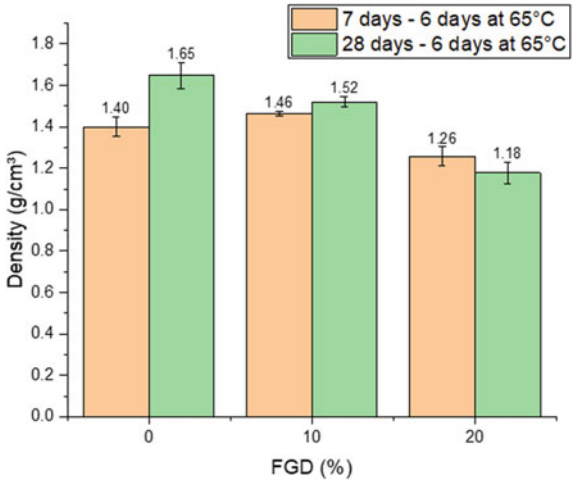

Fig. 2 Density test results in the hardened state at 7 and 28 days with 6 days thermal cure at 65 °C

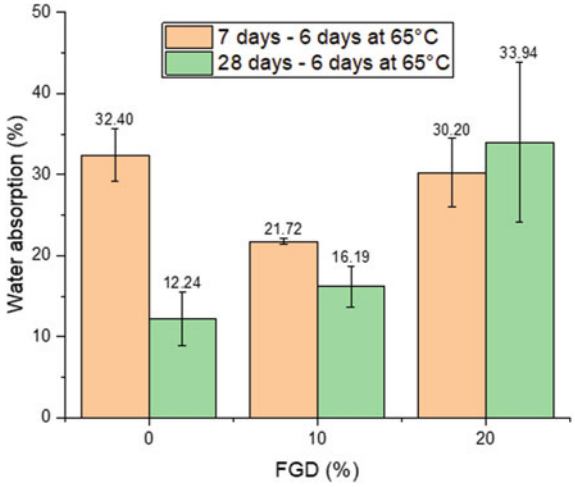

Fig. 3 Results of water absorption tests of alkali activated pastes at 7 and 28 days with 6 days curing at 65 °C

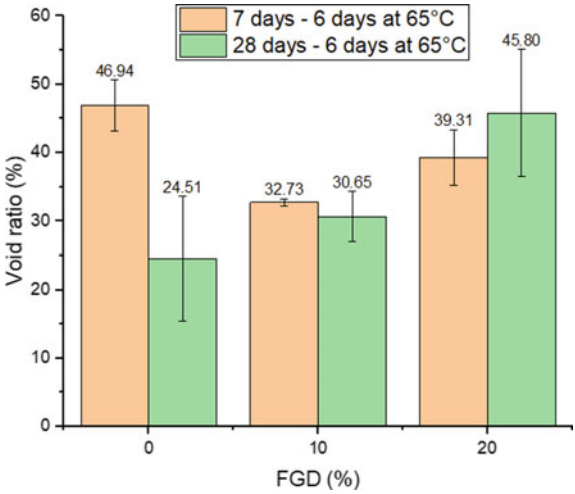

Fig. 4 Void ratio test results of an alkali activated paste at 7 and 28 days with thermal cure at 65 °C

The results of these tests showed considerable variation in relation to 7 and 28 days. At 7 days, the water absorption and void index values do not follow an explanatory relationship with the other tests in the hardened state [21]. However, at 28 days, the lowest value was 0% FGD (reference), with 12.24% and 24.51% for the water absorption and void index tests [22]. As the FGD content increased, the water absorption and the void ratio also increased, reaching average values of 33.94% and 45.80%, respectively [23].

These values are directly related to the results of the compressive strength test. Furthermore, high water absorption values limit in some applications, such as tiles, which have a limit of 20% [21, 24].

Conclusion

The aim of this work was to analyze the replacement of metakaolin by FGD gypsum residue in an alkali activated paste, with replacement percentages of 0, 10, and 20%, in addition to curing in the oven at 65 °C and tests in the hardened state at 7 and 28 days. After the tests, it was possible to conclude the following:

- Replacement of metakaolin by FGD gypsum residue was not effective. The strength test results showed a considerable drop at both 7 and 28 days, with mean values of 40.40 MPa with 0% FGD to 2.36 MPa for 20% FGD at 7 days and 29.60 MPa and 2.25 MPa at 28 days.
- Density, water absorption, and void index tests confirm the deterioration of properties with increasing FGD content.
- One of the explanations for the worsening of properties in the hardened state may be related to the formation of ettringite and the consequent formation of cracks and fissures caused by the expansion of the specimen.
- The difficulty in handling the paste due to the rapid loss of workability with FGD may have impaired the densification and compaction of the specimens, impairing the tests in the hardened state.

Thus, the alkali activated paste did not present good results with the replacement of metakaolin by FGD gypsum in 10% and 20%. One suggestion is to perform substitutions with lower contents to analyze the properties in addition to other complementary microscopic analyzes for studies with more scientific assertiveness.

Acknowledgements This research was funded by the State University of the Northern Fluminense (UENF), partially financed by CAPES (Coordenação de Aperfeiçoamento de Pessoal de Nível Superior—Brazil), CNPq (Coordenação Nacional de Pesquisa), and FAPERJ (Fundação de Apoio à Pesquisa do Estado do Rio de Janeiro). The participation of A.R.G.A. was sponsored by FAPERJ through the research fellowships proc.no: E-26/210.150/2019, E-26/211.194/2021, E-26/211.293/2021, E-26/201.310/2021, and by CNPq PQ2 307592/2021-9.

References

1. Puertas F, González-Fonteboa B, González-Taboada I, Alonso MM, Torres-Carrasco M, Rojo G, Martínez-Abella F (2018) Alkali-activated slag concrete: fresh and hardened behaviour. Cem Concr Compos 85:22–31. https://doi.org/10.1016/j.cemconcomp.2017.10.003
2. Gómez-Casero MA, de Dios-Arana C, Bueno-Rodríguez JS, Pérez-Villarejo L, Eliche-Quesada D (2022) Physical, mechanical and thermal properties of metakaolin-fly ash geopolymers. Sustain Chem Pharm 26. https://doi.org/10.1016/j.scp.2022.100620
3. Li M, Luo R, Qin L, Liu H, Duan P, Jing W (2021) High temperature properties of graphene oxide modified metakaolin based geopolymer paste. Cem Concr Compos 104318. https://doi.org/10.1016/j.cemconcomp.2021.104318
4. Amari S, Darestani M, Millar GJ, Rintoul L, Samali B (2019) Microchemistry and microstructure of sustainable mined zeolite-geopolymer. J Clean Prod 234:1165–1177. https://doi.org/10.1016/j.jclepro.2019.06.237

5. Wan Q, Rao F, Song Morales-Estrella R, Xie X, Tong X (2018) Chemical forms of lead immobilization in alkali-activated binders based on mine tailings. Cem Concr Compos 92:198–204
6. Marvila MT, Azevedo ARG, Vieira CMF (2021) Reaction mechanisms of alkali-activated materials. Rev IBRACON Estrut Mater 14:3. https://doi.org/10.1590/S1983-41952021000300009
7. Mendes BC, Pedroti LG, Vieira CMF, Marvila M, Azevedo ARG, Carvalho JMF, Ribeiro JCL (2021) Application of eco-friendly alternative activators in álcali-activated materials: a review. J Build Eng. https://doi.org/10.1016/j.jobe.2020.102010
8. Ayeni O, Onwualu AP, Boakye E (2021) Characterization and mechanical performance of metakaolin-based geopolymer for sustainable building applications. Constr Build Mater 272:121938
9. Ameri F, Shoaei P, Zahedi M, Karimzadeh M, Musaeei HR, Cheah CB (2021) Physico-mechanical properties and micromorphology of AAS mortars containing copper slag as fine aggregate at elevated temperature. J Build Eng 39:102289. https://doi.org/10.1016/j.jobe.2021.102289
10. Oliveira LB, Azevedo ARG, Marvila MT, Pereira EC, Fediuk R, Vieira CMF (2022) Durability of geopolymers with industrial waste. Case Stud Constr Mater 16:e00839. https://doi.org/10.1016/j.cscm.2021.e00839
11. Zhang Y, Pan F, Wu R (2016) Study on the performance of FGD gypsum-metakaolin-cement composite cementitious system. Constr Build Mater 128:1–11. https://doi.org/10.1016/j.conbuildmat.2016.09.134
12. Caillahua MC, Moura FJ (2018) Technical feasibility for use of FGD gypsum as an additive setting time retarder for Portland cement. J Mater Res Technol 7(2):190–197. https://doi.org/10.1016/j.jmrt.2017.08.005
13. ABNT, NBR 7215 (2019) Portland cement—determination of the compressive strength of cylindrical specimens. Assoc. Brazil Technical Standards (In Portuguese)
14. ABNT, NBR 13280 (2005) Mortar for laying and covering walls and ceilings—determination of apparent mass density in the hardened state. Assoc. Brazil Technical Standards (In Portuguese)
15. ABNT, NBR 9778 (2011) Hardened mortar and concrete determination of water absorption, void ratio and specific mass. Assoc. Brazil Technical Standards (In Portuguese)
16. Chen L, Wang Z, Wang Y, Feng J (2016) Preparation and properties of alkali avtivated metakaolin-based geopolymer. Materials 9:767. https://doi.org/10.3390/ma9090767
17. Villaquirán-Caicedo MA, Mejía de Gutiérrez R, Sulekar S, Davis C, Nino JC (2015) Thermal properties of novel binary geopolymers based on metakaolin and alternative silica sources. Appl Clay Sci 118:276–282
18. Menna C, Asprone D, Ferone C, Colangelo F, Balsamo A, Prota A, Cioffi R, Manfredi G (2013) Use of geopolymers for composite external reinforcement of RC members. Compos Part B Eng 45:1667–1676
19. Bing-hui M, Zhu H, Xue-min C, Yan H, Si-yu G (2014) Effect of curing temperature on geopolymerization of metakaolin-based geopolymers. Appl Clay Sci 99:144–148
20. Khatib JM, Wright L, Mangat PS (2016) Mechanical and physical properties of concrete containing FGD waste. Mag Concr Res 68:550–560. https://doi.org/10.1680/macr.15.00092
21. Marvila MT, de Azevedo ARG, de Oliveira LB, de Castro Xavier G, Vieira CMF (2021b) Mechanical, physical and durability properties of activated alkali cement based on blast furnace slag as a function of $\%Na_2O$. Case Stud Constr Mater 15. https://doi.org/10.1016/j.cscm.2021.e00723
22. Marvila MT, De Azevedo ARG, De Matos PR, Monteiro SN, Vieira CM (2021) Materials for production of high and ultra-high-performance concrete: review and perspective of possible novel materials. Materials 14(15). https://doi.org/10.3390/ma14154304
23. Azevedo ARG, Marvila MT, Zanelato EB, Alexandre J, Xavier GC, Cecchin D (2020) Development of mortar for laying and coating with pineapple fiber. Revista Brasileira De Engenharia Agricola e Ambiental 24(3):187–193. https://doi.org/10.1590/1807-1929/agriambi.v24n3p187-193 (In Portuguese)

24. Carvalho A, Xavier GC, Alexandre J, Pedroti LG, de Azevedo ARG, Vieira CMF, Monteiro SN (2014) Environmental durability of soil-cement block incorporated with ornamental stone waste. https://doi.org/10.4028/www.scientific.net/MSF.798-799.548

Characterization and Mechanical Behavior of Pineapple Fiber Reinforced Geopolymer Composites

J. A. T. Linhares, I. S. A. Pereira, A. R. G. Azevedo, S. N. Monteiro, L. U. D. Tambara, C. M. F. Vieira, and M. T. Marvila

Abstract The cement industry is a protagonist in the current economy; however, it does not act in an environmentally sustainable way, given its high CO_2 emission. In this study, preparing geopolymer composites with the natural fiber reinforcement appears to be a promising solution. The geopolymer is generally made with sources of aluminosilicates and an alkaline activator solution. There are various natural fibers that can be applied as reinforcement; this work aims to elucidate the use of fibers present in the pineapple crown. The fibers were treated in a 5% solution of NaOH; after the treatment, they were characterized by XRD and SEM and then added in a geopolymer matrix in the proportions of 1.6% and 3.2%, on the metakaolin mass, in addition to the production of reference samples. The mechanical properties of the composites were positively evaluated through flexural strength tests.

Keywords Composite · Geopolymer · Pineapple fibers · Mechanical properties

J. A. T. Linhares · I. S. A. Pereira · L. U. D. Tambara · C. M. F. Vieira
LAMAV—Advanced Materials Laboratory, UENF—State University of Northern Rio de Janeiro, Av. Alberto Lamego, 2000, Campos Dos Goytacazes, Rio de Janeiro 28013-602, Brazil
e-mail: vieira@uenf.br

A. R. G. Azevedo
LECIV—Civil Engineering Laboratory, UENF—State University of Northern Rio de Janeiro, Av. Alberto Lamego, 2000, Campos Dos Goytacazes, Rio de Janeiro 28013-602, Brazil
e-mail: afonso@uenf.br

S. N. Monteiro
Department of Materials Science, IME—Military Institute of Engineering, Square General Tibúrcio, 80, Rio de Janeiro 22290-270, Brazil

M. T. Marvila (✉)
UFV—Federal University of Viçosa Campus Rio Paranaíba (UFV-CRP), Rodovia BR 230 KM 7, Rio Paranaíba 38810-000, Brazil
e-mail: markssuel.marvila@ufv.br

M. Zhang et al. (eds.), *Characterization of Minerals, Metals, and Materials 2023*, The Minerals, Metals & Materials Series
https://doi.org/10.1007/978-3-031-22576-5_25

Introduction

Several polymer composites reinforced with artificially produced fibers, such as glass and polypropylene, have been used in the automotive, aerospace, and construction industries [1]. The situation of the industry points to the change from the use of synthetic fibers to natural fibers as potentially positive, from an environmental, economic, and social perspective [2].

Pineapple crown leaf fibers (PALF) have a low cost, low density, good mechanical strength properties, are abundant, and require simple processing, however, there are also limitations linked to natural fibers such as low thermal stability and high water absorption [3]. The City of São Francisco do Itabapoana—RJ, Brazil, is an important pineapple producer. As in many places in the world where it is cultivated on a large scale, a large amount of agricultural waste is generated, such as leaves, roots, and stems, becoming a problem for producers [4].

Geopolymers are inorganic polymers formed from sources of aluminosilicates, with a tetrahedral network structure of Si–O and Al–O, in the presence of an activating alkaline solution [5, 6]. This type of polymer has properties that compare to Portland cement, such as low cost, resistance to corrosion, and high temperatures, and has an advantage in terms of carbon dioxide emissions [7]. In addition to reducing the emission of greenhouse gases, geopolymers can give a useful destination to various waste generated by industrial activity such as fly ash [8].

The objective of this work was to study the mechanical properties of geopolymeric matrix composites with the addition of PALF acting as reinforcement, seeking to evaluate the effectiveness of the alkaline treatment of the fibers in improving the adhesion of the present phases, by means of XRD and SEM. The fibers were collected in the producing in the city of São Francisco do Itabapoana, aiming at sustainability and the destination of agricultural wastes. The flexural strength test was used to evaluate the mechanical behavior of the composites at 7 and 28 days of thermal curing. The specific strength value of the composite was also calculated from the flexural strength.

Materials and Methods

The materials used in this study are sodium hydroxide (99% purity), sodium silicate, distilled water, commercial metakaolin, and agricultural waste from pineapple plantations.

The first stage of the work consisted of the treatment and characterization of the fibers. They were manually separated from the crown and subjected to three cycles of washing in running water and drying at 105 °C in an oven. Then they were processed to a size that facilitates dispersion in the matrix and better workability.

The alkaline surface treatment (mercerization) is very important for a more efficient interaction between the reinforcement/matrix phases, as it removes waxes,

Table 1 Compositions used in this study

Composition	Metakaolin (g)	Sand (g)	PALF (g)	NaOH (g)	Silicate (g)	Water (g)
Reference	320.0	480.0	–	18.0	88.0	182.0
1.6%	320.0	480.0	5.12	18.0	88.0	182.0
3.2%	320.0	480.0	10.24	18.0	88.0	182.0

impurities, and part of the amorphous phases that make up the fibers, such as lignin and hemicellulose. The treatment also contributes to the increase in roughness, which will also reflect in greater adherence [9]. The mercerization was performed with 1 h of exposure of the fibers to an alkaline solution of 5% NaOH.

Three compositions were prepared, and presented in Table 1, with the addition of 1.6 and 3.2% of PALF in the geopolymer matrix. The reference composition was defined through previous studies [6], standardizing the molar ratio of $SiO_2/Al_2O_3 = 4.00$. The purpose of the reference composition is to verify the effect of the addition of fibers, compared with a geopolymer that does not present fibers.

To study the effectiveness of the alkaline treatment of the fibers, X-ray diffraction analyses were carried out to visualize the removal of the amorphous phases that compose the fiber and scanning electron microscopy for topographic analysis. The equipment used were the SSX550 Shimadzu SEDX and the Proto Analytical X-Ray Diffraction Systems (AXRD).

The samples made were of prismatic geometry. The metakaolin used was the commercial brand HP Ultra do Brazil, together with sand oven-dried to constant mass and sieved at 2.4 mm.

To study the mechanical behavior of the composites after the addition of fibers, flexural strength tests were performed, as shown in Fig. 1, based on ASTM C674 [10], commonly used in three-point bending tests. After obtaining the flexural strength data, it was possible to calculate the specific strength, with the volume and mass of the samples.

The equipment used was a universal mechanical testing machine model 5882, brand INSTRON, with a distance between cleavers for bending of 80 mm and a loading rate of 1 mm/min.

Results and Discussion

The images obtained by SEM in Fig. 2 show in (a) the fiber before the alkaline chemical treatment to improve the interface and in (b) the result of the etching. In (a), the cellulosic fibers are not very apparent due to the layers of waxes and lignin, and in (b) the cellulosic fibers are apparent, showing the efficiency of NaOH in removing the components that make it difficult for the fiber to act as a crack bridge. The high roughness in (b) is essential for an efficient adhesion of the fibers with the geopolymer matrix.

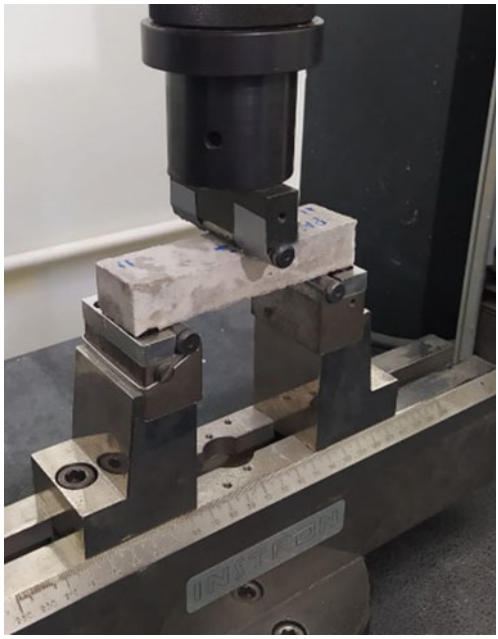

Fig. 1 Specimen being tested in flexion at three points

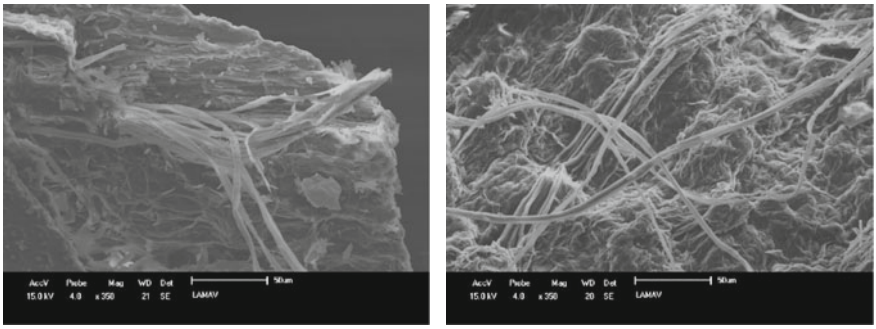

(a) (b)

Fig. 2 Scanning electron microscopy (SEM) of fiber from pineapple crown leaf. **a** Untreated fiber, 350x. **b** Treated fiber, 350x

In Fig. 3, the two diffractograms performed to evaluate the efficiency of mercerization in removing amorphous phases from the material such as lignin are presented. In (a), the untreated fibers present a greater amorphism in relation to (b), with less defined and accentuated peaks, while the treated fibers in (b) already present a greater degree of crystallinity.

Figure 4 presents the results obtained in the flexural strength tests. A subtle drop is observed for specimens subjected to thermal curing for 7 days in relation to the reference, however, this reduction is attenuated in the analysis of Fig. 5, with the

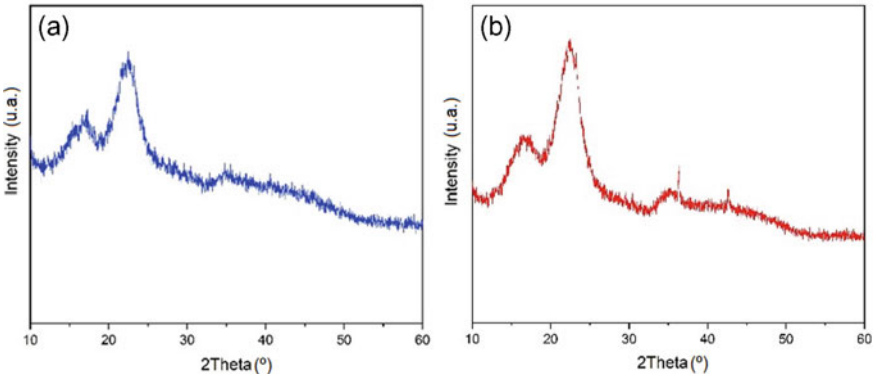

Fig. 3 XRD of the PALF samples, showing the amorphism difference. **a** Not alkaline treated. **b** Subjected to alkaline treatment

resistance to specific mass. For 28 days of curing, there was a considerable increase in this property and a large drop in the reference composition in relation to the 7-day curing; [11] attributes this increase to the potential effectiveness of the fibers to act as bridges of cracks in the brittle matrix.

Although the jump in strength from the reference for the composition containing 1.6% fiber addition was greater than the increase to 3.2%, when analyzing the specific strength in Fig. 5, specimens with 3.2% fiber addition present better results.

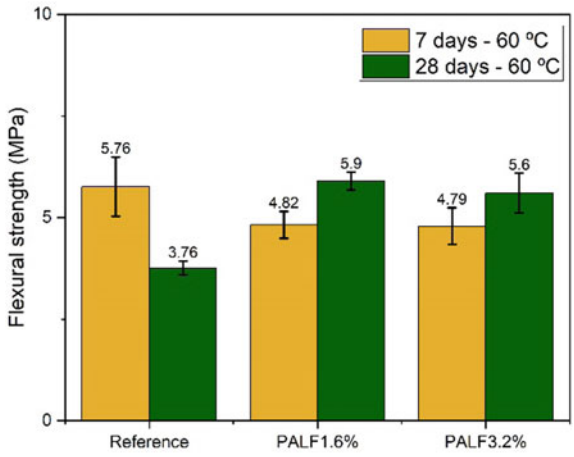

Fig. 4 Flexural strength results

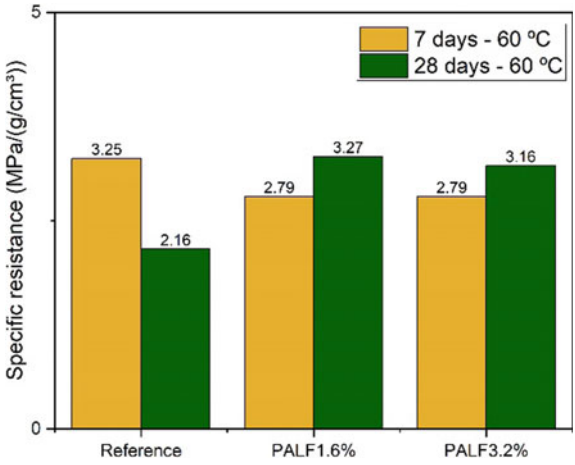

Fig. 5 Specific strength (flexural): ratio between the strength and the density of the samples

Conclusion

In this study, composites of geopolymer matrix reinforced with natural fibers were made from a waste generated by the local economic activity, the pineapple crowns. Based on the results of mechanical flexural strength and characterization techniques, it was possible to conclude that the fibers added as reinforcement were efficient when applied flexural loads, acting as crack bridges. With emphasis on composites subjected to thermal curing for 28 days, with an increase in fibers greater than those exposed to temperature for 7 days. The difference in the mechanical flexural strength obtained was subtle, when compared to the additions of 1.6 and 3.2%, with 1.6% being a little more resistant, which can be disregarded, because in the specific strength the specimens with 3.2% fare a little better. Thus, it is concluded that the addition of 3.2% is more economically viable. The alkaline treatment was efficient in increasing the surface roughness of the fibers, and in removing impurities, components that are harmful to a good fiber/matrix interface.

Acknowledgements The authors thank the Brazilian agencies CNPq, CAPES, and FAPERJ for their support provided to this investigation.

References

1. Silva G, Kim S, Aguilar R, Nakamatsu J (2020) Natural fibers as reinforcement additives for geopolymers—a review of potential eco-friendly applications to the construction industry. Sustain Mater Technol. https://doi.org/10.1016/j.susmat.2019.e00132
2. Ridzuan MJM, Abdul Majid MS, Khasri A, Gan EHD, Razlan ZM, Syahrullail S (2019) Effect of pineapple leaf (PALF), Napier, and hemp fibres as filler on the scratch resistance of epoxy composites. J Market Res 8:5384–5395. https://doi.org/10.1016/j.jmrt.2019.09.005

3. Saravanakumar M, Kumar SS, Babu BS, Chakravarthy CN (2021) Influence of fiber loading on mechanical characterization of pineapple leaf and kenaf fibers reinforced polyester composites. Mater Today Proc 46:439–444. https://doi.org/10.1016/j.matpr.2020.09.804
4. Ravindran L, Sreekala MS, Thomas S (2019) Novel processing parameters for the extraction of cellulose nanofibres (CNF) from environmentally benign pineapple leaf fibres (PALF): structure-property relationships. Int J Biol Macromol 131:858–870. https://doi.org/10.1016/j.ijbiomac.2019.03.134
5. Ren B, Zhao Y, Bai H, Kang S, Zhang T, Song S (2020) Eco-friendly geopolymer prepared from solid wastes: a critical review. Chemosphere. https://doi.org/10.1016/j.chemosphere.2020.128900
6. Junior JAL, Azevedo ARG, Marvila MT, Teixeira SR, Fediuk R, Vieira CMF (2022) Influence of processing parameters variation on the development of geopolymeric ceramic blocks with calcined kaolinite clay. Case Stud Constr Mater. https://doi.org/10.1016/j.cscm.2022.e00897
7. Chen T, Ren B, Wang Z, Meng X, Ning Y, Lv Y (2022) Effect of early strength agent on the hydration of geopolymer mortar at low temperatures. Case Stud Constr Mater. https://doi.org/10.1016/j.cscm.2022.e01419
8. Watanabe Y, Kobayashi T (2022) Synthesis and characterization of metakaolin-based crystalline phase sodium aluminum silicon oxide geopolymers using concentrated alkaline medium. Ceram Int. https://doi.org/10.1016/j.ceramint.2022.07.280
9. Senthilkumar K et al (2021) Compressive, dynamic and thermo-mechanical properties of cellulosic pineapple leaf fibre/polyester composites: influence of alkali treatment on adhesion. Int J Adhes Adhes. https://doi.org/10.1016/j.ijadhadh.2021.102823
10. ASTM C674 (2018) Standard test methods for flexural properties of ceramic whiteware materials
11. Trindade ACC, Liebscher M, Curosu I, Silva FA, Mechtcherine V (2022) Influence of elevated temperatures on the residual and quasi in-situ flexural strength of strain-hardening geopolymer composites (SHGC) reinforced with PVA and PE fibers. Constr Build Mater. https://doi.org/10.1016/j.conbuildmat.2021.125649

Characterization of Açaí Fibers (*Euterpe Oleracea Mart.*) for Application in Cement Composites

T. R. Silva, P. R. de Matos, L. U. D. Tambara Júnior, M. T. Marvila, S. N. Monteiro, and A. R. G. Azevedo

Abstract The waste generated by the agroindustry has been highlighted through reuse in the construction sector, including açaí fibers. Natural fibers have been used in the production of alternative materials, such as cement-based composites. The objective of this work was to characterize the açaí fibers and evaluate the choice of the adequate chemical treatment to improve the fiber-matrix adhesion in view of its application in mortars. Chemical treatments (sodium hydroxide NaOH, calcium hydroxide $CaOH_2$) were performed for 60 min and technological tests for chemical (X-ray diffraction XRD, energy dispersive X-ray analysis EDX) and morphological (scanning electron microscopy (SEM)) characterization of the raw and treated fibers. The results showed that the fibers have an irregular shape and lignin and hemicellulose networks on their surface and a higher presence of silica. As for the fiber treatment, NaOH was the most important, which promoted the removal of most of the amorphous constituents such as hemicellulose, lignin, and waxes of the fibers, also causing an increase in their roughness.

Keywords Technological characterization · Açaí · Natural fibers · Building materials

T. R. Silva · L. U. D. Tambara Júnior · M. T. Marvila
LAMAV—Advanced Materials Laboratory, UENF—State University of Northern Rio de Janeiro, Av. Alberto Lamego, 2000, Campos Dos Goytacazes, Rio de Janeiro 28013-602, Brazil

P. R. de Matos
Civil Engineering Department, UFSM—Santa Maria Federal University, Santa Maria, Rio Grande Do Sul, Brazil

S. N. Monteiro
Department of Materials Science, IME—Military Institute of Engineering, Square General Tibúrcio, 80, Rio de Janeiro 22290-270, Brazil

A. R. G. Azevedo (✉)
LECIV—Civil Engineering Laboratory, UENF—State University of Northern Rio de Janeiro, Av. Alberto Lamego, 2000, Campos Dos Goytacazes, Rio de Janeiro 28013-602, Brazil
e-mail: afonso.garcez91@gmail.com

M. Zhang et al. (eds.), *Characterization of Minerals, Metals, and Materials 2023*, The Minerals, Metals & Materials Series
https://doi.org/10.1007/978-3-031-22576-5_26

Introduction

Natural lignocellulosic fibers (NLFs) have been prominent in the development of alternative materials for different engineering sectors, including construction [1]. These fibers have characteristics such as low specific mass, non-toxicity, biodegradability, low cost, and reduced energy consumption in production [2], which can enhance the technological properties of composite materials, including cement-based composites [3].

In addition, the agroindustry has been responsible for a large volume of discarded solid waste, which contributes to the increase in environmental impacts [4]. In this sense, açaí fibers represent a large part of this sector's discard due to the increased processing of the açaí fruit [5], and thus, they can be considered for their potential application in composite materials, either as reinforcement or as complementary material [6].

Açaí fibers can be called short and represent 83% by weight of the açaí fruit originating from the Euterpe Oleracea Mart. palm, which is cultivated mainly in the Amazon [5, 7]. These fibers have a tendency to interweave, which is one of the main reasons that prevents good fiber-matrix adhesion [8]. Thus, açaí fibers can be treated to achieve better characteristics of their chemical, structural, and morphological properties, thus collaborating to their performance improvement in this sense [9].

In general, NLFs are basically composed of cellulose, hemicellulose, and lignin, thus, their chemical composition must be associated with the choice of the surface treatment to be used [10]. In this sense, different studies have been carried out regarding the treatments of natural fibers such as flax [1], cabuya [11], pineapple [12], and others [13]. Thus, it is possible to state that the choice of treatment, processing conditions, and methods is of fundamental importance, especially for applications in more complex matrices such as cementitious matrices, which demand a more detailed study of parameters related to the interfacial transition zone (ITZ), among them the properties and characteristics of the natural fiber treatment [14].

Thus, the present work aimed to evaluate the chemical and morphological characteristics of açaí fibers, which are still little studied in engineering literature, as well as the choice of treatment to be used on them so that they can be incorporated into Portland cement mortars.

Materials and Methods

The açaí waste was collected in nature, with the help of a shovel, from a company that manufactures açaí-based food products located in the south of the state of Espírito Santo/Brazil. The waste was stored in bags and then transported to the State University of the Northern Rio de Janeiro (UENF), located in Campos dos Goytacazes/RJ/Brazil, where samples were prepared and studied.

Fig. 1 Açaí waste: **a** seeds with fibers; **b** fibers

Firstly, the wastes (seed + fibers—Fig. 1a) were dried on plastic sheets in the open air, at room temperature, to remove the surface moisture of the samples for 48 h. Then, the samples were placed in a stove (BRASDONTO, Model 2) at a temperature of approximately 60 °C for 72 h to remove the remaining moisture. After drying, the samples were manually separated from the açaí fibers (Fig. 1b) and the kernel, and then only the fibers were evaluated.

After being separated, the açaí fibers were sent to the treatments, the first of which was performed through 3 washing cycles (in running water) and drying for 24 h at a temperature of 60 °C. The cycles were performed to remove surface impurities present on the fibers.

After the first treatment, the fibers were subjected to two chemical treatment conditions (second treatment) for a period of 60 min: sodium hydroxide solution (NaOH) and calcium hydroxide solution ($CaOH_2$). For both solutions (2 mol/L), the ratio used for fiber/solution was 1/20 [15], and a period of 5 min was established for homogenization of the mixtures, which was performed by a magnetic stirrer LUCADEMA, model LUCA-01/09, from the Laboratory of Advanced Materials/UENF/RJ/Brazil. After homogenization, the fibers were left to rest in both solutions for 1 h. After 1 h of resting, the fibers treated in both solutions were washed in distilled water until they reached neutral pH. They were then placed in an oven at a temperature of 60 °C for 24 h.

Finally, after the specified conditions, the treated açaí fibers (NaOH, $CaOH_2$) were then assigned to chemical and morphological characterizations. The morphological analysis was performed using a SHIMADZU scanning electron microscope (SEM), model SSX-550, located in the Advanced Materials Laboratory/UENF/RJ/Brazil. The chemical analysis by EDX was performed by the SHIMADZU equipment, model EDX-7000, located in the Physics Department of the Universidade Estadual Paulista—UNESP/SP/Brazil, and by XRD. The XRD—Powder Diffraction System—Proto Manufacturing, located in the Laboratory of Civil Engineering/Advanced Materials at UENF/RJ/Brazil.

Results and Discussion

First, morphological analysis (SEM) was performed for the treated and untreated (reference) acai fibers, as shown in Fig. 2a–c.

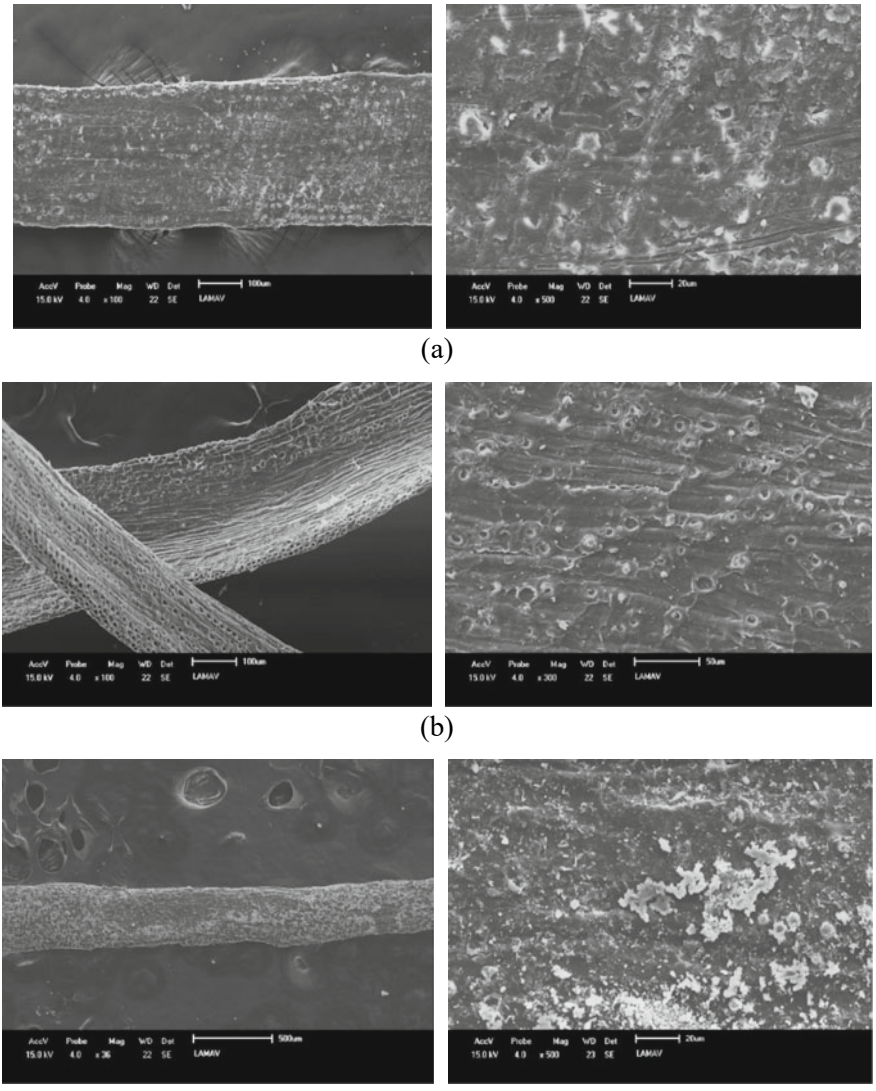

Fig. 2 Açaí fiber: **a** untreated (100x; 500x); **b** treated with NaOH (100x; 300x); and **c** treated with $CaOH_2$ (36x; 500x)

It was possible to observe through SEM images that the surface of the untreated açaí fiber (Fig. 2a) presented a thick layer formed by walls organized by several pores. These characteristics are similar to other plant fibers, because they are composed on their surface (amorphous region) of networks of lignin, hemicellulose, and wax, the overlapping cellulose chains, which are formed by fibrils and microfibrils [6]. In addition, they have part of the surface smooth as a cuticle function. On the outside, the fiber contains a thin primary cell wall that overlies the secondary cell wall, which is thicker [16].

Regarding the fiber with NaOH treatment (Fig. 2b), it can promote the removal of most amorphous constituents such as hemicellulose, lignin, waxes, ash, and oils from the plant fiber and therefore increase the purity of cellulosic fibers [17], as well as its roughness. Roughness is one of the main characteristics for application in composite materials, since it can promote better fiber-matrix adhesion [3]. Furthermore, the images showed that after this type of treatment the surface was more exposed, indicating a partial removal of the components mentioned above and even to have promoted a slight defibrillation of the material. It is also possible to associate that for a medium concentration of NaOH, as in this study, the material tended to have a low alkaline degradation and, consequently, less breakage of cellulose chains in this sense [17].

Compared to the NaOH treatment (Fig. 2c), the $CaOH_2$ treatment on açaí fibers can be considered less aggressive. It was possible to observe in the images a lower roughness in relation to the fibers treated with NaOH, since the surface was less affected regarding the reduction of amorphous components, besides the solution being more concentrated in certain regions of the surface. Although this solution has a significant amount of calcium, an element that is generally beneficial for applications in cement-based matrices, a higher roughness is necessary to improve the necessary fiber-matrix interactions, and especially not to hinder the formation of hydration products and the binder phase [18]. Thus, the NaOH treatment proved to be more efficient regarding the surface characteristics proposed for the study of application in cement matrix.

After choosing the best surface treatment for the açaí fibers (in this case, NaOH) according to the morphology presented above, the chemical analyses of the fibers with NaOH treatment and without treatment (reference) were performed. Thus, the first analysis was performed by EDX, as shown in Table 1.

The second chemical analysis was performed using XRD, as shown in Fig. 3.

It was possible to observe that in the EDX analysis, for both conditions of the açaí fiber (treated and untreated), the highest contents found were of silica, calcium, and potassium already conferred in the literature due to its lignocellulosic characteristics

Table 1 Chemical composition by EDX of açaí fibers (untreated and NaOH treated)

Açaí fiber	Si (%)	Ca (%)	K (%)	S (%)	Fe (%)	Mn (%)	Others (%)
Untreated	55.07	16.88	14.78	6.21	3.36	0.74	2.96
Treated (NaOH)	43.01	38.27	8.30	5.15	1.78	1.16	2.33

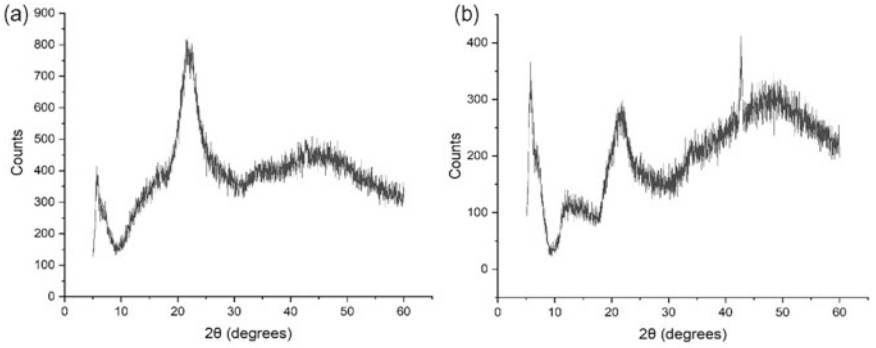

Fig. 3 Açaí fibers: **a** untreated; **b** NaOH treated

[19]. However, after the NaOH treatment, it was possible to observe a significant increase in the calcium element and a decrease in the silica and potassium contents (Table 1).

Thus, it is possible to relate that for the untreated açaí fiber (Fig. 3a), a higher peak in the graph stood out due to the presence of cellulosic structure in the sample that may be associated with the majority presence of potassium and calcium compounds [20]. Cellulose is the most rigid and strongest organic component that gives the fiber strength, stiffness, and stability, and varies according to the characteristics of the individual fibers, such as the type and region of cultivation, climate, and extraction process, among others [6].

In addition, it is also possible to associate the presence of compounds such as quartz, due to the impurities also present that usually end up remaining in the samples despite the treatments [19]. For the fiber treated with NaOH (Fig. 3b), it was possible to note the reduction of this cellulosic structure, caused by the reactions that occurred in contact with NaOH. It is important to note that this may also be related to the presence of glucose in these fibers, occurring saccharide release, thus, being able to interfere later in the application in the cement matrix through calcium ions [21].

Conclusions

According to the present study, it was possible to conclude that

- The choice of surface treatment and analysis of microstructural properties of natural fibers, including açaí fibers, is very important for applications in composite materials, since it can promote changes in characteristics of the fibers to improve their performance in the matrix;
- Among the treatments proposed in the study (NaOH and $CaOH_2$), the best treatment according to the morphological evaluation, regarding surface characteristics,

was the NaOH treatment due to providing better roughness to the açaí fiber, taking into consideration its application in cement-based matrices;

- According to the chemical evaluation, it was possible to verify that the açaí fiber has higher contents of silica, calcium, and potassium, due to its lignocellulosic nature and individual characteristics such as cultivation and extraction, among others. When treated with NaOH, the açaí fiber undergoes changes in the cellulose networks and in the reactions between the potassium and calcium compounds present;
- In addition to the results found, the study also contributes as bibliographical support for the study area, since the literature regarding açaí fibers in the engineering area is still little studied.

References

1. Ferrara G, Pepe M, Martinelli E, Toledo Filho RD (2019) Influence of an impregnation treatment on the morphology and mechanical behaviour of flax yarns embedded in hydraulic lime mortar. Fibers 7(4):1–16. https://doi.org/10.3390/fib7040030
2. Khalid MY, Al Rashid A, Arif ZU, Ahmed W, Arshad H, Zaidi AA (2021) Natural fiber reinforced composites: sustainable materials for emerging applications. Results Eng 11:100263. https://doi.org/10.1016/j.rineng.2021.100263
3. Azevedo ARG, Marvila MT, Tayeh BA, Cecchin D, Pereira AC, Monteiro SN (2021) Technological performance of açaí natural fibre reinforced cement-based mortars. J Build Eng 33:101675. https://doi.org/10.1016/j.jobe.2020.101675
4. Sato MK, Lima HV, Costa AN, Rodrigues S, Pedroso AJS, Maia CMBF (2019) Biochar from Açaí agroindustry waste: study of pyrolysis conditions. Waste Manage 96:158–167. https://doi.org/10.1016/j.wasman.2019.07.022
5. Monteiro GP, Azevedo ARG, Teixeira MT (2021) Effect of the addition of the natural and treated açaí stone in structural mortars. AIMS Mater Sci 8:608–621. https://doi.org/10.3934/matersci.2021037
6. Yan L, Kasal B, Huang L (2016) A review of recent research on the use of cellulosic fibres, their fibre fabric reinforced cementitious, geo-polymer and polymer composites in civil engineering. Compos B 92:94–132. https://doi.org/10.1016/j.compositesb.2016.02.002
7. Tavares FFC, Almeida MDC, Silva JAP, Araújo LL, Cardozo NSM, Santana RMC (2020) Thermal treatment of açaí (Euterpe oleracea) fiber for composite reinforcement. Polímeros: Ciência e Tecnologia 30(1):e2020003. https://doi.org/10.1590/0104-1428.09819
8. Santos NS, Silva MR, Alves JL (2017) Reinforcement of a biopolymer matrix by lignocellulosic agro-waste. Proc Eng 200:422–427
9. Oliveira DNPS, Claro PIC, Freitas RR, Martins MA, Souza TM, Silva BMS, Mendes LM, Bufalino L (2019) Enhancement of the Amazonian açaí waste fibers through variations of alkali pretreatment parameters. Chem Biodivers 16:e1900275. https://doi.org/10.1002/cbdv.201900275
10. Ye H, Zhang Y, Yu Z, Mu J (2018) Effects of cellulose, hemicellulose, and lignin on the morphology and mechanical properties of metakaolin-based geopolymer. Constr Build Mater 173:10–16. https://doi.org/10.1016/j.conbuildmat.2018.04.028
11. Tenazoa C, Savastano H, Charca S, Quintana M (2021) The effect of alkali treatment on chemical and physical properties of ichu and cabuya fibers. J Natural Fibers 18:923–936. https://doi.org/10.1080/15440478.2019.1675211

12. Azevedo ARG, Marvila MT, Zanelato EB, Alexandre J, Xavier GC, Cecchin D (2020) Development of mortar for laying and coating with pineapple fibers e revestimento com fibras de abacaxi. Revista Brasileira de Engenharia Agrícola e Ambiental 24:187–193. https://doi.org/10.1590/1807-1929/agriambi.v24n3p187-193
13. Kesikidou F, Stefanidou M (2019) Natural fiber-reinforced mortars. J Build Eng 25:100786. https://doi.org/10.1016/j.jobe.2019.100786
14. Santos SF, Teixeira RS, Savastano Junior H (2017) Interfacial transition zone between lignocellulosic fiber and matrix in cement-based composites: sustainable and nonconventional construction materials using inorganic bonded. Fiber Compos 3:27–68. https://doi.org/10.1016/B978-0-08-102001-2.00003-6
15. Fonseca RP (2021) Influence of different types of Amazonian plant fibers on the performance of a mortar based on Portland cement and Metakaolin. PhD thesis, Federal University of Santa Catarina, Trindade Campus
16. Yan L, Chouw N, Jayaraman K (2014) Flax fibre and its composites—a review. Compos B 56:296–317. https://doi.org/10.1016/j.composites
17. Pereira PHF, Ornaghi HL, Arantes V, Cioffi MOH (2021) Effect of chemical treatment of pineapple crown fiber in the production, chemical composition, crystalline structure, thermal stability and thermal degradation kinetic properties of cellulosic materials. Carbohyd Res 499:108227. https://doi.org/10.1016/j.carres.2020.108227
18. Lisboa PSA, Machado MS, Brandes R, Hentges TI, Vanin DVF (2021) The influence of microcrystalline cellulose on cement pastes early hydration modulus of rupture. Mater Chem Phys 270:24769. https://doi.org/10.1016/j.matchemphys.2021.124769
19. Marvila MT, Azevedo ARG, Cecchinb D, Costa JM, Xavier GC, Carmo DF, Monteiro SN (2020) Durability of coating mortars containing açaí fibers. Case Stud Constr Mater 13:e00406. https://doi.org/10.1016/j.cscm.2020.e00406
20. Cordeiro L, Paes I, Souza PSL, Azevedo CM (2019) Characterization of the residual ash from the açaí stone for addition to concrete. Ambiente Construído 19:45–55. https://doi.org/10.1590/s1678-86212019000100292
21. Stapper JL, Gauvin F, Brouwers HJH (2021) Influence of short-term degradation on coir in natural fibre-cement composites. Constr Build Mater 306:124906. https://doi.org/10.1016/j.conbuildmat.2021.124906

Characterization of Artificial Stone with Quartzitic Sand and with the Incorporation of Steel Residue

Tatiane Brito Perim da Silva, Elaine Aparecida Santos Carvalho, Maria Luiza Pessanha Menezes Gomes, Gabriela Nunes Sales Barreto, Sérgio Neves Monteiro, and Carlos Mauricio Fontes Vieira

Abstract Artificial stone is a material made of stone aggregates and other minerals agglomerated by a polymeric resin. However, aiming at both sustainability and economy, several studies have produced artificial stones with industrial wastes to reduce the product's final cost and help the environment. Brasil is a big steel producer, generating a lot of waste. The main steel industry wastes are blast furnace dust, sludge, slag, and scale. Blast furnace dust waste is mainly composed of metallic oxides and carbonaceous materials. This work aims at producing artificial stones with high-purity material (pure quartz) and comparing it with artificial stones with 17% steel industry waste, in order to analyze the physical, mechanical, and chemical properties. Both stones presented good performance, but the results showed that the stone with residue had superior properties compared to the one with only pure quartz.

Keywords Artificial stone · Resin · Steel waste · Coating

Introduction

Artificial stone (AS) is defined as a material made of stone aggregates and other minerals agglomerated by a polymeric resin, often obtaining mechanical properties close or superior to natural stone. Aggregates represent around 90–94% of artificial stone [1].

T. B. P. da Silva (✉) · E. A. S. Carvalho · M. L. P. M. Gomes · G. N. S. Barreto · C. M. F. Vieira
Advanced Materials Laboratory (LAMAV), State University of Northern Fluminense—UENF, Av. Alberto Lamego 2000, Campos dos Goytacazes, Rio de Janeiro 28013-602, Brazil

C. M. F. Vieira
e-mail: vieira@uenf.br

S. N. Monteiro
Department of Materials Science, Instituto Militar de Engenharia—IME, Praça General Tibúrcio 80, Praia Vermelha, Urca, Rio de Janeiro, Rio de Janeiro 22290-270, Brazil

M. Zhang et al. (eds.), *Characterization of Minerals, Metals, and Materials 2023*, The Minerals, Metals & Materials Series
https://doi.org/10.1007/978-3-031-22576-5_27

Among these aggregates, high-purity quartz is widely used, in addition to glass waste, natural stone fragments, and others. Furthermore, one of the most important thermosetting polymer classes is epoxy resins, since they offer an excellent combination of properties that are usually unattainable for other thermosetting resins [2, 3].

Artificial stones commonly have certain advantages over natural stones, such as lower weight, due to the low density of the polymer matrix, and lower porosity, which enhances the materials mechanical properties, since pores act like stress concentrators generating mechanical strength decrease. Besides, low porosity offers another advantage, hampering the infiltration of fluids and enabling its application for longer periods in environments with humidity conditions [4, 5].

Although AS has excellent properties, the use of high-purity aggregates elevates the cost, making it more expensive than natural stones. However, aiming at both sustainability and economy, several studies have focused on the production of artificial stones with industrial wastes to reduce the product's final cost simultaneously making a positive contribution to the environment, adding value to the waste while reducing the space occupied for their disposal [6].

According to Instituto Aço Brazil, Brazil is the 9th world crude steel producer and, in 2019, 32.2 million tons of crude steel was produced, generating 22 million tons of co-products. The main steel industry wastes are blast furnace dust, sludge, slag, and scale. Many of these wastes have been reused as aggregates for paving, soil stabilization, fertilizers, cement production, and catalyst in wastewater treatment, among others. Blast furnace dust waste is mainly composed of metallic oxides and carbonaceous materials [7].

Thus, as an alternative for reducing both cost and environmental damage, this work aims at producing artificial stones with high-purity material (pure quartz) and comparing it with artificial stones with 17% steel industry waste, in order to analyze the physical properties (apparent density, apparent porosity, and water absorption), as well as the mechanical properties of bend strength.

Development

Material

The Blast Furnace Dust waste was supplied by ArcelorMittal, located in the city of Serra, Espírito Santo, Brazil. The mineral material (quartz sand) was supplied by the company EcologicStone, located in the city of Cachoeiro de Itapemirim, Espírito Santo, Brazil, which is used in the artificial stone manufacturing. The quartz sand already came with particles of coarse granulometry, from 2 to 0.42 mm and 0.42 to 0.075 mm. The powdery waste had fine particles granulometry, grains with size less than 0.075 mm.

The epoxy used as binding was a diglycidyl ether of bisphenol A (DGEBA) resin mixed with the triethylenetetramine (TETA), both supplied by Epoxyfber, Brazil. The supplier indicated the density of the epoxy as 1.15 g/cm^3.

Determination of the Highest Packaging Granulometric Composition

Based on three ranges of grains obtained, 10 different mixtures with different percentages of rough, medium, and fine particles were proposed.

Figure 1 shows a complete ternary diagram developed in the experimental numeric-modeling grid Simplex Lattice Design (SLD) [8] to obtain greater packaging; each vertex of the triangle corresponds to 100%: large (*L*), medium (*M*), and fine (*F*) particles. The other points in the triangle display (in parentheses) the fractions corresponding to the mixtures. To determine the proportion of the greatest packaging of the 10 mixtures, these were all tested based on the standard ABNT/MB-3388 Brazilian standard (1991) [9]—determination of the minimum index void ratio of non-cohesive. For each composition, the test has been done three times for assuring statistical validation. Each sample from the waste compositional mixture was placed in a steel vessel and left vibrating for 10 min under a load of 10 kg. The mixture was weighed and the apparent density was calculated.

The treatment of the data obtained from the vibrated density has been performed, using analysis of variance (ANOVA) of the completely randomized design (CRC) ($p \leq 0.05$), in order to verify the existence of statistical significance between the treatment performed. Once the statistical difference was confirmed, Tukey's mean comparison test ($p \leq 0.05$) was performed in order to verify which trait obtained

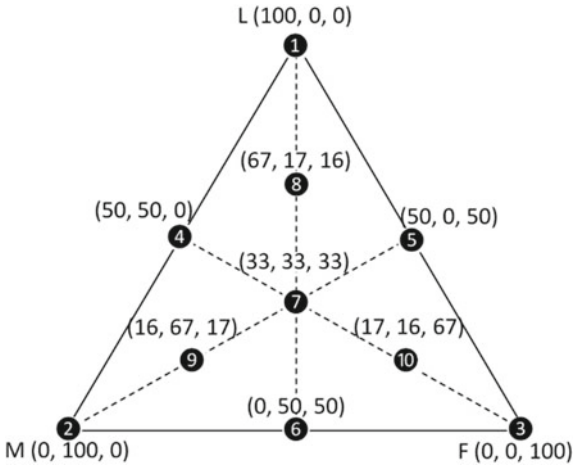

Fig. 1 Ternary diagram with the 10 mixtures based on the complete cubic model of the SLD. Amounts (wt. %) of large (*L*), medium (*M*), and fine (*F*) particles [10]

the best results. The calculations were performed using the excel tool of the office package.

As described by Ribeiro [11], it was necessary to calculate the minimum amount of resin (MAR) of the best statistical results, necessary for the artificial stone production, using Eqs. 1 and 2:

$$VV\% = \left(1 - \frac{\rho_{PA}}{\rho_Q}\right) * 100 \tag{1}$$

where

VV% = Void volume present in the mixture of particles;

ρ_{PA} = Apparent density of particles, calculated by the packaging method;

ρ_Q = Mineral charge density, calculated by pycnometry.

By obtaining the void volume (VV%) value, it was possible to calculate the minimum amount of resin (MAR), through Eq. 2 below

$$MAR\% = \frac{VV\% * \rho_{resin}}{VV\% * \rho_{resin} + (100 - VV\%) * \rho_Q} \tag{2}$$

where

MAR% = Minimum amount of resin to fill the void volume;

VV% = Void volume present in the mixture of particles;

ρ_{resin} = Epoxy resin density;

ρ_Q = Mineral charge density, calculated by pycnometry.

Production of Artificial Stone Plates

For the compositions determined by the statistics, artificial stone slabs were produced with epoxy resin. The plates with 17% of Blast Furnace Dust waste and quartz sand (AS17PB) and the plates with pure quartz sand (ASQS) were produced with 100 × 100 × 15 mm size by the vacuum, vibration, and compression method.

Initially, the waste was dried in an oven at 100 °C to remove moisture, then it was weighed and placed inside the mixer, and the resin was added for completing the entire mixture. After all the mass was mixed, it was deposited in the mold and placed on a vibrating table, to promote the spreading of the mass in the mold cavity and to facilitate the removal of air bubbles that could be in the mass. After the vibration time, the mold, still under vacuum, was removed and placed in the Marcone MA 098-A hydraulic press where specimens were produced with a compression pressure of 3 MPa at 90 °C [3, 4].

Only after pressing, the mold was disconnected from the vacuum system and cooled to room temperature (RT) to remove the plates, after the specimens were placed in an oven at 90 °C for post-curing. At the end, they were sanded and cut according to the pattern for each test.

Characterization of Artificial Stone Plates

The values of density, water absorption, and apparent porosity have been obtained from the standard tests according to the norm ABNT NBR 15,845:2010 [12]. For each condition, 15 specimens were made with dimensions of 30 × 30 × 15 mm.

Ten prismatic specimens, cut from the AS17PB and ASQS plate with dimensions of 10 × 10 × 25 mm, were three points bend tested in a model 5582 Instron machine following the recommendation for agglomerated stones as per the Annex F of the Brazilian NBR 15.845 standard [12].

Abrasive wear resistance was performed using MAQTEST Amsler equipment on two samples measuring 70 × 70 × 40 mm, according to the Brazilian standard ABNT/NBR 12,042 [17, 18].

The thickness measurements of the samples were carried out before the wear test, and measured again after the wear the 500 and 1000 m on a circular track.

It has been evaluated that the microstructure in the fracture region of the specimen bodies were taken to the flexion test by a Scanning Electron Microscope (SEM), making possible the analysis of particle adhesion to the DEGBA-TETA system. The equipment used was the SSX-550 SHIMADZU model operated by secondary electrons.

Results

Table 1 presents the values obtained through the SLD method for the average vibrated density of mixtures of Blast Furnace Dust waste and quartz sand wastes according to Fig. 1.

Table 1 Vibrated density of the blast furnace dust quartz sand sample

Vibrated density (g/cm^3)	
Mixture	Average values
1	1.53 ± 0.02
2	1.75 ± 0.02
3	0.84 ± 0.02
4	1.88 ± 0.01
5	1.54 ± 0.03
6	1.42 ± 0.01
7	1.72 ± 0.01
8	1.83 ± 0.02
9	1.75 ± 0.01
10	1.34 ± 0.01

As it is a parameter of the vibrated densities' average, the data was treated with variance analysis considering a completely randomized design (CRD) performed with a 95% confidence level ($p \leq 0.05$), with subsequent Tukey test average contrasts. Analyzing the results obtained in Tables 2 and 3, it is possible to verify that the treatments studied present statistical differences, meaning that among the 10 mixtures, at least two are differentiated. It is important to have in mind that the variation coefficient for this test was 1.91%, representing the high reliability of the results.

Tukey test was performed in order to differentiate, and results found that mixtures 4 and 8 possess higher density and differ statistically from each other. Once mixtures involving non-spherical particles have an enormous amount of possible particle shapes leading to an infinity of particle combinations, it's hard to develop a model able to predict its behavior. The only accurate prediction is that the more the non-spherical particles become, the lesser the packing density and other related properties.

Table 4 shows the AS17PB and ASQS physical properties.

The density of AS17PB and ASQS was 2.29 g/cm^3 and 2.17 g/cm^3, respectively. It can be observed that the artificial stone containing Blast Furnace Dust waste in its composition presented higher density. It can be explained by the fact that Blast Furnace Dust waste is composed of hematite whose density is ~ 5.26 g/cm^3, while the quartzite density is ~ 2.5 g/cm^3. It is important to evaluate density; the higher its

Table 2 ANOVA test results on the CRD of vibrated density ($p \leq 0.05$)

FV	GL	SQ	QM	F
Treatment	9	2.5960	0.2884	1185.4018
Waste	20	0.0049	0.0002	
Total	29	2.6009		

Conclusion: F calculated > F tabulated, there is a statistical difference
F tulated = 2.39

Table 3 Tukey test for contrasting vibrated density averages ($p \leq 0.05$)

Treatment	Average	Tukey test[a]
4	1.88	A
8	1.83	AB
2	1.75	BC
9	1.75	BC
7	1.72	BC
5	1.54	CD
1	1.53	CD
6	1.42	E
10	1.34	F
3	0.84	G

[a] *Averages followed by the same letter, in the column, do not differ from each other at 5% probability by Tukey's Test*

Table 4 Physical properties of the AS17PB and ASQS artificial stone

Artificial stone	Density (g/m^3)	Water absorption (%)	Apparent porosity (%)
AS17PB	2.29 ± 0.05	0.07 ± 0.02	0.14 ± 0.05
ASQS	2.17 ± 0.07	0.13 ± 0.05	0.29 ± 0.11

value, the better the particle/matrix adhesion, diminishing the occurrence of voids [13, 14].

Lee et al., in their research, manufactured artificial stone using fiberglass and PET, varying the conditions of vacuum, vibration, and compaction pressure and evaluated density values that varied in the range of 2.03–2.45 g/cm^3 [15]. The artificial stones developed in this study had density within this range.

The water absorption of the AS17PB was 0.07% and that of the ASQS was 0.13%, meaning that the water absorption of the AS17PB was approximately half the value of the water absorption of the ASQS. Water absorption is related to the impermeability of the surface of the material, a factor such as artificial stones, as it is used in humid conditions.

Chiodi and Rodriguez, in their "Guide to the Application of Coating Rocks", classified quartzites with water absorption under 0.1% as materials with very low absorption, which reinforces the good performance of both developed stones, with emphasis on AS17PB [16].

The apparent porosity of AS17PB and ASQS were 0.14% and 0.29%, respectively. The ASQS had twice the porosity of the AS17PB. Chiodi and Rodriguez stipulated that quartzites with porosity less or equal to 0.5% as very low porosity materials [16].

Figure 2 shows the Bending Stress x Deformation curves for AS17PB and ASQS.

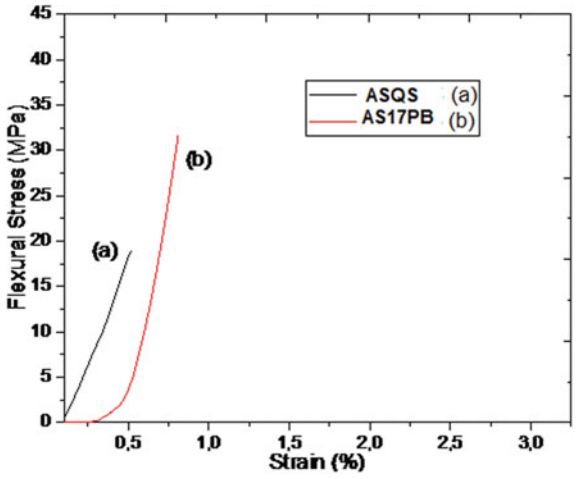

Fig. 2 Flexural rupture stress versus bend strain for artificial stones AS17PB and ASQS

Table 5 Amsler wear associated with the thickness reduction of the artificial stones developed (AS17PB and ASQS)

Material	Wear thickness reduction (mm)	
	500 m	1000 m
AS17PB	0.37	0.84
ASQS	0.92	1.82

The AS17PB and ASQS bend-rupture stresses were 31.8 ± 2.5 and 18.5 ± 1.5 MPa, respectively. The artificial stone developed with Blast Furnace Dust waste (AS17PB) was 58% more resistant than the one with quartz sand ASQS, which can be explained by hematite's greater bend strength when compared to quartzite.

According to Chiodi and Rodriguez (2020) artificial stones applied as coatings are classified as high-strength materials when their bending strength is between 16 and 20 MPa and are considered to be of very high strength when it exceeds 20 MPa. Therefore, both developed stones can be used as coating, with AS17PB being classified as a very high-strength material and ASQS as a high-strength material. It is worth noting that the low-porosity indexes, especially of AS17PB, influenced the materials' good performance, since the pores, as explained, can work as stress concentrators [16].

Chiodi Filho and Rodrigues (2020) classify the material quality as high-traffic floor (< 1.5 mm), medium-traffic floor (< 3 mm), and low-traffic floor (< 6 mm), in terms of abrasive wear, for the application of ornamental stones on floor coverings [16].

Table 5 displays the results obtained in the abrasive wear test for both rocks produced.

Based on the technological parameters mentioned by Chiodi Filho and Rodrigues, AS17PB is indicated for high-traffic floors, due to the efficient rearrangement in the structure and texture of the minerals during the agglutination of the particles in the polymer matrix [16, 17].

The natural quartzite stone wear value of 1.82 mm was the greatest found on the same route. Although quartz has high hardness among minerals (Mohs = 7), the union of quartz with hematite (Mohs = 6.5) contributed to a better performance of AS17PB.

Figure 3 shows the Scanning Electron Microscope (SEM) micrographs of AS17PB and ASQS.

Through the micrographs of both stones shown in Fig. 3a and c, it is possible to confirm the good particles/epoxy matrix interaction proving the optimal adhesion between the filler and the matrix, indicating the quality of the mixture homogenization.

Moreover, it is also possible to observe the low incidence of voids, which appear only in isolation. Through the micrographs, it is possible to confirm that ASQS has higher porosity than AS17PB. Therefore, the microscopic analysis confirmed the physical indices and the bending test results.

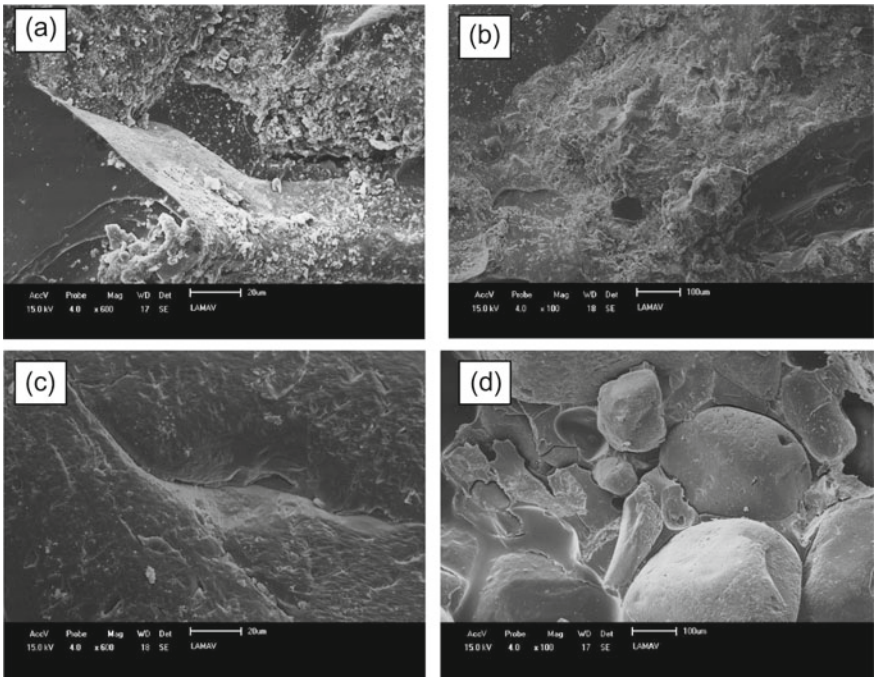

Fig. 3 Micrographs obtained by SEM of AS17PB **a** (600x) and **b** 100X, and of ASQS **c** 600x and **d** 100x

Conclusion

- An innovative artificial stone was developed, using quartzite and both quartzite and Blast Furnace Dust waste, demonstrating the efficiency of the incorporation of this waste incorporation in the artificial stone's development.
- Based on the ternary diagram developed in the experimental numerical-modeling grid simplex, through best packing tests, the aggregate compositions with higher densities were chosen. In order to authenticate the data, Analysis of Variance and Tukey tests were performed.
- Both stones presented satisfactory physical indices, with AS17PB presenting lower porosity and water absorption, enabling its use in moisture environments.
- Regarding bending strength, AS17PB was considered to be a very high-strength material (31.0 $\pm$ 2.5 MPa), while ASQS was considered to be high-strength material (18.5 $\pm$ 1.5 MPa), corroborating the porosity results.
- Through the abrasive wear test, the low thickness (< 1.5 mm) reduction observed in the artificial stone produced with steel waste (0.84 mm for AS17PB) indicates that stone can be used for intense traffic floor areas, while ASQS can be used for medium-traffic floors.

- The SEM micrographs obtained proved the physical index and mechanical property results, displaying the optimal load-matrix interaction for both developed stones.

Acknowledgements The authors are grateful for the support of the Brazilian agencies UENF and FAPERJ in this research. The ArcelorMittal Company and the EcologicStone artificial stone industry for supplying the waste and quartz sand, and we thank technician Renan da Silva Guimarães.

References

1. Suta S, Wattanasiriwech S, Wattanasiriwech D, Duangphet S, Thanomsil C (2019) Preparation of engineered stones. Mater Sci Eng 600:1–6
2. Kirgiz MS (2015) Strength gain mechanisms of blended-cements containing marble powder and brick powder. J Civ Eng 19:165–172
3. Silva F, Ribeiro CE, Rodríguez R (2018) Physical and mechanical characterization of artificial stone with marble calcite waste and epoxy resin. Mater Res 21:1–6
4. Gomes ML, Carvalho E, Dermartini T, Carvalho A, Colorado H, et al (2020) Mechanical and physical investigation of an artificial stone produced with granite residue and epoxy resin. J Compos Mater 1–6
5. Dermartini T, Rodríguez S, Silva F (2018) Physical and mechanical evaluation of artificial marble produced with dolomitic marble residue processed by diamond-plated bladed gang-saws. J Market Res 350:1–6
6. Shishegaran A, Saeedi M, Mirvalad S, Korayem AH (2021) The mechanical strength of the artificial stones, containing the travertine wastes and sand. J Market Res 11:1688–1709
7. Chaves N, Oliveira RM (2020) As alternativas de aproveitamento do pó do alto-forno: uma revisão. Perspectivas da Ciência e Tecnologia 12:188–198
8. Cornell JA (2002) Experiments with mixtures: designs, models, and the analysis of mixture data, 3rd edn. Wiley, New York
9. Brazilian Association of Technical Norms—ABNT. ABNT NBR MB 3388: soil—determination of minimum index void ratio of cohesionless soils—method of test. Rio de Janeiro: ABNT (1991) [in Portuguese]
10. Carvalho EAS, Vilela NF, Monteiro SN, Vieira CMF, Silva LC (2018) Novel artificial ornamental stone developed with quarry waste in epoxy composite. Mater Res 21:1–6
11. Ribeiro CEG, Rodriguez RJ, Carvalho EA (2017) Microstructure and mechanical properties of artifcial marble. Constr Build Mater 149:149–155
12. Brazilian Association of Technical Norms (ABNT). ABN NBR—15845—Rocks of Cladding—Test Methods. São Paulo: ABNT (2010) (in Portuguese)
13. Nikischer A.J. Mindat. Available at: https://www.mindat.org/min-1856.html
14. Nikischer A.J. Mindat. Available at: https://www.mindat.org/min-3337.html
15. Lee DJ, Shin IJ (2002) Effects of vacuum, mold temperature and cooling rate on mechanical properties of press consolidated glass fiber/PET composite. Compos A Appl Sci Manuf 33(8):1107–1114
16. Chiodi CF, Rodriguez EP (2020) Guia de aplicação de rochas em revestimentos. São Paulo: Abirochas, 119 p
17. Agrizzi CP, Carvalho EAS, Gadioli MCB, Barreto GNS, Afonso ARG, Monteiro SN, Vieira CMF (2022) Comparison between synthetic and biodegradable polymer matrices on the development of quartzite waste-based artificial stone. Sustainability 14:1–18
18. Brazilian Association of Technical Norms—ABNT. ABNT NBR 12042: Inorganic Material-Determination of the Resistance to Abrasion. Rio de Janeiro: ABNT; 2002 [in Portuguese]

Characterization of Flotation and Leaching in Cyanide and Thiourea Medium of a Gold, Silver, and Copper Ore

Martín Reyes Pérez, Iván. A. Reyes Domínguez, Mizraim U. Flores Guerrero, Elia Palacios Beas, Julio Cesar Juárez Tapia, Miguel Pérez Labra, Francisco Raúl Barrientos Hernández, Aislinn Michelle Teja Ruiz, and Ian Medina Estrada

Abstract High-grade gold ores are generally associated with iron, copper, and silver sulfides, among other species that during dissolution consume the leaching agent, causing a decrease in the leaching rate. In this work, the flotation, and the comparison of the leaching with cyanide and thiourea (TU) of an ore rich in Au, Ag, and Cu were studied. The flotation was carried out with 100 and 200 mesh particles at pH 6.53, and Eh of 253 mV, and frother MIBC and xanthate 60 and 100 mg/l, respectively. The concentrate was leached with 0.2 M thiourea at pH 1.5 and separately with 2000 PPM-free cyanide at pH 11.1. In the system containing cyanide, 19.7%, 22.8%, and 15.4% of Au, Ag, and Cu of recovery were obtained, respectively, while in the system with only TU 14.36%, 15.75%, and 10.75% extraction.

Keywords Cyanide · Thiourea · Silver · Leaching · Gold

Introduction

The cyanidation process is widely used throughout the world due to its simplicity of operation and low cost; however, when the deposit contains refractory minerals,

M. R. Pérez (✉) · J. C. J. Tapia · M. P. Labra · F. R. B. Hernández · A. M. T. Ruiz · I. M. Estrada
Academic Area of Earth Sciences and Materials, Autonomous University of the State of Hidalgo, Road Pachuca-Tulancingo Kilometer 4.5 Mineral de La Reforma, Hidalgo 42180, México
e-mail: mreyes@uaeh.edu.mx

Iván. A. Reyes Domínguez
Institute of Metallurgy, Autonomous University of San Luis Potosí, SLP, San Luis Potosí 78210, México

M. U. Flores Guerrero
Industrial Electromechanics Area, Technological University of Tulancingo, 43642 Hidalgo, México

E. P. Beas
National Polytechnic Institute Unit ESIQIE. C.P. 07738, México, D.F, México

M. Zhang et al. (eds.), *Characterization of Minerals, Metals, and Materials 2023*, The Minerals, Metals & Materials Series
https://doi.org/10.1007/978-3-031-22576-5_28

there are difficulties in leaching and the values of interest are leached in less than 50% [1, 2]. Currently the term refractory is assigned to minerals that have micrometric gold, which in greater proportion is found encapsulated in the mineral gangue [3]; likewise, the term refractory is assigned when the mineralogy of minerals containing gold and silver is complex [4–6].

Due to the severe environmental requirements for the use and implementation of cyanide, it has been sought to industrially introduce various leaching agents such as thiocyanate ion, thiosulfate, and thiourea, among others. The use of thiourea (TU) and its possible implementation in the industry is the most viable option to replace cyanide. TU has some advantages over cyanide [7], such as reduced environmental impact compared to cyanide, the handling of the reagent presents fewer complications, better selectivity towards gold and silver, in addition to a higher leaching kinetics compared to other leaching agents, together with this it improves the extraction of gold and silver from refractory minerals [8]. As a disadvantage is the high consumption of the oxidizing agent, for example the ferric ion, or hydrogen peroxide [8, 9].

The use of TU at an industrial level could be applied when minerals or concentrates of high grade or grade are processed and those that have a certain refractoriness to be leached; the leaching of gold using thiourea has been previously reported, and 80% leaching in two hours of reaction has been reported; the reduction of the leaching time with respect to the slow dissolution kinetics with cyanide together with high-grade minerals could be the trigger for the use of TU on an industrial scale [10, 11].

In this research, the flotation of the mineralogical species of value was carried out, as well as the comparative study of the leaching of gold, silver, and copper in cyanide-water systems at alkaline pH and thiourea-water in acid conditions, without using an oxidant.

Experimental Methodology

To carry out this experimental study, a high-grade gold ore with silver and copper contents from the state of Michoacán, Mexico, was used. The ore as received was crushed in a jaw crusher, pulverized in a mill roller, and wet-sieved to obtain enough samples of 100 mesh and 200 mesh to carry out the flotation tests using an anionic collector.

The flotation tests were carried out in a Denver-type mechanical cell using an impeller at 1200 rpm and a diffuser located at the bottom of the stainless-steel cell with a capacity of 1 L; 200 g of mineral were used per test (mesh 100 and 200 separately), 60 mg/L frother agent [e] propylene glycol, and 100 mg/L potassium amyl xanthate-type collector [X]. During the conditioning stage, the hydrogen ion potential and the ORP oxidation reduction potential (mV) were continuously measured, which was referred to its value from the standard hydrogen electrode (SHE) adding to the measured value the amount of 242 mV as indicated described in the literature [12]. The concentrate was collected during 5 min of flotation.

Table 1 Concentration (mg/L) of gold, silver, and copper in the feed

Mesh	Feeding mg/L		
	Copper	Silver	Gold
100	98.82	103.81	2.67
200	172.45	54.92	1.66

Table 2 Concentration (mg/L) of gold, silver, and copper in the concentrate

Mesh	Concentrate mg/L		
	Copper	Silver	Gold
100	258.22	185.29	45
200	299.1	199.06	43

Table 3 Concentration (mg/L) of gold, silver, and copper in the tailings

Mesh	Tailings mg/L		
	Copper	Silver	Gold
100	18.1	6.65	0.6
200	16.1	10.6	0.93

The sample of concentrate, feed, and tailings was attacked with aqua regia (1 g) in triplicate, gauged and analyzed via atomic absorption spectrometry, in their concentration of gold, silver, and copper. Tables 1, 2, and 3 show the average values of the concentrations obtained.

Regarding the leaching for each test, 5 g of the 200 mesh flotation concentrate was used; a 1 L glass reactor and deionized water were used for all the experimentation, and the pulp was stirred at 1000 RPM with a four-blade propeller made of inert material; for cyanide leaching, a NaCN sodium cyanide salt was used, weighing the appropriate amount to have 2000 mg/L of free cyanide ion CN- in the solution, and for leaching with thiourea was used at a concentration of 0.2 M, without considering the use of oxidizing agent, during the first three hours of leaching aliquots of 20 ml were taken every 30 min, from the fourth hour and up to eight hours of reaction a sample was taken hourly. All samples were analyzed for their concentration of Au, Ag, and Cu in atomic absorption (AA).

Throughout the cyanidation and thioureation test, pH and oxidation reduction potential were monitored and converted to their standard hydrogen electrode (SHE) value as referred to above.

Results

Figure 1 presents the X-ray diffraction spectrum of the 200-mesh ore concentrated during flotation; the phases of the pyrite and arsenopyrite iron sulfides are

distinguished, for which it is established that it is a silver-bearing arsenopyrite and gold-bearing pyrite mineral.

During the conditioning for the flotation tests, the behavior of the pH and the oxide-reduction potential were monitored, referring the value measured to the equivalent of the hydrogen electro standard (SHE); Fig. 2 shows the results obtained, and it is observed that the addition of the mineral to the solution decreases the pH significantly, indicating the oxidation of the sulfides, later the pH increased with the addition of 0.1 M sodium hydroxide to have an appropriate value for flotation in around 6.5 as reported in the literature [13]. It was also observed that the pH tends to increase towards the end of the test.

Figure 3 shows the values of the potential Eh (mV) of the flotation pulp; this tends to be positive and indicates the strongly oxidizing nature of the mineral; this causes the oxidation of the surface of the metallic elements, leaving a surface rich in sulfur suitable for effect flotation due to the hydrophobic nature of the sulfide and deficient in metal. The potential values at the beginning of the float test are around 250 mV and decrease at the end of the flotation.

The results of the leaching tests are presented in Figs. 4 and 5 for the dissolution using cyanide at pH 11.1 and a potential of around -18 mV and thiourea at pH 1.5, and a potential of around + 528 mV, respectively; it is observed rapid kinetics of formation of metal complexes, in the case of cyanide the maximum extraction is reached in a time of around 120 min, subsequently no significant changes are observed in the leaching process. While for the TU-water system for silver and copper, the highest extraction is obtained in the first 30 min of the test, while the gold

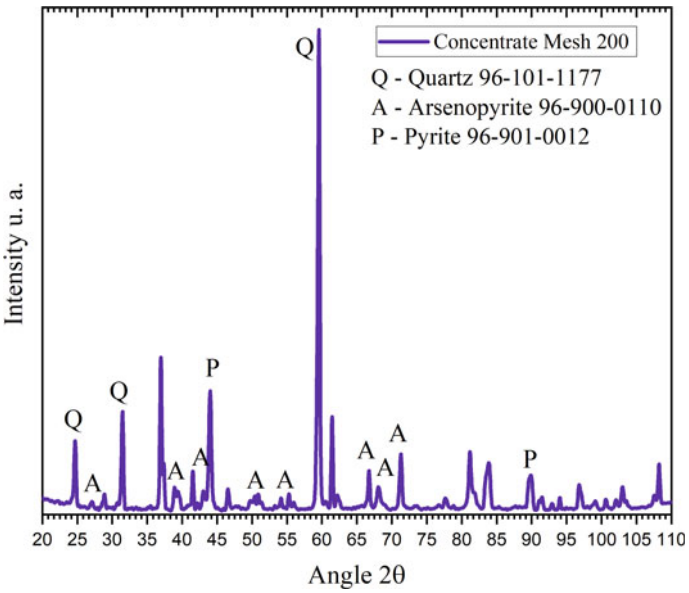

Fig. 1 X-ray diffraction spectrum (XRD) of ore concentrate mesh 200

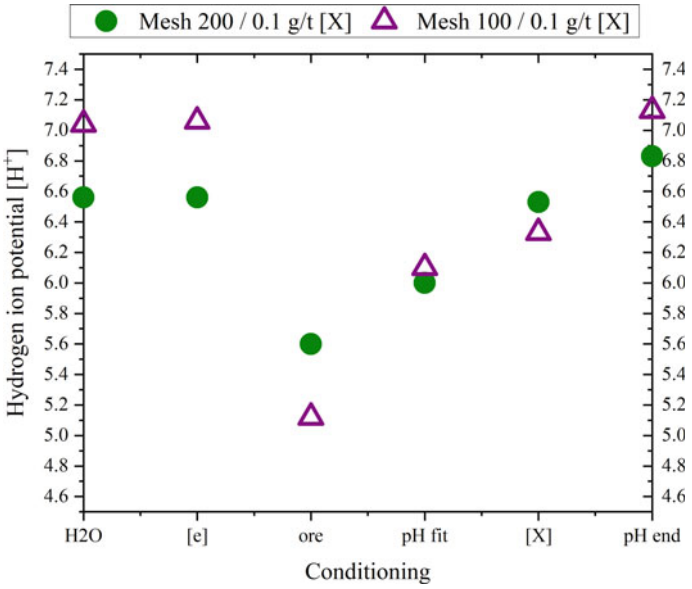

Fig. 2 Behavior of the pH during conditioning and at the end of the flotation test

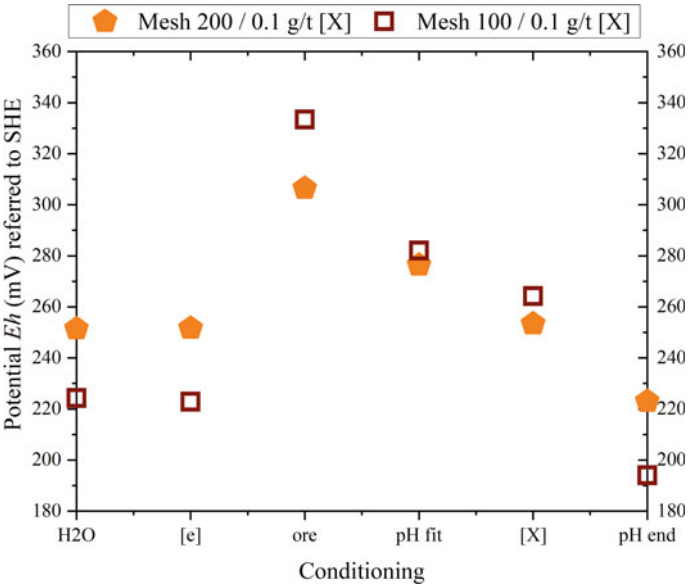

Fig. 3 Behavior of the pulp potential (mV), during conditioning and at the end of flotation

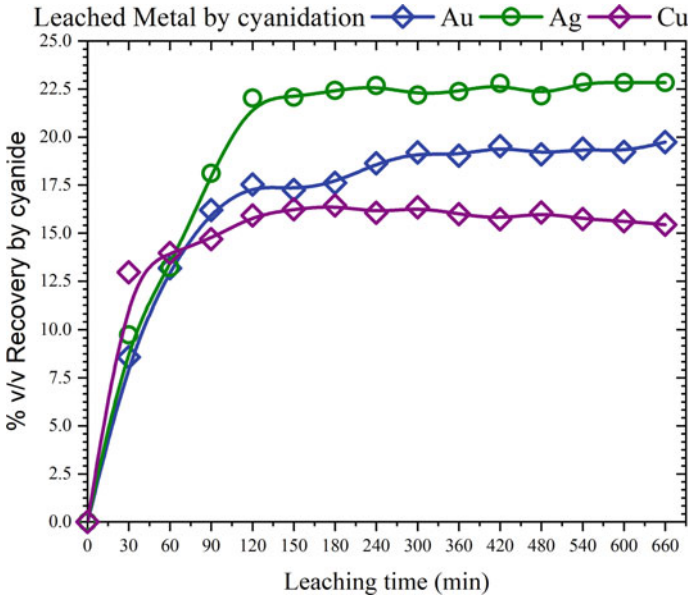

Fig. 4 Recovery curves of gold, silver, and copper % v/v versus the leaching time (min) for the cyanide-water system

dissolution increases gradually over time, thus at 660 min the maximum solution obtained was 14.3% v/v Au.

The expected reactions for the cyanidation of precious metals and copper in the cyanide system are reactions 1–3:

$$4Au + 8CN^- + O_2 + 2H_2O = 4\left[Au(CN)_2\right]^- + 4OH^- \quad (1)$$

$$4Ag + 8CN^- + O_2 + 2H_2O = 4\left[Ag(CN)_2\right]^- + 4OH^- \quad (2)$$

$$4Cu + 8CN^- + O_2 + 2H_2O = 4\left[Cu(CN)_2\right]^- + 4OH^- \quad (3)$$

The thioureation reactions of metals leached with thiourea are expected to be reactions (4), (5), and (6):

$$Au + 2SC(NH_2)_2 + 1/4O_2 + H^+ = Au\left[SC(NH_2)_2\right]_2^+ + 1/2H_2O \quad (4)$$

$$Ag + 2SC(NH_2)_2 + 1/4O_2 + H^+ = Ag\left[SC(NH_2)_2\right]_2^+ + 1/2H_2O \quad (5)$$

$$Cu + 2SC(NH_2)_2 + 1/4O_2 + H^+ = Cu\left[SC(NH_2)_2\right]_2^+ + 1/2H_2O \quad (6)$$

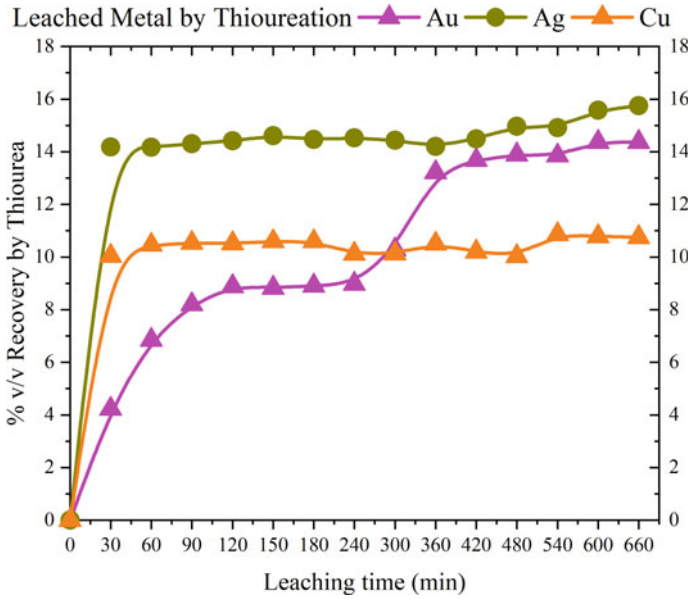

Fig. 5 Recovery curves for gold, silver, and copper % v/v versus leaching time (min) for the thiourea-water system

The results presented in Figs. 4 and 5 show a scarce leaching of metals, which indicates the complex mineralogical nature of this mineral, giving it properties to be considered as a refractory mineral; in the case of the system with thiourea, the use of an agent. The oxidant either ferric ion Fe^{3+} or hydrogen peroxide H_2O_2 could increase the leaching efficiency significantly.

Conclusions

The experimental results obtained in the flotation and leaching with free cyanide of 2000 mg/L at pH 11.6 and Eh −18 mV and with 0.2 M thiourea at pH 1.5 and Eh + 528 mV of an ore containing gold, silver, and copper show that the flotation is carried out efficiently, however during the leaching in both systems the percentage of dissolution for the three elements analyzed Au, Ag, and Cu does not exceed on average 23% of leaching; in the case of the TU, this efficiency can be increased. If an oxidizing agent is used, the results obtained indicate that there is a mineral that is refractory to cyanidation and thioureation due to its complex mineralogical nature, rich in arsenic and iron sulfides, Arsenopyrite FeAsS, and pyrite FeS_2. In future works, the use of an oxidizing agent will be proposed: TU oxidizing agent with the aim of increasing the dissolution efficiency.

Acknowledgements Thanks is given to the Autonomous University of the State of Hidalgo, the PRODEP Teacher Professional Development Program, and the National Polytechnic Institute ESIQUI.

References

1. La Brooy SR, Linge HG, Walker GS (1994) Review of gold extraction from ores. Miner Eng 7(10):1213–1241
2. Alp İ, Celep O, Paktunç D, Thibault Y (2014) Influence of potassium hydroxide pretreatment on the extraction of gold and silver from a refractory ore. Hydrometallurgy 146:64–71
3. Bustos H, Oyola LD, Rojas Y, Alcázar GAP, Balogh AG, Cabri LJ (2011) Quantification of refractory gold in grains of pyrite and arsenopyrite from the "El Diamante" gold mine in Nariño-Colombia. Tumbaga 1(6):153–164
4. Alp İ, Celep O, Deveci H (2010) Alkaline sulfide pretreatment of an antimonial refractory Au-Ag ore for improved cyanidation. JOM 62(11):41–44
5. Celep O, Alp İ, Deveci H (2011) Improved gold and silver extraction from a refractory antimony ore by pretreatment with alkaline sulphide leach. Hydrometallurgy 105(3–4):234–239
6. Celep O, Alp İ, Paktunç D, Thibault Y (2011) Implementation of sodium hydroxide pretreatment for refractory antimonial gold and silver ores. Hydrometallurgy 108(1–2):109–114
7. Li L, Zhu Z, Liu Y, Lin Q, Li Z, Fu J (2014) Optimisation of efficient auxiliary agents of gold leaching in an alkaline thiourea solution for a finely disseminated gold ore. Int J Min Mineral Eng 5(4):315–327
8. Ubaldini S, Fornari P, Massidda R, Abbruzzese C (1998) An innovative thiourea gold leaching process. Hydrometallurgy 48(1):113–124
9. Zheng S, Wang YY, Chai LY (2006) Research status and prospect of gold leaching in alkaline thiourea solution. Miner Eng 19(13):1301–1306
10. Li J, Miller JD (2006) A review of gold leaching in acid thiourea solutions. Miner Process Extr Metall Rev 27(3):177–214
11. Schulze RG (1984) New aspects in thiourea leaching of precious metals. JOM 36(6):62–65
12. Hayes RA, Ralston J (1988) The collectorless flotation and separation of sulphide minerals by Eh control. Int J Miner Process 23(1):55–84
13. Bulatovic SM (2007) Handbook of flotation reagents: chemistry, theory, and practice: volume 1: flotation of sulfide ores. Elsevier

Characterization of Microstructure Changes of Pyrolytic CCCP and Their Effect on Carbon Reactivity by Industrial CT, Mercury Intrusion Porosimetry, and SEM

Xiaomin You, Xuefeng She, Jingsong Wang, and Qingguo Xue

Abstract The microstructure changes of pyrolytic CaO-containing carbon pellets (CCCP) directly determine their ability to produce calcium carbide (CaC_2) in an electric arc furnace. Therefore, the microstructure changes, especially the pore structure changes of CCCP at different pyrolysis temperatures were characterized by industrial CT, mercury intrusion porosimetry (MIP), and SEM from different scales. The reactivity of carbon in pyrolytic CCCP was tested. The relationship between pore structure change and carbon reactivity was established. The results showed that industrial CT could show the overall pore distribution of CCCP in a three-dimensional way; MIP was more accurate for the statistics of the proportion of pores with different pore diameters, and SEM was more intuitive for the local microstructure analysis of CCCP. As temperature increased from 450 to 750 °C, the porosity and average pore diameter of CCCP increased, and decreased over 750 °C. Meanwhile, the reactivity of carbon in CCCP pyrolyzed at 850 °C was the highest.

Keywords CaO-containing carbon pellets · Industrial CT · Mercury intrusion porosimetry · Coal macromolecular · Carbon reactivity

Introduction

China is the largest producer and consumer of calcium carbide (CaC_2). The annual production of CaC_2 in China increased in the past decade to approximately 42 million tons in 2018. Currently, the electrothermal CaC_2 manufacturing process is used in China as the primary process to produce acetylene [1]. The electrothermal CaC_2 manufacturing process is characterized by poor kinetic conditions because of the limited contact area between bulky CaO and char, resulting in a higher reaction

X. You · X. She (✉) · J. Wang (✉) · Q. Xue
State Key Laboratory of Advanced Metallurgy, University of Science and Technology Beijing, Beijing 100083, China
e-mail: shexuefeng@ustb.edu.cn

J. Wang
e-mail: wangjingsong@ustb.edu.cn

M. Zhang et al. (eds.), *Characterization of Minerals, Metals, and Materials 2023*, The Minerals, Metals & Materials Series
https://doi.org/10.1007/978-3-031-22576-5_29

temperature (2000–2200 °C) and high energy consumption (approximately 3000–3500 kW·h/t to obtain 80% CaC_2 yield) [2–6]. The use of new raw materials and processes will be essential for CaC_2 production, considering processes that require lower energy consumption and material efficiency during this process.

The complete contact of the two materials will improve the mass transfer rate of CaO and reduce reaction temperature. Several studies have addressed CaC_2 formation from pellets obtained through well-mixed powder feeds [7–10]. Yin et al. [11–13] proposed a new process of CaC_2 production which included a two-step process. Firstly, the CaO-containing carbon pellets (CCCP) by using mixed lime powder and coal powder were pyrolyzed in a pyrolysis furnace. Then the CCCP was placed in the arc furnace for the production of CaC_2. High compressive strength and high activity are both required properties of pyrolysis CCCP [14]. On the one hand, as mentioned before, both electrothermal and oxy-thermal processes have happened in large moving beds, which require the block material to have a certain cold and thermal strength, especially in the soft melt zone [15]. This is because only the high thermal strength can guarantee the CO permeability and the smooth operation of the moving bed. In the pyrolysis of coking coal, many plastic masses are produced to form high-strength metallurgical coke in the cooling process, ensuring sufficient cold and thermal strength. On the other hand, the production efficiency of CaC_2 also depends on the activity of CCCP. The reactivity of CCCP mainly depends on the oxidation activity, calcium-carbon interface, CO diffusion channel, and carbon reactivity in CCCP after pyrolysis. However, only a few pieces of literature have been found regarding the effect of macromolecular structures on CCCP carbon reactivity, which plays a key role in the reaction of calcium coal pyrolysis pellets to produce CaC_2 in an electric arc furnace. Therefore, it is necessary to study the carbon reactivity of pyrolytic pellets. Previous research is generally focused on the gasification reactivity of chars of coal, petcoke, and biomass, whereas rarely for CCCP [16, 17]. However, it is undeniable that the reactivity of carbon in CCCP, especially the gasification characteristics, is the main method to evaluate the carbon reactivity of pyrolysis pellets.

Industrial CT is the abbreviation of industrial computer tomography technology [18, 19]. It can clearly, accurately, and intuitively display the internal structure, composition, material, and defect status of the tested object in the form of two-dimensional tomographic images or three-dimensional images without damage to the tested object [20]. It is known as the best nondestructive testing and nondestructive evaluation technology today. Mercury intrusion porosimetry (MIP) is also called the mercury porosity method. It is a method to measure the pore size distribution of some mesopores and macropores [14, 21, 22]. Scanning electron microscope (SEM) is an observation method between transmission electron microscope and optical microscope [23]. It uses a narrow focused high-energy electron beam to scan the sample, excites various physical information through the interaction between the beam and the substance, collects, amplifies, and reimages this information to achieve the purpose of characterizing the microscopic morphology of the substance [14, 15, 24].

Table 1 Results of proximate and elemental analysis of coking coal wt%

	Proximate analysis				Ultimate analysis				
Coking coal	M_{ad}	A_d	V_d	FC_d	C_d	H_d	O_{diff}	N_d	S_d
	0.74	12.01	21.93	66.06	78.35	4.51	3.15	1.29	0.69

Note ad air dry basis, *d* dry basis, *diff* difference, *FC* fix carbon, *A* ash, *V* volatile matter, *M* moisture

Table 2 Chemical composition of ash from coking coal wt%

Material	CaO	SiO_2	Al_2O_3	TiO_2	Fe_2O_3	P_2O_5	Other
Ash	1.01	51.4	38.6	1.23	2.81	0.69	4.26

In this study, CaO-containing carbon pellets (CCCP) prepared from well-mixed coking coal (CC) and calcium oxide (CaO) were pyrolyzed at different pyrolysis temperatures (450–850 °C). The carbon reactivity (gasification characteristics) difference of CCCP pyrolysis at different temperatures was analyzed. Industrial CT, MIP, and SEM were adopted to characterized the microstructure changes of CCCP, especially the changes of pore structure. The relationship between the gasification parameter and porosity was established.

Sample Preparation and Experiments

Materials

Analytical grade CaO (AR, > 99.0%) and CC were collected from a Chinese steel plant. They were further dried at 80 °C for 6 h under vacuum and placed in sealed bags. The chemical composition of the CC is presented in Table 1. The ash obtained from coal oxidation was characterized by X-ray fluorescence (AXIOS, Holland), as shown in Table 2.

CCCP Preparation and CCCP Pyrolysis

The coking coal powder (80 μm) was homogeneously mixed with the CaO powder (80 μm) at a C/Ca molar ratio of 3.2:1. The mixtures were placed in a stainless-steel mold and pressed uniaxially using an embedding sample machine (XQ-5, China) under a pressure of 15 MPa for 5 min. Thus, 2.5 gof the CCCP sample with a diameter of 15 mm was prepared.

As shown in Fig. 1, a rapid heating tube furnace with controllable cooling speed was used for CCCP pyrolysis. The tube of the furnace is a rigid jade tube with a diameter of 42 cm, and the thermostatic region is effective in 10 cm. Before conducting the experiments, the temperature was increased to the target temperature (450, 550, 650, 750, or 850 °C) at a rate of 10 °C/min. The CCCP samples were placed in a corundum crucible. Following this, the corundum crucible was placed in a constant temperature zone of the furnace and maintained in an Ar atmosphere for 30 min. After roasting, the sample was cooled to 100 °C at a rate of 22 °C/min and kept at that temperature for 5 min under an Ar atmosphere. The pellets were removed from the furnace at 20 °C. The CCCP can be divided into five categories based on the different pyrolysis temperature (450, 550, 650, 750, and 850 °C). The results of the proximate analysis of the pyrolytic CCCP are shown in Table 3 (Fig. 1).

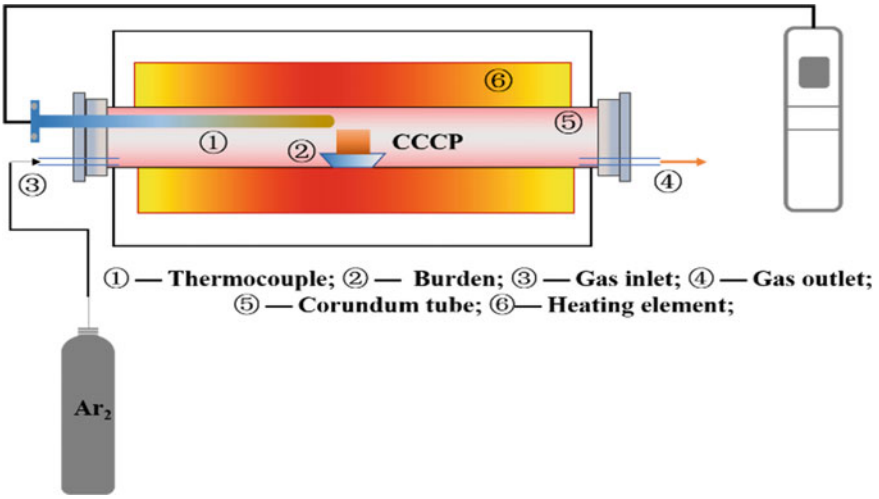

Fig. 1 Schematic diagram of the CCCP pyrolysis preheating device

Table 3 Results of the proximate analysis of CCCP at different pyrolysis temperatures

Sample	Proximate analysis (ad)/wt%			
	M_{ad}	A_{ad}	V_{ad}	FC_{ad}
450 °C-CCCP	0.33	40.39	18.02	28.79
550 °C-CCCP	0.17	36.35	14.97	28.94
650 °C-CCCP	0.05	36.01	14.84	26.9
750 °C-CCCP	0.05	35.83	12.01	27.09
850 °C-CCCP	0.02	36.84	10.02	28.47

Note: *ad* air dry basis, *FC* fix carbon, *A* ash, *V* volatile matter, *M* moisture

CCCP Gasification Experiment

The gasification experiments of pyrolysis CCCP were performed on a thermal gravimetric analyzer (NETZSCH STA 449 F3, Germany). In the gasification experiments, the samples of CCCP were heated from room temperature to 1000 °C at a constant speed (25 °C/min) with 40 mL/min Ar as protective gas and purge gas, and then held at the constant temperature for 30 min. Then, the sample was gasified with 100% CO_2 (>99.9%) gas with a flow rate of 50 mL/min.

Characterization Experiments of CCCP

Three primary test methods were used to evaluate and compare the gasification reactivity. The scanning electronic microscope (SEM) analysis (Hitachi S-4800, Japan) was used to acquire the local micromorphology of CCCP. The pore structural parameters and pore structure properties of the CCCP were calculated by mercury intrusion porosimetry (Autopore IV9773, Micromeritics, USA). In addition, the three-dimensional hole structure distribution was detected by industrial CT (ZEISS Xradia520, Germany).

Results and Discussion

CCCP-CO_2 Gasification Analysis at Different Pyrolysis Temperatures

In order to investigate the carbon reactivity of CCCP after pyrolysis at different temperatures, CO_2 isothermal gasification experiment was carried out at 1050 °C for CCCP after pyrolysis. According to the weight loss during gasification, the gasification conversion curves of different pellets are obtained, as shown in Fig. 2.

As seen in Fig. 2, compared with CCCP at other pyrolysis temperatures, the gasification process of which kept for 150 min, the gasification time of 850 °C-CCCP had shrunk to 40 min, which indicated that after pyrolysis at 850 °C, the carbon reactivity of CCCP is highest. According to the industrial analysis results (see Table 3) of CCCP after pyrolysis, the residual volatile content of CCCP after pyrolysis at 850 °C is the lowest, and the pyrolysis of 850 °C-CCCP is the most complete.

In order to better compare the gasification capabilities of the five different CCCP, we obtained the time ($t_{0.5}$) required for different CCCP when the gasification rate reached 50% according to Fig. 2, and further obtained the parameter R_S by calculating formula (1) [25]:

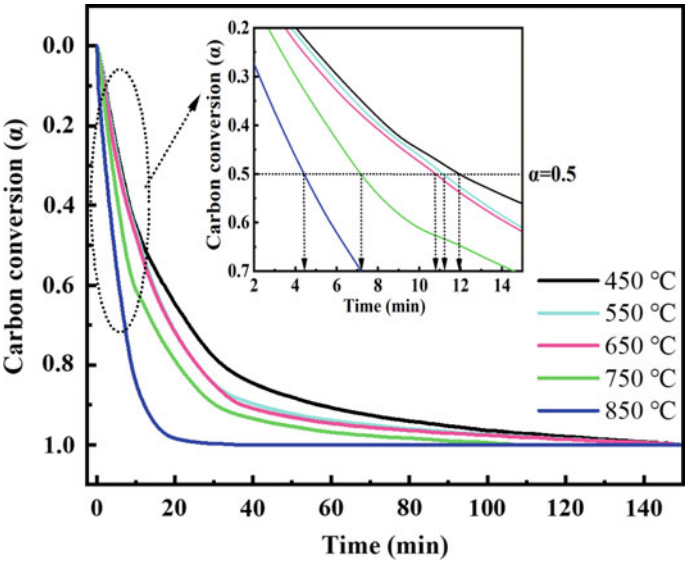

Fig. 2 Conversion of 450–850 °C pyrolysis CCCP in the CO_2 gasification process at 1050 °C

$$R_S = 0.5/t_{0.5}(h) \tag{1}$$

In general, the larger the R_S value, the stronger the gasification ability of the sample [26–28]. According to Table 4, it is obvious that with the increase of pellet pyrolysis temperature, the gasification time ($t_{0.5}$) of pyrolytic CCCP gradually shortened, meanwhile, the gasification parameter R_S gradually increased. It is noticeable that the gasification time ($t_{0.5}$) of 750-850-CCCP was significantly lower than 450-650-CCCP. These results show that the higher the pyrolysis temperature, the stronger the gasification ability (carbon reactivity) of the pellets after pyrolysis.

Table 4 Results of the proximate analysis of CCCP at different pyrolysis temperatures

Sample	$t_{0.5(min)}$	R_s
450 °C-CCCP	11.925	2.516
550 °C-CCCP	11.175	2.685
650 °C-CCCP	10.800	2.778
750 °C-CCCP	7.125	4.211
850 °C-CCCP	4.425	6.780

The Macromolecular Structure Variation of CCCP at Different Pyrolysis Temperatures

In order to analyze the microstructure changes of CCCP more clearly and comprehensively during pyrolysis, we carried out industrial CT, SEM, and mercury intrusion analysis on the pellets after pyrolysis at different temperatures.

Industrial CT Analysis of CCCP After Pyrolysis

Industrial CT was chosen to evaluate the overall morphology and pore distribution of pyrolysis CCCP. As shown in Fig. 3, in the early stage of pyrolysis (450–550 °C), the amount of gas released is small, so the pore volume and size of the pellets are small. When the temperature reached 650 °C, large pores began to appear, and with the further increase of temperature (750 and 850 °C), large pores further increased. It was obvious that industrial CT could show the overall pore distribution of CCCP in a three-dimensional way. Industrial CT images could help us to have a more intuitive understanding of the three-dimensional morphology of holes (Fig. 3).

Interestingly, some cracks began to appear in the pellet at 550 °C-CCCP, which may be related to the rapid degassing process during the decomposition of part of calcium hydroxide and the formation of colloid in the early stage of pyrolysis. When the pyrolysis temperature reached 850 °C, a large number of deep pores and collapsed structures appear in the pellets, which may be related to the catalytic effect of calcium

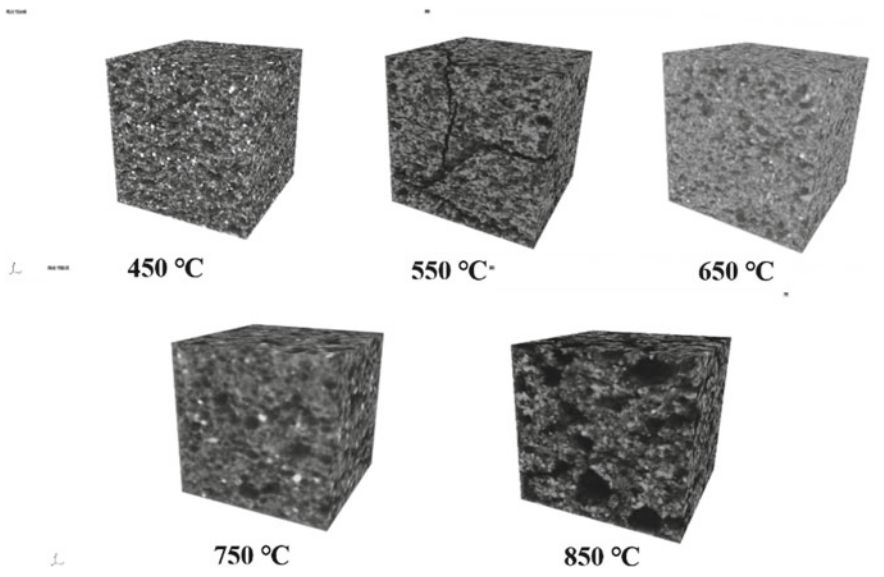

Fig. 3 Industrial CT analysis of pyrolysis CCCP at different temperatures

oxide on the pyrolysis of coal at the later stage of pyrolysis, resulting in the carbon loss caused by the intensification of pyrolysis.

SEM Analysis of CCCP After Pyrolysis

SEM pictures were chosen to evaluate the local microstructure change of CCCP pyrolysis at different temperatures. At 450 °C, because it is in the early stage of pyrolysis, the pore size is small. When the temperature reached 550 °C, large pores began to appear. When the temperature reached 650 °C, the number of macropores further increased, and the interconnected pore structure began to appear. It is obvious that SEM was more intuitive for the local microstructure analysis of CCCP. The binding state of CaO and carbon can be clearly observed at the microscopic level (Fig. 4).

When the temperature reached 750 °C, with the intensification of pyrolysis, the proportion of macropores would further increase. Due to the further progress of polycondensation reaction and the further increase of pore structure, the proportion of pore size would further increase. When the temperature reached 850 °C, the polycondensation process of semi-coke into coke was further enhanced, and the polycondensation degree of coal coke was further increased, resulting in a decrease in the proportion of large pores in the pellet as a whole, and cracks began to appear in some places.

Mercury Injection Analysis of CCCP

In order to study the overall porosity and pore size distribution of pellets, the mercury intrusion method was adopted. At 450 °C, the pore size was mainly concentrated in the range 100–10,000 nm. When the temperature reached 550 °C, except that the proportion of small holes (100–10,000 nm) was further increased, 10,000–100,000 nm pores began to appear. When the temperature increased to 650 °C, the proportion of large pores (10,000–100,000 nm) further increased, while the proportion of small pores decreased. When the temperature was increased to 750 °C, the proportion of pores over 100000 nm increased. At 850 °C, the proportion of macropores decreased. This may be related to the shrinkage process in the process of semi-coke polycondensation (Fig. 5).

As shown in Fig. 5f, with the increase of temperature from 450 to 750 °C, the porosity of pyrolysis CCCP gradually increased. This is because with the increase of temperature, the pyrolysis process did not intensify much, and the amount of gas produced increases constantly, resulting in the increasing porosity. However, when the temperature reached 850 °C, the porosity of pellets decreased slightly. It is very surprising that the average pore size of 500 °C-CCCP was the largest in the pellets. This may be related to the abnormal cracks generated in the 500 °C pellets, and this result has been confirmed by industrial CT data. Besides the abnormal data at 500 °C,

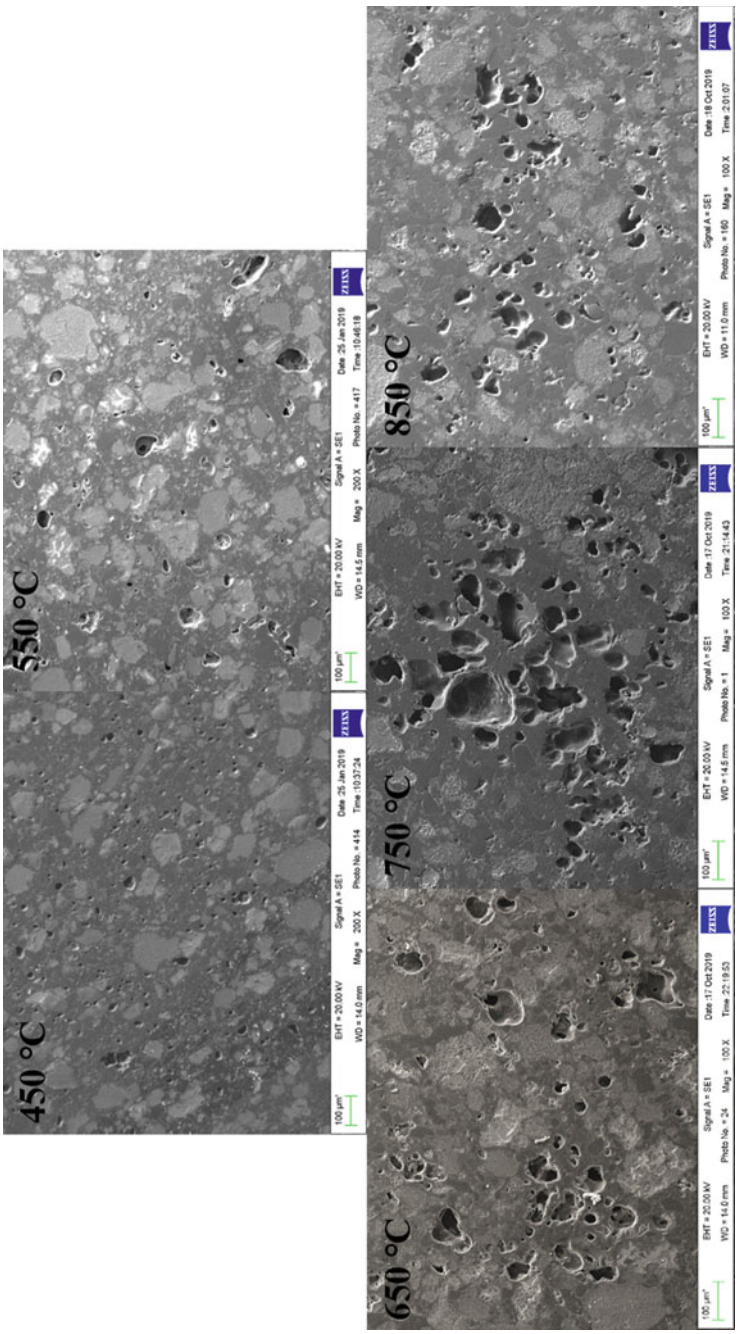

Fig. 4 SEM analysis of pyrolysis CCCP at different temperatures

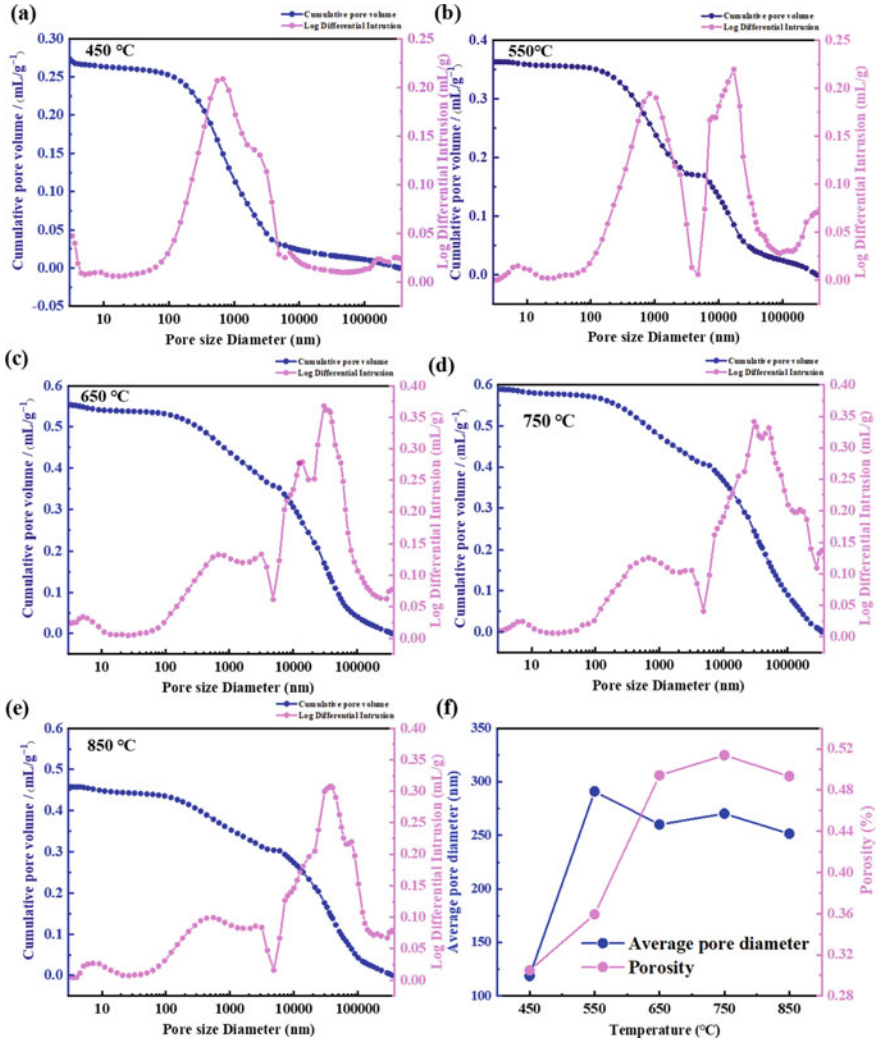

Fig. 5 Mercury injection analysis of CCCP at different temperatures

the average pore size of CCCP at other temperatures was consistent with the change law of porosity.

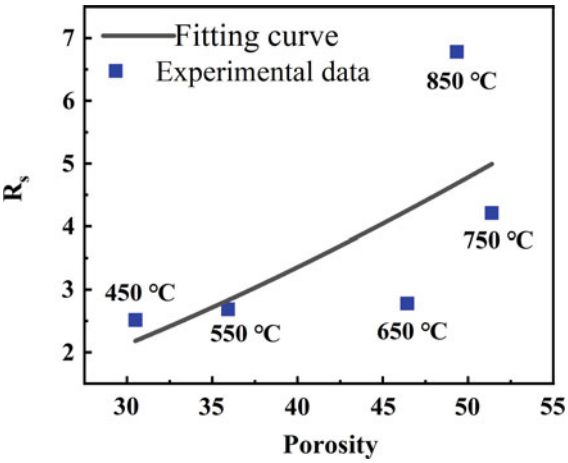

Fig. 6 Relationship between R_s and porosity

Relationship Between Macromolecular Structure and Carbon Reactive

Based on the above gasification data and microstructure change results, we try to explore the direct relationship between the gasification characteristics of CCCP and the pore structure (Fig. 6).

As shown in Fig. 6, as the temperature increased from 450 to 750 °C, the porosity of CCCP gradually increased, and the gasification parameter R_S also gradually increased. Moreover, the gasification parameter R_S showed a positive correlation function relationship with the porosity during the temperature range of 450–750 °C. This may be because the gasification reaction is a gas–solid reaction, and more porosity will be more conducive to the diffusion and reaction of CO to carbon in CCCP. This result was also consistent with that of other researchers [18, 29].

Although the porosity of 850 °C-CCCP was not the highest, the R_S value of CCCP at 850 °C was significantly higher than that at other temperatures. This may be related to the change of the carbon structure at 850 °C and the increase of the disorder degree of the carbon structure caused by the destruction of the carbon structure by CaO at this pyrolysis temperature. Previous studies have also found similar experimental phenomena [30]. This further indicated that the influence of porosity on the gasification ability of carbon was different at different temperature stages.

We further summarized as follows: in the range of 450–750 °C, the higher the porosity of pellets, the stronger the gasification capacity of pyrolysis CCCP.

Conclusions

To investigate the effect of pyrolysis temperature on the carbon reactivity of CCCP, we studied the microstructure of CCCP pyrolysis at different temperatures, especially the pore structure, and established the relationship between gasification characteristic parameters (R_S) and porosity. Industrial CT, SEM, and MIP were used to comprehensively analyze the microstructure of pyrolytic CCCP. The following conclusions are obtained:

1. The gasification parameters (R_S) of pyrolysis CCCP increased with the increase of temperature during the 450–850 °C range.
2. Industrial CT could show the overall pore distribution of CCCP in a three-dimensional way, MIP was more accurate for the statistics of the proportion of pores with different pore diameters, and SEM was more intuitive for the local microstructure analysis of CCCP.
3. At 450 °C, the pore size was mainly concentrated in the range 100–10,000 nm. When the temperature reached 550 °C, 10,000–100,000 nm pores began to appear. When the temperature increased to 650 °C, the proportion of large pores (10,000–100,000 nm) further increased, while the proportion of small pores decreased. When the temperature was increased to 750 °C, the proportion of pores over 100000 nm increased. At 850 °C, the proportion of macropores decreased.
4. As the temperature increases from 450 to 750 °C, the porosity of CCCP increased from what to what, and when the temperature reached 850 °C, the porosity of CCCP decreased due to the intensification of polycondensation reaction.
5. The gasification parameter (R_S) of pyrolysis CCCP was positively correlated with the porosity from 450 to 750 °C.

Acknowledgements This work was financially supported by the National Key R&D Program of China (No.2018YFB0605900).

References

1. Mi Y, Zheng DX, Guo J, Chen XH, Jin P (2014) Assessment of energy use and carbon footprint for low-rank coal-based oxygen-thermal and electro-thermal calcium carbide manufacturing processes. Fuel Process Technol 119:305
2. Xin CF, Qian XR (1994) Reviews on technical routes for chemicals production from carbide acetylene. Prog Chem 6(1):62
3. Li GD, Liu QY, Liu ZY (2013) Kinetic behaviors of CaC_2 production from coke and CaO. Ind Eng Chem Res 52(16):5587
4. Mu JJ, Hard RA (1987) A rotary kiln process for making calcium carbide. Ind Eng Chem Res 26(10):2063
5. Zhang JQ, Wang ZS, Li T, Wang Z, Zhang S, Zhong M, Liu YE, Gong XZ (2019) Preparation of CaO-containing carbon pellet from recycling of carbide slag: Effects of temperature and H_3PO_4. Waste Manage 84:64

6. Xie KC, Li WY, Zhao W (2010) Coal chemical industry and its sustainable development in China. Energy 35(11):4349–4355
7. Zhang S, Gong XZ, Wang Z, Cao JW, Guo ZC (2014) Preparation of block CaO from carbide slag and its compressive strength improved by H_3PO_4. Int J Miner Process 129:6–11
8. Wang RX, Liu ZY, Ji LM, Guo XJ, Lin X, Wu JF, Liu QY (2016) Reaction kinetics of CaC_2 formation from powder and compressed feeds. Front Chem Sci Eng 10(4):517
9. Li ZK, Liu ZY, Wang RX, Guo XJ, Liu QY (2018) Conversion of bio-char to CaC_2 at low temperatures-morphology and kinetics. Chem Eng Sci 192:516–525
10. Xu Q, Li YS, Deng SP, He YL, Li L, Yu HJ (2019) Modeling of multiprocess behavior for feedstock-mixed porous pellet: Heat and mass transfer, chemical reaction, and phase change. ACS Sustain Chem Eng 7(14):12510
11. Yin SW, Wang HY, Wang L, Liu CP, Tong LG (2021) Influencing factors and evaluation system for carbon-calcium pellet performance in a pyrolysis furnace. Energy 214:118991
12. You XM, She XF, Wang JS, Xue QG, Jiang ZY (2021) Preparation of CaO-containing carbon pellets from coking coal and calcium oxide: Effects of temperature, pore distribution and carbon structure on compressive strength in pyrolysis furnace. Int J Miner Metall Mater 28(7):1153–1163
13. You XM, She XF, Wang JS, Xue QG (2022) Coking coal macromolecular structural characteristic and its correlations with the compressive strength of CaO-containing carbon pellets. In: Zhang et al (eds) Characterization of minerals, metals, and materials 2022. The minerals, metals & materials series. Springer, Cham. https://doi.org/10.1007/978-3-030-92373-0_17
14. Gong XZ, Zhang JQ, Wang Z, Wang D, Liu JH, Jing XD, Qian GY, Wang C (2021) Development of calcium coke for CaC_2 production using calcium carbide slag and coking coal. Int J Miner Metall Mater 28(1):76–87
15. Gong X, Zhang T, Zhang J, Wang Z, Liu J, Cao J, Wang C (2022) Recycling and utilization of calcium carbide slag-current status and new opportunities. Renew Sust Energ Rev. 159:112133
16. Sun J, Xing X, He Y, Wang Y, Chen J, Zhu Y (2021) Experimental study on high temperature gasification and melting characteristics of the pyrolysis residue from petrochemical sludge. Fuel 296:120680
17. Pan P, Peng W, Li J, Chen H, Xu G, Liu T (2022) Design and evaluation of a conceptual waste-to-energy approach integrating plasma waste gasification with coal-fired power generation. Energy 238:121947
18. Zhang W, He Y, Wang Y, Li G, Chen J, Zhu Y (2022) Comprehensive investigation on the gasification reactivity of pyrolysis residue derived from ca-rich petrochemical sludge: roles of microstructure characteristics and calcium evolution. Energy Convers Manage 253:115150
19. Hadwiger M, Laura F, Rezk-Salama C, Hollt T, Geier G, Pabel T (2008) Interactive volume exploration for feature detection and quantification in industrial ct data. IEEE Trans Vis Comput Graph 14(6):1507–1514
20. Jia L, Chen M, Sun L, Sun Z, Zhang W, Zhu Q (2013) Experimental study on propagation of hydraulic fracture in volcanic rocks using industrial CT technology. Pet Explor Dev 40(3):405–408
21. Pittman ED (1992) Relationship of porosity and permeability to various parameters derived from mercury injection capillary pressure curves for sandstones. AAPG Bull 76(2):2
22. Schmitt M, Fernandes CP, Neto JC, Wolf FG, Santos VD (2013) Characterization of pore systems in seal rocks using nitrogen gas adsorption combined with mercury injection capillary pressure techniques. Mar Pet Geol 39(1):138–149
23. Song TF, Zhang JL, Wang GW, Wang HY, Xu RS, Pang QH (2018) Influence mechanism of lignite and lignite semi-coke addition on drum strength of coke. ISIJ Int 58(2):253–258
24. Zhao J, Zuo HB, Wang GW, Wang JS, Xue QG (2020) Improving the coke property through adding HPC extracted from the mixture of low-rank coal and biomass. Energy Fuels 34(2):1802–1810
25. Li S, Song H, Hu J, Yang H, Zou J, Zhu Y (2021) CO_2 gasification of straw biomass and its correlation with the feedstock characteristics. Fuel 297:120780

26. Wei R, Ren L, Geng F (2021) Gasification reactivity and characteristics of coal chars and petcokes. J Energy Inst 96:25–30
27. Wang G, Zhang J, Hou X, Shao J, Geng W (2015) Study on CO2 gasification properties and kinetics of biomass chars and anthracite char. Bioresource Technol 177:66–73
28. Liu M, He Q, Bai J, Yu J, Kong L, Bai Z (2021) Char reactivity and kinetics based on the dynamic char structure during gasification by CO_2. Fuel Process Technol 211:106583
29. Sun P, Grace JR, Lim CJ, Anthony EJ (2008) A discrete pore size distribution based gas solid model and its application to the CaO+CO_2 reaction. Chem Eng Sci 63:57–70
30. Chen M, Wang N, Yu J, Yamaguchi A (2007) Effect of porosity on carbonation and hydration resistance of CaO materials. J Eur Ceram Soc 27(4):1953

Characterization of the Dissolution of Gold and Silver Contained in a High-Grade Mineral Concentrate Using Thiourea

Martín Reyes Pérez, Arleth Martínez Escamilla, David Ponce Vergara, Iván. A. Reyes Domínguez, Mizraim U. Flores Guerrero, Elia Palacios Beas, Julio Cesar Juárez Tapia, Miguel Pérez Labra, and Francisco Raúl Barrientos Hernández

Abstract For several decades, attempts have been made to replace cyanide with the reagent thiourea (TU) to reduce the impact on the environment; however, cyanide continues to be the reagent most used industrially, and this is partly due to the higher consumption of TU during leaching. Nevertheless, the use of thiourea could be justified for the leaching of gold and silver from high-grade ores. In this work, a mineral concentrate of gold and silver was characterized by XRD as well as the leaching solutions in their concentration of gold, and silver, by means of atomic absorption spectrometry. The results of leaching in a system only with TU with 0.2, 0.3, and 0.4 M show a higher percentage of Au and Ag leaching at a lower concentration of TU (0.2 M). In just 15 min of leaching, 88 and 59% of gold and silver dissolution are obtained, respectively.

Keywords Thiourea · Gold · Silver · Leaching · Activation

M. R. Pérez (✉) · A. M. Escamilla · D. P. Vergara · J. C. J. Tapia · M. P. Labra · F. R. B. Hernández
Academic Area of Earth Sciences and Materials, Autonomous University of the State of Hidalgo, Road Pachuca-Tulancingo Kilometer 4.5 Mineral de La Reforma, Hidalgo 42180, México
e-mail: mreyes@uaeh.edu.mx

Iván. A. Reyes Domínguez
Institute of Metallurgy, Autonomous University of San Luis Potosí, SLP, San Luis Potosí 78210, México

M. U. F. Guerrero
Industrial Electromechanics Area, Technological University of Tulancingo, 43642 Hidalgo, México

E. P. Beas
National Polytechnic Institute Unit ESIQIE. C.P. 07738, México, D.F, México

M. Zhang et al. (eds.), *Characterization of Minerals, Metals, and Materials 2023*, The Minerals, Metals & Materials Series
https://doi.org/10.1007/978-3-031-22576-5_30

Introduction

The application of thiourea (TU) to leach metals such as gold and silver was established several decades ago [1]; research is currently continuing in search of improvements that can compete with cyanide leaching and be able to replace it; TU is considered an agent non-toxic solution. A green reagent for the gold and silver recovery process [2]. Generally, a common problem in gold and silver beneficiation processes is the presence of valuable species encapsulated in a quartz mineral matrix or minerals considered refractory, that is, difficult to leach with conventional techniques [3, 4].

It has been reported in the literature that the term refractory gold and silver minerals are those that are leached in cyanide solution in proportions less than 50% [5], taking into consideration that the global demand for gold leads mining companies to overexploit mineral deposits containing gold, as well as to process minerals with increasingly complex mineralogy and difficult to leach [4, 6].

Thiourea is a leaching agent that forms stable aqueous species with gold or silver, and many other metal ions, with respect to gold ion thermodynamic stability data for the stable aqueous species $Au[SC(NH_2)_2]\,2+$ is 22.1 which establishes that thiourea is a strong complexing agent with thiourea named gold bisthiourea [7].

In acid solution, thiourea oxidizes and forms formamidine disulfide ($NH_2(NH)CSSC(NH)(NH_2)$); this, in the presence of oxygen, ferric ion, or hydrogen peroxide gold and silver can dissolve rapidly forming complex stable aqueous solutions of gold thiourea or silver thiourea as illustrated by reaction 1 [8].

$$Au + 2SC(NH_2)_2 + 1/4O_2 + H^+ = Au\left[SC(NH_2)_2\right]_2^+ + 1/2H_2O \qquad (1)$$

Previous studies have evaluated the feasibility of leaching gold (4 g/t) with thiourea, obtaining around 80% recovery with a TU consumption of 5 g/kg, 5 g/kg sulfuric acid, and 0.5 g/kg of ferric sulfate [9]. The objective of the current research work is to carry out the flotation and leaching of a high-grade gold mineral concentrate; the concentration was carried out in the presence of potassium amyl xanthate at a pH between 7.2 and 7.5, while the leaching of the flotation concentrate was carried out at pH 1.5 and using various concentrations of TU without using an oxidant.

Experimental Methodology

A mineral from the state of Guadalajara, Jalisco, Mexico, was used. The ore was received in sizes of about 2 inches in section, and the complete sample was crushed, pulverized, and wet-sieved until 500 g of each of the meshes was obtained: 200 (75 μm) and 100 (180 μm). The 200-mesh ore was analyzed by X-ray diffraction technique, using an Equinox 3000 diffractometer with a cobalt X-ray tube.

For the flotation tests, the sieved and homogenized ore was used to carry out the concentration tests, using a Denver flotation machine in a 1L cell equipped with an

Table 1 Chemical characterization of the mineral, gold concentration

Gold Concentration (g/t)						
Mesh; concentration of xanthate	Feed weight of ore used (g)	g/t Au	Concentrate weight of ore obtained (g)	g/t Au	Ore weight in tailings (g)	g/t Au
200; 0.08 g/t [X]	250	0.6	11	6.57	239	0.17
200; 0.16 g/t [X]	250	0.6	19	3.29	231	0.13
100; 0.08 g/t [X]	250	0.57	70	2.27	180	0.24

Table 2 Chemical characterization of the mineral, silver concentration

Silver Concentration (g/t)						
Mesh; concentration of xanthate	Feed weight of ore used (g)	g/t Ag	Concentrate weight of ore obtained (g)	g/t Ag	Ore weight in tailings (g)	g/t Ag
200; 0.08 g/t [X]	250	230	11	502	239	23
200; 0.16 g/t [X]	250	230	19	429	231	44
100; 0.08 g/t [X]	250	216	70	371	180	42

impeller and diffuser. For flotation, 250 g of ore, either 200 mesh or 100 mesh, 1 L of deionized water, 0.06 g/t of foaming propylene glycol [e], and 0.08 g/t of xanthate [X] were used, in addition, independent carried out a test using the 200-mesh containing 0.16 g/t of potassium amyl xanthate and [e] of 0.06 g/t. The concentrate of the flotation test was collected for a time of 5 min, and the chemical characterization of the concentrated product, the feed, and tails was carried out by digestion with aqua regia and analyzed in triplicate by AA atomic absorption spectrometry; the analyses obtained are presented in Tables 1 and 2 for gold and silver, respectively.

The concentrated mineral corresponding to the 200 mesh (74 μm) floated in the presence of 0.08 g/t of [X] and 0.06 g/t of [e] was used to carry out the dynamic leaching tests in a system H2O–Thiourea (TU) without oxidant at acidic pH of 1.5 acidified with sulfuric acid; the pulp (particles plus 1 L deionized water) was continuously stirred using a four-blade mechanical impeller; the evaluated concentrations of TU were 0.2, 0.3, and 0.4 M (mol/L), with established leaching times of 15, 30, 60, 90, 120, 150, 210, 270, and 330 min, for each test, one gram of mineral was used. At each sampling time, an aliquot was collected, filtered, and analyzed via AA in a Perkin Elmer Model 2380 equipment in its concentration of gold and silver. During each of the flotation and leaching tests, pH and redox potential were measured continuously using a Thermo Scientific Orion potentiometer and a platinum sensor glass electrode.

Results

The concentrated ore obtained in the flotation tests was characterized by X-ray diffraction; Fig. 1 shows the spectrum obtained, which consists mainly of a quartz phase, cristobalite pdf 96-901-2602 and arsenopyrite pdf 96-901-6640; the mineralogical nature of this mineral makes it suitable for leaching using a H_2O–TU, because gold and silver may be associated with the matrix and have the characteristics of a refractory mineral that would not be efficient through dissolution with cyanide, as has been described in the literature [10].

The mineral concentrate used for the leaching tests was obtained from the flotation tests carried out in the Denver cell. The mineral pulp prior to flotation was conditioned; adding the proposed concentration of foaming agent 0.06 g/t, 0.08, and 016 g/t of potassium amyl xanthate, the flotation pH was between 7.2 and 7.5. During each conditioning stage, the pH and the ORP oxidation reduction potential (mV) were constantly monitored, which was converted to the value of the standard SHE hydrogen electrode, by adding 236 mV to the measured value of the ORP as expressed in the bibliography [10]; Fig. 2 shows the behavior of pH during conditioning.

Figure 2 shows that the addition of the mineral to the solution causes an increase in pH due to the formation of hydroxyl ions OH^- due to the chemical nature of the mineral, the pH was adjusted with 0.1 M sulfuric acid to a value around 7, recommended pH for the flotation of mineral sulfides such as arsenopyrite [11]; later,

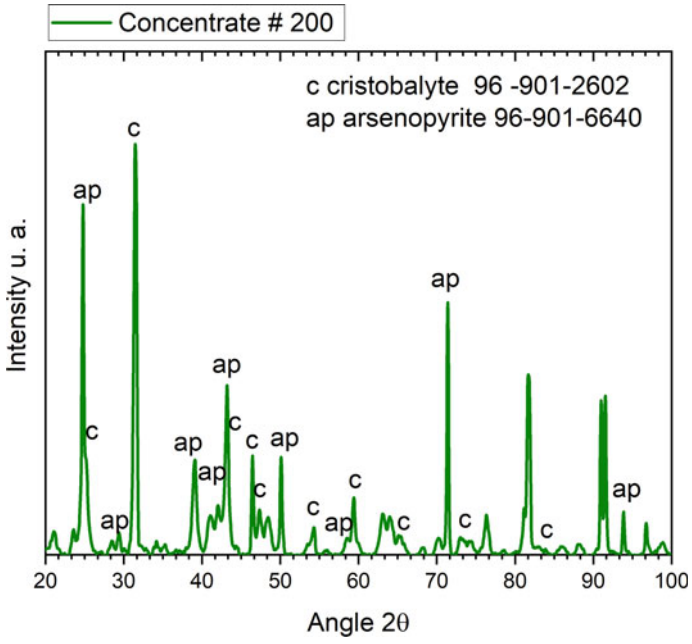

Fig. 1 X-ray diffraction spectrum (XRD) of ore concentrate

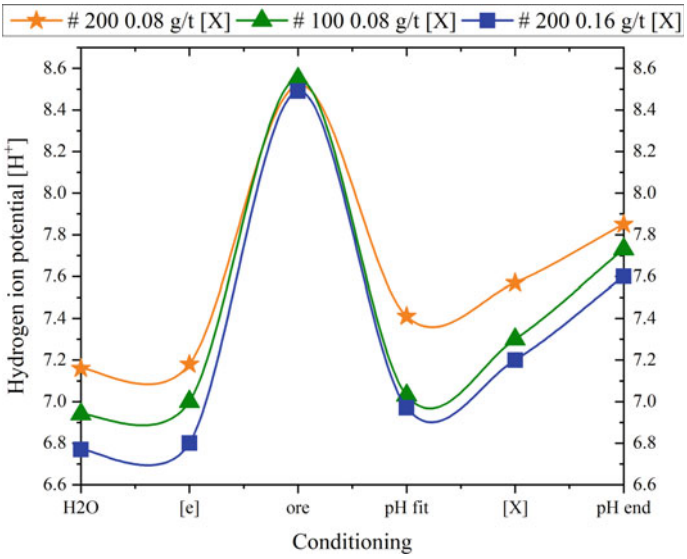

Fig. 2 Behavior of the potential of hydrogen ions, during conditioning and at the end of the flotation test

the xanthate collector was added and the flotation test was started; the concentrate was collected for 5 min; the concentrate, tailings, and feed were characterized based on their concentration of gold and silver as presented in Tables 1 and 2; at the end of the flotation time, it was found that the pH of the pulp increased due to the effect of the formation of hydroxyl ions due to the aeration of the cell.

Figure 3 shows the behavior of the oxidation reduction potential measured and converted to the value of the standard hydrogen electrode (SHE) mV; it is observed that the optimum flotation potential is oxidizing around 180 and 200 mV, that is, the species are mainly metallic, such as iron or arsenic oxidize, and leave a surface rich in sulfur, favoring the flotation of the valuable mineral.

Regarding the leaching tests of gold and silver ore using a TU–H_2O thiourea system at pH 1.5 without using an oxidant in a stirred reactor at 800 rpm, Fig. 4 shows the gold recovery curves as a function of time; the increase in the TU concentration significantly influences the leaching efficiency, however, the use of a concentration of 0.2 M of TU in the first minutes of reaction achieves a better value, % v/v of considerable dissolution, and so on until reaching a maximum extraction of 84% v/v.

The leaching of silver with thiourea as a function of time is presented in Fig. 5; the leaching kinetics compared to that of gold is slower, however, the best efficiency is obtained with a similar concentration of 0.2 M; the application of this leaching system to an ore containing arsenic sulfides achieves elevated separation efficiencies.

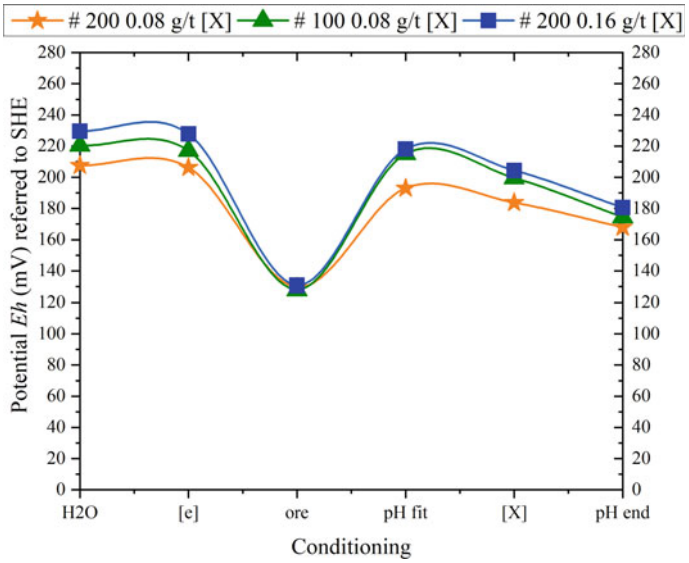

Fig. 3 Behavior of the pulp potential (mV), during conditioning and at the end of flotation

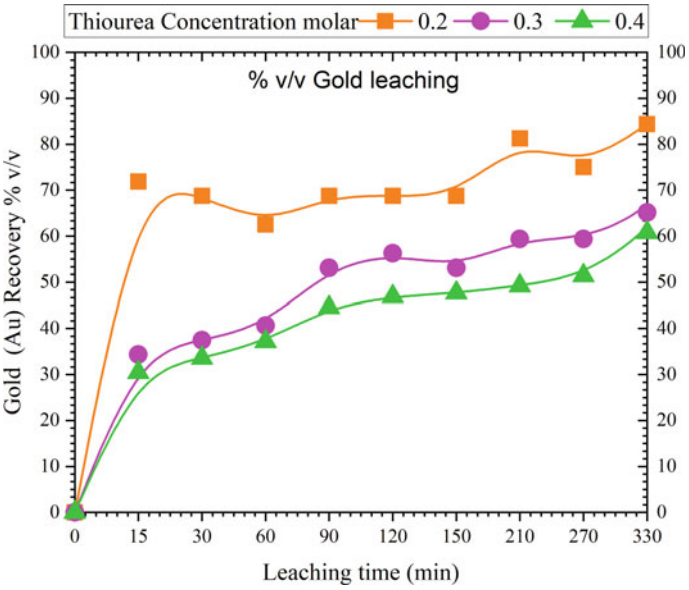

Fig. 4 Gold recovery curves % v/v versus leaching time (min) for different concentrations of thiourea (TU)

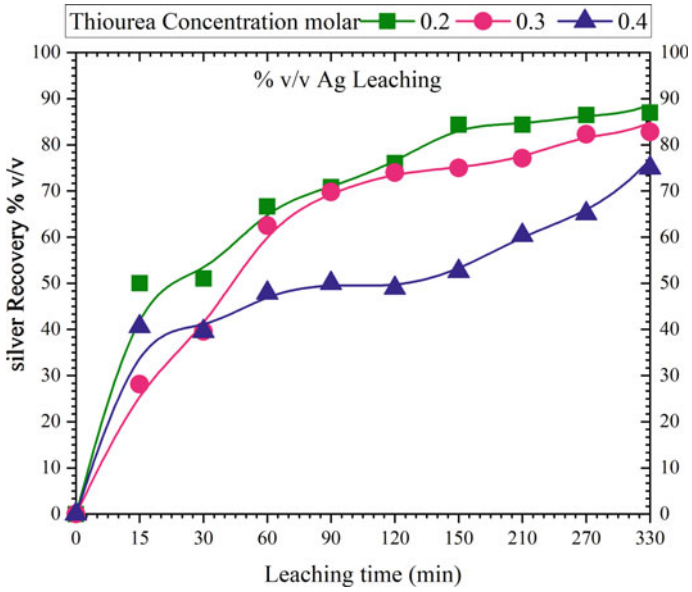

Fig. 5 Silver recovery curves % v/v versus leaching time (min) for different concentrations of thiourea (TU)

Conclusions

Flotation and leaching of an ore containing gold and silver were carried out using xanthate at pH 7.5 and a H_2O–thiourea system at pH 1.5 with concentrations of 0.2–0.4 M, respectively. The experimental results show that the concentration is carried out more efficiently using 200 mesh particles (75 μm) at pH 7.5 and a concentration of 0.08 g/t of xanthate. Regarding the leaching tests, the system with a thiourea concentration of 0.2 M at pH 1.5 and an oxidation reduction potential converted to a pulp potential Eh (standard hydrogen electrode SHE) of 0.5 V, the recovery of gold and silver in 330 min is 84 and 86% v/v, respectively.

Acknowledgements To the Autonomous University of the State of Hidalgo, to the PRODEP Teacher Professional Development Program, and to the National Polytechnic Institute ESIQUIE.

Bibliography

1. Lin JC, Huarng JJ (1994) Electrochemical stripping of gold from Au-Ni-Cu electronic connector scrap in an aqueous solution of thiourea. J Appl Electrochem 24(2):157–165
2. Jaszczak E, Polkowska Ż, Narkowicz S, Namieśnik J (2017) Cyanides in the environment—analysis—problems and challenges. Environ Sci Pollut Res 24(19):15929–15948

3. Konadu KT, Huddy RJ, Harrison ST, Osseo-Asare K, Sasaki K (2019) Sequential pretreatment of double refractory gold ore (DRGO) with a thermophilic iron oxidizing archeaon and fungal crude enzymes. Miner Eng 138:86–94
4. Qin H, Guo X, Tian Q, Yu D, Zhang L (2021) Recovery of gold from sulfide refractory gold ore: oxidation roasting pretreatment and gold extraction. Miner Eng 164:106822
5. Ubaldini S, Veglio F, Beolchini F, Toro L, Abbruzzese C (2000) Gold recovery from a refractory pyrrhotite ore by biooxidation. Int J Miner Process 60(3–4):247–262
6. Nazari AM, Ghahreman A, Bell S (2017) A comparative study of gold refractoriness by the application of QEMSCAN and diagnostic leach process. Int J Miner Process 169:35–46
7. Farinha PA, Correia MJN, Carvalho JR (1992) Leaching of gold from a Portuguese concentrate with thiourea. Miner Eng 5(8):953–959
8. Zheng S, Wang YY, Chai LY (2006) Research status and prospect of gold leaching in alkaline thiourea solution. Miner Eng 19(13):1301–1306
9. Ubaldini S, Fornari P, Massidda R, Abbruzzese C (1998) An innovative thiourea gold leaching process. Hydrometallurgy 48(1):113–124
10. Guy PJ, Trahar WJ (1984) The influence of grinding and flotation environments on the laboratory flotation of galena. Int J Miner Process 12:15–38
11. Bulatovic SM (2007) Handbook of flotation reagents: chemistry, theory and practice: volume 1: flotation of sulfide ores. Elsevier
12. Hayes RA, Ralston J (1988) The collectorless flotation and separation of sulphide minerals by Eh control. Int J Miner Process 23(1):55–84

Chemical Characterization of Filin-Kokuwa Gold Deposit in Northeast Nigeria Towards Its Appraisal

Markus Daniel Bwala, Furqan Abdulfattah, Oladunni Oyelola Alabi, and Suleiman Bolaji Hassan

Abstract Discovering new gold deposits is without a doubt, pertinent to meet the increasing demand for precious minerals like gold. Characterization is done to ascertain the presence of Gold in the Filin-kokuwa deposit. Characterization was carried out using Atomic Absorption Spectroscopy (AAS), Energy Dispersive X-ray Fluorescence Spectrometer (ED-XRF), and Scanning electron microscopy coupled with energy dispersive spectrometry (SEM-EDS). The results revealed that Filin–Kokuwa gold ore approximately assayed 15 ppm, Au. It was observed from the result that the ore contains 66.5% SiO_2, 7.37% K_2O, 3.16% CaO, 0.0015% Au, and other associated minerals. Further qualitative analysis using petrography revealed non-equiaxial mineral grains (light grey), unevenly distributed across the dark-grey ore matrix. This study, therefore, established that the deposit contains gold ore and could be a potential source of gold exploitation in Nigeria.

Keywords Characterization · Gold · Chemical · Mineral · Exploitation

Introduction

The recent drifts in global mineral production and expanding uses of mineral resources predict a bright future, though one with significant challenges, for exploration and development [1]. This projection is premised on the increasing demand for minerals like gold, which is possible to keep on increasing. Thus, discovering new gold deposits is, without a doubt, pertinent to meeting future demands. Emphatically, the development of these discovered deposits has been continuously hampered over the years due to substandard exploration approaches adopted, which affect the environmental and economic viability of the deposits significantly [2]. For instance,

M. D. Bwala · F. Abdulfattah (✉) · S. B. Hassan
Nigerian Institute of Mining and Geosciences, Jos, Nigeria
e-mail: furqanabdul1563@gmail.com

O. O. Alabi
Federal University of Technology, Akure, Nigeria

M. Zhang et al. (eds.), *Characterization of Minerals, Metals, and Materials 2023*, The Minerals, Metals & Materials Series
https://doi.org/10.1007/978-3-031-22576-5_31

the artisanal workings of Nigerian goldfields, both the primary gold-quartz reefs and their associated alluvial existences, harbor harmful minerals in the gold concentrate and release hazardous substances, which pose serious environmental threats [3].

Gold is one of the rare elements in the world, making up roughly 0.003 parts per million (ppm) of the earth's crust. Gold belongs to the precious metal group found in nature as native gold, alloys, sulfides, telluride, antimonite, selenide, and tellurates [4]. Gold has an atomic and mass number of 79 and 197 respectively, a specific gravity of 19.3 (varying with mineral types) and of 1060 °C melting point, a golden yellow streak, a Mohs scale of 2.5–3, and it occurs in octahedral and dodecahedral crystal lattice systems [5]. The topmost five gold-producing countries include China, the United State of America (USA), Australia, South Africa, and Russia. Others are Peru, Indonesia, Ghana, Canada, and Uzbekistan. China was the world's highest gold producer in 2011 when it produced 345 tons of gold. The number one gold producer in the world in 2017 was China, according to the GFMS Gold Survey 2018, mining almost 131 tonnes more than second-place Australia [6]. That's about 13% of worldwide mines production. In 2017, global gold mine production was reported at 3247 tonnes. Australia was the world's second-largest producer of gold; Australia produces around 295.6 tonnes, followed by Russia (270.7 tonnes) and the United States 230.0 (tonnes). In 2011 above 83% of gold production was for jewellery, 6% was designed for medals and official coins, 6% for electronic equipment, 2.2% for dental materials, and 2.8% was consumed in diverse industrial applications [7].

Gold ores are found in alluvial, vein, and lode deposits classified as free-milling and refractory ores. Gold is recoverable from free-milling ores by crushing and amalgamation, while refractory ores such as tellurides are processed through complex routes. Gold ores containing carbonaceous materials are challenging to treat because the gold is tied up with the percentage of carbon present in the ores and therefore reports in the tailings [8].

Specific analyses are done to determine the ore's nature, the ore's metallic content, and the mineralogical assemblage of the ore. These are the precursor to the choice of processing techniques. The equipment used for the analysis includes Atomic Absorption Spectroscopy (AAS) analysis, X-ray fluorescence (XRF) analysis, X-ray diffraction (XRD) analysis, Scanning electron microscopy with energy dispersive X-ray (SEM/EDX) analysis, and petrography study.

Methodology

Materials and Equipment

The material utilized for this research is fifty (50) kg of the crude sample of Filin–Kokuwa gold ore and emery papers (500 μm and 1000 μm grits) for surface preparation. The research equipment employed is a set of sieves, a Laboratory Jaw Crusher, an Automatic Sieve shaker, a Laboratory Roll Crusher, a Laboratory Ball Mill, a

Table 1 Details of selected sampling pits

S/N	sources	Quantity (Kg)	Elevation (m)	Geological location
1	Pit 1	200.0	725	N10°09′59.5″; E9°19′04.4″
2	Pit 2	200.0	719	N10°09′58.667″; E9°19′04.346″
3	Pit 3	200.0	718	N10°09′70.00″; E9°19′04.44”
4	Pit 4	200.0	721	N10°09′58.418″; E9°19′03.760″
5	Pit 5	200.0	724	N10°09′57.1″; E9°19′02.4″

Digital weighing balance, an Atomic Absorption Spectrometer, an Energy Dispersive X-ray Fluorescence Spectrometer (ED-XRFS), Scanning Electron Microscope with Energy Dispersive X-ray Spectrometer (SEM/EDX), and X-ray Diffractometer.

Sample Collection and Preparation

The crude samples of Filin–Kokuwa gold ore were sourced from five different pits of dimension 3 m × 3 m × 5 m with geological locations as depicted in Table 1 at Toro Local Government Area, Bauchi state. The sourced samples were gathered and properly mixed till homogenization was attained, boulders were crushed using a sledgehammer to a size range of 3–5 mm and further reduced to 1 mm using a laboratory jaw crusher. Cone and quartering sampling methods were used to produce a true representative sample for analysis. The representative sample was used for this investigation.

Chemical Characterization of the Ore

The elemental and chemical compositions of the ore were investigated using AAS and ED-XRF, respectively.

Atomic Absorption Spectrometer (AAS)

One (1) g of pulverized sample was weighed into a 100 ml conical flask and moistened with distilled water. 10 ml aqua regia HNO_3: HCl (3:1) was added and boiled with steady heat to almost dryness. It was cooled and leached with 5 ml of 6 M H_2SO_4. 5 ml of distilled water was added and allowed to simmer for 10 min. It was then cooled and filtered. The filtrate was made up to 100 ml and presented for mineral/metal analysis. The analytical technique used for the study of metal concentration was spectrometry, and the equipment used was Atomic Absorption Spectrophotometer (AAS) Buck Scientific model 211 VGP using the calibration plot method. The samples were

analyzed with the metals' concentration being displayed in part per million (ppm) after extrapolation from the standard curve.

Energy Dispersive X-ray Fluorescence Spectrometer (ED-XRF)

About 20 g of the ore sample was finely ground to pass through a 200 mesh (75 μm) sieve and after that thoroughly mixed with cellulose flakes binder in the ratio of 5.0 g sample(s) to 1.0 g binder and pelletized at a pressure of 10–15 tons/square-inch in a pelletizing machine. The pelletized samples were stored in a desiccator and subjected to analysis using the ED-XRF EDX1000 device. The result obtained was reported in percentage (%) composition for trace and significant compounds.

SEM/EDX Analysis of Filin-Kokuwa Gold Ore

Morphological and qualitative analyses of the bulk ore were investigated using SEM/EDX. The SEM provides information on the spatial distribution of mineral phases present in the crude, while EDS includes information on their elemental composition [9]. Five (5) g of the ore was prepared, mounted in epoxy resin, polished, and made conductive by carbon coating in a Denton vacuum, DV-502A. The morphology of the gold ore was then analyzed in the SEM at an accelerating voltage of 20 KVA, real-time of 30 s, and a lifetime of 60 s. The machine was configured with an ultra-thin window energy dispersive X-ray spectrometry, three WDS spectrometers, and a Gellerd Spec automation system controlling the spectrometers and motorized stage. Images were captured using the backscattering electron detectors and the chemical elements of the sample detected by the EDX.

XRD Analysis of Filin-Kokuwa Gold Ore

The mineral phases and their spatial distribution in the ore were determined using a Panalytical Empyrean Diffractometer Scatter—X78 with a Pixel detector, and fixed slits with Fe filtered Co-Kα radiation. The sample was prepared for XRD analysis using a backloading preparation method. The phases were identified using X'Pert Highscore plus software, and the relative phase amounts (%weight) were evaluated using the Rietveld method.

Table 2 AAS analysis of Filin–Kokuwa gold ore in parts per million (ppm)

Sample	Au	Ca	Cr	Fe	Ni	Pb
Crude (ppm)	14.39	13.80	1.75	211.50	13.20	1.22

Results and Discussion

AAS Analysis of Filin-Kokuwa Gold Ore

Elemental constituents of the ore as detected by the AAS in parts per million (ppm) are shown in Table 2. It can be deduced that the ore contains major elements like Fe, Au, Ca, and Ni, of concentrations 211.50, 14.39, 13.80, and 13.20 ppm, respectively, alongside trace elements such as Cr (1.75 ppm) and Pb (1.22 ppm). The considerable gold concentration detected establishes the viability of mining the Filin–Kokuwa deposit after its reserve estimate is determined.

EDS—XRF of Filin-Kokuwa Gold Ore

The chemical analysis result of the crude Filin–Kokuwa gold ore using an Energy Dispersive X-ray Fluorescence Spectrometer (ED-XRFS) is contained in Table 3. It was observed from the result that the ore contains 66.5% SiO_2, 7.37% K_2O, 3.16% CaO, 1.65% TiO_2, 18.33% Fe_2O_3, 8.33% ZrO_2, 0.0015% Au, and other trace compounds. The presence of radioactive compounds such as RuO_2 was also evident. This analysis depicts that the gold in the Filin–Kokuwa deposit occurs free in nature, having a concentration of 0.0015% or 15 ppm. The detected gold content is somewhat synonymous with that of AAS analysis. Further, major associated gangue minerals in the ore are silica, zirconia, and iron oxide which are predominant and possess varying specific gravities and magnetic properties relative to the desired valued gold in the ore. This disparity in their physical properties, if exploited effectively, will facilitate the recovery of gold concentrate from the ore.

Table 3 Chemical composition of crude Filin–Kokuwa gold ore by ED–XRFS

Compound	SiO_2	K_2O	CaO	TiO_2	MnO	Fe_2O_3	ZrO_2	RuO_2	BaO	Au	PbO
Conc. (%)	66.5	7.37	3.16	1.65	0.17	18.39	8.33	0.985	0.51	0.0015	0.10

Conc. concentration

SEM–EDS of Filin-Kokuwa Gold Ore

The SEM micrographs alongside area analysis of the crude sample of Filin–Kokuwa gold ore are presented in Figs. 1 and 2. While Fig. 3 is a diffractogram of the ore revealing the mineral phases therein. From Fig. 1, it can be deduced that the ore contains non-equiaxial mineral grains (light grey), unevenly distributed across the dark-grey ore matrix. The area analysis of the ore revealed the principal elements within the ore as Si, Al, K, C, and O having proportions of 32.8, 21.9, 1.1, 1.1, and 48.1 wt.%, respectively. This finding depicts the likely predominance of alumina, silica, and potassium oxide within the ore, thus complementing the result obtained earlier using ED-XRF (Table 3).

XRD Analysis of Filin-Kokuwa Gold Deposit

The mineralogical characterization of Filin–Kokuwa gold ore deposit using XRD is shown in Fig. 3.

However, further examination at different magnifications, as shown in Fig. 2, these mineral grains appear consolidated, contributing to the non-detection of elemental gold within the ore [10]. Thus, the need for comminution of the ore to a size range where the elemental gold/gold compounds therein can be effectively liberated from associated minerals and, consequently, separated is imperative.

The importance of identifying the nature and occurrence of the gold and associated minerals in the ore cannot be emphasized. This data provides the needful approach or techniques to exploit the recovery of gold concentrate from the said ore. XRD analysis of the gold ore was carried out, and the ensuing result is shown in Fig. 3. The XRD of the gold ore revealed extensive diffraction peaks, which could be attributed to the presence of numerous associated mineral oxides in the gold ore. The identified gold minerals in the ore are Au_2Pb and Na_3AuO_2, alongside other minerals like Cu_4O_3, ZnO, and Pb_3O_4. Also, the observed broad peaks depict that the gold ore possesses some amorphous properties [9]. This further proves the presence of gold in Filin–kokuwa deposit alongside other associated minerals.

Conclusion

This study has shown Filin–Kokuwa gold ore contains approximately 15 ppm Au alongside other associated minerals such as SiO_2, Fe_2O_3, CaO, and TiO_2, which are the significant constituents of associated minerals identified. The SEM/EDX revealed non-equiaxial mineral grains (light grey), unevenly distributed across the dark-grey ore matrix. The area analysis of the ore revealed the principal elements within the ore as Si, Al, K, C, and O; and the ore's diffractogram revealed extensive diffraction

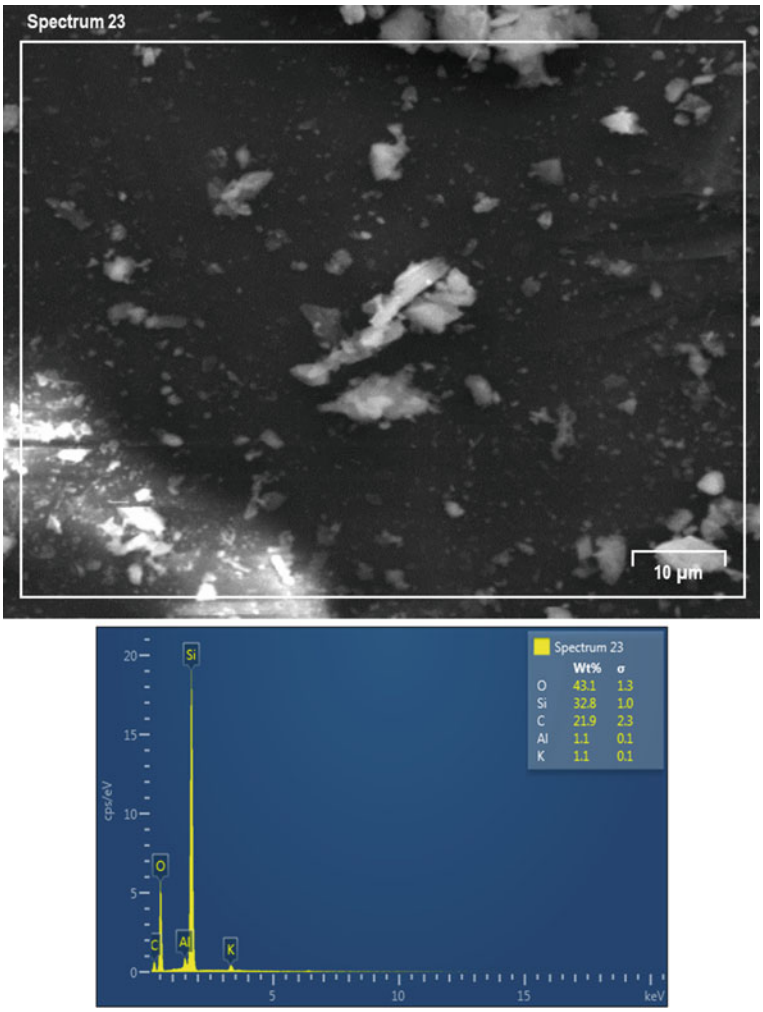

Fig. 1 SEM micrograph of crude Filin–Kokuwa gold ore and EDS of area analysis

of gold mineral peaks such as Au_2Pb and Na_3AuO_2 alongside other minerals like Cu_4O_3, ZnO, and Pb_3O_4. This research has advanced the frontiers of knowledge on the characterization studies of Filin–Kokuwa gold ore deposits, and the information could be a source of data for effective exploration and exploitation of gold from the deposit.

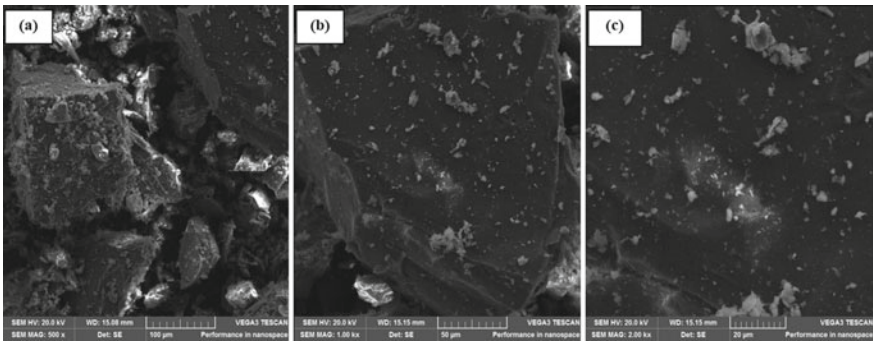

Fig. 2 Micrographs of crude Filin–Kokuwa gold ore taken at different magnifications, **a** 500X, **b** 1000X, and **c** 2000X

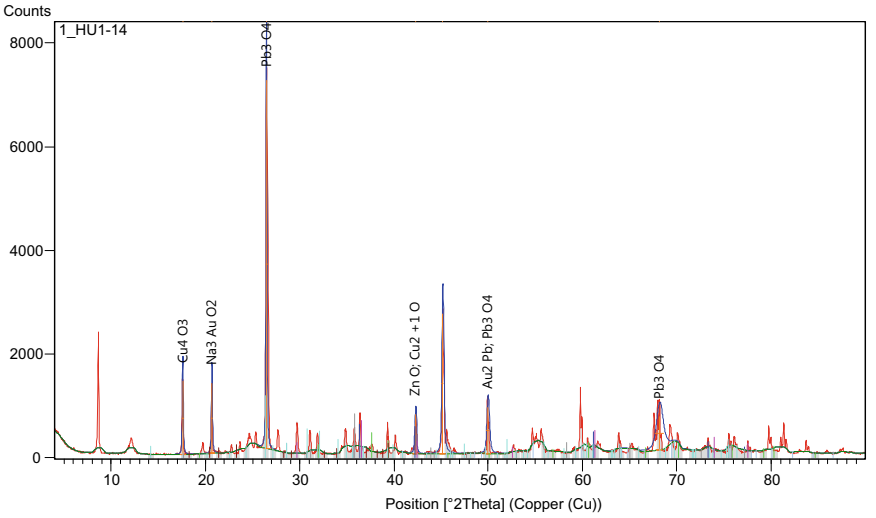

Ref. Code	Score	Compound Name	Displacement [°2Th.]	Scale Factor	Chemical Formula
01-077-0191	26	Zinc Oxide	0.000	0.061	ZnO
00-028-0436	18	Gold Lead	0.000	0.044	Au_2Pb
00-049-1830	13	Copper Oxide	0.000	0.074	Cu_4O_3
00-040-0175	13	Sodium Gold Oxide	0.000	0.015	Na_3AuO_2
00-041-1493	11	Lead Oxide	0.000	0.120	Pb_3O_4
00-002-1067	17	Copper Oxide	0.000	0.059	Cu_2O

Fig. 3 XRD diffractogram showing mineral peaks and weight percent of minerals contained in Filin–Kokuwa gold ore

References

1. Adekeye JID (2010) Impact of conflict on mining in Nigeria. In: Albert IO, Olarinde ON (eds) Trends and tensions in managing conflicts. Society for Peace Studies and Practice (SPSP), Ibadan, Nigeria, pp 254–263
2. Kankara IA, Darma MR (2016) A review of gold metallurgeny in Nigeria. Int J Res Chem Metall Civ Eng (IJRCMCE) 3(2):294–299
3. Aliyu ML (2022) Gold mineralization in Nigeria. https://www.sun.edu.ng/knowledge-update/gold-mineralization-in-nigeria. Assessed 29 Aug 2022
4. Orlich J, Gathje J, Kappes R (2009) The application of froth flotation for gold recovery at Newmont Mining Corporation. In: Recent advances in mineral processing plant design, pp 190–194
5. Wills BA, Napier-Munn TJ (2006) Mineral processing technology, 7th edn. Elsevier, Amsterdam, pp 109–439
6. Dhiraj AB (2018) The world's largest gold producing countries, 2018 rankings. https://ceoworld.biz/2018/06/14/the-worlds-largest-gold-producing-countries-2018-rankings/. Assessed 22 Aug 2022
7. Domínguez A, Valero A (2012) Global gold mining: is technological learning overcoming the declining in ore grades? In: Proceedings of Ecos 2012—the 25th international conference on efficiency, cost, optimization, simulation and environmental impact of energy systems, Perugia, Italy, 277, pp 1–17
8. Abaka-Wood GB, Zanin M, Addai-Mensah J, Skinner W (2019) Recovery of rare earth elements minerals from iron oxide–silicate rich tailings–part 1: magnetic separation. Miner Eng 136:50–61
9. Olubambi PA, Ndlovu S, Potgieter JH, Borode JO (2008) Mineralogical characterization of Ishiagu (Nigeria) complex sulfide ore. Int J Miner Process 87(3–4):83–89
10. Harmon RS, Lawley CJM, Watts J, Harraden CL, Somers AM, Hark RR (2019) Laser-induced breakdown spectroscopy-an emerging analytical tool for mineral exploration. Minerals 9(12):37–40

Creep Behavior at 500 °C of %Cr-0.5Mo Steel

Maribel L. Saucedo-Muñoz, Shin-Ichi Komazaki, and Victor M. Lopez-Hirata

Abstract The creep strength of 5Cr-0.5Mo steel was determined at 600 °C and 78–170 MPa, as well as its relation to the microstructural changes during the creep tests. The microstructural characterization showed that the creep tests were conducted under the presence of a mixture of both intergranular and intragranular M_7C_3 and $M_{23}C_6$ carbides dispersed in the ferrite matrix. The *n* exponent of Norton–Bailey law suggested that the creep deformation process occurred through the ferrite grains, which conducted to a transgranular ductile- fracture mode after creep testing. The creep strength of this steel is directly related to the precipitation size and volume fraction during the creep test.

Keywords 5Cr-0.5Mo steel · Creep properties · Microstructure evolution · Thermo-Calc

Introduction

The creep-resistant Cr–Mo steels are used with great success for applications in the power generation and petrochemical industries. This type of steel has been designed [1–4] to work at temperatures between 350 and 600 °C and pressures of about 15–30 MPa for long periods. The creep resistance of Cr–Mo steel is based on the formation of stable precipitates such as alloyed carbides in a ferritic, bainitic and/or martensitic matrix phase in the normalized steel condition. Nevertheless, the operation conditions of industrial components usually involve exposure to high temperature for prolonged times under stress, which promote different microstructure changes such as grain boundary segregation (temper embrittlement), brittle-phases formation, as well as the coarsening of precipitates [2–6]. These changes may alter the

M. L. Saucedo-Muñoz · V. M. Lopez-Hirata (✉)
Instituto Politécnico Nacional (ESIQIE-ESFM), UPALM Edif. 7, 07300 Mexico, DF, Mexico
e-mail: vlopezhi@prodigy.net.mx

S.-I. Komazaki
Kagoshima University, Kagoshima 8900065, Japan

M. Zhang et al. (eds.), *Characterization of Minerals, Metals, and Materials 2023*, The Minerals, Metals & Materials Series
https://doi.org/10.1007/978-3-031-22576-5_32

mechanical properties of the steel [6]. Therefore, the evaluation of deterioration in mechanical properties such as toughness and creep strength are important issues to be considered for the safe operation of the equipment. Thus, the precipitate of this type of steel plays an important role in obtaining good creep strength. For instance, the ferritic 5Cr-0.5Mo steel [1] is considered as a member of the Cr–Mo steels and it has the presence of abundant precipitation from the as-received condition since this is usually normalized and tempered, which promotes the formation of different carbides, Fe_3C, M_7C_3 and $M_{23}C_6$ [1], related to the precipitation and creep strength of this steel in comparison to the other Cr–Mo steels. Thus, the purpose of the present work is to evaluate the creep strength at 600 °C and test stresses of 78–170 MPa for a 5Cr-0.5Mo steel, as well as the role of the precipitation evolution on the creep strength.,

Experimental Procedure

Table 1 shows the chemical composition of the steel [7]. The steel plates have a size of 200 × 200 × 12 mm. These were normalized from 950 °C and subsequently tempered at 715 °C for 15 min. Uniaxial creep test specimens of 90 mm length, diameter gauge-length of 30 mm and 6 mm diameter were also prepared by machining. The conventional creep tests were carried out at 600 ± 3 °C under different stresses in the range of 78–170 MPa according to the JIS Z 2271(ISO 204) standard [8]. The testing temperature was stabilized in the furnace for 4 h and an atmosphere of high-purity Ar gas was used during testing. The strain was recorded using an extensometer located in the gauge area. Tranversal and longitudinal sections of tested specimens were metallographically prepared, etched with Nital reagent and subsequently observed with Scaning Electron Microscope (SEM) and at 20 kV. In order to compare the precipitation evolution of the tested creep specimens, as-received steel specimens of 12 × 12 × 12 mm were aged at 600 °C for times between 0 and 6000 h. These were also metallographically prepared, etched, and observed with light microscope and SEM. Besides, the precipitates were extracted by electrochemical dissolution of the ferrite matrix from both the as-received and aged specimens. The electrolyte was composed of 2–4 vol. % nitric acid in ethanol with a graphite cathode at room temperature and 2–5 V (d.c.). The extracted residues were analyzed with an X-ray diffractometer with monochromated Kα radiation.

Table 1 Chemical composition of the steel 5Cr-0.5Mo

Steel	C	Mn	Si	Mo	Cr	Ni
wt. %	0.10	0.36	0.35	0.46	4.6	0.12

Results and Discussion

Creep Properties

The creep curves, strain (%) versus time (h), at 600 °C are shown in Fig. 1 for the test stresses between 78 and 170 MPa. The second and third stages of creep are clearly observed in the creep curves. As expected, the time-to-rupture, duration of creep-secondary stage, and total strain increase with the decrease in test stress.

Figure 2 shows the plot of strain rate, $\dot{\varepsilon}$, versus time, where the three creep stages are clearly identified. That is, the strain rate, $\dot{\varepsilon}$, decreases with time, as shown for short times in Fig. 2. The decreasing strain rate in the creep-primary stage has been related to the strain hardening or to a decrease in free or mobile dislocations [1, 2]. In the creep-secondary stage, the strain rate remains almost constant. This strain rate is designated as a steady-state creep rate, $\dot{\varepsilon}_s$, which is commonly associated with a balance between the rate of generation of dislocations contributing to the hardening and the rate of recovery contributing to the softening [3, 4]. In the creep-tertiary stage, the strain rate increases with time until rupture at rupture time t_r and rupture strain, ε_r [1]. This figure also shows that the duration of creep-secondary stage and creep-tertiary stages is shorter as the test stress increases. Likewise, the strain rate at the creep-tertiary stage increases with the test stress.

Since the minimum creep rate, $\dot{\varepsilon}_{min}$, is preferred by engineers and researches to characterize the secondary-creep stages, this was determined from Fig. 2. The stress dependence of minimum creep rate, $\dot{\varepsilon}_{min}$, is usually expressed by a power law, known as the Norton–Bailey Law [1–4]:

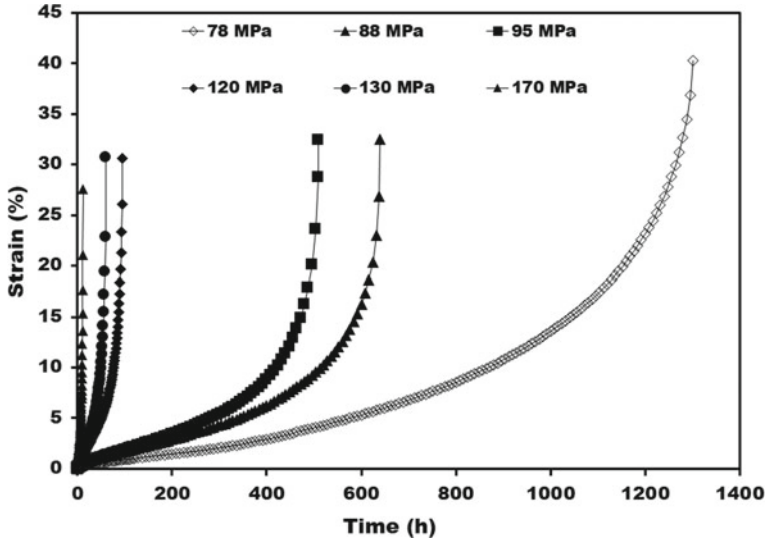

Fig. 1 Creep curves at 600 °C for stresses between 78 and 170 MPa

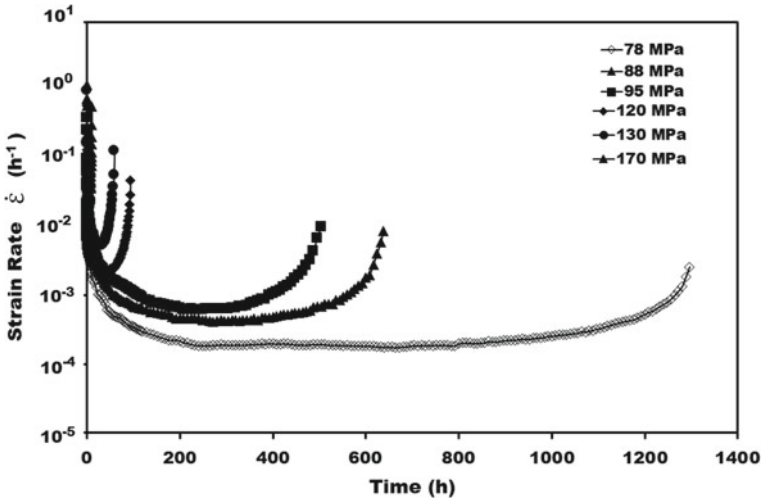

Fig. 2 Plot of strain rate, $\dot{\varepsilon}$, versus time

$$\dot{\varepsilon}_{\min} = A\sigma^n \tag{1}$$

where A and n are exponents stress-independent. Figure 3 shows the stress dependence of minimum creep rate, $\dot{\varepsilon}_{\min}$. This log–log plot shows a clear linear relationship between the minimum creep rate, $\dot{\varepsilon}_{\min}$, and the test stress σ with an R^2 value of approximately 0.9961. This figure also indicates that the stress exponent n is equal to 6.3. The n values have been observed to be from 2.5 to 4 in the case of low stresses, 60–100 MPa for low-alloy ferritic1.25Cr-0.5Mo and 2.25Cr-1Mo steels. In contrast, n values of 6–12 have been reported [1–3] for high stresses at temperatures of 510–620 °C. Besides, the fracture mode changed from intergranular to transgranular at high stresses. Furthermore, a range of n values from 1 at low stresses to 14 at high stresses has been observed to occur in both ferritic and austenitic steels creep-tested at temperatures between 510 and 710 °C. Most of these works [1–4] reported that the deformation process is controlled by the grain boundary sliding at low stresses and by the matrix deformation at high stresses. Thus, an n value of approximately 6.29 suggests that the creep deformation mechanism took place by the deformation of ferrite matrix grains, promoting transgranular ductile-fracture mode for this steel.

Figure 4a–d show the SEM fractograph of tested specimens for 78, 95, 120, and 170 MPa, respectively. A transgranular ductile- fracture mode can be observed for all the tested specimens. The fracture surface shows typical dimpled characteristics of the ductile fracture by microvoid coalescence [1, 2]. The ductile-mode fracture shows an increase with the test stress. Besides, the presence of larger isolated microvoids can also be noted. These were formed after the microvoid coalescence process of ductile fracture. The size and number of these isolated microvoids decreased with the test stress. This behavior seems to be related with the precipitation size, as will

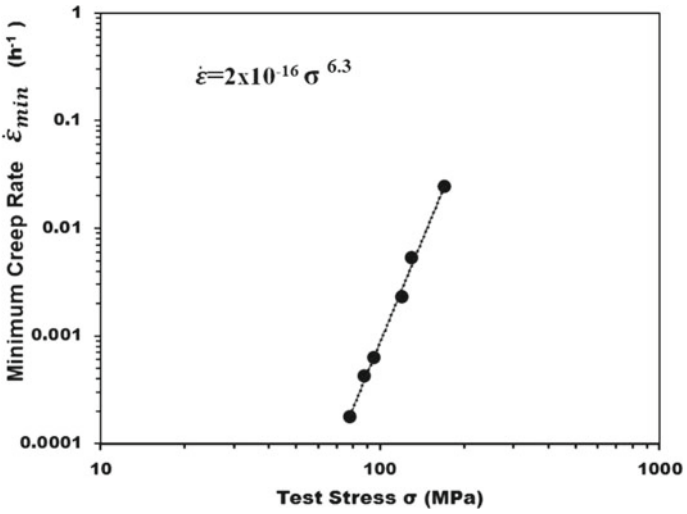

Fig. 3 Plot of minimum creep rate, $\dot{\varepsilon}_{\min}$ versus test stress σ

be shown later. These fracture characteristics are consistent with the deformation mechanism related to the exponent *n*, as described in the previous section.

SEM micrographs for a longitudinal region of the necked specimen are shown in Figs. 5a–d, for instance, after testing at 78, 95, 120 and 170 MPa, respectively. These micrographs show both intragranular and intergranular carbides dispersed in the ferrite matrix. Furthermore, the lowest number density and the largest size of precipitates are observed to occur in the necked region of the 78 MPa-tested specimen, Fig. 7a. In the case of 95 MPa-tested specimen, the number density and size of precipitates are slightly lower and larger, respectively, than the previously described specimen. The 120 MPa-tested specimen shows larger size and lower density number of the precipitates. Likewise, the 170 MPa-tested specimen has similar distribution and size of precipitates than the previous one, but they are slightly elongated in the direction of the test stress, as a result of the high test stress.

Microstructure Evolution of the Aged Steels

SEM micrographs of the steel aged at 600 °C for 0 (as-received), 300, 1000 and 2000 h are shown in Figs. 6a–d, respectively. The microstructure of the as-received steel shows the presence of both intergranular and intragranular precipitates dispersed in the ferrite matrix, Figs. 6a. Bainite constituent is expected to be present according to the Time-Temperature-Transformation (TTT) diagram for this type of steel [9]; however, it is not observable in this micrograph because of the high magnification. In general, the size for intergranular precipitates is larger than that corresponding

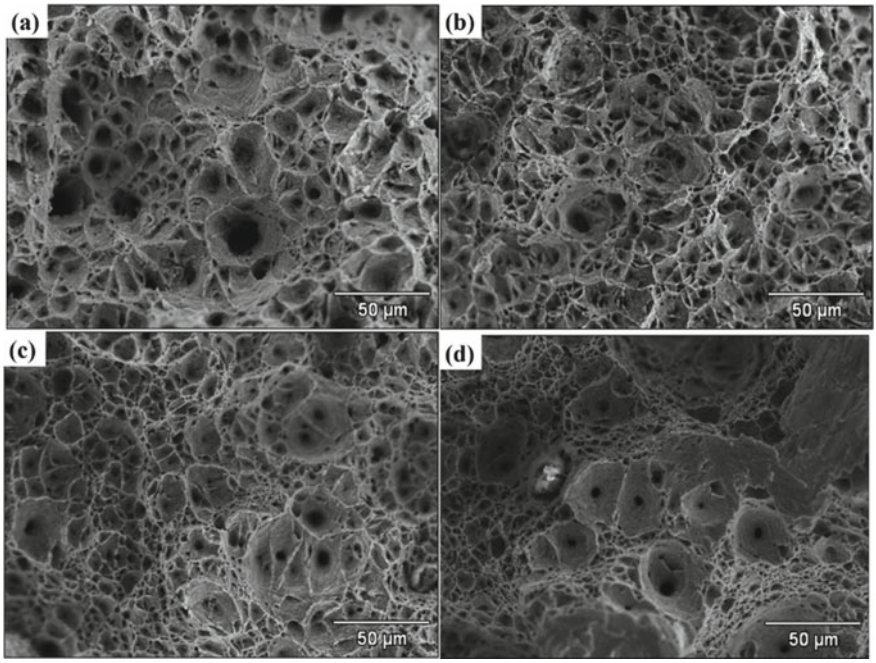

Fig. 4 SEM fractographs of the tested specimens with **a** 78, **b** 95, **c** 120 and **d** 170 MPa

to the intragranular ones. The effect of aging process at 600 °C can be noted in the microstructure evolution, as shown in Fig. 6b–d. That is, there is an increase in the size, from 35 to 45 nm and a decrease in the number density of precipitates, from 2.3 $\times$ 10^{12} to 1.9 $\times$ 10^{12} particles m^{-2}, in the steel after aging for 300 h, Fig. 6b. This fact suggests that some precipitates were dissolved, while others were being formed during the aging process. As the aging process progresses, the precipitate number density decreases, while the precipitate size continues increasing. This characteristic clearly indicated the presence of precipitate coarsening [10].

To identify the precipitate type, the XRD patterns of extracted residues from the specimens are shown in Fig. 7a, b. These XRD patterns also include the corresponding SEM micrograph of extracted residues. The identified precipitates were Cr_7C_3 and $Cr_{23}C_6$ carbides for the as-received steel, Fig. 7a. These carbides were formed after the normalizing and tempering treatments. Several works [4–6] have reported that the precipitation sequence that occurs in the ferrite matrix is as follows: $M_3C \rightarrow M_7C_3 \rightarrow M_{23}C_6$. The M_3C carbide is similar to the Fe_3C cementite phase with an orthorhombic structure (space group Pnma), M_7C_3 is a metastable Cr-rich carbide with an orthorhombic structure (space group Pnma) and $M_{23}C_6$ is the equilibrium stable Cr-rich carbide, with cubic structure (space group Fm $\overline{3}$ m), at 600 °C for the chemical composition of this steel [6]. It is important to note that M in both carbides means that the main element is Cr, but also it contains Fe and Mo [9]. This precipitation reaction is expected to occur not only by isothermal heating, but also

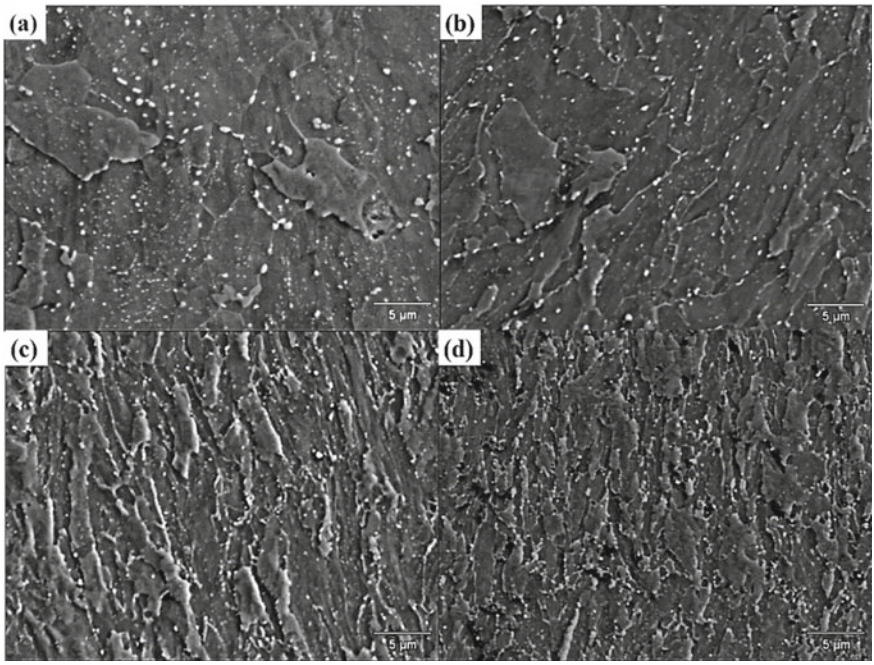

Fig. 5 SEM micrographs for the longitudinal section of tested specimens with **a** 78, **b** 95, **c** 120 and **d** 170 MPa

by continuous cooling from normalizing temperature [7]. That is, the presence of M_7C_3 and $M_{23}C_6$ carbides for the as-received steel can be attributable to the cooling process of normalizing and the isothermal heating of tempering at 715 °C for 15 min. The absence of M_3C cementite for the as-received steel seems to be related to the fact that this phase can be formed at the early stages of precipitation in the air-cooling of the normalizing treatment. This cementite M_3C is subsequently dissolved to permit the nucleation of M_7C_3 during the tempering treatment. M_7C_3 and $M_{23}C_6$ carbides can be present simultaneously since the transformation of M_7C_3 carbide into $M_{23}C_6$ carbide is a concurrent process [10]. As the aging process progresses, see Figs. 7b, the X-ray diffraction intensity from peaks corresponding to the M_7C_3 carbide decreases, while those from $M_{23}C_6$ show an increase in intensity. Furthermore, the XRD of steel aged for 2000 h mainly indicates the presence of peaks corresponding to $M_{23}C_6$ carbide.

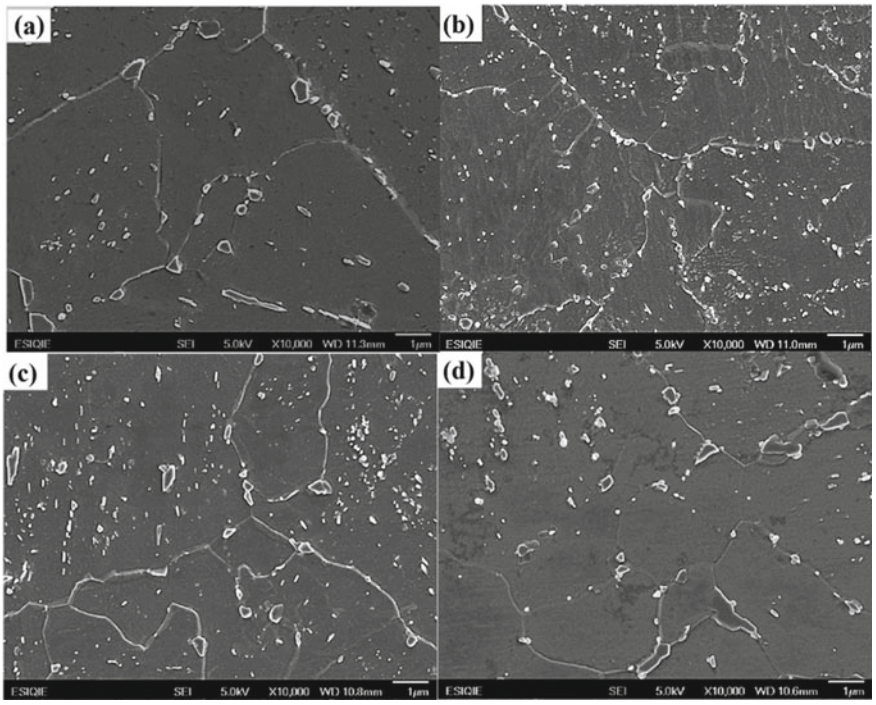

Fig. 6 SEM micrographs of the steel aged at 600 °C for **a** 0 h, **b** 300 h, **c** 1000 h and **d** 2000 h

Conclusions

The creep strength for creep resistant 5Cr-0.5Mo steel were determined at 600 °C, as well as its relation to the microstructure evolution during test, and the conclusions are:

1. The n exponent of 6.3 determined from the Norton–Bailey law, suggested that the deformation process occurred through the ferrite grains causing transgranular ductile-fracture mode after creep tests, which also observed in the creep-tested specimens.
2. The XRD patterns indicate that the creep test at 600 °C and 78–170 MPa took place under the presence of M_7C_3 and $M_{23}C_6$ carbides.
3. The creep resistance, expressed by time-to-rupture t_r, of this work steel was determined to be higher than those reported in the literature for this type of steel tested at the same stress level.

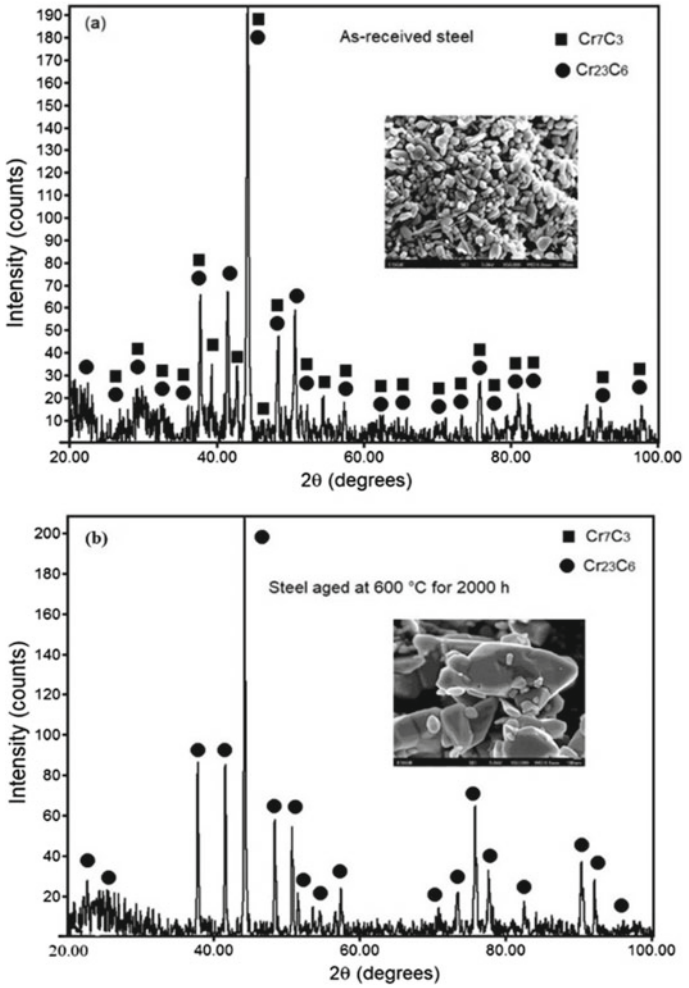

Fig. 7 XRD patterns of the extracted residues from the steel aged at 600 °C for **a** 0 h and **b** 2000 h

Acknowledgements The authors wish to thank the financial support from SIP-COFAA-IPN and CONACYT A1-S-9682.

References

1. Viswanathan R (1993) Damage mechanisms and life assessment of high-temperature components. ASM International, Ohio, USA
2. Abe F, Ulf-Kern T, Viswanathan R (2008) Creep resistant steels. Woodhead Publishing Limited, Cambridge

3. Viswanathan R (1977) Effect of stress and temperature on the creep and rupture behavior of a 1.25 Pct. Chromium-0.5 Pct. molybdenum steel. Met Trans A 8:877–884
4. Igwemezie VC, Ugwuegbu CC, MarkU (2016) Physical metallurgy of modern creep-resistant steel for steam power plants: microstructure and phase transformations. J Metall 3:1–19
5. Bhadeshia HKDH, Strange A, Gooch DJ, Ferritic power plant steels: remanent life assessment and approach to equilibrium, Inter Mater Rev 43:45–69
6. Bhadeshia HKDH (2001) Design of ferritic creep-resistant steels. ISIJ Int 41:626–640
7. A387/A387M 11 (2011) Standard specification for pressure vessel plates, alloy steel, Chromium-Molybdenum, ASTM International
8. JIS Z 2271 (2011) Metallic materials –Uniaxial creep testing in tension- Method of test, Japanese Industrial Standard
9. Thermo-Calc, Thermo-Calc version 2022ª, TCFe11 and MobFe6
10. Kostorz G (2001) Phase transformations in materials. Wiley, Germany

Durability of Alkali Activated Tiles Produced with Residual Gray from the Ceramic Industry

A. S. A. Cruz, L. U. D. Tambara, M. T. Marvila, C. M. F. Vieira, A. L. Marques, S. N. Monteiro, and A. R. G. Azevedo

Abstract Alkali activated materials present themselves as a viable solution to reduce the consumption of Portland cement, and for the management of industrial waste, including the residual ash from ceramic production. Thus, this research aimed to evaluate the physical and mechanical behavior of activated alkali materials, with the insertion of ash from ceramic industries, in the face of durability tests. For this, alkali activated specimens containing 0 and 10% of residue insertion were produced. The samples were submitted to curing for 7 and 28 days. Compressive strength, water absorption, wetting, and drying and salt attack cycles were carried out. The masses of the specimens were measured every day during the durability cycles to evaluate the loss of mass. Furthermore, the mechanical strengths of the samples were evaluated before and after the durability tests to analyze the influence of the tests on the mechanical behavior of the alkali activated material.

Keywords Alkali activated materials · Ash · Durability

Introduction

In recent years, the environmental cause has been gaining more and more notoriety, as processes such as global warming, deforestation, and pollution increasingly threaten the continuity of human life on the planet. In this context, with the advance

A. S. A. Cruz · A. L. Marques · A. R. G. Azevedo (✉)
LECIV—Civil Engineering Laboratory, UENF—State University of Northern Rio de Janeiro, Av. Alberto Lamego, 2000, Campos Dos Goytacazes, Rio de Janeiro 28013-602, Brazil
e-mail: afonso.garcez91@gmail.com

L. U. D. Tambara · M. T. Marvila · C. M. F. Vieira
LAMAV—Advanced Materials Laboratory, UENF—State University of Northern Rio de Janeiro, Av. Alberto Lamego, 2000, Campos Dos Goytacazes, Rio de Janeiro 28013-602, Brazil
e-mail: vieira@uenf.br

S. N. Monteiro
Department of Materials Science, IME—Military Institute of Engineering, Square General Tibúrcio, 80, Rio de Janeiro 22290-270, Brazil

M. Zhang et al. (eds.), *Characterization of Minerals, Metals, and Materials 2023*, The Minerals, Metals & Materials Series
https://doi.org/10.1007/978-3-031-22576-5_33

of industrialization around the globe, not only developed countries, but also developing countries face serious problems regarding the disposal of industrial waste, whose generation grows every year, proportionally to industrialization, economic and to population growth. Damage to the environment increases when such waste is disposed of in nature without proper treatment or proper disposal procedures. Thus, the correct management of waste is of paramount importance in the current world scenario [1, 2].

Likewise, civil construction plays a decisive role in terms of pollution through the emission of CO_2 into the atmosphere. Specifically, Portland cement production is responsible for more than 7% of the CO_2 released annually into the atmosphere [3]. Portland cement is the main constituent of mortars and concretes, materials used worldwide in the civil construction sector, due not only to the abundance of raw materials for its production, but also to its good mechanical properties [4].

In this scenario, the study and development of materials that can play the role that Portland cement has in civil construction, without, however, any lag in terms of mechanical properties, when compared to traditional mortars and concretes, is fundamental in order to align civil construction with sustainable development.

In order to reduce the consumption of Portland cement, and thus minimize the impacts of its production on the environment, the geopolymer was developed by Davidovts in 1978. Geopolymers are inorganic polymers whose main raw material is industrial waste rich in aluminosilicates [5] Geopolymer materials are recognized as potential substitutes for Portland cement-based materials due to the wide availability of raw materials for their production, their good mechanical properties, and excellent durability [4].

As a result, and aiming to have an important aspect of geopolymer synthesis, that is, its potential for reuse of industrial waste, contributing to waste management and to the practice of a circular economy, this research aims to produce geopolymer tiles with the insertion of ash from the burning of biomass used in red ceramic brick kilns, and above all, the evaluation of the durability of this material, with the purpose of evaluating the performance of activated alkali when subjected to normal application conditions.

With this objective, activated alkali samples were produced based on metakaolin, with ash insertions in the levels of 0%, for reference, and 10%, in relation to the amount of metakaolin. Sodium hydroxide (NaOH) and sodium silicate (Na_2SiO_3) were used for the activator solution. The specimens were subjected to thermal curing at 65 °C during the first three days followed by curing at room temperature until the end of the curing periods, which corresponded to 7 and 28 days. In addition, tests of compressive strength, water absorption, wetting and drying cycles and saline attack cycles were carried out.

Materials and Methods

The residue used in this research originates from the red ceramic brick firing ovens of Cerâmica Sardinha located in the municipality of Campos dos Goytacazes, RJ. It is configured as an ash resulting from the burning of biomass (wood) in the ovens to generate heat. To be used in the activated alkali material, the ash was sieved through a 100 sieve.

To obtain the chemical analysis of the residue, the ash was submitted to the Energy Dispersive Spectroscopy test (EDX). The results of this analysis are shown in table 1.

In turn, sodium hydroxide (NaOH) and sodium silicate (Na_2SiO_3) were used for the activator solution, in a Si/Al ratio of 3.5. The precursor used in the geopolymer synthesis was metakaolin. To make the specimens, the dry materials, that is, ash, metakaolin and sand were first manually mixed until homogeneity. The solution was then added to the dry materials, and the compost was again manually mixed to ensure that the solution was in contact with most of the dry material. Finally, the mixture was taken to an electric mixer, where it underwent mechanical homogenization for approximately 3 min.

For the conformation of the specimens, cylindrical molds of 5 cm in diameter by 10 cm in height were used.

Two curing periods were used: 7 and 28 days. In both cases, the specimens, already demolded, spent the first 3 days in an oven, subjected to thermal curing at 65 °C. After this period, the samples were removed from the oven and remained at room temperature until the end of the determined curing period.

Subsequently, the compressive strength and water absorption tests were carried out to evaluate the mechanical behavior of the composite. In addition, to evaluate the durability of the activated alkali material, the samples were subjected to cycles of wetting and drying and also of salt attack.

For the wetting and drying cycles, the specimens were subjected, alternately, to 24 h of immersion in water and 24 h of permanence in an oven at 65 ºC. This test lasted 30 days, totaling 15 complete cycles. During its execution, the masses of the specimens were measured every day, so that, at the end of the test, the mass loss of the activated alkali material was analyzed under the conditions to which it was submitted.

Likewise, to perform the saline attack test, the specimens were kept in constant submersion in saline solution for 30 days. The solution used consisted of water and table salt, that is, NaCl, without iodine. The concentration used in the solution was 5%, which in practice resulted in a ratio of 10 L of water to 500 g of salt. Again, as performed throughout the wetting and drying test, the masses of the samples were measured every day during the test.

Table 1 EDX results for the residue used

	CaO	K_2O	SiO_2	MnO	Fe_2O_3	SO_3	SrO	Rb_2O	ZrO_2
Ash	86.48%	7,66%	2.32%	1.08%	1.07%	1.03%	0.31%	0.03%	0.03%

At the end of the 30 days during which the durability tests were carried out, the specimens, after drying at room temperature, were submitted to the compression resistance test, so that, establishing a parallel with the performance of the samples that did not pass by the durability cycles, it was analyzed how the exposure of the activated alkali material to the adverse conditions simulated in the test affects its mechanical behavior.

Results and Discussion

Table 1 shows the result of the chemical analysis performed on the ash using an x-ray spectroscopy assay (EDX). It shows the strong presence of calcium in the ash, a relevant factor because, during alkaline activation, calcium reacts with silica and alumina to form hydrated calcium silicate (C–S–H) and hydrated calcium aluminum silicate (C–A–S–H), that catalyze geopolymerization reactions and optimize the microstructure of the material, making it more resistant [6].

Figure 1 shows the results found for the water absorption test performed on samples at the ages of 7 and 28 days of curing, with 0 and 10% of residue insertion. The performance of the samples indicates that, at the age of 7 days, the insertion of ash had a beneficial effect on the behavior of the alkali activated material, reducing water absorption. This effect is related to the action of ash in the reactions that form the composite. The calcium present in the ash is directly responsible for the formation of products such as C–S–H gel, or C–A–S–H, when alumina participates in the reaction. This product, in coexistence with the N–A–S–H gel, resulting from geopolymerization reactions, makes the alkali activated material denser, with fewer pores [5, 6]. The reduction of pores has a direct influence on the reduction of water absorption of the samples, since it reduces the possibility of the existence of interconnected pores, which would increase the permeability of the sample, by creating paths for water to penetrate the material.

On the other hand, it can be seen that, at the age of 28 days, the presence of ash in the composite did not translate into a reduction in absorption, as occurred with the samples cured for 7 days. In fact, at 28 days the water absorption of the reference samples, that is, without residue insertion, and of those with 10% residue insertion remained statistically constant. In turn, when comparing the samples with 10% residue, at the two curing ages, 7 and 28 days, it is noted that there is an increase in water absorption for the longer curing samples, a performance that goes against the trend expected. It is believed that this behavior is linked to the phenomenon of efflorescence, which reached the samples cured for 28 days, as can be seen in Fig. 2.

In alkali activated materials, the dissolution of the aluminosilicate precursor is generally incomplete. Therefore, a portion of the alkali remains in excess in the material, free and easily charged from the N–A–S–H gel. Efflorescence in alkali activated materials is a process that occurs due to the movement of free alkali through the pore network of the material towards the surface. In contact with carbon dioxide, the alkalis crystallize on the surface of the sample, as seen in Fig. 2 [7].

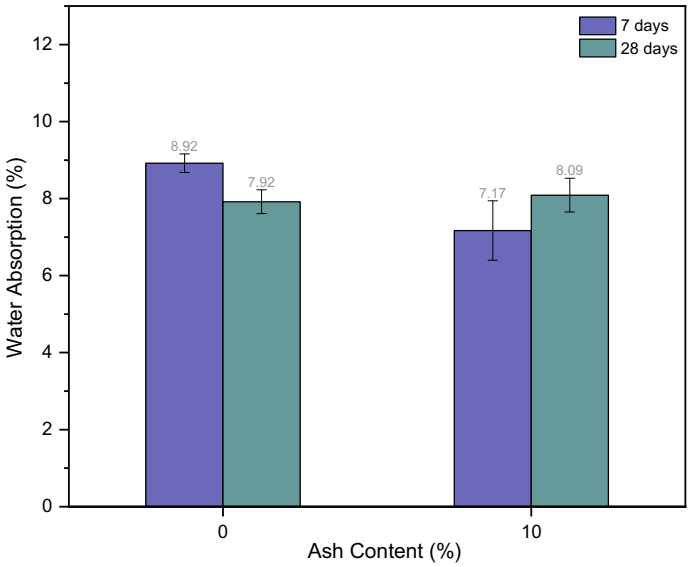

Fig. 1 Results of the water absorption test

Fig. 2 Specimens under efflorescence process

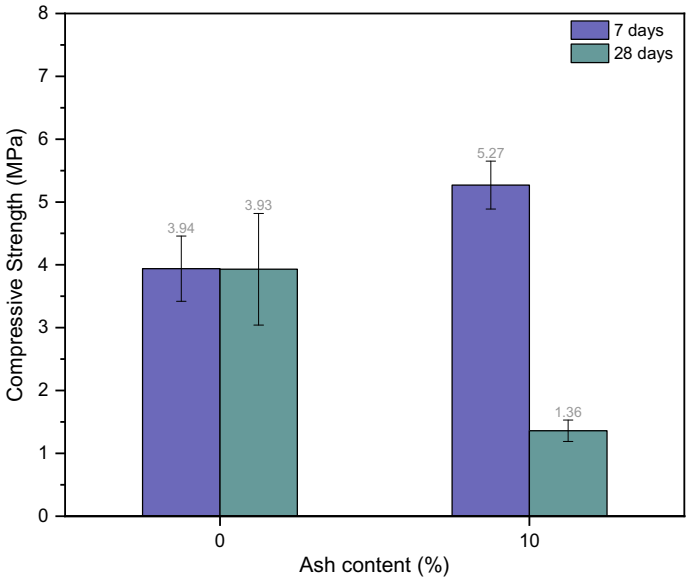

Fig. 3 Results of compressive strength test

Excessive efflorescence is related to changes in the microstructure of the composite, such as increased porosity, which justifies the increased water absorption experienced by samples affected by this phenomenon. In addition, this pathology also has the consequence of reducing the compressive and flexural strength of the material [8], as can be seen in Fig. 3.

The results obtained for the specimens after the compressive strength test can be seen in Fig. 3. It can be seen that the performance of the samples confirms the trends observed in the water absorption test, that is, at the age of 7 days the influence exerted by the ash on the geopolymerization reactions allowed an increase in the compressive strength of the alkali activated material. However, for samples at the age of 28 days, the occurrence of efflorescence compromised the microstructure of the material, reducing its strength [9].

In turn, Figs. 4 and 5 present the analysis of the weight loss of the samples after carrying out the saline attack and wetting and drying tests, respectively. It can be seen that, for all compositions, except the composition with 10% of residue insertion and age of 28 days, there was a weight loss of less than 5% at the end of 30 days of exposure to the saline environment [10]. Knowing the excellent properties of alkali activated materials in terms of durability, this result is in agreement with what was expected, according to the literature [4, 5].

On the other hand, it is observed that the worst performance was obtained for the samples with 10% of residue insertion and 28 days of age, a fact that is in accordance with the behavior presented by the composition also in the compression strength and water absorption tests [11]. The increase in the porosity of the samples,

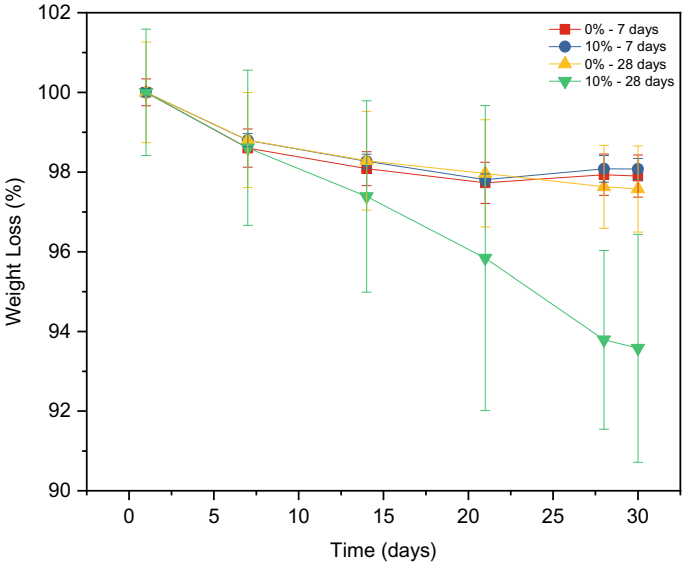

Fig. 4 Sample weight loss after saline attack cycles

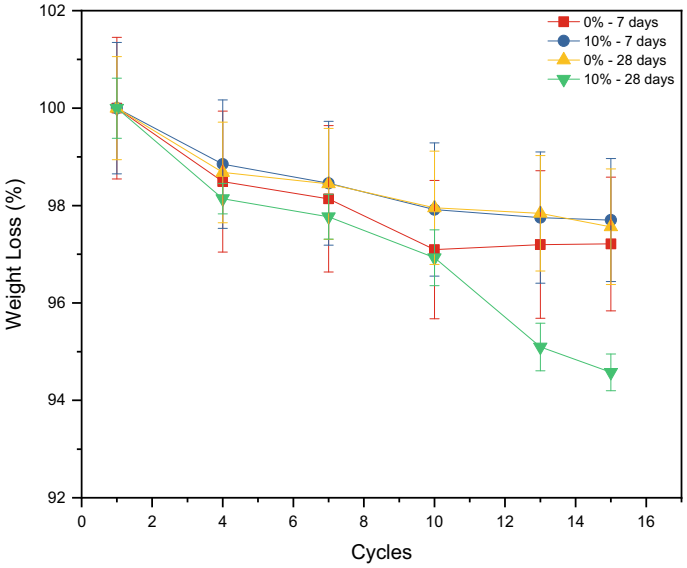

Fig. 5 Sample weight loss after wetting and drying cycles

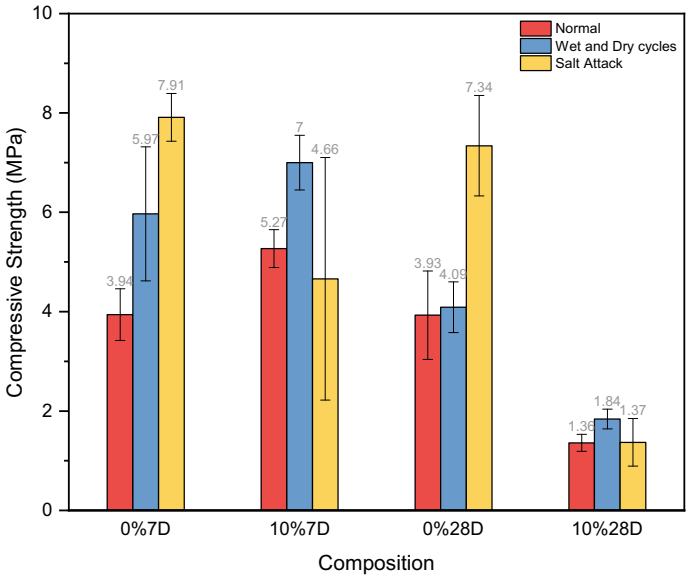

Fig. 6 Compressive strength test results after durability tests

a consequence of the efflorescence process experienced by the composition, made the material more susceptible to the action of external agents, potentiating the weight loss of the samples in the face of the durability tests performed [12].

The results of the post-durability compression strength test are shown in Fig. 6. Again, the composition with 10% residue and age of 28 days performed well below the other compositions tested. Based on the performance observed in the other tests for the same composition, such behavior is within the expected range [10].

On the other hand, it can be seen that, for all other compositions, there was an increase in the compressive strength after the salt attack tests and wetting and drying cycles. Although more analysis is necessary to conclude what caused the improvement of the resistance after wetting and drying, it is understood that, for the samples submitted to salt attack, there was the crystallization of salts in the pores of the material, which reduced the porosity and led to the increased strength observed in the test [8].

Conclusion

The strong concern with environmental preservation, currently, intensifies the search for construction materials that are eco-friendly. Activated alkali materials, in this

context, offer advantages over Portland cement, not only because they have a non-polluting production method, but because they offer the possibility of reuse for numerous industrial wastes.

Therefore, this research was successful in proving the feasibility of using biomass ash, residual from the production of ceramic artifacts, as a precursor in activated alkali materials, allied to metakaolin.

Furthermore, considering the intended application for the produced activated alkali material, that is, the use as ceramic tile, the research was successful in showing that the activated alkali produced with biomass ash manages to maintain good physical and mechanical performance under conditions of adverse applications, such as its use in environments with constant cycles of sun and rain, or places close to the sea.

However, further research is needed so that methods are adopted that aim to mitigate the efflorescence suffered by the composition with 10% insertion of residue and 28 days of curing age.

Acknowledgements This research was funded by the State University of the Northern Fluminense (UENF), partially financed by CAPES, CNPq, and FAPERJ. The participation of A.R.G.A. was sponsored by FAPERJ through the research fellowships proc.no: E-26/210.150/2019, E-26/211.194/2021, E-26/211.293/2021, E-26/201.310/2021, and by CNPq PQ2 307592/2021-9.

References

1. Goutam MA, Ramesh WU, Chakraborty R, Renu K, Vellingiri B, George A (2021) A review on modern and smart technologies for efficient waste disposal and management. J Environ Manage. https://doi.org/10.1016/j.jenvman.2021.113347
2. Yang Z, Chen H, Du L, Lu W, Qi K (2021) Exploring the industrial solid wastes management system: empirical analysis of forecasting and safeguard mechanisms. J Environ Manage. https://doi.org/10.1016/j.jenvman.2020.111627
3. Miller SA, Habert G, Myers RJ, Harvey JT Achieving net zero greenhouse gas emissions in the cement industry via value chain mitigation strategies. One Earth 4(10):398–411
4. Fu Q, Xu W, Zhao X, Bu MX, Yuan Q, Niu D (2021) The microstructure and durability of fly ash-based geopolymer concrete: a review. Ceram Int. https://doi.org/10.1016/j.ceramint.2021.07.190
5. Lekshmi S, Sudhakumar J (2022) An assessment on the durability performance of fly ash-clay based geopolymer mortar containing clay enhanced with lime and GGBS. Cleaner Mater. https://doi.org/10.1016/j.clema.2022.100129
6. Peyne J, Gautron J, Doudeau J, Joussein E, Rossignol S (2017) Influence of calcium addition on calcined brick clay based geopolymers: a thermal and FTIR spectroscopy study. Constr Build Mater. https://doi.org/10.1016/j.conbuildmat.2017.07.047
7. Longhi MA, Zhang Z, Walkley B, Rodríguez ED, Kirchheim AP (2021) Strategies for control and mitigation of efflorescence in metakaolin-based geopolymers. Cem Concr Res. https://doi.org/10.1016/j.cemconres.2021.106431
8. Marvila MT, De Azevedo ARG, De Matos PR, Monteiro SN, Vieira CM (2021) Materials for production of high and ultra-high-performance concrete: review and perspective of possible novel materials. Materials. https://doi.org/10.3390/ma14154304

9. Azevedo ARG, Marvila MT, Zanelato EB, Alexandre J, Xavier GC, Cecchin D (2020) Development of mortar for laying and coating with pineapple fiber. Revista Brasileira De Engenharia Agricola e Ambiental. https://doi.org/10.1590/1807-1929/agriambi.v24n3p187-193(InPortuguese)
10. Carvalho A, Xavier GC, Alexandre J, Pedroti LG, de Azevedo ARG, Vieira CMF, Monteiro SN (2014). Environmental durability of soil-cement block incorporated with ornamental stone waste. https://doi.org/10.4028/www.scientific.net/MSF.798-799.548
11. Marvila MT, de Azevedo ARG, de Oliveira LB, Xavier GC, Vieira CMF (2021) Mechanical, physical and durability properties of activated alkali cement based on blast furnace slag as a function of $\%Na_2O$. Case Studies in Construction Materials. https://doi.org/10.1016/j.cscm.2021.e00723
12. Zeyad AM, Magbool HM, Tayeh BA, Azevedo ARG, Abutaleb A, Hussain Q (2022) Production of geopolymer concrete by utilizing volcanic pumice dust. Case Stud Constr Mater. https://doi.org/10.1016/j.cscm.2021.e00802

Eco-Friendly Mortar with Partial Replacement of the Fine Aggregate by Polyethylene Terephthalate (PET)

I. D. Batista, K. M. S. Tavares, M. M. D. Pereira, I. S. A. Pereira, J. Alexandre, S. N. Monteiro, and A. R. G. Azevedo

Abstract The planet has been facing several environmental problems, most of which come from civil construction waste, which, in addition to being a major polluting source, still requires a large amount of raw materials removed from the environment. In order to minimize these damages, the present work aims to reduce the extraction of sand from river beds and reduce the incorrect disposal of packaging produced with polyethylene terephthalate (PET) through the partial replacement of the fine aggregate by PET in the production of mortars. Prismatic specimens were be produced with curing in 28 days of 25 °C and partial replacement of 10, 20 and 30% of the natural sand by the waste. Tests were performed on consistency, viscosity, density, mechanical strength and capillarity will be performed tests. The results showed that the partial replacement of natural sand by PET is feasible, despite some observed viscosity losses, making this mortar more ecological.

Keywords Building materials · Industrial solid waste · PET · Sustainability

Introduction

With the growth of the world population, more and more natural resources are needed to meet the needs of the planet; with this, the damage caused to the environment

I. D. Batista · K. M. S. Tavares · M. M. D. Pereira · I. S. A. Pereira
LAMAV – Advanced Materials Laboratory, UENF—State University of Northern Rio de Janeiro, Av. Alberto LamegoCampos Dos Goytacazes, Rio de Janeiro 200028013-602, Brazil

J. Alexandre · A. R. G. Azevedo (✉)
LECIV - Civil Engineering Laboratory, UENF—State University of Northern Rio de Janeiro, Av. Alberto Lamego, 2000, Campos Dos Goytacazes, Rio de Janeiro 28013-602, Brazil
e-mail: afonso.garcez91@gmail.com

J. Alexandre
e-mail: jonas@uenf.br

S. N. Monteiro
Department of Materials Science, IME—Military Institute of Engineering, Square General Tibúrcio, 80, Rio de Janeiro 22290-270, Brazil

M. Zhang et al. (eds.), *Characterization of Minerals, Metals, and Materials 2023*, The Minerals, Metals & Materials Series
https://doi.org/10.1007/978-3-031-22576-5_34

has grown exponentially. With the aim of mitigating environmental degradation, sustainable materials and methods have been increasingly researched.

According to the World Bank, about 2.01 billion tons of urban waste were generated per year [1]. Most of this waste is sent to landfills or incinerated, both options being unfavorable to sustainable development.

Solid waste can be used by being inserted into concrete and mortar, improving their properties, in addition to benefiting the environment, the economy and contributing to technological advancement [2]. When waste is incorporated into concrete or mortar, it significantly collaborates with the environment, preventing more raw material from being extracted from the environment, and more polluting gases being emitted during extraction and preparation for use [3].

The use of wastes in mortars, when used correctly, can improve the mechanical properties, in addition to removing large amounts of waste from the environment [4]. Such use also generates considerable savings, as the cost of extracting and processing the raw material will be reduced [5], along with the costs of maintaining landfills or incinerating waste.

Among the various types of waste there is plastic waste, which mostly has non-biodegradable and non-reactive properties, making it possible to pollute the environment for many years until it degrades [6]. Polyethylene terephthalate (PET) is a very common plastic nowadays, and its waste can act in the partial replacement of the fine aggregate in mortars and concrete, thus reducing the extraction of rivers and conserving their natural courses [7].

In order to reduce the environmental impacts caused by plastic waste, the 3R policy is adopted, which aims at the reuse, recycling and reduction of materials [8].

Materials and Methods

To carry out the present research, Portland Cement composed with slag (CP II E-32), natural quartz sand, removed from the bed of the Paraíba do Sul River, Polyethylene Terephthalate (PET), waste made available by the company Lubian—Telhas Translúcidas, was used and water supplied by the Águas do Paraíba concessionaire.

The mixture used was 1:4, by mass. Reference specimens were made, 0% PET, and specimens with 10, 20 and 30% replacement of the fine aggregate, sand, by PET. Table 1 presents the values of the mixtures, in mass.

Table 1 Mass mixture values

Mixture	PET (%)	Cement: sand: PET (kg)
1:4 Cement: sand/PET	0	1:4:0
	10	1:3.6:0.4
	20	1:3.2:0.8
	30	1:2.8:1.2

Fig. 1 Mortar production

The mortars were prepared according to NBR 13,276:2002 [9], and the consistency index was found for the reference mix, and the water/cement ratio was fixed for the other mixes. The specimens were molded into prismatic shapes with dimensions of 4 cm × 4 cm × 16 cm and after demolding they were stored for 28 days at an average temperature of 25 ºC. The manufacture of the mortar can be seen in Fig. 1.

The viscosity test was performed using the MVD-8 digital viscometer device, and the configurations and the cylinder were according to the material to be analyzed. The result was the average of the immediate values after making the mortar. In Fig. 2 the equipment used in the test.

The flexural and compressive strength tests were performed according to NBR 13,279:2005 [10], with a load applied at a speed of 0.5 mm/min for flexion and 2.0 mm/min for compression. The equipment used for these tests was the INSTRON 5582. Figure 3 illustrates these tests.

The capillary water absorption test and determination of the capillarity coefficient were performed according to NBR 15,259:2005 [11]. The specimens remain with water at a constant height of 5 mm for 90 min, having their mass measured before the test, at 10 and at 90 min.

Results and Discussion

The results can be found in the figures below, with Fig. 4 on the consistency index determination test. Due to the w/c ratio being fixed according to the reference, the replacement percentages did not show good workability, thus limiting the possibilities of using the mortar. The workability with replacement of 30% of PET was poor to

Fig. 2 Apparatus used for viscosity testing

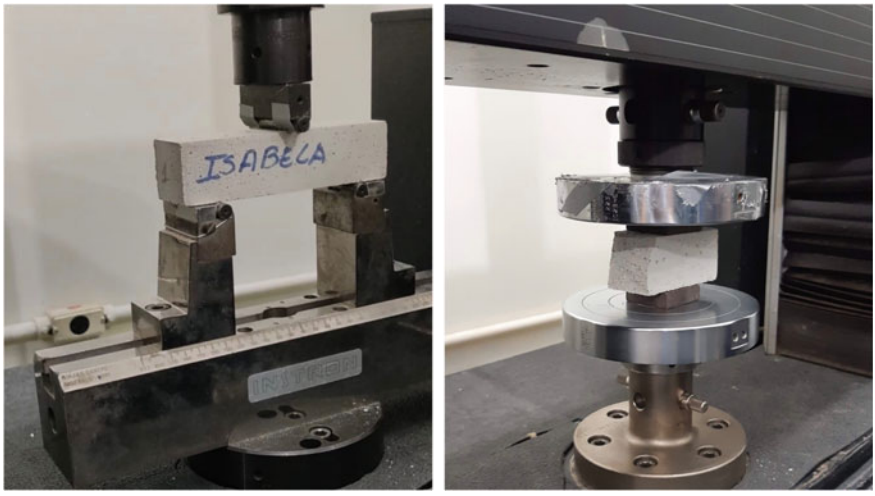

Fig. 3 Flexural and compressive strength tests

the point that it was not possible to mold the specimens, being possible to do only the tests in the fresh state in this percentage of replacement [12].

The viscosity test demonstrates that the higher the percentage of replacement of the fine aggregate by PET, the higher the viscosity of the mortar, as shown in Fig. 5. This result is consistent with the consistency test, because the higher the viscosity, the lower the workability of the material.

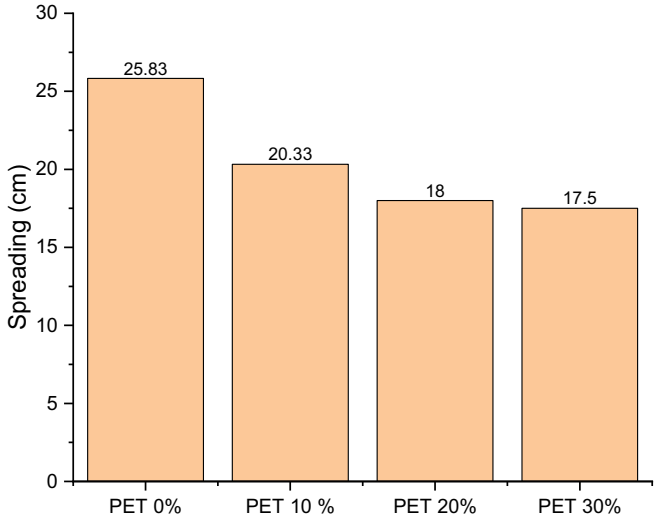

Fig. 4 Spread of each composition (in cm)

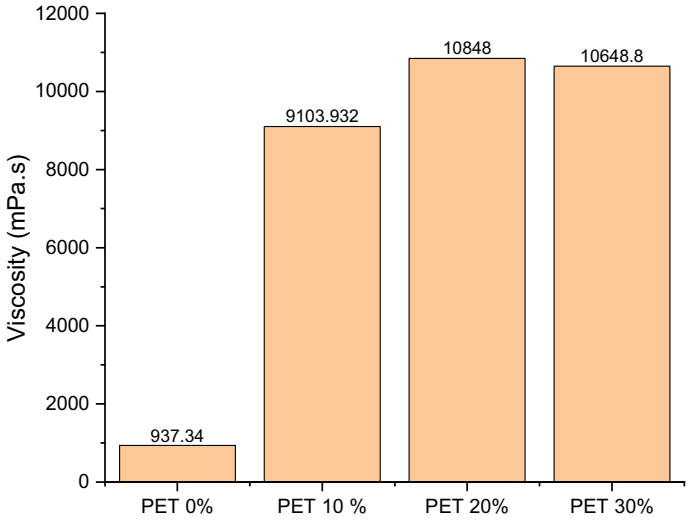

Fig. 5 Results of viscosity (in mPa s)

The density test was performed in the fresh and hardened states, and it is possible to notice that the higher the percentage of PET present in the mortar, the lower its density, due to the low specific weight that PET has, and because the plastic aggregate increases the porosity of the mortar. [12, 13]. Figure 6 demonstrates the difference in density in the different percentages and in the two physical states studied.

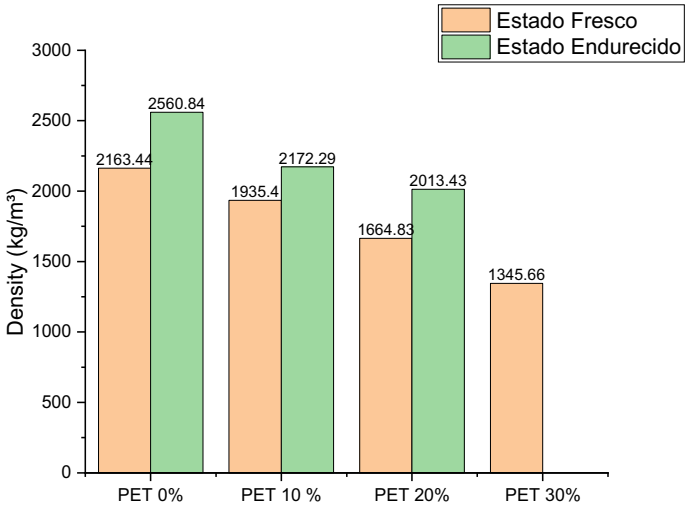

Fig. 6 Density tests in the fresh and hardened state (in kg/m^3). In orange the fresh state and in green the hardened state

The mechanical tests of flexural and compressive strength were carried out on the reference specimens, which have 0% replacement, and on the specimens with 10 and 20% replacement, since the mortar with 30% PET was not molded due to its consistency [14]. Figures 7 and 8 demonstrate, respectively, the flexural and compressive strength, both performed at the ages of 7 and 28 days. It is possible to notice that the resistance with aggregate replacement was lower than the conventional one, but still meets the minimum requirements of the standard [15, 16].

According to experimental tests, the presence of plastic aggregates reduces water absorption by capillarity [13]. However, as illustrated in Fig. 9, the values obtained showed a disordered variation, which may have occurred due to the compactness of the material, which may be studied in a future work.

Conclusion

After the results obtained, it is concluded that the mortars with partial replacement of PET did not meet the workability required for coating mortar, but this fact occurred because the water/cement ratio was fixed; in a future work the workability will be fixed, in order to meet the use of coating mortar without affecting the workability. However, the mortar studied meets the requirements for subfloor, not being totally discarded. Since the viscosity is inversely proportional to the workability of the mortar, this parameter will be corrected along with the workability, thus, when the consistency meets the requirement of 260 $\pm$ 5 mm, the consistency will have acceptable values. It is also concluded that the mortar with partial replacement of PET has

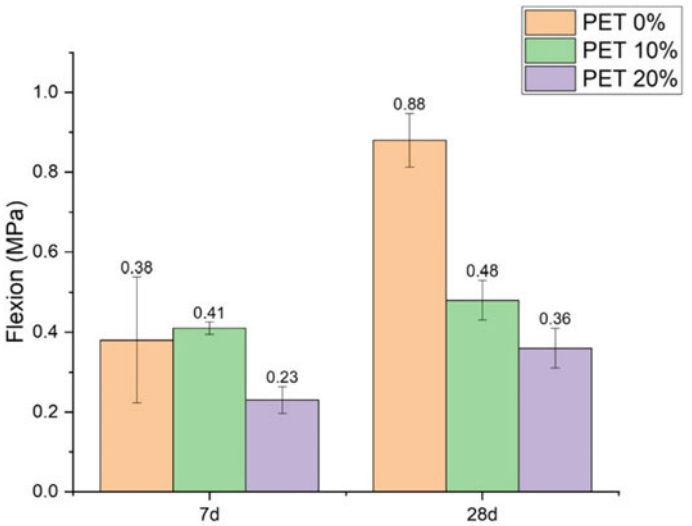

Fig. 7 Results of the flexural strength test (MPa)

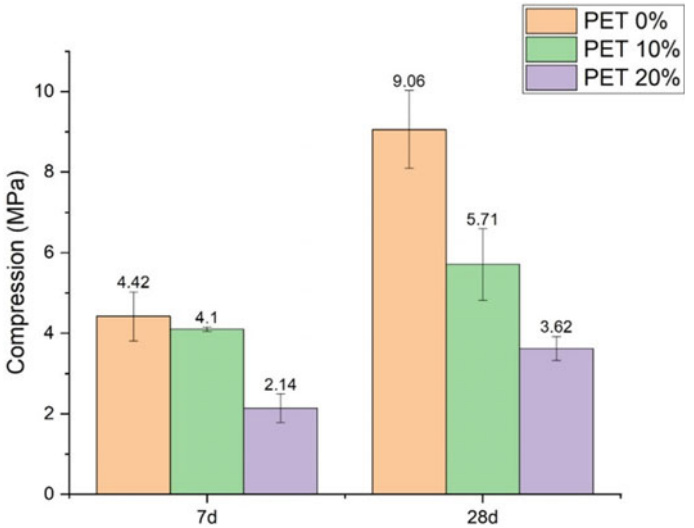

Fig. 8 Results of the compressive strength test (MPa)

a significantly lower density than the conventional mortar, reducing the structure's own weight and the cost of handling and transport.

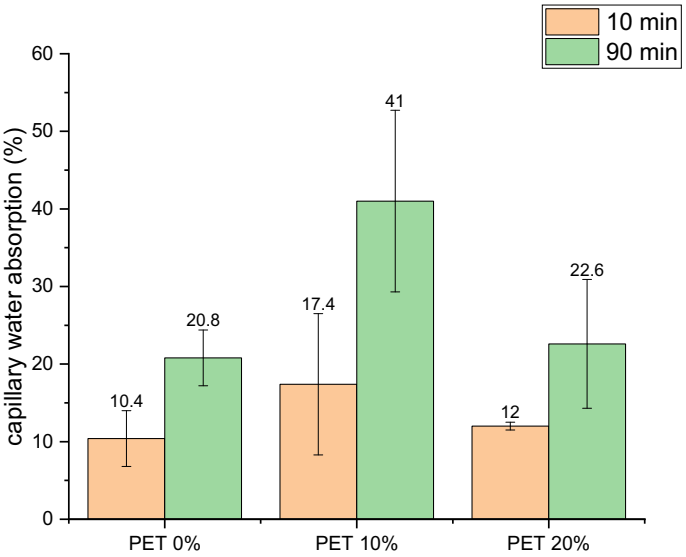

Fig. 9 Capillary water absorption (%)

Acknowledgements This research was funded by the State University of the Northern Fluminense (UENF), partially financed by CAPES (Coordenação de Aperfeiçoamento de Pessoal de Nível Superior—Brazil), CNPq (Coordenação Nacional de Pesquisa) and FAPERJ (Fundação de Apoio à Pesquisa do Estado do Rio de Janeiro). The participation of A.R.G.A. was sponsored by FAPERJ through the research fellowships proc.no: E-26/210.150/2019, E-26/211.194/2021, E-26/211.293/2021, E-26/201.310/2021, and by CNPq PQ2 307592/2021-9.

References

1. Fanran M, Aritha D, Simon JMM, Gavin HT, Alex C, Jon M (2021) Bioethanol from self-contained municipal solid waste: environmental and financial feasibility assessment under political contexts, aplic. Energy. https://doi.org/10.1016/j.apenergy.2021.117118
2. Nikita G, Rafat S, Rafik B (2021) Sustainable and greener self-compacting concrete incorporating industrial by-products: a review. J Clean Prod. https://doi.org/10.1016/j.jclepro.2020.124803
3. Wahid F, Allan M, Rafat S, Priyan M, Yan Z, Hong SW, Weena L, Thiru A, Peter S (2021) Recycling of landfill wastes (tyres, plastics and glass) in construction—a review on global waste Generation, performance, application and future opportunities. Resour Conserv Recycl. https://doi.org/10.1016/j.resconrec.2021.105745
4. Laura JG, Sam AW, Claire LC, Susan AB, Valentin L, Martin CS, John LP, Neil CH (2021) Temperature transformation of blended magnesium potassium phosphate cement binders. Cemente Concr Res. https://doi.org/10.1016/j.cemconres.2020.106332
5. Syed MSK, Muhammas JM, Yu-Fei W (2021) Application of waste tire rubber and recycled aggregates in concrete products: a new compression casting approach. Resour Conserv Recycl. https://doi.org/10.1016/j.resconrec.2020.105353

6. Mikael K, Dominique F, Gwénael LM, Stéphane B (2020) Why is there plastic packaging in the natural environmente? Understanding the roots of our individual plastic waste management behaviours, science of the total environmente. https://doi.org/10.1016/j.scitotenv.2020.139985
7. Khawla C, João PC, Ahmed W, Ana VG, Olfa H, Armando CD, Teresa RS, Mohamed K (2019) Microplastic pollution in the sediments of Sidi Mansour Harbor in Southeast Tunisia. Mar Pollut Bull. https://doi.org/10.1016/j.marpolbul.2019.06.004
8. Yasuhiko H, Chettiyapan V, Michikazu K, Agamuthu P (2016) Development of 3R policy indicators for the Asia-Pacific region: experience of the 3R Regional Forum in Asia and the Pacific. J Mater Waste Manage Cycl. https://doi.org/10.1007/s10163-015-0442-3
9. NBR 13276 (2002) Mortar for laying and coating walls and ceilings—preparation of the mixture and determination of the consistency index. Brazilian Technical Standards Association
10. NBR 13279 (2005) Mortar for laying and coating walls and ceilings—determination of tensile strength in bending and compression. Brazilian Technical Standards Assoc
11. NBR 15259 (2005) Mortar for laying and coating walls and ceilings—determination of water absorption by capillarity and capillarity coefficient
12. Nabajyoti S, Jorge B (2012) Use of plastic waste as aggregate in the preparation of cement and concrete mortar: a review. Constr Build Mater. https://doi.org/10.1016/j.conbuildmat.2012.02.066
13. Luciano DM, Bartolomeo C, Luc C, Frédéric M, Loredana I, Paola S (2018) Data on termal conductivity, water vapour permeability and water absorption of a cementitious mortar containing end-of-waste plastic aggregates. Constr Build Mater. https://doi.org/10.1016/j.dib.2018.03.128
14. Marvila MT, Azevedo ARG, Alexandre J, Zanelato EB, Azeredo NG, Simonassi NT, Monteiro SN (2019) Correlation between the properties of structural clay blocks obtained by destructive tests and ultrasonic pulse tests. J Build Eng. https://doi.org/10.1016/j.jobe.2019.100869
15. Azevedo ARG, Marvila MT, Zanelato EB, Alexandre J, Xavier GC, Cecchin D (2020) Development of mortar for laying and coating with pineapple fiber. Revista Brasileira De Engenharia Agricola e Ambiental 24(3):187–193. https://doi.org/10.1590/1807-1929/agriambi.v24n3p187-193(InPortuguese)
16. Carvalho A, Xavier GC, Alexandre J, Pedroti LG, de Azevedo ARG, Vieira CMF, Monteiro SN (2014) Environmental durability of soil-cement block incorporated with ornamental stone waste. https://doi.org/10.4028/www.scientific.net/MSF.798-799.548

Effect of Fly Ash as Additive or Substitute for Portland Cement on the Initial Absorption of Concrete Blocks (Vibro-Compacted)

Hugo García Ortiz, Édgar Martínez Rojo, Julio Cesar Juárez Tapia, Martín Reyes Pérez, and Aislinn Michelle Teja Ruiz

Abstract During this investigation, the effect of fly ash as an additive or substitute for Portland cement on the initial absorption of concrete blocks (Vibro-compacted) is reported. For comparison, a standard specimen was manufactured with Portland cement without any substitution or addition of fly ash, this standard with an initial absorption coefficient of 24.2 g/(cm^2 × min $^{.5}$), was compared with four specimens with a replacement or addition of fly ash. With this reference parameter, they were compared with the modified specimens, the first 15% of fly ash was added, reaching an initial absorption coefficient of 26.1 g/(cm^2 × min $^{.5}$) to the last three Portland cement was partially replaced in 15, 30 and 50% by fly ash with an initial absorption coefficient of 17.0, 19.5 and 22.6 g/(cm^2 × min $^{.5}$) respectively. The physical tests were carried out under the ONNCCE regulations.

Keyword Fly ash · Initial absorption · Concrete · Additive · Vibro-compacted

Introduction

About 26,913 Terawatt-hours (TWh) of electricity are produced annually [1] around the world, where more than 80% of this energy is generated by fossil fuels [2]. A relevant activity for these fuels is the burning of natural coal because it is a common

H. G. Ortiz (✉) · É. M. Rojo · J. C. J. Tapia · M. R. Pérez · A. M. T. Ruiz
Universidad Autónoma del Estado de Hidalgo, Área Académica de Ciencias de La Tierra Y Materiales, Pachuca-Tulancingo Highway, Kilometer 4.5, 42180 Mineral de La Reforma Hidalgo, Pachuca, Mexico
e-mail: hugo_garcia@uaeh.edu.mx

J. C. J. Tapia
e-mail: jcjuarez@uaeh.edu.mx

M. R. Pérez
e-mail: mreyes@uaeh.edu.mx

A. M. T. Ruiz
e-mail: aislinn_teja@uaeh.edu.mx

M. Zhang et al. (eds.), *Characterization of Minerals, Metals, and Materials 2023*, The Minerals, Metals & Materials Series
https://doi.org/10.1007/978-3-031-22576-5_35

practice in countries with reserves of this mineral, derived from this one of the main by-products of this process is “fly ash”.

The ASTM-C-618-03 standard defines this term as: “Finely divided residues from the combustion of mineral or finely ground coal transported in air currents” [3]. These ashes have been used by various researchers as high-strength cement additives or substitutes to increase compressive strength.

For several years, this ash has covered large areas of land and is known to be harmful to groundwater, which is why various studies have reported that when rainwater comes into contact with this ash, it is filtered, attracting harmful particles that cause contamination of the soil and groundwater [4].

National Geographic conducted a study titled “Finding a Safer Future for Discharged Ash from Coal-Fired Power Plants,” describing fly ash and other residues from coal combustion as one of the largest waste streams in the United States. United States and Europe, with more than 136 and 100 million respectively [5]. Meanwhile, researchers from the China Academy of Building Materials and the Building Materials Industry Technical Information Institute estimate that their countries have accumulated about 2.5 billion tons of ash from coal burning [5].

Taking into account the exorbitant amount of ash produced and its harmful effects on the environment, it is important to investigate the use of these residual products, coming from coal-fired power plants.

Qian Huang et al. in 2021 show the effect of nanosilica on compressive strength, water absorption, hydration products, microstructure and pore structures of fly ash-added concrete pastes [6].

Regarding the above, in 2003 Yasar et al. produced a mixture of lightweight concrete, where said test 20% fly ash was added as a replacement for cement based on weight, it was tested with cylindrical specimens of 150 mm in diameter and a height of 300 mm, the results obtained from the specimens with the addition of fly ash were favorable and significant and the compressive strength was reported to be 29 MPa, and the density of the concrete changed from 1955 kg/cm^2 to 1932 kg /cm^2 [7].

However, one of the main goals in recent years is to reduce the amount of cement used in the production of concrete. In this regard, in 2008, Chen B. and co-workers conducted several tests on high-strength lightweight concrete with fly ash replacing Portland cement in the range of 10% to 40% and found that the compressive strength was optimized from 10 to 20%, with the highest values at 2.5 and 6 MPa compared to a control test with a strength of 50 MPa [8].

It can be seen that the central analysis of the study by Yasar et al. [7] was the use of different percentages of ash as a substitute for Portland cement, however, the analysis of the initial absorption coefficient in concrete blocks is of vital importance in order to maintain in the quality standards of the norms for the use of these elements.

Experimentation

One of the main components in the preparation of these vibro-compacted blocks was the use of fly ash as an additive or substitute for Portland cement, for which a mineralogical and morphological characterization was carried out by means of Inel brand X-Ray Diffraction (XRD). Equinox 2000 model, in the range from 5° to 100° with Cobalt radiation (CoKα1), and a JOEL model JSM-IT300 Scanning Electron Microscope (SEM) at different magnifications.

For the manufacture of the specimens that were evaluated, ordinal Portland cement CPO-40R [9], fine stone material (sand), coarse material (gravel) and water were used as materials; using a water-cement ratio of 0.48, the block dimensions were 20 × 40 × 12 cm with two central holes under the NMX-C-038-2013 standard [10].

5 specimens were manufactured in triplicate, which were evaluated at 3, 7 and 14 days, the first we will call standard with which Portland cement was not added or substituted, specimen 2 has an addition in weight (kg) of 15% of fly ash with respect to Portland cement, specimen 3, 4 and 5 have a substitution in weight (kg) of 15, 30 and 50% of Portland cement for fly ash.

The vibro-compacted blocks were manufactured under the standard, for the reduction and separation between coarse and fine aggregates, the NMX-C-030-2004, NMX-C-170-1997 and NMX-C-077-199 standards were used [11-13]. Subsequently, to determine the specific densities of the fine and coarse aggregates, the NMX-C-164-2014 and NMX-C-165-2014 standards were used [14, 15], respectively.

Once the raw materials were obtained, the specimens were prepared, in a previously moistened mixer, 50% of the stone materials (gravel and sand) were added first, together with 50% of water. Once these materials were wet, the cement and fly ash were added at the same time the remaining 50% of water was added [16].

The mixture is left in the mixer until it is completely homogeneous, later this mixture is emptied into the molds and placed in the vibro-compaction machine for a time of 7 s, where the mold is vibrated and the mixture compacted, after In this process, the mold is removed and at this time a block has been produced in a fresh state; this only has sufficient resistance to maintain its shape and its mechanical properties such as resistance to compression or initial absorption will be acquired over time.

The initial absorption test was carried out at 7, 14 and 28 days after its manufacture under the NMX-C-037-2005 standard [17]. When the specimen has reached the age for evaluation, drying is carried out for 24 h where it must be left to rest for 6 h before the test. Once it has gone through this process, the dimensions of height, length and width are measured, the dry block is weighed, the tray, separators and water are placed for the test as in Fig. 1, and the test was carried out for a time of 10 min. After this it is removed from the tray and with a dry cloth the excess moisture is removed, the wet block is weighed, and finally the values obtained were calculated by means of the formula of the initial absorption coefficient (Cb).

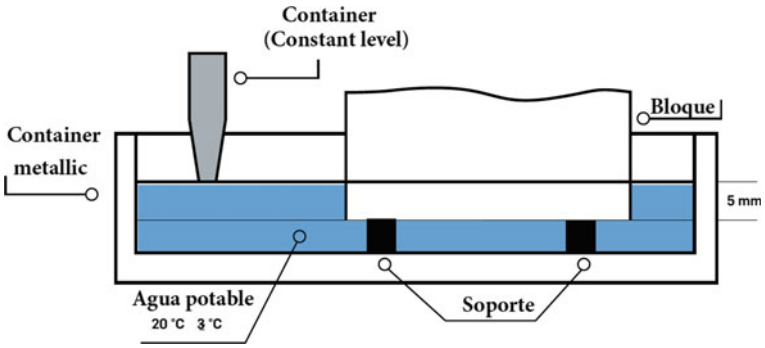

Fig. 1 Initial absorption

$$C_{\mathrm{b}} = \frac{100\,M}{S\sqrt{t}} = \frac{100(M_1 - M_2)}{S\sqrt{10}}$$

C_{b}initial absorption coefficient in g/(cm^2 × min $^{.5}$)
Mwater absorbed by the block during the test in g ($M = M_1 - M_{\mathrm{s}}$)
M_1wet mass in (g)
M_{s}dry mass in (g)
Ssurface of the submerged face in (cm^2)
$t$immersion time ($t = 10$ min)

Results

Difracción De Rayos X (DRX)

Figure 2 shows the diffractogram of the fly ash obtained by X-Ray Diffraction. It can be seen that the most important signals are quartz SiO_2 with the main peak at $2\theta \approx 31.02°$, iron oxide $Fe_2\,O_3$ (hematite) with the main peak at $2\theta \approx 41.50°$, and a species of alluminum oxide Al2O3 with the main peak at $2\theta \approx 29.71°$; these results are very similar to the diffractograms reported in the literature used, it is important to highlight that these results are characteristic of a typical mineralogical composition of fly ash and are consistent with those reported by Gomes and François in 2000 [18].

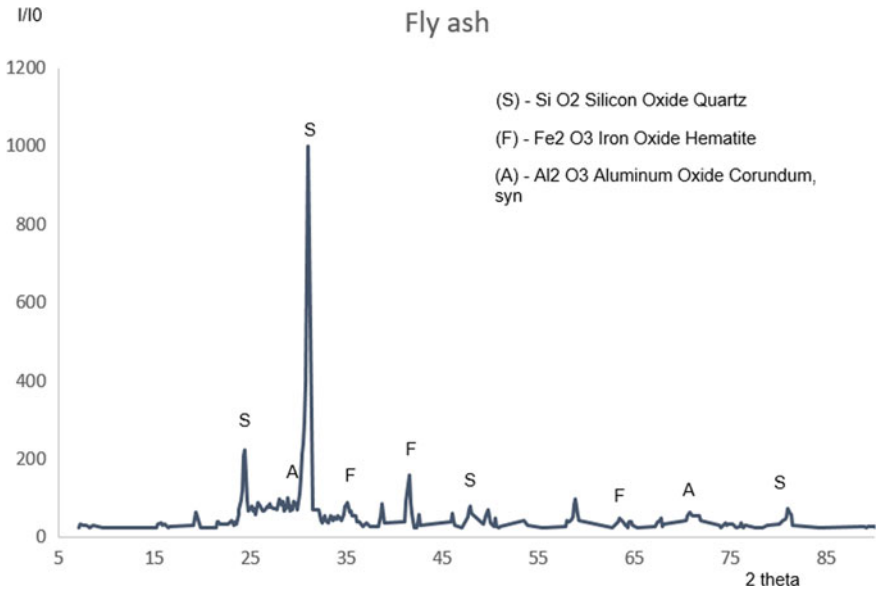

Fig. 2 Fly ash diffractogram

Scanning Electron Microscopy (SEM)

The morphology of the fly ash was analyzed by Scanning Electron Microscopy (SEM). Figure 3 shows a micrograph of the fly ash, taken with a working distance of 9.5 mm, 30 kV at 500×. A spherical morphology was observed, with a solid and smooth surface, with the size of the particles being non-uniform. Some particles present agglomeration and these results are characteristic of the fly ash, previously reported by Kutchko and Kim [19]. It can be highlighted that the morphology is a function of the carbon particle used, the combustion temperature and the cooling rate [20], so from these variables the size and shape of the fly ash can vary.

Initial Absorption Coefficient

Tables 1, 2 and 3 show the results obtained from the initial absorption coefficient, the compressive test of the vibro-compacted concrete blocks after 7, 14 and 28 days, of the different mixes including the standard sample. These results are relevant and are used to determine if the modified concrete mix undergoes changes with respect to the absorption coefficient.

In the results obtained we can see that in the different mixtures the initial absorption coefficient (C_b) has changed and we can measure the difference with the standard block. In Table 1 we can observe the results obtained after 7 days, where the highest

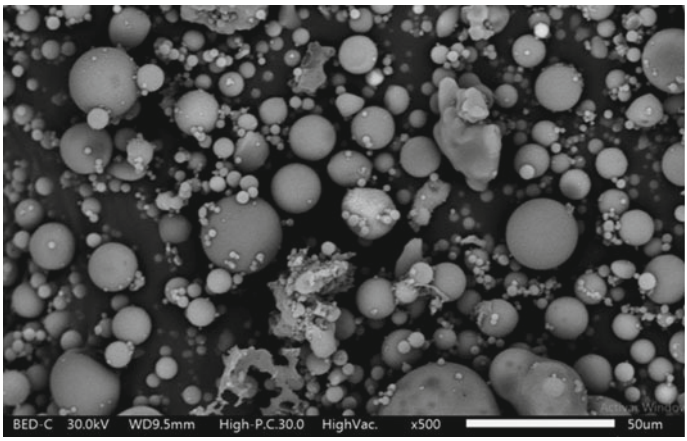

Fig. 3 Fly ash micrograph

Table. 1 Initial absorption coefficient g/(cm^2 x min $^{.5}$) at 7 days

7 days					
Sample	Standard	15% addition	15% substitution	30% substitution	50% substitution
Tall	19.9	19.9	19.9	19.9	19.9
Width	12.1	12	12.1	12.1	12
Length	39.9	39.9	40	39.9	39.9
M	550	470	520	570	680
M_1	11,090	11,280	11,230	11,150	11,210
M_s	10,540	10,810	10,710	10,580	10,530
S	794.01	794.01	796	794.01	794.01
t	10	10	10	10	10
C_b	21.9	18.7	20.7	22.7	27.1

Table. 2 Initial absorption coefficient g/(cm^2 x min $^{.5}$) at 14 days

Sample	Standard	15% addition	15% substitution	30% substitution	50% substitution
14 days					
Tall	20	19.9	20	20	19.9
Width	11.9	12	12	12	12
Length	39.9	40	40	40	40
M	650	470	470	640	630
M_1	11,410	11,180	11,610	11,240	11,390
M_s	10,760	10,710	11,140	10,600	10,760
S	798	796	800	800	796
t	10	10	10	10	10
C_b	25.8	18.7	18.6	25.3	25.0

Table. 3 Initial absorption coefficient g/(cm^2 x min $^{.5}$) at 28 days

Sample	Standard	15% addition	15% substitution	30% substitution	50% substitution
28 days					
Tall	19.9	20	20	19.9	19.9
Width	12	12	12	12	12
Length	40	40	39.9	40	40
M	610	660	430	490	570
M_1	11,390	11,050	11,260	11,460	11,300
M_s	10,780	10,390	10,830	10,970	10,730
S	796	800	798	796	796
t	10	10	10	10	10
C_b	24.2	26.1	17.0	19.5	22.6

absorption coefficient initial belongs to the vibro-compacted block with 50% substitution, with a value of 27.1 g/(cm^2 × min $^{.5}$), and the lowest value is from the block with 15% addition that is 18.7 g/(cm^2 × min $^{.5}$).

In Table 2 we can see the results obtained after 14 days, the highest initial absorption coefficient belongs to the standard vibro-compacted block, with a value of 25.8 g/(cm^2 × min $^{.5}$) and the lowest value from the block with 15% substitution is 18.6 g/(cm^2 × min $^{.5}$). In Table 3 we can see the results obtained at 28 days, the highest initial absorption coefficient belongs to the vibro-compacted block with 15% addition, with a value of 26.1 g/(cm^2 × min $^{.5}$) and the lowest value of the block with 15% substitution is 17.0 g/(cm^2 × min $^{.5}$).

In Fig. 4 we can see the behavior of the initial absorption coefficient of the 5 mixtures made at 7, 14 and 28 days of manufacture, obtaining the best result at 28 days with the vibro-compacted block with a 15% Portland cement substitution by fly ash.

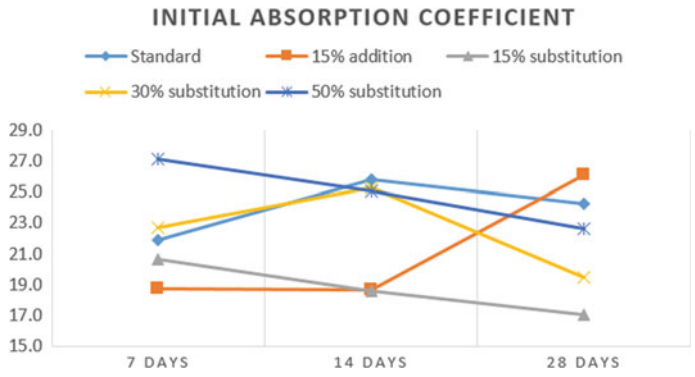

Fig. 4 Initial absorption coefficient at 7, 14 and 28 days

Fly ash is not only used as a substitute for cement, but it has also been used by Mien et al. in 2019 as an additive to improve the workability of concrete mixtures [21], because the substitution or addition of ash does not only affect the absorption coefficient but also its behavior over time.

A behavior that is observed with the mixtures in which a percentage of Portland cement was substituted for fly ash is that the values of the initial absorption coefficient are lower at 28 days compared to 14 days of manufacture.

Conclusions

The addition and substitution of fly ash affects the initial absorption coefficient in vibro-compacted blocks, having the best value with a 15% substitution of Portland cement for fly ash with $C_b = 17.0$ g/(cm^2 × min $^{.5}$).

The highest value found for the initial absorption coefficient is found after 7 days with a substitution of portland cement for 50% fly ash with $C_b = 27.1$ g/(cm^2 × min $^{.5}$).

There is a trend in the mixtures that replaced 15, 30 and 50% of portland cement with fly ash, at 14 days $C_b = 20.7, 22.7$ and 27.1 g/(cm^2 × min $^{.5}$) are higher compared to those found at 28 days $C_b = 17.0, 19.5$ and 22.6 g/(cm^2 × min $^{.5}$), respectively.

At 28 days of manufacture of the vibro-compacted blocks, the standard has a value of $C_b = 24.2$ g/(cm^2 × min $^{.5}$) being higher than the blocks with a Portland cement substitution of 15, 30 and 50% for fly ash with a $C_b = 17.0, 19.5$ and 22.6 g/(cm^2 × min $^{.5}$), finding an improvement of up to 30% in the reduction of the absorption coefficient.

References

1. Enerdata (2020) Consumo energético mundial | Consumo eléctrico | Enerdata". https://datos.enerdata.net/electricidad/datos-consumo-electricidad-hogar.html. Consultado el 4 de septiembre de 2020
2. Banco mundial (2020) Consumo de energía procedente de combustibles fósiles (% del total) | Data . https://datos.bancomundial.org/indicator/EG.USE.COMM.FO.ZS?view=map. consultado el 4 de septiembre de 2020
3. ASTM C618 – 03 (2003) Standard Specification for Coal Fly Ash and Raw or Calcined Natural Pozzolan for Use in Concrete
4. Viera SMM, Silvia M (2014) Estudio microestructural y de los procesos de hidratación de cementos con adiciones, Ph.D. thesis, ETSI Caminos, Canales y Puertos (UPM)
5. @NatGeoES (2011) Buscando un futuro más seguro para la ceniza desechada de las centrales eléctricas de carbón. *National Geographic*, el 15 de agosto de 2011. https://www.nationalgeographic.es/ciencia/buscando-un-futuro-mas-seguro-para-la-ceniza-desechada-de-las-centrales-electricas-de. consultado el 22 de agosto de 2020
6. Huang Q, Zhu X, Liu D, Zhao L, Zhao M (2021) Modification of water absorption and pore structure of high-volume fly ash cement pastes by incorporating nanosilica. J Build Eng 33:101638, ene. https://doi.org/10.1016/j.jobe.2020.101638

7. Yasar E, Atis CD, Kilic A, Gulsen H (2003) Strength properties of lightweight concrete made with basaltic pumice and fly ash. Mater Lett 57(15):2267–2270. https://doi.org/10.1016/S0167-577X(03)00146–0
8. Chen B, Liu J (2008) Experimental application of mineral admixtures in lightweight concrete with high strength and workability. Constr Build Mater 22(6):1108–1113. https://doi.org/10.1016/j.conbuildmat.2007.03.001
9. NMX-C-061-ONNCCE-2015 (2015) Industria de la Construcción—Cementantes Hidráulicos—Determinación de la Resistencia a la Compresión de Cementantes Hidráulicos
10. NMX-C-038-ONNCCE-2013 (2004) Industria de la construcción—mampostería—determinación de las dimensiones de bloques, tabiques o ladrillos y tabicones—método de ensayo
11. NMX-C-030-ONNCCE-2004 (2004) Industria de la Construcción—Agregados—Muestreo
12. NMX-C-170-1997-ONNCCE (1997) Industria de la Construcción—Agregados—Reducción de las Muestras de Agregados Obtenidas en el Campo al Tamaño Requerido para las Pruebas
13. NMX-C-077-1997-ONNCCE (1977) Industria de la Construcción—Agregados para Concreto—Análisis Granulométrico—Método de Prueba
14. NMX-C-164-ONNCCE-2014 (2014) Industria de la construcción—Agregados—Determinación de la densidad relativa y absorción de agua del agregado grueso
15. NMX-C-165-ONNCCE-2014 (2014) Industria de la construcción—Agregados—Determinación de la densidad relativa y absorción de agua del agregado fino—Método de ensayo
16. NMX-C-414-ONNCCE-2017 (2017) Industria de la construcción—Cementantes hidráulicos—Especificaciones y métodos de ensayo
17. NMX-C-037-ONNCCE-2013 (2013) Industria de la construcción—Mampostería—Determinación de la absorción total y la absorción inicial de agua en bloques, tabiques o ladrillos y tabicones—Método de ensayo
18. Gomes S, François M (2000) Characterization of mullite in silicoaluminous fly ash by XRD, TEM, and 29Si MAS NMR. Cement Concr Res 30(2):175–181. https://doi.org/10.1016/S0008-8846(99)00226-4
19. Kutchko BG, Kim AG (2006) Fly ash characterization by SEM–EDS. Fuel 85(17–18):2537–2544. https://doi.org/10.1016/j.fuel.2006.05.016
20. At H, Vories KC, Throgmorton D, Throgmorton D (1996) Coal combustion by-products and western coal mines: a technical interactive forum. Golden, Colorado
21. Van Mien T, Phuc NH, Yen CTH (2019) Effect of fly ash on shrinkage of self-compacting concrete using restrained ring test. J Sci Technol Civ Eng (STCE)-NUCE 13(3):26–33. https://doi.org/10.31814/stce.nuce2019-13(3)-03

Effect of High-Power Nanosecond Electromagnetic Pulses on the Microhardness, Physicochemical and Flotation Properties of Rare Metal Minerals

Igor Zh. Bunin, Natalia E. Anashkina, Irina A. Khabarova, and Maria V. Ryazantseva

Abstract One of the actual problems in flotation of complex niobium-tantalum ores is to develop the advanced methods to improve rare metals mineral processing efficiency by enhancing the contrast of the structural-chemical (phase) surface state and technological properties of ore and rock-forming minerals. In the recent years, various types of energy impacts have been used to enhance the contrast of the physicochemical and technological properties of minerals, and the techniques used are the radiation, ultrasound, electrochemical, laser, plasma, microwave, electromagnetic pulse, high-voltage electric pulse, and other effective methods of energy impact. In this paper, we report the results of experimental studies on the directional modification of the surface morphology (SEM–EDX), microhardness (Vickers), physicochemical (electrokinetic and electrochemical potentials, surface hydrophobicity, sorption activity) and flotation properties of columbite, tantalite, zircon, feldspar, and quartz as a result of the nonthermal effect by high-power nanosecond electromagnetic pulses. The rational pretreatment with nanosecond pulses ($t_{\text{treat}} = 100$ s is the treatment minerals time, $f = 100$ Hz is the pulse repetition rate, and $U_{\text{A}} \cong 25$ kV is the amplitude of pulses) of rare metal minerals provided higher selectivity of columbite and zircon flotation separation, without any appreciable boost in flotation activity of rock-forming minerals (feldspar and quartz).

Keywords Rare metal minerals · High-power nanosecond electromagnetic pulses · Scanning electron microscopy · Surface morphology · Microhardness · Electrode potential · Sorption · Flotation

I. Zh. Bunin (✉) · N. E. Anashkina · I. A. Khabarova · M. V. Ryazantseva
N. V. Melnikov's Institute of Comprehensive Exploitation of Mineral Resources, Russian Academy of Science (ICEMR RAS), Moscow 111020, Russia
e-mail: bunin_i@mail.ru

M. Zhang et al. (eds.), *Characterization of Minerals, Metals, and Materials 2023*, The Minerals, Metals & Materials Series
https://doi.org/10.1007/978-3-031-22576-5_36

Introduction

In recent decades, rare metals have been consumed on an ever increasing scale by industries such as microelectronics and optoelectronic (Ge, In, Ta), laser technology (Ga, Sc), automotive industry (Li), new classes of permanent magnets (Nd, Sm, Dy), high-temperature superconductors (Y, La, Sr, Bi, Tl), innovative structural ceramics (Zr, Y), materials for the aerospace industry (Ta, Nb, Li, V, Be, Re, Sc), atomic energy technology (Zr, Hf), fusion energy (Li, Be, V), powersaving solar energy (cadmium telluride, CaTe), and medicine (Ta).

A significant share of rare metal deposits in Russia have low grade of rare metals and are located in areas with challenging climatic conditions with a complete lack of infrastructure, for example Tomtor deposit in an undeveloped part of Yakutia holding unique reserves of niobium and rare-earth metals (8–12% of REM oxides). Ores from Russian rare metal deposits are in most cases polymetallic and can only be processed at a profit if all valuable components are recovered. For example, commercial development of Goltsovoye pegmatite deposit and Chuktukonskoe deposits of niobium-rare earth ore (Krasnoyarsk Territory, Boguchansky District) is economically feasible only if, in addition to niobium, tantalum, and lithium, such elements as beryllium, rubidium, cesium, and nonmetallic feldspars are recovered [1].

In the enrichment of complex niobium-tantalum ores (with Nb/Ta ratio ranging from 5 to 20) with a wide range of impregnation of industrially valuable components, the flotation method (in addition to gravity) can be used as a principal beneficiation process. However, flotation of niobium-tantalum ores remains a technological challenge because of the proximity of the physicochemical properties of the mineral surfaces of ore and rock-forming minerals belonging in terms of their flotation properties to the same class of silicates and oxides. In addition, the surfaces of both the commercial minerals (columbite, tantalite, columbite-tantalite (coltan), zircon) and the rock-forming minerals (quartz, feldspar) are often heavily ferruginized, which brings their process properties even closer, and the use of highly efficient flotation reagents such as hydroxamic acids does not always produce the desired results [2, 3].

In recent years, various types of energy impacts have been used to enhance the contrast of the physicochemical and technological properties of natural minerals: electrochemical, radiation, ultrasound, laser, plasma, microwave, electric pulse impact and high-power electromagnetic pulse effect, and other methods [2-8]. In [9], we presented the results of comprehensive experimental investigations of the mechanism for structural and chemical surface transformations of tantalite, columbite, and zircon in leaching with acid solutions, including activation of dissolution of iron- and silicate-containing films from the mineral surface, and intensive oxidation of iron atoms in the surface layer of tantalite and columbite with transition of Fe(II) to Fe(III) and destruction of zircon surface with formation of oxygen-vacancy defects of SiO_3^{2-}, SiO_2^0-types under anolyte (pH < 5) treatment. In [9] a higher efficiency of acid water electrolysis product (anolyte) for targeted alteration of chemical and phase composition of the surface, microhardness, physicochemical, electrochemical, and electrical properties of rare metal minerals and feldspar as compared to HCl solution

was experimentally demonstrated and practiced in conventional finishing preparation of rough tantalum–niobium gravity concentrates for flotation.

In this paper, we report the results of experimental investigations on the mechanism of modification of the surface structure (SEM–EDX), microhardness (Vickers), physicochemical (electrochemical and electrokinetic potentials, surface hydrophobicity, sorption activity) and flotation properties of columbite, tantalite, zircon, feldspar, and quartz as a result of the nonthermal treatment by high-power nanosecond electromagnetic pulses (HPEMP [10, 11]). The study purpose is to examine and substantiate the rational mode of preliminary electromagnetic pulse effect and appropriate reagent flotation modes to improve the selective flotation process parameters of rare metal minerals.

Experimental

Minerals

We performed our studies using monomineral fractions of rare metal minerals (columbite, tantalite, zircon), and rock-forming (host rock) minerals (feldspar, quartz) produced from rough gravity concentrates in the gravity–magnetic–electrical flowsheet. The gross elementary composition of specimens was evaluated by atomic–emission spectroscopy with inductively coupled plasma (Varian Vista CCD Simultaneous ICP–AES).

The *columbite* with the formula $(Mn_{0.91}Fe^{2+}_{0.08}Fe^{3+}_{0.01})_{1.00}(Nb_{1.79}Ta_{0.20}Ti_{0.01})_{2.00}O_{6.00}$ (stoichiometric formula, (Fe, Mn)(Nb, Ta)$_2$O$_6$) was in granular form with grain sizes of (–3 + 0.5) mm. The *tantalite* we used contained small amounts of Ti^{4+} and Sn^{4+} admixtures and was essentially a manganese-containing niobio–tantalite mineral with the formula $Mn_{0.80}Fe^{2+}_{0.15}Fe^{3+}_{0.05})_{1.00}(Ta_{1.15}Nb_{0.80}Ti_{0.03}Sn_{0.02})_{2.00}O_{6.00}$ (stoichiometric formula, (Fe, Mn)(Ta, Nb)$_2$O$_6$. The *zircon* grains of –300 μm in size contained isomorphic impurity Hf^{4+} and hydroxyl groups; the composition of specimens was described by formula $(Zr_{0.85}Hf_{0.03})_{0.88}[Si_{1.00}O_{3.52}(OH)_{0.48}]$. The minerals of the host rocks (rock-forming minerals) are represented by *feldspar*, mass %: Si–70.57, Al–10.58, K–11.09, Na–1.16, Ca–0.67, Fe_{total}–0.92, Fe(II) – 0.52, Fe(III) – 0.40, and *quartz* (SiO_2), mass %: Si–91.32, Fe_{total}–0.35, Fe(II) – 0.22, Fe(III) – 0.13. Data on the chemical composition, morphology, and crystallographic properties of these studied minerals are detailed in [2, 3, 9].

Impulse Generators

We treated mineral samples under normal conditions in air with high-power nanosecond electromagnetic pulses using a 100 Hz repetition pulses rate special high-voltage pulse generator (ICEMR RAS, and NPP FON, Ryazan) based on capacitive energy storage. The output pulse amplitude was 20–30 kV, the duration of the leading edge of the pulse varies from pulse to pulse within 2–5 ns, and the pulse duration varies within 4–10 ns. Repetitive voltage pulses of a bipolar shape are generated, pulse energy was ~ 0.1 J, electric field strength in the inter-electrode gap was (0.5–1) $\times$ 10^7 V $\times$ m^{-1}, time range of the minerals pulsed treatment was t_{treat} = 10–150 s.

Analysis Methods

The morphological features of the surface of minerals were studied on individual crystals and grains specially selected from the entire sample of minerals. We used analytical scanning electron microscopy (SEM–EDX) on a LEO 1420VP microscope equipped with an INCA Oxford 350 analyzer. Mineral specimens were fixed by two-sided graphite scotch, and the thin conductive graphite layer was plated on the specimen's surface, if required. Microhardness of mineral specimens before and after high-power electromagnetic pulse treatment was on thin polished sections according to Vickers method (*HV*, MPa) using a PMT-3 M (LOMO, Russia) microhardness tester. The load on the indenter was 100 g for rare metal minerals, and 200 g for quartz and feldspar specimens; the period of loading was 10–15 s. The technique for measuring the microhardness of the minerals surface described in detail in [12].

Electrokinetic potential (ζ-potential, mV) of rare metal minerals and feldspar particles of less than 10 μm in size was measured by the dynamic (electrophoretic) light dispersion with the use of Zetasizer Nano ZS system for examination of nanoparticles (Malvern Instrum's); ζ-potential was assessed in distilled water at pH 6–6.5. Electrochemical properties of tantalite and zircon (electrode currentless potential; *E*, mV) were measured by potentiometric titration with concurrent control of mineral potential and medium pH, whose value was adjusted by adding 0.1 n NaOH solution; medium pH variations ranged within 2.1–11. Working electrodes were made of separated mineral grains of ~ 5 $\times$ 5 $\times$ 5 mm in size, with none of inclusions or defects visible under binocular microscope. Saturated chlorum-silver electrode was selected as a reference electrode.

The surface hydrophobicity of columbite, tantalite, and zircon particles of –2 + 1 mm in size before and after HPEMP treatment was evaluated in 500 mg/l caprylhydroxamic acid solution (C8), pH 2.1 with a special device (V. A. Glembotsky's contact device). Based on the data on mineral surface hydrophobicity the test crystals were classified into hydrophobic and hydrophilic ones [2]. Hydrophobic were particles which adhered to an air bubble in contact for less than 50 ms. Hydrophilic were particles which failed to adhere during more than 5 s. The balance were grains

that attached to an air bubble within an interval from 50 ms to 5 s, and they were classified as mixed type crystals.

The procedure for conducting the experiments based on the adsorption measurements had a number of following steps. Mineral samples with weighing 1.00 g (particle size, − 100 + 63 μm) in the initial state and after HPEMP treatment were mixed (agitated) in a laboratory flotation chamber at pH 2.5 (HCl, S: L = 1: 10) for 3 min; a reagent solution (caprylic hydroxamic acid; 800 mg × L^{-1}) was then added to the chamber, and the mineral particles remained in contact with this reagent for 3 min. The solid phase was then separated by filtration, washed with a tenfold volume of distilled water, dried in air, and analyzed via Diffuse reflectance infrared Fourier transform spectroscopy (DRIFTS).

DRIFT spectra were recorded in the spectral range of 4000 to 400 cm^{-1} with a resolution of 4 cm^{-1}, using a Shimadzu IR-Affinity IR Fourier spectrometer equipped with a Pike Technologies Diffuse IR adaptor. At least ten spectra were recorded for each sample, and 100 scans were made for each spectrum. To establish the semi-quantitative characteristics of reagent adsorption on mineral particles before and after the action of an HPEMP, IR–spectra were processed and analyzed using Shimadzu IR Solution special software.

Flotation activity of monomineral powdered specimens of columbite, zircon, and feldspar was evaluated by a mineral recovery to the froth product in presence of caprylhydroxamic acid at acid pH 2.1. Flotation tests were conducted before and after electromagnetic pulsed pretreatment of mineral specimens of 1 g of –80 + 40 μm in size at a laboratory flotation machine with a chamber of 20 ml at 1 min agitation time with a reagent, 2 min flotation time.

Results and Discussion

Minerals of rare metals had a surface of fracture (break) from stepwise uneven to conchoidal. In the initial state (before effect of HPEMP), the surface of columbite and tantalite was smooth and characterized by the presence of individual genetic microcracks (Fig. 1ad). According to SEM data the electromagnetic pulse treatment of rare metal minerals (t_{treat} = 10–100 s) caused the opening of mineral intergrowths along the grain boundaries of ore and rock-forming minerals, formation of intercrystalline and transcrystalline microcracks (Fig. 1b, f), and disintegration (separation) of mineral fragments (Fig. 1e). The result of HPEMP processing (t_{treat} = 100 s) resulted in such additional defects as erosion pits on the columbite and tantalite surfaces (Fig. 1c).

The surfaces of tantalite and zircon (and, to a lesser extent, feldspar and quartz) were characterized by atomic redistribution of the substance of the surface phases, and the enlargement and localization of secondary phase fragments, mainly in areas of surface defects, likely, due to desorption and surface diffusion processes. Analysis of X-ray radiation distribution over SEM–EDX scanning area indicates some slight rise of iron and oxygen neoformation content at concurrent reduction in niobium,

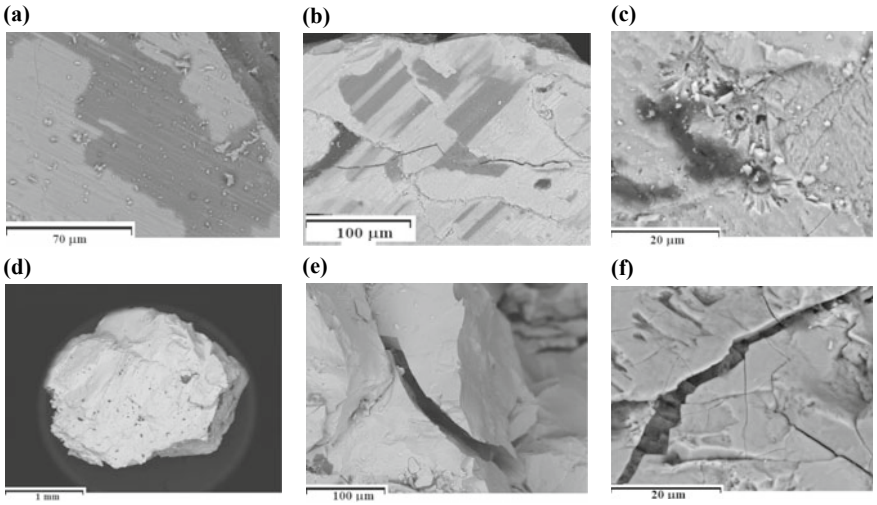

Fig. 1 SEM micrographs of **a**–**c** columbite, **d**, **e** tantalite, and **f** zircon surfaces **a**, **d** before and **b**, **c**, **e**, **f** after exposure to a high-power nanosecond electromagnetic pulses (t_{treat} = 50–100 s). Scale: **a** 70, **b**, **e** 100, **c**, **f** 20 μm, and **d** 1 mm

manganese and tantalum amount (Fig. 2). The recorded contrast between surface Nb and O was mainly due to specific features of relief on the tantalite surface. The observed changes in the minerals' surface morphology were apparently due to the nonthermal action [10, 13] of the microwave components of nanosecond electromagnetic pulses generating an additional motive force that caused mass transfer in the semiconductor crystals [14].

Microstructural transformations in the surface layers of the rare-metal minerals, feldspar, and quartz caused by the effect of nanosecond HPEMP, resulted in changes in surface morphology and the effective softening of the minerals, particularly the coarsening of the samples' surfaces with increasing altitude (amplitude) of roughness, and relative variations (reductions) of 29–37% in the microhardness of the minerals. The electromagnetic pulse treatment of columbite and tantalite (hardness

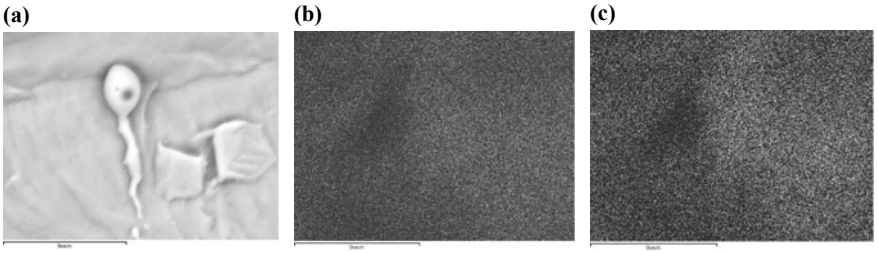

Fig. 2 **a** New formations on the tantalite surface caused by HPEMP (t_{treat} = 50 s); **b** Nb and **c** O distribution maps; **a**–**c** SEM–EDX, scale 9 μm

after Mohs scale being ~ 5.5–6.5) led to reduction in microhardness of minerals from 990 and 1020 MPa in the initial state to 700 and 710 MPa (after HPEMP treatment for $t_{treat} = 300$ s) for columbite and tantalite, respectively. The relative reductions in the microhardness ΔHV after HPEMP treatment was observed at $t_{treat} = 30$–50 s and was equal to ~ 20%. For zircon and feldspar (Mohs hardness being 7–8 and ~ 5.5–6.5, respectively) 32–35% appreciable relative reduction in hardness from 1590 to 1090 MPa for zircon and from 1530 to 990 MPa for feldspar was recorded at large radiation doses ($t_{treat} = 100$–150 s). The impact of pulse energy substantially softened the quartz surfaces (Mohs hardness 7) and monotonically lowered the microhardness of the mineral as the duration of HPEMP treatment grew ($t_{treat} = 10$–150 s). The maximum relative change (drop) in quartz microhardness was recorded at $t_{treat} = 150$ s, which was 29% (from 1425 to 1015 MPa).

The greatest changes in the mineral electrokinetic potential (ζ-potential, mV) were caused by preliminary electromagnetic pulse processing of the mineral samples in the range of time treatment variation $t_{treat} = 10$–100 s. Columbite and tantalite were characterized by nonlinear variations in the ζ-potential with local maxima toward growing negative values of columbite at $t_{treat} = 50$ s (from -16.7 to -18.6 mV), followed by reductions in the absolute potential value at $t_{treat} = 100$ s. Zircon was characterized by antibate changes in its electrokinetic potential: a drop in the absolute ζ-potential at $t_{treat} = 50$ s (from -17.1 to -11.8 mV) and a rise in it at $t_{treat} = 100$ s (up to -17.4 mV). The contrasting (antiphasic) change in the potentials of tantalite and feldspar upon increasing the time of HPEMP treatment should be noted, so that, at $t_{treat} = 100$ s, the absolute value of the electrokinetic potential of tantalite (-19.6 mV) was less than the ζ-potential of feldspar (-22.1 mV).

Studying into the electrochemical properties of tantalite and zircon surface revealed that in HPEMP treatment of minerals ($t_{treat} = 100$ s) the currentless electrode potential (E, mV) shifted to the positive-value domain by 30–90 mV under the pH variations within 2–8 for tantalite and lowered by 43 mV (pH 2.1) for zircon as compared to the initial mineral state without electromagnetic pulsed treatment. The maximum difference $\Delta E = E_{puls} - E_0$ in values is recorded in alkaline medium at pH 10; for tantalite it is $\Delta E_{max} \cong 90$ mV. The HPEMP treatment ($t_{treat} = 100$ s) generated dehydroxylation (dehydratation) of columbite (tantalite) surface with removal of adsorbed hydroxyl ions and possible partial destruction of the surface iron hydroxide films, inducing a shift of the electrode potential to the positive value domain. Such alteration of tantalite potential can also relate to variations in equilibrium concentration of free charge carriers and formation of an excess number of electron vacancies (holes) under the effect of high-voltage electric fields. Apparently, alteration of tantalite and columbite surface charge creates favorable conditions for attachment of a flotation reagent (caprylhydroxamic acid) on mineral surface and improves of their floatability. The reverse situation was observed for zircon: the increase in the number of free electrons and the reduction in the electrode potential created conditions to lower sorption of the reagent on the mineral surface and to diminish its flotation activity.

According to our IR Fourier spectroscopy data, the flotation reagent (caprylhydroxamic acid) was fixed on the initial (without effect of HPEMP) columbite surface

mainly as hydroxamic complexes (Fe(III), Ta and Nb hydroxamates, with peaks at 1530 cm^{-1} and 1600 cm^{-1}) [15], testifying to the chemical sorption of the reagent. There was no appreciable reagent fixing in the molecular (physical) form (peak at 1670 cm^{-1}). Electromagnetic impulse treatment of mineral particles had no appreciable effect on the sorption character of reagent molecules, but it did contribute to the sorption activity of the columbite surface. The transformation of the 1670 cm^{-1} shoulder on the IR–spectra of the initial samples into the absorption band of the HPEMP treated columbite particles points to a higher number of physically fixed reagent molecules.

Quartz was characterized by physical (a peak at 1678 cm^{-1}) and chemical (peaks at 1512 and 1612 cm^{-1}) reagent sorption on the surfaces of the initial particles, while zircon was characterized by chemical sorption (a 1540–1600 cm^{-1} doublet) reagent fixing. Preliminary HPEMP treatment of minerals resulted in lower sorption activity of quartz particles: a 1.3–1.6-fold reduction in area of the 2750–3000 cm^{-1} multiplet corresponding to vibrations of the C–H bonds of the reagent's hydrocarbon skeleton. This testifies to the lower sorption activity of the mineral surface due to the nonthermal action of high-voltage nanosecond pulses. The integral characteristics of reagent adsorption on the feldspar surface did not change during HPEMP processing throughout the all time range of the mineral pulsed treatment.

The obtained results of SEM–EDX and spectroscopic studies comply with the data on changes in the hydrophobicity and floatability of minerals under conditions of pulsed energy impacts. Most columbite, tantalite, and zircon particles in the initial (before HPEMP treatment) state in the presence of caprylhydroxamic acid had a hydrophobic or mixed type surface. As a result of preliminary electromagnetic pulse treatment of minerals for $t_{treat} = 50$–100 s, the hydrophobicity of columbite and tantalite particles' surface increased by an average of 6–9% due to the removal of hydroxyl groups and chemisorbed water from the surface of minerals. With an increase in the pulse treatment time up to $t_{treat} = 150$ s, a decrease in the hydrophobic properties of the surface of mineral particles was observed down to the initial state.

Alternatively to columbite and tantalite, the hydrophobocity of zircon surface reduced in average by 1–6% with increase in HPEMP treatment time by up to $t_{treat} = 50$ s owning to the adsorption of hydroxyl ions and water molecules on the mineral surface. Growth of a radiation dose up to $t_{treat} = 150$ s caused local heating of mineral particles. This effect promoted the removal of hydroxyl ions and water molecules from zircon surface, thus improving the hydrophobic properties of the mineral.

In the range of short treatment time ($t_{treat} \leq 50$ s) floatability of columbite (caprylhydroxamic acid concentration being 500 ml/l) remained actually constant, and the flotation recovery of the mineral was $\varepsilon \cong 72\%$. The pulse pretreatment of columbite with variation in $t_{treat} = 50$–300 s allowed 4–9% improvement of flotation activity of columbite. Thereat, the best parameter $\varepsilon = 81\%$ was gained at pulse treatment within $t_{treat} = 100$ s. In this range of $t_{treat} = 50$–300 s HPEMP pretreatment of zircon aggravated floatability of the mineral in average by 5% (from 62 to 57%); the maximum fall of ε was observed at $t_{treat} = 100$ s.

The optimal mode of pulse energy effect ($t_{treat} = 100$ s) at a higher concentration of caprylhydroxamic acid up to 800 mg/l contributed to higher results of ore mineral

flotation: columbite and zircon recovery into the froth product was 91 and 59%, respectively. The nonthermal HPEMP effect on feldspar and quartz specimens did not induce an appreciable variation in flotation activity of the rock-forming minerals.

Conclusions

As a result of the comprehensive studies of the effect of directed modification of structural-chemical, physicochemical, and technological (flotation) properties of rare metal minerals by applying the high-power nanosecond electromagnetic pulses we enabled to substantiate the rational mode of preliminary electromagnetic pulse treatment of rare metal minerals $t_{\text{treat}} \cong 100$ s. The HPEMP pretreatment of rare metal mineral provides higher selectivity of columbite–zircon separation (columbite separation from zircon), as the difference values in mineral recovery into the froth product $\Delta\varepsilon$ before and after impulse treatment amounted to 11 and 24.5%, respectively. The optimal mode of pulse energy effect at a higher concentration of caprylhydroxamic acid up to 800 mg/l contributed to higher results of ore mineral flotation: columbite and zircon recovery into the froth product was 91% and 59%, respectively, without any appreciable boost in flotation activity of feldspar and quartz.

Our results demonstrate the actual feasibility to apply the nonthermal high-power nanosecond electromagnetic pulses effects to improve disintegration and opening of finely disseminated rare metal mineral aggregates, to realize the directed modification of their structural-chemical, electrochemical, physicochemical, and flotation properties and to boost the process parameters in flotation of rough tantalum-niobium gravity concentrates.

Acknowledgements This work supported in part by the President of the Russian Federation under contract number NSh 7608.2016.5 (Academician V.A. Chanturiya's scientific school), and in part by the Russian Science Foundation, project no. 16-17-10061. The authors are grateful to Cand. Sci. (Geol.−Mineral.) E.V. Koporulina of Moscow State University for her help with the SEM−EDX experiments.

References

1. Serdyuk SS, Lomaeva VG., Kuzminb VI (eds) (2015) Krasnojrskiy Cluster—strategic development priorities rare metal industry Russia. J Siberian Federal Univ Eng Technol 8(7):816−834. https://doi.org/10.17516/1999-494X-2015-8-7-816-834
2. Chanturiya VA, Chanturiya EL, Ryzantseva MV, Khabarova IA (2016) The effect of acid-pretreatment upon hydroxamic acids sorption and rare metals' minerals flotation. Obogashchenie Rud (Miner Processing J). 5:19–24. https://doi.org/10.17580/or.2016.05.04
3. Chanturiya VA, Ryzantseva MV, Chanturiya EL (eds) (2017) The mechanism of structural and chemical transformations of tantalite, columbite, and zircon surfaces in the process of acid and electrochemical treatment of mineral suspensions. Dokl. Earth Sc 473:472–476. https://doi.org/10.1134/S1028334X1704016X

4. Bunin IZh, Ryazantseva MV, Samusev AL, Khabarova IA (2017) Composite physicochemical and energy action on geomaterials and aqueous slurries: theory and practice. Gornyi Zhurnal (Min J) 11:77−83. https://doi.org/10.17580/gzh.2017.11.14
5. May F, Hamann S, Quade A, Bruser V (2017) Froth flotation improvement by plasma pretreatment of sulfide minerals. Miner Eng 113(11):95–101. https://doi.org/10.1016/j.mineng.2017.08.009
6. Ran J, Qiu X, Hu Z, Liu Q, Song B, Yao Y (2019) Enhance flotation separation of arsenopyrite and pyrite by low-temperature oxygen plasma surface modification. Appl Surf Sci 480(6):1136–1146. https://doi.org/10.1016/j.apsusc.2019.02.172
7. Huang W, Chen Y (2021) The application of high voltage pulses in the mineral processing industry. Powder Technol 393(11):116–130. https://doi.org/10.1016/j.powtec.2021.07.003
8. Rostovtsev VI, Bryazgin AA, Korobeinikov MV (2020) Improvement of milling selectivity and utilization completeness through radiation modification of mineral properties. J Miner Sci 56:1000–1009. https://doi.org/10.1134/S1062739120060125
9. Chanturiya VA, Chanturiya EL, Bunin IZh (eds) (2016) Effect of acid and electrochemical treatment on physicochemical and electrical properties of tantalite, columbite, zircon and feldspar. J Miner Sci 52:778–792. https://doi.org/10.1134/S1062739116041190
10. Bunin IZh, Bunina NA, Vdovin VA, Voronov PS, Gulyaev YuV, Korzhenevsskii AV, Lunin VD, Chanturiya VA, Cherepenin VA (2001) Experimental studies of non-thermal effect of high-power electromagnetic pulses on rebellious gold-bearing raw materials. Bull Russ Acad Sci Phys 65(12):1788–1792
11. Chanturiya VA, Bunin IZh, Ryazantseva MV, Filippov LO (2011) Theory and applications of high-power nanosecond pulses to processing of mineral complexes. Miner Process Extr Metall Rev 32(2):105−136. https://doi.org/10.1080/08827508.2010.530722
12. Bunin IZh, Chanturiya VA, Anashkina NE (eds) (2015) Experimental validation of mechanism for pulsed energy effect on structure, chemical properties and microhardness of rock-forming minerals of kimberlites. J Miner Sci 51:799−810. https://doi.org/10.1134/S1062739115040177
13. Cherepenin VA (2006) Relativistic multiwave oscillators and their possible applications. Phys Usp 49(10):1097–1102. https://doi.org/10.1070/PU2006v049n10ABEH006109
14. Zayats NS, Konakova RV, Milenin VV (eds) (2015) Microwave-radiation-induced structural transformations in homo- and heterogeneous GaAs-based systems. Tech Phys 60:432–436. https://doi.org/10.1134/S1063784215030299
15. Cui J, Hope GA, Buckley AN (2012) Spectroscopic investigation of the interaction of hydroxamate with bastnaesite (cerium) and rare earth oxides. Miner Eng 36–38:91–99. https://doi.org/10.1016/j.mineng.2012.03.001

Evaluation of Coating Mortars with the Addition of Natural and Treated Açaí Seed (*Euterpe Oleracea Mart.)*

G. P. Monteiro, M. T. Marvila, R. Fediuk, S. N. Monteiro, and A. R. G. Azevedo

Abstract The açaizeiro is a palm tree found on a large scale in the northern region of Brazil, one of the main non-timber forest products with great economic potential. However, the residues, which represent about 85% of the total fruit, cause a serious environmental problem, since about 365 tons of açaí seeds are discarded daily, with no provision for reuse. This research studies the feasibility of adding these residues to the coating mortars through the partial replacement of sand, in 10% of the mass. four compositions were used, one being a reference (trace 1:3) and the others with the presence of the residue. The mortars were subjected to tests in the plastic and hardened state. It is concluded that the addition of seed in all compositions generates a reduction in mechanical strength and few changes in properties in the fresh state.

Keywords Açaí · Mortar · Construction

Introduction

The construction industry, in the last year, was responsible for 660 million tons of aggregates in Brazil, affecting the civil form due to environmental consumption [1]. At the same time that it generates a negative impact through the construction of a manufacturing device, civil construction has the ability to absorb the different

G. P. Monteiro · M. T. Marvila
LAMAV—Advanced Materials Laboratory, UENF—State University of Northern Rio de Janeiro, Av. Alberto Lamego, 2000, Campos Dos Goytacazes, Rio de Janeiro 28013-602, Brazil

R. Fediuk
Far Eastern Federal University, Ulitsa Mordovtseva, 12, Vladivostok 690091, Russia

S. N. Monteiro
Department of Materials Science, IME—Military Institute of Engineering, Square General Tibúrcio, 80, Rio de Janeiro 22290-270, Brazil

A. R. G. Azevedo (✉)
LECIV—Civil Engineering Laboratory, UENF—State University of Northern Rio de Janeiro, Av. Alberto Lamego, 2000, Campos Dos Goytacazes, Rio de Janeiro 28013-602, Brazil
e-mail: afonso.garcez91@gmail.com

M. Zhang et al. (eds.), *Characterization of Minerals, Metals, and Materials 2023*, The Minerals, Metals & Materials Series
https://doi.org/10.1007/978-3-031-22576-5_37

generated both by other industrial sectors, reusing them in construction materials [2].

Agribusiness is a production modality of enormous importance in the Brazilian context, it is estimated that the production of grains, cereals, and legumes in Brazil reached 260.5 million tons in 2021 [3]. In view of the large production, there is also a large availability of waste without a final destination from this industry [4]. Numerous works have been carried out with the aim of uniting the capacity of construction materials to absorb waste with the wide availability of these through the agroindustry for the production of new cementitious materials, aiming to improve their properties [5–7].

Among the countless residues generated by the agro-industry, the açaí seed is highly available, since only 15% of the fruit (pulp) is used for commercial purposes by ice cream and beverage agro-industries, and the other 85% is discarded daily without estimates of reuse [8]. Data show that in 2019 (pre-pandemic period) approximately 223 thousand tons of açaí were produced in Brazil, with 365 tons being discarded daily in the Brazilian state of Pará [9].

In this context, the objective of this work is to use the açaí seed as a partial substitute in mass of sand, the content of 10%, for the manufacture of mortars for coating walls and ceilings.

Materials and Methods

The Portland cement adopted was (CP-II-E-32), from the Champion brand, well used in the study region. The dry natural sand used was extracted from the bed of the Paraíba do Sul River, in the city of Campos dos Goytacazes—RJ, with a density of 2.65 g/cm^3, granulometry of 2.35 mm (average) and a chemical composition of 98% SiO_2. The water used in the manufacture of mortars came from the Águas do Paraíba concessionaire, responsible for sanitation in Campos dos Goytacazes since 1999.

The açaí seeds came from an açaí ice cream industry, located in the state of Espírito Santo. The pits have an average diameter of 9 mm (10 pieces chosen at random), the density of 1.48 g/cm^3, and chemical composition distributed in 75.34% carbon, 21.66% oxygen, and 3% other elements.

In addition to the reference composition (without residue), three compositions were defined with the presence of açaí residue in different processing conditions. Table 1 shows all the samples adopted.

The lumps were cleaned with running water to remove dust, soil, and roots present in the collected residue. Afterwards, it was exposed to drying at room temperature of $\pm$ 27 °C for 24 h (or until it reached constant mass). Then the stones went through the crushing process until they reached a granulometry similar to that of the adopted sand. For this, equipment such as Crusher and Forage Mincer was used, responsible for crushing, grinding, chopping, and disintegrating products such as fodder, sugar cane, grass, cassava branches, cereal husks, and corn, among others.

Table 1 Adopted samples

Mixture (1:3)	Description	Replacement content (%)
R1	Reference mortar	0
R2	Mortar with stone calcined at 800 °C	10%
R3	Mortar with crushed stone	10%
R4	Mortar with crushed stone treated with liquid paraffin	10%

Part of the crushed lumps was used for surface treatment with liquid paraffin in order to waterproof the pits as they are highly hydrophilic residues [10, 11]. The treatment consisted of immersion of the residues in a clean and oil-free container and the subsequent addition of liquid paraffin until all the residue was submerged. The lumps were in contact with the paraffin for 10 min (enough time for a film or camcorder). Afterwards, they were hit for a long time and kept to dry at temperature for 4 h or until they reached a mass.

Another part of the residues benefited by means of the calcination process, where they were taken to the oven until reaching a temperature of 800 °C, at a rate of 5 °C per minute, without a plateau, cooling soon after reaching the indicated peak.

All mortars were made in accordance with the Brazilian standard (NBR 16541/2016), which specifies the preparation of mortars dosed in the laboratory [12]. The properties of consistency, water retention, and density were evaluated in the fresh state. The consistency index was evaluated according to the NBR 13276/2016 standard that governs mortar for laying and covering walls and ceilings—determination of the consistency index [13]. Water retention was analyzed according to the requirements of NBR 13277/2005 [14]. The mass density test was performed according to the ABNT 13278/2005[a] standard [15].

The tests carried out in the hardened state were mass density and mechanical compressive strength at 7 and 28 days. For mass density, the requirements of NBR 13280/2005 [16] were observed and the compressive strength was performed in accordance with NBR 13279/2005 [17].

Results and Discussion

Figure 1 demonstrates the results of the mortar consistency index. A water/cement content of 0.55 was fixed for all samples. The horizontal spreading is related to the fluidity and consequent workability of the mortar [18].

Among the values found, only the R2 sample showed an improvement in the consistency index, with an increase of 12.89% compared to R1. The mortar with the crushed stone (R3) showed a significant drop in this important property, which is very harmful for the proposed application, reducing by 19.28%.

Sample R4, despite reducing by 5.83%, shows greater consistency when compared to sample R3, which shows the effectiveness of the treatment in controlling the

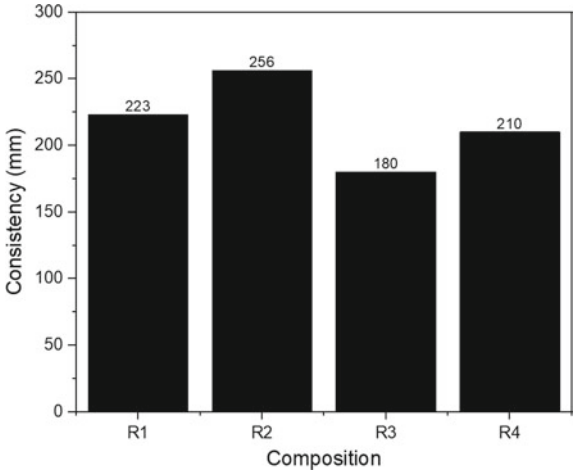

Fig. 1 Consistency test results

water absorption of the residue, allowing a greater amount of water available for workability. This reduction occurs because the presence of natural fibers affects the rheology of the material since the hydrophilic character and intrinsic porosity of the fibers cause loss of consistency and workability [7].

Several studies attest that the presence of lignocellulosic residues, whether stone or fiber, contribute to the reduction of the consistency index, as evidenced by the results found [19, 20]

Figures 2 and 3 demonstrate the density and water retention results respectively.

The results demonstrate that the density remains practically at the same values for mortars R3 and R4 when compared to the reference, with a slight increase in R4 of 5.14% due to the presence of liquid paraffin absorbed by the residue during

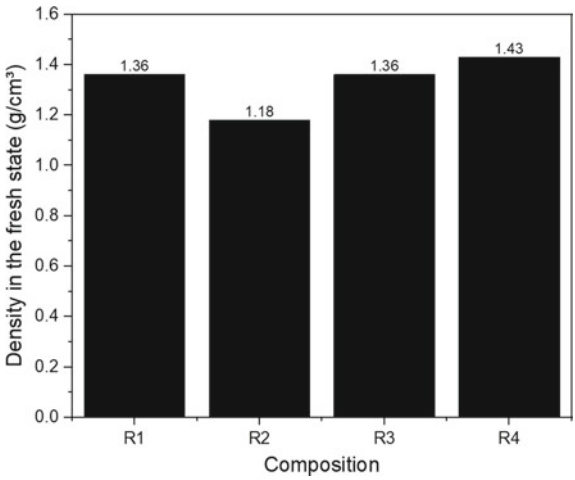

Fig. 2 Density test results in fresh state

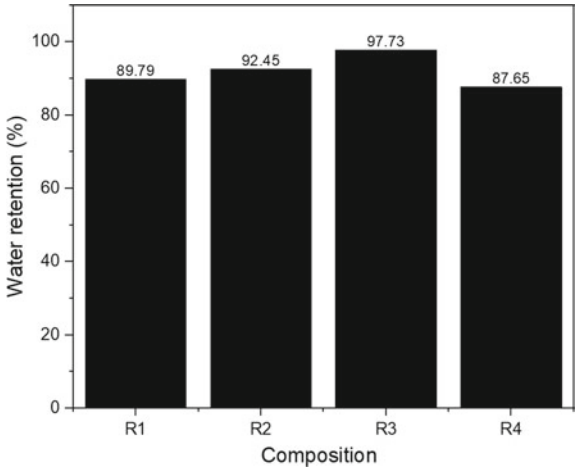

Fig. 3 Water retention test results

treatment. Sample R2 shows a reduction of 13.26% in relation to R1, which ends up generating lighter and more malleable mortars with the presence of calcined residue.

Water retention is a property that is related to the ability of fresh mortar to maintain its workability when subjected to efforts that cause loss of mixture, either by evaporation or by absorption of water from the base. The samples submitted to the water retention test showed interesting small variations. The compositions R2 and R3 presented values above 90% in this property, which according to the Brazilian standard NBR 13281/2005 characterizes them as high-capacity mortars to retain water, is a favorable point, since the high retention tends to allow better hydration of the cement, the maintenance of its workability for a long period and, consequently, results in gains in mechanical strength and adhesion [21].

This increase can be explained by the fact that the residue is highly hydrophilic, therefore, part of the water destined for kneading is incorporated by the stone and is not available for loss when submitted to the test. In this sense, the residue is advantageous because it has the tendency to release this water over time, making the loss difficult [11].

Figure 4 demonstrates the results obtained for the density test in the hardened state. It was possible to notice that all the compositions with the presence of the residue had lower mass density than the reference mortar, which has a positive impact, characterizing mortars that will also bring a lower overload when, for example, applied to masonry.

As in the fresh state, the samples with the calcined stone maintain the greatest reduction in this index, presenting about 15.52% lighter. In the characterization results of the açaí kernel, it is possible to notice that the average density of the residue of the whole açaí without treatment is smaller than the density of the average sand in about 22.15%, thus resulting in lighter mortars as the contents replacement rates increase [22].

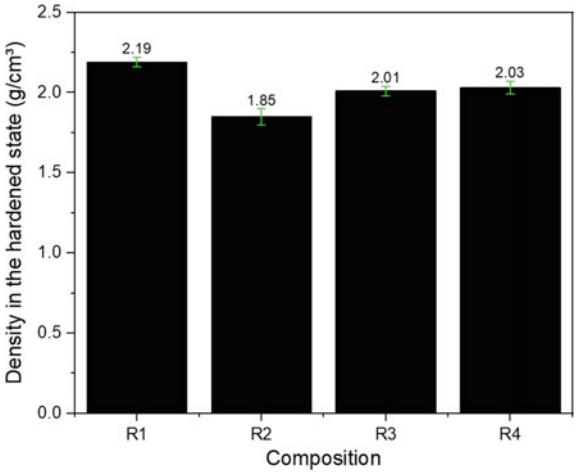

Fig. 4 Density test results in the hardened state

Figure 5 shows the results obtained in the mechanical compressive strength tests at 7 and 28 days.

It was observed that the mortars with the incorporation of açaí seed, present lower resistance to compression when compared to the reference, which is an adequate behavior in cementitious materials that present multiple fine aggregates in their composition [23].

The sample that stands out the most is R4, reaching 90% of the resistance of R1, leaving evidence of improvement when using the treatment, which allows a greater amount of free water for hydration and consequently a gain in mechanical resistance, as well as a lower amount of porosity, since the pits have ample absorption. Compositions R2 and R3, reach approximately 53.64% of the reference strength at

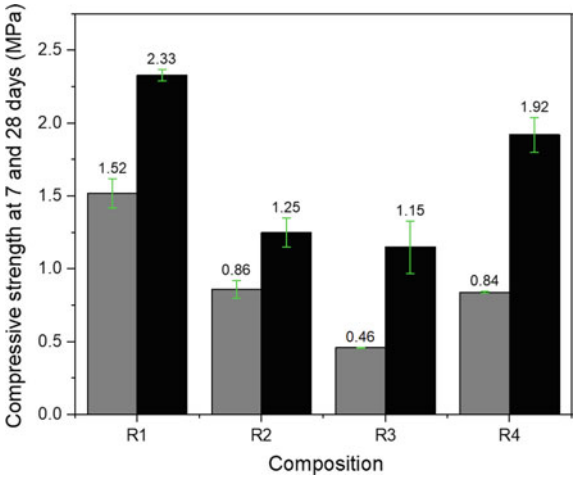

Fig. 5 Compressive strength test results

28 days, showing an expressive drop in strength with the presence of the residue in these conductions.

Conclusion

The objective of this work was to analyze the incorporation of açaí seed as a partial substitute, 10% by mass, of the fine aggregate (sand) in mortars intended for coating. After carrying out the tests, it was possible to conclude that.

- In the fresh state, it was possible to highlight the composition R2, which presented better consistency, lighter mortar, and with a slightly greater capacity to retain water. The other compositions significantly reduce the consistency index, presenting values that are not suitable for the proposed use.
- The presence of açaí residue reduces the compressive strength of all samples at both 7 and 28 days compared to the reference sample.
- It was observed that the presence of residues provided a greater amount of pathologies in the specimens, which may have influenced the mechanical strength and would certainly affect other important properties of the material.
- It is necessary to carry out a greater number of tests for a more detailed understanding of the behavior of the açaí residue in cementitious matrices. It is suggested to carry out tests of tensile strength, tensile adhesion, shrinkage, and microstructural analyses.

Acknowledgements This research was funded by the State University of the Northern Fluminense (UENF), partially financed by CAPES (Coordenação de Aperfeiçoamento de Pessoal de Nível Superior—Brazil), and CNPq (Coordenação Nacional de Pesquisa). The participation of A.R.G.A. was sponsored by FAPERJ through the research fellowships proc.no: E-26/210.150/2019, E-26/211.194/2021, E-26/211.293/2021, E-26/201.310/2021 and by CNPq PQ2 307592/2021-9.

References

1. Valverde FM (2022) Year 3 of the pandemic. Areia and Brita Magazine. Sao Paulo, pp 77, 3–38. Ten. 2021. (In Portuguese)
2. Smith J, Petrovic P, Rose M, De Souza C, Muller L, Nowak B, Martinez J (2021) J Citation Styles, Many Styles. 3
3. Siqueira MU, Contin B, Fernandes PRB, Ruschel-Soares R, Siqueira PU, Baruque-Ramos J (2022) Brazilian agro-industrial wastes as potential textile and other raw materials: a sustainable approach. Mater Circular Econ 4 (2022). https://doi.org/10.1007/s42824-021-00050-2
4. Costa CF, Silva AJ, Silva PA, Sousa FC (2017) Utilization of agro-industrial residues in the elaboration of by-products. II International Congress of Agricultural Sciences (In Portuguese)
5. De Monteiro GP, Azevedo ARG, Marvila MT (2021) Effect of the addition of the natural and treated açaí stone in structural mortars. AIMS Mater. Sci. 8(3):608–621. https://doi.org/10.3934/matersci.2021037

6. Azevedo AR, Marvila MT, Zanelato EB, Alexandre J, Xavier GC (2020) Development of mortar for laying and coating with pineapple fibers. Rev Bras de Engenharia Agrícola e Ambiental 24(3):187–193. https://doi.org/10.53660/CLM-150-166
7. De Azevedo ARG, Marvila MT, Tayeh BA, Cecchin D, Pereira AC, Monteiro SN (2021) Technological performance of açaí natural fibre reinforced cement-based mortars. J Build Eng 33:1–11. https://doi.org/10.1016/j.jobe.2020.101675
8. Marques ES, Froder JG, Oliveira PR, de. Perazzo FF, Rosa PCP, Gaivão IO, de M, Mathias MIC, Maistro EL (2019) Cytotoxic effects of Euterpe oleraceae fruit oil (açaí) in rat liver and thyroid tissues. Braz J Pharmacognosy 29:54–6. https://doi.org/10.1016/j.bjp.2018.12.001
9. Medina G, da S, Cruz JE (2021) Studies in Agribusiness: Brazilian participation in production chains. Goiânia, vol. 5, p 390. (In Portuguese)
10. Guimarães Junior JB, Mendes LM, Mendes RF, Guimaraes BMR, Melo RR (2013) Effect of paraffin content on physical-mechanical properties of particleboard panels of Pinus oocarpa. Madeira Sci Mag RCM 4(1):72–82. (In Portuguese)
11. Rodrigues J, Souza JA, Fujiyama R (2015) Polymer composites reinforced with natural fibers from the Amazon, manufactured by infusion. Mater Mag 20(4):946–960 (In Portuguese)
12. ABNT, NBR 16541 (2016) Mortar for laying and covering walls and ceilings—Preparation of the mixture for carrying out the tests, Assoc. Braz Tech Stand (In Portuguese)
13. ABNT, NBR 13276 (2016) Mortar for laying and covering walls and ceilings—Determination of consistency index, Assoc. Braz Tech Stand (In Portuguese)
14. ABNT, NBR 13277 (2005) Mortar for laying and covering walls and ceilings—Determination of water retention, Assoc. Braz Tech Stand (In Portuguese)
15. ABNT, NBR 13278 (2005) Mortar for laying and covering walls and ceilings—Determination of mass density and air content, Assoc. Braz Tech Stand (In Portuguese)
16. ABNT, NBR 13280 (2005) Mortar for laying and covering walls and ceilings—Determination of apparent mass density in the hardened state Assoc. Braz Tech Stand (In Portuguese)
17. ABNT, NBR 13279 (2005) Mortar for laying and covering walls and ceilings—Determination of tensile strength in bending and compression, Assoc. Braz Tech Stand (In Portuguese)
18. Azevedo ARG, Alexandre J, Marvila MT et al (2019) Development of methodology for the characterization and incorporation of waste from the paper industry in cementitious materials. In: Li B, Li J, Ikhmayies S et al (eds) Characterization of minerals, metals, and materials 2019. Springer, Cham, pp 583–590
19. Cruz J, Araújo S, Bonfim FP (2021) Influência da cinza do caroço de açaí nas propriedades de argamassas de chapisco. Engenharia e Tecnologia 13(3):216–226
20. Pascarolo A, Da silva SHL, Pinto MCC, Da costa MRA (2022) Influência de microfibras de celulose no estado fresco de argamassas. Ambiente Construído, Porto Alegre 22(1):179–190
21. Carasek H, Araújo RC, Cascudo O, Angelim R (2016) Parâmetros da areia que influenciam a consistência e a densidade de massa das argamassas de revestimento. Rev Matéria 21(3):714–732
22. Barbosa A, deRabelo VSMM, Martorano LG, Giacon VM (2019) Characterization of acai waste particles for civil construction use. Rev Matéria 24(3):1–11

Evaluation of Different Treatment Methods of Natural Açai Fibers (*Euterpe Oleracea Mart.*) for Cement Composites

D. L. Rocha, M. T. Marvila, D. Cecchin, M. C. C. S. da Silva, and A. R. G. Azevedo

Abstract The use of natural lignocellulosic fibers (NLF) favors a series of properties, such as mechanical strength, when used in cementitious composites. Brazil, due to its climatic and geographical characteristics, has a variety of natural fibers that can be used in cementitious composites. The objective of this work was to evaluate the characteristics of different mortars in the hardened state reinforced with the addition of açaí fiber, exposed to three different methodologies of surface treatment: (i) immersion in a solution of sodium; (ii) potassium hydroxides and (iii) calcium hydroxides, all in a concentration of 10% in relation to the mass of water. Mortars with a mixture of 1:3 (cement: sand) ratio, in mass, were made to reinforce structures with additions 1.5, 3.0, 4.5, and 0% (reference) of the açaí fiber, in relation to the cement mass. The results were analyzed by statistical tests and demonstrated that the treatments with potassium hydroxide (KOH) showed the best results.

Keywords Natural açai fiber · Superficial treatment · Cement composite

D. L. Rocha
IFES—Espirito Santo Federal Institute, Coordination of the Technical Mechanics, Rodovia BR Norte Km 58, 101 - Litorâneo, São Mateus, Espírito Santo 29932-540, Brazil

D. L. Rocha · M. T. Marvila
LAMAV – Advanced Materials Laboratory, UENF—State University of Northern Rio de Janeiro, Av. Alberto Lamego, 2000, Campos Dos Goytacazes, Rio de Janeiro 28013-602, Brazil

D. Cecchin · M. C. C. S. da Silva
TER—Department of Agricultural Engineering and Environment, UFF—Federal Fluminense University, Rua Passos da Patria, Niterói, Rio de Janeiro 2056-562, Brazil

A. R. G. Azevedo (✉)
LECIV—Civil Engineering Laboratory, UENF—State University of Northern Rio de Janeiro, Av. Alberto Lamego, 2000, Campos Dos Goytacazes, Rio de Janeiro 28013-602, Brazil
e-mail: afonso.garcez91@gmail.com

M. Zhang et al. (eds.), *Characterization of Minerals, Metals, and Materials 2023*, The Minerals, Metals & Materials Series
https://doi.org/10.1007/978-3-031-22576-5_38

Introduction

Fiber-reinforced composites are increasingly being used because their addition improves mechanical properties. The natural fiber-reinforced composites, the fact that they are a less harmful alternative to the environment and since they come from plants, are being increasingly used by industries in various sectors [1].

These composites have advantages over synthetic fibers, such as glass fiber composites. Glass fibers require greater energy consumption for their manufacture. On the other hand, natural fibers have biodegradability, non-toxicity, easy availability, non-abrasiveness, low density, good specific strength, and great resistance to corrosion and fatigue. However, natural fibers also have disadvantages such as fiber degradation, material heterogeneity, and low durability when compared to synthetic fiber [2].

The cementitious composite reinforced with natural fibers can achieve mechanical characteristics superior to those of conventional materials already used in the industry. The fibers inhibit the initiation and propagation of cracks as they attenuate the progression of microcracks, thus preventing sudden rupture. Because of this, the crack length in the hardened matrix is shorter, which considerably improves the impermeability and durability of composites exposed to the environment [3]. The use of fibers indicates a potential for reinforcing the matrices of fragile materials, based on Portland cement, which may increase their ductility [4].

A major problem related to the use of natural fibers in cementitious matrices is due to their high alkalinity, which ends up deteriorating the fibers when naturally incorporated [5]. One possibility is the use of different surface treatment methodologies, through impregnation in solutions that form a protective film [6].

To develop composites with good properties, it is necessary to improve the fiber-matrix interface and reduce moisture absorption. To ensure the durability of composites reinforced with plant fibers, it is necessary that these fibers undergo surface modifications in order to infer better characteristics in them as a reinforcing material [7, 8].

Brazil has a great diversity of natural fibers, which are generally used in the production of handcrafts, generating fewer added values to this natural product. Scientific research has been encouraging the use of natural fibers in other economic sectors, such as civil construction. Açaí, for example, is a typical Amazonian açaí fruit, widely used in the production of foodstuffs, cosmetics, and medicines, and which generates huge amounts of agro-industrial waste, usually with a seed and natural fiber [9]. The objective of this work was to evaluate the characteristics of different mortars in the hardened state reinforced with the addition of açaí fiber, exposed to three different methodologies of surface treatment: (i) immersion in a solution of sodium; (ii) potassium hydroxides and (iii) calcium hydroxides, all in a concentration of 10% in relation to the mass of water.

Fig. 1 Acai waste collection site: **a** View of the storage yard; **b** Natural tree of origin of açaí

Materials and Methods

The main materials used in this research were açaí fibers and materials for the production of the cement matrix: fine aggregate and cement. The fine aggregate is composed of: natural sand derived from river beds sieved in 24 mesh, following the same pattern used by literature [10].

The açaí fibers were collected from the municipality of Rio Novo do Sul, Brazil, in an agro-industry that produces açaí for ice cream. Figure 1 shows a collection of images of the place where the açaí wastes of the açaí fiber is deposited. From the images it is possible to observe the amount of waste generated, which would be wasted if it were not introduced in mortar. Currently, these residues from the açai agroindustry are sent to sanitary landfills.

The research methodology of this study is demonstrated in the flowchart in Fig. 2.

Results and Discussion

After a curing period of 28 days, the mortars were evaluated for properties in the hardened state. It was observed that, as in the fresh state, the density in the hardened state also reduced as more fiber was incorporated into the mixture, as reported by literature [10, 11].

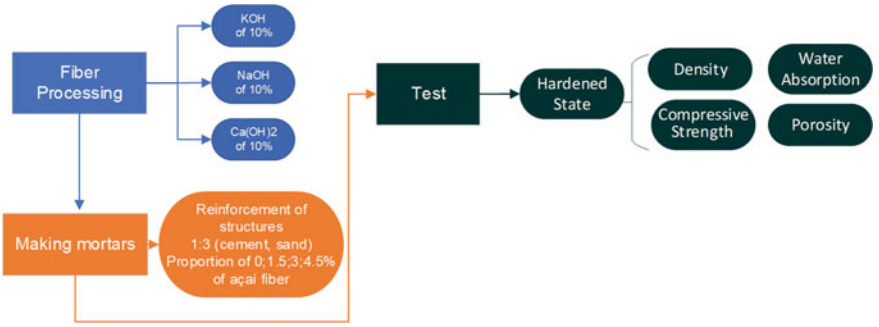

Fig. 2 Flowchart with the process steps

The reduction in density found in cementitious composites reinforced with natural açaí fibers is due to the lower specific mass that the isolated fiber has in relation to traditional cementitious materials [12]. Figure 3 shows the result with density values in the hardened state.

It is observed that the same mixtures that showed lower densities in the fresh state also continue to be the lightest in the hardened state. The mixtures of 4.5% of the $Ca(OH)_2$ and KOH treatment, with densities of 1.88 g/cm^2 and 1.86 g/cm^2. Note that there were small variations in densities in the treatment with NaOH, but all of them varied within the margin of error.

In the void index test (porosity), it was noted that the more the fiber was inserted into the mixture, the greater the porosity. This is in line with the fresh state properties, such as air retention, related in the literature [10]. As more fiber is added to the mix, they increase the amount of space within the composite by increasing the space for air to enter through these porous channels. Figure 4 demonstrates the results of the void ratio test.

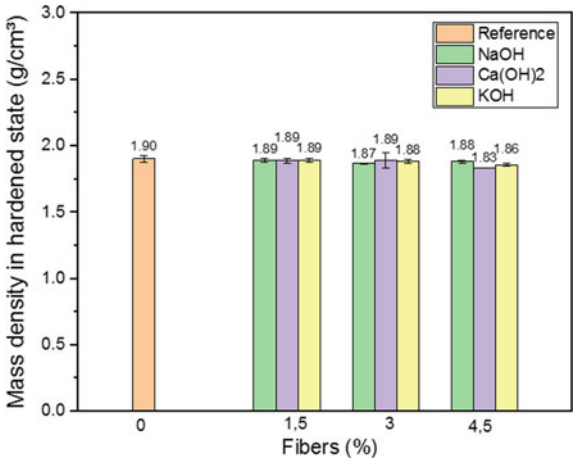

Fig. 3 Density results in the hardened state of composites

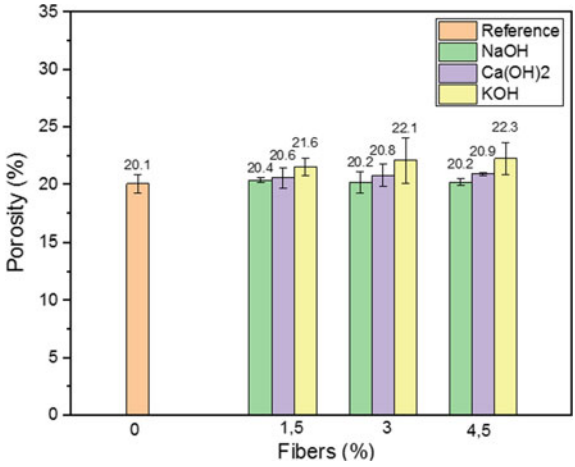

Fig. 4 Results of void ratio of cementitious composites

Comparing the void index values of the hardened state of mortars in this research with those of other researchers, it can be seen that açaí fibers imply in mortars with a higher void index, greater porosity and, consequently, they are in the range of the lightest.

Mortar with coconut fiber content from 0.125 to 0.75% had 19.1% to 28.8% void content [13]. The addition of flax fibers, modified by the plasma treatment, increases the porosity of the mortar to values ranging from 18.5 to 20.8% [14].

Regarding the void index or porosity, the incorporation of açaí fibers greatly increases the porosity of the mortars [15]. However, exists relating this increase to the porosity of the fibers, but also to the antiparticle spaces created between the fibers. Furthermore, the introduction of fibers results in the formation of an additional porosity, located in the interfacial transition zone existing around the fibers. This transition zone is formed during the mortar manufacturing process and is believed to be due to the high-water absorption coefficient of the raw vegetable fibers, which generates a migration of water from the cement paste in the fresh state to the fibers. This leads to more porosity in this zone in the hardened state. Figure 5 shows the results of water absorption in the different mixtures.

There was a tendency to increase water absorption as a function of the increase in the content of natural fiber addition, corroborating with porosity results presented above. In addition, treatment with KOH showed the greatest percentage increase, in agreement with other studies in the literature [11, 13].

The open porosity of fibrous composites is linked to the water absorption capacity of the fibers. This property can be detrimental to certain applications that are directly related to the strength of the composite. Because the addition of natural fibers in cementitious matrices increases the amount of space in the composite, the greater the space for water absorption in composites with some type of natural fiber. Finally, the last characteristic analyzed was the compressive strength. After incorporation of natural fibers, the strength of the composite has increasing nominal values in the

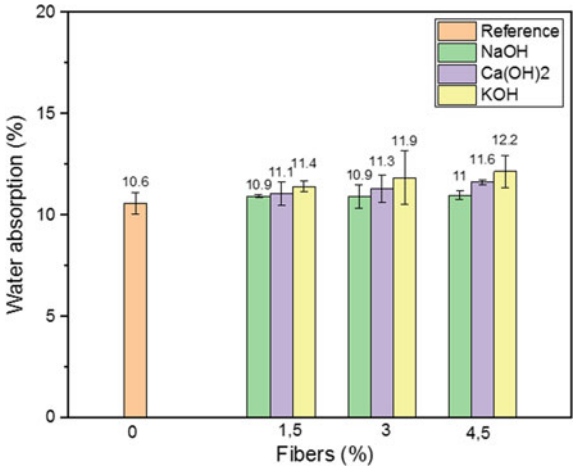

Fig. 5 Results of water absorption of composites

literature. The addition of açaí fibers provided a characteristic increase in compressive strength due to greater internal matrix compaction. The gain in strength was observed in some blends with fiber, as shown in Fig. 6.

The experiments showed that in the comparison of treatments, the more aggressive treatment (KOH) was more beneficial than the treatments more focused on adhesion (NaOH and $Ca(OH)_2$. Because it was the highest cellulose content of the samples treated with KOH 3% and 4.5% which provided higher strengths than samples treated with NaOH and $Ca(OH)_2$ which are not as aggressive and therefore remove less lignin, in agreement with other similar studies in the literature [10, 11].

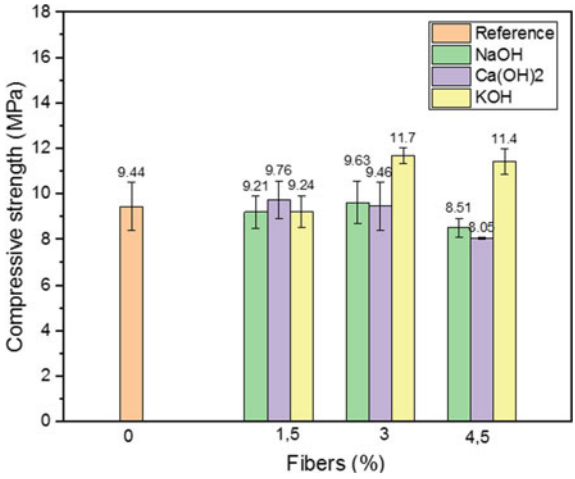

Fig. 6 Results of the uniaxial compression tests of the composites

Conclusion

In this work, treated açaí lignocellulosic fibers were used to improve the mechanical characteristics of the mortar used to reinforce structures. It can be concluded that acai fibers were successful in improving certain characteristics.

The best methodology for surface treatment of açaí fiber was the treatment with KOH. As it is a more aggressive treatment to the non-cellulosic constituents of the fiber, it proved to be useful in the reduction of lignin and hemicellulose and in the increase of cellulose in the fiber. What caused samples with higher resistances.

Lignocellulosic fibers present as a great disadvantage in relation to synthetic fiber, the low durability within the matrix, making it necessary to propose methods to increase this characteristic. Treatments in alkaline medium can achieve this goal, with NaOH treatment being the most used in the literature. However, it was noted that the treatment with KOH was successful in increasing the compressive strength even with a higher porosity than the other samples. This was due to the preservation of cellulose crystals that are not destroyed during the treatment process, which occurs in NaOH.

Density, both fresh and hardened, was also affected. It was noted that the samples treated with KOH showed a much higher porosity, resulting in lighter composites. Because of this, these mortars were less dense than the one treated with NaOH and the reference grade. However, after 28 days of curing, in the hardened state, there was little variation in density between the cementitious composites. Due to the evaporation of water during the curing time, the hardened mortar becomes less dense than the mortar in the fresh state, thus reducing the differences between the composites. Even so, the mixtures of 4.5% KOH and $Ca(OH)_2$ remain the lightest.

The maximum wettability of the composites varied with the treatments used. Since the levels of maximum compressive strength in composites with the three types of treatments were totally different (3% in NaOH, 1.5% in $Ca(OH)_2$) and undetermined in KOH, since only tests with levels above of 4.5%, it would be possible to observe the point where the values of compressive strength of this treatment begin to decrease.

Therefore, it can be better defined that the sample that presents as characteristics was 4.5% KOH. Because this sample obtained values according to the required standards (with the exception of consistency), both international and Brazilian standards, as well as the literature. And in the state resists this sample of greater resistance to resistance and the lowest density. And in relation to the number of voids index and water absorption, it was statistically equal to the reference.

References

1. Queiroz FA, Silva GRB, Barros LHV, Felipe RCTS (2021) Analysis of the degradation of reinforced plastic in fiberglass when exposed to sea water and sand. RSD 10(4):e19510413981. https://doi.org/10.33448/rsd-v10i4.13981

2. Ferreira TRM, Silva AB, Dias F (2016) Mechanical properties evaluation of glass fiber and hollow glass bubble reinforced polyamide 6 composites. In: Paper presented at the CBECiMat, Natal, Rio Grande do Norte, 11–15 Nov 2016
3. Zhang P, Yang Y, Wang J, Jiao M, Ling Y (2020) Fracture models and effect of fibers on fracture properties of cementitious composites—A review. Materials 13(23):5495. https://doi.org/10.3390/ma13235495
4. Savastano H, Agopyan V, Nolasco AM, Pimentel L (1999) Plant fibre reinforced cement components for roofing. Constr Build Mater 13(8):433–438. https://doi.org/10.1016/S0950-0618(99)00046-X
5. Azevedo ARG, Klyuev S, Marvila MT, Vatin N, Alfimova N, Lima TES, Fediuk R, Olisov A (2020) Investigation of the potential use of curauá fiber for reinforcing mortars. Fibers 8(11):69. https://doi.org/10.3390/fib8110069
6. Silva CC, Freire Júnior RCS, Ford ETLC, Dantas CM, Santos JKD, Aquino EMF (2018) Mechanical behavior and water absorption in sisal/glass hybrid composites. Matéria (Rio J.) 23(4):e-12246. https://doi.org/10.1590/s1517-707620180004.0580
7. Kılınç AÇ, Durmuşkahya C, Seydibeyoğlu MÖ (2017) Natural fibers. Fiber technology for fiber-reinforced composites, Elsevier, New York, pp 209–235
8. Liu K, Zhang C, Madbouly SA (2016) Fiber reinforced plant oil-based composites. Bio-based plant oil polymers and composites, Elsevier, New York, pp 167–189
9. Marvila MT, Azevedo ARG, Cecchin D, Costa JM, Xavier GC, Carmo DF, Monteiro SN (2020) Durability of coating mortars containing açaí fibers. Case Stud Constr Mater 13:e00406. https://doi.org/10.1016/j.cscm.2020.e00406
10. Azevedo ARG, Marvila MT, Tayeh BA, Cecchin D, Pereira AC, Monteiro SN (2021) Technological performance of açaí natural fibre reinforced cement-based mortars. J Build Eng 33:101675. https://doi.org/10.1016/j.jobe.2020.101675
11. Lilargem D, Tambara Júnior LUD, Marvila MT, Pereira EC, Souza D, Azevedo ARG (2022) A review of the use of natural fibers in cement composites: concepts, applications and Brazilian history. Polymers 14(10):2043. https://doi.org/10.3390/polym14102043
12. Jaramillo N, Hoyos D, Santa JF (2016) Compuestos de fibra de hoja de piña fabricados mediante moldeo por compresión por capas. Ingeniería y Competitividad 18(2):151–162. https://doi.org/10.25100/iyc.v18i2.2163
13. Rupasinghe M, Bhasura HMP, Sathiparan N (2016) Use of coconut coir reinforced plaster mortar for strengthening of unreinforced masonry. In: Annual research symposium, faculty of engineering, vol. 10, University of Ruhuna, pp 1–5. https://doi.org/10.13140/RG.2.2.23160.19202
14. Page J, Khadraoui F, Gomina M, Boutouil M (2019) Influence of different surface treatments on the water absorption capacity of flax fibres: rheology of fresh reinforced-mortars and mechanical properties in the hardened state. Constr Build Mater 199:424–434. https://doi.org/10.1016/j.conbuildmat.2018.12.042
15. Haba B, Agoudjil B, Boudenne A, Benzarti K (2017) Hygric properties and thermal conductivity of a new insulation material for building based on date palm concrete. Constr Build Mater 154:963–971. https://doi.org/10.1016/j.conbuildmat.2017.08.025

Evaluation of the Degradation Effects of Durability Cycles in Geopolymer Mixtures with Glass Waste Incorporation

L. R. Cruz, A. S. A. Cruz, M. T. Marvila, L. U. D. Tambara Junior, S. N. Monteiro, C. M. F. Vieira, and A. R. G. Azevedo

Abstract The global technological advance has been encouraging the development of several more sustainable materials. The current research develops a geopolymeric mixture with the incorporation of waste glass, given the high strength gain capacity of geopolymer materials, and eliminates the need to burn artifacts as in ceramics. Thus, mixtures of SiO_2/Al_2O_3 molar ratios fixed at 3.0 and 3.5 with 10% incorporation of waste glass were tested, such as water absorption and uniaxial compression tests. In addition, to simulate the exposure conditions of the material, durability tests were carried out through wetting and drying cycles and saline attack, evaluating the loss of mass and mechanical strength. The results of the water absorption test showed that the glass waste considerably reduced the water absorption of the materials, presenting reductions of up to 63%. Durability tests by saline attack showed undesirable interactions of the salt with the geopolymer matrix.

Keywords Geopolymer · Durability · Waste glass

Introduction

The world society has been changing around more sustainable daily habits. The insight that our primary sources of raw materials are finite has caused a number of

L. R. Cruz · A. S. A. Cruz · A. R. G. Azevedo (✉)
LECIV—Civil Engineering Laboratory, UENF—State University of Northern Rio de Janeiro, Av. Alberto Lamego, 2000, Campos Dos Goytacazes, Rio de Janeiro 28013-602, Brazil
e-mail: afonso.garcez91@gmail.com

M. T. Marvila · L. U. D. T. Junior · C. M. F. Vieira
LAMAV—Advanced Materials Laboratory, UENF - State University of Northern Rio de Janeiro, Av. Alberto Lamego, 2000, Campos Dos Goytacazes, Rio de Janeiro 28013-602, Brazil
e-mail: vieira@uenf.br

S. N. Monteiro
Department of Materials Science, IME—Military Institute of Engineering, Square General Tibúrcio, 80, Rio de Janeiro 22290-270, Brazil

M. Zhang et al. (eds.), *Characterization of Minerals, Metals, and Materials 2023*, The Minerals, Metals & Materials Series
https://doi.org/10.1007/978-3-031-22576-5_39

environmental problems. Following this trend, the glass industry is shaped by this concern for the environment and seeks to make its production processes less harmful.

The production process of ceramic artifacts, in addition to involving stages of exploitation of natural resources, also requires a stage of conformation of the artifacts through the stage of burning this material, and this procedure is responsible for the consolidation of certain properties such as increase in mechanical strength, density increase, pore reduction, and water absorption capacity [1]. This step, in addition to presenting high costs, also collaborates strongly with the emission of CO_2 gases, largely responsible for the worsening of the so-called greenhouse effect [2].

In this segment, activated alkali materials, more specifically geopolymers, are materials rich in silica and alumina and react in a strongly alkaline medium [3]. These materials as a good alternative to ceramic materials, mainly given their characteristic of obtaining similar mechanical properties to conventional ceramics. Geopolymer materials still have the advantage that they do not need to be burned at high temperatures [4].

Knowing the ability of geopolymers to incorporate agro-industrial wastes, combined with the chemical affinity between the composition of glass and aluminosilicates, the glass waste showed strong potential for aggregation to geopolymer mixtures. The glass waste chosen for the development of this work is a waste from the process of cutting flat glass sheets with high contents of soda-lime glass [5]. In addition, the glass industry is one of those that generate the most waste [6], so incorporating these wastes is extremely important since it leads to the clearance of the landfills to which these materials are destined.

Thus, the objective of this work is to evaluate the durability of a geopolymer mixture with the incorporation of waste glass, from degradation tests by means of wetting and drying and saline attack, in order to reproduce the effects of weathering and chemical attacks such as those from coastal regions.

Materials and Methods

The materials used for the development of this work were the following materials: HP Ultra metakaolin, sand, commercial sodium silicate (Na_2SiO_3) and sodium hydroxide (NaOH) and glass waste from the flat glass cutting process from the company New Temper (Campos dos Goytacazes, Brazil). Metakaolin and glass waste acted as precursor materials and silicate and sodium hydroxide as components of the activator solution. The preparation of the samples was made by mixing the precursors with the alkaline solution mechanically mixed for 3 min.

The traces used for sample preparation were given through the SiO_2/Al_2O_3 ratio, which was set at 3.5 and 3.0. After that, two mixtures were prepared, one for reference and one with incorporation of 10% of waste by substitution in the precursor material to then be molded in cylindrical specimens of 5 $\times$ 10 cm, where they were tested according to the resistance tests to compression and water absorption.

In addition to the tests for the mechanical characterization of the samples, durability tests were carried out, through wetting and drying cycles as well as saline attack. The cycles of both tests were carried out for 30 days, with cycles lasting 24 h of exposure to the etching agent, pure water in the case of wetting and drying cycles and saltwater in the case of saline attack, and 24 h in an oven alternately until the end of the test period. At the end of the cycles, the specimens were ruptured under compression so that they could be compared with the results obtained in the reference samples.

The water absorption tests followed the normative precepts imposed by NBR 15310 [7] and the compressive strength tests followed the reports provided for in the Brazilian association of technical standards NBR 5739:2018 [8].

Results and Discussion

Figure 1 shows the results related to water absorption at 7 and 28 days of exposure of the specimens.

The water absorption results were satisfactory with regard to the effects expected by the incorporation of the glass waste. In a general outlook, the behavior of the material from the addition of the waste to the matrix is of reduction in the rates of water absorption. However, it is worth mentioning the considerable reduction of 63% in the rate of water absorption in the samples of molar ratio 3.5 [9]. This result is attributed to higher silica content in the N-A-S–H gel formation [10]. Figure 2 refers to the results obtained from the compressive strength tests.

The compressive strength results were slightly different from what was expected based on the results obtained in the water absorption tests. The expectation, in view of the reduction in water absorption rates from the incorporation of the waste, was

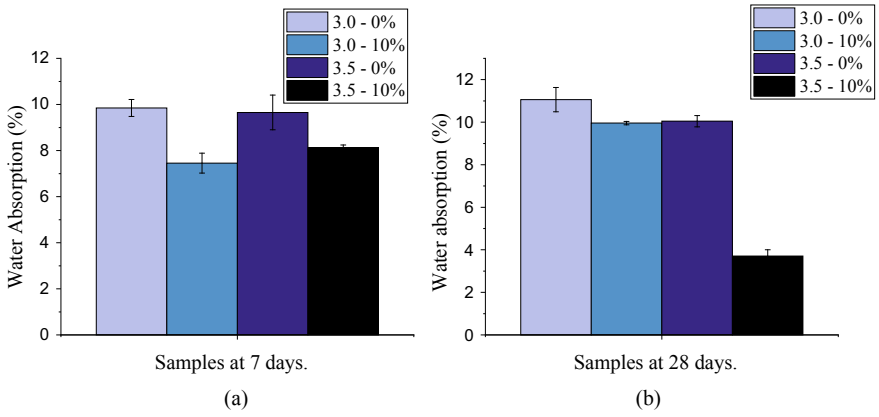

Fig. 1 Absorption water results at **a** 7 and **b** 28 days. (See the legend in the Figure with the contents)

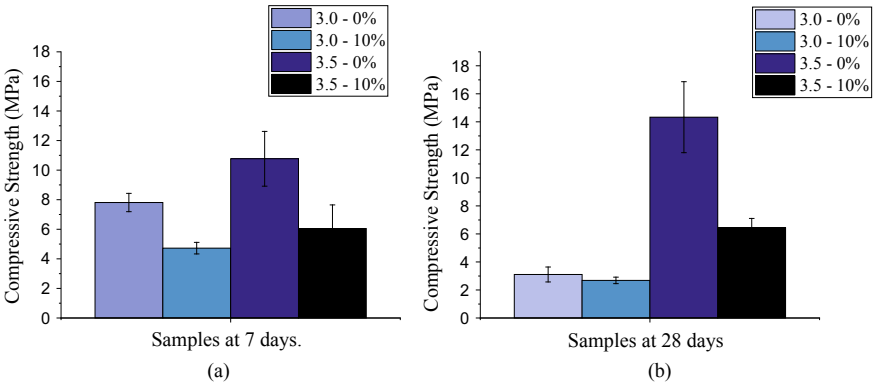

Fig. 2 Mechanical compressive strength result at **a** 7 and **b** 28 days. (See the legend in the Figure with the contents)

that the mechanical compressive strength of the material would increase. However, in addition to observing lower resistances at older ages, it is possible to notice a reduction in resistances in a range of 40–55%. This is possibly due to a high silica/alumina ratio, which causes greater silica networks in the N-A-S-H gel, which gives the material strength. Large silica chains result in a low denser gel and cause the matrix to weaken, that is, loss of strength. In addition, because it is a gel phase, the formation of the N-A-S-H gel prevents water from entering the matrix, which justifies the reduction in water absorption rates and the drop in strength [11]. Figure 3 refers to durability tests by the saline attack.

At the end of the saline attack cycles, the mass loss of the material was evaluated together with the mechanical strength. However, in the saline attack durability tests on

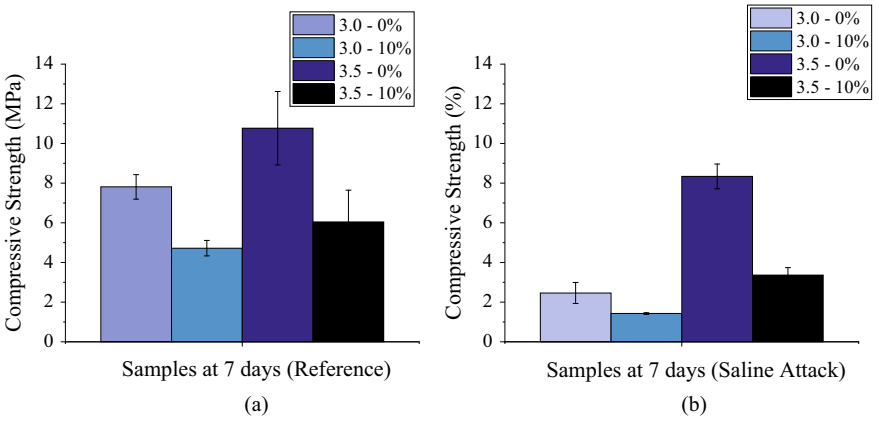

Fig. 3 Results of saline attack tests at 7 days: **a** Reference and **b** Saline Attack. (See the legend in the Figure with the contents)

the 7-day samples, only one sample actually degraded, but not significantly, totaling about 1% of mass loss. In general, the behavior of the material at this stage of the work was one of mass gain and loss of strength [12]. Figure 4 shows the results obtained in the saline attack durability tests at 28 days.

The results obtained from the samples at the ages of 28 days were different from those at the age of 7 days (Fig. 5). This time, all samples suffered mass gain, quite possibly due to the interactions of geopolymerization reactions with the salt present in the attacks.

The 3.0 molar ratio samples showed an increase in strength, which leads us to believe that the crystallization of the salts inside the sample ended up increasing the strength of the material since it was a less dense sample. On the other hand, it can

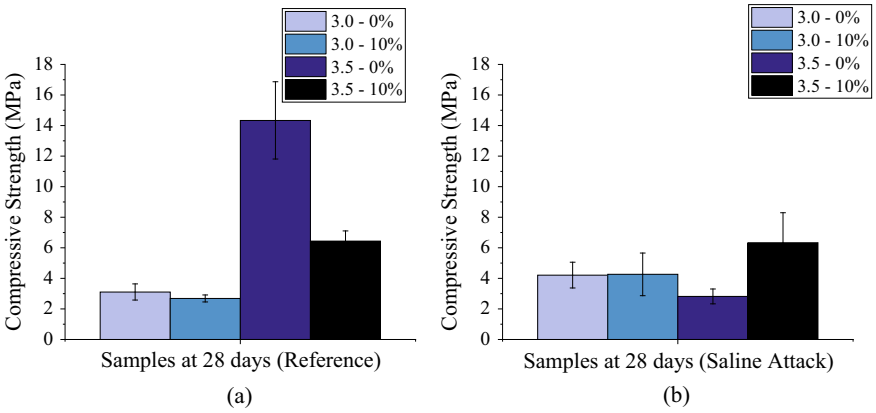

Fig. 4 Results of saline attack tests at 28 days: **a** Reference and **b** Saline Attack. (See the legend in the Figure with the contents)

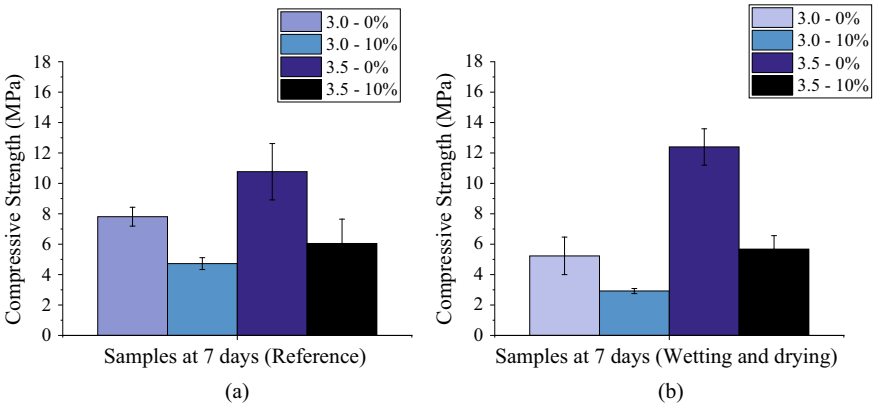

Fig. 5 Results of wetting and drying test at 7 days: **a** Reference and **b** Wetting and drying. (See the legend in the Figure with the contents)

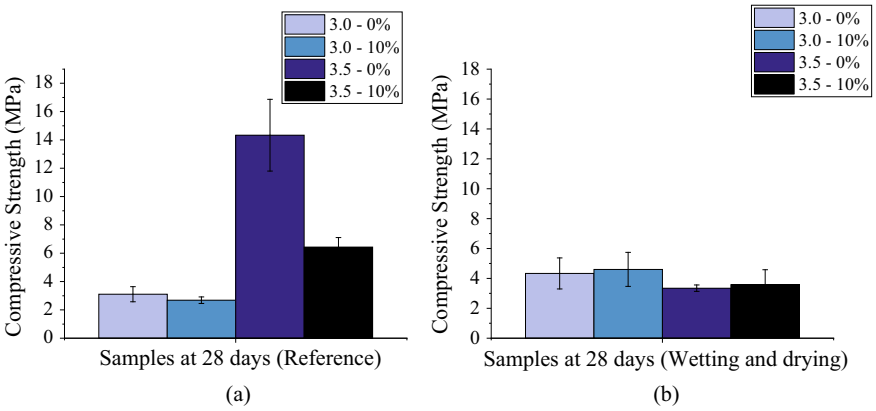

Fig. 6 Results of wetting and drying test at 28 days: **a** Reference and **b** Wetting and drying. (See the legend in the Figure with the contents)

be observed that composition 3.5, which had the best performance so far, suffered a considerable loss of resistance. This drop can also be attributed to the formation of salts inside the samples. Considering that this was a denser composition, the crystallization of the salts inside it caused the appearance of cracks, compromising its mechanical performance [13].

The wetting and drying cycles presented what was expected. A small degradation and a slight loss of strength, however nothing very significant at 7 days, given the stability of the samples [14]. Figure 6 shows the results obtained from the wetting and drying cycles at 28 days.

At 28 days, the wetting and drying cycles caused less degradation in the samples. However, the drops in resistance were more significant, especially in the 3.5 compositions [15]. One hypothesis is that the wetting and drying cycles ended up leaching the silicate formed in these samples with higher silica/alumina ratios, thus increasing the porosity of the samples and consequently reducing the mechanical strength. On the other hand, the 3.0 molar ratio compositions remained more stable, not showing major changes in strength [16].

Conclusion

After the results, it can be concluded that.

- Waste glass proved to be effective in terms of reducing water absorption rates from its incorporation.
- The mechanical strength tests proved to be satisfactory, however, it is necessary to adjust the waste incorporation rates in order to avoid the large silica chains that reduce the strength of the material.

- In the durability tests by means of saline etching, the interaction of salts with the geopolymer matrix was evident. Therefore, it is necessary to carefully assess the effects of these interactions.
- The material has great potential for use for its intended application in an ecologically and economically convenient way.

Acknowledgements This research was funded by the State University of the Northern Fluminense (UENF), partially financed by CAPES, CNPq, and FAPERJ. The participation of A.R.G.A. was sponsored by FAPERJ through the research fellowships proc.no: E-26/210.150/2019, E-26/211.194/2021, E-26/211.293/2021, E-26/201.310/2021, and by CNPq PQ2 307592/2021-9.

References

1. Silva JB (2006) Evaluation of heat losses in a Hoffmann model oven. In: Proceedings of the 50th annual meeting of the Brazilian ceramic society. Blumenau, Santa Catarina, 22–25 May 2006
2. Da Silva AC, Méxas MP, Gonçalves Quelhas OL (2017) Restrictive factors in implementation of clean technologies in red ceramic industries. J Clean Prod. https://doi.org/10.1016/j.jclepro.2017.09.086
3. Severo CGS, Costa DL, Bezerra IMT, Menezes RR, Neves GA (2013) Characteristics, particularities and scientific principles of alkaline activated materials. Electron Mag Mater Process 8(2):55–67
4. Santos GZB, Melo Filho JA, Manzato L (2018) Proposal of a ceramic obtained by geopolymerization of calcined ETA sludge. Cerâmica. https://doi.org/10.1590/0366-69132018643702353
5. De Azevedo ARG, Alexandre J, Zanelato EB, Marvila MT (2017) Influence of incorporation of glass waste on the rheological properties of adhesive mortar. J Clean Prod. https://doi.org/10.1016/j.conbuildmat.2017.04.208
6. Cruz LR, Marvila MT, Cruz ASA, Júnior JATL, Cerqueira NA, Monteiro SN, Vieira CMF (2021) Influence of the mixing processes of the constituents of incorporated geopolymer materials with glass waste. In: Characterization of minerals, metals, and materials 2021. The Minerals, Metals & Materials Series. Springer, Cham, pp 483–490
7. Brazilian Association of Technical Standards (2009) NBR 15310: Ceramic components—Tiles—Terminology, requirements and test methods. Rio de Janeiro. (In Portuguese)
8. Brazilian Association of Technical Standards (2005) Concrete—Compression test of cylindrical specimens ABNT NBR 5739:2018 (In Portuguese)
9. Peyne J, Gautron J, Doudeau J, Joussein E, Rossignol S (2017) Influence of calcium addition on calcined brick clay based geopolymers: a thermal and FTIR spectroscopy study. Constr Build Mater 15(152):794–803
10. Tambara Júnior LUD, Malik C, Rocha JC (2018) Development of alcaline-activated self-leveling hybrid mortar ash-based composites. Materials. https://doi.org/10.3390/ma11101829
11. Longhi MA, Zhang Z, Walkley B, Rodríguez ED, Kirchheim AP (2021) Strategies for control and mitigation of efflorescence in metakaolin-based geopolymers. Cem Concr Res. https://doi.org/10.1016/j.cemconres.2021.106431
12. Marvila MT, De Azevedo ARG, De Matos PR, Monteiro SN, Vieira CM (2021) Materials for production of high and ultra-high-performance concrete: review and perspective of possible novel materials. Materials 14(15). https://doi.org/10.3390/ma14154304

13. Azevedo ARG, Marvila MT, Zanelato EB, Alexandre J, Xavier GC, Cecchin D (2020) Development of mortar for laying and coating with pineapple fiber. Revi Bras De Engenharia Agricola e Ambiental 24(3):187–193. https://doi.org/10.1590/1807-1929/agriambi.v24n3p187-193
14. Carvalho A, Xavier GC, Alexandre J, Pedroti LG, de Azevedo ARG, Vieira CMF, Monteiro SN (2014) Environmental durability of soil-cement block incorporated with ornamental stone waste. Mater Sci Forum. https://doi.org/10.4028/www.scientific.net/MSF.798-799.548
15. Marvila MT, de Azevedo ARG, de Oliveira LB, Xavier GC, Vieira CMF (2021) Mechanical, physical and durability properties of activated alkali cement based on blast furnace slag as a function of %Na2O. Case Stud Constr Mater. https://doi.org/10.1016/j.cscm.2021.e00723
16. Zeyad AM, Magbool HM, Tayeh BA, Azevedo ARG, Abutaleb A, Hussain Q (2022) Production of geopolymer concrete by utilizing volcanic pumice dust. Case Stud Constr Mater. https://doi.org/10.1016/j.cscm.2021.e00802

Evaluation of the Durability of Adobe Bricks Made with Cattle Manure

M. R. Brito, S. A. Dutra Júnior, A. R. G. Azevedo, and M. T. Marvila

Abstract In recent decades, the development of new building materials that meet technological, economic, and environmental criteria, especially those that use alternative raw materials or new production methodologies, have become increasingly necessary. In this context, adobe bricks, known for decades in the field of civil construction, proved to be great models of experimentation, since they result from an adequate mixture of soil, sand, and natural fibers, apart from also air drying, with no need for calcination. In this work, cattle manure was used as an alternative of natural fiber for the development of adobe bricks, in the levels of 5%, 10%, and 15%, to analyze which, one would be ideal. The use of cattle manure in the development of adobe bricks is based on the notion of sustainability, given that this waste is normally disposed of in an improper way, apart from being less polluting than the chemical-industrial fibers. In search for the composition that best meets the regulatory requirements of civil construction, the effects of corrective materials such as Portland cement and hydrated lime were also evaluated, as the main disadvantage of using cattle manure is related to its low durability in places with high humidity. Thus, through this work, we sought to evaluate the durability of adobe blocks, with the proposed formulations, through wetting and drying cycles. In conclusion, it was noticed that the temporal degradation mechanisms of the adobe blocks made of cattle manure could be reduced using corrective materials, stabilizing their durability.

M. R. Brito · S. A. D. Júnior · M. T. Marvila (✉)
Material Engineering Laboratory, UFV CRP—Federal University of Viçosa, Campus Rio Paranaíba, Km 7 - Zona Rural MG-230, Rodoviário, Rio Paranaíba 38810-000, Brazil
e-mail: markssuel.marvila@ufv.br

M. R. Brito
e-mail: marina.brito@ufv.br

S. A. D. Júnior
e-mail: samuel.junior@ufv.br

A. R. G. Azevedo
LECIV—Civil Engineering Laboratory, UENF—State University of Northern Rio de Janeiro, Av. Alberto Lamego, 2000, Campos Dos Goytacazes, Rio de Janeiro 28013-602, Brazil
e-mail: afonso@uenf.br

M. Zhang et al. (eds.), *Characterization of Minerals, Metals, and Materials 2023*, The Minerals, Metals & Materials Series
https://doi.org/10.1007/978-3-031-22576-5_40

Keywords Adobe bricks · Cattle manure · Durability

Introduction

One of the most consumed building materials comes from ceramic materials. Its' production consumes a significant amount of natural soil material, such as clays, in addition to the high energy consumption arising from the firing process of the pieces [1]. Its production process begins with the extraction of the clay, which is subsequently processed, then goes through a drying and firing process. A major problem related to the production of ceramic artifacts is due to the control of the firing temperature, this directly interferes with the final quality of the products, and it also increases environmental damage, such as the use of natural resources and gases released into the atmosphere.

In this context, there is a need to develop alternative, eco-friendly materials that reduce the amount of gases released into the atmosphere as a result of the burning of ceramic materials. One of the viable materials to perform this substitution is the adobe block, obtained by mixing clay, sand, and natural fibers in adequate proportions, with no need for calcination [2]. Also, the possibility of incorporating agro-industrial wastes in the production of adobe makes this material even more environmentally advantageous [3]. The present project proposes the use of cattle manure as a source of natural fibers.

In addition to the environmental advantages, it is possible to highlight economic advantages as a result of the application of adobe blocks replacing ceramic materials. This is because the absence of the calcination process and the use of materials in their natural state, with almost no processing, makes the production of adobe blocks low-priced. Other relevant advantages are the ease of manufacturing the blocks, which consists of a basic three-step cycle (molding, drying, and storage); good thermal insulation properties due to high porosity; possibility of use in different formats and dimensions; material with the full possibility of recycling after the end of its lifespan; it is not necessary to use qualified labor for the production of adobe blocks; the raw material used is widely available and abundant [4–6].

However, the use of the material involves some disadvantages, which will be explored in this research project, aiming to mitigate these problems. It is mentioned: the construction process is slow, reducing the productivity of the material; adobe blocks have low tensile and flexural strength compared to conventional blocks; hand-crafting the component requires considerable human effort; need for a considerable area for drying the adobe blocks; difficulty obtaining regular dimensions in the adobe block; and one of the main problems is the fact that the blocks absorb a lot of water due to their high porosity, compromising their durability in places with high humidity [4–6].

Although most of the disadvantages of adobe blocks are controllable with an adequate production of the material, the durability problems of this type of block

need further investigation. As a result, in this work, the mechanisms of durability of adobe blocks produced with clay and cattle manure will be investigated.

Materials and Methods

The materials used to produce the adobe blocks were clay from the region, quartz sand to correct the plasticity of the adobe; cattle manure as a source of organic matter, and natural fibers to improve the tensile strength properties of adobe and reduce the shrinkage effect; Ordinary Portland cement as a corrective to improve compressive strength and Hydrated Lime as a corrective to improve the stability of adobe in reaction to humidity. These materials were subjected to a series of characterization techniques, such as chemical composition, granulometric analysis, and Atterberg limits.

Initially, two compositions were proposed, one as a reference, containing only clay and manure; and another modified, containing sand in addition to clay and manure. The amount of sand added must be sufficient to adjust the ideal particle size fractions. As highlighted by Gandia et al. [7], the ideal material to be used as adobe should have a clay fraction of approximately 40%, between 35 and 45%, and a sand fraction of approximately 55%, necessarily less than 65%, it was used 55% of sand and 45% of clay. As also highlighted by Gandia et al. [7, 8], and Santos et al. [9], the added water content must be adequate so that the mixture has a moisture content between the liquidity limit and the plasticity limit, by that it was added 40% of water into the adobes. The amounts of manure were also evaluated based on bibliographic works that analyzed similar materials, such as organic waste from a sewage treatment plant. Trang et al. [10] and Gandia et al. [8] used waste levels between 5 and 15%.

The best composition from a mechanical point of view was the modified—10% showing a compressive strength of approximately 157 kPa. After this definition, the effects of two important additions to adobe were evaluated: Ordinary Portland cement, with the objective of improving compressive strength, and hydrated lime, aiming to improve the stability in water of adobe blocks. The two binders were used separately, in a percentage of 10%, according to the bibliographic consultation in Santos et al. [9] and Dhandhukia et al. [5], and used together in individual percentages of 5%. All formulations are illustrated in Table 1.

The materials used to produce the adobe blocks were mixed manually, in the appropriate proportions, then the specimens were molded, using a form in the dimensions of 0.20 × 0.10 × 0.08 m. The samples were dried in the sun for a curing period of 7 days, then used to carry out the proposed tests (Fig. 1). The adobes had their physical–mechanical characteristics characterized through water absorption (AA) test of the specimens will be carried out in accordance with the procedures described by the ASTM C373 [11] standard, represented by the expression (1):

$$WA = \frac{W_w - W_d}{W_d} \times 100 \tag{1}$$

Table 1 Studies compositions

Composition	Clay (%)	Sand (%)	Cattle Manure (%)	Cement (%)	Hydrated Lime (%)	Water (%)
Reference—5%	45	55	5	–	–	40
Reference—10%	45	55	10	–	–	40
Reference—15%	45	55	15	–	–	40
Modified—5%	45	55	5	–	–	40
Modified—10%	45	55	10	–	–	40
Modified—15%	45	55	15	–	–	40
Controlled Cement	45	55	10	10	–	40
Controlled Lime	45	55	10	–	10	44
Controlled Mix	45	55	10	5	5	40

Fig. 1 Samples produced

where

WA Is the water absortion as a percentage;
W_w Is the saturated weight of sample;
W_d Is the dry weight of sample.

The compressive strength of the specimens will be performed using a universal testing machine, brand INSTRON, at a loading rate of 0.5 mm/min. The resistance of the specimens is calculated by expression (2):

$$CS = \frac{F}{A} \tag{2}$$

where

CS Is the compressive strength;
F Is the force or load at point of failure;
A Is the initial cross-sectional surface area.

Results and Discussion

Initially, an analysis of the characterization of the soil used in the research was carried out, which must be within the limits recommended by the authors. Table 2 presents the chemical composition of the soil. It is observed that the presence of high levels of Al_2O_3, typical of the soils of the region, is known as red latosols. The high presence of Fe_2O_3 is responsible for the red color of the material [12]. Table 3 presents the Atterberg limits of the soil, while Fig. 2 presents the granulometry curve of the material. Regarding the plasticity limits, it is possible to notice that the humidity used in the production of adobe blocks must be between 29.48 and 41.21%. As a result, the use of 40% was adopted, meeting the criteria defined by other authors, such as Gandia et al. [7, 8], and Santos et al. [9]. Regarding the granulometry (Fig. 2) it is highlighted that the soil used in the research does not meet the criteria established by Gandia et al. [7], which indicates that the clay fraction should be approximately 40%. As a result, it was necessary to add sand to the material, to obtain a mass compatible with the application of adobe blocks.

At seven days of curing, the blocks of the corrective compositions with Portland cement and hydrated lime were submitted to the tests. In Fig. 3 it is possible to observe the average compressive strength obtained by three specimens of each composition. The formulation of 10% of cement stands out and obtained greater amplitude, which was expected due to the properties of the material. It is important to emphasize that the blocks were made manually, without the use of compaction equipment, which reduces the maximum force supported by them. In short, the objective of these results is to present the difference in amplitude of the proposed formulations, aiming to find an adequate formulation that includes not only good results in terms of compressive strength, but mainly in terms of water absorption presented by them, as they acquire satisfactory durability.

Adobe, composed of water, soil, and natural fibers materials, cannot maintain its characteristics when submerged in water, as seen by Charai et al. [11] who studied adobe with the use of Pennisetum setaceum fibers, so it's necessary to use water-proofing materials capable of allowing the adobe to not decompose in water. As seen in Fig. 4, the blocks of the three compositions did not decompose immersed in water, except for one block of the composition composed of 5% lime and 5% cement, which had an isolated water absorption of approximately 28% and fell apart. Despite

Table 2 Chemical composition of the clay

%	SiO_2	Fe_2O_3	CaO	Al_2O_3	TiO_2	SO_3	Others
Clay	12.97	21.87	0.96	50.65	10.80	1.87	0.88

Table 3 Atterberg limits of the clay

Liquidity limit (%)	Plasticity limit (%)
41.21	29.48

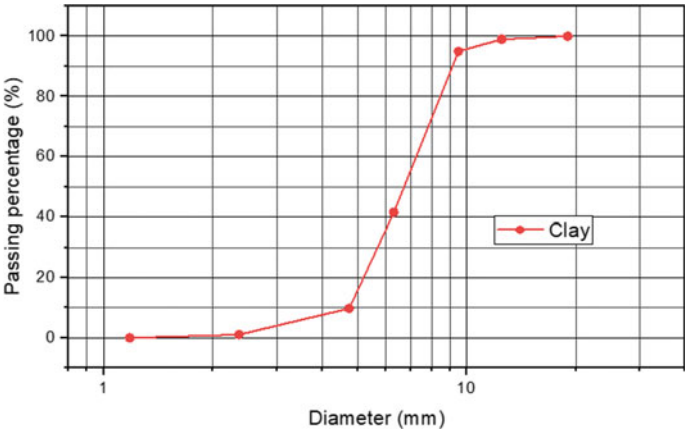

Fig. 2 Granulometry of clay

Fig. 3 Compressive strength results

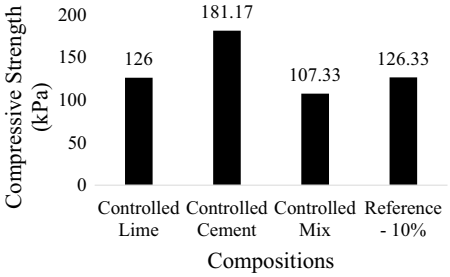

this, the average values of all compositions were satisfactory, with emphasis on the formulation of 10% hydrated lime, which presented results below the average of all compositions, proving to be an excellent material to correct plasticity, workability, as well as control the water content absorbed by the adobes. The results are expressed in Fig. 5.

Fig. 4 Specimens submerged in water

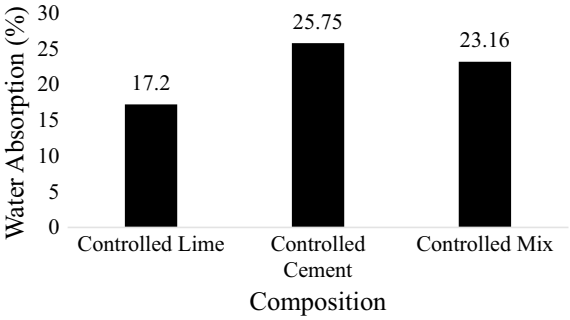

Fig. 5 Water absorption results

Conclusion

After discussing the results, it can be concluded that:

- The compositions presented similar results in all compositions; however, the formulation of 5% lime and 5% cement presented inferior results in all the tests to which they were submitted so far, giving scope to study compositions with different contents of both compositions, since the use of both materials would provide a brick with attractive properties for the civil construction sector.
- The 10% lime composition proved to be a viable option in terms of low water absorption and satisfactory compressive strength for the methods and materials chosen.
- It is expected that the results of the durability test will remain close in magnitude, but with better use of the formulation only composed of 10% lime, since its characteristics propose a more concise block.
- Although it is known that the form of execution influences the results of the adobe, more investigations are needed around this to quantify how compaction is directly linked to the mechanical strength of the adobe.

Acknowledgements The authors thank the Brazilian agencies FAPEMIG and UFV CRP for the support provided to this investigation.

References

1. Girondi GD, Marvila MM, de Azevedo ARG, de Souza CC, Souza D, de Brito J, Vieira CMF (2020) Recycling potential of powdered cigarette waste in the development of ceramic materials. J Mater Cycles Waste Manag 22:1672–1681. https://doi.org/10.1007/s10163-020-01058-7
2. Dormohamadi M, Rahimnia R (2020) Case Studies in Construction Materials Combined effect of compaction and clay content on the mechanical properties of adobe brick. Case Stud Constr Mater 13:e00402. https://doi.org/10.1016/j.cscm.2020.e00402

3. Pezo LL, Radojevic Z (2020) Optimization of adobe clay bricks based on the raw material properties (mathematical analysis) 244. https://doi.org/10.1016/j.conbuildmat.2020.118342
4. Silveira D, Varum H, Costa A (2013) Influence of the testing procedures in the mechanical characterization of adobe bricks. Constr Build Mater 40:719–728. https://doi.org/10.1016/j.conbuildmat.2012.11.058
5. Dhandhukia P, Goswami D, Thakor P, Thakker JN (2013) Soil property apotheosis to corral the finecompressive strength of unbaked adobe bricks. Constr Build Mater 48:948–953. https://doi.org/10.1016/j.conbuildmat.2013.07.043
6. Olacia E, Laura A, Chiodo V, Maisano S, Frazzica A, Cabeza LF (2020) Sustainable adobe bricks with seagrass fibres. Mechanical and thermal properties characterization. Constr Build Mater 239:117669. https://doi.org/10.1016/j.conbuildmat.2019.117669
7. Gandia RM, Corrêa AAR, Gomes FC, Marin DB, Santana LS (2019) Physical, mechanical and thermal behavior of adobe stabilized with "synthetic termite saliva." Eng Agrícola 39:139–149. https://doi.org/10.1590/1809-4430-eng.agric.v39n2p139-149/2019
8. Gandia RM, Gomes FC, Corrêa AAR, Rodrigues MC, Marin DB (2019) Physical, mechanical and thermal behaviour of adobe stabilized with the sludge of wastewater treatment plants. Eng Agrícola 39:684–697. https://doi.org/10.1590/1809-4430-eng.agric.v39n6p684-697/2019
9. Miranda L, Santos A, Anselmo J, Figueirêdo A, De Azerêdo N (2020) Soil characterization for adobe mixtures containing Portland cement as stabilizer
10. Minh Trang NT, Dao Ho NA, Babel S (2021) Reuse of waste sludge from water treatment plants and fly ash for manufacturing of adobe bricks. Chemosphere 284:131367. https://doi.org/10.1016/j.chemosphere.2021.131367
11. Charai M, Salhi M, Horma O, Mezrhab A, Karkri M, Amraqui S (2022) Thermal and mechanical characterization of adobes bio-sourced with Pennisetum setaceum fibers and an application for modern buildings
12. Oliveira TS, Costa LM, Schaefer CE (2005) Water-dispersible clay after wetting and drying cycles in four Brazilian oxisols. Soil Tillage Res 83(2):260–269

Evaluation of the Impact of the Incorporation of Pineapple Crown Particles on the Compressive Properties of Composites

J. A. T. Linhares, D. C. R. Velasco, A. R. G. Azevedo, S. N. Monteiro, F. P. D. Lopes, C. M. F. Vieira, and M. T. Marvila

Abstract Due to pineapple production, the amount of crown residue of this fruit is significant in Brazil. This material has been studied as reinforcement in materials especially when in fiber format. However another part of waste consists of particulates. This work aims to evaluate the technological feasibility of using these particulates as reinforcement/filler in polymer matrix composites, having as a reference their compressive strength. The matrix used was a Diglycidyl ether bisphenol A (DGEBA)/triethylene-tetramine (TETA) system, with a stoichiometric ratio of 20 phr. The formulations evaluated consist of the 0, 25, 50, and 100 percentiles of the maximum volume in which it was possible to incorporate the particulates. The test was performed using the Instron Model 5582, according to the ASTM D695-15. The results presented demonstrated the variation in the behavior of the material as a function of the amount of charge, as well as the technological feasibility of its incorporation.

Keywords Compressive strength · Waste · Particulates · Polymer

J. A. T. Linhares · D. C. R. Velasco · F. P. D. Lopes · C. M. F. Vieira
LAMAV—Advanced Materials Laboratory, UENF—State University of Northern Rio de Janeiro, Av. Alberto Lamego, 2000, Campos Dos Goytacazes, Rio de Janeiro 28013-602, Brazil
e-mail: vieira@uenf.br

A. R. G. Azevedo
LECIV—Civil Engineering Laboratory, UENF—State University of Northern Rio de Janeiro, Av. Alberto Lamego, 2000, Campos Dos Goytacazes, Rio de Janeiro 28013-602, Brazil
e-mail: afonso@uenf.br

S. N. Monteiro
Department of Materials Science, IME—Military Institute of Engineering, Square General Tibúrcio, 80, Rio de Janeiro 22290-270, Brazil

M. T. Marvila (✉)
UFV—Federal University of Viçosa Campus Rio Paranaíba (UFV-CRP), Rodovia BR 230 KM 7, Rio Paranaíba 38810-000, Brazil
e-mail: markssuel.marvila@ufv.br

M. Zhang et al. (eds.), *Characterization of Minerals, Metals, and Materials 2023*, The Minerals, Metals & Materials Series
https://doi.org/10.1007/978-3-031-22576-5_41

Introduction

The need to obtain materials with specific properties, which sometimes could not be observed in conventional materials, made man combine different materials. There are records of the use of natural fibers to reinforce materials since ancient Egypt for the construction of pyramids [1].

However, over the years, natural fibers were replaced by synthetic materials. This measure has been rethought in view of the socio-environmental advantages of using natural fibers, as well as the by-products of their production, which sometimes appear in the form of particulates. The use of these materials allows us to solve two of the biggest problems of this century, the excessive demand of natural resources and the inadequate disposal of residues [2–4].

According to data from the Food and Agriculture Organization of the United Nations (FAO), pineapple production grew by 34% in the last 10 years listed (2010–2019), reaching a production of 30.5 million tons in 2019 [5].

Such production generates opportunities for waste recovery. In this sense, fibers from the pineapple crown leaf, PALF, have had their application studied. It is also added that in addition to being incorporated as long and short fiber, its use as particulate in composites has also been evaluated. [6, 7].

Thus, the particulates obtained by removing the fibers from the pineapple crown can be used in composites, similarly to what is already done with coconut husk powder in epoxy matrix composites [4, 8].

In this sense, this work aims to evaluate the compressive properties of epoxy matrix composites with the addition of particulates that come from the process of extracting fibers from the pineapple leaf.

Materials and Methods

The residue used in this work, Fig. 1, was obtained as a by-product of the extraction of short fibers from the pineapple crown leaf, which were separated from the latter through a sieving with a 40 mesh sieve. The matrix used in this work was an epoxy system DGEBA/TETA, using an amount of hardener (TETA) equal to 20% of the resin mass (DGEBA).

The evaluated formulations have volumetric fractions of 0.0, 4.5, 9.0, and 18% of particulates, being produced 7 specimens for each formulation in silicone mold. After curing, the specimens were sanded in order to obtain dimensions equal to 12.7 × 12.7x4 mm and submitted to the compression test according to ASTM D695-15 [9]. To perform this test, a universal mechanical testing machine, Instron, model 5582, Fig. 2.

An analysis of variance (ANOVA) and Tukey's test was performed to verify any statistical differences between the sample groups, with a significance level

Fig. 1 Pineapple crown leaf particulates

Fig. 2 Universal testing machine—Instron 5582

of 5%. Such analyzes were performed using the PAST software, according to the Copenhagen and Holland algorithm [10].

Results and Discussion

Figure 3 shows the variation of the modulus of elasticity as a function of the amount of load. By means of this result it is possible to observe that the addition of particulates in small amounts (4.5%) tends to increase the elastic modulus of the material, this increase being significant according to the Tukey test. The latter also indicated that the other formulations, with 9 and 18% load, do not generate a significant variation in the modulus of elasticity [11, 12].

Figure 4 demonstrates the variation in compressive strength as a function of the amount of load. A resistance gain of approximately 10% was observed when adding 4.5% of particulates, this resistance gain being significant according to Tukey's test, even with the observed variance. The Tukey test also indicated that there is no significant variation in strength when inserting 9% of particulates, as well as that the compressive strength of the formulation with 18% of particulates had a significantly lower strength than the other formulations.

The observed behavior can be attributed to the lower concentrations of particulates favoring a better dispersion and distribution of the same, as well as the addition of excess particulates tends to make it difficult to mix between resin and hardener. In extreme circumstances, it is possible to observe that the incorporation of particulates

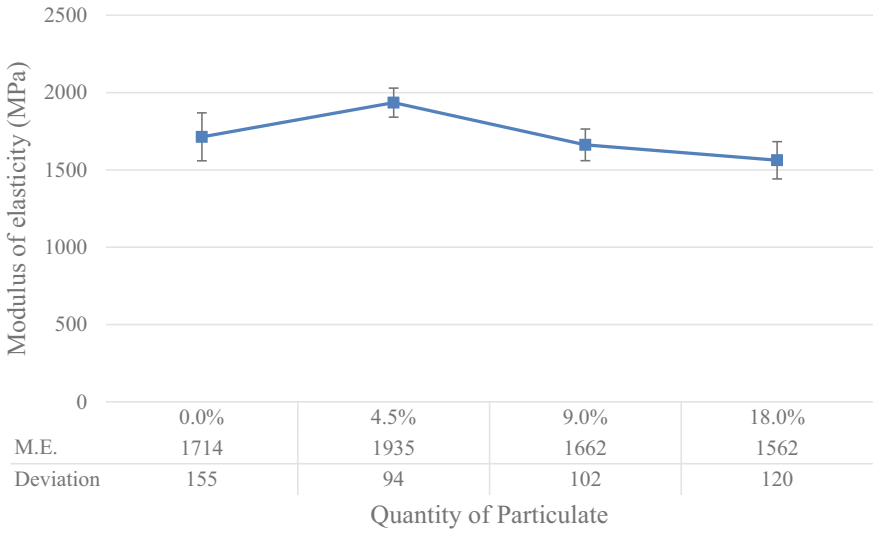

Fig. 3 Modulus of elasticity depending on the amount of load

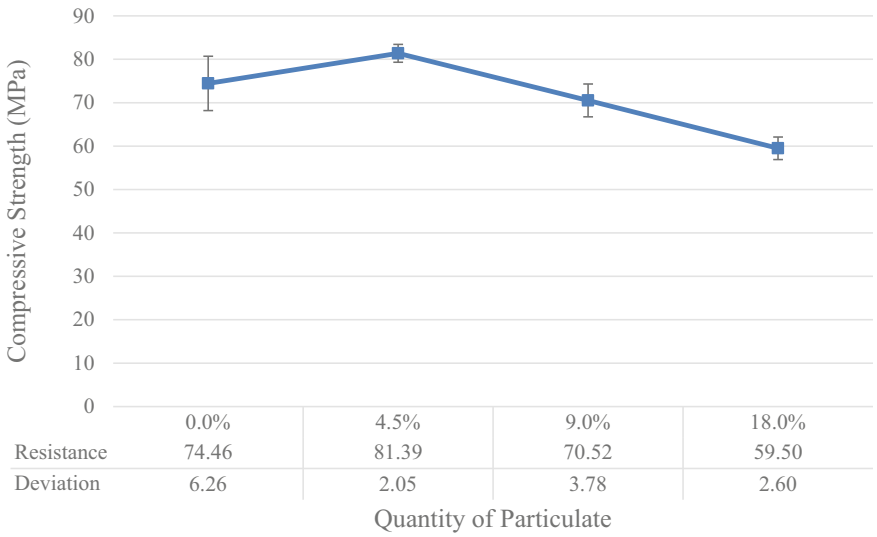

Fig. 4 Compressive strength limit as a function of the amount of load

can generate agglomerates of particulates that are not properly bonded to the matrix [8].

Conclusions

The results of this work indicated that the addition of particulates from the pineapple crown leaf at 4.5% of volumetric fraction resulted in the best results. The Tukey test indicated that the formulation has a significantly higher modulus of elasticity and compressive strength than the others.

It was also observed that the addition of particulates in higher amounts generated a reduction in the compressive strength of the composites, which is attributed to the higher concentrations of particulates impairing the distribution and dispersion of the particulates and hardener in the resin.

References

1. Low IM, Alomayri T, Assaedi H (2021) Cotton and flax fibre-reinforced geopolymer composites. Compos Sci Technol. https://doi.org/10.1007/978-981-16-2281-6
2. Güven O, Monteiro SN, Moura EAB, Drelich JW (2016) Re-emerging field of lignocellulosic fiber—Polymer composites and ionizing radiation technology in their formulation. Polym Rev 56:1176037

3. Azevedo ARG et al (2020) Potential use of ceramic waste as precursor in the geopolymerization reaction for the production of ceramic roof tiles. J Build Eng 29:101156
4. Velasco DCR, Lopes FPD, Simonassi NT, Vieira, CMF (2022) Influência da incorporação de resíduos na permeabilidade ao vapor de água de compósitos de matriz epoxídica/Influence of the incorporation of waste on the water vapor permeability of epoxide matrix composites. Braz J Dev 8. https://doi.org/10.34117/bjdv8n4-101
5. Food and Agriculture Organization of the United Nations (2022) Food balances (2010). https://www.fao.org/faostat/en/#data/FBS. Accessed 23 Aug 2022
6. Komal UK, Lila MK, Singh I (2021) Processing of PLA/pineapple fiber based next generation composites. Mater Manuf Process 36:1942904
7. Najeeb MI, Sultan MTH, Andou Y, Shah AU, Eksiler K, Jawaid M, Ariffin AH (2020) Characterization of silane treated Malaysian Yankee Pineapple AC6 leaf fiber (PALF) towards industrial applications. J Market Res 9(01):058
8. Velasco DCR, Simonassi NT, Lopes FPD, Vieira CMF, Guimarães RS (2022) Resistência ao impacto de compósitos reforçados com pó da casca de coco em duas configurações: processados e não processados. Congresso Anual da Associação Bras de Metal Materiais e Mineração (ABM) 75. https://doi.org/10.5151/2594-5327-34632
9. ASTM D695-15 (2016) Standard test method for compressive properties of rigid plastics
10. Copenhaver MD, Holland B (1988) Computation of the distribution of the maximum studentized range statistic with application to multiple significance testing of simple effects. J Stat Comput Simul 30. https://doi.org/10.1080/00949658808811082
11. de Azevedo ARG, Marvila MT, Antunes MLP, Rangel EC, Fediuk R (2021) Technological perspective for use the natural pineapple fiber in mortar to repair structures. Waste Biomass Valorization 12. https://doi.org/10.1007/s12649-021-01374-5
12. Mohammad J et al. (2021) A comparative evaluation of chemical, mechanical, and thermal properties of oil palm fiber/pineapple fiber reinforced phenolic hybrid composites. Polym Compos 42. https://doi.org/10.1002/pc.26305

Experimental Study of Pretreatment of a Refractory Gold Mineral for the Recovery of Gold in the Goldmins SRL Mining Company

Nemy Villca Aro and Agustín Moisés Cárdenas Revilla

Abstract A significant sample of "refractory tails" product of a gravimetric concentration of primary ore, provided by Empresa Minera Goldmins SRL, with an approximate gold content of 31 g/t, was treated experimentally at the laboratory level. It was subjected to a mineralogical characterization by Fluorescence and X-Ray Diffraction, reporting a sulfur (S) content of 15%, iron (Fe) 23%, silica (SiO_2) 7%, and arsenic (As) 3% as the main cyanicide. Based on the result of the characterization, two important stages were developed for the recovery of gold from these tailings: pretreatment and conventional cyanidation. The pretreatment involved grinding to two particle sizes (75 and 105 μm) followed by oxidation using hydrogen peroxide (H_2O_2). Subsequently, stirred tank cyanidation was carried out. It was possible to develop nine experimental tests considering constant the parameters of the percentage of solids, temperature, speed of agitation, and pH. Including a leaching without oxidation, whose recovery was less than 10% for 24 h. The remaining eight tests, oxidized and cyanide, reported recoveries above 59% for the same time. The best recovery, 84% for 24 h, was under the following conditions: grinding at −75 μm, oxidation with H_2O_2 at 25 g/L, and leaching at a NaCN concentration of 3.77 g/L.

Keywords Pretreatment · Oxidation · Cyanidation

Introduction

The exploitation of gold in Bolivia is from two sources: vein gold deposits (primary) and alluvial gold (secondary). Mostly developed by the cooperative sector and small informal mining. With regard to the exploitation of vein gold, many times in its mineralogy there is a diversity of compounds such as pyrites, arsenopyrites, as well

N. Villca Aro (✉) · A. M. Cárdenas Revilla
Universidad Mayor de San Andrés UMSA, La Paz, Bolivia
e-mail: nemyvillca@gmail.com

A. M. Cárdenas Revilla
e-mail: acardenasrevilla@gmail.com

M. Zhang et al. (eds.), *Characterization of Minerals, Metals, and Materials 2023*, The Minerals, Metals & Materials Series
https://doi.org/10.1007/978-3-031-22576-5_42

as other elements such as copper, antimony, and arsenic. Likewise, it is known that the recovery of free gold from this type of deposit is by conventional gravimetric methods and the use of mercury from grinding, which is inadequate. It should be noted that in the presence of sulfides and/or arsenides in these ores (hence the name refractory), the recovery of gold is not possible, therefore, it is necessary to consider other exploitation techniques for the recovery of these resources that, at They are generally unknown by the cooperative sector that works with them. Consequently, their gravimetric tailings show significant contents of unrecovered gold with gold tenors of up to 30 g/t. And in order to carry out the chemical oxidation of sulfur species; In the present study, an experimental study of the use of oxidizing agents in the "pretreatment" stage is carried out, which not only includes regrind to different particle sizes for greater surface exposure to oxidation, but also includes oxidation with peroxide. of hydrogen (H_2O_2) to a refractory gold charge provided by Empresa Minera Goldmins S.R.L. followed by conventional cyanidation for the recovery of gold in the rich solution.

Materials and Methods

Mineralogical Characterization of the Tailings Load

The ore sample (tails from the gravimetric concentration process) provided by Empresa Minera Goldmins S.R.L. was 50 kg, it was crushed, homogenized, and quartered for the various stages of the process.

The X-Ray Fluorescence (XRF) analysis was developed in the "Laboratorios Conde Morales" laboratory in the city of Oruro. On the other hand, the X-Ray Diffraction (XRD) analysis was carried out by the Laboratory of the Institute of Geological and Environmental Research (IGEMA-UMSA).

Pretreatment of the Refractory Gold Charge

The pretreatment stage included the re-grinding of the ore to two particle sizes: 75 and 105 μm in size (−200# and −150#), which was at various sizes between the 20 mesh range and 1.06" from the ASTM series.

Pre-oxidation with Hydrogen Peroxide

The pre-oxidation using hydrogen peroxide was carried out considering two different concentrations: 25 and 34 g/L of hydrogen peroxide H_2O_2 (at 50%m/m) that generates an exothermic reaction.

Cyanidation of the Refractory Gold Charge

The cyanidation process was developed considering two concentrations: 0.94 and 3.77 g/L NaCN, reaching the following tests.

Conventional Cyanidation at −200# Particle Size Without Pre-oxidation at 0.94g/L NaCN

Next, the operating conditions and parameters for conventional leaching without performing pre-oxidation are presented.

Cyanidation conditions	
Natural pH pulp	4.5–5
%solids	25%
Rpm	From the stirring equipment
NaOH	12.3 [g]
Leaching pH	10.5
CN^-	500 [ppm]

Cyanidation Preoxidizing with H_2O_2 to 34[g/L] ≈1[M], −200# y 0.94 g/L NaCN

Likewise, the operating conditions and parameters for conventional leaching after pre-oxidation with hydrogen peroxide at a concentration of 34 g/L are presented.

Cyanidation conditions	
Natural pH Pulp	4.5–5
%solids	25%
Rpm	Del of the stirring equipment
NaOH	12.3 [g]
Leaching pH	10.5
CN^-	500 [ppm]

Cyanidation Preoxidizing with H_2O_2 to 25[g/L], −200# Particle Size y 3.77 g/L NaCN

Likewise, the operating conditions and parameters for conventional leaching after pre-oxidation with hydrogen peroxide at a concentration of 25 g/L are presented.

Cyanidation conditions	
Natural pH pulp	4.5–5
% solids	25%
Rpm	Del of the stirring equipment
NaOH	10 [g]
Leaching pH	10.5
CN^-	500 [ppm]

Cyanidation Preoxidizing with H_2O_2 to 25[g/L], −150# y 3.77 g/L NaCN

The operating conditions and parameters for conventional leaching are presented after pre-oxidation with hydrogen peroxide at a concentration of 25 g/L but at a particle size of 150#.

Cyanidation conditions	
Natural pH Pulp	4.5–5
%solids	25%
Rpm	Del of the stirring equipment
NaOH	9 [g]
Leaching pH	10.5
CN^-	[ppm]

Results and Discussion

Mineralogical Characterization of the Ore Sample

X-Ray Fluorescence

Table 1 shows which elements are in greater proportion, these being iron, sulfur, and arsenic; typical of pyrites and arsenopyrites.X-Ray Diffraction.

And in the next figure it can be seen a diffractogram from the material before pretreatment.

Table 1 XRF test report (Values for reference only) to the original sample

Chunks (%)													
Zn	*Pb*	*Sn*	*As*	*Cu*	*Sb*	*Pb*	WO_3	*Ca*	*Fe*	*S*	SiO_2	*Bi*	*Al*
0.039	0.128	0.004	3.968	0.032	0.014	0.134	0.205	0.24	23.62	15.33	7.128	0.013	0.279
K	*Ti*	*V*	*Cr*	*Co*	*Ni*	*Ga*	*Rb*	*Sr*	*Y*	*Zr*	*Ba*	*Hg*	*U*
0.769	0.313	0.04	0.029	0.002	0.001	0.003	0.005	0.003	0.004	0.003	0.037	0.001	0.002

Source Conde Morales Laboratory

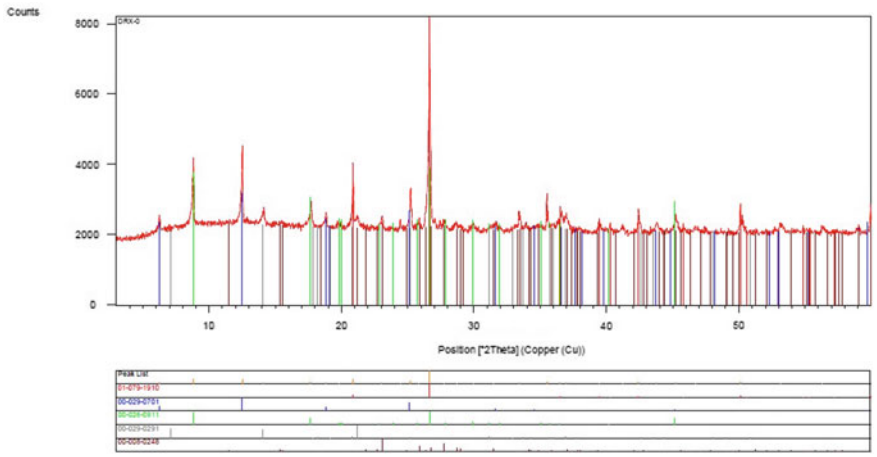

Fig. 1 X-ray diffraction of the head sample. *Source* Institute of Geological and Environmental Research—IGEMA

Identification of Crystalline Phases

A. **Major components**

(1) Clinochloro: $(Mg, Fe)_6\ (Si, Al)_4O_{10}(OH)_8$
(2) Illita: $(K, H_3O)\ Al_2Si_3AlO_{10}(OH)_2$

B. **Minority components**

(1) Quartz: SiO_2
(2) Vertuminita: $Ca_4Al_4Si_4O_6(OH)_{24}I_3H_2O$
(3) Brimstona: S

In the diffractogram presented in Fig. 1, it is observed that the majority of compounds have iron, sulfur, and silicates, confirming once again that in the sample under study gold is associated and encapsulated in sulfides.

Pretreatment of the Refractory Gold Charge

Pre-oxidation with Hydrogen Peroxide

In the previous table it can be seen that after pretreatment and oxidation the proportion of the elements originally present have not been altered, indicating that the oxidation caused microfractures in the particle for the penetration of the leaching solution and attacking the gold, also indicating that there was no leaching of unwanted elements (Fig. 2 and Table 2).

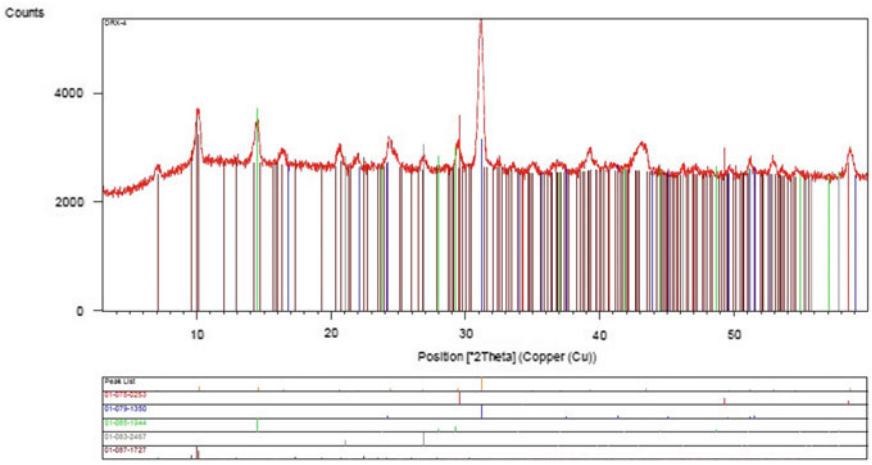

Fig. 2 Diffractogram of preoxidized and cyanidated sample. *Source* Institute of Geological and Environmental Research—IGEMA

Identification of Crystalline Phases

A. **Major components**

1. Ankerita: $Ca_{.997}(Mg_{.273}\ Fe_{.676}\ Mn_{.054})(CO_3)_2$
2. Pyrochloro: $K_{.056}\ Sr_{.014}\ Ca_{.017}\ (H_2O)_{0.704}\ Nb_{1.04}\ Ti_{.288}\ (O_{2.595}(OH)_{1.234})(H_2O)_{2.405}$
3. Stilbita: $Na_{7.67}\ Ca_{4.84}\ (Al_{17.35}\ Si_{54.65}O_{144})(H_2O)_{17.04}$

B. **Minority components**

1. Cuarzo: SiO_2
2. Chalcopyrita: $CuFeS_2$

In this second diffractogram performed on a pretreated and oxidized sample, it is also observed that the composition of its compounds did not change, observing that there are compounds with iron content.

Sample Ore Cyanidation

Conventional Cyanidation at −200# Without Pre-oxidation at 0.94g/L NaCN

The following table shows the metallurgical balance of the experimental test described before.

According to Table 3 and Fig. 3, it is observed that the recovery of gold for a period of 24 h is approximately 9% for conventional cyanidation without pretreatment.

Table 2 XRF analysis (reference value) of preoxidized and cyanidated sample

Chunks (%)													
Zn	*Pb*	*Sn*	*As*	*Cu*	*Sb*	WO_3	*Ca*	*Fe*	*S*	SiO_2	*Al*	*K*	*Ti*
0.058	0.121	0.012	6.186	0.024	0.018	0.416	0.21	24.33	11.16	5.169	0.277	0.65	0.316
V	*Cr*	*Co*	*Ni*	*Ga*	*Rb*	*Sr*	*Y*	*Zr*	*Ba*	*Hg*	*Th*	*U*	
0.005	0.014	0.006	0.012	0.002	0.001	0.003	0.001	0.012	0.03	0.03	0.001	0.006	

S*ource* Conde Morales Laboratory

Table 3 Metallurgical balance of conventional cyanidation at −200# particle size and 0.94 g/L NaCN

Metallurgical balance							
Product	Weight [Kg]	Volume [L]	mg/L Au	Au [g/t]	Fine Au [g]	%Recovery	Hour
PLS 1		3.00	0.467		0.00140	4.29	1
PLS 2		3.00	0.582		0.00175	5.35	2
PLS 3		3.00	0.659		0.00198	6.06	3
Calc. Tailings	1.00			30.67	0.03067	93.94	
Calc. Feeding	1.00			32.65	0.03265	100.00	

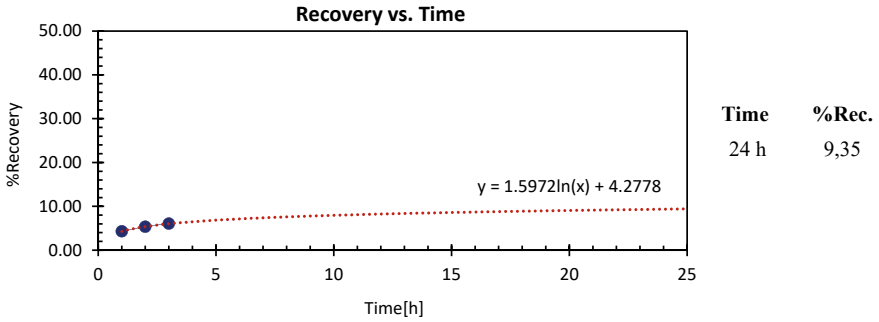

Fig. 3 Recovery versus Time of conventional cyanidation at −200# particle size and 0.94 g/L NaCN

Cyanidation by Pre-oxidation with H_2O_2 at 34[g/L], −200# and 0.94 g/L NaCN

The following table shows the metallurgical balance of the experimental test described before.

According to Table 4 and Fig. 4, it can be seen that the recovery of gold for 24 h is approximately 66% for a cyanidation process prior to oxidation pretreatment with hydrogen peroxide.

Cyanidation Preoxidizing with H_2O_2 at 25[g/L], −200# Particle Size and 3.77 g/L NaCN

The following table shows the metallurgical balance of the experimental test described before.

Table 4 Metallurgical balance of cyanidation preoxidizing with H_2O_2 at 34 g/L, −200# and 0.94 g/L NaCN

Metallurgical balance							
Product	Weight [Kg]	Volume [L]	mg/L Au	Au [g/t]	Fine Au [g]	%Recovery	Hour
PLS 1		3.00	1.36		0.0041	13.03	1
PLS 2		3.00	2.61		0.0078	25.00	2
PLS 3		3.00	3.75		0.0113	35.93	4
Calc. Tailings	1.00			20.06	0.0201	64.07	
Calc. Feeding	1.00			31.31	0.03131	100.00	

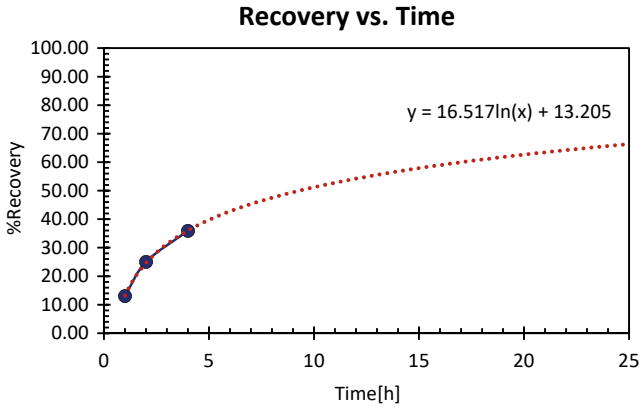

Time	%Rec.
24 h	65,7

Fig. 4 Recovery versus time of cynidation preoxidizing with H_2O_2 at 34 g/L, −200# and 0.94 g/L NaCN

According to the metallurgical balance presented in Table 5 and Fig. 5, a gold recovery of approximately 83% is observed for 24 h, after carrying out the corresponding oxidation pretreatment.

Table 5 Metallurgical balance of cyanidation preoxidizing with H_2O_2 at 25[g/L], −200# particle size and 3.77 g/L NaCN

Metallurgical balance							
Product	Weight [Kg]	Volume [L]	mg/L Au	Au [g/t]	Fine Au[g]	%Recuperation	Hour
PLS 1		3.00	2.56		0.0077	24.53	2
PLS 1		3.00	6.04		0.0181	57.87	8
PLS 3		3.00	6.74		0.0202	64.57	11
PLS 4		3.00	7.17		0.0215	68.69	14
Calc. Tailings	1.00			9.80	0.0098	31.31	
Calc. Feeding	1.00			31.31	0.0313	100.00	

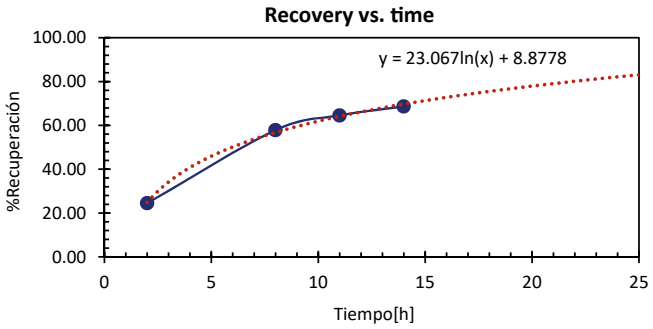

Time	%Rec.
24 h	83,85

Fig. 5 Recovery versus time of cyanidation of pre-oxidation with H_2O_2 at 25[g/l], −200# particle size and 3.77 g/L NaCN

Cyanidation Preoxidizing with H_2O_2 at 25[g/L], −150# and 4 g/L NaCN

The following table shows the metallurgical balance of the experimental test described before.

Finally, in Table 6 and Fig. 6, a gold recovery of approximately 73% is observed for 24 h under the pretreatment conditions mentioned above.

Table 6 Balance of cyanidation preoxidizing with H_2O_2 at 25[g/L], −150# and 4 g/L NaCN

Metallurgical balance							
Product	Weight [Kg]	Volume [L]	mg/L Au	Au [g/t]	Fine Au [g]	%Recuperation	Hour
PLS 1		3.00	3.67		0.0110	35.16	2
PLS 1		3.00	6.25		0.0188	59.88	8
PLS 3		3.00	6.59		0.0198	63.13	14
Calc. Tailings	1.00			11.54	0.0115	36.87	
Calc. Feeding	1.00			31.31	0.0313	100.00	

Conclusions

According to the mineralogical characterization, there is a refractory gold load of 31 g/t, likewise the XRF analysis reported iron [Fe] 23.62%, sulfur [S] 15.33%, silica [SiO_2] 7.13%, as majority elements. Observing arsenic [As] as the greatest cyanicide with a reference content of 3.968%. On the other hand, the XRD analysis reported major compounds of pyrites and arsenopyrites which encapsulate gold.

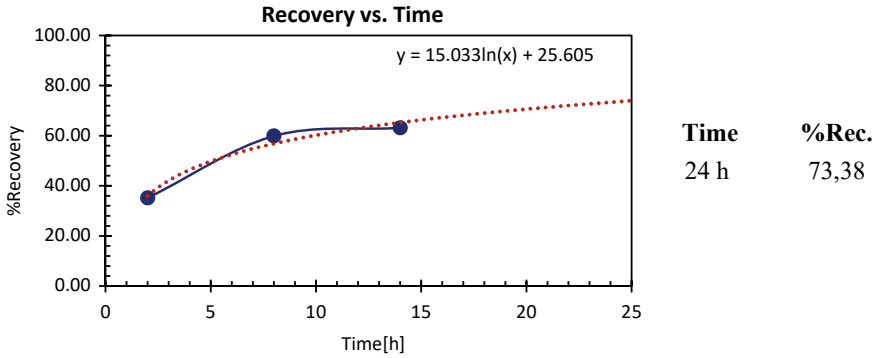

Fig. 6 Recovery versus time of cyanidation preoxidizing with H_2O_2 at 25[g/L], −150# and 4 g/L NaCN

The following experimental treatment mechanism in the laboratory of the refractory gold ore is proposed, provided by Empresa Minera Goldmins S.R.L. based on the tests carried out, which consists of re-grinding at a particle size of 74 microns, pre-oxidation with hydrogen peroxide at a concentration of 25 g/L and leaching with a concentration of sodium cyanide of 3.77 g/L. L where an approximate recovery of 84% is achieved for a leaching time of 24 h.

Influence of the Time of Staining Agents on Ornamental Rocks

B. R. Maciel, E. D. Fizzera, T. E. S. Lima, N. A. Cerqueira, M. N. Barreto, S. N. Monteiro, C. M. F. Vieira, and A. R. G. Azevedo

Abstract The characterization of ornamental rocks has the purpose of predicting the behavior of the rocks when exposed to various requests present in their place of application, seeking to know the feasibility of using the material. The objective of this work is to analyze the staining of the rocks after variations in exposure times. Four types of rocks were selected for the test: Dallas White, São Gabriel Black, Castelo Grey, and Siena White. The staining agents chosen were: lemon, oil, coffee, steel sponge and detergent, bleach, and degreaser. As a result, it was noticed that the stains caused were more evident and accentuated as the time of exposure of the rocks to the staining agents increased, developing more accentuated and permanent stains.

Keywords Ornamental rocks · Technological characterization · Stain

B. R. Maciel · E. D. Fizzera
Department of Mining Engineering, IFES—Espirito Santo Federal Institute, Eng. Fabiano Vivácqua Highway, 1.568, Cachoeiro de Itapemirim 29322-000, Brazil
e-mail: bianca@uol.com.br

E. D. Fizzera
e-mail: evanizis@ifes.edu.br

T. E. S. Lima · N. A. Cerqueira · C. M. F. Vieira
LAMAV—Advanced Materials Laboratory, UENF—State University of Northern Rio de Janeiro, Av. Alberto Lamego, 2000, Campos Dos Goytacazes, Rio de Janeiro 28013-602, Brazil
e-mail: coord.niander@gmail.com

M. N. Barreto
IFF—Fluminense Federal Institute, Campus Centro, Rua Dr. Siqueira, 273, Campos dos Goytacazes, Campos 28035-048, Brazil
e-mail: marnevesbar@ibest.com.br

S. N. Monteiro
Department of Materials Science, IME—Military Institute of Engineering, Square General Tibúrcio, 80, Rio de Janeiro 22290-270, Brazil

A. R. G. Azevedo (✉)
LECIV—Civil Engineering Laboratory, UENF—State University of Northern Rio de Janeiro, Av. Alberto Lamego, 2000, Campos Dos Goytacazes, Rio de Janeiro 28013-602, Brazil
e-mail: afonso.garcez91@gmail.com

M. Zhang et al. (eds.), *Characterization of Minerals, Metals, and Materials 2023*, The Minerals, Metals & Materials Series
https://doi.org/10.1007/978-3-031-22576-5_43

Introduction

The rocks, because they have different mineralogical compositions, have different characteristics that are responsible for their physical and chemical behavior. Knowing these properties is essential for an adequate applicability of the materials, since each available environment of its particularity may have variations in temperature, humidity, constant use of water and cleaning chemicals [1, 2].

Technological characterization has a purpose of determination through tests and evidence such as rocks, exhibiting chemical, physical parameters and mechanical properties, which allow indicating an adequate suitability for each environment [3]. The improper use of cleaning, which contains components of beauty, the appearance of ornamental stones is responsible for causing stains, shine, identification and consequently loss of brightness, identification and consequently, resulting in the appearance of ornamental stones [3]. According to Frascá [4], the irregular areas present in the characterization formation or general expression of the formation are irregular. Changes in most cases are not properties of physical characteristics, as they are displayed normally and loss of dates.

The stain resistance test aims to determine the susceptibility to chemical reagents contained in household or commercial products that may eventually come into contact with the rock. Although there is no specific technical standard for the stain resistance test, in this work the standard for ceramics of ABNT NBR 13818 [5], Annex G, with some adjustments, will be used. The various lithotypes for ornamental purposes have different resistance to staining when accidentally exposed to staining agents. Observing the relevance of this information for the market of these products, this study becomes a necessary contribution, since the objective of this work is to evaluate four types of rocks in terms of resistance to staining, seeking to analyze the behavior of the rocks when exposed to different substances of domestic, culinary and cleaning use, present in everyday life at three different time intervals.

Materials and Methods

To carry out the stain resistance test, 4 types of granite were chosen, which are commercially classified as Dallas white, Siena white, Saint Gabriel black, and Castle grey.

Nineteen specimens of each type of granite were made, 1 of which was used as a reference specimen to assist in the future staining analysis. The dimensions of the specimens are in accordance with NBR 13818 [5], being 7 cm wide and 7 cm long, with a thickness of approximately 2 cm.

The staining agents used in the stain resistance test were described in Table 1. For the removal of stains caused by exposure to staining agents, three attempts were carried out with different cleaning agents also described in Table 1.

Table 1 Composition of staining and cleaning agents

Staining agent	Composition
Lemon	100% lemon juice
Oil	Soybean oil (genetically modified from Agrobacterium) and antioxidants: TBHQ and citric acid
Coffee	Roasted and ground coffee powder with water
Steel sponge, detergent and water	Carbon steel and detergent (Sodium alkylbenzene sulfonate, sodium lauryl ether sulfate, sequestrant, coadjuvant, thickeners, hydrotope, Glycerin, collagen, solvent, neutralizer, preservatives, pH control agent, fragrance, dye, and vehicle)
Bleach	Stabilizers, sodium hypochlorite and vehicle. active chlorine content—2.0% at 2.4 plpm
Degreaser	Sodium alkyl benzene sulfonate, lauramine oxide, alkalizing agent, coadjutants, preservative, pH control agents, fragrances, water
Cleaning agent	*Composition*
Warm water	Running water from the tap
Detergent	Sodium alkylbenzene sulfonate, sodium lauryl ether sulfate, sequestrant, coadjuvant, thickeners, hydrotope, glycerin, collagen, solvent, neutralizer, preservatives, pH control agent, fragrance, dye, and vehicle
Multipurpose paste	Soap, Anionic Surfactant, Neutralizer, Coadjuvants, Abrasive, Dye, Essence, and Vehicle

Initially, specimens were made with dimensions defined in the ABNT NBR 13818 [5] standard, 7 cm wide and 7 cm long. The 76 specimens were prepared, totaling 19 of each type of rock, however, 1 specimen of each material was reserved to be used as a reference, that is, for later comparative use.

After making, the specimens were washed in running water and placed in the oven for a period of one hour for drying. The initial gloss measurement was performed by inserting the Gloss Meter into the center of the surface of each rock sample. A sample of each type of rock was separated for each staining agent, which was exposed at three different times to each of them: 30 min, 4 h, and 24 h.

After exposure, the specimens were washed in running water and placed in the oven at a temperature of approximately 70 °C for a period of 30 min for drying, later analyzed and then the brightness measurement of each sample was performed. All samples that were identified with stains underwent cleaning processes. The first cleaning process was the attempt to remove the stains using warm water, the specimens were submerged for a period of 5 min. At the end of this period, the samples were taken to the oven for a period of 30 min, then the analysis and brightness measurement of each specimen was performed.

The second cleaning attempt was carried out with the aid of detergent, sponge, and water being applied to the surface of the specimens and then washed in running

water and placed in the oven at a temperature of approximately 70 °C for a period of 30 min. Soon after, the staining analysis and gloss measurement were performed for each sample. Noting the existence of staining in some samples, it was necessary to perform the third cleaning step, which consists of the use of multipurpose paste, sponge, and water that were applied to the surface of each specimen and subsequently washed in running water, soon after, inserted into the oven at a temperature of 70 °C for 30 min.

Results and Discussion

To obtain the gloss loss result after each cleaning step, the final reading used was the measurement after the 1st cleaning step and the initial reading used was the measurement after staining. To calculate the result of loss of gloss in the 2nd cleaning stage, the measurements obtained in the 2nd cleaning stage were used as final reading and as initial reading, the gloss measurements of the 1st cleaning stage were used. And to arrive at the result of loss of gloss from the 3rd cleaning stage, the gloss measurements obtained in the 3rd cleaning stage were used as a final reading, and the gloss measurements obtained in the 2nd cleaning stage were used as an initial reading [6].

Tables 2, 3, and 4 show the results obtained in measuring the brightness of the specimens that were exposed to the staining agents during the period of 30 min, 4 h, and 24 h, respectively, where the initial brightness measurement appears, that is, before staining and the gloss measurement after staining. Gloss losses are also found after staining and after each cleaning step.

Observing the first group of rocks that were exposed to staining agents within 30 min, it was possible to identify that of the 24 specimens used in the staining test, only 8 suffered from the appearance of stains after exposure. Analyzing the rocks exposed to lime in this interval, it was found that there was a loss of brightness in Dallas white, Saint Gabriel black, Castle grey, and Siena white, but only Saint Gabriel black and Castle grey suffered staining. The stains that appeared were very mild and only caused lightning in the region where the lemon was attacked. At each cleaning step, a small change in brightness intensity decrease was visually identified [7].

The rocks that came into contact with the oil during the 30-min interval showed visually more pronounced stains in Dallas white, Castle grey, and Siena white. Saint Gabriel black was resistant to oil and did not show any type of stain.

The specimens that were exposed to coffee for 30 min showed very soft spots visually on Dallas white, Castle grey, and Siena white. Saint Gabriel black showed resistance to coffee and did not suffer staining [8]. As the contact with the coffee lasted a short time, it was possible to remove the stains after the first cleaning step.

The rocks that came in contact with the steel sponge and the detergent, bleach, and degreaser in this staining test during the 30 min did not suffer any type of stains, but it was possible to observe loss of brightness after performing the measurement.

Table 2 Brightness variation of rocks exposed to staining agents for 30 min

Rock type	Staining agent	Initial brightness (GU)	Brightness after exposure to staining agent (GU)	Loss of brightness after exposure to staining agent (%)	Loss of brightness after 1st cleaning step (%)	Loss of brightness after 2nd cleaning step (%)	Loss of brightness after 3rd cleaning step (%)	Stain removal
Dallas white	Lemon	47.35	45.03	4.9	–	–	–	–
Saint Gabriel black		63.21	40.36	36.15	−3.69	10.16	19.95	Not removed
Castle grey		63.01	60.15	4.54	−2.88	5.2	8.11	Not removed
Siena white		70.31	67.35	4.21	–	–	–	–
Dallas white	Oil	61.33	62.46	– 1.84	−4.16	3.7	6.58	Not removed
Saint Gabriel black		61.85	57.56	6.94	–	–	–	–
Castle grey		62.65	61.25	2.23	0.57	1.05	13.08	Not removed
Siena white		68	70	−2.94	−1.93	3.71	9.74	Not removed
Dallas white	Coffee	68.63	64.23	6.41	−3.74	–	–	Removed
Saint Gabriel black		75.4	68.38	9.31	–	–	–	–
Castle grey		61.95	59.38	4.15	−2.61	–	–	Removed
Siena white		62.85	60.23	4.17	−2.21	–	–	Removed
Dallas white	Steel sponge + detergent	63.6	61.88	2.7	–	–	–	–
Saint Gabriel black		65.31	62.5	4.3	–	–	–	–
Castle grey		66.08	62.86	4.87	–	–	–	–

(continued)

Table 2 (continued)

Rock type	Staining agent	Initial brightness (GU)	Brightness after exposure to staining agent (GU)	Loss of brightness after exposure to staining agent (%)	Loss of brightness after 1st cleaning step (%)	Loss of brightness after 2nd cleaning step (%)	Loss of brightness after 3rd cleaning step (%)	Stain removal
Siena white		60.81	61.46	−1.07	–	–	–	–
Dallas white	Bleach	54.38	0.65	6.86	–	–	–	–
Saint Gabriel black		72.98	64.56	11.54	–	–	–	–
Castle grey		63.95	52.98	17.15	–	–	–	–
Siena white		69.48	69.48	0	–	–	–	–
Dallas white	Degreaser	59.38	57.21	3.65	–	–	–	–
Saint Gabriel black		65.88	59.4	9.84	–	–	–	–
Castle grey		62.01	60.46	2.5	–	–	–	–
Siena white		69.6	67.65	2.8	–	–	–	–

(−) There wasn't staining

Table 3 Brightness variation of rocks exposed to staining agents for 4 h

Rock type	Staining agent	Initial brightness (GU)	Brightness after exposure to staining agent (GU)	Loss of brightness after exposure to staining agent (%)	Loss of brightness after 1st cleaning step (%)	Loss of brightness after 2nd cleaning step (%)	Loss of brightness after 3rd cleaning step (%)	Stain removal
Dallas white	Lemon	60.63	57.28	5.53	–	–	–	–
Saint Gabriel black		71.38	47.65	33.24	−16.79	14.14	27.27	Not removed
Castle grey		61.55	58.36	5.18	–	–	–	–
Siena white		68.86	68.28	0.84	–	–	–	–
Dallas white	Oil	62.2	61.35	1.37	−3.63	3.62	9.5	Not removed
Saint Gabriel black		74.65	49.98	33.05	–	–	–	–
Castle grey		58.6	45.81	21.83	−28.92	1.54	6.31	Not removed
Siena white		71.61	53.78	24.9	−20.12	−9.38	2.31	Not removed
Dallas white	Coffee	53	52.1	1.7	−0.58	−34.85	32.49	Not removed
Saint Gabriel black		64.16	51.78	19.3	–	–	–	–
Castle grey		67.26	65.43	2.72	−1.33	23.82	−21.66	Not removed
Siena white		74.1	70.45	4.93	−2.41	10.77	−6.42	Not removed
Dallas white	Steel sponge + detergent	61.78	60.63	1.86	−3.91	4.13	−1.66	Not removed
Saint Gabriel black		70.85	57.13	19.36	–	–	–	–
Castle grey		63.01	61.03	3.14	−3.56	3.86	–	Removed

(continued)

Table 3 (continued)

Rock type	Staining agent	Initial brightness (GU)	Brightness after exposure to staining agent (GU)	Loss of brightness after exposure to staining agent (%)	Loss of brightness after 1st cleaning step (%)	Loss of brightness after 2nd cleaning step (%)	Loss of brightness after 3rd cleaning step (%)	Stain removal
Siena white		71.5	65.4	8.53	–	–	–	–
Dallas white	Bleach	62.92	53.68	14.69	–	–	–	–
Saint Gabriel black		75.61	58.73	22.33	–	–	–	–
Castle grey		60.81	58.93	3.09	–	–	–	–
Siena white		62.9	55.36	11.99	–	–	–	–
Dallas white	Degreaser	60.12	58	3.53	–	–	–	–
Saint Gabriel black		62.56	50.38	19.47	–	–	–	–
Castle grey		61.33	60.33	1.63	–	–	–	–
Siena white		64.11	66.28	– 3.38	–	–	–	–

(–) There wasn't staining

Table 4 Brightness variation of rocks exposed to staining agents for 24 h

Rock type	Staining agent	Initial brightness (GU)	Brightness after exposure to staining agent (GU)	Loss of brightness after exposure to staining agent (%)	Loss of brightness after 1st cleaning step (%)	Loss of brightness after 2nd cleaning step (%)	Loss of brightness after 3rd cleaning step (%)	Stain removal
Dallas white	Lemon	58.66	56.61	3.49	–	–	–	–
Saint Gabriel black		73.91	53.03	28.25	−9.01	5.24	8.85	Not removed
Castle grey		58.41	55.61	4.79	–	–	–	–
Siena white		59.7	61.15	−2.43	–	–	–	–
Dallas white	Oil	68.45	62.81	8.24	−0.67	– 4.22	6.28	Not removed
Saint Gabriel black		73.78	63.36	14.12	–	–	–	–
Castle grey		62.8	57.7	8.12	−5.94	−0.9	3.7	Not removed
Siena white		64.16	54.55	14.98	−22.11	−1.04	5.97	Not removed
Dallas white	Coffee	66.45	60.1	9.56	−2.33	1.04	7.61	Not removed
Saint Gabriel black		72.3	60.33	16.56	–	–	–	–
Castle grey		66	62.61	5.14	−2.75	0.78	3.18	Not removed
Siena white		68.25	64.71	5.19	−1.34	−0.35	11.44	Not removed
Dallas white	Steel sponge + detergent	50.95	46.25	9.22	−11.03	−0.51	8.64	Not removed
Saint Gabriel black		79.46	63.63	19.92	–	–	–	–
Castle grey		61.56	55.96	9.1	−3.79	−2.62	8.59	Not removed

(continued)

Table 4 (continued)

Rock type	Staining agent	Initial brightness (GU)	Brightness after exposure to staining agent (GU)	Loss of brightness after exposure to staining agent (%)	Loss of brightness after 1st cleaning step (%)	Loss of brightness after 2nd cleaning step (%)	Loss of brightness after 3rd cleaning step (%)	Stain removal
Siena white		61.95	55.8	9.93	−2.96	−0.97	5.43	Not removed
Dallas white	Bleach	61.61	41.5	32.64	−17.73	−1.06	0.95	Not removed
Saint Gabriel black		73.2	49.65	32.17	–	–	–	–
Castle grey		61.93	40.4	34.77	–	–	–	–
Siena white		77.66	68.9	11.28	–	–	–	–
Dallas white	Degreaser	68.18	61.05	10.46	−4.6	0.8	5.24	Not removed
Saint Gabriel black		78.6	60.36	23.21	–	–	–	–
Castle grey		63.1	56.95	9.75	−3.97	0.39	5.14	Not removed
Siena white		68.81	59.98	12.83	–	–	–	–

(–) There wasn't staining

Analyzing the results obtained in the group of rocks exposed to staining agents in the interval of 4 h, it was possible to verify that of the 24 specimens used in the test, only 9 suffered from staining. The specimens exposed to lemon during this interval showed greater resistance, namely Dallas white, Castle grey, and Siena white. Saint Gabriel black was the only one that suffered from staining and the stain caused was very mild visually, only causing a decrease in the intensity of the color in the region of the attack with the lemon [9]. Although the stain was visually not very noticeable, it was not possible to remove it after all the cleaning steps.

The oil applied to the group of rocks exposed for 4 h, caused visually more pronounced stains than the first group. Dallas white, Castle grey, and Siena white were the rocks that did not show resistance to oil. Saint Gabriel black showed resistance to the staining agent, so it did not suffer any type of staining, there was only a loss of brightness verified by the measurement performed.

Rocks in contact with the coffee for 4 h developed permanent stains after exposure. Dallas white, Castle grey, and Siena white did not show resistance to coffee, that is, they suffered staining and loss of brightness. Saint Gabriel black showed resistance and did not suffer staining. Visually, Dallas white and Siena white developed more pronounced stains than Castle grey [10].

The steel sponge and the detergent, when in contact with the rocks for 4 h, showed soft and very small stains on the Dallas white and Castle grey. Saint Gabriel black and Siena white showed resistance to this staining agent, but it was found that all the rocks after measurement lost brightness.

As in the first test of exposing the rocks to 30 min, the bleach and the degreaser did not cause stains on the rocks when in contact for 4 h.

In the group exposed to rocks within 24 h, the 24 specimens used in test 13 suffered from the appearance of stains after contact with the staining agents. The rock that did not show resistance to lime was Saint Gabriel black [5]. Comparing the three groups that were exposed to lemon, it was found that the time the rock is in contact with the staining agent does not intensify the stain caused, in the three groups the stain was not removed after the cleaning steps.

The rocks that came into contact with the oil during the 24 h interval showed very intense spots in Dallas white, Castle grey, and Siena white. Saint Gabriel black did not suffer staining, but had a loss of shine. Comparing the three groups of rocks exposed to oil, it is possible to verify that as the exposure time increases, the rocks present more visually intense stains.

The coffee in contact with the specimens during the 24-h interval caused stains in Dallas white, Castle grey, and Siena white. Comparing the three groups, it can be concluded that coffee causes permanent staining if it maintains contact with the rock for a period equal to or greater than 4 h. in contact with the staining agent [4].

The steel sponge and the detergent in contact with the rocks during the 24 h period showed stains on the Dallas white, Castle grey, and Siena white. Comparing the three groups exposed to sponge and detergent, it is possible to verify that as the exposure time increases, the rocks develop permanent stains [3].

The bleach when in contact with the rocks in the period of 24 h showed staining only in the Dallas white and the stain caused was not removed after the cleaning

steps. And the rocks exposed to the degreaser in 24 h showed stains in Dallas white and Castle grey.

Conclusion

The staining test seeks to simulate the external stresses that the rocks will suffer when applied, and in this work, it was possible to verify how the four types of rocks chosen reacted when in contact with the selected staining agents. In the group in which the rocks were exposed to staining agents for 30 min, it was possible to verify that only five of the specimens showed permanent stains after carrying out all the cleaning steps. In the group of rocks exposed to staining agents for 4 h, it was found that 8 specimens suffered from the emergence of permanent stains. As in the first group tested, there was loss of gloss after the cleaning steps. In this second trial, the spots were more pronounced when compared to the first group. The group of rocks exposed to 24 h showed permanent stains in 13 specimens, causing more visually accentuated stains than the second group studied. Like the other groups, there were gloss losses after each cleaning step.

It is concluded that the rocks that suffered from staining, as the exposure time increased, developed more visually accentuated and permanent stains. Each rock, due to mineralogical composition, reacted differently to the contact with the chosen staining agents. It was possible to verify that the culinary staining agents caused more stains on the rocks than the staining agents used on a daily basis for cleaning.

Acknowledgements The authors thank the Brazilian agencies CNPq, CAPES, and FAPERJ for the support provided to this investigation.

References

1. Bahiense AV, Alexandre J, Xavier GC, Azevedo ARG, Monteiro SN (2021) Dosage of interlocking paving with ornamental rock waste: an experimental design approach, particle packing and polluting potential. Case Stud Constr Mater 15:e00596
2. Marvila MT, Azevedo ARG, Barroso LS, Barbosa MZ, Brito J (2020) Gypsum plaster using rock waste: a proposal to repair the renderings of historical buildings in Brazil. Constr Build Mater 250:118786
3. Dönmez S, Sari YD (2005) A digital image analysis basedsurface polish measurement system. J Eng Sci 11(3):401–405
4. Frascá MHBO (2014) Tipos de rochas ornamentais e características tecnológicas. In: Tecnologia de Rochas ornamentais: pesquisa, lavra e beneficiamento, vol. 2. CETEM/MCTI, Rio de Janeiro, pp 44–98
5. Brazilian Association of Norms Technical (1997) NBR 13818. Ceramic tiles for coating—Specification and test methods: determination of stain resistance. Annex G, Rio de Janeiro (In Portuguese)

6. Marvila MT, De Azevedo ARG, De Matos PR, Monteiro SN, Vieira CM (2021) Materials for production of high and ultra-high-performance concrete: review and perspective of possible novel materials. Materials 14(15). https://doi.org/10.3390/ma14154304
7. Azevedo ARG, Marvila MT, Zanelato EB, Alexandre J, Xavier GC, Cecchin D (2020) Development of mortar for laying and coating with pineapple fiber. Rev Bras De Engenharia Agricola e Ambiental 24(3):187–193. https://doi.org/10.1590/1807-1929/agriambi.v24n3p187-193(InPortuguese)
8. Carvalho A, Xavier GC, Alexandre J, Pedroti LG, de Azevedo ARG, Vieira CMF, Monteiro SN (2014) Environmental durability of soil-cement block incorporated with ornamental stone waste https://doi.org/10.4028/www.scientific.net/MSF.798-799.548
9. Marvila MT, de Azevedo ARG, de Oliveira LB, Xavier GC, Vieira CMF (2021) Mechanical, physical and durability properties of activated alkali cement based on blast furnace slag as a function of $\%Na_2O$. Case Studies in Constr Mater 15. https://doi.org/10.1016/j.cscm.2021.e00723
10. Zeyad AM, Magbool HM, Tayeh BA, Azevedo ARG, Abutaleb A, Hussain Q (2022) Production of geopolymer concrete by utilizing volcanic pumice dust. Case Stud Constr Mater 16. https://doi.org/10.1016/j.cscm.2021.e00802

Investigation on the Delayed Cracking Performance of the 22MnB5 Hot Roll Bending Pipe

Ping Zhu, Tianhan Hu, Kai Ding, and Yulai Gao

Abstract 22MnB5 steel possesses a promising application in the structural components in automobile industry mainly attributing to its low cost combined with the high mechanical properties. The delayed cracking behavior of the 22MnB5 steel in the solution of 0.1 mol/L HCl with various times is comparatively investigated. By observing the crack initiation and propagation during the delayed cracking test, it can be found that the initiation of the cracks exists an incubation period, and the cracks appear after being soaked in acid for 3 h. In particular, the crack initiation location is highly related to the position of the pipe, especially the inner bending zones reflect much higher susceptibility of the delayed cracks. The hydrogen can easily accumulate in the bending zones with large residual stress. The interaction between hydrogen and metal atoms can possibly weaken the cohesion of the grain boundaries, eventually trigger the initiation of the cracks.

Keywords Hot roll bending · 22MnB5 steel pipe · Delayed cracking · Crack initiation · Failure mechanism

Introduction

The development and application of lightweight materials in automotive are significant to the energy saving, emission reduction, safety etc. In the past decades, lightweight materials have gradually become the preferable choice in automobile

P. Zhu · T. Hu · K. Ding (✉) · Y. Gao (✉)
State Key Laboratory of Advanced Special Steel, Center for Advanced Solidification Technology, School of Materials Science and Engineering, Shanghai University, Shanghai 200444, People's Republic of China
e-mail: dingkaiwsj@shu.edu.cn

Y. Gao
e-mail: ylgao@shu.edu.cn

Y. Gao
Shanghai Engineering Research Center for Metal Parts Green Remanufacture, Shanghai 200444, People's Republic of China

M. Zhang et al. (eds.), *Characterization of Minerals, Metals, and Materials 2023*, The Minerals, Metals & Materials Series
https://doi.org/10.1007/978-3-031-22576-5_44

industry [1, 2]. Among which, the advanced high strength steels (AHSSs) have been widely applied for the purpose of energy saving and emission reduction attributing to their high strength, which can appropriately reduce the thickness of steel plate [3, 4]. With the increased tendency for lightweight, the workpiece needed to be designed and manufactured by the materials with higher strength and more complex shapes. Due to the poor plastic properties of high strength steels, the cracks and wrinkle could be possibly occurred in the bending area during the cold forming process. Compared with the cold stamping, the hot stamping could effectively relief the problems e.g. serious rebound and poor dimensional accuracy of complex parts [5–8]. Based on these advantages, hot stamping has been rapidly developed as one of the preferred manufacturing techniques in the field of automobile manufacturing [9].

22MnB5 steel is widely used in automobile industry mainly attributing to its low cost and high mechanical properties. The initial microstructure of the 22MnB5 steel is mainly composed of ferrite and pearlite, and the corresponding tensile strength is around 600 MPa. After hot roll bending, the microstructure of the 22MnB5 steel is transformed to the lath martensite with high dislocation density and a small amount of residual austenite. The ultimate tensile strength (UTS) of 22MnB5 steel after hot roll bending can be over 1500 MPa. Unfortunately, the poor delayed cracking performance of such AHSSs has become the key point to limit their application when their strength exceeds 1000 MPa [10–13].

Generally speaking, martensite possesses a high susceptibility of delayed cracking behavior, yet austenite can produce a positive effect to improve the delayed cracking resistance [14]. Junichiro et al. [15] found that the hydrogen diffusivity in martensite was around 5–6 orders higher than that in austenite. Lian et al. [16] pointed out that the stress state could significantly affect the crack initiation, and the cracking strain differed greatly under various stress states. In a word, the delayed cracking performance is the result of coupled effects among the hydrogen in steel, microstructure and stress–strain state etc. Thus, there exists a necessity to study the delayed cracking behavior of the hot stamping steels with ultra-high strength.

In the present study, the 22MnB5 steel pipes formed by hot roll bending are chosen to evaluate their delayed cracking performance. The pH and temperature are in situ recorded during the test. By observing the crack initiation and propagation of hot roll bending pipe after being soaked in acid for different time, the delayed cracking behavior of the 22MnB5 hot roll bending pipe is correspondingly analyzed and discussed.

Experimental Procedures

The 22MnB5 steel pipes after hot roll bending are chosen, and the chemical composition of the 22MnB5 steel pipe is listed in Table 1. The schematic of hot roll bending pipe of the 22MnB5 steel is shown in Fig. 1. Considering the bend and straight sections existed in the actual service process, the performance of both the typical sections should be comparatively studied in the delayed cracking test. Compared with

Table 1 The chemical composition of the 22MnB5 steel pipe (wt%)

Elements	C	Si	Mn	P	S	Cr + Mo	B	Al	Ti
22MnB5	0.25	0.4	0.14	0.025	0.01	0.5	0.0035	0.015	0.05

straight section, the stress distribution of bent section is more complicated due to the addition of further bending process, and the characterization of delayed cracking performance is more meaningful for practical application.

Before the delayed cracking test, the specimens are initially cleaned with degreaser at room temperature, then the specimen surfaces are scrubbed successively with alcohol and acetone. The appearances of specimens before and after cleaning are displayed in Fig. 2.

As for the delayed cracking test, the cleaned specimens are dipped in the solution of 0.1 mol/L hydrochloric acid, and the ratio of solution volume to specimen

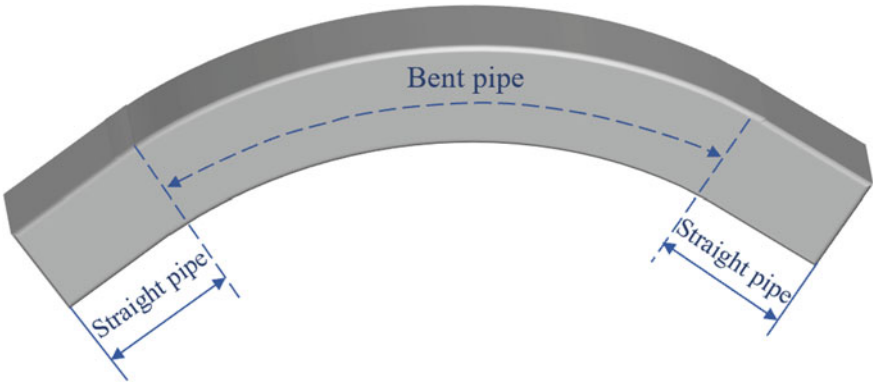

Fig. 1 Schematic of the hot roll bending pipe of the 22MnB5 steel

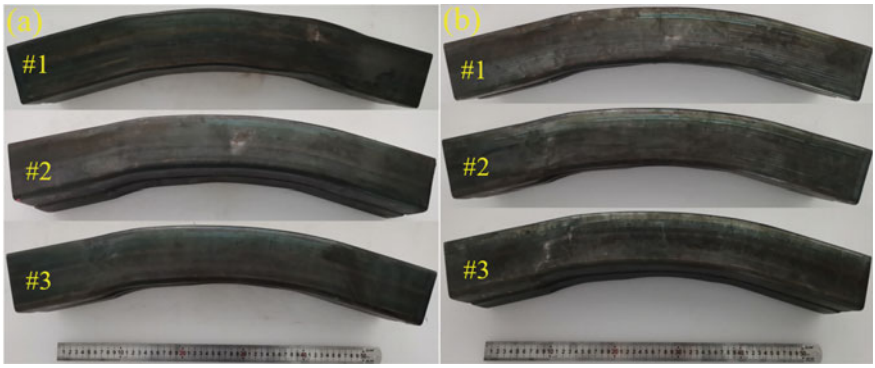

Fig. 2 Appearance of the 22MnB5 steel pipe specimens #1, #2, #3 before delayed cracking test: **a** before cleaning, and **b** after cleaning

weight is 7 mL/g. The whole duration of the delayed cracking test is 300 h. The pH value and temperature of the solution are monitored in real-time during the delayed cracking test. The specimens are taken out for photo recording, weighing, and crack observation at 1 h, 3 h, 5 h, 7 h, 9 h, 100 h, 200 h, and 300 h. In order to ensure the accuracy of the test, three specimens are tested under the same conditions. To emphasize the comparability, the performance of delayed cracking for specimen #1 is selected for analysis.

Results and Discussion

The pH value and temperature change during the delayed cracking test are shown in Fig. 3. It can be found that the pH value increases with the increase of the time, which keeps nearly unchanged at about 4 after 150 h. It should be noted that the sharp decrease in the pH value at 100 h is because of the artificial mixing of acid during the test. The temperature of delayed cracking test is always in the range of 20–24 °C.

Figure 4 shows the appearance of the 22MnB5 steel pipe specimen after delayed cracking test for 1 h. No obvious crack can be detected on the surface of the specimens. The appearance of the 22MnB5 steel pipe specimen after delayed cracking test for 3 h is shown in Fig. 5. Clearly several cracks appear at the inner bending zones of the specimen, but no crack can be found at the outer bending zones. Figure 6 displays the appearance of the 22MnB5 steel pipe specimen after delayed fracture for 7 h. The cracks at the inner bending zones of the specimen obviously extend to the side of the specimen and the outer bending zones. The appearance of the 22MnB5 steel pipe specimen after delayed cracking test for 100 h is presented in Fig. 7. Compared with the specimen after delayed cracking for 3 h, the cracks at the inner bending zones extend significantly to the side and outer bending zones of the specimen.

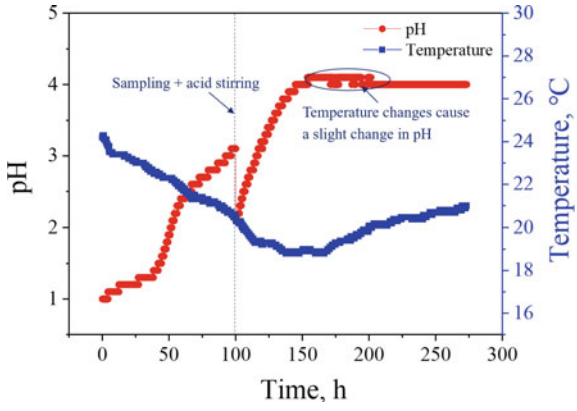

Fig. 3 The change of the pH value and temperature during delayed cracking test

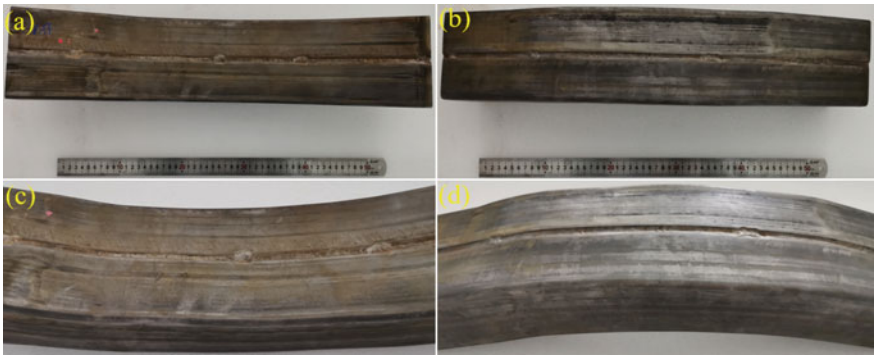

Fig. 4 Appearance of the 22MnB5 steel pipe after delayed cracking for 1 h: **a** inner surface, **b** outer surface, **c** details of the inner surface, and **d** details of the outer surface

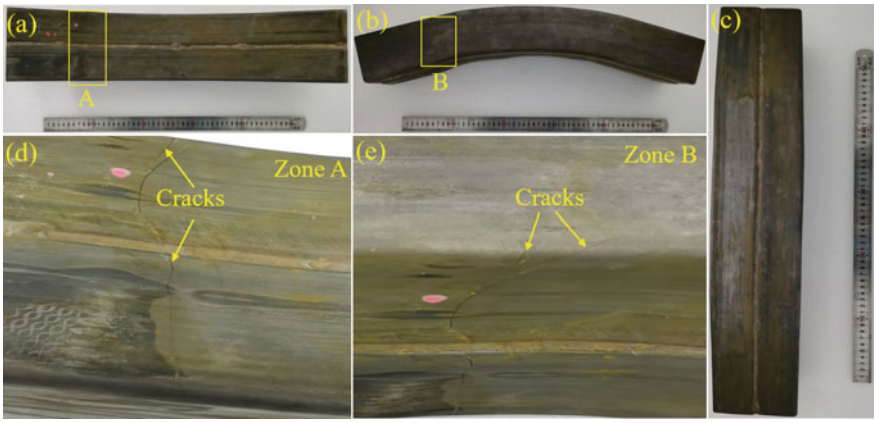

Fig. 5 Appearance of the 22MnB5 steel pipe after delayed cracking for 3 h: **a** inner surface, **b** side surface, **c** outer surface, **d** details of the inner surface crack in the region marked with yellow rectangle in (**a**), and **e** details of the side surface crack in the region marked with yellow rectangle in (**b**)

The variation of specimen weight of three specimens and crack length of specimen #1 with delayed cracking time is exhibited in Fig. 8. With the delay cracking time of 9 h, the weight reduction ratio of the specimen is about 0.6%, yet the weight reduction ratio of the specimen is about 1.6% when the delay cracking time is prolonged to 100 h. No crack can be found within 1 h of delayed cracking, and crack propagation mainly occurs in 3–7 h of delayed cracking. Only one crack exceeding 80 mm in the specimen can be observed within 100 h of the delayed cracking test.

Figures 4 and 5 exhibit the cracks appear in 22MnB5 steel pipe after the delayed cracking test for 3 h, indicating that there exists an incubation period for crack initiation. Usually, crack initiation is related to hydrogen content [17]. That is to say, the delayed cracking occurs only when the local hydrogen concentration reaches a

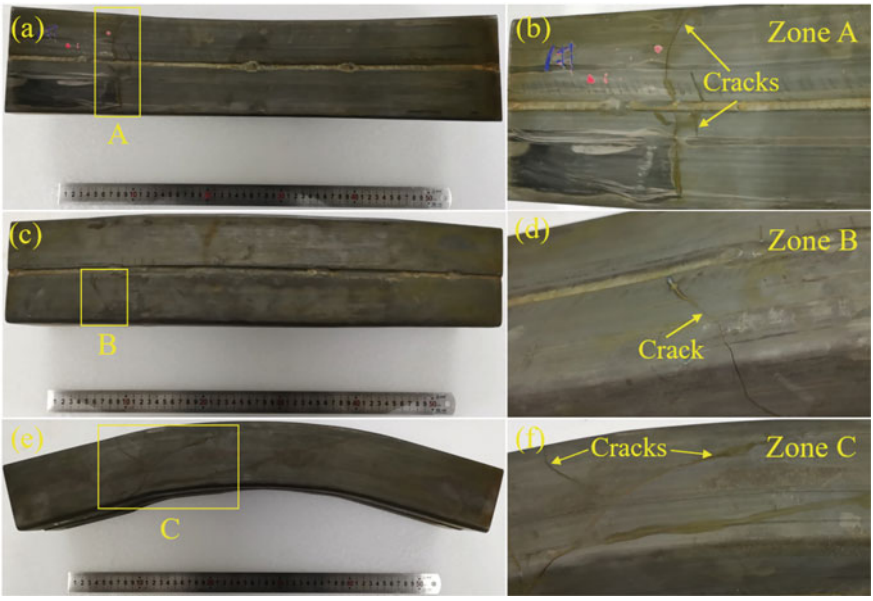

Fig. 6 Appearance of the 22MnB5 steel pipe after delayed cracking for 7 h: **a** inner surface, **b** details of the inner surface crack in the region marked with yellow rectangle in (**a**), **c** outer surface, **d** details of the outer surface crack in the region marked with yellow rectangle in (**c**), **e** side surface, and **f** details of the side surface crack in the region marked with yellow rectangle in (**e**)

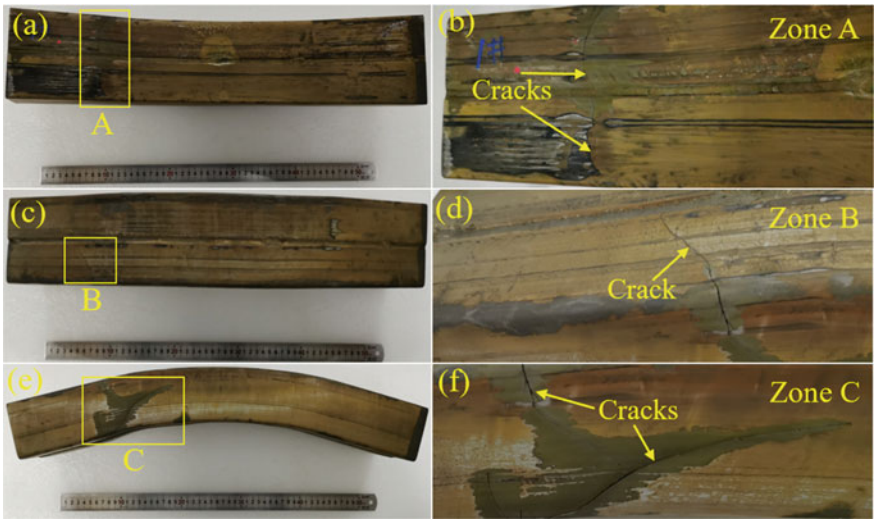

Fig. 7 Appearance of the 22MnB5 steel pipe after delayed cracking for 100 h: **a** inner surface, **b** details of the inner surface crack details in the region marked with yellow rectangle in (**a**), **c** outer surface, **d** details of the outer surface crack in the region marked with yellow rectangle in (**c**), **e** side surface, and **f** details of the side surface crack in the region marked with yellow rectangle in (**e**)

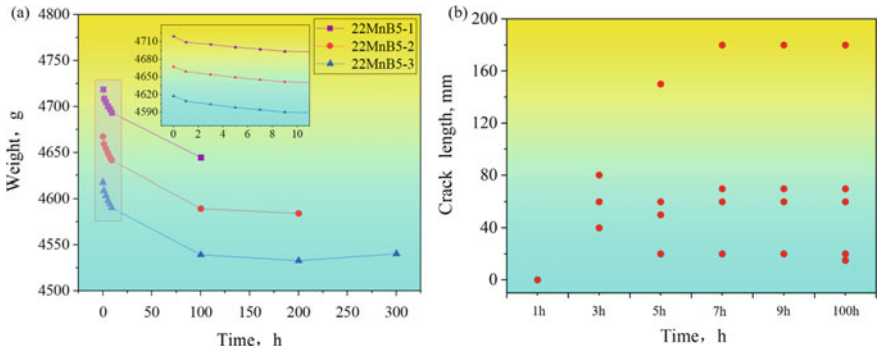

Fig. 8 **a** Variation of weight with delayed cracking time, **b** variation of the crack length with delayed cracking time

critical levels, and the incubation time is determined by the time to attain critical hydrogen concentration. Corresponding to the crack region in Figs. 5, 6, 7, it can be seen that the cracks tend to occur and extend at the inner bending zones. The stress gradient causes by the residual stress in the hot roll bending is the driving force of the hydrogen diffusion. The hydrogen can weak the atomic bonding energy and the cohesion of the grain boundaries and therefore lead to the crack initiation and propagation [18, 19]. As a result, the hydrogen is accumulated in the inner bending zones with large residual stress, reflecting much higher susceptibility of delayed cracks.

The schematic of delayed cracking failure mechanism for the 22MnB5 steel pipe is displayed in Fig. 9. The microstructure of the 22MnB5 steel specimen is lath martensite, and a large residual stress concentration in the bending zones after the hot roll bending process is existed. The stress gradient promotes the diffusion and accumulation of hydrogen to the stress concentration zones. Due to the reduction in atomic bonding energy caused by hydrogen, the cracks tend to firstly initiate at the bending zones with aggregated hydrogen. After crack initiation, stress concentration occurs at the crack tip, and hydrogen atoms further accumulate at the crack tip. When the accumulated hydrogen concentration at the crack tip reaches a critical level, the initial microcracks extend further and finally lead to hydrogen-induced delayed cracking.

Conclusions

The delayed cracking behavior of the 22MnB5 steel pipes in the solution of 0.1 mol/L HCl with various time is comparatively investigated. The results show that there exists an incubation period for the crack initiation. In the first step, no obvious crack could be detected. Then the cracks appear after the delayed cracking test for 3 h. The crack propagation is triggered with the prolonged soaking time in acid. Based on the crack

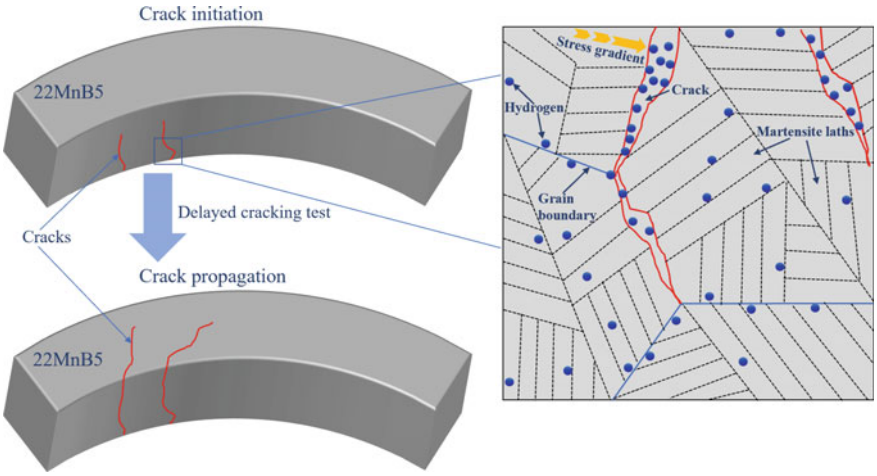

Fig. 9 Schematic of delayed cracking mechanism of the 22MnB5 steel pipe

observation, it can be found that the crack initiation location is highly related to the position of the pipe, and the inner bending zones reflect much higher susceptibility of delayed cracks. The nonuniform stress distribution can be generated inside the 22MnB5 steel pipe after hot roll bending, leading to the accumulation of hydrogen in the bending zones with large residual stress. The interaction between hydrogen and metal atoms could possibly weaken the cohesion of the grain boundaries, eventually trigger the initiation and propagation of the cracks.

Acknowledgements This work is supported by the National Natural Science Foundation of China (Grant no. 52101042) and the China Postdoctoral Science Foundation (Grant no. 2021M702082).

References

1. Farooq MA, Roth R, Kirchain R (2018) Lightweighting technologies: analyzing strategic and economic implications of advanced manufacturing processes. Int J Prod Econ 206:268–279
2. Chu Y, Sun L, Li L (2019) Lightweight scheme selection for automotive safety structures using a quantifiable multi-objective approach. J Clean Prod 241:118316
3. Jambor A, Beyer M (1997) New cars-new materials. Mater Des 18(4):203–209
4. Jing R, Yuan C, Rezaei H, Qian J, Zhang Z (2020) Assessments on emergy and greenhouse gas emissions of internal combustion engine automobiles and electric automobiles in the USA. J Environ Sci 90:297–309
5. Sun CY, Bai Q, Lin JG, Matsumoto T, Dean T (2013) The effect of process and model parameters in temperature prediction for hot stamping of boron steel. Adv Mech Eng 829379
6. Zhu B, Xu ZQ, Wang K, Zhang YS (2020) Nondestructive evaluation of hot stamping boron steel with martensite/bainite mixed microstructures based on magnetic Barkhausen noise detection. J Magn Magn Mater 503(6):166591–166598

7. Lobbe C, Hering O, Hiegemann L, Tekkaya E (2016) Setting mechanical properties of high strength steels for rapid hot forming processes. Materials 9(4):229–248
8. Donders S, Brughmans M, Hermans L, Tzannetakis N (2005) The effect of spot weld failure on dynamic vehicle performance. Sound Vib 39(4):16–25
9. Knoerr L, Faath T, Dykeman J, Malcolm S (2016) Evaluation of hot forming effects mapping for CAE analyses. J Phys Conf Ser 734:032041
10. Komatsuzaki Y, Joo H, Yamada K (2008) Influence of yield strength levels on crack growth mode in delayed fracture of structural steels. Eng Fract Mech 75(3–4):551–559
11. Sanchez J, Lee SF, Martin-Rengel MA, Fullea J, Andrade C, Ruiz-Hervias J (2015) Measurement of hydrogen and embrittlement of high strength steels. Eng Fail Anal 59:467–477
12. Wei X, Jin L, Wei K (1998) Crack growth retardation of single overload for A537 steel in a 3.5% NaCl solution under cathodic potential and free corrosion condition. Int J Fatigue 20(3):225–231
13. Nei YH, Hui WJ, Fu WT, Weng YQ (2007) Effect of boron on delayed fracture resistance of medium-carbon high strength spring steel. J Iron Steel Res Int 14(6):53–57
14. Zhu X, Li W, Hsu TY, Zhou S, Wang L, Jin XJ (2015) Improved resistance to hydrogen embrittlement in a high-strength steel by quenching partitioning tempering treatment. Scr Mater 97:21–24
15. Yamabe J, Takakuwa O, Matsunaga H, Itoga H, Matsuoka S (2017) Hydrogen diffusivity and tensile-ductility loss of solution-treated austenitic stainless steels with external and internal hydrogen. Int J Hydrog Energy 42(18):13289–13299
16. Lian J, Sharaf M, Archie F, Munstermann S (2013) A hybrid approach for modelling of plasticity and failure behaviour of advanced high-strength steel sheets. Int J Damage Mech 22(2):188–218
17. Homma T, Chiba T, Takai K, Akiyama E, Oshikawa W, Nagumo M (2022) Cracking process in delayed fracture of high-strength steel after long atmospheric exposure. ISIJ Int 62(4):776–787
18. Liu Y, Chen Y, Yang C, Han XH (2022) Study on hydrogen embrittlement and reversibility of hot-stamped aluminized 22MnB5 steel. Mater Sci Eng A 848:143411
19. Novak P, Yuan R, Somerday BP, Sofronis P, Ritchie RO (2010) A statistical, physical-based, micro-mechanical model of hydrogen-induced intergranular fracture in steel. J Mech Phys Solids 58(2):206–226

Izod Impact Characterization of Engineered Artificial Stone Reinforced by Arapaima Gigas Fish Scales

Elaine A. S. Carvalho, Rafael Bittencourt Miranda, Noan Simonassi, Maria Luiza Gomes, Henry Colorado, Sérgio Neves Monteiro, and Carlos Maurício Vieira

Abstract In recent decades, with the advance of industrialization, the huge amount of waste discarded by industries has generated discussions about self-sustainable solutions. One of these solutions is artificial stone, as the use of waste can be a good alternative for the production of this type of material. Therefore, the main objective of the present work was to evaluate the influence of young scales of arapaima gigas on the reinforcement of artificial stones made with quarry dust and epoxy resin, by the process of vibration, compression, and vacuum. The residue was divided into three granulometric ranges by the sieving method: Coarse and medium (quarry dust) and fine (quartzite). Data were treated through statistical analysis, using analysis of variance (ANOVA). The proportions obtained were 5, 7, and 8 (50% coarse and medium), (33% coarse, medium and fine) and (67% coarse, 17% medium, and 16% fine). The 3 developed compositions were submitted to the physical index test. The result obtained classified the composition 7 for the incorporation of arapaima scales, and the physical index, bending, and charpy impact tests were performed to characterize the developed stone. The results obtained indicate that the artificial stone with pirarucu scale had a porosity of 0.67% greater than the one without scale, indicating lack of adhesion of the scale with the residues. The mechanical strength was higher, 34.7 ± 2.7 Mpa due to the arapaima scales having a high strength. The impact energy of charpy was 28.3 ± 4.6 J/m for the scaled artificial stone and 24.1 ± 4.9 J/m for the scaleless stone.

Keywords Artificial stone · Fine gravel · Quartzite · Arapaima scales

E. A. S. Carvalho (✉) · R. B. Miranda · N. Simonassi · M. L. Gomes · C. M. Vieira
Advanced Materials Laboratory—LAMAV, State University of Northern Rio de Janeiro—UENF, Av. Alberto Lamego, 2000, Campos dos Goytacazes 28013-602, Brazil
e-mail: elainesanttos@yahoo.com.br

H. Colorado
CCComposites Laboratory, Universidad de Antioquia UdeA, Calle 70 No. 52-21, Medellín, Colombia

S. N. Monteiro
Materials Science Department, Military Institute of Engineering—IME, Praça General Tibúrcio, 80, Urca, RJ, Rio de Janeiro, RJ 22290-270, Brazil

M. Zhang et al. (eds.), *Characterization of Minerals, Metals, and Materials 2023*, The Minerals, Metals & Materials Series
https://doi.org/10.1007/978-3-031-22576-5_45

Introduction

The search for the delicate balance between economic growth and sustainability has been one of the core issues. The underlying idea is that economies should be able to maintain sustained growth over time, but consuming fewer natural resources and avoiding the degradation of the environment [1]. The most challenging task is to use the waste from the industry in the right place. Waste comes out of the industry in many ways. Some waste causes air pollution and some waste is responsible for soil pollution [2].

Tons of ornamental stone residues are produced throughout the world every year. These residues are improperly discarded in the environment, causing serious public health problems, since they release a powder into the atmosphere. When inhaled, these substances cause respiratory complications [3].

The Brazilian ornamental stone sector assumes a privileged position in the global mineral market, producing an equivalent of 8.3 million tons in 2017 with the south-eastern region of Brazil responsible for approximately 60% of this amount. Although this sector is already consolidated, its production process is still rudimentary and inefficient, and the waste is primarily disposed of in a disorderly manner [4].

Arapaima gigas, also known as pirarucu in Brazil, is considered one of the largest water fish, reaching a maximum weight close to 200 kg and length between 2 and 3 m. how many fish are covered with scales that can reach 10 cm in length, that is, aids to self-defense due to their natural habitat in rivers of the Amazon basin, which become infested by piranhas with the advance of the dry season. Arapaima scales are an example of material that evolved to provide protection from predators. They feature laminated composite structures coated with a pattern of compensated collagen layers and reinforced with nanocrystals. Collagen fibers are arranged in a cross-lamellar arrangement, resulting in a laminated composite [5–7].

The study of these biological materials has become increasingly attractive and reveals a range of new structures, mechanical responses, and design principles that match and often surpass synthetic materials with similar functions. The fish industry has pointed to promising prospects due to the existing demands in the markets of Asia, Africa, Latin America, and the Caribbean, this contrasts with the difficulties that the fishing sector faces, especially with regard to waste from the fish process, with highlighting the scales which are solid waste that can correspond to 1% of the total mass of the fish [7].

The quarry dust stone residue considered waste from the process of obtaining crushed stone, is called quarry fines with granulometry (<4.8 mm). It is almost always present in large quantities, they are harmful to the environment due to the dust generated, the silting produced by the drainage, and the space occupied in the quarry itself. These quarries generate a significant amount of fines mainly in the rock-crushing process. Quarry fines are accumulated in restricted areas around crushing plants, on the surface, as they are not properly used [8].

Artificial stones have demonstrated a high market value and also an increasing demand in recent times. Typically named as stone industrialized consists of 95%

natural aggregates, that is, substantially a natural material. Among the advantages artificial stones are solid, impermeable, good mechanic resistant, and had liquid penetration resistant, remaining only on the surface. This is caused by resin used in the manufacturing process, that provide adhesion between the stone particles and also penetrate between the interstices, eliminating the porosity of natural stones [9].

The physical and mechanical properties of the artificial stone are the main influencing factors to its use in the construction industry. These properties are directly related to the resin content and the microstructure which can be seen in the production process [10].

Therefore, the present work main goal was to evaluate the influence of young arapaima gigas fish scales reinforcing engineered artificial stone made with waste quarry dust and epoxy resin.

Materials and Methods

The quarry dust fine particles waste was collected as tail from a pebble separation process in the Itereré quarry located in the mountain region of Serra da Bela Vista, at 17 km from the city of Campos dos Goytacazes, north of state of Rio de Janeiro, Brazil. After collection, the waste was subjected to ball milling for further reduction in particle size. By means of dry sieving, the reduced waste was then separated into three granulometric classes: (i) large, from 2 to 0.71 mm, (ii) medium, from 0.71 to 0.063 mm, and (iii) fne particles, grains with size less than 0.063 mm. The quartzite residue was supplied by the Mineral Technology Center (CETEM), located in the city of Cachoeiro, state of Espirito Santo, Brazil. Whose granulometry was below 0.063 mm. The arapaima was acquired frozen at 3 to 4 months of age, the scales were removed with pliers and placed in an oven at 60 °C until constant mass was acquired (Fig. 1).

The epoxy used as binding for the waste particles was a diglycidyl ether of bisphenol A (DGEBA) resin mixed with the triethylene tetramine (TETA) supplied by Epoxyfber, Brazil. The supplier indicated the density of the epoxy as 1.15 g/cm^3.

Determination of the Highest Packaging Granulometric Composition

Based on three ranges of grains obtained, 10 different mixtures with different percentages of rough, medium and fine particles were proposed. Figure 2 shows a complete ternary diagram developed in the experimental numeric-modeling grid Simplex (Simplex-Lattice Design) to obtain greater packaging, each vertex of the triangle corresponds to 100%: large (L), medium (M) and fine (F) particles. The other points in the triangle display (in parenthesis) the fractions corresponding to the mixtures.

Fig. 1 Arapaima scale used in the production of artificial stone

To determine the proportion of the greatest packaging of the 10 mixtures. (Tcharllis) For each composition, the test was done three times for assuring statistical validation. Each sample of waste compositional mixture was placed in a steel vessel and left vibration for 2 min under a load of 10 kg. The mixture was weighed and the apparent density was calculated.

The treatment of the data obtained from the vibrated density was performed, using analysis of variance (ANOVA) of the completely randomized design (DIC) ($p \leq 0.05$), in order to verify the existence of statistical significance between the treatment performed. Once the statistical difference was confirmed, Tukey's means comparison test ($p \leq 0.05$) was performed in order to verify which trait obtained

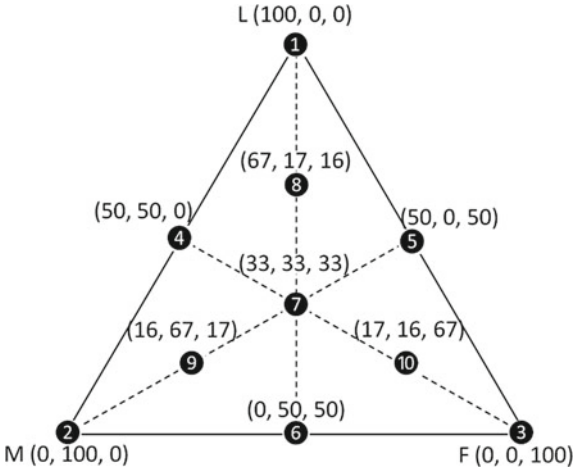

Fig. 2 Ternary diagram with the 10 mixtures based on the complete cubic model of the Simplex. Amounts (wt%) of Large (L), Medium (M), and Fine (F) particles [8]

the best results. The calculations were performed using the excel tool of the office package.

Production of Artificial Stone Plates

Thus, for the 3 compositions, artificial stone slabs with 85% by weight of the residue with 15% by weight of epoxy resin with dimension 100 × 100 × 15 mm were produced by processing under vacuum, vibration and compression.

Initially, the residue was dried in an oven at 100 °C to remove moisture, then it was weighed and placed inside the mixer, and the resin was added to complete the entire mixture. After all the mass was mixed it was deposited in the mold and connected to a vacuum system. Already under vacuum, the mold was placed on a vibrating table, to promote the spreading of the mass in the mold cavity and facilitator the removal of air bubbles that might be in the mass. After the vibration time, the mold, still under vacuum, was taken and placed in the Marcone MA 098-A hydraulic press where specimens were produced with a compression pressure of 3 MPa at 90 °C [10, 11].

Only after pressing was the mold disconnected from the vacuum system and cooled at room temperature to remove the artificial stone plate, which was then sanded and cut according to the standard for each test.

For the plates with the arapaima scales, the process was the same. The scales were placed in the middle of the plate, representing the structure of the arapaima scales and then taken to the press.

Characterization of Artificial Stone Plates

The values of density, water absorption and apparent porosity were obtained from the standard tests according to the norm ABNT NBR 15,845–2: 2015 [12]. For each condition, 15 specimens were made with dimensions of 30 × 30 × 15 mm.

Ten prismatic specimens, with dimensions of 10 × 10 × 25 mm, were three points bend tested in a model 5582 Instron machine following the recommendation for agglomerated stones as per the Brazilian NBR 15.845–6:2015 standard [13].

A total of 8 specimens for Charpy impact test were obtained by cutting each plates and sanded to suit the ASTM D256 standard [14] recommendations of 62 × 12 × 10 mm. Later a notch with 45° was made and tests were conducted in a PANTEC model XC-50 pendulum with a 22 J hammer.

Results

Table 1 presents the values obtained through the SLD method for the average density of vibrated mixtures of waste from fluorescent lamps according to Fig. 1.

As it is a parameter of the mean of the vibrated densities, the data were treated with analysis of variance considering a completely randomized design (DIC) carried out with a 95% confidence level ($p \leq 0.05$), with subsequent contrasts of means by Tukey's test (Table 2).

Analyzing the results obtained in Table 2, it is possible to verify that the treatments studied present statistical difference, which means that among the 10 mixtures, at least three are differentiated. An important point to remember is that the coefficient of variation for the test was 1.91%, which represents that the results obtained are highly reliable.

Table 1 Vibrated density of quarry dust (large and medium granulometry) and quartzite waste (fine granulometry)

Vibrated density (g/cm^3)	
Mixture	Average values
1	1.01 ± 0.1
2	1.68 ± 0.02
3	1.47 ± 0.01
4	1.43 ± 0.07
5	1.70 ± 0.04
6	1.53 ± 0.01
7	1.73 ± 0.01
8	1.69 ± 0.03
9	1.40 ± 0.04
10	1.62 ± 0.03

Table 2 Tukey's test for contrast of vibrated density averages ($p \leq 0.05$)

Treatment	Average	Tukey test
5	1.79	A
7	1.73	AB
8	1.7	AB
2	1.68	BC
10	1.62	CD
6	1.53	DE
3	1.47	EF
4	1.44	EF
9	1.41	F
1	1.02	G

To differentiate, the Tukey test was used, where it was possible to conclude that the treatments with the highest densities are at 5, 7, and 8. The Tukey test statistically proves that the addition of fine granulometry presents one of the highest densities, due to the fact that the smaller particles fill the voids between the larger ones. At the same time, it is very difficult to develop a model that can predict the behavior of mixtures involving non-spherical particles due to the high possible number of particle shapes, as well as the infinity of combinations that can arise through them. The only prediction that can be made is that as the particles become non-spherical, there will be a decrease in packing density and other related properties.

Table 2 presents the values of density, water absorption, and porosity of the artificial stone produced. It can be noted that the composition of ASQ-7 obtained the best result and was chosen for the addition of arapaima scale. It can be noted that, as expected, artificial stone is less dense.

Manufacturers of artificial stones corroborate the information above, because they report density values that are in the range between 2.4 and 2.5 g/cm^3. Due to the presence of polymer in its composition, which is a lighter material; this fact makes it so that the transportation cost of this material is lower. For instance, one container has a maximum weight capacity that can be transported and the freight cost varies in terms of destination and other individual characteristics of the freight [8, 10].

When talking about water absorption, its reduction follows that of porosity, but not in a directly proportional way, since the interconnection of pores directly or through cracks can vary.

Water absorption is always lower than porosity, as not all pores are interconnected and allow the percolation of liquids. The water absorption values for ASQ-5, 7, 8, and ASQ-7 with scale are 0.14 ± 0.10%, 0.06 ± 0.02%, 0.17 ± 0.07, and 0.27 ± 0.63, which are the values within those reported in the artificial rock manufacturing industry, between 0.09% and 0.4%, considered then materials of low water absorption. The three different proportions of ASQ without fish scale have absorption below indicated by the standard of $\leq$ 0.2% (ASTM C503), recommended for natural marble [15].

For apparent porosity values 0.31 ± 0.23% (ASQ-5), 0.14 ± 0.05% (ASQ-7), 0.38 ± 0.14 were found and can be classified as porcelain, as their porosity values are less than 0.5%, therefore they can be used as coating materials. The ASQ-7 with scale obtained values above the expected, this may be due to unsatisfactory adhesion of the scale with the residue and resin, thus increasing porosity and water absorption. Despite this, the results are in accordance with Brazilian technical standards, according to NBR 15844, the apparent density of artificial granites must be less than 2.5 g/cm^3, with a maximum absorption of 0.4% and maximum porosity of 1% (Table 3).

In the absence of a specific standard that regulates the use of artificial stones in humid environments, when framed within the limits established by the standard, it is competent to replace natural stones in the same applications.

As is known, the physical indices are closely intertwined and reflect on the improvement of characteristics such as mechanical strength, as will be observed in the mechanical tests.

Table 3 Physical property of artificial stones produced with 3 different compositions and with arapaima scale

Artificial Stone	Density (g/m^3)	Absorption (%)	Porosity (%)
ASQ-5	2.20 ± 0.05	0.14 ± 0.10	0.31 ± 0.23
ASQ-7	2.32 ± 0.03	0.06 ± 0.02	0.14 ± 0.05
ASQ-8	2.28 ± 0.09	0.17 ± 0.07	0.38 ± 0.14
ASQ-7 (scale)	2.27 ± 0.4	0.27 ± 0.63	0.67 ± 0.14

Figure 3 shows the bending stress versus deformation curves of the artificial stone with crushed stone and quartzite residue, composition 7, with and without arapaima scale (ASQ-7 and ASQ-7 with scale). ASQ-7 without scale obtained a maximum tension of 30.9 ± 2.3 Mpa and ASQ-7 with scale 34.7 ± 2.7 Mpa, it is observed that despite the higher porosity of ASQ with scale in relation to the lowest index of porosity of the scaleless, the flexural strength was higher. This can be explained by the fact that the arapaima scales have a high resistance, due to the collagen in their composition and the grooves that make up their surface as they represent barriers. The calcium content is responsible for the mineralization of the scale, which leads to greater hardness, and the layers can be thought of as laminated structures formed by collagen fibers [5–7].

Costa et al. (2021) define that the rocks for coating must have very high strength or excellent quality when the value of the tensile strength is greater than 20/22Mpa, respectively [16]. The NBR 15,844 [17] standard stipulates the minimum flexural strength value at three points of 10 MPa for the use of rocks in coatings, while ASTM C503 determines 7 MPa [15]. ASQ-7 with and without scale have strength values to be used as a coating.

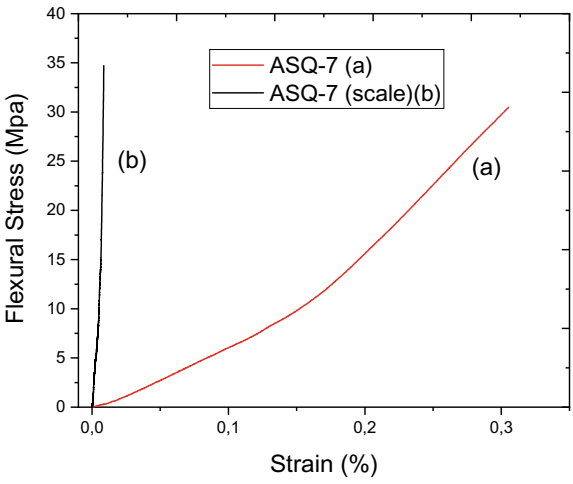

Fig. 3 Flexural stress versus strain curves for **a** ASQ-7 and **b** ASQ-7 with scale

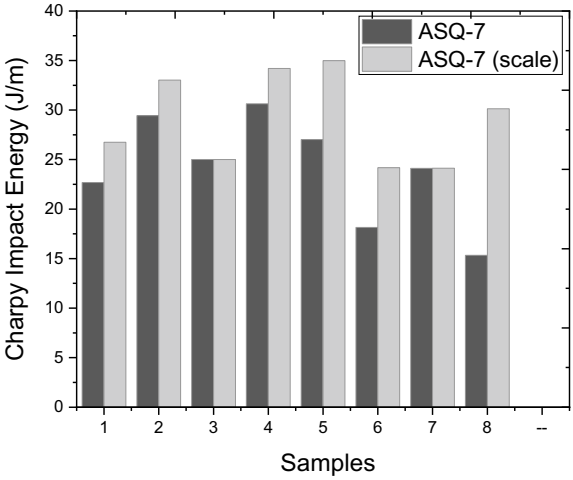

Fig. 4 Results of Charpy impact test for the artificial stone, ASQ-7, and ASQ-7 (scale)

Figure 4 presents the results obtained in the Charpy impact resistance test for artificial stones with crushed stone and quartzite residue, with and without arapaima scale (ASQ-7 and ASQ-7 scale). The two basic mechanisms of energy absorption of materials are the creation of new fracture surfaces and the deformation of the material. In the impact test, the first mechanism to operate is the deformation of the material and, when the incident energy is high enough, the crack initiation and propagation occurs, acting as a second energy absorption mechanism.

It can be seen that the impact energy of charpy for ASQ-7 is 24.1 ± 4.9 J/m and ASQ-7 (scale) is 28.3 ± 4.6 J/m. The arapaima scale obtained a higher impact energy than the rock without the scale, mainly due to the fact that the fish scales are constructed in a similar way to a laminated fiber reinforced composite material. The failure mechanisms observed in impacted fish scale samples show some correspondence with the mechanisms that occur in fiber-reinforced composites. These include fiber breakage, delamination, and crack propagation in the matrix. The higher collagen content in the inner layers of fish scales (83%) is responsible for a more ductile behavior in fish scales when subjected to impact [18].

As for the macroscopic fracture, Fig. 5, all specimens were split into two parts after the impact of the Charpy hammer. The rupture of the specimen occurred in the notch as required by the standard.

Conclusion

This study investigated the technique of developing the artificial stone with residue of crushed stone and quartzite and to reinforce it, pirarucu scale was incorporated, and its physical and mechanical properties were evaluated. From the results, statistical

Fig. 5 Macroscopic aspect of impact-tested da ASQ-7 scale

analysis, among the 10 compositions 3 are differentiated (5, 7, and 8) and through these compositions the artificial stones were developed;

The 3 compositions, with different granulometry percentages with crushed stone and quartzite residue, had porosity results of 0.31 ± 2.3% (ASQ-5); 0.14 ± 0.05% (ASQ-7) and 0.38 ± 0.14% (ASQ-8). Water absorption 0.14 ± 0.1% (ASQ-5), 0.06 ± 0.02% (ASQ-7) and 0.17 ± 0.07% (ASQ-8). According to standards, the results of all compositions were low porosity and water absorption, which could be used for coating.

ASQ-7 obtained the best results and was chosen for the incorporation of the pirarucu scale. The result of porosity 0.67 ± 0.14% and for water absorption 0.27 ± 0.63% (ASQ-7 scale), even the result being lower than ASQ-7 to ASQ-7 (scale), was in accordance with the standard and can be used with coating, only in an area with little use of water. The result of bending and charpy impact was superior to ASQ-7 without scale, 34.7 ± 2.7 Mpa and 28.4 ± 4.6 J/m.

This study is characterized as authentic, in the matter of pirarucu scales, with the first encouraging results, and in the future, it may serve several segments of architecture and/or civil construction. Once commercialized, the artificial stones developed would generate a new economic cycle that ranges from waste collection to cutting, including the use of waste, creating new stakeholders in addition to adding socioeconomic value.

Acknowledgements The authors thank the Brazilian agency FAPERJ for financing this research and for providing scholarships. They also thank UENF and coach Renan da Silva Guimarães for their support.

References

1. Alcay A, Montañés A, Simón-Fernández M (2021) Waste generation and the economic cycle in European countries. Has the Great Recession decoupled waste and economic development. Sci Total Env https://doi.org/10.1016/j.scitotenv.2021.148585
2. Kumar S, Dwivedi VK, Dwivedi SP (2021) Waste material produced from industry and its utilization in development of green composite material: a review. Mat Today Proc 43:490–496. https://doi.org/10.1016/j.matpr.2020.12.021
3. Valensca S, Barros A, Marciano JEA, Ferreira HC, Menezes RR, Neves GA (2016) Addition of quartzite residues on mortars: analysis of the alkali aggregate reaction and the mechanical behavior. Const Build Mat 118:344–351. https://doi.org/10.1016/j.conbuildmat.2016.05.079
4. Silva MCA, Leão VA, Reis EL (2021) Incorporation of quartzite fines in the production of red ceramics. J Clean Prod 288:125098. https://doi.org/10.1016/j.jclepro.2020.125098
5. Bezerra WBA, Monteiro SN, Oliveira MS, Santos da Luz F, Garcia Filho FC, Cruz LC, Ulisses Oliveira Costa DUO (2020) Processing and characterization of *Arapaima gigas* scales and their reinforced epoxy composites. Jmr&t 9(3):3005–3012. https://doi.org/10.1016/j.jmrt.2020.01.051
6. Torres FG, Malásquez M, Troncoso OP (2015) Impact and fracture analysis of fish scales from Arapaima gigas. Mater Sci Eng C 51:153–157. https://doi.org/10.1016/j.msec.2015.02.034
7. Yang W, Quan H, Meyers MA, Ritchie RO (2019) Arapaima fish scale: one of the toughest flexible biological materials. Matter 1557–1566. https://doi.org/10.1016/j.matt.2019.09.014
8. Gomes MAPM, Carvalho EAS, Demartini TJC, Carvalho EA, Colorado HA, Vieira MF (2020) Mechanical and physical investigation of an artificial stone produced with granite waste and epoxy resin. J. Compos. Mater. https://doi.org/10.1177/0021998320968137
9. Silva FS, Ribeiro CE, Rodriguez RJS (2018) Physical and mechanical characterization of artificial stone with marble calcite waste and epoxy resin. Mater. Res. 21(1):1–6. https://doi.org/10.1590/1980-5373-MR-2016-0377
10. Demartini TJC, Rodriguez RJS, Silva FS (2018) Physical and mechanical evaluation of artificial marble produced with dolomitic marble waste processed by diamond–plated bladed gangsaws J Mater Res Technol 7(3):308–313. https://doi.org/10.1016/j.jmrt.2018.02.001
11. Ribeiro CEG, Rodriguez RJ, Carvalho EA (2017) Microstructure and mechanical properties of artificial marble. Constr Build Mater 149:149–155. https://doi.org/10.1016/j.conbuildmat.52017.05.119
12. Associação Brasileira de Normas Técnicas (2015) Rochas para revestimento—Parte 2: Determinação da densidade aparente, da porosidade aparente e da absorção de água—NBR 15.845-2. Rio de Janeiro
13. Associação Brasileira de Normas Técnicas (2015). Rochas para revestimento—Parte 6: Determinação do módulo de ruptura (flexão por carregamento em três pontos)—NBR 15.845-6. Rio de Janeiro
14. American Society for Testing and Materials (2018) Standard test methods for determining the izod pendulum impact resistance of plastics—ASTM D256
15. American Society for Testing and Materials (2016) Standard specification for marble dimension stone—ASTM C503
16. Costa FP, Fernandes JV, Melo LRL, Rodrigues AM, Menezes RR, Neves GA (2021) The potential for natural stones from northeastern Brazil to be used in civil construction. Minerals 11(5):440
17. Associação Brasileira de Normas Técnicas (2015) Rocks for cladding—requirements for granite—NBR 15.844, Rio de Janeiro
18. Nascimento LFC, Monteiro SN, Louro LHL, Santos da Luz F, Santos JL, Braga FO, Marçal RLSB (2018) Charpy impact test of epoxy composites reinforced with untreated and mercerized mallow fibers. JMR&T 7(4):520–527

Mechanical and Rheological Characterization of Cement Pastes with Marble Dust Waste

K. M. S. Tavares, I. D. Batista, M. M. D. Pereira, I. S. A. Pereira, G. C. Xavier, S. N. Monteiro, and A. R. G. Azevedo

Abstract The manufacturing process of materials used in civil construction generates large-scale waste. In order to create a solution that can alleviate this problem, it was proposed to use marble dust waste as a replacement of the cement that will be used in the production of cement paste. Specimens were made with replacement proportions of 10 and 20% of the cement, observed for a period of 28 days in order to assess your strengths (at 7 days is at 28 days), in order to perform consistency index tests, viscosity and compressive strength. The results obtained through these tests allowed the analysis of mechanical properties, as well as workability characteristics, setting time of the paste and verification of the influence of partial replacement of the marble waste in the cement paste in the hardened state.

Keywords Cement · Waste · Marble dust · Cement paste

Introduction

Marble is one of the most used materials in civil construction, generally used as a decoration article [1]. Because it is considered a rock derived from limestone, it has mineralogical constituents that vary according to its origin [2]. In the process of processing ornamental rocks the blocks are sawed by looms and consequently result

K. M. S. Tavares · I. D. Batista · M. M. D. Pereira · I. S. A. Pereira
LAMAV—Advanced Materials Laboratory, UENF—State University of Northern Rio de Janeiro, Av. Alberto Lamego, 2000, Campos Dos Goytacazes, Rio de Janeiro 28013-602, Brazil

G. C. Xavier · A. R. G. Azevedo (✉)
LECIV—Civil Engineering Laboratory, UENF—State University of Northern Rio de Janeiro, Av. Alberto Lamego, 2000, Campos Dos Goytacazes, Rio de Janeiro 28013-602, Brazil
e-mail: afonso.garcez91@gmail.com

G. C. Xavier
e-mail: gxavier@uenf.br

S. N. Monteiro
Department of Materials Science, IME—Military Institute of Engineering, Square General Tibúrcio, 80, Rio de Janeiro 22290-270, Brazil

M. Zhang et al. (eds.), *Characterization of Minerals, Metals, and Materials 2023*, The Minerals, Metals & Materials Series
https://doi.org/10.1007/978-3-031-22576-5_46

in cutting wastes, lime shot and water that have seen a highly abrasive mud, and in turn contaminate reservoirs, lakes, and streams [3]. Generally, natural rocks generate 2 types of waste in their processing stages, which are solid and semi-liquid slums (slums) (contains percentage of water) [4]. This waste has great potential for addition to cementitious matrices, as it has high stability and abrasion resistance [5]. Because it is a thin material, its addition is expected to significantly modify the rheological properties of mortars.

Due to this fact, it is evident the importance of the use of this waste, especially in Brazil, in the region of Espíto Santo, because it has a large number of Quarries and Marmorarias [6]. It is necessary to concern and foster studies that enable the application of this type of waste, providing adequate destinations that will reduce environmental impacts, in addition to fostering innovative and technological use, also ensuring quality and durability.

Industries are responsible for causing major environmental damage, as estimates indicate that the production of 1 ton of Portland Cement releases the same amount of carbon dioxide (CO_2) into the atmosphere [7]. In order to minimize such damage, it was proposed the partial replacement by materials composed of fine particles and characteristics similar or complementary to those of cement, called supplementary cementitious materials, obtained most often by benefaction of industrial waste and mining [8]. Composite materials have some advantages, such as increasing the strength and durability of materials that use cement as a binder, besides presenting sustainable characteristics, depending on the pozolanic effect [9].

Since in the region of Cachoeiro do Itapemirim - ES - Brazil, marble shops and quarries are predominant, it was observed that these industries generate a large amount of waste, in which most of them do not have an adequate purpose. With the objective of reducing the pollution of rivers, lakes, and springs and the environmental impacts caused by the production of cement, which releases a large amount of CO_2, studies were carried out in which we evaluated the feasibility of using and applying the waste of marble processing, through the tests of consistency, viscosity and compression, using proportions of 10 and 20% of cement replacement.

Materials and Methods

To make the specimens, cp II E 32 cement, from the same batch, the waste of marble processing, from the marble shops de Cachoeiro de Itapemirim - ES and the water supplied by the local concessionaire were used. As the waste arrives in the form of mud, it was necessary to first place it in the sun (Fig. 1) and after in the oven for 24 h, at a temperature of approximately 60 °C, then it was crushed and sieved, in mesh sieve #50, in order to obtain a fine powder and the larger particles were eliminated. For the preparation of the paste, the waste was used in proportions of 10 and 20% of the cement.

Fig. 1 Marble powder waste in a semi-liquid state was placed in the sun to dry and then crushed

After that, the tests of paste consistency index, viscosity and compression were performed, all according to the respective NBRs. First, the reference paste consistency test was performed, shown in Fig. 2 where the consistency obtained was 25.66 mm and subsequently the tests referring to the substitution proportions of 10 and 20%, where the consistencies obtained were 25.66 mm and 23, 3 mm, respectively [10].

In the viscosity test, the paste was placed in a container that was filled halfway, according to Fig. 3. Subsequently, the viscometer was activated, using a temperature

Fig. 2 Reference paste consistency test - Flow table

Fig. 3 Viscosity test of the reference paste using the digital viscometer

of 24 °C and rotation of 60 RPM and the viscosity was measured for a time of 60 s, then all viscosity results were recorded, finally, the average of these values was made.

The compressive strength tests were performed at 7 and 28 days after curing at room temperature (23 °C). The specimens were positioned in the center of the press, between two iron plates, where a load of approximately 50 N/s was applied until the rupture occurred [11].

Results and Discussion

The results of the consistency index assay represented in Fig. 4 show that in the substitution of 20% of the waste, the consistency decreased about 9.08% when compared to the indexes of the reference pastes and a proportion of 10%. This decrease can be explained because marble powder is a waste that has fine particles, thus retaining more water for itself and as it was added in greater quantity, this effect was potentiated. This implies reducing the workability of the folder.

Figure 5 below shows that the replacement additions of the waste greatly increase the viscosity of the paste, in the case of the paste with a ratio of 20%, increased more

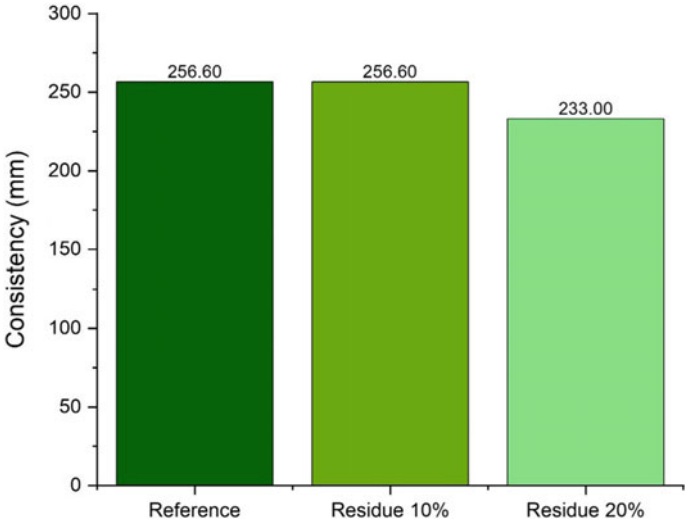

Fig. 4 Results of the consistency test of the reference pastes and with partial replacements of 10% and 20%

than double the reference paste. The explanation for this increase is due to the fact that the particles are very thin and consequently have a large surface area, in addition, the greater the amount of replacement of marble powder, the greater the possibility of forming clusters that end up intensifying internal friction.

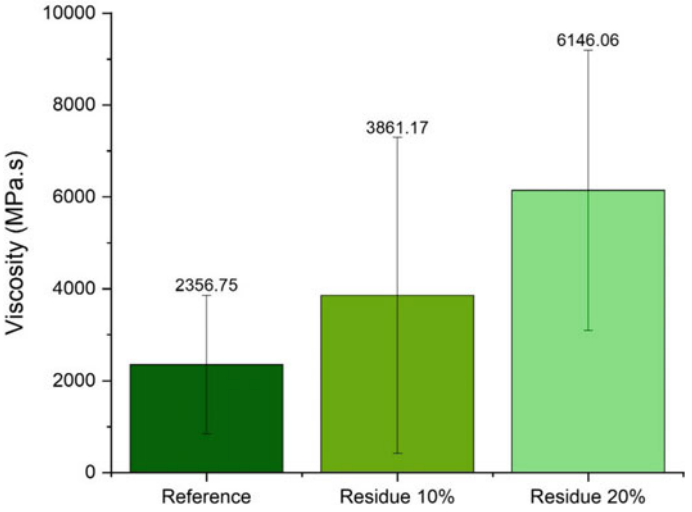

Fig. 5 Viscosity test results of the reference pastes and with partial replacements of 10 and 20

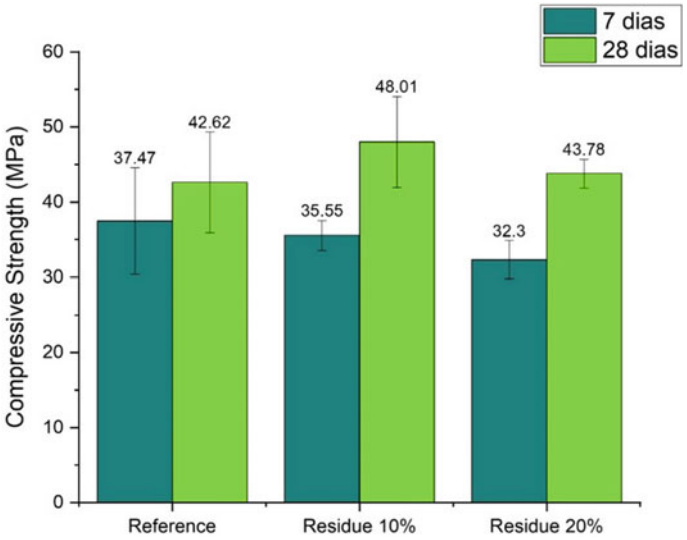

Fig. 6 Compressive strength test results of pastes at 7 and 28 days

Figure 6 represents the results of axial compression tests, performed in the periods of 7 and 28 days. The averages of the results were made and the graphs were generated, which show that there was resistance gain in the healing time from 7 to 28 days. In the graphs referring to the 7-day period, it was possible to observe that the measure that waste was added to the paste, its resistance decreased, while the results of 28 days oscillated considerably, but the resistances of the specimens with substitution proportions were higher than that of the reference specimen. When 10% of marble powder was used in the paste, there was an increase in resistance to understanding compared to the mixture without adding marble powder. However, when 20% of marble powder was used, a drop in resistance to understanding was noticed compared to the paste that was used in 10% marble powder. Therefore, it is possible to affirm that at some percentage value between 0 and 20%, the incrementation of marble powder increases the resistance to understanding of the mixture and from this value any percentage value above marble powder would cause a gradual fall in the resistance value to the understanding of the mixture.

Conclusion

Through the experiments, it was concluded that the consistency of the paste in the proportion of 20% did not meet the normative parameters, which implies the poor workability of the paste and causes its handle to start faster. The 10% reference and

replacement specimens met the standard and therefore tend to have good workability and the pick-up time starts later.

It was also possible to observe that the viscosity of the paste increases as marble waste is added, reaching values higher than twice the reference paste, due to the fact of the very fine granulometry of the waste, causing it to absorb a greater amount of water. Viscosity also affects workability, so it can be affirmed that pastes with additions of marble powder have lower workability. In the period of 7 days, the waste contributed to the decrease in strength and the higher the proportion of waste, the lower the resistance, already in the period of 28 days, the additions of 10 and 20% of the marble powder were beneficial for the increase of compressive strength.

Acknowledgements This research was funded by the State University of the Northern Fluminense (UENF), partially financed by CAPES (Coordenação de Aperfeiçoamento de Pessoal de Nível Superior—Brazil), CNPq (Coordenação Nacional de Pesquisa), and FAPERJ (Fundação de Apoio à Pesquisa do Estado do Rio de Janeiro). The participation of A.R.G.A. was sponsored by FAPERJ through the research fellowships proc.no: E-26/210.150/2019, E-26/211.194/2021, E-26/211.293/2021, E-26/201.310/2021 and by CNPq PQ2 307592/2021-9.

References

1. Singh M, Choudhary K, Srivastava A, Singh Sangwan K, Bhunia D (2017) A study on environmental and economic impacts of using waste marble powder in concrete. J Build Eng 13:87–95. https://doi.org/10.1016/j.jobe.2017.07.009
2. Malkani MS (2020) Cement resources, agrominerals, construction, marble, dimension and decor stone resources, gemstone and jewelry resources of Pakistan. Open J Geol 10(08):900–942. https://doi.org/10.4236/ojg.2020.108041
3. Danish A, Mosaberpanah MA, Salim MU, Fediuk R, Rashid MF, Waqas RM (2021) Reusing marble and granite dust as cement replacement in cementitious composites: A review on sustainability benefits and critical challenges. J Build Eng 44. https://doi.org/10.1016/j.jobe.2021.102600
4. Aukour FJ (2009) Feasibility study of manufacturing concrete eco-blocks using marble sludge powder as raw materials. WIT Trans Ecol Environ 120:845–852. https://doi.org/10.2495/SDP090792
5. Ricardo Silva Santos G, Carmo de Abreu Apolinário E, Véras Ribeiro D (2013) Influence of the addition of marble and granite cutting waste (RCMG) on the rheology of mortars. Alta Paulista Environ Forum 9(1):70–86 (In Portuguese)
6. Sato VY, Galina APL, Teixeira JESL (2018) Contribution to the rheological study of cementitious pastes with addition of wastes from the processing of ornamental rocks. Revista IBRACON de Estruturas e Materiais 11(6):1284–1307. https://doi.org/10.1590/s1983-41952018000600007
7. Benjeddou O et al (2020) Utilisation of waste marble powder as low-cost cementing materials in the production of mortar. J Build Eng 32. https://doi.org/10.1016/j.jobe.2020.101642
8. Paul SC, Mbewe PBK, Kong SY, Šavija B (2019) Agricultural solid waste as source of supplementary cementitious materials in developing countries. Materials 12(7). MDPI AG. https://doi.org/10.3390/ma12071112
9. Arif E, Clark MW, Lake N (2016) Sugar cane bagasse ash from a high efficiency co-generation boiler: applications in cement and mortar production. Constr Build Mater 128:287–297. https://doi.org/10.1016/j.conbuildmat.2016.10.091

10. Brazilian Association of Technical Norms (2016) NBR 13276: Mortar for laying and covering walls and ceilings—determination of consistency index. ABNT, Rio de Janeiro (In Portuguese)
11. Brazilian Association of Technical Norms (2005) NBR 13279: Mortar for laying and covering walls and ceilings—determination of tensile strength in flexion and compression. ABNT, Rio de Janeiro, Rio de Janeiro (In Portuguese)

Mechanical Behavior of Geopolymer Matrix Composites with the Addition of Steel Fibers

J. A. T. Linhares, S. A. A. Malafaia, A. R. G. Azevedo, S. N. Monteiro, L. U. D. Tambara, C. M. F. Vieira, and M. T. Marvila

Abstract The production of clinker uses a high amount of energy and releases a large volume of greenhouse gases. The search for more sustainable production processes has permeated several sectors of academy and industries, in this context, geopolymers have been widely studied as an alternative proposal to conventional cement. Steel fibers are an important reinforcement for high mechanical performance concretes and mortars. In this work, composites were prepared with a geopolymeric mortar matrix, reinforced with 1.5 and 3.0% of steel fiber, in relation to the mass of metakaolin used as precursor element. Studies were carried out on the gain of mechanical properties, with compression and flexural strength. In addition to the mechanical properties, water absorption and density tests in the hardened state were performed. The tests showed good properties of the composites produced.

Keywords Composite · Steel fibers · Geopolymer · Mechanical properties

J. A. T. Linhares · L. U. D. Tambara · C. M. F. Vieira
LAMAV—Advanced Materials Laboratory, UENF—State University of Northern Rio de Janeiro, Av. Alberto Lamego, 2000, Campos Dos Goytacazes, Rio de Janeiro 28013-602, Brazil
e-mail: vieira@uenf.br

S. A. A. Malafaia · A. R. G. Azevedo
LECIV – Civil Engineering Laboratory, UENF—State University of Northern Rio de Janeiro, Av. Alberto Lamego, 2000, Campos Dos Goytacazes, Rio de Janeiro 28013-602, Brazil

S. N. Monteiro
Department of Materials Science, IME—Military Institute of Engineering, Square General Tibúrcio, 80, Rio de Janeiro 22290-270, Brazil

M. T. Marvila (✉)
UFV—Federal University of Viçosa Campus Rio Paranaíba (UFV-CRP), Rodovia BR 230 KM 7, Rio Paranaíba 38810-000, Brazil
e-mail: markssuel.marvila@ufv.br

M. Zhang et al. (eds.), *Characterization of Minerals, Metals, and Materials 2023*, The Minerals, Metals & Materials Series
https://doi.org/10.1007/978-3-031-22576-5_47

Introduction

Civil construction has a high importance in the world economy, accounting for approximately 13% of the total GDP (Gross domestic product) of countries, employing, according to data from the World Economic Forum, more than 100 million people [1]. In this scenario, Portland cement is a material that meets the various demands of the sector, however its manufacture generates many problems such as high energy consumption and the large volume of harmful gases emitted to the environment, such as carbon dioxide. It is estimated that for every ton of binder produced, a ton of CO_2 is also generated. The production problems of Portland cement, there is still a great extraction of natural resources [2].

Faced with the negative scenario of conventional cement Portland in the face of sustainable perspectives, several materials are studied as ecological alternatives, such as geopolymers, which have similar properties and are more environmentally friendly [3]. Geopolymers are materials formed after the dissolution of amorphous phases from sources of aluminosilicates in a strong alkaline solution. They have a three-dimensional network structure and have good mechanical and durability properties [4].

Given the fragile characteristics of geopolymers, several studies are conducted to add various fibers such as steel, inorganic, natural, and synthetic in different sizes, geometries, and mechanical properties, to produce composites with optimized characteristics [5]. Fibers can mitigate the brittle behavior of materials, controlling the mechanisms that form cracks, increasing tenacity and energy absorption [6].

Steel fibers can improve technological properties of interest such as flexural strength and ductility. The importance of studying the addition of steel fibers and the behavior of the properties of the composites in the face of the variation in content and size, occurs due to the high cost of this fiber, which must be applied correctly [7]. This study aimed to analyze the variation of the addition of steel fibers, in 1.5 and 3.0% in geopolymer matrix, to evaluate if the ends of conventional fibers, acquired commercially, would increase their mechanical properties since these parts do not impact the workability due to its dimensions. Thermal curing processes were carried out at 60 ºC for 7 and 28 days. The mechanical properties evaluated were the flexural and compressive strength, complemented with the influence of the fibers on the density and water absorption in the composites.

Materials and Methods

To carry out this work, commercially produced A1 type fibers were used. The diameter of the reinforcement material was 0.75 mm and only the ends were used in this study, with approximately 10 mm in length, Fig. 1 shows the fibers acquired and those used.

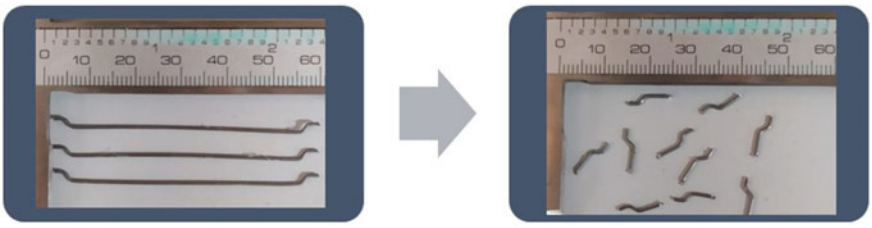

Fig. 1 Dimensional adequacy of steel fibers

Table 1 Compositions used

	Metakaolin (g)	Sand (g)	Steel (g)	NaOH (g)	Silicate (g)	Water (g)
Reference (%)	320.0	320.0	–	18.0	88.0	182.0
1.5	320.0	320.0	4.8	18.0	88.0	182.0
3.0	320.0	320.0	9.6	18.0	88.0	182.0

The matrix phase compositions, together with the 1.5% and 3.0% reinforcement contents are shown in Table 1.

The molded samples were of prismatic geometry, subjected to thermal curing for a period of 7 and 28 days for the analysis of their technological properties. The 3-point bending strength tests followed ASTM C674 guidelines [8], commonly used in this type of test. The distance between the supports was 80 mm and the loading rate was 1 mm/minute, the same rate used for the mechanical behavior tests under compressive stresses. The compression tests followed guidelines adapted from the NBR 13,279 [9] in an adapted way. Both mechanical tests were performed on a universal machine, model 5882, brand INSTRON.

To determine the influence of the addition of steel fibers on the density in the hardened state and water absorption, the procedures adapted from the NBR 13,280 [10] and NBR 9778 [11] were applied respectively, for 7 days of thermal curing.

The density was determined with the dimensions of the specimens, measured with a digital caliper. With the measurements it was possible to calculate the volume of each specimen. The masses were recorded to determine this property. Water absorption was calculated with the masses being measured before and after immersion of the samples in distilled water for 24 h, as described in the standard.

Results and Discussion

The density of the samples produced did not change significantly, subtly reducing from 1.6 g/cm^3 of the reference composition to 1.58 and 1.57 g/cm^3 for the specimens with 1.5% and 3.0% of steel fiber addition, as shown in Fig. 2. This difference is mainly due to the difference between the density of each phase, the matrix, and the

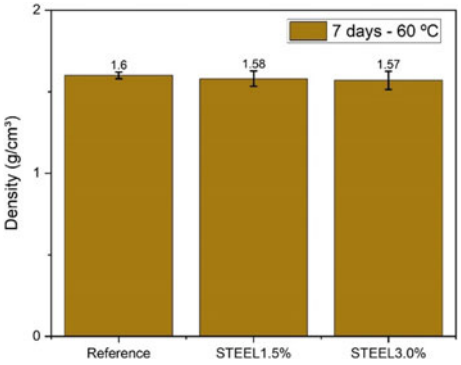

Fig. 2 Density results

reinforcement, corroborating that steel fibers have a high density, which contributes to improvements in mechanical behavior [12].

Figure 3 presents the results of water absorption and, as well as the behavior of the density, this property remained linear, without major significant changes. The almost imperceptible variation of density and water absorption point to the fibers as the only potential modifiers of the mechanical properties, acting as tension bridges and potentiating the tenacity of the composites, mitigating the high fragility characteristic of the geopolymer matrix.

The flexural strength results are shown in Fig. 4. The behavior of samples when subjected to bending loads is similar when they are subjected to compressive stresses. For 7 days of thermal curing, the strength declined in relation to the reference, demonstrating low polymerization of the matrix in this period. For 28 days of curing, with the maturation of the matrix, the fibers could act as a reinforcement phase for the addition of 1.5%, with a significant increase of 79.6% in strength. When 3.0% of fiber was added, there was an increase in relation to the reference of 42.4%, that is, lower than the intermediate addition of 1.5%, indicating a potential limit for addition.

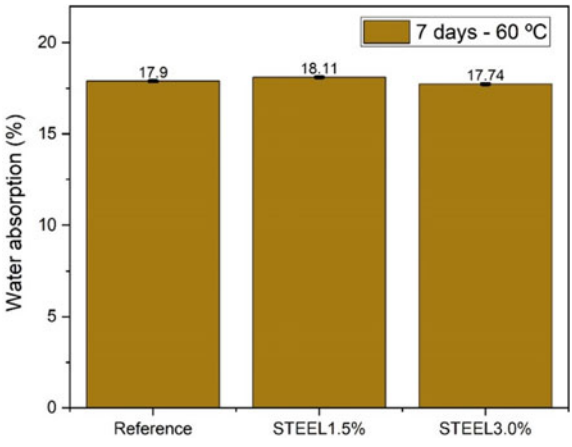

Fig. 3 Water absorption results

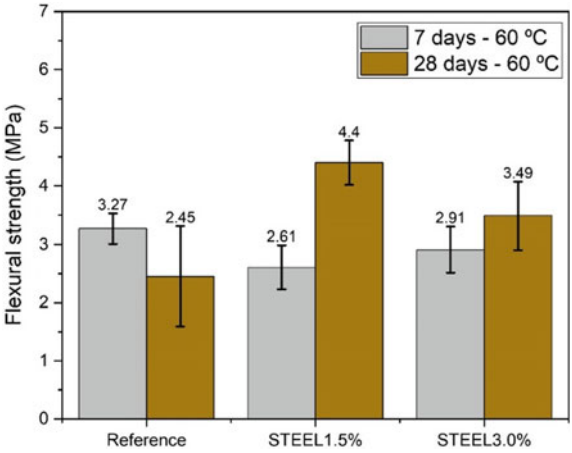

Fig. 4 Flexural strength results

The increase in flexural strength is due to several factors, one of them as analyzed by [13] is the increase in flexural toughness of composites reinforced with steel fibers.

Figure 5 presents the results obtained with the compression tests. For 7 days of curing, the fibers apparently subtly weakened the matrix, with drops of 21.7 and 13.76% in strength. When exposed to thermal curing for a period of 28 days, specimens with the addition of 1.5% of steel fiber responded most positively, with a 77% increase in strength. The reference and 3.0% fiber specimens showed a similar behavior.

Several factors may be responsible for the results obtained, such as the increase in the percentage of fiber being responsible for the generation of interfaces and microcracks that weaken the composite in a similar way to the results obtained by [14], where the compressive strength declined beyond the addition of 1.25% steel fiber as reinforcement.

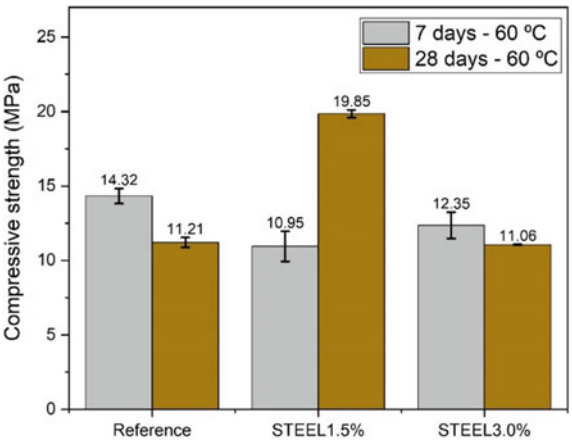

Fig. 5 Compressive strength results

The mechanical results are in accordance with previous studies, with an increase in these properties occurring due to the good interaction between the geopolymer mortar and the steel fiber, which are efficient in transferring stresses, inhibiting the growth of cracks [15].

Conclusion

Mechanical bending and compression tests were carried out to evaluate the efficiency of steel fibers with approximately 10 mm in length at contents of 1.5 and 3.0%. Due to the influence of the geopolymerization process, analyzes of water absorption and density were used, properties directly linked to the porosity of the samples, which would affect the mechanical behavior, which could make it difficult to determine the efficiency of the fibers in acting as a reinforcement phase.

It is concluded with the linearity of the density and water absorption results, that all the increase in flexural and compression strength can come from the addition of steel fibers. If there are no changes in the matrix that could interfere with the results.

The best fiber addition was 1.5%, confirming the results found in the literature. When higher increments such as 3.0% were used, the fibers got in the way, generating more interfaces and micro-cracks that weakened the matrix. The most significant increases in strength were 79.6% for bending forces and 77% for compressive strength, both for the compositions with the addition of 1.5%, with thermal cure at 60 °C for 28 days.

Based on the results, it is concluded that the ends of commercial fibers can be used as reinforcement in an assertive way in geopolymer composites, enhancing the tenacity and mitigating the fragility characteristics of materials of this nature, due to the good connection of steel fibers with the matrix up to 1.5% addition percentage.

Acknowledgements The authors thank the Brazilian agencies CNPq, CAPES, and FAPERJ for the support provided to this investigation.

References

1. Raza MH, Zhong RY (2022) A sustainable roadmap for additive manufacturing using geopolymers in construction industry. Resour Conserv Recycl 186:106592
2. Qaidi SMA et al (2022) Rubberized geopolymer composites: A comprehensive review. Ceram Int 48(06):123
3. Neupane K (2022) Evaluation of environmental sustainability of one-part geopolymer binder concrete. Cleaner Mater 6:100138
4. Yang J et al (2022) An efficient approach for sustainable fly ash geopolymer by coupled activation of wet-milling mechanical force and calcium hydroxide. J Cleaner Prod 372:133771
5. Abbas AGN, Aziz FNAA, Abdan K, Nasir NAM, Huseien GF (2022) A state-of-the-art review on fibre-reinforced geopolymer composites. Constr Build Mater 330:127187

6. Larsen IL, Thorstensen RT (2020) The influence of steel fibres on compressive and tensile strength of ultra high performance concrete: a review. Constr Build Mater 256:119459
7. Aisheh YIA, Atrushi DS, Akeed MH, Qaidi S, Tayeh BA (2022) Influence of steel fibers and microsilica on the mechanical properties of ultra-high-performance geopolymer concrete (UHP-GPC). Case Stud Constr Mater 17:e01245
8. ASTM C674 (2018), Standard Test Methods for Flexural Properties of Ceramic Whiteware Materials.
9. NBR 13279 (1995) - Argamassa para assentamento de paredes e revestimento de paredes e tetos – Determinação da resistência à compressão, Assoc. Bras. Normas Técnicas.
10. NBR 13280 (2005) - Argamassa para assentamento e revestimento de paredes e tetos - Determinação da densidade de massa aparente no estado endurecido, Assoc. Bras. Normas Técnicas.
11. NBR 9778 (2011) Argamassa e concreto endurecidos -Determinação da absorção de água, índice de vazios e massa específica, Assoc. Bras. Normas Técnicas.
12. Kuranlı ÖF et al (2022) Evaluation of slag/fly ash based geopolymer concrete with steel, polypropylene and polyamide fibers. Constr Build Mater 325:126747
13. Bellum RR (2021) Influence of steel and PP fibers on mechanical and microstructural properties of fly ash-GGBFS based geopolymer composites. Ceram Int 48(11):232
14. Zada Farhan K, Azmi Megat Johari M, Demirboğa R (2022) Evaluation of properties of steel fiber reinforced GGBFS-based geopolymer composites in aggressive environments. Constr Build Mater 345:128339
15. Ghasemzadeh Mousavinejad SH, Gashti MF (2021) Effects of alkaline solution to binder ratio on fracture parameters of steel fiber reinforced heavyweight geopolymer concrete. Theoret Appl Fract Mech 113:102967

Mechanical Properties of Silica Fume-Based Mortars Alkaline Activated by NaOH

P. H. C. H. Caldas, A. R. G. Azevedo, and M. T. Marvila

Abstract It is known that the use of Portland cement is essential for civil construction in all countries of the world; however, it is well known that this material is highly harmful to the environment. That said, the development of new binders such as activated alkali cement (AAC), produced from silica fume and activated by sodium hydroxide, opens the door to the study of less polluting and harmful materials. The results obtained in this research indicate the feasibility of using this material as a substitute for conventional binders.

Keywords Activated alkali cement · Active silica · Environment

Introduction

The use of new cementitious materials for the progress of civil constructions with less environmental attacks is gaining more and more space about a great global concern: sustainable development, which can combine development efficiency without losing care with the environment [1]. It is mentioned, then, as an object of study, the activated alkali cement (AAC).

Ordinary Portland Cement (OPC), due to the clinker calcination process and the common extraction of minerals that are not renewed in nature [2] is harmful to the environment, while the use of ACC has advantages such as environmental and economic gains, in the which can be mentioned the use of by-products from the

P. H. C. H. Caldas · M. T. Marvila (✉)
UFV—Federal University of Viçosa Campus Rio Paranaíba (UFV-CRP), Rodovia BR 230 KM 7, Rio Paranaíba 38810-000, Brazil
e-mail: markssuel.marvila@ufv.br

P. H. C. H. Caldas
e-mail: pedro.caldas@ufv.br

A. R. G. Azevedo
LECIV – Civil Engineering Laboratory, UENF – State University of Northern Rio de Janeiro, Av. Alberto Lamego, 2000, Campos Dos Goytacazes, Rio de Janeiro 28013-602, Brazil
e-mail: afonso@uenf.br

M. Zhang et al. (eds.), *Characterization of Minerals, Metals, and Materials 2023*, The Minerals, Metals & Materials Series
https://doi.org/10.1007/978-3-031-22576-5_48

industry, such as slag and ash, for the production of this material, in addition to mitigating the tons of CO_2 emitted by the clinkerization process [3].

The ACC has, like several other materials, disadvantages, important to be mentioned, such as: Loss of workability, requirement of a greater demand for water, the lack of knowledge of all its mechanisms and reactions [4]. In the exclusive case of AAC, it can be noted that the eventual excess of air incorporated in the mortar can be more harmful, in this case, due to the preference of alkalines, such as sodium, to accumulate in the voids generated by the air [5]. Basically, the structural difference between AAC and OPC is the formation of C-S–H and C-A-S–H chains [4], illustrated in Fig. 1.

It is then observed that the CP hydration reaction will produce calcium (C) chains, which are linked to silica (S) and water (H) tetrahedra, whereas in CAA, the same hydration reaction will produce tetrahedra of alumina (A), in which some will replace the silica tetrahedra, causing cross-links between the chains, thus providing greater

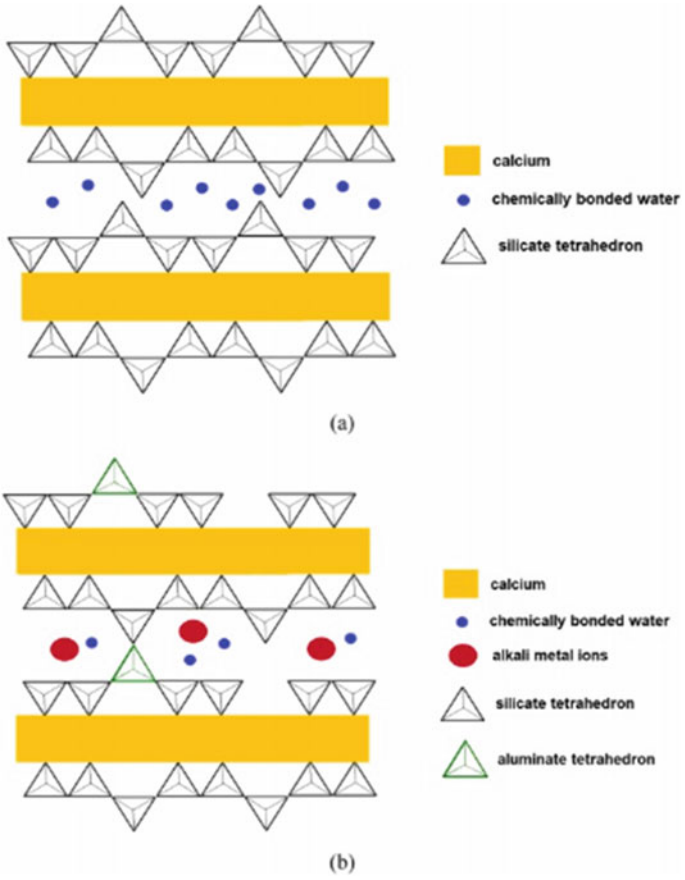

Fig. 1 **a** Structural representation of C-S–H, **b** structural representation of C-A-S–H [4]

strength to the material [6, 7]. In this context, the objective of this work was to evaluate the alkaline activation of silica fume, with the use of sodium hydroxide (NaOH), and their respective partial replacements of OPC in mortar.

Materials and Methods

The materials used for the development of the study in question were commercial Portland cement type CP-II-E; and washed river sand, between the 2.4 mm and 0.15 mm sieves, where the part that was retained on the 2.4 mm sieve was discarded, and the part that was retained on the 0.15 mm sieve was used for the study in question. Silica fume was used, which is a material from the metallurgical industry, precisely from ferrosilicon. Figure 2 shows the granulometry of the materials used in the research.

For the activation of the previously mentioned silica, sodium hydroxide (NaOH) was used, an alkali-containing material capable of producing alumina tetrahedra, as highlighted in the introduction. It is necessary to emphasize that the sodium content in the SCC will form a barrier between the mortar grains, causing it to change the workability of the material [8]. Table 1 presents the composition of the specimens for the development and production of AAC based on silica fume and sodium hydroxide.

The compositions presented in Table 1 were defined by adopting partial substitution of Portland cement to produce the mortar, that is, 90% of OCP and 10% of silica

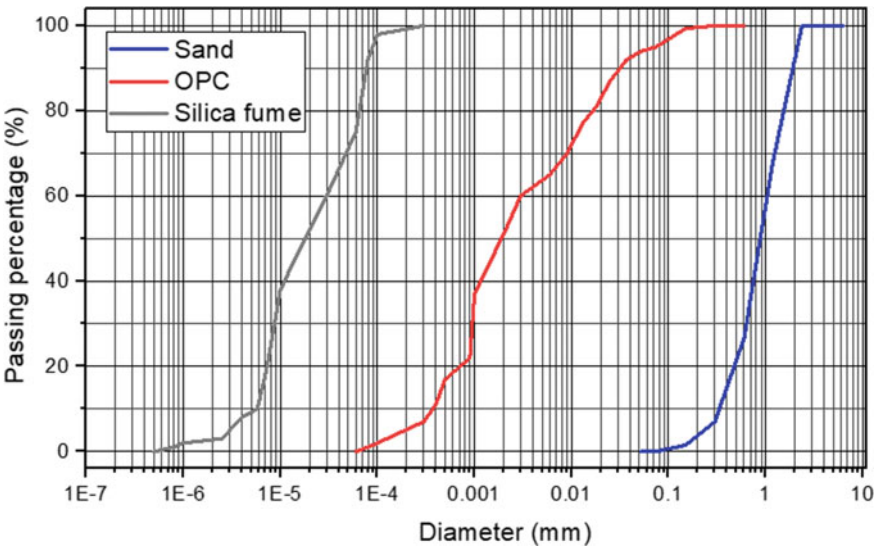

Fig. 2 Granulometry of the materials used in the research

Table 1 Compositions of mortar

Composition (%)	OPC (g)	Silica fume (g)	Sand (g)	NaOH (g)	Water (g)
0	900.00	0.00	1800.00	0.00	405.00
10	810.00	81.00	1800.00	11.61	405.00
20	720.00	162.00	1800.00	23.23	405.00

fume were used, then 80% of OCP and 20% of silica fume, and finally, it should be noted that 0% is the reference mortar with 100% OCP.

The mixing process of the mortar specimens was carried out as follows: water, OPC and silica fume were added to the mortar bowl, and then the mixer was turned on at low speed for 30 s. Subsequently, sand was added for 30 s, without turning off the equipment, and then, after this period, the speed was increased to high for 30 s. In sequence, the mixer was turned off for 1 min and 30 s, the first 15 s being used to, with the aid of a spatula, remove the mortar that was retained on the walls of the vat, and thus, letting the mortar rest for 1 min and 15 s left. Finally, the mixer was turned on at high speed for another 60 s, according to the normative procedure [9]. The specimens were molded in 4 layers of approximately the same height, with 30 socket strokes in each layer.

With the specimens duly ready, the curing process began. For the study in question, curing in a lime tank was used for 28 days, in which this type of curing is used so that the moisture of the specimen is not lost to the environment [10]. For this study, 6 specimens were made for the compositions of 0% (reference mortar), 10% and 20%.

The tests performed are highlighted below: mass density in the hardened state, water absorption, axial compression and diametral compression. For the density test, 3 specimens molded using the procedure described above were used. The test consists of weighing the specimens after drying in an oven for 24 h. Using the standard volume of the specimens, it is possible to obtain this parameter, according to the normative procedure [11]. The water absorption test was carried out according to the regulation [12], in which the 3 wet specimens were weighed, after being removed from curing in a lime tank, and after drying in an oven for a minimum period of 24 h. The mass difference, proportionally, indicates the water absorption of the material.

The axial compressive strength test was performed based on the NBR 7215 [9] standard, in which the specimen was subjected to rupture using an Instron hydraulic press, using a rate of (0.25 ± 0.05) MPa/ s. Tree samples were used for this assay. Finally, the diametral compressive strength test was performed using the normative procedures [13]. The rate adopted is the same as the axial compression test, as well as the geometry and number of specimens. The essential differential is in the direction of application of the load, along the diagonal of the specimens.

Results and Discussion

Figure 3 presents the density results obtained in the survey. A practically linear reduction in density is observed with the use of fumed silica. This is an advantage from a material application point of view, since one of the main loads that occur in building materials is the self-weight [14]. This weight reduction is positive for cement-based mortars.

Figure 4 presents the water absorption results obtained in the survey. In these results, there is no linearity of information. Therefore, it is possible to highlight that the composition containing 10% of silica fume presented an increase in behavior compared to the composition containing only OPC, since there was a significant reduction in water absorption. It is known that the main mechanisms of degradation of cementitious materials happens due to water absorption [15]. Therefore, the reduction of this property is also a positive parameter.

Figure 5 presents the axial compressive strength results obtained in the research. It is observed that there was a reduction in the resistance properties. This reduction can be attributed to the type of curing used, immersion in lime. As highlighted by Marvila et al. (2021) [4], the use of this type of cure in AAC is not the most recommended, due to the loss of sodium due to diffusion. Therefore, performing other types of curing (thermal cure or in sodium solutions) will be carried out in later stages to evaluate improvements in strength properties. However, it is noteworthy that the 10% composition has strength values compatible with structural applications, above 20 MPa [16], and contributes to the reduction of the OPC content by 10%. This is a significant contribution as each ton of OPC produced emits an average of 1.2 tons of CO_2 into the atmosphere. A material that allows the reduction of 10% of OPC, consequently makes it possible to reduce 0.12 tons of CO_2 in the atmosphere in a proportional way [17]. This is a big environmental advantage.

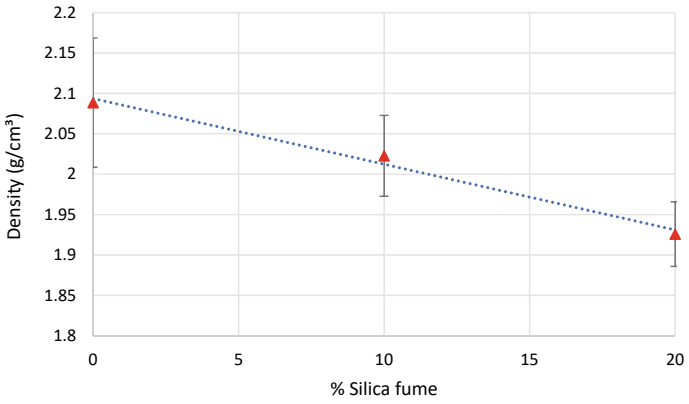

Fig. 3 Density of the studied compositions

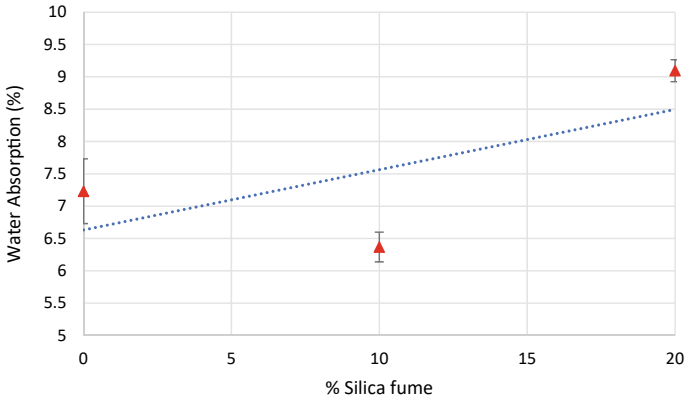

Fig. 4 Water absorption of the studied compositions

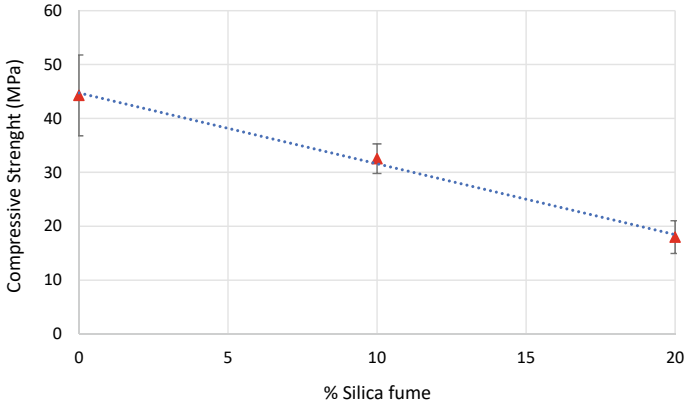

Fig. 5 Compressive strength of the studied compositions

Figure 6 presents the results of diametral compressive strength obtained in the research. It is observed that the values are consistent as they follow the trend of the results highlighted in Fig. 5. To improve the mechanical results of the compositions containing AAC, it is suggested to perform other types of curing, as highlighted in the previous paragraph. This is confirmed by the illustrations in Fig. 7, where it is clear the occurrence of a differential phase on the surface and inside the specimen with 20%. This happened due to the curing adopted, which does not favor the strength of AAC compositions and causes loss of sodium from the material [16].

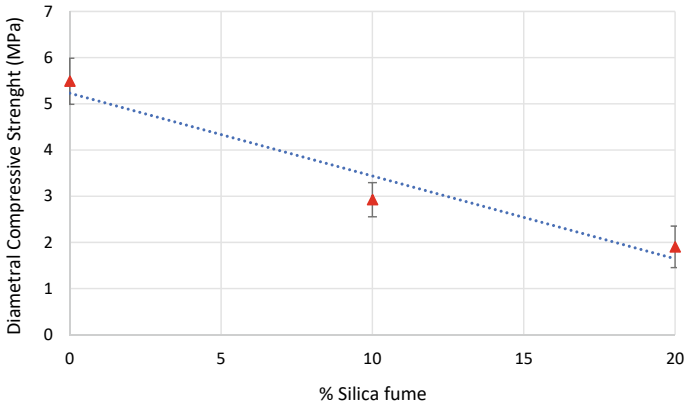

Fig. 6 Diametral compression strength of the studied compositions

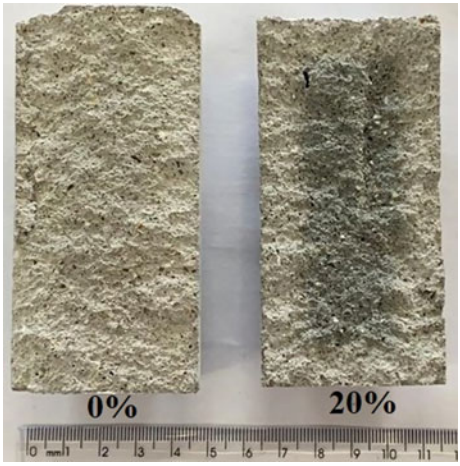

Fig. 7 Ruptured surface of the studied mortars

Conclusion

Based on the results obtained in this research, it is possible to verify that the use of activated silica activated alkaline by NaOH as a partial substitute for OPC is viable. Density and water absorption results were beneficial, especially for the composition with 10% replacement.

In addition, the results of compressive strength and diametral compression indicate the feasibility of using active silica in structural functions. However, it is necessary to point out that there was a reduction in the mechanical properties as a function of the type of curing adopted, which does not favor AAC compositions. As a result, a future stage of the work is to evaluate other types of curing, through thermal curing and in sodium hydroxide solutions.

References

1. Marvila MT, de Azevedo ARG, Vieira CMF (2021) Reaction mechanisms of alkali-activated materials. Revista IBRACON de Estruturas e Materiais 14. https://doi.org/10.1590/s1983-41952021000300009
2. Campanhão AF, Marvila MT, de Azevedo ARG, da Silva TR, Fediuk R, Vatin N (2021) Recycled PET sand for cementitious mortar. Materials 15:273. https://doi.org/10.3390/ma15010273
3. Kleib J, Aouad G, Abriak N-E, Benzerzour M (2021) Production of Portland cement clinker from French municipal solid waste incineration bottom ash. Case Stud Constr Materials. 15:e00629. https://doi.org/10.1016/j.cscm.2021.e00629
4. Marvila MT, de Azevedo ARG, de Oliveira LB, de Castro Xavier G, Vieira CMF (2021) Mechanical, physical and durability properties of activated alkali cement based on blast furnace slag as a function of %Na2O. Case Stud Constr Mater 15:e00723. https://doi.org/10.1016/j.cscm.2021.e00723
5. Marvila MT, de Azevedo ARG, de Matos PR, Monteiro SN, Vieira CMF (2021) Rheological and the fresh state properties of Alkali-activated mortars by blast furnace slag. Materials 14:2069. https://doi.org/10.3390/ma14082069
6. Provis JL (2014) Geopolymers and other alkali activated materials: Why, how, and what? Mater Struct Materiaux Constr 47:11–25. https://doi.org/10.1617/s11527-013-0211-5
7. Duxson P, Provis JL (2008) Designing precursors for geopolymer cements. J Am Ceram Soc. https://doi.org/10.1111/j.1551-2916.2008.02787.x
8. Marvila MT, Azevedo ARG, Delaqua GCG, Mendes BC, Pedroti LG, Vieira CMF (2021) Performance of geopolymer tiles in high temperature and saturation conditions. Constr Build Mater 286:122994. https://doi.org/10.1016/j.conbuildmat.2021.122994
9. ABNT (2019) NBR 7215: Cimento Portland—Determinação da resistência à compressão de corpos de prova cilíndricos (in Portuguese). Associação Brasileira de Normas Técnicas
10. Associação Brasileira De Normas Técnicas (2014) ABNT NBR 5752- Materiais pozolânicos — Determinação do índice de desempenho com cimento Portland aos 28 dias. Associação Brasileira de Normas Técnicas
11. ABNT (2005) ABNT NBR 13280—Argamassa para assentamento e revestimento de paredes e tetos - Determinação da densidade de massa aparente no estado endurecido. Associação Brasileira de Normas Técnicas
12. ABNT (2011) NBR 9778—Argamassa e concreto endurecidos—Determinação da absorção de água, índice de vazios e massa específica. Associação Brasileira de Normas Técnicas
13. ABNT (2011) NBR 7222—Concreto e argamassa—determinação da resistência à tração por compressão diametral de corpos de prova cilíndricos. Associação Brasileira de Normas Técnicas
14. Wang H-Y, Tsai S-L, Hung C-C, Jian T-Y (2022) Research on engineering properties of cement mortar adding stainless steel reduction slag and pozzolanic materials. Case Stud Constr Mater 16:e01144. https://doi.org/10.1016/j.cscm.2022.e01144
15. Marvila MT, de Azevedo ARG, Ferreira RLS, Vieira CMF, de Brito J, Adesina A (2022) Validation of alternative methodologies by using capillarity in the determination of porosity parameters of cement-lime mortars. Mater Struct 55:19. https://doi.org/10.1617/s11527-021-01877-6
16. Marvila MT, de Azevedo ARG, de Matos PR, Monteiro SN, Vieira CMF (2021) Materials for production of high and ultra-high performance concrete: review and perspective of possible novel materials. Materials 14:4304. https://doi.org/10.3390/ma14154304
17. Wu T, Ng ST, Chen J (2022) Deciphering the CO2 emissions and emission intensity of cement sector in China through decomposition analysis. J Clean Prod 352:131627. https://doi.org/10.1016/j.jclepro.2022.131627

Microscopic Structure Characterization of Coke in Different Sizes

Xin Dai, Dongtao Li, Peng Li, Yang Liu, Deying Guo, and Yong Zhang

Abstract Optical microscope and X-ray diffraction study were conducted to investigate the microscopic mechanism of coke size distribution. The results show that an increase in coke size resulted in a slight decrease in moisture and an increase in the volatile matter content. However, the mineral catalysis index (MCI) varied slightly with the change in coke size. Besides, the cell dimension did not change much with the coke size variation. Furthermore, cell spacing and graphitization degree increased when the coke size decreased. Therefore, it is possible to improve the coke size distribution and control the coke graphitization degree in the coking process.

Keywords Coke size distribution · Microcrystalline structure · Porous structure · Coke size

Introduction

With the gradual advancement of large-scale blast furnace, the skeleton role of metallurgical coke in blast furnace is becoming more and more irreplaceable. The coke particle size and its distribution are important parameters to ensure the blast furnace permeability and the stability at tuyere raceway [1–3]. In coking production process, quenched coke was sent to screening system. The screening method difference is also one of the key affecting factors. Coke is a kind of porous carbon material. Hu Desheng et al. found that microcrystalline structure is the essential factor to the coke macroscopic properties. The larger the microcrystalline layer spacing of coke, the looser the structure, the higher the coke reactivity and the lower the strength of coke after

X. Dai (✉) · D. Li · Y. Liu · D. Guo · Y. Zhang
Research Institute of Technology of Shougang Group Co., Ltd, Beijing 100043, China
e-mail: dennisdaixin@163.com

Beijing Key Laboratory of Green Recyclable Process for Iron & Steel Production Technology, Beijing 100043, China

P. Li
ShougangJingtang United Iron & Steel Co., Ltd, Hebei, Tangshan 063200, China

M. Zhang et al. (eds.), *Characterization of Minerals, Metals, and Materials 2023*, The Minerals, Metals & Materials Series
https://doi.org/10.1007/978-3-031-22576-5_49

reaction [4]. Zhang Shouyu et al. found that the heat treatment of coking coal above 900°C would change microcrystalline structure of coke and decrease coke reactivity [5]. In addition, studies have shown that the variation of coke microcrystal structure under different conditions would lead to serious deterioration of coke quality [6].

The microscopic structure mechanism of coke particle size change has not been clear. In this paper, the coke produced by Shougang Jingtang United Iron & Steel Co., Ltd. was adopted, and the variation mechanism of particle size was analyzed. The coke porous structure and crystal structure were characterized to illuminate the microscopic structural mechanism of coke particle size variation, and it could play a guiding role in the control of coke size distribution.

Experiments

Sample Preparation

The cokes produced by Shougang Jingtang United Iron & Steel Co,.Ltd. were selected as the samples to simulate the coke screening process. In the first step, the coke was divided into large coke (coke with particle size greater than 60 mm) and small coke (coke with particle size less than 60 mm), and these obtained cokes were primary coke. In the second step, the large coke and small coke obtained in the first step are screened by five sizes sieves, and the obtained coke are secondary large coke and secondary small coke respectively. In the third step, all the coke obtained in the second step was mixed, and then screened with a five sizes sieves. Finally, coke samples with different particle sizes (five particle sizes of > 80 mm, 60 mm–80 mm, 40 mm–60 mm, 25 mm–40 mm and < 25 mm, respectively) were obtained, and the obtained coke was tertiary coke.

According to GB/T212—2008, GB/T217—2007, GB/T30733—2014 and GB/T37673—2019 the approximate analysis and ultimate analysis, total sulfur content and ash component content were obtained.

Pore Structural Analysis

The coke pore structure was measured by Leica MARXE optical microscope combined with MCA Smart scope automatic coal rock analysis system. After coarse grinding, fine grinding and polishing, the porosity and pore size distribution of coke samples were measured under 50 times optical microscope. Five representative samples were selected for each particle size coke test, and then the average value was taken.

Microcrystalline Structure Analysis

Bruke-AXS D8 X-ray analyzer (produced by Bruke, Germany) was mainly used to qualitatively and quantitatively analyze the microcrystalline structure of coke with different particle sizes. The instrument adopted copper target (working voltage is 40 kV, working current is 40 mA), scanning diffraction angle (2θ) scanning range is 10°–90°, and scanning step length is 0.02. The samples were prepared by tabletting method, the test samples were ground below 100 meshes, and the data were analyzed by the phase analysis software EVA Bruke.

Results and Discussion

Effect of Screening Method on Coke Size Distribution

Coke size distribution after screening was shown in Table 1.

It could be seen from Table 1 that the coke mean size after first screening was 58.84 mm, and the coke mean size after twice screening decreased from 58.84 to 58.11 mm. From the perspective of coke particle size composition, the proportion of coke particle size greater than 60 mm after first screening was 45.45%, and the proportion of coke particle size greater than 60 mm after two screenings was 42.76%.

In order to analyze the influencing factors of coke with different particle sizes, approximate analysis, ultimate analysis and ash component analysis were analyzed. The results are shown in Tables 2, 3 and 4. The calculation formula of MCI value in Table 4 is as follows [11]:

$$\mathrm{MCI} = A_{d\times}\frac{\omega(\mathrm{Fe_2O_3}+1.85\omega(\mathrm{K_2O})+2.2\omega(\mathrm{Na_2O})+1.6\omega(\mathrm{CaO})+0.83\omega(\mathrm{MgO})+0.9\omega(\mathrm{MnO})}{(100-V_d)+(\omega(\mathrm{SiO_2})+0.41\omega(\mathrm{Al_2O_3})+2.5\omega(\mathrm{TiO_2}))}$$

Table 1 Shougang Jingtang company coke size distribution

Sample	Proportion/wt%					Mean size/mm
	> 80 mm	60 ~ 80 mm	40 ~ 60 mm	25 ~ 40 mm	< 25 mm	
primary coke	16.23	29.22	38.10	13.35	3.10	58.84
secondary large coke	30.14	49.12	18.82	0.96	0.96	71.36
secondary small coke	1.06	4.10	64.60	24.44	5.81	44.79
tertiary coke	14.40	28.36	41.33	13.20	2.71	58.11

Table 2 Approximate analysis of various particle size coke

Coke size/mm	M_{ad}/%	A_d/%	V_d/%	FC_d/%
> 80	0.54	11.99	1.51	86.50
60–80	0.55	11.96	1.49	86.55
40–60	0.62	12.31	1.40	86.29
25–60	0.67	12.04	1.39	86.57
< 25	0.65	12.14	1.39	86.47

M_{ad}: air dried basis moist content,A_d: dried basis ash content, V_d: dried basis volatile matter content, FC_d: dried basis fixed carbon content

Table 3 Ultimate analysis of various particle size coke

Coke size/mm	$S_{t,d}$/%	C_d/%	H_d/%	O_d/%	N_d/%
> 80	0.76	86.66	< 0.3	0	1.16
60–80	0.74	86.51	< 0.3	0	1.08
40–60	0.78	85.72	< 0.3	0	1.15
25–60	0.76	86.46	< 0.3	0	1.12
< 25	0.77	86.71	< 0.3	0	1.08

$S_{t,d}$: dried basis total sulfur content, C_d: dried basis carbon content, H_d: dried basis hydrogen content, N_d: dried basis nitrogen content, O_d: dried basis oxygen content.

It could be seen from Tables 2, 3, 4 that with the decrease of coke particle size, the moisture content increased slightly while the volatile content decreased. Besides, the ash content was a W-type variation. The elemental composition of cokes with different coke particle sizes shared little difference, and the mineral catalytic index of coke changed slightly. Therefore, the basic properties of coke were not the main factors affecting coke particle size.

Pore Structure of Coke with Different Particle Sizes

Porosity, average pore size and average coke wall thickness with different particle sizes are shown in Table 5.

It could be seen that the porosity of coke greater than 80 mm was the smallest, but the average coke wall thickness was the largest. The porosity of coke with 60–80 mm and 40–60 mm was similar, but the average pore diameter and average coke wall thickness of coke with 40–60 mm were smaller. The porosity and average pore diameter of coke with 25–60 mm increased, and the average wall thickness was slightly smaller. By comparing the coke pore structure, the coke particle size and the average wall thickness decreased but the porosity increased.

Table 4 Ash component of various particle size coke

Coke size/mm	SiO_2/%	Al_2O_3/%	Fe_2O_3/%	CaO/%	MgO/%	K_2O/%	Na_2O/%	TiO_2/%	MnO/%	MCI
> 80	50.79	37.22	4.38	2.30	1.22	0.50	0.61	1.23	0.12	2.02
60–80	51.08	36.77	4.44	2.43	1.24	0.48	0.52	1.21	0.11	2.02
40–60	50.42	36.49	4.65	2.66	1.33	0.48	0.60	1.16	0.15	2.26
25–60	51.26	36.93	4.42	2.24	1.14	0.49	0.56	1.21	0.11	1.97
< 25	51.65	36.20	4.57	2.27	1.17	0.48	0.60	1.23	0.10	2.03

Table 5 Porosity, average pore size and average coke wall thickness of various cokes

Coke size/mm	porosity/%	average pore size/μm	average coke wall thickness/μm
> 80	44.6	87.9	110.68
60–80	56.5	117.1	93.90
40–60	56.0	103.2	83.20
25–60	60.6	131.9	87.70

Microcrystalline Structure of Coke with Different Particle Sizes

It could be seen from Fig. 1 that the 002 and 100 peaks of coke with different particle sizes were obviously different, and the peak position moved to right with the decrease of coke particle size. Combined with Bragg's law, Scherrer equation and Franlkin's formula, the calculation formulas of crystal plane spacing dhkl, stacking height or cell size Lhkl and crystal plane graphitization degree ghkl are as follows:

$$d_{hkl}=\frac{\lambda}{2\sin\theta_{hkl}} \tag{1}$$

$$L_{hkl}=\frac{K\lambda}{\beta\cos\theta_{hkl}} \tag{2}$$

$$g_{hkl}=\frac{d_{max}-d_{hkl}}{d_{max}-d_{min}} \tag{3}$$

where λ is the wave length of X-ray; θ_{hkl} is the diffraction angle; K is the content; β is FWHM of diffraction peak; d_{max} is coke surface spacing for ungraphitization, 3.894 Å[7–10]; d_{min} is coke surface spacing for idea graphitization, 3.354 Å[7–10]。

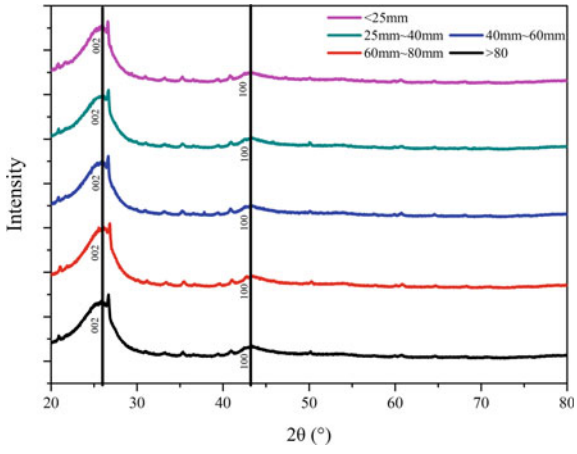

Fig. 1 XRD of various coke particle sizes

Table 6 The microcrystalline structure parameters of different coke sizes

Coke size/mm	$2\theta_{002}$/(°)	$FWHM_{002}$	d_{002}	L_c	g_{002}	$2\theta_{100}$/(°)	L_a
> 80	25.25	4.65	3.52	17.70	0.68	43.24	68.78
60 ~ 80	25.54	4.42	3.48	18.63	0.76	43.33	69.10
40 ~ 60	25.93	4.29	3.43	19.21	0.85	43.41	68.59
25 ~ 40	26.05	4.18	3.42	19.72	0.88	43.30	69.46
< 25	26.22	4.00	3.40	20.62	0.92	43.21	69.48

$2\theta_{002}$: 002 peak position, $FWHM_{002}$: 002 peak full width half maximum, d_{002}: 002 peak surface spacing, L_c:stack height, g_{002}:graphitization; $2\theta_{100}$:100 peak position, L_a:cell size。

The microcrystalline structure parameters of different coke particle sizes were calculated by formula (1–3) and the results were shown in Table 6.

From Table 6, it could be seen that the crystal plane spacing of coke greater than 80 mm was the largest, but the stacking height was the smallest. The stacking height and cell size of coke 60–80 mm increased slightly compared with coke greater than 80 mm, and the cell spacing decreased slightly. The cell spacing of coke 40–60 mm and coke 25–40 mm was similar, but the stacking height and cell size of coke 25–40 mm are higher. On the whole, the microcrystalline structure of different particle sizes was different. The peak position of 002 peak shifted to right with the decrease of particle size, and the peak position of 100 peak changed little. The crystal plane spacing decreased with the decrease of coke particle size, and the crystal plane spacing increased. The porosity of coke increased.

Conclusion

1. With the decrease of coke size, the moisture content increased slightly, the volatile content decreased slightly, and the ash content was a W-type variation. The elemental composition of cokes with different sizes had little difference, and the catalytic index of coke changed slightly. Therefore, the basic properties of coke were not the main factors affecting coke particle size.
2. The porosity of coke greater than 80 mm is the smallest, but the average wall thickness is the largest. The porosity of coke 60–80 mm and 40–60 mm was similar, but the average pore diameter and average wall thickness of coke 40–60 mm were smaller. The porosity and average pore diameter of coke 25–60 mm increased, and the average coke wall thickness was slightly smaller. By comparing the pore structure of coke, the particle size of coke decreased, the porosity increased, and the average wall thickness decreased.
3. The microcrystalline structure of different particle sizes was quite different. The peak position of 002 peak shifted to the right with the decrease of particle size, and the peak position of 100 peak changed little. The crystal plane spacing decreased with the decrease of coke particle size, and the crystal plane spacing increased.

The porosity of coke increased. Controlling the graphitization degree of coke in coking process could improve the particle size distribution of coke.

References

1. Sun C (2019) Effect of graphitization process on microstructure and metallurgical properties of blast furnace coke [D]. University of Science and Technology Liaoning
2. Guo T (2015) Fundermental study on innovative process of low-carbon blast furnace ironmaking by coke oven gas injection [D]. Northeastern University
3. Wu R, Xia H, Zhang D (2008) Advances in coke researched by use of X-ray diffraction. Shandong Metallurgy30:1-4
4. Hu D (2006) Crystallite structure characteristics of coke. Iron Steel 41:10–12,41
5. Zhang S, Lv J, Wang W et al (2004) Effect of Heat treatment on the reactivity and microstructure of coal-char. J Fuel Chem Technol 32:673–678
6. He Z, Yu Y, Chen W (2004) Influence of Sodium on coke microstructure in different reaction atmosphere. J Univ Sci Technol 39:321–326
7. Zhang Q, Zhang W, Cao Y et al (2019) Study on the effect of particle size on XRD test of coke. Nonferrous Metal Mater Eng 40:27–31
8. Zhang Z, Zheng Y, Gao N et al (2020) Study on the degree of microcrystalline order of coke determined by XRD. Coal Qual Technol 35:12–17
9. Iwashita N,Park CR, Fujimoto H et al (2004) Specification for a standard procedure of X-ray diffraction measurements on carbon materials. Carbon 42:704–714
10. Wu (1999) Study of XRD on the crystallite structure characteristics of high temperature coke of coals. J Xi'an Univ Sci Technol (2):158–160
11. Zhang D, Lin H, Wang X et al (2017) Influence of Ash of coking coals on its coking property. Iron Steel 8:10–18

Microstructure Analysis of TRIP Fe-1.39Si-2.57Mn-0.17C Steel

Victor M. Lopez-Hirata, Maribel L. Saucedo-Muñoz, Brenda A. Sandoval-Reyes, Felipe Hernandez-Santiago, Héctor Dorantes-Rosales, Mauel Beltrán-Zuñiga, and Diego I. Rivas-Lopez

Abstract In this work, the phase transformations were studied during the intercritical treatment in TRIP steel with chemical composition of Fe-1.39Si-2.57Mn-0.17C. Steel specimens were heated in the intercritical region, ferrite and austenite, at 750° C for 30 min, austempered at 430 °C, quenched in water without agitation, and normalized by air cooling. Microstructural analysis was performed by optical microscopy and scanning electron microscopy, and by X-ray diffraction. All samples were mechanically characterized by uniaxial tension and Rockwell tests. Microstructural and phase analysis was also carried out with the Thermo-Calc software. The microstructural characterization results showed that the phases and microconstituents were ferrite, austenite, cementite, and austenite. Thermo-Calc results are consistent with the phases and microconstituents found for each heat treatment condition. On the other hand, the tension test results showed that the yield strength and ultimate tensile strength are between 763–818 MPa, and 1190–1255 MPa, respectively, for these heat-treated steels.

Keywords TRIP Fe-1.39Si-2.57Mn-0.17C steel · Microstructure evolution · Thermo-Calc · Heat treatment · Mechanical properties

Introduction

The high-strength steels with excellent ductility have an increasing demand, for instance in automotive steel [1]. Transformation induced by plasticity TRIP steels can present tensile strengths above 900 MPa with 20% elongation and reduction of the structural weight up to 20% [1]. In order to increase the elongation above 25%, the austenite stabilized C-Si-Mn TRIP steels were developed [2]. The selection of an appropriate Si and Mn content and heat treatment permit to improve the mechanical properties. The use of Calphad-based software, Thermo-Calc, is a good alternative

V. M. Lopez-Hirata (✉) · M. L. Saucedo-Muñoz · B. A. Sandoval-Reyes · F. Hernandez-Santiago · H. Dorantes-Rosales · M. Beltrán-Zuñiga · D. I. Rivas-Lopez
Instituto Politécnico Nacional (ESIQIE-ESFM), UPALM Edif. 7, D.F. 07300, Mexico
e-mail: vlopezhi@prodigy.net.mx

M. Zhang et al. (eds.), *Characterization of Minerals, Metals, and Materials 2023*, The Minerals, Metals & Materials Series
https://doi.org/10.1007/978-3-031-22576-5_50

Table 1 Chemical composition of the TRIP steels

Steel	C	Mn	Si	Al	Ti	Cu	V	Nb
HP40	0.17	2.60	1.40	0.023	0.024	0.012	0.01	0.01

to analyze the phase transformations of this steel during the heat treatment and to understand the effect of microstructure evolution on the mechanical properties [3–5].

Thus, the aim of the present work is to carry out experimental and numerical analyses of microstructure evolution of a TRIP Fe-1.39Si-2.57Mn-0.17C steel during heat treatment, as well as the effect of microstructure on their mechanical properties.

Experimental Procedure

The chemical composition of the Trip steel in Table 1. Tension test specimens were prepared from a steel sheet of 40 × 50 × 0.12 cm according to the ASTM E-8 standard [6]. Three heat treatments were conducted: Normalizing, quenching, and austempering- quenching from an austenitizing at an intercritical temperature at 750 °C for 30 min using an electric tubular furnace. The austempering temperature was 430 °C for 10 min. The heat-treated specimens were metallographically prepared, etched with Nital etchant, and then observed with optical (OM) and scanning electron (SEM) microscopes. The heat-treated specimens were also analyzed by X-Ray Diffraction (XRD) with Co Kα radiation. According to the standard procedure, the Rockwell "45 N" hardness was determined in all the specimens using 45 kg_f with a diamond indenter, ASTM E-12 standard [7].

Numerical Procedure

Thermo-Calc, TC, software was used to analyze the stability of phases in the TRIP steel and to calculate the Time-Temperature-Transformation (TTT) diagram. The kinetic and thermodynamic data was determined from the Thermo-Calc databases for TCFe11 and MobFe6 [8]. TC-Prisma was used to calculate the intergranular precipitation of ferrite in austenite [8].

Results and Discussion

Microstructure Evolution of the Heat-Treated Steel

Figures 1a–c show the SEM micrographs of the steel in the condition of austempered, normalized, and quenched, respectively. The microconstituents are bainite, ferrite, and retained austenite in the case of the austempered steel. As expected, the microconstituents are martensite and ferrite for the quenched steel. The microstructure shows the presence of ferrite and pearlite in the case of the normalized steel. The amount of all phases in equilibrium as a function of temperature was calculated with Themo-Calc and is shown in Fig. 2. This figure indicates a ratio of 50:50 of austenite to ferrite at about 750 °C. Besides, this plot shows that the equilibrium phases are ferrite and cementite at temperatures lower than 700 °C. This fact suggests that the presence of pearlite is expected for the normalized steel. The TC calculated Time-Temperature- Transformation TTT diagram is shown in Fig. 3, and this one also verifies the transformation of austenite into pearlite during the cooling of normalizing. That is, the microconstituents of pearlite and ferrite are the expected ones for the normalizing process. The TTT diagram of the TRIP steel also predicts, Fig. 3, that it is possible to form martensite by quenching from the intercritical temperature, and this characteristic is consistent with the microconstituents, martensite and ferrite observed in the quenched steel. Besides, Fig. 4 shows the TC calculated plot of martensite percent as a function of temperature for different intercritical temperatures, and it can be noticed that the maximum amount of martensite can be obtained by quenching from 750 °C. In the case of the austempering treatment at 430 °C, the diagram suggests the formation of ferrite, bainite, and retained austenite, which provides more ductility to the steel.

Figure 4 presents the XRD pattern for the austempered, quenched, and normalized steel. The XRD pattern of the austempered steel and the main diffraction peaks correspond to the ferrite, cementite and austenite, which confirms the phases and microconstituents predicted by Thermo-Calc, and the experimental observations. In the tempered steel, the XRD peaks of ferrite and martensite are overlapped. Nevertheless, the ferrite and cementite peaks are clearly observed for the normalized steel, which is consistent with TC calculations and the experimental observations.

Tension Properties of Heat-Treated Steels

The plot of uniaxial tension test, engineering stress versus engineering strain is shown in Fig. 5 for the austempered, quenched, and normalized steel specimens. This plot clearly shows that the highest tensile strength and the lowest ductility correspond to the quenched steel. The austempered steel presented the longest elongation percent, as shown in Table 2. This table also shows that the highest yield strength corresponds to the austempered steel.

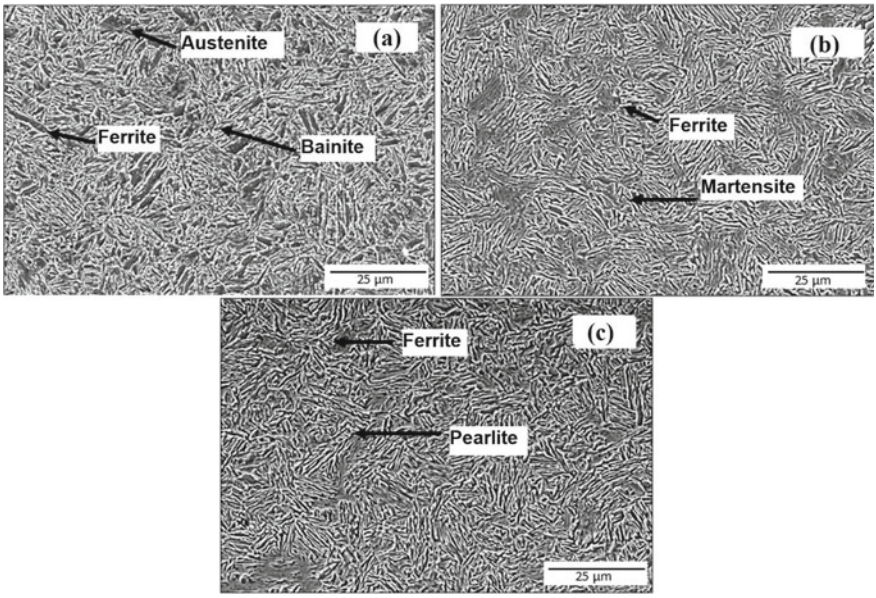

Fig. 1 SEM micrographs for the **a** austempered specimen, **b** quenched specimen and c normalized specimen

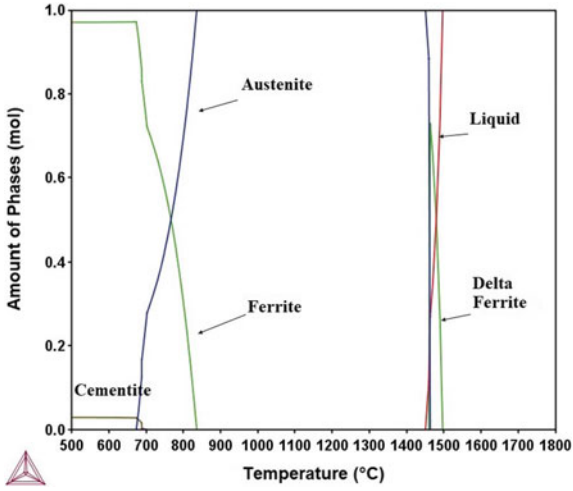

Fig. 2 TC calculated a plot of the amount of all phases in equilibrium against temperature for the TRIP steel

The SEM fractographs of the tension-tested specimen are shown in Fig. 6a–c for the austempered, quenched, and normalized specimens, respectively. A ductile fracture is clearly observed for the austempered steel, and the quenched specimen shows transgranular brittle fracture. The normalized specimen also presents ductile fracture.

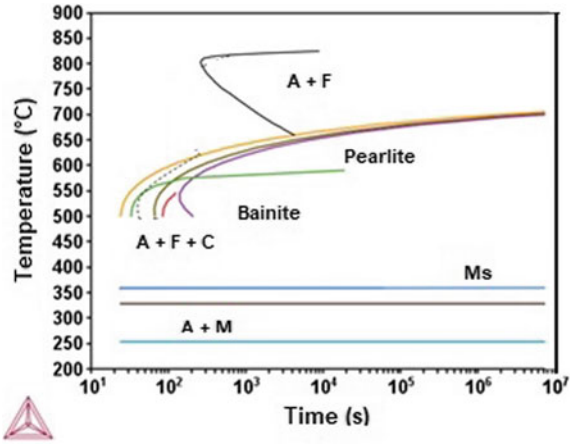

Fig. 3 TC calculated TTT diagram for the TRIP steel

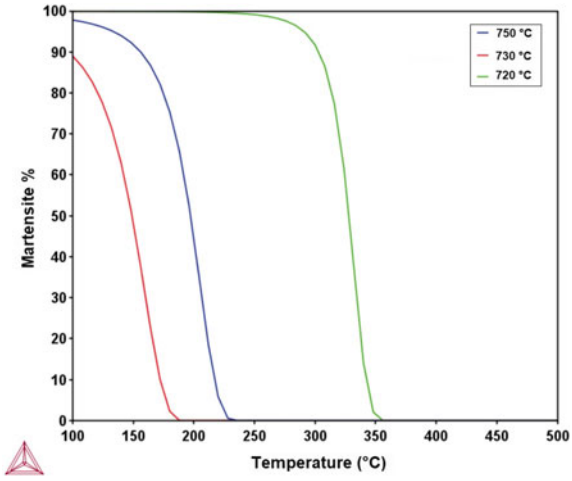

Fig. 4 TC calculated plot of martensite % versus temperature for the intercritical temperatures of 720, 730 and 750 °C

Table 3 shows the Rockwell hardness corresponding to the austempered, quenched, and normalized specimens, and it can be noted that the highest hardness is for the quenched steel and the martensite and ferrite microconstituents. The lowest one corresponds to a mixture of ferrite and pearlite.

It is important to note that the presence of retained austenite in the austempered steel contributes to the ductility observed in this heat-treating condition. This behavior is favored by the high Si content in this steel [8] (Fig. 7)

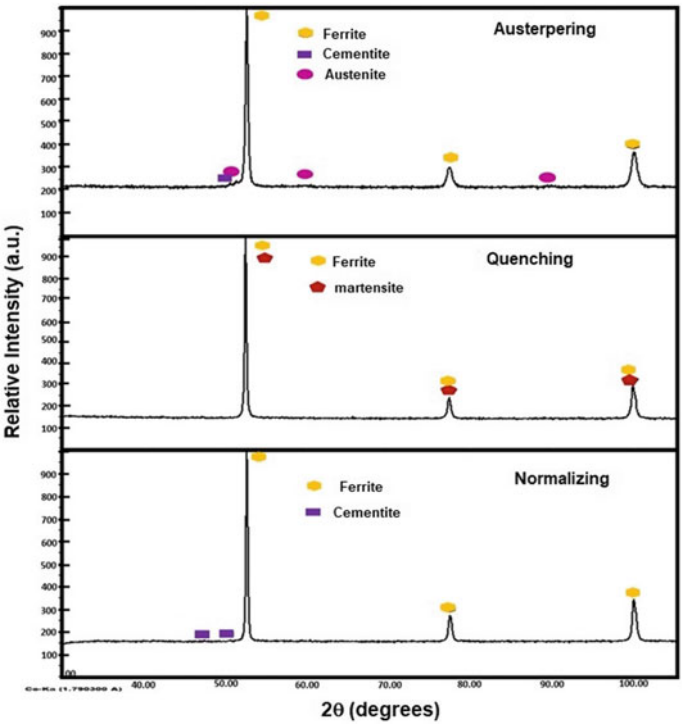

Fig. 5 XRD pattern for the TRIP steel

Table 2 Tension test results

Steel	Yield Strength (MPa)	Tensile Strength (MPa)	Elongation (%)
Austempered	818	1202	23.5
Quenched	763	1255	11
Normalized	792	1190	15

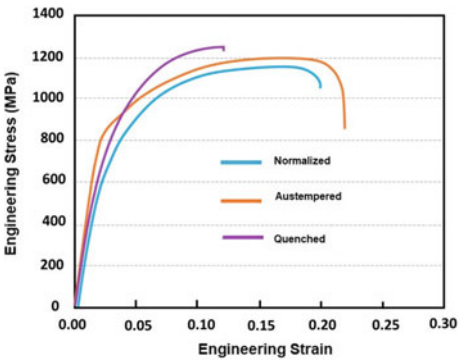

Fig. 6 Plot of Engineering stress versus engineering strain for the austempered, quenched and normalized TRIP steel

Table 3 Rockwell hardness test results

Steel	Rockwell 45 N	Rockwell *C*
Austempered	47	43
Quenched	51	47
Normalized	44	41

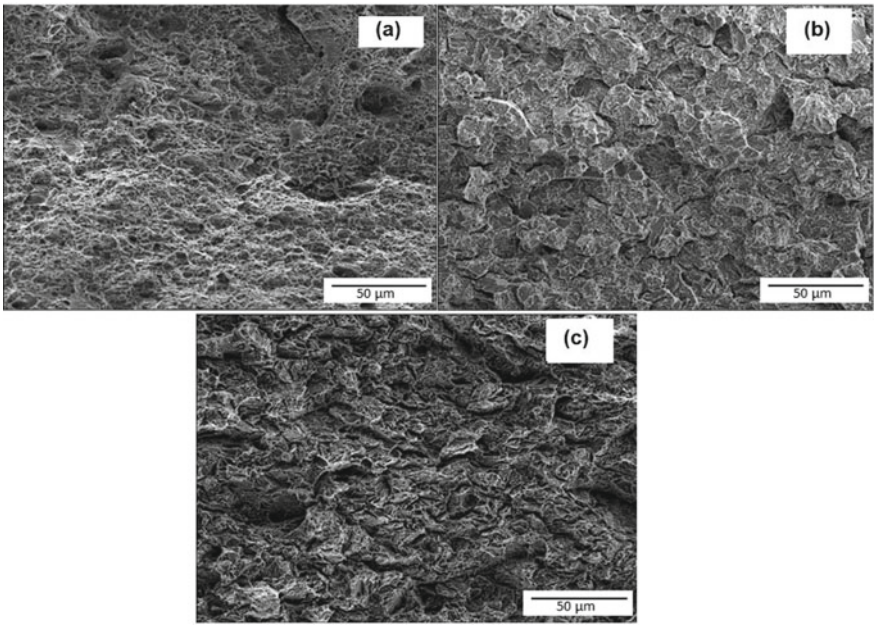

Fig. 7 SEM fractographs for the **a** austempered, **b** quenched and **c** normalized TRIP steel for the TRIP steel

Conclusions

A study of the microstructure evolution of a TRIP Fe-1.39Si-2.57Mn-0.17C steel was conducted, and the conclusions are summarized as follows:

1. The microstructure evolution developed during the heat treatment of this steel is consistent with the Thermo-Calc calculation.
2. The austempered steel presented a tensile strength similar to that of the quenched steel, but with more ductility.
3. The retained austenite plays a very important role in the ductility of the austempered steel.

Acknowledgements The authors wish to thank the financial support from SIP-COFAA-IPN and CONACYT A1-S-9682.

References

1. Shome M, Tumuluru M (2015) Introduction to welding and joining of advanced high-strength steel. Woodhead Publishing, UK
2. Founstein N (2015) Advanced high strength sheet steels: physical metallurgy, design, processing, and properties. Springer, Cham
3. Tisza M (2020) Development of lightweight steel for automotive applications. Hungary: IntechOpen
4. Mohsen A, Massoud G, Shahram K (2008) Kinetics of Austenite formation in dual phase steel. ISIJ Int 48:1251–1255
5. Huper T, Endo S, Ishikawa N, Osawa K (1999) Effect of volume fraction of constituent phases in the stress-strain relationship of dual phase steels. ISIJ Int 39:288–249
6. ASTM (2016) ASTM E8/E8M-16a, Standard test methods for tension testing of metallic materials
7. ASTM (2020) ASTM E8–20, Standard test methods for Rockwell hardness of metallic materials
8. Kim S-J, Lee C, Choi I, Lee S (2001) Effects of heat treatment and alloying elements on the microstructures and mechanical properties of 0.15 Wt Pct C transformation-induced plasticity-aided cold-rolled steel sheets. Metall Mater Trans A 32:505–514

Performance Evaluation of Pineapple Crown Fibers (*Ananas Comosus*) in Cementitious Composites

S. A. A. Malafaia, T. R. Silva, L. U. D. Tambara Júnior, J. A. T. Linhares Júnior, I. S. A. Pereira, S. N. Monteiro, and A. R. G. Azevedo

Abstract Brazil has been standing out in the agro-industrial production in which large volumes of waste are generated, including pineapple fibers. Natural fibers have been studied in different composites, especially cementitious. This research aimed to evaluate fibers from the pineapple crown for their application in coating mortars. The residue was submitted to wetting and drying cycles and, was treated in variable parameters: reagent concentration (5 and 10%), exposure time to chemical attack (30 min and 60 min), and type of reagent (NaOH and Ca $(OH)_2$). The fibers were incorporated with 1.5% in relation to the mass of cement of the produced mortar and compared with the reference mortar (0%), which were evaluated in the fresh state. It was found that the treatment with NaOH was the one that most degraded the external surface of the fiber and the produced mortars showed satisfactory performance, thus contributing to the development of alternative materials.

Keywords Technological characterization · Pineapple · Natural fibers · Building materials

Introduction

Currently, the construction sector has been seeking more sustainable alternatives due to environmental problems arising from the impacts of human actions, including the destination of solid waste in the environment [1]. In this context, studies have been

S. A. A. Malafaia · A. R. G. Azevedo (✉)
LECIV—Civil Engineering Laboratory, UENF—State University of Northern Rio de Janeiro, Av. Alberto Lamego, 2000, Campos dos Goytacazes, Rio de Janeiro 28013-602, Brazil
e-mail: samuelazevedoeng@gmail.com

T. R. Silva · L. U. D. Tambara Júnior · J. A. T. Linhares Júnior · I. S. A. Pereira
LAMAV—Advanced Materials Laboratory, UENF—State University of Northern Rio de Janeiro, Av. Alberto Lamego, 2000, Campos dos Goytacazes, Rio de Janeiro 28013-602, Brazil

S. N. Monteiro
Department of Materials Science, IME—Military Institute of Engineering, Square General Tibúrcio, 80, Rio de Janeiro 22290-270, Brazil

M. Zhang et al. (eds.), *Characterization of Minerals, Metals, and Materials 2023*, The Minerals, Metals & Materials Series
https://doi.org/10.1007/978-3-031-22576-5_51

developed using the incorporation of natural fibers, which represent a large part of the disposal of agro-industrial waste, including pineapple, banana, sugarcane, açaí, coconut and rice fibers, among others [2, 3].

Countries with tropical climates such as Brazil stand out as major agro-industrial producers, as they have favorable climatic factors for large-scale fruit planting and may highlight pineapple fruit (*Ananas comusus*). In these productive processes, about 30% to 40% of the cultivated materials become waste [4], which implies the need for alternatives for the use of these wastes. Natural fibers are strongly used in different types of composites, including cementitious, due to their good characteristics such as low density and biodegradability and can provide improvements in technological properties depending on their application [5]. They can be highlighted mainly by their composition, basically formed of cellulose, hemicellulose and lignin [6].

As a result, natural fibers are submitted to surface treatments, which provide changes in surface characteristics of the fiber, so that it is possible to use these fibers in composites for different applications. In these circumstances, these treatments mainly improve the interaction between fiber/matrix, consequently collaborating with the adhesion between the fibrous material and the composite matrix [2].

Considering these factors, the present study sought to make use of the fibrous material present in the pineapple crown (PALF) and define the appropriate surface treatment for its application in cementitious coating mortars, as well as to evaluate the performance of natural fiber incorporation in mortar. Fresh state technological tests such as consistency, water retention, embedded air content and mass density were performed.

Materials and Methods

The following materials were used in this study: Portland CP II-F-32 cement, CH-III hydrated lime, river natural sand and distilled water for the preparation of mortar mixtures for coating. The fibrous material of the pineapple crown was collected directly from a rural production unit, located in the municipality of São Francisco do Itabapoana (RJ/Brazil), which is an important regional center of pineapple production, being responsible for supplying part of the southeast region of Brazil. The crown of the fruit is discarded after harvest, upon preparation for the sale of the fruit, since the pineapple is marketed without this part.

The sand used has $D_{MAX} = 2.40$ mm and was dried in a greenhouse for Sterilization and Drying Brasdonto MOD2 at 105ºC until constant mass so that the mixture would not be influenced by the moisture retained by this material. To obtain distilled water, the Mars Water Distiller MB1005 Pilsen 5 L 220v was used.

After separation and collection, the materials were stored in sealed containers, in the premises of the Ceramic Materials Laboratory of the Science and Technology Center of the State University of Norte Fluminense Darcy Ribeiro (UENF), located in Campos do Goytacazes/RJ/Brazil. The project steps are shown in Fig. 1.

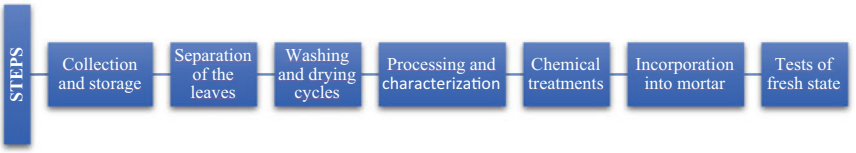

Fig. 1 Flowchart with project steps

Then, the leaves of the pineapple crown were removed and the degraded parts of the fruit were discarded. After this step, the samples were destined to three cycles of washing and drying in the oven until the samples obtained constant mass. This process aimed to remove possible impurities from fruit production.

Subsequently, the samples were processed in an industrial mixer and submitted to chemical treatments. The process consisted of the analysis of three parameters with eight variables: reagent concentration in 5% and 10%, chemical attack time in 30 min and 60 min and type of reagent, where NaOH and $Ca(OH)_2$ were used, as shown in Fig. 2.

The chemical treatment process took place as follows: initially, the amount of reagent was calculated in relation to the volume of the solution. The fiber mass to be treated occurred at the concentration of 1/20 in relation to the same volume, multiplied by the fiber density, which was obtained through the pycnometer, with a value of 1.397 g/cm^3.

In the chemical treatments, after the indicated time, the samples of the fibers treated with their reagents were washed in running water until the washing water was transparent (pH neutral), indicating that the reagent material had been diluted.

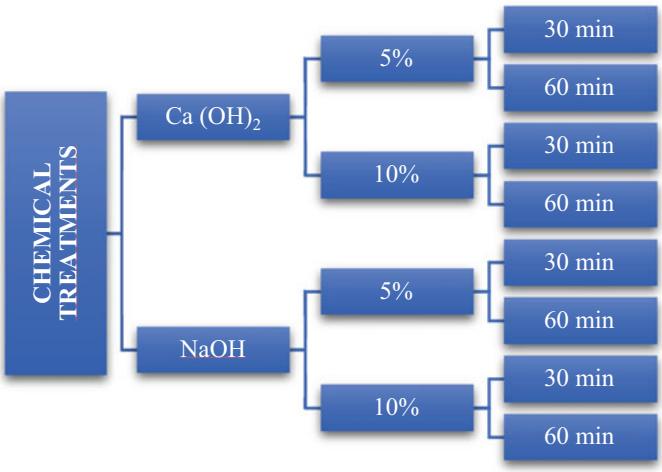

Fig. 2 Flowchart with chemical treatments

Then, the material was dried in an oven at 105 ºC until constant mass. Subsequently, the fibers were again processed in order to incorporate dwell in the mortar, they had a lower segregation in the mixture.

In all steps, characterizations of the 8 variables were made, so that it was possible to understand the influence of treatments on the microstructure of fibers. After this stage, the best treatment was chosen: NaOH with 5% concentration in 60 min., joining the attack to the outermost layer of cellulose, which has little adhesion with the mixture, increasing adhesion with the cement matrix, in an intermediate concentration, when compared to 10%.

The mortars were made in accordance with ABNT NBR 16,541:2016 [7]. Fresh state tests were performed, where it is possible to evaluate: consistency, water retention, embedded air content and mass density, thus analyzing the behaviors of this addition. The mortar was made in the planetary mixer. Consistency was obtained through the Solotest MC-119 220v Table, according to ABNT NBR 13,276:2016 [8]. Then, the embedded air content test was performed in the Air Meter device incorporated into the Solotest mortar, according to ABNT NBR 13,278:2005 [9]. The mass density was determined using the Solotest Mass Density Container, with methodology available in ABNT NBR 13,278: 2005 [9]. Finally, the water retention test was performed in the forced filtration system with a Büchner funnel, proposed at ABNT NBR 13,277: 2005 [10]. Figure 3 shows the tests carried out at this stage of the project.

The mixture was based on the proportions 1:1:6 (cement, hydrated lime and sand), since this composition is widely used in the research region. The amount of water was defined by trial and error, where the consistency was fixed, being used in the amount necessary for the spreading of the mixture in the range of 260 mm ± 5 mm, as suggested by ABNT NBR 13,276: 2016 [8]. The composition of the mixtures and the water/cement ratio (w/c) are arranged in Table 1.

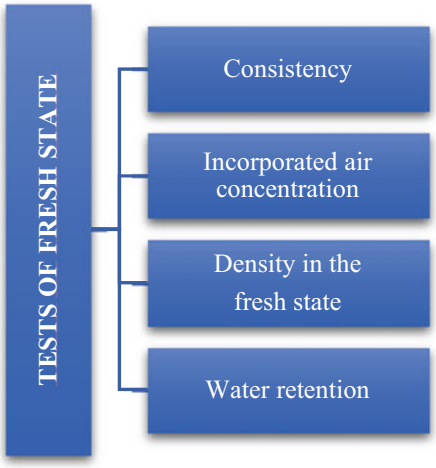

Fig. 3 Flowchart with fresh state tests

Table 1 Composition of mixtures

Mixture	Cement(g)	Lime(g)	Sand(g)	Water(g)	Palf(g)	*w/c*
REF	200 g	200 g	1200 g	275 g	–	1.375
PALF1.5%	200 g	200 g	1200 g	280 g	3 g	1.400

Two mixtures were made, where in the first composition there was no residue incorporation (REF), and in the second the PALF fibers were incorporated in the ratio of 1.5% in relation to the cement mass (PALF1.5%). The fibers were treated with the reagent, concentration and time previously defined (NaOH 5% in 1 h).

Results and Discussion

Figure 4 exposes the consistency results. The water/cement ratio in the mixtures was defined after trial and error, in order to achieve the ideal consistency for coating mortars, according to ABNT NBR 13,276: 2016 [8]. For this to be possible, in the mixture of 1.5% it was necessary to add 1.81% in relation to the total water in the reference mixture. This can be related to the property of water absorption fibers [11]. The result of the consistencies indicated that, for the PALF1.5% line of way, the consistency, which directly influences the workability, was 1.14% lower, indicating that the workability was not significantly impaired [12].

The incorporated air content assay was then performed, where it was verified that the increase of this index was 12.70% in the MIXTURE PALF1.5%, in relation to the reference mixture. This situation accompanied the reduction of the plasticity of the mixture [13]. The inverse relationship of these two properties has already been

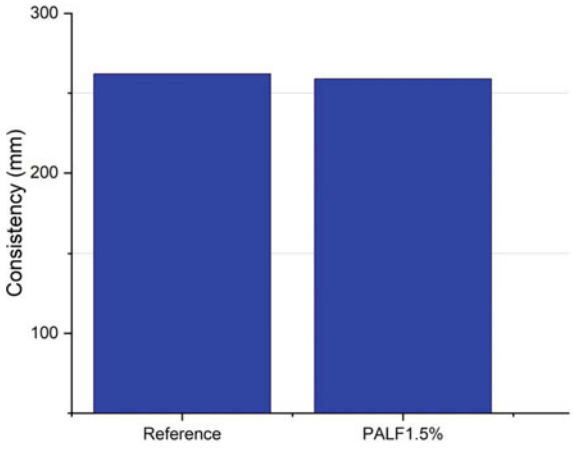

Fig. 4 Consistency in the fresh state of the mixtures

verified in the literature [11], and indicates that the data are in agreement with the expected. Figure 5 correlates the results of the two mixtures.

The density of the mass in the fresh state for the two mixtures was made after the previous tests, where it was possible to verify that the mixture with PALF obtained a relative reduction of specific mass (0.78%) [14]. This situation can be tied to the fact that the fibers have lower density compared to the other materials used in the cement mixture. It can be said that PALF fibers collaborate with the reduction of the compound's own weight in this case, as shown in Fig. 6 [15].

The water retention of the mixtures was analyzed (Fig. 7), where there were little significant changes in relation to this data. The variation between the mixtures with PALF was 0.82% lower when compared to the reference [16]. However, it is understood that the addition of fiber reduced this content. The cause for this purpose

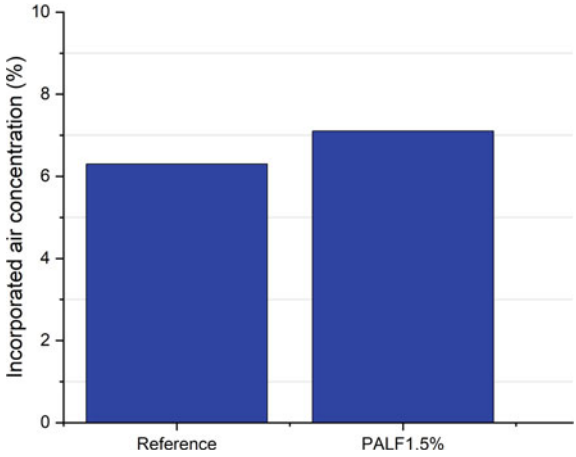

Fig. 5 Incorporated air concentration in the fresh state of the mixtures

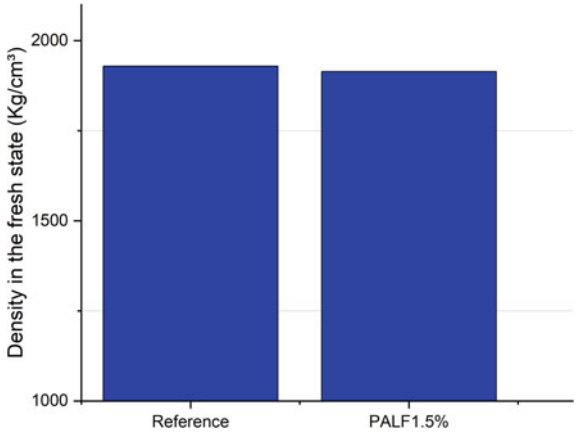

Fig. 6 Density in the fresh state of the mixtures

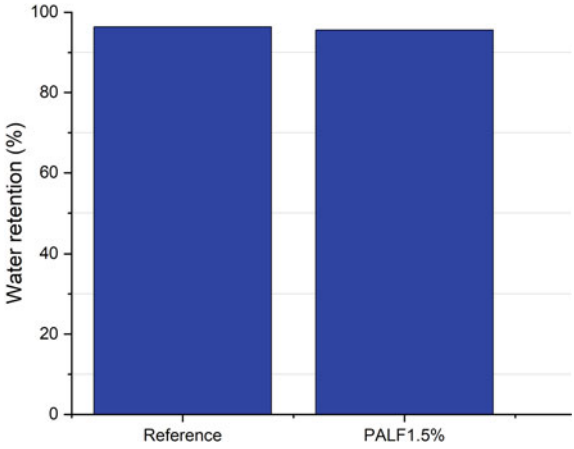

Fig. 7 Water retention of mixtures on the fresh state

may be related to the impregnation of part of the water from the mixture into the inner wall of the fibers [11].

Conclusion

Through the fresh state technological tests performed, it was possible to conclude that the addition of PALF at the ratio of 1.5% behaved beneficially in the cementitious mixture. The workability of the mixture was reduced, but reached the recommend for the function of the mortar produced.

The mass density was reduced, indicating that the addition of PALF contributed to the reduction of the mixture's own weight. The embedded air content behaved as expected, indicating a higher percentage than the reference mixture. The variation in water retention was not significant, indicating that the results were close to those without PALF incorporation. It is concluded that PALF fibers are beneficial when used in 1.5% in relation to the cement mass, for coating mortars, but the durability of these composites needs to be studied so that it is possible to use and popularize them in the construction sector.

Acknowledgements This research was funded by the State University of the Northern Fluminense (UENF), partially financed by CAPES (Coordenação de Aperfeiçoamento de Pessoal de Nível Superior—Brazil), CNPq (Coordenação Nacional de Pesquisa) and FAPERJ (Fundação de Apoio à Pesquisa do Estado do Rio de Janeiro). The participation of A.R.G.A. was sponsored by FAPERJ through the research fellowships proc.no: E-26/210.150/2019, E-26/211.194/2021, E-26/211.293/2021, E-26/201.310/2021 and by CNPq PQ2 307592/2021-9.

References

1. Zavadskas EK, Šaparauskas J, Antucheviciene J (2018) Sustainability in construction engineering. Sustainability (Switzerland), vol. 10, no. 7. MDPI, Jun. 29, 2018. doi: https://doi.org/10.3390/su10072236.
2. de Azevedo ARG et al (2022) Possibilities for the application of agro-industrial wastes in cementitious materials: a brief review of the Brazilian perspective. Cleaner Materi 3. https://doi.org/10.1016/j.clema.2021.100040
3. Sriram M, Aswin Sidhaarth KR (2022) Various properties of natural and artificial fibers with cementitious composites in hybrid form—a review. Mater Today Proc 60:2018–2025. https://doi.org/10.1016/j.matpr.2022.01.266
4. Asim M et al (2015) A review on pineapple leaves fibre and its composites. Int J Polym Sci 2015. Hindawi Limited. https://doi.org/10.1155/2015/950567
5. Monteiro SN, Satyanarayana KG, Lopes FPD (2010) High strength natural fibers for improved polymer matrix composites. Mater Sci Forum 638–642:961–966. https://doi.org/10.4028/www.scientific.net/MSF.638-642.961
6. Pereira PHF, Ornaghi HL, Arantes, Cioffi MOH (2021) Effect of chemical treatment of pineapple crown fiber in the production, chemical composition, crystalline structure, thermal stability and thermal degradation kinetic properties of cellulosic materials. Carbohydr Res 499. https://doi.org/10.1016/j.carres.2020.108227
7. NBR 16541 (2016) Argamassa para assentamento e revestimento de paredes e tetos—preparo da mistura para a realização de ensaios. Assoc Bras Normas Técnicas
8. NBR 13276 (2016) Argamassa para assentamento e revestimento de paredes e tetos—determinação do índice de consistência. Assoc Bras Normas Técnicas
9. NBR 13278 (2005) Argamassa para assentamento e revestimento de paredes e tetos—determinação da densidade de massa e do teor de ar incorporado. Assoc Bras Normas Técnicas
10. NBR 13277 (2005) Argamassa para assentamento e revestimento de paredes e tetos—determinação da retenção de água, Assoc Bras Normas Técnicas
11. Azevedo AR, Marvila MT, Zanelato EB, Alexandre J, Xavier GC, Cecchin D (2020) Development of mortar for laying and coating with pineapple fiber. Revista Brasileira de Engenharia Agricola e Ambiental. 24. https://doi.org/10.1590/1807-1929
12. Marvila MT, De Azevedo ARG, De Matos PR, Monteiro SN, Vieira CM (2021) Materials for production of high and ultra-high-performance concrete: review and perspective of possible novel materials. Materials 14(15). https://doi.org/10.3390/ma14154304
13. Azevedo ARG, Marvila MT, Zanelato EB, Alexandre J, Xavier GC, Cecchin D (2020) Development of mortar for laying and coating with pineapple fiber. Revista Brasileira De Engenharia Agricola e Ambiental 24(3):187–193. https://doi.org/10.1590/1807-1929/agriambi.v24n3p187-193
14. Carvalho A, Xavier GC, Alexandre J, Pedroti LG, de Azevedo ARG, Vieira CMF, Monteiro SN (2014). Environmental durability of soil-cement block incorporated with ornamental stone waste. https://doi.org/10.4028/www.scientific.net/MSF.798-799.548
15. Marvila MT, de Azevedo ARG, de Oliveira LB, Xavier GC, Vieira CMF (2021) Mechanical, physical and durability properties of activated alkali cement based on blast furnace slag as a function of %Na2O. Case Stud Constr Mater 15. https://doi.org/10.1016/j.cscm.2021.e00723
16. Zeyad AM, Magbool HM, Tayeh BA, Azevedo ARG, Abutaleb A, Hussain Q (2022) Production of geopolymer concrete by utilizing volcanic pumice dust. Case Stud Constr Mater 16. https://doi.org/10.1016/j.cscm.2021.e00802

Physicochemical and Environmental Features of Rice Husk Ash from Brazil to Use in Cement Materials

A. Muller, L. Simão, E. F. Olivo, A. R. G. Azevedo, M. T. Marvila, C. M. F. Vieira, and F. Raupp-Pereira

Abstract The rice beneficiation process annually produces tons of rice husk ash (RHA). In this work, RHA from companies in southern Brazil is characterized physically and chemically, seeking to apply them in cementitious materials. In addition, the waste was analyzed concerning the literature considering aspects related to its environmental characterization, generation data, recycling availability, and applicability in cementitious materials. The preliminary results of ash characterization demonstrate potential for use in cementitious materials. The ash has a high content of silica (amorphous) and crystalline phases, such as cristobalite. Regarding feasibility, maps of the generating companies and possible recipients of these residual materials in the study region confirm the proposed application. Using RHA in cementitious materials demonstrates an excellent alternative for sustainability and economic circularity in the study region.

Keywords Sustainability · Cements · Circular economy

A. Muller · L. Simão · E. F. Olivo · F. Raupp-Pereira
Postgraduate Program in Materials Science and Engineering (PPGCEM), UNESC – University of the Extreme South of Santa Catarina, Av. Universitária, 1105, Santa Catarina, Criciúma 88806-000, Brazil
e-mail: anderson.muller@ifsc.edu.br

E. F. Olivo
e-mail: eduardaolivo@unesc.net

F. Raupp-Pereira
e-mail: fraupp@unesc.net

A. R. G. Azevedo (✉)
LECIV – Civil Engineering Laboratory, UENF - State University of Northern Rio de Janeiro, Av. Alberto Lamego, 2000, Campos Dos Goytacazes, Rio de Janeiro 28013-602, Brazil

M. T. Marvila · C. M. F. Vieira
LAMAV – Advanced Materials Laboratory, UENF - State University of Northern Rio de Janeiro, Av. Alberto Lamego, 2000, Campos Dos Goytacazes, Rio de Janeiro 28013-602, Brazil
e-mail: vieira@uenf.br

M. Zhang et al. (eds.), *Characterization of Minerals, Metals, and Materials 2023*, The Minerals, Metals & Materials Series
https://doi.org/10.1007/978-3-031-22576-5_52

Introduction

In the modern world, large amounts of waste are generated. Consequently, it becomes necessary to reuse these materials in a valuable and efficient way [1]. Due to the amounts of biomass generated in harvesting and agricultural production, agroindustrial activity is considered critical in some countries, such as the United States, China, India, Africa, Brazil, and Pakistan [2].

Rice husk is the by-product of the grain beneficiation process that is generally used as a source of biomass for low-cost energy production to replace other energy sources partially. Combustion of rice husk at 600–700 °C removes organic matter and converts about 20 to 25% to ash, corresponding to an 80% reduction in mass [3]. Rice husk has a high calorific value (4000 cal/g), which can be compared with eucalyptus sawdust which is approximately 4100 cal/g [4]. During a process of controlled combustion of biomass, residual ash with high concentrations of highly reactive silica can be generated [2]. These pozzolanic and highly reactive residual materials can be used in concrete and are called mineral admixtures [1, 5].

This work aims to physically and chemically characterize the rice husk ash (RHA) of a company in southern Brazil seeking to apply them to cementitious materials. Scopus database was used to investigate the potential cementitious applications using RHA. Primary papers were filtered using the following keywords: "rice husk ash", "cement", "mortar", and "concrete". The highest cited and relevant papers in the last five years were evaluated using the defined analysis criteria, CPQvA. Five decision-making criteria guided this systematic method, namely, classification, potential, quantity, viability, and applicability, which were associated with the environmental regulations and standards, physicochemical characteristics, production data, recycling challenges, and possible applications, respectively. This systematic guideline was adopted by the authors in previous studies for aluminum anodizing waste [6], stone cutting waste [7] and iron ore tailings [8].

Quantity and Feasibility

Rice (Oryza sativa) production is one of the most significant agricultural activities in the world, second only to sugarcane and corn. Currently, ~ 510 million tons of rice are processed worldwide annually. China is the biggest producer with 28.5%, followed by India with 24%, Indonesia and Bangladesh with 7%, Vietnam with 5%, and Thailand with 4%. Rice production in Brazil in the 2021/2022 harvest reached the mark of 10,783.5 thousand tons [9]. The South region has the most significant production with about 8,992.4 thousand tons, whereas the state of Rio Grande do Sul is the largest producer (7654,4 thousand tons) and Santa Catarina ranks second nationally with 1,178.3 thousand tons representing [9]. Considering that 20% of the harvested rice corresponds to husk and 4% corresponds to RHA, it is concluded that 431.34 thousand tons of RHA are generated in the country. Of this total, the state

of Santa Catarina produces 47.13 thousand tons of RHA per year. Therefore, rice husk and RHA are generated in large quantities, so their use as a by-product can be a viable way to avoid environmental problems due to improper disposal while reducing costs for the rice processing company [10].

According to a survey carried out in the Extreme South region of Santa Catarina, which includes the Association of Municipalities in the Extreme South of Santa Catarina (AMESC), the Association of Municipalities in the Coal Region (AMREC), and the Association of Municipalities in the Laguna Region (AMUREL), there are currently 32 rice processing and 121 companies manufacturing cement materials and products (Fig. 1). Therefore, using RHA from the study region in cementitious formulations shows a potential application concerning generation and possible recipient companies.

Rice husk ash is currently used for various purposes and in greater volume, especially in the agroindustry of the studied region. This method is used indirectly by most rice producers since a good part of the generated husk is deposited in the soil as the only way to dispose of this waste [11]. However, in this sector, its use has a low added value [10] and some associated environmental problems, such as decomposition time, a large volume of methane (CH_4) released, and the large volume required for its disposal due to its low density [10].

The need for technological advances for a better cost/benefit ratio of materials has encouraged diversification in the supply of raw materials, seeking to integrate

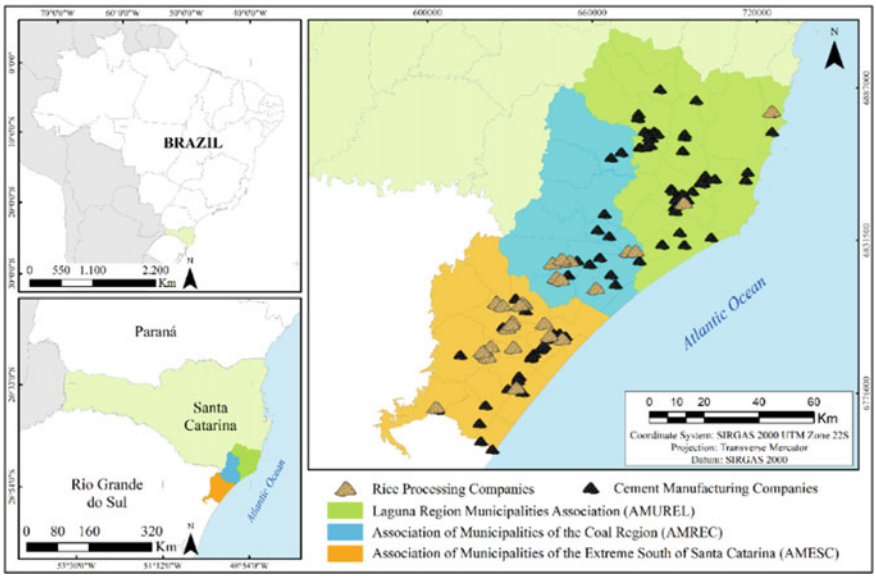

Fig. 1 Location of the rice processing companies with respect to the cement-material industries in southern Santa Catarina, Brazil

different production chains [12]. The search for new alternatives for greater profitability of cement production was based mainly on significant percentage data at the state and federal levels about the products mentioned. According to the Federation of Industries of the State of Santa Catarina (2015), Santa Catarina is the largest producer of cementitious materials in the southern region of Brazil, with a production of approximately 1,800 thousand tons/year, corresponding to a share of 5.9% in the GDP from Santa Catarina [13].

Applications of RHA in Cement Materials

In the literature (Table 1), it can be seen that most works are focused on using RHA as a cement substitute, and few address the replacement of fine aggregates by RHA. Gill and Siddique [1] studied the durability and microstructural properties of self-compacting concrete (SCC) composed of metakaolin (MK) replacing cement and rice husk ash (RHA) replacing 10% of fine aggregates, with significant improvements in their properties of durability [1].

Kang et al. [5] studied high-performance concretes using RHA as a reactive filler to improve mechanical properties. The idea of the study was to replace the inert quartz filler with the reactive RHA-based filler with high amorphous silica content. Due to the high porosity of RHA, internal curing is adequate and promotes the hydration reaction for a longer time. Experimental results show a strength of ~ 200 MPa after 91 days at ambient conditions of 20 °C and 60% relative humidity. The authors

Table 1 Main studies about rice husk ashes to use in cement materials

Ref	Applications	Objective	Mains results
[5]	Use in high performance concrete	Replacing the inert quartz filler	~ 200 MPa after 91 days
[14]	Use in high performance concrete	Addition of nanometer RHA	Improved compressive strength and waterproofing
[1]	Use in self-compacting concrete	Replace 10% of fine aggregates	Significantly improved properties and durability
[15]	Use in concrete with recycled aggregates (RCA)	Addition of RHA	Increased hydration rate, improved acid resistivity and reduced chloride diffusivity
[16]	Geopolymer	Replacement of 20% of MK by RHA	Improved waterproof properties
[17]	Geopolymer concrete	Partial cement replacements by RHA	Improve the resistance of geopolymers to sulfate attack
[18]	Geopolymer	Replace commercial sodium silicate with RHA (after hydrothermic process)	Compressive strength similar to commercial silicate samples

concluded that this good result was due to the pozzolanic reaction of the amorphous silica in the system and the reduction in capillary pore volume [5].

In addition to the chemical composition of the RHA, the burning temperature of this ash is an essential factor in the properties obtained in cementitious materials. Faried et al. [14] concluded that the firing condition at 700 °C for five hours generates more amorphous silica than other mixtures.

The use of recycled aggregates (RCA) has been studied recently as a substitute for natural aggregates in mortars and concretes [15, 19]. The use of RCA usually obtains inferior properties concerning concretes that use natural aggregates. The use of silica fume and fly ash are exciting additions to improve the performance of RCA-based concretes. Koushkbaghi et al. [15] studied the addition of RHA to improve the performance and durability of concretes with RCA. The results revealed that RHA could be used to mitigate the low performance of concrete with RCA and improve the adhesion between concrete and fibers. The addition of RHA increased the hydration rate of the concrete at advanced ages, improved the resistivity against acids (due to the lower content of calcium hydroxide in the concrete obtained), and reduced the diffusivity of chlorides [15].

Materials rich in SiO_2, such as nano-silica and RHA, were used by Nuaklong et al. [20] to improve the properties of geopolymer concretes made with RCA. The study aimed to replace commercial nano-silica with RHA in geopolymers. The results of mechanical compression at 28 days containing RHA were similar to those with nano-silica, ranging from 36.0 to 38.1 MPa [20]. The compressive strength of RHA-based geopolymers is directly proportional to the amount of alkaline activator and molarity of the activator solution. An increase in the molar concentration of the alkaline activator increases the strength, bringing a denser and more homogeneous microstructure. This is because the higher amount of NaOH promotes the dissolution of RHA and improves the bond between the particles [21].

Studies indicate that using 30% of rice husk ash instead of metakaolin increases compressive strength, in addition to gains in the thermal stability of the material obtained [16, 22, 23]. The ash has a filler effect, high reactivity, and can refine the microporosity of geopolymer gel [23]. Other works indicate that the incorporation of 10–20% by weight of rice husk ash improves the geopolymer's short- and long-term properties, making it a sustainable and environmentally friendly way to valorize these materials [24]. Rice husk ash-based geopolymers can minimize the total porosity of the concrete, change its pore composition and significantly decrease the permeability, which reduces the effect of harmful ions that contribute to the reduction of the concrete matrix strength [16, 17, 25].

The interest in valuing industrial waste and the need to reduce the production cost of geopolymeric binders has promoted the development of alkaline activators based on the combination of alkalis with waste sources of amorphous silica [26]. These activators may have a similar or even greater effect than traditional soluble silicate-based alkaline activators. Tong et al. [18] studied a hydrothermal process before dissolving RHA in sodium hydroxide solution to increase silicon solubility. A concentration of 3 M NaOH, heating temperature of 80 °C, and three hours of heating were necessary to later mix the obtained solution with fly ash and granulated

blast furnace slag. The compressive strength obtained from the mortar was 60 MPa at 28 days, like the samples with commercial silicate. Furthermore, the method could reduce almost 55% of the cost of activating these materials [18]. Therefore, rice husk ash is an excellent biogenic source of Si to synthesize low-cost sodium/potassium silicate that is generally used as an activator in geopolymers. The efficiency of Si dissolution depends on the concentration of the NaOH solution, the temperature (80–100 °C), and the crystallinity of the silica present in the ash. In addition, the amorphous silica present in the ash can reduce the cost of processing sodium silicate compared to conventional processes using autoclaves [24].

Materials and Methods

After the RHA quantity/viability evaluation and their applications in cement materials, a sample from the region of the study was characterized by loss on ignition (LoI) test according to ASTM D7348 standard [27] and subsequent chemical analysis by energy-dispersive X-ray fluorescence spectrometry (EDX 7000, Shimadzu, Japan). Mineralogical analysis was performed using an X-ray diffractometer (XRD, Shimadzu XRD-6000, Japan; CuKα radiation, 10–80° 2θ range, 0.02° step). The thermal behavior was determined by thermogravimetry (STA449F3, NETZSCH, Germany) in synthetic air atmospheres at a heating rate of 20 °C min^{-1} and a threshold of 1000 °C. In addition, some information about the environmental aspects of RHA is described.

Classification and Environmental Impacts

Waste is a material that needs to be classified according to its hazardous when disposed of in landfills or when used in other processes and products. Thus, leaching tests are essential to assess the classification of these materials [28]. Leach tests are adopted by the European Economic Community (EEC) and other environmental agencies worldwide to classify their waste [29, 30]. In the United States, hazardous and non-hazardous waste is managed according to the Environmental Protection Agency (EPA) recommendations. Likewise, the Brazilian standard NBR 10,004/2004 [30] classifies waste into three classes: hazardous (Class I) when corrosive, pathogenic, flammable, or toxic characteristics are revealed; non-hazardous, but not inert (Class II-A) when biodegradability, combustibility or water solubility is demonstrated; and non-hazardous and inert (Class II-B), when none of the characteristics mentioned above are demonstrated. Detailed waste classification procedures based on the NBR 10,004 standard were reported in previous studies [7, 31].

According to Walter and Rossato [32], Rice husk receives a Class IIA classification according to NBR 10.004 for presenting characteristics of biodegradability

and combustibility. In this way, the material can be considered non-inert and non-hazardous to human health and the environment. When it goes through the burning process, the generated rice husk ash is considered highly harmful to human health due to the high silica content and the consequent risk factor for lung disease known as "silicosis" [33]. When these rice husks are incinerated indoors (e.g., in boilers and ovens), they result in highly polluting ash, releasing harmful gases that contribute to global warming [34, 35]. On the other hand, when rice husks are discarded in crops and river bottoms, their decomposition releases methane gas, which is about 50% more harmful than CO_2 to the environment [36]. Therefore, despite not being considered a hazardous waste, the rice husk generated in the rice processing process needs adequate treatment so that it does not result in negative environmental impacts for the environment [32].

According to the NBR 10,004 standard, rice husk ash is classified as Class II-A, as it does not fall into the Class I class of hazardous characteristics, which causes pathogenicity, flammability, corrosivity, and reactivity [33]. The rice husk leaching and solubilization tests with their respective normative limits are described in Table 1 [33], where we can see that the Mn element was the only one above the limits of the Brazilian normative for the solubilization test.

Potentialities: Chemical and Physical Features

Among the biomass ash, some, such as rice husk ash, have a high pozzolanic content resulting from their abundant silica concentration [37]. The characteristics of these materials include more than 95% amorphous silica, high reactivity, and high specific surface area [17, 23]. The percentages related to amorphous silica may vary according to the process of burning. According to the characterizations performed and studies in the literature (Tables 2 and 3), a high silica content with crystalline and amorphous phases can be observed.

Through the result presented in Fig. 2a, it can be verified that the cristobalite phase is present, confirming the presence of SiO_2 evidenced in the XRF. Furthermore, it can be seen that the central peak has a considerable broadening, between 15° 2θ and 36° 2θ, indicating the presence of amorphous compounds. As the formation of crystalline peaks increases, there is an indication of a reduction in the degree of amorphism, and the formation of the cristobalite peak indicates that the burning temperature of the rice husk has reached high temperatures [38].

As the temperature of the firing process increases, there is a tendency to increase the specific area of the ash obtained. On the other hand, the fusion of silica at high temperatures, responsible for more significant structure densification, demands greater energies for the adequate combination of the ash [38]. In addition to the temperature, it is also essential to observe the time of the firing process for eventual favoring of the material's melting [39]. These facts corroborate the great importance of control over the firing process.

Table 2 Rice husk ashes leaching and solubilization test results found in the literature

Chemical constituents	Floriano[33]	USA Leaching limits (mg/L)	Brazilian Leaching limits (mg/L)	Floriano [33]	Brazilian Solubilized limits (mg/L)
Al		–	–	0.10	0.20
As	< 0.001	5.0	1.0	< 0.0015	0.01
Ba	0.692	100.0	70.0	0.071	0.70
Cd	< 0.05	1.0	0.5	< 0.005	0.005
Pb	< 0.005	5.0	1.0	< 0.005	0.01
Cl		–	–	29.7	250.00
Cu		–	–	< 0.001	2.00
Cr	< 0.003	5.0	5.0	< 0.003	0.05
Fe		–	–	0.001	0.30
F	0.04	–	150.0	0.05	1.50
Mn		–	–	1.2	0.10
Nitrate		–	–	2.512	10.00
Ag	< 0.005	5.0	5.0		0.05
Se	< 0.008	1.0	1.0		0.01
Na		–	–	45.0	200.00
Surfactants		–	–	0.066	0.50
Sulfates		–	–	159.1	250.00
Zn		–	–	0.668	5.00
Hg	< 0.00015	0.2	0.1	< 0.0001	0,001
Fenol				0.0012	0,01
Cianetos				< 0.001	0,07

The mineralogical composition of RHA varies depending on combustion conditions (particularly maximum temperature). At high temperatures (> 700 °C), crystalline silica is generated that can be used in the ceramic and steel industries. Below 700 °C amorphous silica is produced, used as a supplemental cementitious material (SCM) in building materials, and as a filler in rubber or paint. The ideal combustion temperature to obtain the highest amorphous silica content is between 500 and 700 °C, with contents reaching more than 90%. We can still have black ash with a high carbon content when burned at temperatures lower than 500 °C [5].

Thermogravimetric analysis was performed for the proper characterization of the material under study, and the results are shown in Fig. 2b. The initial mass loss refers to the loss of surface moisture from the sample up to 110 °C. Above this temperature, up to approximately 200 °C, there is a loss of water adsorbed in the sample. Above 300 °C, the loss of volatile materials, water of constitution, and decomposition of

Table 3 XRF and XRD of rice husk ash studied in this work and others from literature

Ref	SiO_2	Al_2O_3	Fe_2O_3	CaO	K_2O	Na_2O	MgO	P_2O_5	SO_3	LoI	XRD
This work	88.92	–	0.30	1.30	1.39	–	v	0.79	0.31	6.75	C
[25]	89.47	0.83	0.53	0.68	0.17	0.22	0.37	–	0.12	7.61	–
[5]	92.00	0.31	0.38	0.97	3.87	0.20	0.47	0.75	–	0.76	Am
[5]	88.30	0.25	0.37	0.91	3.63	0.16	0.40	0.69	–	5.02	Am
[19]	87.14	0.89	0.34	1.12	2.51	1.10	0.49	0.98	0.28	5.15	–
[16]	93.10	0.30	0.20	1.50	2.30	0.06	0.60	–	-	0.80	Q., Al., Ca
[1]	93.50	0.55	0.23	1.11	1.40	0.10	0.31	–	0.07	-	–
[15]	91.15	0.41	0.21	0.41	6.25	0.05	0.45	–	0.62	0.45	–
[40]	88.46	0.17	0.31	0.75	1.69	0.22	0.47	0.69	0.05	9.22	C., S
[18]	90.50	0.30	0.20	0.90	2.00	0.10	0.40	–	0.40	3.80	Q
[20]	81.60	–	6.50	1.70	8.90	0.20	0.90	–	0.20	2.30	C., Q., M

C: Cristobalite; A: Amorphous; Q: Quartz; Al: Alminum oxide; Ca: Calcium aluminum oxide; S: Sodium phosphorus silicon oxide; M: Magnesioferrite.

carbonate materials occur. The characteristic variation of carbon combustion at ~ 493 °C stands out. This mass variation was less than 7%, indicating the elimination of most of the carbonaceous compounds in the burning process. At temperatures above 1000 °C, new phases may form as the maximum crystallization of cristobalite occurs [41].

Rice husk ash is granular, with a particle size similar to husk before burning. Figure 2c and d present images obtained from a stereoscopic magnifying glass of rice husk ash. The milling process promotes physical properties such as fineness and specific surface [38]. An adequate degree of grinding must be foreseen depending on the intended application. The average particle size is generally between 5 and 20 μm [5]. According to the Brazilian Standard NBR 12,653, a pozzolanic material must present physical, chemical, and physical–mechanical requirements that indicate reactivity with Portland cement and lime [42]. RHA of this study is mainly composed of SiO_2 (88.9%), with the total of $SiO_2 + Al_2O_3 + Fe_2O_3$ equal to 89.2%, higher than the minimum required by the standard [42]. Likewise, the SO_3 content observed is lower than the maximum allowed and its loss on ignition is 6.75%. According to NBR 12,653, the studied RHA can be classified as a class N pozzolanic material [42].

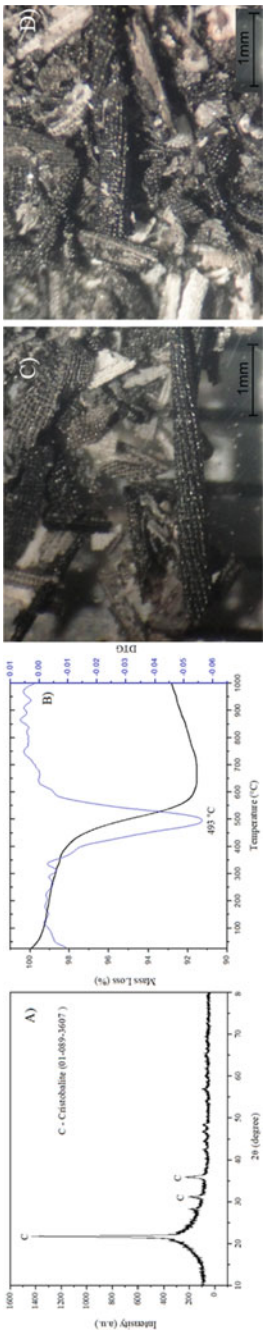

Fig. 2 **a** XRD, **b** TGA/DTG, **c** and **d** pictures of RHA samples

Final Remarks

The present study evaluated the valuation of the RHA generated by a Brazilian company concerning its classification, potentiality, quantity/feasibility, and applicability in cementitious materials. Some obstacles to applying rice husk ash as a complementary cementitious material in geopolymers and cement, in general, can be commented on: The combustion control conditions of rice husk ash can cause air pollution and produce poor quality ash when done incorrectly. Rice cultivation, which is usually located in specific regions of producing countries, can increase transport costs. In this sense, it was observed that the study region has a great potential for application since several companies generate the waste and potential recipients of this material for application in cement products.

References

1. Gill AS, Siddique R (2018) Durability properties of self-compacting concrete incorporating metakaolin and rice husk ash. Constr Build Mater 176:323–332. https://doi.org/10.1016/j.conbuildmat.2018.05.054
2. Thomas BS, Yang J, Mo KH et al (2021) Biomass ashes from agricultural wastes as supplementary cementitious materials or aggregate replacement in cement/geopolymer concrete: a comprehensive review. J Build Eng 40:102332. https://doi.org/10.1016/j.jobe.2021.102332
3. Toniolo N, Boccaccini AR (2017) Fly ash-based geopolymers containing added silicate waste: a review. Ceram Int 43:14545–14551. https://doi.org/10.1016/j.ceramint.2017.07.221
4. Diniz J, De A, Cardoso L et al (2004) Poder calorífico da casca de arroz, caroço de pêssego, serragem de eucalipto e de seus produtos de pirólise. Ciência e Nat 26:25–32
5. Kang S-H, Hong S-G, Moon J (2019) The use of rice husk ash as reactive filler in ultra-high performance concrete. Cem Concr Res 115:389–400. https://doi.org/10.1016/j.cemconres.2018.09.004
6. Souza MT, Simão L, Montedo ORK et al (2019) Aluminum anodizing waste and its uses: An overview of potential applications and market opportunities. Waste Manag 84:286–301. https://doi.org/10.1016/j.wasman.2018.12.003
7. Simão L, Souza MT, Ribeiro MJ et al (2021) Assessment of the recycling potential of stone processing plant wastes based on physicochemical features and market opportunities. J Clean Prod 319:128678. https://doi.org/10.1016/j.jclepro.2021.128678
8. Vilaça ASI, Simão L, Montedo ORK et al (2022) Waste valorization of iron ore tailings in Brazil: assessment metrics from a circular economy perspective. Resour Policy 75:102477. https://doi.org/10.1016/J.RESOURPOL.2021.102477
9. CONAB. Brazilian National Food Supply Agency (2022) Acompanhamento da Safra Brasileira. Bol da Safra 2021 9:60
10. França AA, Schultz J, Borges R et al (2017) Rice husk ash as raw material for the synthesis of silicon and potassium slow-release fertilizer. J Braz Chem Soc 28:2211–2217. https://doi.org/10.21577/0103-5053.20170072
11. Mayer FD, Hoffmann R, Ruppenthal JE (2006) Gestão energética, econômica e ambiental do resíduo casca de arroz em pequenas e médias agroindústrias de arroz. 1–11
12. Schwanke AJ, Melo DMA, Silva AO, Pergher SBC (2013) Use of rice husk ash as only source of silica in the formation of mesoporous materials (Emprego da cinza da casca de arroz como única fonte de sílica na formação de materiais mesoporosos). Cerâmica 59:181–185
13. Fiesc (2015) Santa Catarina em dados - 2015

14. Faried AS, Mostafa SA, Tayeh BA, Tawfik TA (2021) The effect of using nano rice husk ash of different burning degrees on ultra-high-performance concrete properties. Constr Build Mater 290:123279. https://doi.org/10.1016/j.conbuildmat.2021.123279
15. Koushkbaghi M, Kazemi MJ, Mosavi H, Mohseni E (2019) Acid resistance and durability properties of steel fiber-reinforced concrete incorporating rice husk ash and recycled aggregate. Constr Build Mater 202:266–275. https://doi.org/10.1016/j.conbuildmat.2018.12.224
16. Liang G, Zhu H, Zhang Z et al (2019) Investigation of the waterproof property of alkali-activated metakaolin geopolymer added with rice husk ash. J Clean Prod 230:603–612. https://doi.org/10.1016/j.jclepro.2019.05.111
17. Farooq F, Jin X, Faisal Javed M et al (2021) Geopolymer concrete as sustainable material: A state of the art review. Constr Build Mater 306:124762. https://doi.org/10.1016/J.CONBUILDMAT.2021.124762
18. Tong KT, Vinai R, Soutsos MN (2018) Use of Vietnamese rice husk ash for the production of sodium silicate as the activator for alkali-activated binders. J Clean Prod 201:272–286. https://doi.org/10.1016/j.jclepro.2018.08.025
19. Padhi RS, Patra RK, Mukharjee BB, Dey T (2018) Influence of incorporation of rice husk ash and coarse recycled concrete aggregates on properties of concrete. Constr Build Mater 173:289–297. https://doi.org/10.1016/j.conbuildmat.2018.03.270
20. Nuaklong P, Jongvivatsakul P, Pothisiri T et al (2020) Influence of rice husk ash on mechanical properties and fire resistance of recycled aggregate high-calcium fly ash geopolymer concrete. J Clean Prod 252:119797. https://doi.org/10.1016/j.jclepro.2019.119797
21. Kaur K, Singh J, Kaur M (2018) Compressive strength of rice husk ash based geopolymer: The effect of alkaline activator. Constr Build Mater 169:188–192. https://doi.org/10.1016/j.conbuildmat.2018.02.200
22. Liang G, Zhu H, Zhang Z, Wu Q (2019) Effect of rice husk ash addition on the compressive strength and thermal stability of metakaolin based geopolymer. Constr Build Mater 222:872–881. https://doi.org/10.1016/j.conbuildmat.2019.06.200
23. Ren B, Zhao Y, Bai H et al (2021) Eco-friendly geopolymer prepared from solid wastes: A critical review. Chemosphere 267:128900. https://doi.org/10.1016/J.CHEMOSPHERE.2020.128900
24. Hossain SS, Roy PK, Bae C-J (2021) Utilization of waste rice husk ash for sustainable geopolymer: a review. Constr Build Mater 310:125218. https://doi.org/10.1016/j.conbuildmat.2021.125218
25. Mehta A, Siddique R (2018) Sustainable geopolymer concrete using ground granulated blast furnace slag and rice husk ash: Strength and permeability properties. J Clean Prod 205:49–57. https://doi.org/10.1016/j.jclepro.2018.08.313
26. Passuello A, Rodríguez ED, Hirt E et al (2017) Evaluation of the potential improvement in the environmental footprint of geopolymers using waste-derived activators. J Clean Prod 166:680–689. https://doi.org/10.1016/j.jclepro.2017.08.007
27. ASTM (2007) ASTM D7348: Standard test methods for loss on ignition (LOI) of solid combustion residues. EUA
28. Viguri J, Andrés A, Ibañez R et al (2000) Characterization of metal finishing sludges: influence of the pH. J Hazard Mater 79:63–75. https://doi.org/10.1016/S0304-3894(00)00248-X
29. Council of the European Union, 2003/33/EC (2003) Council decision establishing criteria and procedures for the acceptance of waste at landfills pursuant to Article 16 of and Annex II to Directive 1999/31/EC. Off J Eur Communities 27–49
30. ABNT (2004) NBR 10004—Resíduos sólidos—Classificação
31. Simão L, Hotza D, Raupp-Pereira F, et al (2019) Characterization of pulp and paper mill waste for the production of waste-based cement. Rev Int Contam Ambient 35:237–246. https://doi.org/10.20937/RICA.2019.35.01.17
32. Walter JP, Rossato MV (2010) Destino do resíduo casca de arroz na microrregião de restinga seca - rs: um enfoque à responsabilidade sócio ambiental. In: VI Congresso nacional de excelência em gestão

33. Floriano FJ (2014) Valorização dos resíduos do processo de anodização de alumínio e cinza de casca de arroz por meio da obtenção de zeólitas. Federal University of Santa Catarina
34. Padilha SA (2017) Potencialidade do uso de cinza de casca de arroz em blocos de concreto de alvenaria estrutural: segundo NBR 6136. Federal University of Pelotas
35. Padilha SA, Paliga CM, Torres AS (2019) Potencialidade do uso de cinza de casca de arroz em blocos de concreto para alvenaria estrutural: de acordo com as normas brasileiras. Rev Estud Ambient 21:17. https://doi.org/10.7867/1983-1501.2019v21n1p17-28
36. Ripoli Filho F, Baesso MH, Rizzatti E, Soares JMD (2021) Caracterização E aplicação de casca e cinza da casca de arroz para emprego em argamassa de cimento Portalnd. Rev Científica Multidiscip Núcleo do Conhecimento 174–193. https://doi.org/10.32749/nucleodoconhecimento.com.br/engenharia-civil/cimento-portalnd
37. Moayedi H, Aghel B, Abdullahi MM et al (2019) Applications of rice husk ash as green and sustainable biomass. J Clean Prod 237:117851. https://doi.org/10.1016/j.jclepro.2019.117851
38. Cordeiro L de NP (2009) Analysis of variation of the index of amorfization of the rice husk ash on the pozzolanic activity (in Portuguese). Pp 1–98
39. Furtado RG (2020) Universidade Federal De Santa Catarina Campus Universitário Reitor João David Ferreira Lima Programa De Pós-Graduação Em Engenharia E Gestão Do Conhecimento Évora : Gestão De Objetos Digitais De Ensino E
40. Luukkonen T, Abdollahnejad Z, Yliniemi J et al (2018) Comparison of alkali and silica sources in one-part alkali-activated blast furnace slag mortar. J Clean Prod 187:171–179. https://doi.org/10.1016/j.jclepro.2018.03.202
41. Della VP, Kühn I, Hotza D (2001) Caracterização de cinza de casca de arroz para uso como matéria-prima na fabricação de refratários de sílica. Quim Nova 24:778–782. https://doi.org/10.1590/s0100-40422001000600013
42. Associação brasileira de normas técnicas (2014) NBR 12653: Materiais Pozolânicos. In: ABNT (ed) NBR 12653: Materiais Pozolânicos. Rio de Janeiro, p 10

Production of Sustainable Artificial Stone from Granite Waste and Steel Waste and Polyurethane from Castor Oil

Maria Luiza Pessanha Menezes Gomes, José Lucas Decotê de Carvalho Lírio, Elaine Aparecida Santos Carvalho, Gabriela Nunes Sales Barreto, Sérgio Neves Monteiro, and Carlos Maurício Fontes Vieira

Abstract Waste generation and its improper disposal have been growing substantially nowadays, among them, steel wastes, ornamental stones and polymers instigating serious environmental problems. The development of artificial stones using a polymeric matrix from a renewable source is a great alternative to reincorporate these types of waste, creating a novel sustainable stone with properties that make them suitable for use as a coating in civil construction. This work's main objective was to produce and characterize an artificial stone (ASGS) with 85% of wastes (granite and steel) in a 15% vegetable polyurethane matrix. Initially, the most close-packed granulometric composition was determined, followed by the plates production using vibration, compression, and vacuum. ASGS presented 2.24 g/cm^3 density, which was within the expected range, 0.46% of water absorption, which was at the limit to be considered a low water absorption stone and 1.04% of apparent porosity, denoting its high porosity content. The ASGS bend strength classified it as a stone of very high mechanical strength. Through SEM micrographs, the high content of apparent porosity was confirmed, and a low load/matrix interaction was verified. However, analyzing the ASGS bend strength, it was possible to conclude that it did not impair its mechanical strength.

Keywords Artificial stone · Granite waste · Siderurgic waste · Polyurethane

M. L. P. M. Gomes (✉) · J. L. D. de Carvalho Lírio · E. A. S. Carvalho · G. N. S. Barreto · C. M. F. Vieira
Advanced Materials Laboratory—LAMAV, State University of Northern Rio de Janeiro—UENF, Av. Alberto Lamego, Campos dos Goytacazes 2000, 28013-602, Brazil
e-mail: malu_pmg@hotmail.com

C. M. F. Vieira
e-mail: vieira@uenf.br

S. N. Monteiro
Department of Materials Science, Military Engineering Intitute – IME, Praça General Tibúrcio, 80, Praia Vermelha, Urca, Rio de Janeiro 22290-270, Brazil

M. Zhang et al. (eds.), *Characterization of Minerals, Metals, and Materials 2023*, The Minerals, Metals & Materials Series
https://doi.org/10.1007/978-3-031-22576-5_53

Introduction

The waste generation is an unavoidable problem that is a characteristic of many production processes, instigating an increase in both environmental pollution and the tailings number in landfills [1]. Nonetheless, several wastes can be recycled and reused with an innovative approach in diversified sectors too, besides contributing to the environment, enabling the development of technically and economically viable materials [2].

The mining of decorative stones is quite prosperous worldwide, while Brazil plays a major role as an ornamental stone producer, extracting thousands of tons of blocks in the quarries [3]. Brazilian exports of natural stone materials totaled US$ 1.34 billion and 2.40 Mt in 2021, surpassing the 2013 historical records both in the revenue figures and in annual variation (US$ 1, 30 billion and 22.8%) [4].

Beneficiation of the stones, an operation that includes mining, cutting, and polishing, converts approximately 50% of the extracted mineral materials into dry waste. Generally, to produce a 20 mm thick natural stone, 5 mm is cut from the surface. These cuts represent about 50% of all dry waste that is normally generated in the stone production process [5]. These wastes are often carried by trucks out of factories and dumped in nature, an improper disposal that can prompt severe environmental bruises [6].

According to Instituto Aço Brasil, Brazil is the world's ninth largest crude steel producer. As the steel industry engenders an extensive assortment of solid wastes, liquid effluents and gaseous emissions in its different stages of processing [7, 8], this sector encourages the transformation of these wastes into co-products that can be used to replace natural resources. This replacement has the potential to decrease production costs, enhance the performance of the developed materials and lessen environmental impacts [9].

In this context, novel materials called artificial stones, composed of a high percentage of particulate aggregates agglomerated by a polymeric matrix, were developed. The mechanical properties of artificial stones are superior compared to the ornamental stones, due to their lower porosity index [10, 11]. This type of material can work as an alternative for the reincorporation of waste, reused as a raw material in its manufacture, once it can be produced with assorted types of aggregates and resins, from a wide range of compositions, and under distinct manufacturing conditions and variables (such as vacuum, vibration and compaction pressure), a fact that also makes artificial stones to have divergent properties and aesthetic [12, 13].

Artificial stones are customarily produced with synthetic polymers petroleum derived, mostly polyester and epoxy resins. Sarami and Mahdavian [14] evaluated the properties of artificial stones developed with unsaturated polyester resin, travertine and marmarit stone with cement. Borselino et al. [15] developed artificial marbles with epoxy and polyester resin and Demartini et al. [16] developed an artificial stone with dolomitic marble waste processed by diamond circular saws agglomerated by epoxy resin.

With the current burgeoning of polymer consumption, in their most varied types, the amount of polymeric waste, a material that takes many years to decompose and is often discarded inappropriately, has also been growing over the years, adding to the already huge problem of waste's inadequate disposal, which is leading to a high level of environmental pollution [17]. The use of a polymeric matrix from a renewable source, which does not emanate toxic substances, to produce artificial stones is also another attractive alternative in view of mitigating the environmental impact [18].

Polyurethane (PU) castor oil is a low-cost, renewable, widely found oil that has attracted the attention of researchers owing to its use in coatings, adhesives, inks, sealants, and encapsulating compounds. Castor oil-based PUs possesses low mechanical strength and limited ductility thanks to their flexible, highly cross-linked and permanent network structure. Within the concepts of sustainability, it is interesting to replace polymers with this type of PU from a renewable source [19, 20].

This work's main goal is to develop and characterize an artificial stone using aggregate particles of granite and steel waste (FGD) agglomerated in a PU matrix derived from castor oil, the so-called ASGS, a sustainable material capable of being used as a coating in civil construction.

Materials and Methods

Materials

White granite waste from the slab finishing process was supplied by the Brumagran company, located in Cachoeiro de Itapemirim, Brazil. The steel waste, called FGD (Flue Gas Desulfurization), a waste dust from the gas treatment of the steel coking ovens, supplied by ArcelorMittal Serra, Brazil, was also used.

The authors used a hammer and a jaw crusher to diminish the wastes for them to be sieved according to the Brazilian standard NBR 7181 [ref] and then classified into three granulometric ranges: large (2 to 0.42 mm), medium (between 0.42 to 0.075 mm), and fine (grains with particle sizes less than 0.075 mm) [21]. The granite waste was sieved to fit coarse and medium granulometry, while FGD was already supplied by ArcelorMittal in the fine granulometry.

The resin, vegetable polyurethane (PU) synthesized from castor oil, was formulated by cold mixing of a prepolymer (component A) and a polyol (component B), in a proportion of 1:1,2, respectively, as recommended by the supplier, company IMPERVEG, Brazil.

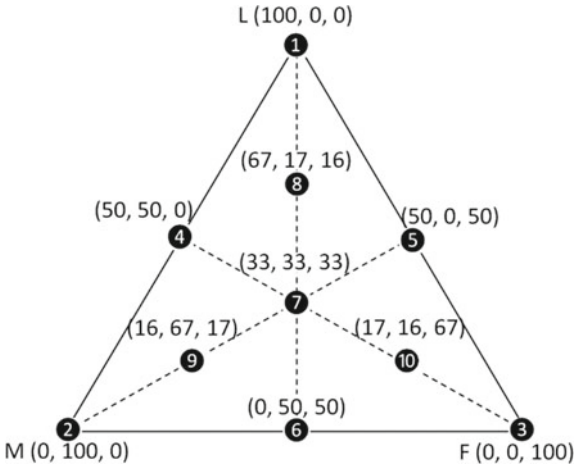

Fig. 1 Simplex-Lattice Design ternary diagram representing the granulometric composition of the 10 mixtures proposed

Determination of the Most Close-packed Composition

For the determination of the most close-packed composition, 10 mixtures were proposed, with different percentages of large, medium, and fine particles, based on the three granulometric ranges described above.

Figure 1 displays the Simplex-Lattice Design ternary diagram developed in the experimental numeric-modeling grid Simplex to better describe the composition of the 10 mixtures. Each triangle vertex is equal to 100%: large (L), medium (M) and fine (F) particles and the other diagram points shows (in parenthesis) the fractions corresponding to the particle's percentage in the mixtures.

To determine the most close-packed composition, the 10 mixtures were tested according to the Brazilian standard MB-3388 [22]. Each mixture was placed into a steel container of known weight and volume, pressed with 10 kg under 6 Hz vibration for 10 min and weighed to calculate the vibrate density. This procedure was repeated three times for each mixture to statistically guarantee the results.

Each mixture was placed in a steel container of known volume (volume, or weight, mass, I don't remember) under 6 Hz vibration for 10 min and weighed to calculate the vibration density. This procedure was repeated three times for each mixture to statistically guarantee the results.

Production of Artificial Stone Plates

Artificial stone plates were manufactured with 85 wt% of wastes (a mixture of granite and FGD) and 15 wt% of still fluid vegetable polyurethane resin inside a 100 × 100 × 15mm^3 steel mold. The waste was dried in a stove at 100 °C for 24 h to release

moisture water and then put in a desiccator jar until it returned to room temperature (RT), around 25 °C. The wastes and the resin were mixed under 600 mmHg vacuum and put into the mold, which was vibrated for 2 min and then hot pressed for 20 min under 90ºC and 10 MPa.

Characterization of Artificial Stone Plates

The Brazilian standard NBR 15,845–2 [23] was used to determine density, water absorption and apparent porosity of the ASGS, using 10 specimens with 50 × 50 × 15mm^3.

A three-point bending test was carried out in accordance with EN 14,617–2 [24] and NBR 15,845–6 [25] standards to determine ASGS and PU bend strength. For each material, six specimens of 15 × 25x100 mm^3 were used and the test was performed in an Instron model 5582 with 0.25 MPa/s speed, which was kept constant until the specimen broke.

For microstructural analysis, scanning electron microscopy (SEM) was performed on the fractured surface of the ASGS specimens submitted to the bending test, using a SHIMADZU's Super Scan SSX-550 at 20 kV of secondary electrons. The samples were cut and prepared with an adhesive carbon tape wrapped in a metallic sample holder gold surface.

Results and Discussion

Table 1 shows the vibrate density values of the 10 mixtures proposed by the Centroid Simplex Diagram.

To determinate, the mixture with higher vibrate density is important because this represents the most close-packed composition of the granulometric ranges, which is equal to the composition with lower incidence of voids, which contributes to better physical and mechanical properties of the stone.

The mixture with the highest vibrated density, mixture 8, was chosen to produce ASGS plates. Mixture 8 had 1.80 g/cm^3 density and according to the Simplex Centroid Diagram shown in Fig. 1, corresponds to 67% of the large, 17% of the medium and 16% of the fine particles.

Table 2 shows the ASGS density, water absorption and apparent porosity results after the performed tests.

Natural ornamental stone's density is important because the higher its value the better the adhesion between the particles and the matrix, therefore, there is less occurrence of voids [18]. Anyhow, for artificial stones, on behalf of the fact that they

Table 1 Vibrate density results of the 10 mixtures

Mixture	Coarse	Medium	Fine	Vibrate density (g/cm^3)
1	1	0	0	1.49 ± 0.03
2	0	1	0	1.77 ± 0.01
3	0	0	1	0.60 ± 0.01
4	½	½	0	1.61 ± 0.02
5	½	0	½	1.12 ± 0.04
6	0	½	½	1.03 ± 0.02
7	1/3	1/3	1/3	1.62 ± 0.01
8	2/3	1/6	1/6	1.80 ± 0.01
9	1/6	2/3	1/6	1.72 ± 0.01
10	1/6	1/6	2/3	1.19 ± 0.01

Table 2 ASGS' physical properties

Physical Propertirs	ASGS
Density (g/cm$^{3)}$	2.24 ± 0.01
Water absorption (%)	0.46 ± 0.03
Apparent porosity (%)	1.04 ± 0.07

have polymeric matrices in their composition, which is a material of lower density compared to minerals, their density is often lower than natural stones [13].

Lee et al. in their research used glass crystals and PET to produce artificial stones with various levels of compression, vacuum and vibration and the density values found by them varied in the range of 2.03 to 2.45 g/cm^3 [26]. As the ASGS density result was found to be 2.24 g/cm^3, it can be considered to be within the expected range compared to similar materials.

Water absorption indicates how much water could penetrate the stone through its pores. However, as not all pores are interconnected, the water absorption values are invariably lower than the porosity ones. Water absorption levels are especially relevant for stones that will be applied as a coating, as they will be frequently wetted [11].

According to Chiodi and Rodriguez [27] in their "Guide to Application of Stones in Coating", a coating should have water absorption values between 0.1 – 0.4% to be considered a low absorption coating. ASGS had 0.46% of water absorption, therefore, it can be considered that the ASGS is at the limit of the stipulated value.

According to Chiodi and Rodriguez [27], high quality coating materials must have porosity values below 0.5%. ASGS had 1.04% porosity, a value twice as high as recommended, a fact that can jeopardize the mechanical properties of ASGS and which was analyzed in micrographs obtained by SEM and will be further discussed.

Figure 2 shows the stress vs strain curves of ASGS and PU after the 3-point bend strength test.

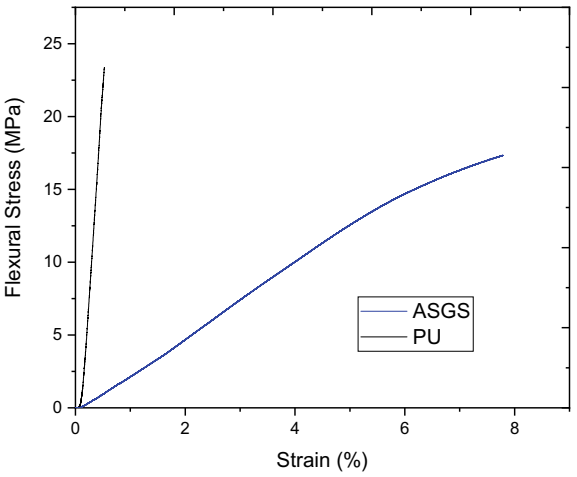

Fig. 2 Stress vs strain curves of ASGS and PU

The bend strength results of ASGS and PU were of 23.36 ± 2.32 MPa and 17.31 ± 0.82 MPa respectively. Thereupon, as expected, it can be verified that the addition of filler (granite waste and FGD) in the resin contributed to stiffen the material. Ergo, the incorporation of rigid particles in the polymer matrix elevated the material's elastic modulus.

According to Chiodi and Rodriguez [27], for coating stones to be classified as high strength, the bend strength must be between 16 and 20 MPa, while bending strengths exceeding 20 MPa would classify the coating stones as of very high strength. Hence, the ASGS, which obtained 23.36 MPa bend strength, demonstrated a good performance, being considered very high strength. Agrizzi et al. [11] produced an artificial stone using quartzite waste in the same matrix of PU using vibration, vacuum and compression and obtained 10.77 ± 0.64 MPa, a lower rupture tension than the presented by ASGS.

Through the results obtained, it can be observed that despite the high porosity of 1.04% and considering that the pores can work as stress concentrators and contribute to the material's rupture, the material's bend strength was not jeopardized.

Figure 3 a,b,c shows the SEM micrographs of the ASGS fractured surface region obtained after the three-point bending test

Through Fig. 2 it is possible to observe the presence of voids or pores between the grains, evidencing there was no good load/PU matrix interaction.

The micrographs shown in Fig. 2 confirm the ASGS high apparent porosity results, that could have been attributed to both the considerable amount of pores, which can be observed in Figs. 2 (b,c and d) by the white circles, and the poor interactions between the waste particles and the polymer matrix, which is shown in Fig. 2a by the white arrows.

Debnath et al. [28] in their study concluded that a good interfacial interaction in composites improves its mechanical properties and that this interaction is directly related to the strength of the adhesive force provided by the interfacial

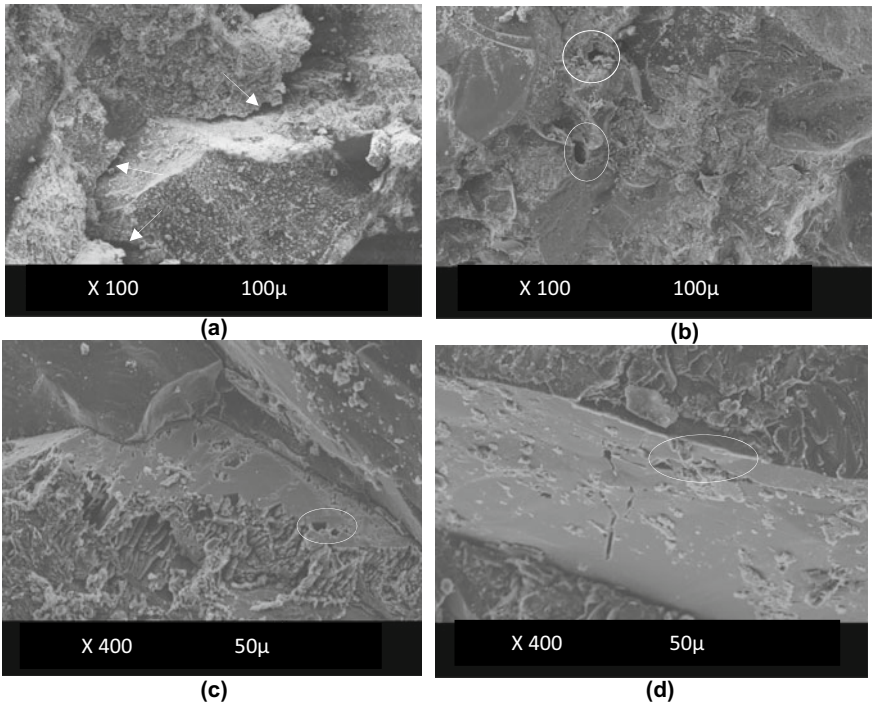

Fig. 3 **a**, **b**, **c**, **d**: SEM micrographs of ASGS fractured surface with **a**, **b** 100 × and **b**, **c** 400 × magnification

regions' successful wettability. On that account, despite the high porosity and the low load/matrix interaction harming the ASGS mechanical strength, its performance was still satisfactory. To further increase the ASGS properties, a good alternative would be a better homogenization of the mixture.

Conclusion

- The most close-packed granulometric composition of the granite and FGD waste particles was determined, with 67% of the large, 17% of the medium and 16% of the fine particles.
- It was possible to produce a novel type of sustainable artificial stone (ASGS) from the reuse of granite and steel waste (FGD) in a polyurethane matrix, a resin derived from a natural source.
- ASGS showed 2.24 g/cm^3 of apparent density, which was within the expected range for artificial stone. As for water absorption, ASGS was considered a low absorption coating since its value of 0.46% was the stipulated limit. Regarding

the apparent porosity, ASGS, of 1.04% apparent porosity, was considered to be a high apparent porosity material.

- ASGS proved to be mechanically resistant with a 23.36 MPa bend strength, classified the novel material developed as an artificial stone of very high strength for coating.
- Through SEM micrographs, the high incidence of voids in the material was shown, confirming the high apparent porosity results. Furthermore, it was possible to verify that there was not a good interaction between the waste (load) and the polyurethane matrix. Notwithstanding, the ASGS bend strength was not jeopardized.

Acknowledgements The authors thank FAPERJ (process grant number E-26/200.139/20220) for funding the research, UENF for their support, and the companies ArcelorMittal and Brumagran for providing the wastes.

References

1. Das O, Babu K, Shanmugam V, Sykam K, Tebyetekerwa M, Neisiany RE, Forsth M, Sas G, Libreros JG, Capezza AJ, Hedenqvist MS, Berto F, Ramakrishna S (2022) Natural and industrial wastes for sustainable and renewable polymer composites. Renew Sustain Energy Rev. https://doi.org/10.1016/j.rser.2021.112054
2. Arumugaprabu V, Johnson RDJ, Vigneshwaran S (2020) Mechanical performance of nanocomposites and biomass-based composite materials and its applications: an overview. In: Handbook of nanomaterials and nanocomposites for energy and environmental applications. Cham: Springer International Publishing. pp. 1–14. https://doi.org/10.1007/978-3-030-11155-7_123-1
3. Mosaferi M, Dianat I, Khatibi MS, Mansour SN, Fahiminia M, Hashemi A (2014) Review of environmental aspects and waste management of stone cutting and fabrication industries. J Master Cycles Waste Mang. 16:721–730
4. ABIROCHAS - Brazilian Association of the Ornamental Stone Industry. Available online: https://abirochas.com.br/wp-content/uploads/2022/03/Informe-01_2022-Exportacoes-2021.pdf
5. Ahmadi SF, Reisi M, Amiri MC.(2022) Reusing granite waste in eco-friendly foamed concrete as aggregate. J of Building Eng. 46. https://doi.org/10.1016/j.jobe.2021.103566
6. Guo Z, Tu A, Chen C, Lehman DE (2018) Mechanical properties, durability, and life-cycle assessment of concrete building blocks incorporating recycled concrete aggregates. J of Cleaner Production. 199(20):136–149
7. Instituto Aço Brasil – Available online. https://acobrasil.org.br/site/wp-content/uploads/2022/08/Estatistica-da-Siderurgia_2o_TRI_2022.pdf
8. Andrade LN, Amorim CC, Santos SV, Teixeira IF, Leão MMD, Lago RM (2015) Efficient demulsification of wastewater by steel furnace dust with amphiphilic and surface charge properties. Chemical Eng. J. 271:281–286
9. Vieira CMF, Andrade PM, Vernilli F, Monteiro SN (2006) Incorporation of fine steel sludge waste into red ceramic. Mat. Sci. and Eng. 427(2):142–147
10. Silva SF, Ribeiro CEG, Rodriguez RJS (2018) Physical and Mechanical Characterization of Artificial Stone with Marble Calcite Waste and Epoxy Resin. Mater Reser. 21(1)

11. Agrizzi CP, Carvalho EAS, Gadioli MCB, Barreto CNS, Azevedo ARG, Monteiro SN, Vieira CMF (2022) Comparison between synthetic and biodegradable Polymer matrices on the development of quartzite waste-based artificial stone. Sustainability.14(11)
12. Hamoush, S, Abu-Lebdeh T, Picornell M, Amer S (2011) Development of sustainable engineered stone cladding for toughness, durability, and energy conservation. Constr Build Mater 25:4006–4016
13. Gomes, MLPM, Carvalho EAS, Sobrinho LN, Monteiro SN, Rodriguez RJS, Vieira CMF (2019) Physical and mechanical properties of artificial stone produced with granite waste and vegetable polyurethane. In: Ikhmayies S, Li J, Vieira C, Margem J, de Oliveira Braga, F (eds) Green materials engineering. The minerals, metals & materials series. Springer, Cham. https://doi.org/10.1007/978-3-030-10383-5_3
14. Sarami N, Mahdavian L (2015) Effect of inorganic compound on artificial stones' properties. Int J Ind Chem. 6:213–219. https://doi.org/10.1007/s40090-015-0045-9
15. Borselino C, Calbrese L, di Bella G (2009) Effects of powder concentration and type of resin on the performance of marble composite structures. Constr Build Mater 23:1915–1921. https://doi.org/10.1016/j.conbuildmat.2008.09.005
16. Demartini TJC, Rodriguez RJS, Silva FS (2018) Physical and mechanical evaluation of artificial marble produced with dolomitic marble residue processed by diamond–plated bladed gangsaws. J Market Res 7:308–313. https://doi.org/10.1016/j.jmrt.2018.02.001
17. Yu ZY, Gu Ruonan, S Jingang, Cheng S, Chu J (2022) Polymeric solid wastes for efficient and stable solar desalination and the outdoor clean water production performance prediction. Separation and Purification Technology. https://doi.org/10.1016/j.seppur.2022.121938
18. Gomes, MLPMG, Carvalho EAS, Barreto GNS, Rodriguez RJS, Monteiro SN, Vieira CMF (2022) Development of sustainable artificial stone using granite waste and biodegradable polyurethane from castor oil. Sustainability. 14(11) https://www.mdpi.com/journal/sustainability
19. Clarinval A-M, Halleux J (2005) Classification of biodegradable polymers. Biodegradable Polym Industr Appl 3–31. https://doi.org/10.1533/9781845690762.1.3
20. Rajalakshmi P, Marie JM, & Maria Xavier, A. J (2019) Castor oil-derived monomer ricinoleic acid based biodegradable unsaturated polyesters. Polymer Degradation and Stability 170. https://doi.org/10.1016/j.polymdegradstab.2019.109016
21. Brazilian Association of Technical Norms – ABNT. ABNT NBR 7181: soil – grain size analysis. Rio de Janeiro: ABNT; 2016 (In Portuguese).
22. Brazilian Association of Technical Norms – ABNT NBR MB 3388 (1991) Soil - Determination of the minimum void index of non-cohesive soils. Rio de Janeiro. (In Portuguese)
23. Brazilian Association of Technical Norms - ABNT NBR 15845–2 (2015). Rocks for cladding – Part 2: Determination of bulk density, apparent porosity and water absorption. Rio de Janeiro: ABNT. (In Portuguese)
24. Spanish Association of Standards and Certification - UNE-EN 14617–2 (2016) Test methods - Part 2: Determination of the flexural strength. Madrid: UNE-EN. (In Spanish)
25. Brazilian Association of Technical Norms - ABNT NBR 15.845–6:2015 – Rocks for classing-Part 6: Determination of modulus of rupture (three point bending). Rio de Janeiro: ABNT. (In Portuguese)
26. Lee DJ, Shin IJ (2002) Effects of vacuum, mold temperature and cooling rate on mechanical properties of press consolidated glass fiber/PET composites. Compos. Part A. 33:1107–1114.
27. Chiodi FC, Rodriguez EP (2020) Aplication guide for stone in coating (in Portuguese). São Paulo, Brazil: Abirochas. (In Portuguese).
28. Debnath S, Ranade R, Wunder SL, Mccool J, Boberick K, Baran G. (2004) Interface effects on mechanical properties of particle-reinforced composites. Dent Mater 20:677–86

Sulfidation of Nickel in Laterite Ore with Sulfur

Sujun Lu, Jingfeng Yu, Yutian Ma, Qiang Zhong, Mingjun Rao, and Zhiwei Peng

Abstract Temperature is an important factor affecting the sulfidation of laterite ore. The effect of temperature on the sulfidation of nickel in laterite ore was studied. The thermodynamic analysis shows that the sulfidation reactions of nickel oxide and iron oxide can be carried out at temperatures above 400 ℃ and increasing temperature will promote the reactions. High sulfidation of nickel at high temperature will be achieved by regulating the partial pressure of sulfur and oxygen. In the atmosphere of high sulfur and low oxygen pressure, nickel and iron mainly exist in the form of sulfides. With the increase of temperature from 400 °C to 1200 °C, the sulfidation degree of nickel in the ore increased initially and then decreased. At 1100 ℃, the sulfidation degree of nickel in the ore was the highest, reaching 84.43%. The size of nickel sulfide particles increased to about 10 μm.

Keywords Thermodynamic analysis · Sulfidation degree · Nickel · Laterite ore

Introduction

Nickel is a strategic metal with high strength, good stability, strong corrosion resistance, great ductility, high thermal and electrical conductivity, and great aesthetic property.[1] It is widely used in stainless steel, electroplating, catalyst and petrochemical engineering.[2, 3] In recent years, the world's demand for nickel has kept increasing. In 2020, the global nickel production was about 25 million tons.[4] The world's nickel resources mainly come from nickel sulfide ore and laterite ore. The

S. Lu · Y. Ma
State Key Laboratory of Nickel and Cobalt Resources Comprehensive Utilization, Jinchang 737104, Gansu, China

J. Yu (✉) · Q. Zhong · M. Rao · Z. Peng (✉)
School of Minerals Processing and Bioengineering, Central South University, Changsha 410083, Hunan, China
e-mail: jf2020@csu.edu.cn

Z. Peng
e-mail: zwpeng@csu.edu.cn

M. Zhang et al. (eds.), *Characterization of Minerals, Metals, and Materials 2023*, The Minerals, Metals & Materials Series
https://doi.org/10.1007/978-3-031-22576-5_54

former accounts for 28% of the world's nickel resources while the latter accounts for 72%.[5] With the shortage of nickel sulfide ore and the increasing demand for nickel, laterite ore has become the main resource for nickel extraction recently.

Laterite ore is featured by low grade, complex composition and high moisture content.[6] At present, there are two types of treatment methods, including hydrometallurgical and pyrometallurgical methods. The hydrometallurgical methods include atmospheric pressure acid leaching, [7] pressurized acid leaching [8] and ammonia leaching.[9] The pyrometallurgical methods, including those based on smelting, are dominant in the laterite ore treatment. However, they suffer from high energy consumption and low metal recovery percentage.[10]

Currently, it is critical to develop a new process to improve the nickel grade of laterite ore prior to the smelting process. Laterite ore can be physically upgraded to increase its nickel grade by flotation when nickel oxide in the ore has sufficient sulfidation by adding sulfurizing agent at appropriate temperatures. To reduce production cost, the sulfidation of iron oxide should be controlled as the oxide will consume a large amount of the sulfurizing agent. Hence, selective sulfidation of nickel oxide is preferred.

It was reported that nickel in laterite ore could have selective sulfidation to form nickel sulfide.[11, 12] Further flotation of the sulfidation product showed that the nickel grade in the flotation product could reach $6 - 7$ wt%. However, due to grinding of the sulfide product before flotation, there was serious metal entrainment, leading to low recovery percentage of nickel (about 50%). Obviously, the sulfidation process of laterite ore needs to be further explored.

Temperature is expected to have a very important effect on the sulfidation process of laterite ore. In this study, the effect of temperature on the sulfidation of nickel in laterite ore with sulfur was explored. It was shown that great sulfidation of nickel in the ore could be achieved at a proper temperature.

Experimental

Materials

The main chemical composition of laterite ore is shown in Table 1. The ore contained 33.28 wt% iron and 1.48 wt% nickel. The XRD pattern of the ore is shown in Fig. 1. It was found that the main phases of laterite ore were $(Fe,Mg)(Cr,Fe)_2O_4$, FeOOH and $Al_2Si_2O_5(OH)_4$. According to the chemical phase analysis and distribution of nickel in Table 2, the element mainly existed in the form of oxide and silicate in the ore.

Table 1 Main chemical composition of laterite ore (wt%)

TFe	SiO_2	Al_2O_3	MgO	Cr_2O_3	MnO	Ni	Co	LOI
33.28	14.36	9.76	8.15	2.34	1.21	1.48	0.15	21.49

LOI: loss on ignition.

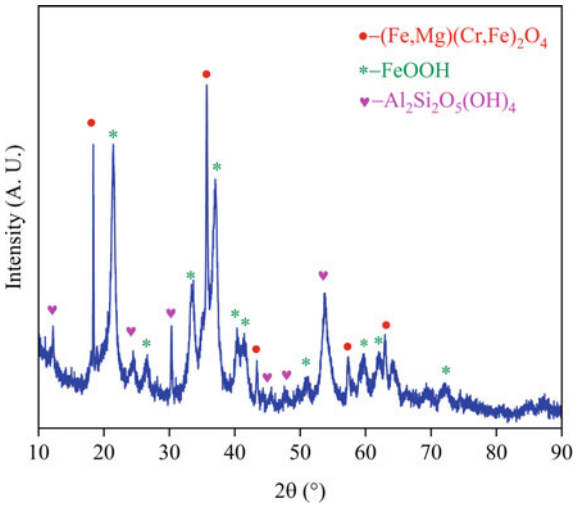

Fig. 1 XRD pattern of laterite ore

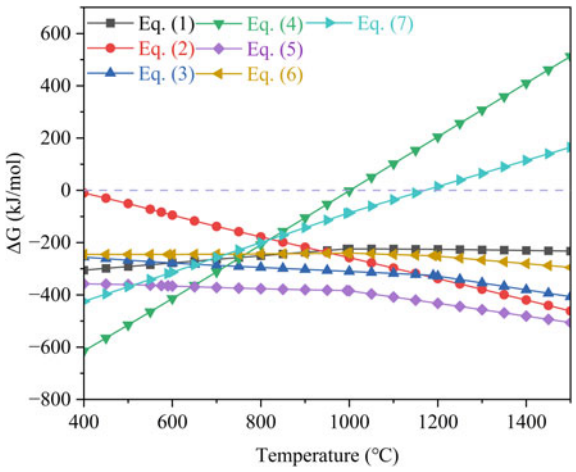

Fig. 2 Standard Gibbs free energy changes of possible reactions as a function of temperature

Table 2 Chemical phase analysis and distribution of nickel in laterite ore

Phase	Nickel sulfide	Nickel silicate	Nickel oxide	Total
Ni content (wt%)	0.03	0.31	1.14	1.48
Proportion (%)	2.03	20.94	77.03	100

Methods

All raw materials were ground to particles less than 0.074 mm prior to the experiments. Firstly, 50 g of laterite ore was mixed with sulfur with the predetermined mass ratio of sulfurizing agent to laterite ore of 20%. The mixture was then pressed into briquettes at 10 MPa.

The briquettes were initially loaded into a tube furnace for preheating at 400 ℃ for 1 h under N_2 atmosphere. They were then heated to the target temperature for sulfidation for a given time. After the briquettes were cooled to below 200 ℃ under N_2 atmosphere, they were taken out for determination of nickel sulfidation degrees by chemical titration.

For analysis of sulfidation mechanism, the standard Gibbs free energy changes of possible reactions in the process of sulfidation and the stability diagrams of the Ni-S–O and Fe-S–O systems were calculated using FactSage 8.1 and HSC 5.0. The chemical compositions of the samples were analyzed using inductively coupled plasma atomic emission spectrometry (ICP-AES, IRIS Intrepid II XSP). The phase compositions of the samples were determined by X-ray diffraction (XRD, Rigaku, TTR-1I1). The microstructures and particle sizes of the samples were determined by scanning electron microscopy (SEM, JEOL, JSM-6490LV).

Results and Discussion

Thermodynamic Analysis

For nickel oxide and other relevant components in laterite ore, the possible sulfidation reactions during the heating process in the presence of sulfur are as follows.

$$4NiO + 3S_2 = 4NiS + 2SO_2 \tag{1}$$

$$12Fe_2O_3 + S_2 = 8Fe_3O_4 + 2SO_2 \tag{2}$$

$$4Fe_2O_3 + 7S_2 = 8FeS + 6SO_2 \tag{3}$$

$$4Fe_2O_3 + 11S_2 = 8FeS_2 + 6SO_2 \tag{4}$$

$$6NiFe_2O_4 + 5S_2 = 6NiS + 4Fe_3O_4 + 4SO_2 \quad (5)$$

$$2NiFe_2O_4 + 5S_2 = 2NiS + 4FeS + 4SO_2 \quad (6)$$

$$2NiFe_2O_4 + 7S_2 = 2NiS + 4FeS_2 + 4SO_2 \quad (7)$$

The standard Gibbs free energy changes of these reactions between 400 °C and 1500 °C were calculated using FactSage 8.1. As shown in Fig. 2, the sulfidation of nickel oxide and iron oxide with sulfur is thermodynamically feasible. The increase in temperature favors most of the sulfidation reactions. Equations 4 and 7 are difficult to proceed with increasing temperature because FeS_2 has decreased stability at high temperature. For the above reactions, intimate contact between the metal oxides and the sulfur is necessary for sufficient sulfidation. Increasing the temperature is beneficial to the formation of NiS.

To further study the phase transition of nickel and iron components in laterite ore during sulfidation, it is assumed that all phases are pure substances. The stability diagrams of the Ni-S–O (solid line) and Fe-S–O (dotted line) systems at 1100 °C were plotted. The results are shown in Fig. 3.

The stability of condensed phases involved are expressed as a function of the partial pressure of S_2 and O_2, labeled Ps_2 and Po_2, respectively. As shown in Fig. 3, the shaded region is the stability region for sulfidation. It shows that nickel oxide in laterite ore can be selectively converted into sulfides by controlling the partial pressure of S_2 and O_2. Under high Ps_2 and low Po_2, the stable phases of nickel and iron are NiS_2 and FeS_2, respectively. With the decrease of sulfur partial pressure, FeS_2 is firstly converted into FeS and then into Fe, FeO, and Fe_3O_4. NiS_2 is converted to NiS, Ni_3S_4, Ni_3S_2, Ni and NiO, depending on the difference of the oxygen partial

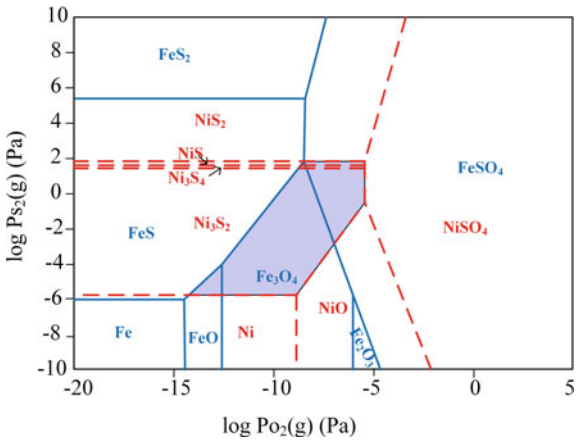

Fig. 3 Superimposed stability diagrams of the Fe-S–O (solid line) and Ni-S–O (dotted line) systems at 1100 ℃

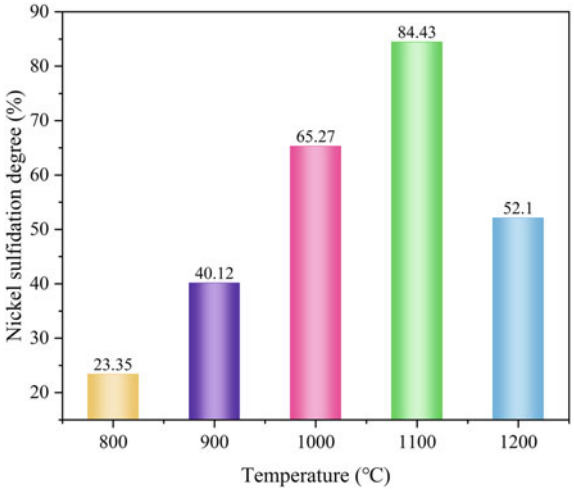

Fig. 4 Effect of temperature on the nickel sulfidation degree of laterite ore

pressure. In addition, at higher Po_2, nickel and iron are converted into $NiSO_4$, $FeSO_4$ and Fe_2O_3, respectively.

Sulfidation Degree Analysis

Temperature is an important factor for sulfidation of laterite ore. The effect of temperature on the nickel sulfidation degree of laterite ore for 2 h was studied. The results are shown in Fig. 4. Increasing temperature from 800 °C to 1100 °C significantly increased the sulfidation degree, which reached the maximum value at 1100 °C (84.43%). By increasing the temperature to 1200 °C, the sulfidation degree declined to 52.10%, probably due to partial re-oxidation of nickel sulfide at high temperature.

XRD Analysis

Figure 5 shows the XRD patterns of laterite ore samples after sulfidation at different temperatures for sulfidation. It was found that the main phase of the sulfidation product was $Mg(Al,Fe)_2O_4$. The peak of pyrrhotite ($Fe_{1-x}S$) appeared, indicating partial sulfidation of iron oxide in the ore. As the temperature increased, pyrrhotite began to decompose. At 1200 °C, a small amount of silicate was formed with gradual decrease of FeS.

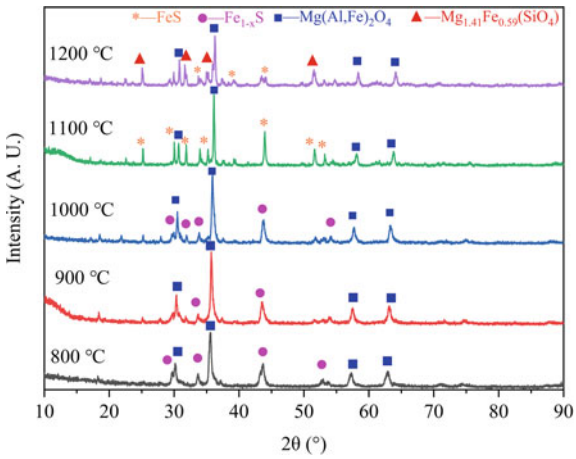

Fig. 5 XRD patterns of laterite ore samples after sulfidation at different temperatures

Microstructural Evolution

Figure 6 shows the microstructures of laterite ore samples after sulfidation at 800 − 1200 ºC. With the increase of temperature, the generated nickel sulfide particles, as indicated by the arrows, grew significantly. At 800 °C, the sulfide particles were distributed around the gangue particles. As the temperature increased, the size of nickel sulfide particles increased evidently. At 1100 °C, the size of nickel sulfide particles grew to about 10 μm. Note that the nickel sulfide particles were identified by energy dispersive spectroscopy whose results were not provided for brevity.

Conclusions

In this study, sulfur was used for sulfidation of laterite ore at different temperatures. According to thermodynamic analysis, the selective sulfidation of nickel and iron can be achieved by adjusting the atmosphere. In the atmosphere of high Ps_2 and low Po_2, both nickel and iron exist in the form of sulfides. With the decrease of sulfur partial pressure, the stable phases gradually change to oxides. The sulfidation experiments showed that the sulfidation degree of nickel gradually increased with temperature. At 1100 °C, it had the highest value, 84.43%. As the temperature increased to 1200 °C, it dropped to 52.1% due to re-oxidation of nickel sulfide at high temperature. The main phase of the ore after sulfidation was $Mg(Al,Fe)_2O_4$ with partial sulfidation of iron to $Fe_{1-x}S$. According to the microstructural analysis at 800 °C, nickel sulfide was found to adhere to the surface of gangue particles. When the temperature increased to 1100 ºC, the size of nickel sulfide particles reached about 10 μm.

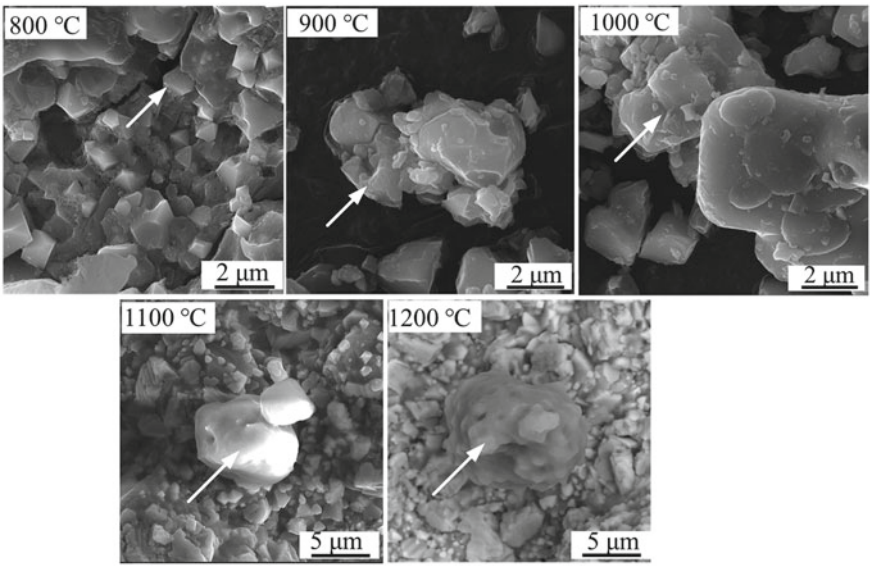

Fig. 6 SEM images of laterite ore samples after sulfidation at 800−1200 °C

Acknowledgements This work was supported by the Project of State Key Laboratory of Nickel and Cobalt Resources Comprehensive Utilization (738010570) and the Science and Technology Planning Project of Hunan Province, China (2019RS2008).

References

1. Supriyatna YI, Sihotang IH, Sudibyo (2019) Preliminary study of smelting of Indonesian nickel laterite ore using an electric arc furnace. Mater Today Proc 13:127–131
2. Chen S, Guo S, Jiang L, Xu Y, Ding W (2015) Thermodynamic of selective reduction of laterite ore by reducing gases. T Nonferr Metal Soc 25(9):3133–3138
3. Pintowantoro S, Abdul F (2019) Selective reduction of laterite ore. Mater Trans 60(11):2245–2254
4. Pandey N, Tripathy S, Patra S, Jha G (2022) Recent progress in hydrometallurgical processing of nickel lateritic ore. Trans Indian Inst Metal. https://doi.org/10.1007/s12666-022-02706-2
5. Xu D, Liu L, Quast K, Addai-Mensah J, Robinson D (2013) Effect of nickel laterite agglomerate properties on their leaching performance. Adv Powder Technol 24(4):750–756
6. Quast K, Addai-Mensah J, Skinner W (2017) Preconcentration strategies in the processing of nickel laterite ores Part 5: effect of mineralogy. Miner Eng 110:31–39
7. Luo W, Feng Q, Ou L, Zhang G, Lu Y (2009) Fast dissolution of nickel from a lizardite-rich saprolitic laterite by sulphuric acid at atmospheric pressure. Hydrometallurgy 96(1–2):171–175
8. Ma B, Yang W, Yang B, Wang C, Chen Y, Zhang Y (2015) Pilot-scale plant study on the innovative nitric acid pressure leaching technology for laterite ores. Hydrometallurgy 155:88–94

9. Ilyas S, Srivastava R, Kim H, Ilyas N, Sattar R (2020) Extraction of nickel and cobalt from a laterite ore using the carbothermic reduction roasting-ammoniacal leaching process. Sep Purif Technol 232:115971
10. Gao J, Li W, Ma S, Du Z, Cheng F (2021) Spinel ferrite transformation for enhanced upgrading nickel grade in laterite ore of various types. Miner Eng 163(4):106795
11. Harris C, Peacey J, Pickles C (2013) Selective sulphidation and flotation of nickel from a nickeliferous laterite ore. Miner Eng 54:21–31
12. Harris C, Peacey J, Pickles C (2010) Selective sulphidation of a nickeliferous lateritic ore. Miner Eng 24(7):651–660

Shine Behavior of Ornamental Rock Plates with the Reduction of Water Consumption in Polishing

L. M. Santos, E. D. Fizzera, T. E. S. Lima, C. M. F. Vieira, S. N. Monteiro, N. A. Cerqueira, M. N. Barreto, and A. R. G. Azevedo

Abstract The polishing process is an important phase in the processing of ornamental stones, through which it is possible to obtain materials with a high aesthetic standard desired by the international market. This process requires good equipment and a constant flow of water, in order to provide higher quality products. A well-polished material has a higher level of shine and is valued more. Thus, the present work aimed to propose a reduction in the water flow during the polishing process to evaluate the feasibility of reducing water consumption while increasing the quality of the final product. To carry out the study, three types of rocks were chosen: Corumba Grey, Dallas White and Itabira Ochre. The experiments proved to be efficient and the quantitative analysis can be an important tool in obtaining a brighter final product and, also, an opportunity to save water.

L. M. Santos · E. D. Fizzera
Department of Mining Engineering, IFES—Espirito Santo Federal Institute, Eng. Fabiano Vivácqua Highway, 1.568, Cachoeiro de Itapemirim 29322-000, Brazil
e-mail: arissa@uol.com.br

E. D. Fizzera
e-mail: evanizis@ifes.edu.br

E. D. Fizzera · T. E. S. Lima · C. M. F. Vieira · N. A. Cerqueira
LAMAV—Advanced Materials Laboratory, UENF—State University of Northern Rio de Janeiro, Av. Alberto Lamego, 2000, Campos dos Goytacazes, Rio de Janeiro 28013-602, Brazil
e-mail: vieira@uenf.br

S. N. Monteiro
Department of Materials Science, IME—Military Institute of Engineering, Square General Tibúrcio, 80, Rio de Janeiro 22290-270, Brazil

M. N. Barreto
IFF—Fluminense Federal Institute, Campus Centro, Rua Dr. Siqueira, 273, Campos dos Goytacazes 28035-048, Brazil
e-mail: marnevesbar@ibest.com.br

A. R. G. Azevedo (✉)
LECIV—Civil Engineering Laboratory, UENF—State University of Northern Rio de Janeiro, Av. Alberto Lamego, 2000, Campos dos Goytacazes, Rio de Janeiro 28013-602, Brazil
e-mail: afonso.garcez91@gmail.com

M. Zhang et al. (eds.), *Characterization of Minerals, Metals, and Materials 2023*, The Minerals, Metals & Materials Series
https://doi.org/10.1007/978-3-031-22576-5_55

Keywords Ornamental rocks · Polishing · Water flow · Shine

Introduction

The ornamental stone market has gained prominence in recent years. Gradually, as more varieties of materials were found and explored, and new technologies were employed in the mining and processing processes, the level of consumer demand increased.

In order to guarantee the customer such characteristics in the final product, the dimension stone entrepreneurs sector invests in increasingly elaborate techniques during extraction, processing (which comprises the unfolding or sawing of rock blocks into slabs and polishing, responsible for finishing the product) and in the marketing options [1, 2].

The production of ornamental stones consists of three stages: extraction, processing and commercialization. The polishing stage, inserted in the processing, is carried out by a machine called a polisher, using water and abrasives of different granulometries, creating the abrasive slurry [3, 4].

The shine level obtained after the sheet polishing process is linked to several factors and one of them is the amount of water used in the process [5–7]. In this way, this work will point out suggestions for reducing the water flow during the polishing process of granite slabs to result in savings on this natural resource and, at the same time, to evaluate the changes in the value of the shine level of these slabs. Therefore, the objective of this work is to study the polishing process of three types of ornamental stone slabs in order to analyze whether the reduction of the process water flow can interfere in the final shine level of the materials.

Materials and Methods

The experimental program was carried out in the sawmill of a marble and granite company, located in the municipality of Cachoeiro de Itapemirim. The company has 12 conventional looms and an automatic polishing machine, made up of 16 CPC model heads, CIMEF brand, which has a general control panel, which monitors the polished area in m^2, the number of sheets and other parameters of the process, thus producing a monthly average of 13,270 m^2 of sawn slabs.

The ornamental rocks chosen for analysis in this work were Dallas white, Corumba grey and Itabira ochre. The study comprised the analysis of the flow of water in liters per minute (L/min) that is used in the polisher and evaluated the level of shine of the plate at four different times, for each material, reducing the flow of water used for each measurement. The satellite rotation was 550 RPM and a pressure of 1.5 bar.

To measure the water flow, a hydrometer of the type of turbine with electronic operation and model k24 of the Ofa brand was used. This equipment has a manual

doser that started the dosage with manual opening of the valve, providing the flow of water, so its meter registered the volume drained from zero and when it reached the volume of 30 L, which is the volume used in the company's polisher, the valve was closed, finishing the dosage. The volume of water used in the polishing machine was 27 L in the first experiment, 24 L in the second experiment and 21 L in the third experiment.

A Professional Portable Digital Glossmeter was used to measure the shine of the plates. According to Neves [8], the measurement scale, shine units (GU), of a shine meter is a scale based on a highly polished black reference glass standard with a defined refractive index having a specular reflectance of 100 GU at the specified angle. This standard is used to establish a top point calibration of 100 with the bottom end point set to 0 on a perfectly matte surface. This scale is suitable for most coatings and non-metallic materials (paints and plastics) as they generally fall within this range. For other highly reflective looking materials (mirrors, coated/raw metal components), higher values can be achieved up to 2000 GU [9]. For transparent materials, these values can also be increased due to various reflections within the material.

After finishing the polishing process, the polished sheets went through the dryers and then the value of the shine level was measured at several different points on the sheets.

Results and Discussion

After carrying out the entire polishing process, it was observed that the reduction of water flow increases the shine level of the different ornamental stone slabs, with the increase in shine being proportional to the reduction of water. Such results can be seen in Table 1 and Figs. 1, 2 and 3.

In Fig. 1 the Cinza Corumbá material increased by 3.8% in the shine level value when the water flow was reduced to 27 L/min. Subsequently, with the reduction to 24 L/min, the shine level was increased by 6.05% and in the last analysis, with the reduction of the water flow to 21 L/min, it was noticed that the shine level of the material had an increase of 8.45% in relation to the initial level with the company's usual flow of 30 L/min [10].

In Fig. 2 it was also noted that the water reduction was able to provide an increase in shine. The Dallas white granite underwent a total increase of 10.63% in relation

Table 1 Shine level results with reduced water flow for different ornamental rocks

	Corumba grey				Dallas white				Itabira ochre			
Water flow (L/min)	30	27	24	21	30	27	24	21	30	27	24	21
Shine (GU)	71	73.7	75.3	77	70.5	72.1	76	78	75.11	76.26	76.34	77.62

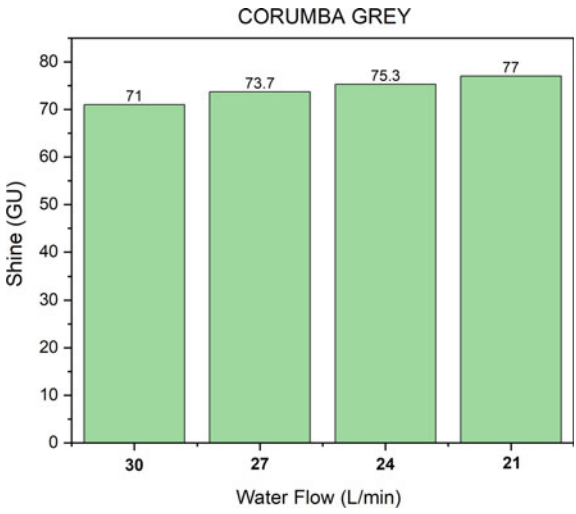

Fig. 1 Shine level of Corumba gray material

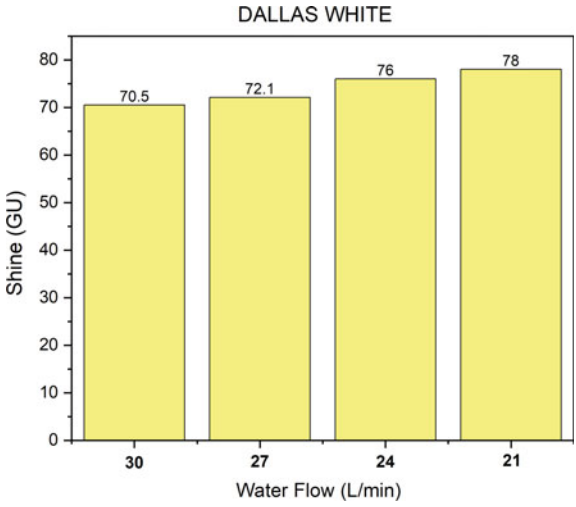

Fig. 2 Shine level of Dallas white material

to the usual shine level of 70.5 GU at a flow rate of 30 L/min. At the reduced flow rate at 27 L/min the increase was 2.27% and at 24 L/min it was 7.8% [11].

In Fig. 3, the Itabira ochre material experienced a 1.53% increase in the shine level value when the initial flow rate was decreased by 3 L/min. When the flow was reduced by 6 L/min, it was found as the shine value increased by 1.64% and in the last flow reduction for this material, totaling 9 L/min less in the water flow, a level of 3.34% more brightness than sheets that were polished with a water flow rate of 30 L/min [12, 13].

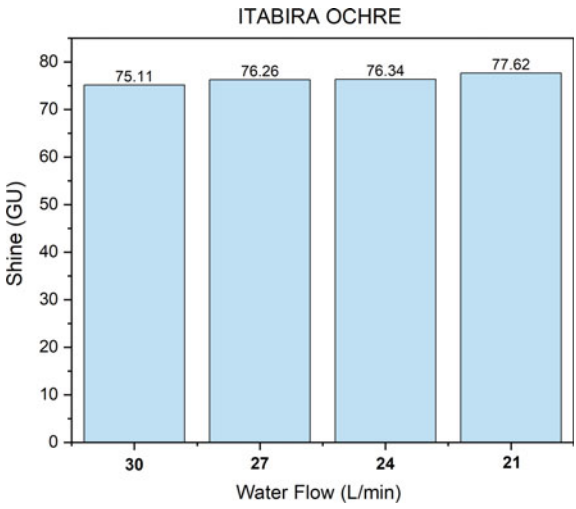

Fig. 3 Shine level of Itabira ochre material

Conclusion

Through four experimental steps, in which the flow of water that enters the polishing process was gradually reduced, it was possible to obtain a considerable increase in the level of shine in the materials studied: 10.63% in Dallas white, 8.45% in Corumba grey and 3.34% in Itabira ochre. All this with the reduction of the flow of water used in the polisher from 30 to 21 L/min.

In this way, it was possible to reduce water consumption, automatically generating a certain production economy and environmental sustainability, without harming the quality of the product, since there was an improvement in the shine level of all the analyzed rocks.

Acknowledgements The authors thank the Brazilian agencies CNPq, CAPES and FAPERJ for the support provided to this investigation.

References

1. Bahiense AV, Alexandre J, Xavier GC, Azevedo ARG, Monteiro SN (2021) Dosage of interlocking paving with ornamental rock waste: An experimental design approach, particle packing and polluting potential. Case Stud Constr Mater 15:e00596
2. Marvila MT, Azevedo ARG, Barroso LS, Barbosa MZ, Brito J (2020) Gypsum plaster using rock waste: a proposal to repair the renderings of historical buildings in Brazil. Constr Build Mater 250:118786
3. Dönmez S, Sari YD (2005) A digital image analysis basedsurface polish measurement system. J Eng Sci 11(3):401–405
4. Aukour FJ, Al-Qinna MI (2008) Marble production and environmental constrains: case study from Zarqa Governorate, Jordan. Jordan J Earth Environ Sci 1(1):11–21

5. Soltan AM, Taman Z, El-Kaliouby B (2011) Recycling of ornamental stones Hazardous wastes. Nat Resour 2:244–249
6. Souza AJ, Pinheiro BCA, Holanda JNF (2010) Processing of floor tiles bearing ornamental rock-cutting waste. J Mater Process Technol 210:1898–1904
7. Uliana JG, Calmon JL, Vieira GL, Teixeira JESL, Nunes E (2015) Heat treatment of processing sludge of ornamental rocks: application as pozzolan in cement matrices. Ibracon Struct Ans Mater J 8(2):100–123
8. Neves MC (2010) Geotechnics—experimental study of the polishing of different "granites" and the relationship with mineralogy. In: Master's Thesis—EESC-USP University of São Paulo. Sao Carlos/SP, 113p (In Portuguese)
9. Marvila MT, De Azevedo ARG, De Matos PR, Monteiro SN, Vieira CM (2021) Materials for production of high and ultra-high-performance concrete: review and perspective of possible novel materials. Materials 14(15) https://doi.org/10.3390/ma14154304
10. Azevedo ARG, Marvila MT, Zanelato EB, Alexandre J, Xavier GC, Cecchin D (2020) Development of mortar for laying and coating with pineapple fiber. Revista Brasileira de Engenharia Agricola e Ambiental 24(3):187–193. https://doi.org/10.1590/1807-1929/agriambi.v24n3p187-193(InPortuguese)
11. Carvalho A, Xavier GC, Alexandre J, Pedroti LG, de Azevedo ARG, Vieira CMF, Monteiro SN (2014) Environmental durability of soil-cement block incorporated with ornamental stone waste. Mater Res. https://doi.org/10.4028/www.scientific.net/MSF.798-799.548
12. Marvila MT, de Azevedo ARG, de Oliveira LB, Xavier GC, Vieira CMF (2021) Mechanical, physical and durability properties of activated alkali cement based on blast furnace slag as a function of $\%Na_2O$. Case Stud Constr Mater 15. https://doi.org/10.1016/j.cscm.2021.e00723
13. Zeyad AM, Magbool HM, Tayeh BA, Azevedo ARG, Abutaleb A, Hussain Q (2022) Production of geopolymer concrete by utilizing volcanic pumice dust. Case Stud Constr Mater 16. https://doi.org/10.1016/j.cscm.2021.e00802

Structural Characterization of Europium-Doped $BaTiO_3$ Obtained by Solid-State Reaction Synthesis

J. P. Hernández-Lara, A. Hernández-Ramírez, J. A. Romero-Serrano, M. Pérez-Labra, F. R. Barrientos-Hernández, R. Martinez-Lopez, and M. I. Valenzuela-Carrillo

Abstract Barium Titanate ($BaTiO_3$)-based ceramic materials are widely used in the electroceramic industry. Conventional processing of these materials is primarily in high-temperature solid-state reactions between mixed oxides. To produce a better quality of the initial powder, factors such as the quality of raw materials, homogeneity of the mixture and the nature of the reaction atmosphere must be controlled. In this research, an analysis of $BaTiO_3$-based ceramic products doped with Europium (Eu^{3+}) were carried out, by means of solid-state reaction synthesis. A review of the compositions ($x = 0.007$ and $x = 0.01\%$ by weight Eu^{3+}) was carried out, grinding was carried out for 5 h and the resulting powders were calcined at 900 °C and sintered at 1350 °C. The experimental results by x-ray diffraction showed the tetragonal $BaTiO_3$ phase. Raman spectroscopy analysis shows the phase transition of $BaTiO_3$ ceramics. Scanning electron microscopy results showed randomly round particles.

Keywords Solid state reaction · Europium · Raman spectroscopy

Introduction

$BaTiO_3$ ceramics are widely used in electronic devices as high permittivity capacitors, due to their high dielectric constant and low loss characteristics. It is well known that the ferroelectric and optical properties of ferroelectric ceramics depend on the grain size. Basically, Barium Titanate is prepared by a solid-state reaction between oxides [1–4].

$BaTiO_3$ is an insulating material with a large energy band (3.05 eV) at room temperature and can become a semiconductor when doped with small concentrations

J. P. Hernández-Lara (✉) · A. Hernández-Ramírez · J. A. Romero-Serrano
Higher School of Chemical Engineering and Extractive Industries (ESIQIE)-IPN, Zacatenco 07738, México
e-mail: juanp_hernandezlara@hotmail.com

M. Pérez-Labra · F. R. Barrientos-Hernández · R. Martinez-Lopez · M. I. Valenzuela-Carrillo
Academic Area of Earth Sciences and Materials, Autonomous University of the State of Hidalgo, Pachuca-Tulancingo Km 4.5, Mineral de la Reforma 42184, Hidalgo, México

M. Zhang et al. (eds.), *Characterization of Minerals, Metals, and Materials 2023*, The Minerals, Metals & Materials Series
https://doi.org/10.1007/978-3-031-22576-5_56

of anisovalent ions as donor elements. Incorporation of isovalent impurities has no effect on the defect population; however, anisovalent impurities (valence different from those it replaces) require the formation of compensation defects of opposite charge to maintain electrical neutrality. If the replacement cation has a lower valence than the original cation, electron holes could be released, and if the replacement cation has a higher valence than the original cation, electrons could be released. Conductivity is therefore closely related to the existence of these ionic defects, such as cationic and anionic vacancies and cationic and anionic gaps [5–8].

Rare earth (RE) dopants are a special class of doping and are often used in $BaTiO_3$ due to their long-term reliability advantages in strength degradation, grain size refinement, high permittivity behavior, and stability of dielectric temperature [9].

A small ~ 1 atom% substitution of a large number of higher valence ions (3+, 5+, 6+) usually changes the volume resistivity of ceramic $BaTiO_3$. Intermediate ions can replace either the Ba^{2+} or Ti^{4+} site depending on the Ba/Ti ratio of the starting powder, or the intermediate ions will occupy both sites with a different partition for each ion [9, 10].

In this research, the results of new ceramic compounds are reported by x-ray diffraction, Raman spectroscopy, as well as scanning electron microscopy of the samples ($x = 0.007$ and $x = 0.0.1\%$ by weight Eu^{3+}) which were synthesized by the technique solid state reaction.

Experimental Methodology

The compositions of the precursor powders previously calculated from the Ba1-xEuxTi1-x/4O_3 mechanism were ground in PET containers with a capacity of 0.5 L with a zirconia ball as a grinding medium for 3 h, and acetone as a control agent. Resulting powders were recovered by filtration allowing the acetone to evaporate. Subsequently, they were heated to 900 °C in order to decarbonate the samples, followed by sintering at a temperature of 1300 °C for 5 h.

Results and Discussion

X-ray Diffraction

The x-ray diffraction patterns corresponding to the sintered samples with $x = 0.007$ and $x = 0.01\%$ by weight of Eu^{3+} at 1300 °C, as well as undoped $BaTiO_3$ are shown in Fig. 1. The characteristic peaks of undoped $BaTiO_3$ can be observed and the doped samples $x = 0.007$ and $x = 0.01$ coincide with the $BaTiO_3$ species, which shows the consolidation of Tetragonal $BaTiO_3$ (JCPDS 05-0626) and can be seen at positions

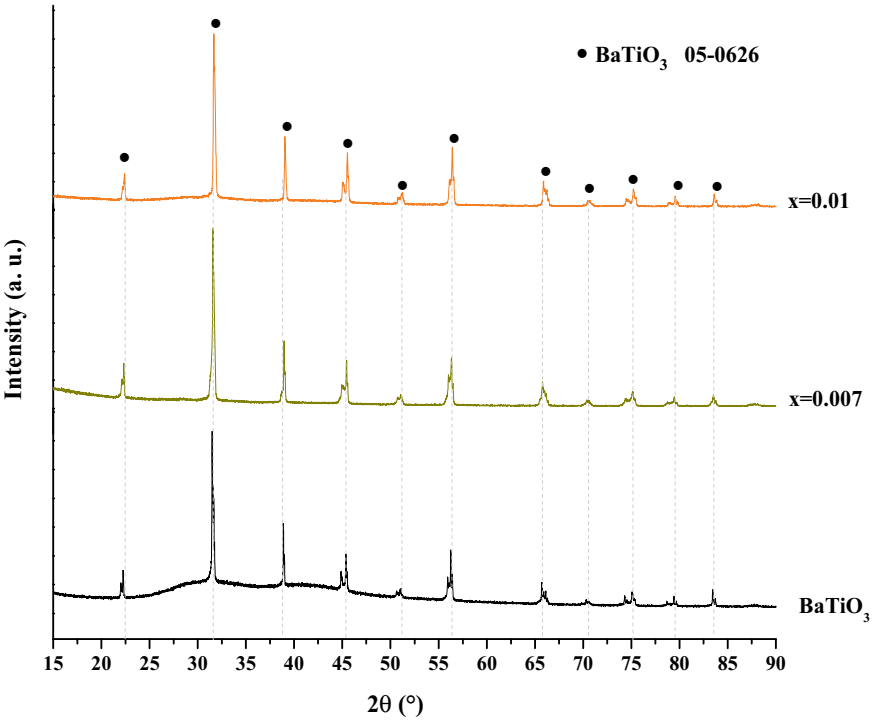

Fig. 1 Diffractograms of the samples undoped $BaTiO_3$, $x = 0.007$ and $x = 0.01\%$ by weight Eu^{3+}

$2\theta \approx 22.41°, 31.49°, 39.07°, 45.54°, 51.20°, 56.37°, 65.92°, 70.45°, 75.31°, 79.50°, 83.55°$.

Figure 2 shows the highest intensity peak at $2\theta \approx 31.49°$, as well as the absence of the species corresponding to the precursor powders. Kolthoum et al. [11] mention that the amount of $BaTiO_3$ formed after calcination increases with increasing calcination temperature at a constant calcination time of 1 h. Therefore, at 900 °C, the reaction between $BaCO_3$, TiO_2 and Eu_2O_3 comes to an end with the formation of 100% of $BaTiO_3$ without the presence of secondary phases and precursor powders of the samples $x = 0.007$ and $x = 0.01\%$ by weight of Eu^{3+}.

Raman Spectroscopy

Figure 3 shows the Raman spectra for undoped $BaTiO_3$ and doped $BaTiO_3$ with $x = 0.007$, 0.01, % by weight Eu^{3+} prepared by the solid-state reaction. The frequency coverage area is from 100 to 1000 cm^{-1}. The graphs show the characteristic Raman peaks of $BaTiO_3$ at room temperature, consistent with those reported by Gardiner et al. [12–14] located at 205 cm^{-1}, (E (TO + LO), A1(LO)), 265 cm^{-1} (A1(TO)),

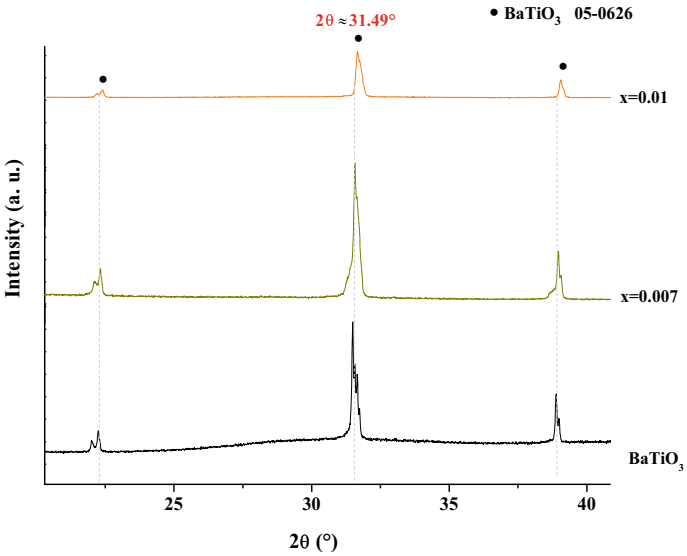

Fig. 2 Diffractogram of the highest intensity peak in the undoped $BaTiO_3$ samples, $x = 0.007$, $x = 0.01\%$ by weight Eu^{3+}

304 cm^{-1} (B1, E (TO + LO)), 513 cm^{-1} (A1(TO), E(TO)) and 717 cm^{-1} (A1(LO), E(LO)); Similar bands for $BaTiO_3$-based ceramics were observed in studies by Matsuoka et al. and Ikushima et al. [12, 14].

Scanning Electron Microscopy (SEM)

The Scanning Electron Microscopy analyzes reported in this research were performed on undoped $BaTiO_3$ and the sintered powders at 1300 °C for 5 h for the samples $x = 0.007$ and $x = 0.01\%$ by weight Eu^{3+}.

Figure 4 shows the morphology of undoped $BaTiO_3$ using an acceleration voltage of 5.0 kV, a magnification of ×10,000. The sample consists of individual particles and aggregates with various sizes, and they have a random orientation with porosity in different areas in the same way some agglomerates are formed.

Figure 5 shows the SEM image of the sample $x = 0.007$ using an acceleration voltage of 5.0 kV and a magnification of ×10,000. In this image porosity is observed in different areas of the sample, this results in pores not eliminated inside the grain and agglomeration of the particles. Zhao et al. [15] report that in order to avoid abnormal grain growth, it is very important to carry out a good synthesis of the powders and thus prevent $BaTiO_3$ particles with poor powder morphology from hindering compact packing during the formation process before sintering and that prevent the densification of the ceramic.

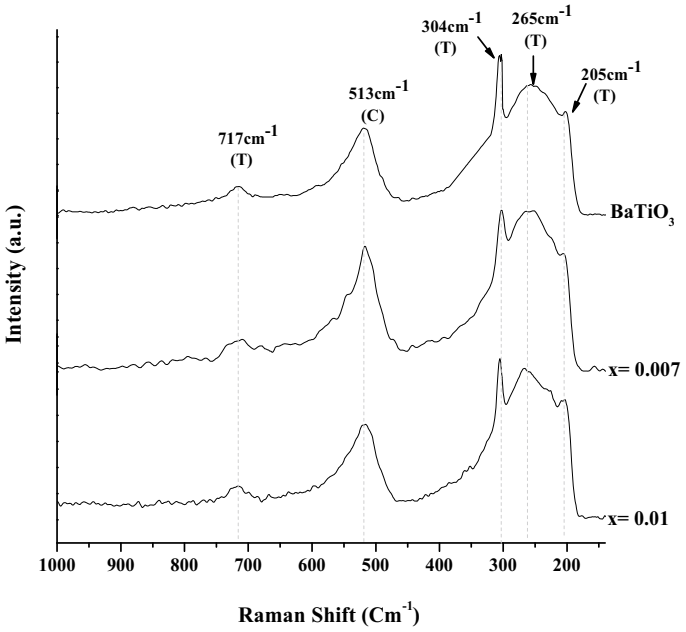

Fig. 3 Raman spectra of undoped $BaTiO_3$, $x = 0.007$, $x = 0.01\%$ by weight Eu^{3+}

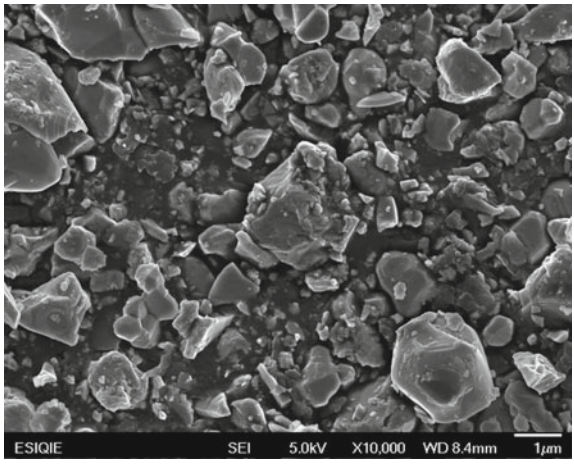

Fig. 4 Micrograph of the undoped $BaTiO_3$ sample

The image in Fig. 6, $x = 0.01\%$ by weight Eu^{3+}, uses an accelerating voltage of 5.0 kV and a magnification of ×10,000, semi-consolidated rounded and sub-rounded particles can be observed in the range of sizes of 1 μm with various sizes which present the characteristic necks of a sintering process. However, it can also be seen that the material has a significant percentage of porosity. F.R. Barrientos

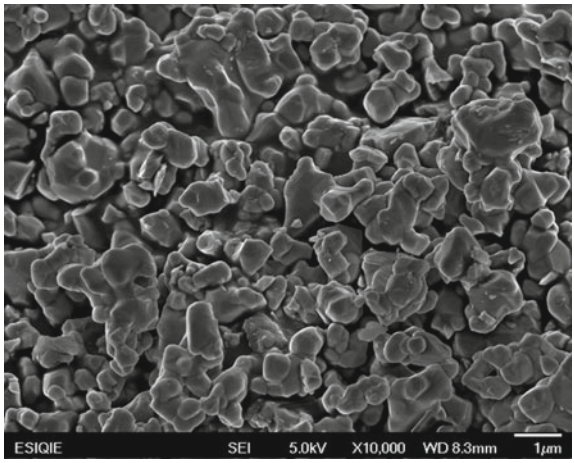

Fig. 5 Micrograph of the sample $x = 0.007\%$ by weight Eu^{3+} sintered at 1300 °C

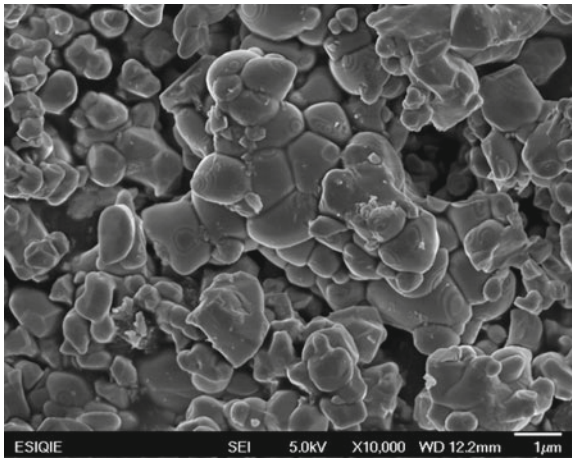

Fig. 6 Micrographs of the samples $x = 0.01\%$ by weight Eu^{3+} sintered at 1300 °C

Hernández et al. [16] carried out studies on $BaTiO_3$ doped with Nb where they found particles of different sizes, which they attributed to the increase in the amount of dopant used in the synthesis, as well as porosity in different zones and spherical grains with random orientation.

Conclusions

X-ray diffraction patterns confirmed the consolidation of tetragonal $BaTiO_3$ according to the identification letter (JCPDS 05-0626) at positions $2\theta \approx 22.41°$, 31.49°, 39.07°, 45.54°, 51.20°, 56.37°, 65.92°, 70.45°, 75.31°, 79.50°, 83.55° as

well as the highest intensity peak is found at $2\theta \approx 31.49°$ and there is no presence of the species corresponding to the precursor powders. The Raman spectra show the characteristic peaks of $BaTiO_3$ at room temperature, located at 205 cm^{-1}, (E (TO + LO), A1(LO)), 265 cm^{-1} (A1(TO)), 304 cm^{-1} (B1, E (TO + LO)), 513 cm^{-1} (A1(TO), E(TO)) and 717 cm^{-1} (A1(LO), E(LO)) this is consistent with what is reported in the literature. The Scanning Electron Microscopy analyzes reported for the undoped $BaTiO_3$ sample show individual particles with different sizes, however, for the doped samples $x = 0.007$ and $x = 0.01$ they show grains of different sizes which present the characteristic necks of a sintering process, there is porosity in different areas and agglomeration of the particles.

Acknowledgements This work has been carried out thanks to the support of IPN-ESIQIE, the Autonomous University of the State of Hidalgo, and Conacyt.

References

1. Nalwa HS (1999) Handbook of low and high dielectric constant materials and their applications. Academic Press, USA
2. Sakabe Y, Minai K, Wakino K (1981) High-dielectric constant ceramics for base metal monolithic capacitors. Jpn J Appl Phys Suppl 20–4:147–150
3. Hreniak D, Łukowiak E, Maruszewski K, Pązik R, Stręk W (2002) Structure, spectroscopy and dielectric properties of $BaTiO_3$:Eu^{3+} nanocrystallites prepared by the sol–gel method. Mater Sci 20(1):43–50
4. Simon-Seveyrat L, Hajjaji A, Emziane Y, Guiffard B, Guyomar D (2007) Re-investigation of synthesis of $BaTiO_3$ by conventional solid-state reaction and oxalate coprecipitation route for piezoelectric applications. Ceram Int 33:35–40
5. Smyth DM (2000) The defect chemistry of metal oxides. Oxford University Press, Oxford
6. Levinson LM (1988) Electronic Ceramics. Marcel Dekker Inc., New York
7. Yanagida H (1996) The chemistry of ceramics. Wiley, Tokyo
8. Buchanan RC (1998) Ceramic materials for electronics; processing, properties and applications, 2nd
9. Tsur Y, Dunbar TD, Randall CA (2001) Crystal and defect chemistry of rare earth cations in $BaTiO_3$. J Electroceram 7:25–34
10. Jankowska-Sumara I, Sitko D, Podgórna M, Pilch M (2017) The electromechanical behavior of europium doped $BaTiO_3$. J Alloy Compd 724:703–710
11. Othman KI, Hassan AA, Abdelal OAA, Elshazly ES, El-Sayed Ali M, El-Raghy SM, El-Hout S (2014) Formation mechanism of barium titanate by solid-state reaction. Int J Sci Eng Res 5(7)
12. Ikushima H, Hayakawa S (1967) National technical reports, vol 13, pp 209–216
13. Gardiner DJ, Graves PR (1989) Practical Raman spectroscopy. Springer, Berlin
14. Matsuoka T, Fujimura M, Matsuo Y (1972) PTCR behavior of $BaTiO_3$ with Nb_2O_5 and MnO2 additives. J Am Ceram Soc 55:108–116
15. Zhao X, Liu W, Chen W, Zhong L (2013) Effect of particle size of $BaCO_3$ and TiO_2 powders on the properties of $BaTiO_3$ ceramics. In: Annual report conference on electrical insulation and dielectric phenomena, pp 603–606
16. Barrientos Hernández FR, Lira Hernández IA, Gómez Yáñez C, Arenas Flores A, Cabrera Sierra R, Pérez Labra M (2014) Structural evolution of $Ba_8Ti_3Nb_4O_{24}$ from $BaTiO_3$ using a series of $Ba(Ti_{1-5x}Nb_{4x})O_3$ solid solutions. J Alloy Compd 583:587–592

Study of Cement-Based Mortars Reinforced with Guaruman Fibers in the Fresh State

T. E. S. Lima, L. B. Oliveira, V. S. Candido, A. C. R. Silva, M. T. Marvila, S. N. Monteiro, and A. R. G. Azevedo

Abstract Guaruman fiber is a natural lignocellulosic fiber (NFL) extracted from the stalk of an Amazon plant (*Ishinosiphon Koern*) in the northern region of Brazil. The present work investigates the addition of 2.5, 5.0 and 7.5 wt.% of guaruman fiber, in cement mass, and a reference mortar (0%). The fibers were mercerized in NaOH solution for improved adhesion to a mortar matrix made with 1:1:6 ratio of Ordinary Portland Cement (OPC), lime and natural sand. Technical properties, such as density, consistency, content of air incorporated and water retention were evaluated for the processed fresh state of the mortar reinforced with guaruman fiber. The preliminary results in association with the relatively low density of the mortars incorporated with NaOH-treated guaruman fibers reveal a promising material to be applied as mortar for wall covering in civil construction, in a proportion of 7.5 wt.%, which shows a great potential for the use of this fiber.

Keywords Guaruman fiber · Amazon lignocellulosic fiber · Mortar · Technical properties

T. E. S. Lima · L. B. Oliveira · M. T. Marvila
LAMAV—Advanced Materials Laboratory, UENF—State University of Northern Rio de Janeiro, Av. Alberto Lamego, 2000, Campos dos Goytacazes, Rio de Janeiro 28013-602, Brazil

V. S. Candido · A. C. R. Silva
Faculty of Materials Engineering, UFPA—Federal University of Pará, Colégio Intelectual - Tv. We Vinte e Seis, 2, Ananindeua 67130-660, Brazil
e-mail: scarpini@ufpa.br

A. C. R. Silva
e-mail: alissonrios@ufpa.br

S. N. Monteiro
Department of Materials Science, IME—Military Institute of Engineering, Square General Tibúrcio, 80, Rio de Janeiro 22290-270, Brazil

A. R. G. Azevedo (✉)
LECIV—Civil Engineering Laboratory, UENF—State University of Northern Rio de Janeiro, Av. Alberto Lamego, 2000, Campos dos Goytacazes, Rio de Janeiro 28013-602, Brazil
e-mail: afonso.garcez91@gmail.com

M. Zhang et al. (eds.), *Characterization of Minerals, Metals, and Materials 2023*, The Minerals, Metals & Materials Series
https://doi.org/10.1007/978-3-031-22576-5_57

Introduction

The replacement of synthetic materials by recycled natural ones is growing in association with the concept of sustainable civil construction [1, 2]. Natural lignocellulosic fibers (NLFs), in particular, have in recent years been considered as substitute for synthetic steel and polymer fibers in cementitious matrix composites, mainly concrete and mortars, used by the construction industry [1–6]. Indeed, the incorporation of NLFs in cementitious composites like mortars has relevant advantages such as cost-effectiveness, relatively low density, wide availability and easy to recycle owing to their biodegradability. Moreover, NLFs serve as acoustic insulation and possess CO_2 neutrality [7]. In addition, they have mechanical properties that enhance the application on construction materials [8, 9]. In fact, vegetable fibers in cementitious matrix tend to improve the compressive strength and confer ductility to the composite [10].

However, NLFs present some disadvantages due to non-uniform properties arising from natural heterogeneity such as variation in diameter, length and chemical content within the same fiber species [11]. Other disadvantages that limit the use of as-extracted vegetable fibers are the durability and hydrophilicity in contact with a cement matrix. To overcome these problems and improve the interfacial fiber/cement adhesion, NLFs should be subjected to surface pretreatments such as mercerization with sodium hydroxide (NaOH) [3, 4].

The guaruman fiber is extracted from an Amazonian *Ischinasiphon Koern* plant, which is endemic in humid places on the river's banks and streams, located in the northern region of Brazil, mainly in the states of Amazonas and Para. From these plants are extracted the stalks, splint and fibers that have great potential for producing local handicrafts.

Reis et al. [12] reported on the properties of guaruman fiber indicating that it has one of the lowest 0.50–0.64 g/cm^3, NLFs densities as well as crystallinity index of 60–67%, tensile strength of 614 MPa and favorable microfibrillar angle of 7.3–8.2°. Similar results related to fiber characterization were found in other works in the literature [13–15]. In this way, the authors considered the guaruman fiber adequate for composite reinforcement. Therefore, this work aims to analyze the behavior that the addition of guaruman fiber, in the natural and treated condition, performs in mortars in the fresh state, aiming at its application in civil construction.

Materials and Methods

The guaruman fibers were cleaned in running water and dried in a stove at 60 °C for 24 h. The mortar used as matrix for the fiber incorporation was prepared using a standard mixture of ordinary Portland cement (OPC), lime and sand in the ratio of 1:1:6, respectively. A Brazilian OPC type III (CPIII) was purchased in the local Campos dos Goytacazes specialized commercial store. Similarly, the sand and lime were commercially available in construction stores. The use of lime in mortar provides

several advantages, which ensure greater durability under weather exposure in a tropical country like Brazil [3]. The sand used as aggregate was naturally collected from river and sieved to homogenize the granulometry.

It was determined, after the analysis of physical characteristics of the guaruman fiber, it has density of 0.61 g/cm^3, average tensile strength of 670 MPa, average Young's modulus of 22 GPa, microfibrillar angle of 8.1° and average absorbed energy of 522 J/m. The chemical characterization of the fiber found a concentration of 38.40% of cellulose, 41.23% of hemicellulose, 10.87% of Lignin and 9.71% of general extractives. The other materials, such as OPC and lime, were not evaluated as they are commercial with well-known characteristics and have already been used in other recent research [16–18].

The guaruman fibers were added to the mortar in different proportions in relation to the total cement mass of the reference mixture without any addition, which was used for comparison purposes. Thus, additions of 2.5, 5.0 and 7.5 wt.% were considered, together with the reference mixture, for the manufacture of mortars.

Technological tests were carried out in the fresh state, just after composite preparation. The consistency determination was performed by measuring the horizontal spreading of the mixed paste on a slump table, which enabled the evaluation of the mortar´s workability [19]. The consistency makes it possible to measure the workability of the mortar in its horizontal spread, which for the application of wall and ceiling coverings is 260 mm in average values. Mortars with high fluidity and workability are difficult to apply. The water retention test was determined for each mixture using the Buchner funnel method [20]. This allowed obtaining the capacity to fill the internal pores of the mortar with water. The content of incorporated air was measured by using the pressiometric method, which indicates the volume of air in the mortar. Together with the water retention, it gives the capacity of the mortar to retain and to suction water from the applied substrate [21–23]. Finally, the mass density in the fresh state was determined using the standard process of the Brazilian standard to determine this property [22].

Results and Discussion

Table 1 presents the results of the technological tests in terms of the corresponding parameters. Based on the results shown in this table, the corresponding graphical interpretations are shown in Figs. 1, 2, 3 and 4.

As for the consistency results in Fig. 1, only slight decrease, from 265 to 210 mm, occurred with incorporation of guaruman fibers. Moreover, practically no change occurred as a consequence of fiber NaOH treatment. In principle one may conclude that the mortar workability is not significantly affected by addition of guaruman fibers up to 7.5 wt.%. The incorporation of NFLs traditionally reduces the average spread measured in the consistency test. This has already been observed in other works in the literature, and occurs due to the anchoring that the fibers promote in the cementitious paste in the fresh state, which may even contribute to a potential

Table 1 Technological fresh state parameters for mortars incorporated with guaruman fiber

Composition	Consistency (mm)	Mass density in fresh state (g/cm^3)	Water retention (%)	Incorporated air (%)
Reference	264.2	2.00	95.90	7.5
2.5% untreated fiber	259.8	1.96	94.56	7.9
2.5% treated fiber	262.4	1.98	95.20	7.7
5% untreated fiber	252.4	1.91	93.40	8.5
5% treated fiber	246.7	1.96	94.98	8.15
7.5% untreated fiber	209.8	1.88	92.7	8.8
7.5% treated fiber	225.6	1.94	94.24	8.3

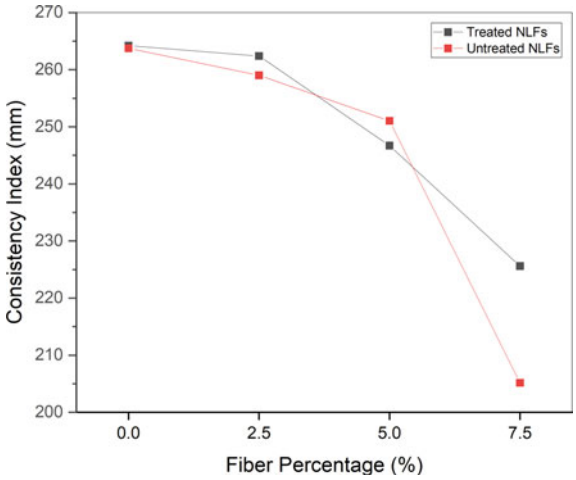

Fig. 1 Consistency of the different mortars

increase in the mechanical strength of the composite in the hardened state [24–26]. For wall and ceiling cladding applications, the standard and literature stipulate an average spread of 260 mm with a tolerance ≈ 5 mm, which allows us to prove that the addition of only 2.5 wt.% meets this requirement [25]. On the other hand, it has already been shown in the literature that small differences in these values, such as those observed in the 5 wt.%, guaruman fiber-added mortar are still allowed, provided that other parameters in the fresh state are adequate [1].

Regarding the relative volume of incorporated air in Fig. 2, there is a moderate, 7.5–9%, increase from the reference mixture with plain mortar. It is also important to note that air incorporation was sensibly higher for the mortar added with non-treated

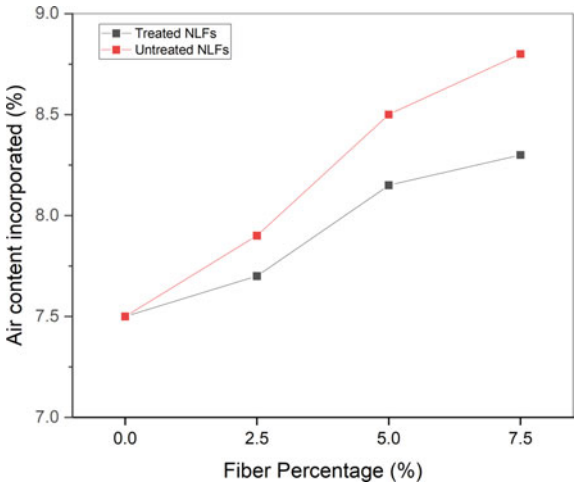

Fig. 2 Content of air incorporated in the different mortars

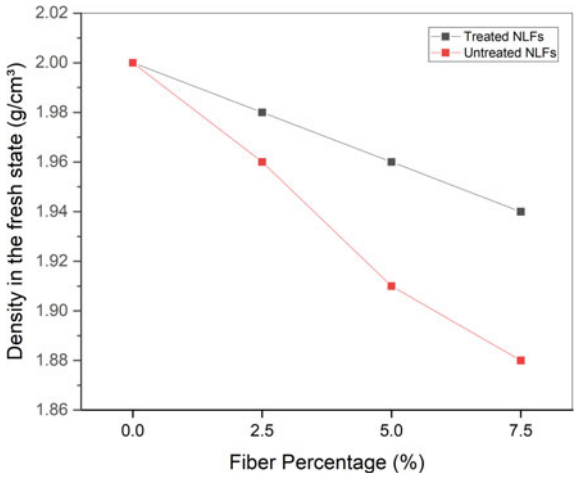

Fig. 3 Density in the fresh state of different mortars

guaruman fibers compared to those treated with NaOH solution. The addition of untreated NLFs in cementitious composites promotes the appearance of internal voids in the interfacial region, which are detected in the fresh state through the analysis of entrained air, and can translate into fragility of the matrix in the hardened state. The surface treatment with NaOH promoted greater adhesion between the fiber and the matrix, which certainly justifies the reduction in the amount of air incorporated in each mixture evaluated Fig. 2, when compared to non-treated NFL [27]. Another point is that the morphological characteristics of guaruman fibers, which are extremely thin and short, promote a smaller reduction in the amount of incorporated air than that observed in other studies reported in the literature on NFL added mortars [27, 28].

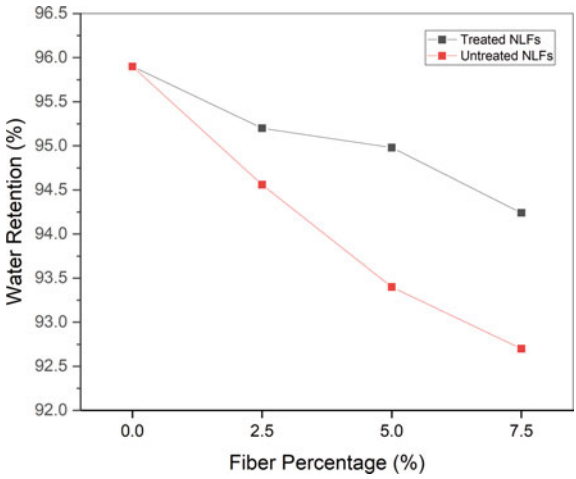

Fig. 4 Water retention for the different mortars

The density in fresh state curves shown in Fig. 3 display the expected tendency towards a slightly decrease owing to the relatively lower density of the guaruman fibers. As expected, this decrease in mortar density is more effective in mortars incorporated with NFLs, which tend to lose more wax and lignin [26]. Mortars with lower density are more applicable for civil construction, as they provide greater lightness to the sealing elements of constructions. Nevertheless, some studies have shown that values between 1.9 g/cm^3 and above are adequate because, for lower values, problems were detected in the integrity and durability of the mortar [21, 29]. Parallel to this, the addition of NFLs improves the acoustic and thermal properties of the mortars, which with an adequate average mass density, between 2.0 and 1.9 g/cm^3, can be easily applied [29]. Thus, blends with treated NFLs in all evaluated addition ratios can be used.

Figure 4 shows the variation of water retention with incorporation of guaruman fibers into the mortar. Contrary to what one would expect, the presence of guaruman fibers caused a decrease in water retention associated with both untreated and treated fibers. A possible explanation is that the guaruman fibers promote a better adhesion with the mortar OPC as previously suggested by Marvila et al. [4] for açai added mortars. In the present case of guaruman fibers, the surface roughness might be responsible for the improved interfacial bonding with the mortar's cement past as happens with a polymer (epoxy) matrix [21, 22]. In addition, the fiber treatment process in NaOH solution promoted the formation of a protective film in the interfacial region, contributing to the reduction of water retention, which would be expected in NFLs that display this characteristic [30]. The untreated condition of guaruman fiber, which does not promote this traditional absorption is already a positive factor and shows its great potential for application in civil construction.

The results presented in Figs. 1, 2, 3 and 4 make it possible to sustain that the treatment with NaOH solution could be neglected, which, in principle, would be economical for a real application. However, as it is known, the deleterious effect of

the cement matrix on NFLs due to its alkalinity, makes the treatment essential and even indispensable. Thus, any mixture with NaOH treatment satisfies this property, with the value of 7.5 wt.% incorporation being recommended because it uses a greater amount of less expensive guaruman fiber.

Conclusion

The preliminary technical results of guaruman fibers incorporated mortar in the fresh state permit to conclusion: (i) The mortar consistency is only slightly reduced without practically no effect due to the guaruman fibers NaOH treatment; (ii) The content of incorporate air is increased, with significant changes, associated with untreated guaruman fibers. This is attributed to a higher amount of surface open porosity generated by the alkali attack; (iii) The mass density in fresh state is reduced with incorporation of guaruman fibers owing to their relatively lower density; (iv) The incorporation of guaruman fibers caused a decrease in water retention despite the hydrophilicity of these natural lignocellulosic fibers. It is suggested that the guaruman fibers promote a better adhesion to the mortar cement paste due to their characteristic rougher surface; (v) Based on these technical findings, it is also possible to conclude that fabrication of mortars incorporated with up to 7.5 wt.% of guaruman fibers offers a novel material for wall lining in building material; (vi) As an addition to cementitious mortars in fresh state, guaruman fiber has a promising potential for civil construction applications, in contents of 7.5 wt.% under treatment conditions with NaOH solution. Emphasizing that this natural fiber has never been used for applications in cementitious materials.

Acknowledgements The authors thank the Brazilian agencies CNPq, CAPES, and FAPERJ for the support provided to this investigation.

References

1. Azevedo ARG, Alexandre J, Marvila MT, Xavier GC, Monteiro SN, Pedroti LG (2020) Technological and environmental comparative of the processing of primary sludge waste from paper industry for mortar. J Clean Prod 249:119336
2. Nasr MS, Shubbar AA, Abed ZAAR, Ibrahim MS (2020) Properties of eco-friendly cement mortar contained recycled materials from different sources. J Build Eng 31:101444
3. Azevedo ARG, Marvila MT, Tayeh BA, Cecchin D, Pereira AC, Monteiro SN (2021) Technological performance of açaí natural fibre reinforced cement-based mortars. J Build Eng 33:101675
4. Marvila MT, Azevedo ARG, Cecchin D, Costa JM, Xavier GC, Carmo DDF, Monteiro SN (2020) Durability of coating mortars containing açaí fibers. Case Stud Constr Mater 13:e00406
5. Fediuk RS, Lesovik VS, Svintsov AP, Mochalov AV, Kulichkov SV, Stoyushko NY, Timokhin RA (2018) Self-compacting concrete using pretreatmented rice husk ash. Mag Civ Eng 79(3):66–76

6. Zukowski B, Silva FA, Toledo Filho RD (2018) Design of strain hardening cement-based composites with alkali treated natural curaua fiber. Cem Concr Compos 89:150–159
7. Reis JM (2013) Fracture properties of curaua fibers reinforced polymer mortars. Adv Mater Res Trans Tech Publ Ltd 687:490–494
8. Fediuk R, Smoliakov A, Muraviov A (2017) Mechanical properties of fiber-reinforced concrete using composite binders. Adv Mater Sci Eng 1:1–13
9. Pimentel MG, Borges JPDC, Picanço MDS, Ghavami K (2016) Response to flexural and toughness analysis of mortars reinforced with curaua fiber. Matéria (Rio J) 21(1):18–26
10. Picanço MDS, Ghavami K (2008) Compressive behavior of mortars reinforced with Amazon vegetable fibers. REM Rev Esc De Minas 61:13–18
11. Seydibeyoglu MO, Mohanty AK, Misra M (2017) Natural fibers. Fiber technology for fiber-reinforced composites. Woodhead Publishing, Cambridge, pp 09–235
12. Reis RHM, Nunes LF, Oliveira MS, Veiga Junior VF, Garcia Filho FDC, Pinheiro MA, Monteiro SN (2020) Guaruman fiber: another possible reinforcement in composites. J Mater Res Technol 9(1):622–628
13. Monteiro SN, Lopes FPD, Barbosa AP, Bevitori AB, Silva ILA, Costa LL (2011) Natural lignocellulosic fibers as engineering materials—an overview. Metall Mater Trans 42(10):2963–2974
14. Monteiro SN, Lopes FPD, Ferreira AS, Nascimento DCO (2009) Natural-fiber polymer-matrix composites: cheaper, tougher, and environmentally friendly. Jom 61(1):17–22
15. Satyanarayana KG, Guimarães JL, Wypych F (2007) Studies on lignocellulosic fibers of Brazil. Part I: Source, production, morphology, properties and applications. Compos Part A Appl Sci Manuf 38(7):1694–1709
16. Azevedo ARG, Nascimento M, Carmo D, Marvila MT, Xavier GC, Monteiro SN (2022) Environmental and durability perspective of the use of curaua fiber treatedin mortars. J Renew Mater 10(6):1–21
17. Azevedo ARG, Vilumev SV, Marvila MT, Vatin NI, Alfimova NI, Lima TES, Fediur R, Olisov AV (2020) Investigation of the potential use of curaua for reinforcing mortars. Fibers 8(11):69
18. Soltan DG, Neves P, Olvera A, Junior HS, Li VC (2017) Introducing a curaua fiber reinforced cement-based composite with strain-hardening behavior. Ind Crops Prod 103:1–12
19. NBR 13276 (2016) Mortar for laying and covering walls and ceilings—determination of consistency index. Brazilian Association of Technical Standards
20. Lertwattanaruk P, Suntijitto A (2015) Properties of natural fiber cement materials containing coconut coir and oil palm fibers for residential building applications. Constr Build Mater 94:664–669
21. Arce C, Garzon E, Sanchez-Soto PJ (2019) Phyllite clays as raw materials replacing cement in mortars: properties of new impermeabilizing mortars. Constr Build Mater 224:348–358
22. Azevedo ARG, Marvila MT, Zanelato EB, Alexandre J, Xavier GC, Cecchin D (2020) Development of mortar for laying and coating with pineapple fibers. Rev Bras De Eng Agric e Ambient 24:187–193
23. Azevedo ARG, Marvila MT, Barroso LS, Zanelato EB, Alexandre J, Xavier GC, Monteiro SN (2019) Effect of granite residue incorporation on the behavior of mortars. Materials 12(9):1449
24. Fediuk RS, Smoliakov AK, Timokhin RA, Batarshin VO, Yevdokimova YG (2017) Using thermal power plants waste for building materials. IOP Conf Ser: Earth Environ Sci 87(9):092010
25. Marvila MT, Azevedo ARG, Alexandre J, Vieira CMF, Zanelato EB, Delaqua GCG (2020) Study of the compressive strength of mortars as a function of material composition, workability, and specimen geometry. Model Simul Eng 4:1–6
26. Okada K, Ooyama A, Isobe T, Kameshima Y, Nakajima A, MacKenzie KJD (2009) Water retention properties of porous geopolymers for use in cooling applications. J Eur Ceram Soc 29(10):1917–1923
27. Suwan T, Maichin P, Fan M, Jitsangiam P, Tangchirapat W (2022) Influence of alkalinity on self-treatment process of natural fiber and properties of its geopolymeric composites. Constr Build Mater 316:125817

28. Bui H, Sebaibi N, Boutouil M, Levacher D (2020) Determination and review of physical and mechanical properties of raw and treated coconut fibers for their recycling in construction materials. Fibers 8(6):37
29. Wei J, Meyer C (2015) Degradation mechanisms of natural fiber in the matrix of cement composites. Cem Concr Res 73:1–16
30. Shi Z, Geiker MR, Weerdt K, Lothenbach B, Kaufmann J (2015) Durability of portland cement blends including calcined clay and limestone: Interactions with sulfate, chloride and carbonate ions. RILEM Book 10:133–141

Study of Mortar with Incorporation of Different Proportions of Coconut Fiber With and Without Previous Treatment

M. M. D. Pereira, I. D. Batista, I. S. A. Pereira, K. M. S. Tavares, S. N. Monteiro, L. U. D. Tambara Júnior, and A. R. G. Azevedo

Abstract Coconut fiber is a renewable material that has high potential for use in civil construction. Proving to be a profitable and promising alternative, this study intends to analyze and compare the effects of the addition of coconut fiber in the mortar through tests, such as consistency, density, viscosity, compressive and flexural strength. The comparison was made with 0.3 and 0.6% of addition in cement mass, treating the fibers previously with sodium hydroxide with 0.3 and 0.6% and in natural condition. The results showed that the treatment was beneficial for this type of fiber, showing that its application in mortals is feasible.

Keywords Coconut Fiber · Waste · Incorporation · Renewable

Introduction

With the rapid global urbanization, the demand for construction materials has increased, generating the search for effective and sustainable alternatives to replace conventional materials [1]. Mortar is one of the materials that has wide use in civil construction, obtained from a homogeneous mixture between binder, aggregate and water, and may contain the addition of minerals in its composition, in order to modify or improve properties of the cement mixture [2].

On the other hand, the destination of agro-industry waste is a matter of concern in many countries. The by-product generated by fruits presents a significant increase,

M. M. D. Pereira · I. D. Batista · I. S. A. Pereira · K. M. S. Tavares · L. U. D. T. Júnior
LAMAV—Advanced Materials Laboratory, UENF—State University of Northern Rio de Janeiro, Av. Alberto Lamego, 2000, Campos dos Goytacazes, Rio de Janeiro 28013-602, Brazil

S. N. Monteiro
Department of Materials Science, IME—Military Institute of Engineering, Square General Tibúrcio, 80, Rio de Janeiro 22290-270, Brazil

A. R. G. Azevedo (✉)
LECIV—Civil Engineering Laboratory, UENF—State University of Northern Rio de Janeiro, Av. Alberto Lamego, 2000, Campos dos Goytacazes, Rio de Janeiro 28013-602, Brazil
e-mail: afonso.garcez91@gmail.com

M. Zhang et al. (eds.), *Characterization of Minerals, Metals, and Materials 2023*, The Minerals, Metals & Materials Series
https://doi.org/10.1007/978-3-031-22576-5_58

where the coconut waste stands out as one of the main agricultural wastes generated [2]. It is estimated that about 1.6 billion tons of food produced for human consumption are lost or wasted per year, and about 50% is composed of fruits, vegetables and roots [3].

The reuse of these wastes becomes an alternative as it is a way to minimize the impacts to the environment inherent to sanitary landfills by practicing the 3R's (reduce, reuse, recycle) [4].

Characterized for being an available, recoverable and renewable resource, natural fibers stand out for being cheap, low density and non-toxic, in addition to excellent mechanical properties, increasing ductility when incorporated into cementitious matrices. Added in mortar, they control cracks and increase tensile strength, tenacity and durability, with coconut fiber being one of the most used to improve the properties of mortar mixtures [5, 6].

Thus, the present work aims to study and compare the workability and strength of mortar with the addition of pre- treated coconut fiber at 0.3 and 0.6 wt%.

Materials and Methods

For the research, Portland Cement (CP II E-32) was used, which has slag addition and is widely used in the region, natural quartz sand washed from the Paraíba do Sul River with a fineness modulus of 2.21, classified as "average" according to NBR 7211 [7], natural coconut fiber from São Fidélis-RJ, as shown in Fig. 1, and water supplied by the Águas do Paraíba concessionaire in Campos dos Goytacazes. When all materials arrived at the laboratory, they were packed in plastic bags and properly sealed.

Fig. 1 Coconut fiber

Table 1 Recipe for making the mortar samples

Feature	Coconut fiber	Water/cement ratio
1:4 cement: sand	0%	0.9
	0.3% treated	0.9
	0.3% untreated	0.9
	0.6% treated	0.9
	0.6% untreated	0.9

A pre-treated fiber was carried out with a mixer for a solution of water + sodium hydroxide, and then, after cooling, the fiber was placed in treatment in the mixture. Subsequently, it was washed, for maximum elimination of the hydroxide, and later placed in an oven until reaching constant mass.

Reference specimens were made, with 0% addition, and specimens with 0.3 and 0.6% addition of fibers in relation to the cement mass, in natural condition and previously treated with sodium hydroxide, according to Table 1.

The water-cement ratio was defined by trial and error in the reference mortar (0% addition), where necessary spreading was found according to NBR 13,276 [8], and this ratio was fixed for all the others.

All prismatic specimens of dimensions 40 × 40 × 160 mm, as shown in Fig. 2, were molded in three level layers and densified with 30 drops of flow table, totaling the production of 3 specimens for each test performed.

In the fresh state, the viscosity was analyzed using the MVD-8 digital viscometer, where the result was the average of the values found in the first 60 s of the test. Still

Fig. 2 Specimens molded

Fig. 3 The viscosity measurement (left) and density testing device (right)

in the fresh state, the density was performed, through the mass and volume made in a cylindrical container (Fig. 3).

For the hardened state tests, the Instron 5582 Universal Tester equipment was used, where the flexural strength and compressive strength tests were carried out, according to NBR 13,279 [9]. A load was applied at 0.5 mm/min for the bending test and 2.0 mm/min for the compression test.

Results and Discussion

In the test where the consistency index was determined, it can be seen, through Fig. 4, that the previously treated fibers achieved greater workability. The NBR 13,276 standard specifies the spreading value for mortar, and considers values between 25.5 and 26.5 cm as ideal for a workable material [8]. Thus, it is observed that both proportions of previously treated fibers reached values higher than those determined by the standard. However, even presenting values in disagreement, no mortar had the possibility of limited use, being possible to carry out all tests, fresh and hardened, for all percentages of additions.

As shown in Fig. 5, in the viscosity test, the addition of 0.6% of treated fiber in the mortar generated a significant increase in viscosity [9]. This means that its resistance to flow is greater, and this result does not match the values found in other mortars. When compared to the additions of 0.3% fiber, the untreated fiber had a higher viscosity, which would justify a lower workability in consistency. More in-depth studies are needed to understand whether the fixation of the water/cement ratio, instead of spreading, had an influence on these results [10].

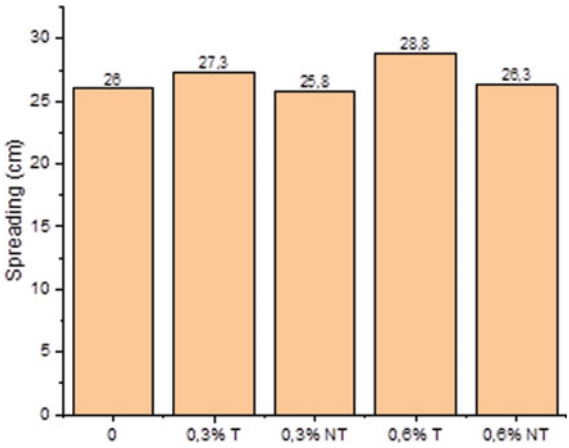

Fig. 4 Consistency index—Spread. T = treated fiber; NT = Untreated fiber

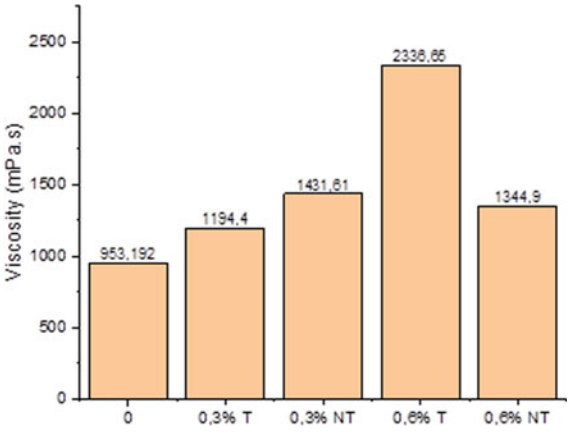

Fig. 5 Viscosity

The density test was performed in the fresh state, as can be seen in Fig. 6. The results show that the density does not have significant changes, since the addition of a relatively small percentage of fibers and because this waste is extremely light when compared to other wastes. Thus, it demonstrates that there is no compromise in the use of coconut fibers in mortars [11].

Tests in the hardened state to define the flexural and compressive strength are shown in Figs. 7 and 8, respectively. It is possible to notice that the flexural strength with the addition of 0.3% of coconut fiber was higher in the first 7 days, with a significant change in strength after 28 days. It can be seen that the addition of 0.6% of treated coconut fiber reached higher values when the reference mortar was purchased [12].

In compressive strength tests, the reference mortar presents a better performance in terms of initial strength. However, at 28 days, the addition of coconut fibers showed higher values compared to the reference mortar, with emphasis on the addition of

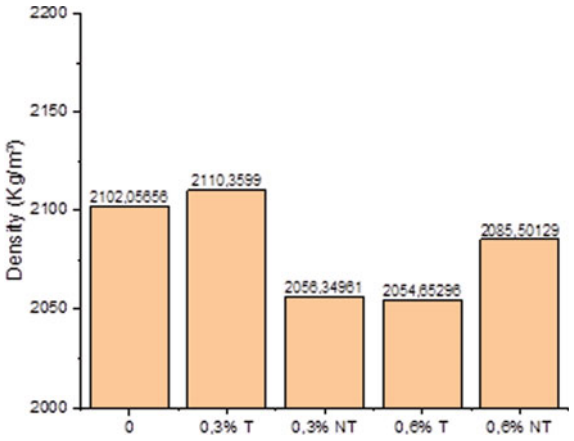

Fig. 6 Density tests in the fresh state

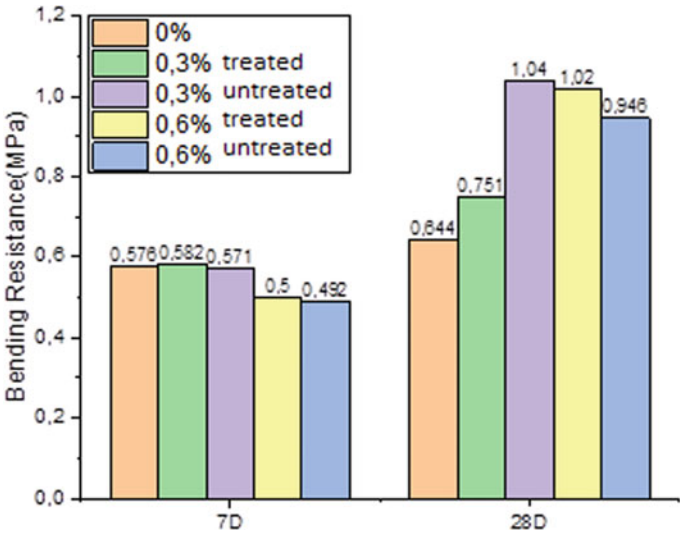

Fig. 7 Bending strength test results

0.3% without treatment, which has the highest value [13]. The results show that the addition of more than 0.3%, without any type of treatment, reduces the resistance, but still maintains a value above the reference [14].

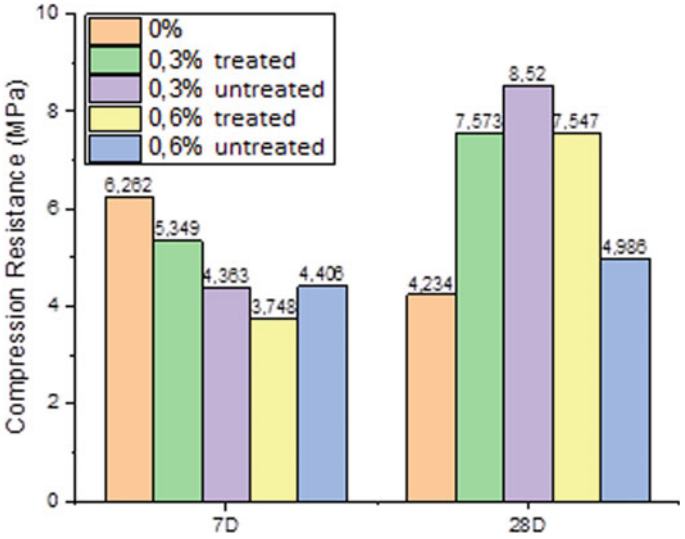

Fig. 8 Compression strength test results

Conclusion

The reuse of agricultural waste in construction materials is presented as a viable solution for a more sustainable construction and conservation of natural resources for future generations. Highlighting for being a cheap, light, durable material and available in abundance.

Based on the results, coconut fiber offers beneficial responses when added to the mortar. It increases workability and contributes to better strength even when added without treatment, showing that for an addition greater than 0.3%, treatment with sodium hydroxide positively influences the results.

It is necessary in future works a detailed analysis of its structure, as well as characteristics related to porosity, fire resistance and thermal conductivity. In addition to fixing the workability required by the norm, instead of the water-cement ratio, to achieve even more favorable parameters.

It is concluded that the mortar with the addition of coconut fiber can be studied as a reinforcement taking into account not only the previous treatment of the fibers, but also the size of the added fibers, which were not considered in the present work.

Acknowledgements This research was funded by the State university of the Northern Fluminense (UENF), partially financed by CAPES (Coordination for the Improvement of Higher Education Personnel—Brazil), CNPq (National Research Coordination) and FAPERJ (Rio de Janeiro State Research Support Foundation). The participation of ARGA was sponsored by FAPERJ through the research fellowships proc.no: E-26/210,150/2019, E-26/211,194/2021, E-26/211,293/2021, E-26/201,310/2021 and by CNPq PQ2 307592/2021-9.

References

1. Madurwar MV, Ralegaonkar RV, Mandavgane SA (2013) Application of agro-waste to sustainable building materials: a review. Constr Build Mater
2. Carasek HM (2010) ISAIA, GC civil construction materials, 2nd edn. IBRACON, São Paulo, vol 1 (In Portuguese)
3. Freitas LC, Barbosa JR, Fernanda ALCC, Bezerra WF, Pinto RHH, Carvalho Junior RN (2021) From waste to sustainable industry: how can agro-industrial waste help in the development of new products?
4. Marchi CMD (2011) World scenario of solid waste and Brazilian corporate behavior facing reverse logistics
5. Hwang C-L, Tran V-A, Hong J-W, Hsieh Y-C (2016) Effects of coconut short fiber on mechanical properties, plastic cracking behavior and impact strength of cementitious composites
6. Rashmi J, Bochen NJ, Gołaszewska M (2022) Experimental studies of the effect of natural and synthetic fibers on the properties of fresh and hardened mortars
7. Brazilian Association of Technical Norms (2005) NBR 7211: aggregates for concrete—specification. ABNT, Rio de Janeiro
8. NBR 13276 (2002) Mortar for laying and covering walls and ceilings—mixture preparation and consistency index determination. Association of Brazilian Technical Standards (In Portuguese)
9. NBR 13279 (2005) Mortar for laying and covering walls and ceilings—determination of tensile strength in bending and compression. Association of Brazilian Technical Standards (In Portuguese)
10. Marvila MT, De Azevedo ARG, De Matos PR, Monteiro SN, Vieira CM (2021) Materials for production of high and ultra-high-performance concrete: review and perspective of possible novel materials. Materials 14(15). https://doi.org/10.3390/ma14154304
11. Azevedo ARG, Marvila MT, Zanelato EB, Alexandre J, Xavier GC, Cecchin D (2020) Development of mortar for laying and coating with pineapple fiber. Revista Brasileira De Engenharia Agricola e Ambiental 24(3):187–193. https://doi.org/10.1590/1807-1929/agriambi.v24n3p187-193(InPortuguese)
12. Carvalho A, Xavier GC, Alexandre J, Pedroti LG, de Azevedo ARG, Vieira CMF, Monteiro SN (2014) Environmental durability of soil-cement block incorporated with ornamental stone waste. Mater Sci Forum. https://doi.org/10.4028/www.scientific.net/MSF.798-799.548
13. Marvila MT, de Azevedo ARG, de Oliveira LB, Xavier GC, Vieira CMF (2021) Mechanical, physical and durability properties of activated alkali cement based on blast furnace slag as a function of $\%Na_2O$. Case Stud Constr Mater 15. https://doi.org/10.1016/j.cscm.2021.e00723
14. Zeyad AM, Magbool HM, Tayeh BA, Azevedo ARG, Abutaleb A, Hussain Q (2022) Production of geopolymer concrete by utilizing volcanic pumice dust. Case Stud Constr Mater 16. https://doi.org/10.1016/j.cscm.2021.e00802

Study of the Properties of Geopolymeric Mortars with the Addition of Natural Pineapple Fibers in the Fresh State

J. A. T. Linhares, I. S. A. Pereira, A. R. G. Azevedo, S. N. Monteiro, L. U. D. Tambara, C. M. F. Vieira, and M. T. Marvila

Abstract Portland cement is widely used in civil construction due to various convenient properties, however, in its production processes a large volume of polluting gases is dispersed in the atmosphere, harming the environment. Composites of geopolymer matrices reinforced with natural fibers emerge as potential mitigators of the use of conventional cement, reducing the emission of pollutants. Pineapple crowns are a residue generated on a large scale in fruit producing places, making their use in composites possibly viable. This work carried out a chemical treatment of the fibers of the pineapple crown leaves in a 5% NaOH solution to study the properties of a geopolymeric mortar in the fresh state, with the addition of 2 and 4% of the reinforcing elements, on the mass of metakaolin. Consistency tests, density in the fresh state and viscosity were carried out, which verified a good workability of the mortars.

Keywords Geopolymer · Consistency · Pineapple fibers · Composite

J. A. T. Linhares · I. S. A. Pereira · L. U. D. Tambara · C. M. F. Vieira
LAMAV—Advanced Materials Laboratory, UENF—State University of Northern Rio de Janeiro, Av. Alberto Lamego, 2000, Campos dos Goytacazes, Rio de Janeiro 28013-602, Brazil
e-mail: vieira@uenf.br

A. R. G. Azevedo
LECIV—Civil Engineering Laboratory, UENF—State University of Northern Rio de Janeiro, Av. Alberto Lamego, 2000, Campos dos Goytacazes, Rio de Janeiro 28013-602, Brazil
e-mail: afonso@uenf.br

S. N. Monteiro
Department of Materials Science, IME—Military Institute of Engineering, Square General Tibúrcio, 80, Rio de Janeiro 22290-270, Brazil

M. T. Marvila (✉)
UFV—Federal University of Viçosa Campus Rio Paranaíba (UFV-CRP), Rodovia BR 230 KM 7, Rio Paranaíba 38810-000, Brazil
e-mail: markssuel.marvila@ufv.br

M. Zhang et al. (eds.), *Characterization of Minerals, Metals, and Materials 2023*, The Minerals, Metals & Materials Series
https://doi.org/10.1007/978-3-031-22576-5_59

Introduction

Lignocellulosic fibers have gained space in several sectors of the economy such as the automotive industry, packaging, furniture and, in particular, civil construction. This is mainly because they are environmentally friendly and have a low cost [1]. Natural fibers are generally composed of cellulose, lignin and hemicellulose. A fiber structure is summarized in microfibrillary units that unite to form single bundles [2].

Brazil is among the largest agricultural producers in the world, along with China, the United States, India, among others. In this context, the generation of agricultural solid waste has intensified and one of the most efficient ways to apply them for some purpose is in civil construction [3]. Pineapple is a characteristic fruit of tropical and subtropical regions, being widely cultivated in Brazil. One of the major problems generated by the fruit is in the extraction of the crown, which is not consumed, leading to the generation of waste in large quantities that can be used as fertilizers or as reinforcement for composites [4].

Currently, a lot of virgin raw material is consumed by the construction industry, negatively impacting the environment, generating a certain risk of exhaustion [5]. Portland cement, being the most used material, has caused serious environmental problems, as its production processes demand large amounts of energy and generate a large volume of carbon dioxide, which causes the greenhouse effect [6]. In this context, the search for alternative cementitious materials has been intensified, aiming to mitigate these impacts and the geopolymer has been presented as one of the potential alternatives [7].

Geopolymers are made by aluminosilicate sources activated by a strong alkaline solution. Geopolymer materials emit less CO2 and require less energy to manufacture [8]. The formation of the geopolymer consists of a first stage, in the dissolution of the aluminosilicates giving rise to the first gel, in the second stage, the dissolved components condense forming an inorganic polymer that has greater stability and finally in the last stage of formation, the crystallized zeolites appear [9].

Faced with the search for a more circular and green economy, the elaboration of composites of geopolymer matrices reinforced by natural fibers, from the leaves of the pineapple crowns (PALF) are a potentially viable alternative. The region of São Francisco do Itabapoana, located in the north of the state of Rio de Janeiro, Brazil, is an important producer of the fruit. With production, a large amount of agricultural waste is generated, which makes it necessary to carry out studies that enable their application for economic purposes. This work aimed to study the properties in the fresh state of geopolymeric mortars with the addition of fibers from residues generated by pineapple plantations in the city of São Francisco do Itabapoana-RJ. Compositions were prepared with the addition of 2 and 4% in relation to the mass of metakaolin. Then, the table tests of consistency, density in the fresh state and viscosity were carried out, to evaluate the impact of the addition of fibers on the workability of the mortar.

Materials and Methods

Initially, the natural fibers of the pineapple crown (PALF) were individually separated and subjected to three cycles of washing and drying in an oven at 105 ºC. Then they were processed for dimensional adequacy and then treated in an alkaline medium, in a 5% NaOH solution. These processes are generally used in the elaboration of composites that use PALF as the reinforcement phase, for a better interaction and transfer of tensions between matrix and reinforcement [10].

Geopolymer compositions reinforced with 2 and 4% of PALF were prepared for this work, in relation to the mass of precursor material, according to Table 1.

The activating solution was prepared 24 h in advance. The fibers were previously homogenized in the solution and then all the components were joined in a mortar. Immediately after the preparation of the mortars, the table tests of consistency, density in the fresh state and viscosity were performed.

The consistency table test followed the procedures of the NBR 13,276 [11] standard. The standard marked out the test in an adapted way, since it is applied to conventional Portland cement mortars. The ideal index prescribed is 260 ± 5 mm, however geopolymer mortars have their particularities. The frustoconical mold was positioned in the center of the table and was filled in three layers, each layer being necessary to perform a homogeneous densification, using a socket. In all, 15 blows were applied to the first layer, 10 to the second and 5 to the third. Then the mold was removed for the manual execution of 30 drops in a period of 30 s. After the falls, three diameters were measured evenly distributed in the mortar, using a ruler. The consistency index was then obtained from the average of these three measures. The equipment used in the test is shown in Fig. 1.

The density in the fresh state was measured based on the NBR 13,278 [12] standard, in which the mass and volume of the empty container were obtained, shown in Fig. 2. The mortar prepared was added to the container in three equal fractions, making 20 strokes with a socket to consolidate each layer. Then, three drops were performed to eliminate voids. The surface was then scraped and then the mass of the filled container was recorded. After obtaining the parameters, it was possible to calculate the density in the fresh state.

To supply was provided, of the mortars shown in Fig. 3. Immediately after homogenization of the components, a beaker was filled halfway and the viscosity was measured for a period of 1 min, recording 45 measurements, from which the average was taken. The temperature used was 24 ºC at a rotation of 60 RPM.

Table 1 Compositions of mortar

Composition	Metakaolin (g)	Sand (g)	PALF (g)	NaOH (g)	Sodium silicate (g)	Water (g)
Reference	480	480	–	27	132	273
2.0%	480	480	9.6	27	132	273
4.0%	480	480	19.2	27	132	273

Fig. 1 Consistency table, frustoconical mold, ruler and socket used

Fig. 2 Cylindrical container used to obtain the density in the fresh state

Results and Discussion

The consistency table tests are shown in Fig. 4. There was a considerable drop in consistency from 17.63% for 2% PALF addition and 33.5% for 4% addition. The added fibers subtract part of the water from the reaction medium, that is, the water present in the activator solution, leading to a great reduction in the workability of the geopolymeric mortar. Despite the alkaline treatment making the fibers less hygroscopic, in this case they still retained a large part of the free water that would contribute to the greater fluidity of the material [4].

Fig. 3 MVD-8 digital viscometer

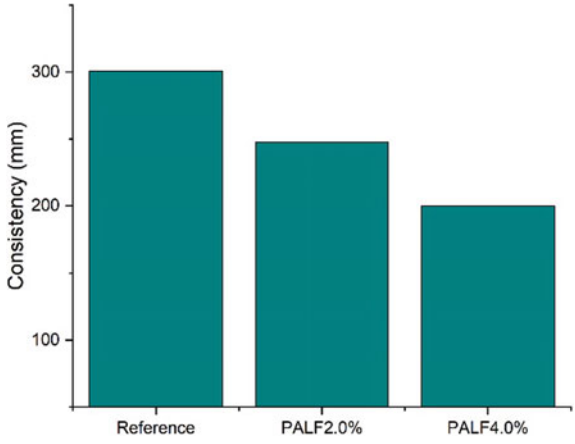

Fig. 4 Results of the consistency index

The density in the fresh state, as expected, reduced considerably as shown in Fig. 5. The drop occurs mainly due to the difference in the specific density of each material, the fiber being much lower than the geopolymer matrix. Composites with lower mass densities are better for civil construction, as they are lighter, however, some studies show that values below 1900 kg/m^3 can generate problems that may compromise the integrity of the material [13].

The addition of natural fibers directly impacts the rheological properties of the mortars, causing a large increase in viscosity as shown in Fig. 6. The viscosity

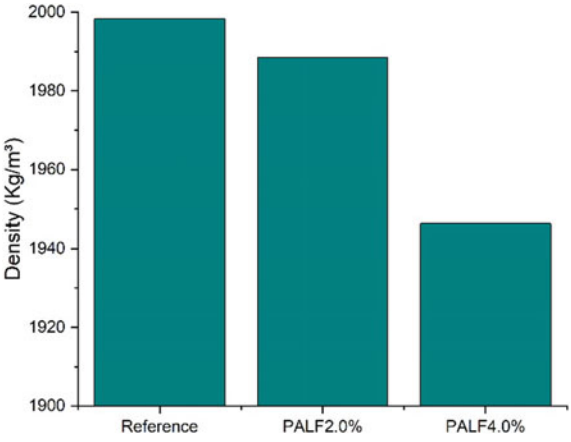

Fig. 5 Density in the fresh state of geopolymeric mortars

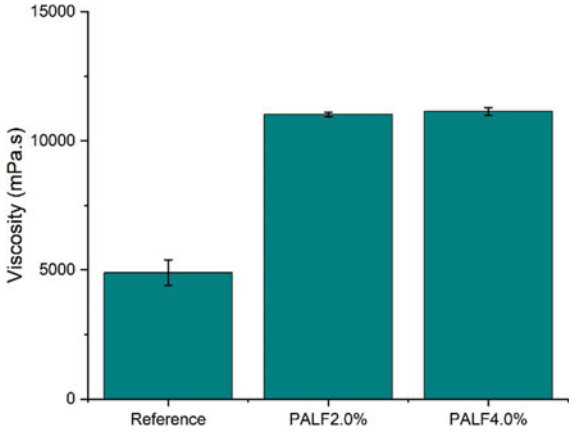

Fig. 6 Viscosity results

increased approximately twice compared to the reference composition and this occurs mainly by the absorption of free water, by the added fibers, and this increases the solid fraction of the composition, which is a preponderant fact in the increase in viscosity [14]. The high viscosity reduces workability, corroborating the consistency results.

Conclusion

Based on the results obtained, it is generally concluded that the compositions with the addition of 2 and 4% of PALF impacted in a great reduction of the workability of the mortars. The addition of 4% reduced the consistency by one third in relation

to the reference, indicating the composition with an intermediate addition of 2% as closer to the 260 mm predicted by the standard.

The density results in the fresh state were satisfactory, since both fiber additions reduced it, being positive for the weight of the constructions. No composition resulted in density below 1900 kg/m^3, so it is concluded that the addition of 4% was the most efficient in this property. The viscosity doubled with the addition of fibers, however, there was little difference between 2 and 4%. It is concluded that the addition of 4% was the best due to the low impact between the compositions in this property.

It is concluded with the study of the properties in the fresh state that in cases that demand more plasticity and application time of the geopolymer mortar with the addition of fibers, the addition of 2% is used, since it was the one that presented the most adequate consistency, however in other faster applications that demand less plasticity, the addition of 4% would be the most indicated.

Acknowledgements The authors thank the Brazilian agencies CNPq, CAPES, and FAPERJ for the support provided to this investigation.

References

1. Luz FS, Ramos FJHTV, Nascimento LFC, Figueiredo ABHDS, Monteiro SN (2018) Critical length and interfacial strength of PALF and coir fiber incorporated in epoxy resin matrix. J Market Res 7(04):025
2. Uppal N, Pappu A, Gowri VKS, Thakur VK (2022) Cellulosic fibres-based epoxy composites: from bioresources to a circular economy. Ind Crops Prod 182:114895
3. Azevedo ARG et al (2022) Possibilities for the application of agro-industrial wastes in cementitious materials: a brief review of the Brazilian perspective. Cleaner Mater 3:100040
4. Azevedo AR, Marvila MT, Zanelato EB, Alexandre J, Xavier GC, Cecchin D (2020) Development of mortar for laying and coating with pineapple fiber. Revista Brasileira de Engenharia Agricola e Ambiental 24. https://doi.org/10.1590/1807-1929
5. Sandanayake M, Law D, Sargent P (2022) A new framework for assessing the environmental impacts of circular economy friendly soil waste-based geopolymer cements. Build Environ 210:108702
6. Zhu X et al (2022) Effects of carbon nanofibers on hydration and geopolymerization of low and high-calcium geopolymers. Cement Concr Compos 133:104695
7. Mohd Tahir MF et al (2022) Potential of industrial By-Products based geopolymer for rigid concrete pavement application. Constr Build Mater 344:128190
8. Mendes BC et al (2022) Evaluation of eco-efficient geopolymer using chamotte and waste glass-based alkaline solutions. Case Stud Constr Mater 16:e00847
9. Junior JAL, Azevedo ARG, Marvila MT, Teixeira SR, Fediuk R, Vieira CMF (2022) Influence of processing parameters variation on the development of geopolymeric ceramic blocks with calcined kaolinite clay. Case Stud Constr Mater 16:e00897
10. Silva G, Kim S, Aguilar R, Nakamatsu J (2020) Natural fibers as reinforcement additives for geopolymers—a review of potential eco-friendly applications to the construction industry. Sustain Mater Technol 23:e00132
11. NBR 13276 (2002) Argamassa para assentamento e revestimento de paredes e tetos—Preparo da mistura e determinação do índice de consistência. Assoc. Bras. Normas Técnicas.
12. NBR 13278 (2005) Argamassa para assentamento e revestimento de paredes e tetos - Determinação da densidade de massa e do teor de ar incorporado. Assoc. Bras. Normas Técnicas

13. Azevedo ARG, Lima TES, Reis RHM, Oliveira MS, Candido VS, Monteiro SN (2022) Guaruman fiber: a promising reinforcement for cement-based mortars. Case Stud Constr Mater 16:e01029
14. González-Fonteboa B, González-Taboada I, Carro-López D, Martínez-Abella F (2021) Influence of the mixing procedure on the fresh state behaviour of recycled mortars. Constr Build Mater 299:124266

Study on Conductivity of Molten Mold Flux

Yijia Wang, Mingxing Wang, Yu Wang, Hongpo Wang, Bo Bai, and Fushen Li

Abstract To investigate the effect of electromagnetic field on molten mold flux, the electrical conductivity of the $CaO–SiO_2–Al_2O_3–MgO–CaF_2–Na_2O$ system was tested by the AC four-electrode method, and the influencing factors and change in the law of conductivity of the molten mold flux was analyzed. The results show that the conductivity of molten mold flux increases with the increasing content of Na_2O, CaF_2, and other components, and the basicity of mold flux. In this work, the electrical conductivity of the molten mold flux is approximately 0.026–0.810 Ω^{-1} cm^{-1}. For every 0.1 increase in optical basicity, the conductivity increases by about 58.7%. As the temperature increases every 25 K, the conductivity increases by about 27.2%.

Keywords Molten mold fluxes · Electrical conductivity · AC four-electrode method

Introduction

Mold flux, an important functional material in the continuous casting process, plays a role in controlling heat transfer, lubricating, absorbing assimilation inclusions, preventing secondary oxidation of molten steel, and thermal insulation, which can effectively improve the efficiency of continuous casting and the surface of the slab quality. With the deepening of research, electromagnetic field technology is widely used in metallurgy, material preparation and other fields due to its unique thermal and mechanical effects.

By using the thermal effect and force effect generated by the electromagnetic field, the fluid motion properties, shape and momentum transfer in the metallurgical process are affected [1]. The application of electromagnetic technology in the continuous casting process has greatly improved the efficiency of continuous casting and the quality of the slab [2–4]. It is now recognized that the electronic conductance of slag is accomplished by transition metal oxides (such as iron oxides) in the

Y. Wang · M. Wang · Y. Wang (✉) · H. Wang · B. Bai · F. Li
College of Materials Science and Engineering, Chongqing University, Chongqing 400045, China
e-mail: wangyu@cqu.edu.cn

M. Zhang et al. (eds.), *Characterization of Minerals, Metals, and Materials 2023*, The Minerals, Metals & Materials Series
https://doi.org/10.1007/978-3-031-22576-5_60

slag, while other oxides form ionic conductance. In general, the percentage of ionic bonds of the M–O bond in molten basic oxide is relatively large, and the ability to release simple ions is relatively strong, so it has a relatively large conductivity, that increases with the alkalinity [5]. Diaz [6] measured the electrical conductivity of pure oxidizing substances and obtained the following order: SiO_2 (10^{-5} Ω^{-1} cm^{-1}) < Al_2O_3 (15 Ω^{-1} cm^{-1}) < MgO (35 Ω^{-1} cm^{-1}) $^{-1}$) < CaO (40 Ω^{-1} cm^{-1}). Since SiO_2 is a network former oxide, in the slag based on SiO_2, the ion migration is greatly resisted by the network former, and the number of ions that can move freely is small, so the electrical conductivity will decrease. In contrast, Diaz measured the conductivity of pure FeO slag at 1643 K (iron crucible) to be 122 Ω^{-1} cm^{-1}. For the slag mediated by electronic conduction, Lu et al. [7] studied the effect of electrical conductivity on the decarburization reaction, and found that there are a large number of free electrons and holes in the slag containing transition metal oxides (such as TiO, Fe_2O_3). The increase of electron conductivity in the slag can promote the rate of decarburization reaction between slag and Fe–C droplets, reduce the mass fraction of carbon to a lower level, and improve the efficiency of decarburization reaction. Heika [8] used deionized water as a slurry, air-cooled slag and water-cooled slag as raw materials, and measured the conductivity value of calcium portland cement (CAC) paste containing different mass fractions of slag at low temperatures as a function of hydration time It is found that the electrical conductivity is an effective method to divide the phase composition change of calcium aluminate cement at different temperatures. Regarding the research on the measurement of slag conductivity, Yu et al. [9] analyzed the conductivity mechanism of continuous casting mold flux., the conductivity of mold flux for medium carbon steel slabs with CaO/SiO_2 between 1.0 and 1.1 increases with the increase of basicity and temperature, and the conductivity of mold flux is approximately 0.195–0.72 Ω^{-1} cm^{-1}. Regarding analyzing the influencing factors of slag electrical conductivity, electrical conductivity is a physical property greatly affected by the structure. In the ion-conductive slag structure, the main determinants of electrical conductivity are the mobility of alkali metal cations, ion concentration and ion interaction force. In molecular, atomic, or solid systems, density functional theory treats single-electron density as an independent variable and uses functionals to represent energy and other physical quantities. Combining the electronegativity equilibrium theory with density functional theory, Shen Erzhong revised the calculation formula of effective electronegativity and energy [10].

In this paper, continuous casting mold flux is taken as the research object, and the main factors and mechanism of influence on the conductivity of mold flux are analyzed based on the experimental measurement data of electrical conductivity. It positively affects quantitatively analyzing the influence of components and temperature on the conductivity of mold flux, optimizing and regulating the function of mold flux under the action of electromagnetic field, and enriching the design and development ideas of mold flux.

Experimental Methods and Materials

Experimental Method

In this paper, the AC four-electrode method is used. The principle of AC four-electrode test is shown in Fig. 1a–d are four electrodes. The current flows into the slag to be measured through electrodes a and b, and a voltage drop is formed between electrodes b and c. According to Ohm's law, the melt resistance Rx between is obtained electrodes b and c:

$$R_x = \frac{Ex}{I_S} \tag{1}$$

$$I_S = \frac{E_S}{R_\mathrm{f}} \tag{2}$$

$$R_x = \frac{Ex}{E_S} \cdot R_\mathrm{f} \tag{3}$$

It can be seen from Eq. 3 that when R_f is known, the bulk resistance of the slag to be measured can be calculated only by measuring E_x and E_S, and the slag conductivity κ can be obtained by combining the conductivity the cell constant C.

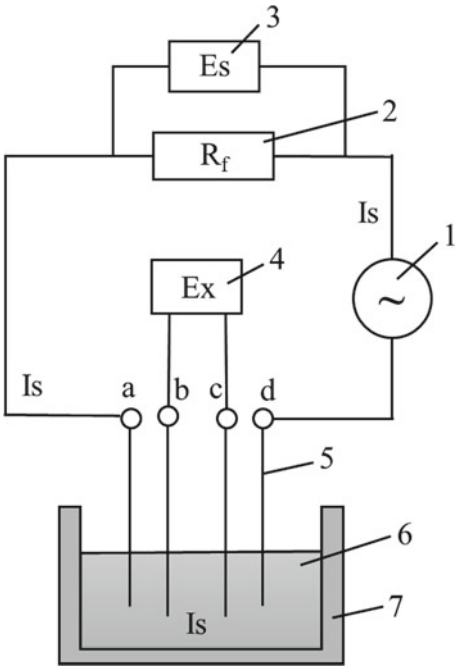

Fig. 1 Schematic diagram of ac quadrupole method. 1—AC power supply; 2—standard resistance; 3—standard resistance voltage drop; 4—slag voltage drop; 5—electrode; 6—slag; 7—crucible

Table 1 Composition and basic parameters of slag produced in a factory

	CaO	SiO_2	Al_2O_3	MgO	F^-	Na_2O	$C_{固}$
Factory slag	32.96	27.52	2.57	3.05	7.84	11.17	5.31

Table 2 Chemical composition of slags for the experiment (wt%)

Numbering	CaO	SiO_2	Al_2O_3	MgO	Na_2O	CaF_2	合计
A1	38.170	31.800	2.720	4.570	5.810	16.930	100
A2	37.070	30.900	2.720	4.570	7.810	16.930	100
A3	35.990	29.980	2.720	4.570	9.810	16.930	100
A4	34.860	29.110	2.720	4.570	11.810	16.930	100
A5	33.824	28.186	2.720	4.570	13.800	16.900	100
B1	35.630	29.680	2.720	3.230	11.810	16.930	100
B2	36.180	29.130	2.720	3.230	11.810	16.930	100
B3	36.920	28.390	2.720	3.230	11.810	16.930	100
B4	37.520	27.790	2.720	3.230	11.810	16.930	100
B5	38.100	27.208	2.720	3.230	11.810	16.930	100
C1	38.590	32.150	2.720	3.930	11.810	10.800	100
C2	37.480	31.220	2.720	3.930	11.810	12.840	100
C3	36.740	30.620	2.720	3.230	11.810	14.880	100
C4	35.630	29.680	2.720	3.230	11.810	16.930	100
C5	34.468	28.724	2.720	3.230	11.810	19.048	100

Mold Flux Design

This paper uses a commercial mold flux as the base slag, and the composition is shown in Table 1. On the basis of the original slag, the composition was adjusted, and the change of the electrical conductivity and the effect on the performance were studied by changing the composition of the flux. Three groups of experimental slag were designed, namely Group A (A1–A5), Group B (B1–B5) and C Groups (C1–C5), and the composition of the experimental slag samples is shown in Table 2.

Results and Analysis

Influence of Na_2O on the Conductivity of Mold Flux

Figure 2 shows the experimental results of the effect of Na_2O on the conductivity of slag in group A slag at different temperatures.

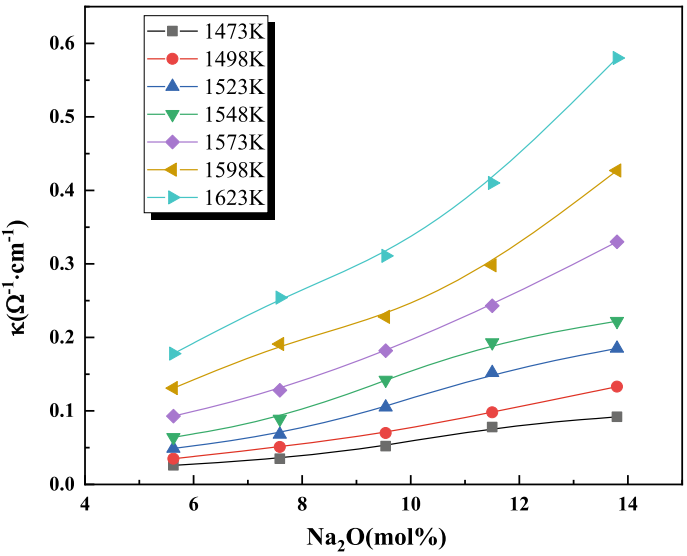

Fig. 2 Change of conductivity of protective slag under different Na_2O content

It can be seen from the figure that when the temperature is constant, the electrical conductivity increases with the increase of Na_2O content. Under the same Na_2O content, the higher the temperature, the greater the electrical conductivity. In the lower temperature range (1473–1548 K), the electrical conductivity rises relatively gently with the increase of Na_2O content. For every 1% increase of Na_2O content, the minimum conductivity increase rate is 13.06% and the maximum is 37.32%; in the higher temperature range (1573–1623 K), the conductivity increases more greatly with the increase of Na_2O content. For every 1% increase of Na_2O content, the minimum increase rate of conductivity is 18.32%, and the maximum is 45.80%. In the experimental temperature range, the average increase rate of conductivity is 17.6% for every 1% increase of Na_2O. At 1473 K, the conductivity is only 0.026–0.092 Ω^{-1} cm−1, and at 1523 K, the conductivity increases to 0.049–0.185 1623 KΩ^{-1} cm^{-1}, and when the temperature rises to 1623 K, the conductivity rapidly increases to 0.178–0.580 Ω^{-1} cm^{-1}, and the change of conductivity is more significantly affected by temperature with the increase of Na_2O content, and the increase range is larger.

At 1473 K, the conductivity is only 0.026–0.092 Ω^{-1} cm^{-1}, at 1523 K, the conductivity increases to 0.049–0.185 Ω^{-1} cm^{-1}, and when the temperature rises to 1623 K, the conductivity rapidly increases to 0.178–0.580 Ω^{-1} cm^{-1}, and the change of conductivity is more significantly affected by temperature with the increase of Na_2O content, and the increase range is larger.

Influence of CaF_2 on the Conductivity of Mold Flux

For group C slag, the experimental results of the effect of CaF_2 content on the conductivity of the slag at different temperatures are shown in Fig. 3.

It can be seen from the figure that when the temperature is constant, the electrical conductivity increases with the increase of the CaF_2 content. Under the same CaF_2 content, the higher the temperature, the greater the electrical conductivity; as the CaF_2 content increases, the magnitude of the electrical conductivity changes with the temperature increases.

In the lower temperature range (1473–1523 K), the electrical conductivity rises relatively gently with the increase of CaF_2 content. For every 1% increase in CaF_2 content, the minimum conductivity increase rate is 10.25% and the maximum is 31.82%; in the higher temperature range (1548–1623 K), the electrical conductivity increases with the increase of CaF_2 content, and the increased rate of electrical conductivity increases by 1% for every 1% increase of CaF_2 content. In the experimental temperature range, the average increase rate of conductivity is 18.6% for every 1% increase in CaF_2 content.

When the temperature is 1498 K, the electrical conductivity of the C group slag (C1–C5) is 0.062 Ω^{-1} cm^{-1}, 0.072 Ω^{-1} cm^{-1}, 0.085 Ω^{-1} cm^{-1}, 0.098 Ω^{-1} cm^{-1} and 0.121 Ω^{-1} cm^{-1} respectively. Under the same increment of CaF2, the maximum conductivity change rate is 19.01%; when the temperature is 1623 K, the C The group conductivities were 0.281 Ω^{-1} cm^{-1}, 0.308 Ω^{-1} cm^{-1}, 0.326 Ω^{-1} cm^{-1}, 0.411 Ω^{-1} cm^{-1} and 0.535 Ω^{-1} cm^{-1}, respectively. It can be seen that the higher the CaF_2

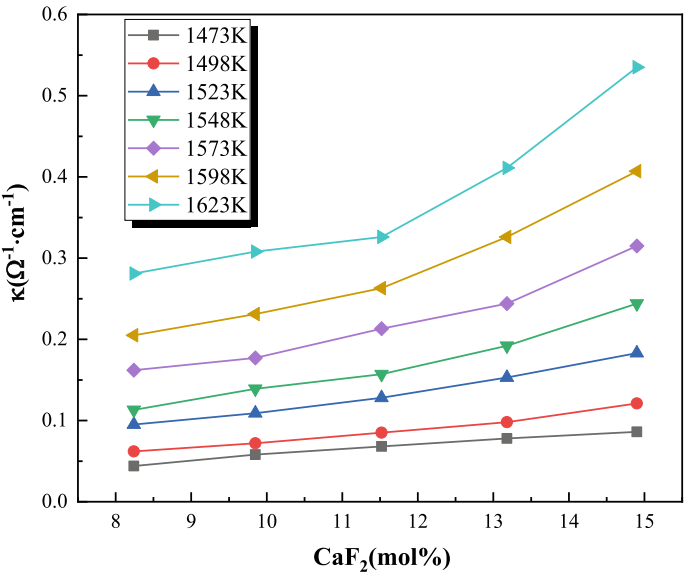

Fig. 3 Change of conductivity of protective slag under different CaF_2 content

content, the more obvious the change of conductivity, and the greater the increase with the increase of temperature.

The Effect of Alkalinity on the Conductivity of Mold Flux

Using the corrected optical alkalinity mentioned above, the influence of temperatures on the conductivity was analyzed. The experimental results are shown in Fig. 4.

It can be seen from Fig. 4 that when the corrected optical alkalinity increases from 0.75 to 0.79, the conductivity of the mold flux shows an upward trend, and the larger the value, the greater the rate of change of the conductivity under the same temperature difference.

The temperature range is 1473–1548 K, and for every 0.1 increase in Λ^{corr}, the minimum conductivity increase rate is 15.62%, and the maximum is 117.18%; the temperature range is 1573–1623 K, for every 0.1 increase in Λ^{corr}, the conductivity increase rate is minimum 30.98%, maximum 90.33%; The average increase in conductivity was 58.7%. The higher the temperature, the more obvious the upward trend of the electrical conductivity with the increase of the corrected optical alkalinity, and the greater the increase range.

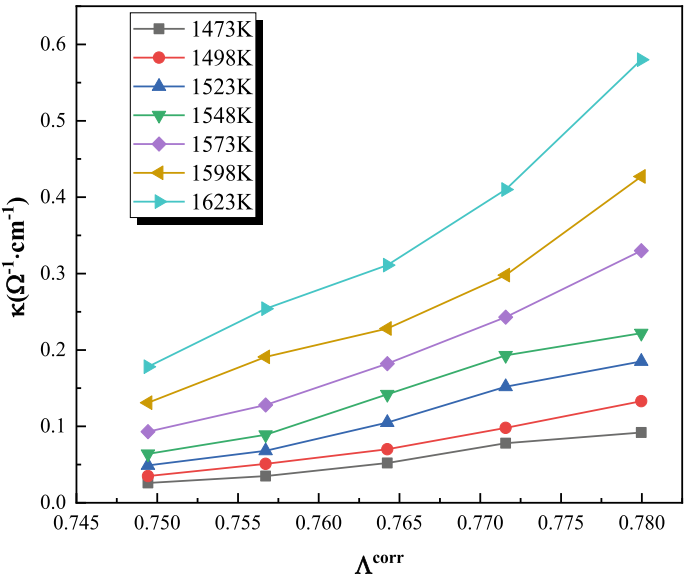

Fig. 4 Electrical conductivity of slag of different Λ^{corr}

The Effect of Temperature on the Conductivity of Mold Flux

Generally, the relationship between the conductivity and temperature of the slag follows the Arrhenius equation [11].

$$\kappa = A \exp(-E/RT)$$

or

$$\ln \kappa = \ln A - E/RT \tag{4}$$

In the formula, κ is the conductivity, Ω^{-1} cm^{-1}; A is the pre-exponential factor; E is the conductivity activation energy, J/mol; T is the temperature, K.

In order to study the effect of temperature on conductivity when the composition and alkalinity of the mold flux are constant, take 104/T as the abscissa and the logarithm of the conductivity as the ordinate to draw a graph to obtain the conductivity of the mold flux in groups A, B and C. The relationship between rate and temperature is shown in Fig. 5.

It can be seen from Fig. 5a that when the Na_2O content is constant, for every 25 K increase in temperature, the minimum conductivity increase rate is 16.66%, the maximum is 35.53%, and the average increase is 26.25%.

It can be seen from Fig. 5b that when the alkalinity is constant, for every 25 K increase in temperature, the minimum conductivity increase rate is 14.96%, the maximum is 28.9%, and the average increase is 21.93%.

It can be seen from Fig. 5c. When the content of CaF_2 is constant, the minimum increase rate of conductivity is 18.94%, the maximum is 56.12%, and the average increase rate is 33.49% when the temperature increases by 25 K.

In summary, due to the increase in temperature, the mobility of ions is enhanced, and the mobility of the conductive ions is improved. When the component content is constant, the temperature increase will improve the slag's conductivity. When the content of mold flux components is constant, the average increase of electrical conductivity is about 27.2% for every 25 K increase in temperature.

Conclusion

In this paper, the AC four-electrode method is used to test the electrical conductivity of the CaO–SiO_2–Al_2O_3–MgO–CaF_2–Na_2O series continuous casting mold flux, and the influence of the main components of the mold flux and the temperature on the conductivity of the molten mold flux is studied. Under the conditions of this study, the electrical conductivity of the molten mold flux increases with the increase of temperature. The temperature is 1473–1623 K, the corrected optical basicity is 0.749–0.787, and the conductivity range of the mold flux is 0.026–0.810 Ω^{-1} cm^{-1}.

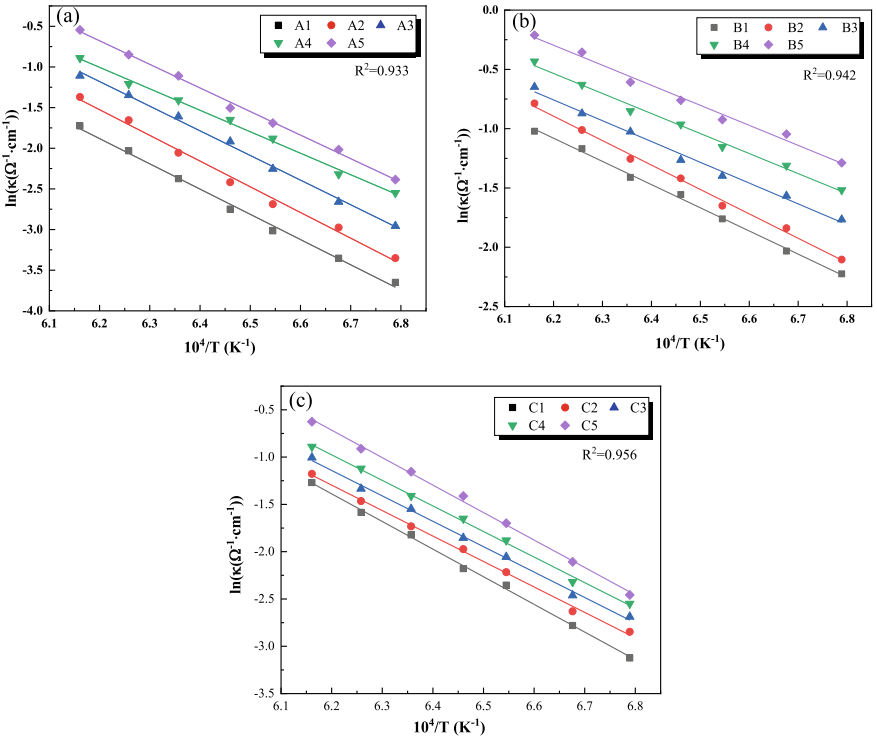

Fig. 5 Change of conductivity of protective slag at different temperatures. **a** group A. **b** group B. **c** group C

Among them, for every 1% increase of Na_2O content, the conductivity increases by about 17.6% on average; for every 0.1 increase in Λ^{corr}, the conductivity increases on average by about 58.7%; for every 1% increase of CaF_2 content, the conductivity increases on average by about 18.6%. For every 25 K increase in temperature, the conductivity increases by about 27.2% on average.

References

1. Shumei K (2017) Electromagnetic metallurgy. Metallurgical Industry Press
2. He J, Lei H, Wang Q (2019) Computational metallurgy. Science Press
3. He F, He X (2020) Physical properties of materials and their applications in materials research. Harbin Institute of Technology Press
4. Ayata K, Lnoue T, Mori H et al (2002) Improvement of billet surface quality by ultra-high-frequency electromagnetic casting. Revue De Métallurgie 42(11):1025–1032
5. Mills KC, Yuan L, Jones RT (2011) Estimating the physical properties of slags. J South Afr Inst Min Metall 111(10):649–658
6. Diaz C (1974) The thermodynamic properties of copper-slag systems. International Copper Research Association

7. Lu X, F Li, Li L et al (1998) Influence of conductivity of slag on decarburization reaction. J Univ Sci Technol Beijing (Eng Edn) 1998(01):20–22
8. Heikal M, Morsy MS, Radwan M (2005) Electrical conductivity and phase composition of calcium aluminate cement containing air-cooled and water-cooled slag at 20, 40 and 60°C. Cem Concr Res 35(7):1438–1446
9. Wang Y, Wei Z, Liu Y et al (2010) Research on the electrical conductivity of molten mold flux. In: 2010 national metallurgical physical chemistry conference
10. Shen E, Yang Z (1996) Molecular electronegativity under density functional theory: III. Direct calculation of total molecular energy. Acta Chem Sinica 54(002):152–159
11. Jiang Z et al (2015) Electroslag metallurgy. Science Press

Synthesis and Characterization of SnO_2 Nanoparticles Obtained by Sol–Gel Method

Frida S. Yañez, Atxayacalt O. Flores, Iraís Cardenas, Iván A. Reyes, Laura García, Pedro A. Ramírez, Rubén H. Olcay, and Mizraim U. Flores

Abstract Tin oxide nanoparticles were synthesized using the sol–gel technique, where metallic tin, ammonia hydroxide, nitric acid, ascorbic acid, ethanol, and deionized water were used. A white powder characteristic of tin oxide was obtained. X-ray diffraction was performed on the synthesis product and identified as cassiterite (SnO_2), with a tetragonal unit cell, which lattice parameters are at $a = 4.74$ Å and $c = 3.19$ Å, the ICDD-PDF letter is 96-210-4755. Scanning electron microscopy characterization showed that nanoparticles have a spherical morphology and sizes ranging from 23 to 67.6 nm. Analysis performed by infrared spectroscopy show that it has the tin bond oxygen 667 cm^{-1} region.

Keywords Synthesis · Characterization · SnO_2 nanoparticles · Sol–gel method

Introduction

Nanotechnology has had a huge impact on science, because the small size can allow the automation of tasks that were previously inaccessible due to physical constraints. The main benefits of nanotechnology include improved manufacturing methods, water purification systems, energy systems, physical improvement, nanomedicine,

F. S. Yañez · A. O. Flores · I. Cardenas · L. García · P. A. Ramírez · M. U. Flores (✉)
Área de Electromecánica Industrial, Universidad Tecnológica de Tulancingo, Camino a Ahuehuetitla #301 Col. Las Presas, Tulancingo, Hidalgo 43642, México
e-mail: mflores@utectulancingo.edu.mx

I. A. Reyes
Instituto de Metalurgia, Universidad Autónoma de San Luis Potosí, San Luis Potosí 78210, México

Catedrático CONACYT, Consejo Nacional de Ciencia y Tecnología, Benito Juárez, 03940 Ciudad de México, México

R. H. Olcay
Departamento de Ingeniería Metalúrgica, Facultad de Ingeniería y Arquitectura, Universidad Arturo Prat, Iquique, Chile

M. Zhang et al. (eds.), *Characterization of Minerals, Metals, and Materials 2023*, The Minerals, Metals & Materials Series
https://doi.org/10.1007/978-3-031-22576-5_61

better food production methods, nutrition and large-scale self-manufacturing infrastructure. So nanotechnology is the study of the synthesis, characterization and application of matter at the nanometric scale, which in recent years has seen a great interest in nanoparticles, especially metal nanoparticles, such as zinc oxide (ZnO), silver (Ag), gold (Au), copper (Cu) titanium dioxide (TiO_2) and tin oxide (SnO), although the latter have not been very studied because they show some limitations to obtain them because it is complex. Tin oxide is a wide band, n-type semiconductor (about 3.5 eV) and, in the form of thin sheets, is a transparent conductive material, characterized by a high optical transmission (80–90%). Tin oxide has two crystalline phases, romarchite (SnO) and cassiterite (SnO_2), the latter being the most stable due to the tetragonal arrangement of atoms [1–4]. The heat of formation of cassiterite structure is $\Delta H = 1.9 \times 103$ J mol^{-1} and the heat capacity of the material is Cp = 52.59 J mol^{-1} K^{-1}; its density at 25 °C is 6.95 g cm^{-3} and the melting point of the material is 1630 °C. This crystalline structure contains metal atoms in octahedral coordination and oxygen in planar coordination; the lattice parameters are a = 4.737 Å and c = 3.186 Å [1–3]. The physical and chemical properties of crystalline tin oxide are often different from crystalline or amorphous. These properties depend on the crystalline structure and morphology, as well as on the grain size. The synthesis of tin oxide nanostructures with the desired structure and morphology is of great scientific and technological interest, due to their superior physical and chemical properties and their wide range of applications, such as gas sensors, photocatalysts, nanofiltration membranes, thermal mirrors and glass coatings. Therefore, it is very important to develop ways to control its dimensions, structure, surface and interface properties.

Tin oxide nanoparticles (SnO_2 NP's) can be synthesized by different methods, generally classified as chemical, physical and biosynthesis methods. Chemical methods are effective, because the process and equipment required are simple, and they also offer the advantage of being easy and economical to perform. These can be synthesized by sol–gel [1], mechanochemical [2], co-precipitation [3], hydrolysis [4], microwave [5] and precipitation [6].

Applications reported by various authors of tin oxide nanoparticles have been reflected as optoelectronic devices [7], catalysis [8], dye-based solar cells [9], medicine [10], photosensors and antistatic coatings [11].

Therefore, in this work the synthesis of tin oxide nanoparticles (SnO_2 NP's) was performed using a methodology of Zhang et al. [12] but with a novel reagent: ascorbic acid, in which nanoparticles of SnO_2 in the form of cassiterite with a diameter size of 23–67.6 nm were favorably obtained with a spherical morphology. By X-ray diffraction it was possible to determine that there is a crystalline phase of tin oxide, which has been confirmed as cassiterite and by FTIR-ATR was confirmed the presence of metal oxides.

Materials and Methods

For the synthesis of tin oxide nanoparticles, 8 M of HNO_3 was added to a mixture of 3 g of metallic tin shot and 10 g of ascorbic acid in a flask, stirred at 300 rpm. The solution was filtered to remove lead in solid form, because tin was a Sn–Pb alloy. Ammonium hydroxide (25%) was added drop by drop to the solution with agitation until a pH of 8 was reached, the solution slowly developed into a turbid colloidal solution. The solution was centrifuged at 300 rpm for 20 min to recover the precipitate, and washed several times with 50/50 ethanol and water solution. It dried at 100 °C for 5 h in a muffle. The powder obtained was ground in a mortar, and finally roasted in an oven at 400 °C for 2 h. This whole process is shown in Fig. 1.

To identify the synthesized compound, X-ray diffraction was performed, and equipment used is a Bruker D8 powder diffractometer, with Ni filtered radiation from a Cu anode, $k_{\alpha 1} = 1.5406$ Å; 40 kV and 35 mA. Diffraction patterns were recorded in the angular range 2θ of 10–80°, with a step size = 0.01° and a step time = 3 s. Scanning electron microscopy (SEM) was used to determine the morphology and size of nanoparticles, the equipment is a Field Emission Scanning Electron Microscopy-Energy Dispersive X-Ray Spectrometry (FESEM-EDS a JEOL JSM-670 IF, JEOL, Tokyo, Japan). The metal oxide was confirmed by FTIR-ATR y in a PerkinElmer Spectrum Two with Universal ATR (PerkinElmer Inc. Waltham, MA, USA) 2500-450 cm^{-1}.

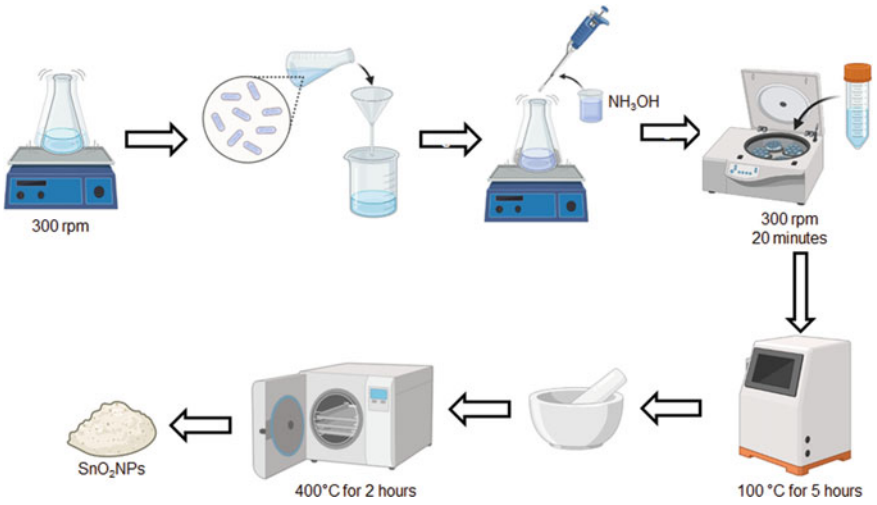

Fig. 1 Schematic methodology for synthesis of tin oxide nanoparticles

Results and Discussion

The presence of tin dioxide was confirmed by X-ray diffraction, as the peaks match with the crystallographic chart of the International Centre for Diffraction Data-Powder Diffraction File (ICDD-PDF) 00-041-1445, which belongs to the cassiterite (SnO_2). The crystalline structure of a cassiterite is tetragonal, with lattice parameters of $a = 4.7382$ Å and $c = 3.1871$ Å. Figure 2 shows the diffractogram where it is observed that the crystallographic planes match with those of the cassiterite, however, noise is shown, which is attributed to the organic acid that was used.

To determine particle size and morphology, scanning electron microscopy was used (Fig. 3), where particles with spherical morphology and size of approximately 23–67.6 nm are observed. Figure 4 shows the spectrum of energy dispersive x-ray spectroscopy, where tin, chlorine, carbon and oxygen are observed; tin and oxygen check the presence of nanoparticles of SnO_2, the chlorine is due to the washing that was given to the sample and the presence of carbon is due to the ascorbic acid that remains even after the washing of the nanoparticles.

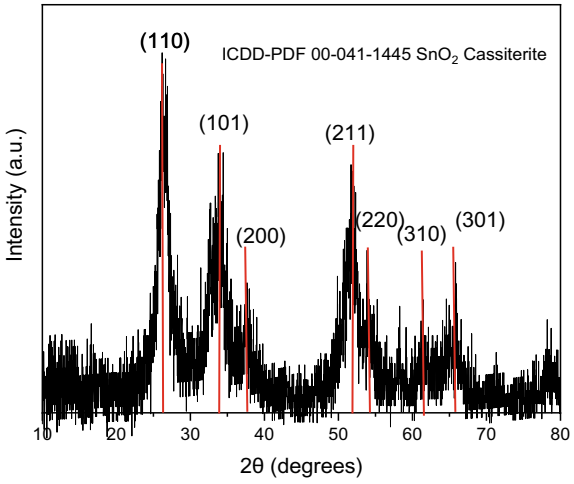

Fig. 2 X ray diffractogram of the SnO_2 synthesized

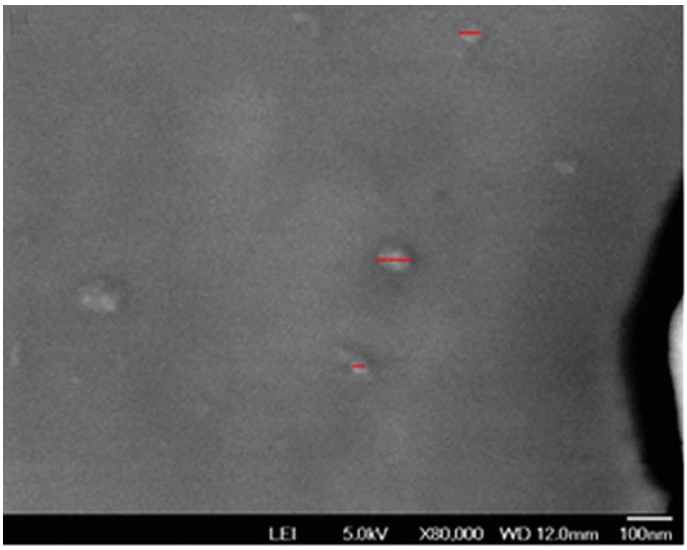

Fig. 3 SEM image of the SnO_2 nanoparticles

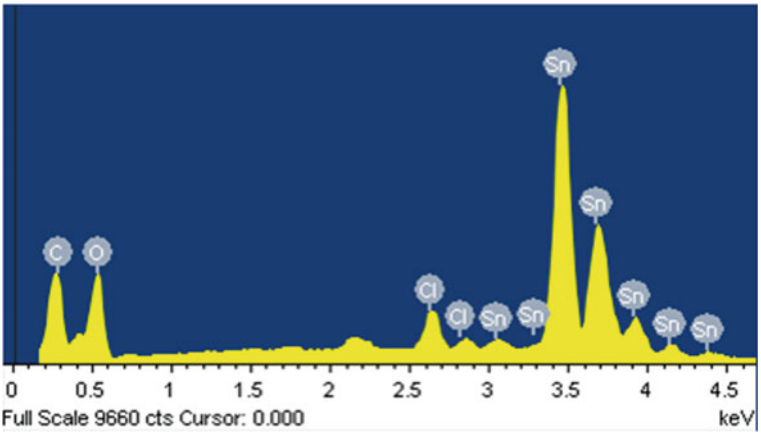

Fig. 4 EDS spectrum of the SnO_2 nanoparticles

Figure 5 shows the spectrum of FTIR-ATR made to the nanoparticles of SnO_2, which shows the presence of organic compounds even after washing the sample, these organic compounds belong to ascorbic acid and ammonium hydroxide. However, the absorption bands at 856 and 667 cm^{-1} belong to the Sn = O bond with which the presence of metal oxide is confirmed and suggests that it should be washed with some solvent to remove the excess of organic material.

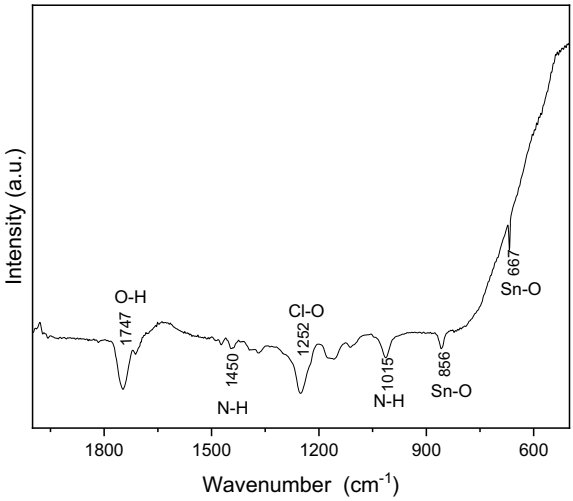

Fig. 5 FTIR-ATR spectrum of SnO_2 nanoparticles

Conclusions

The tin oxide nanoparticles were synthesized using the sol–gel method and ascorbic acid was added. The sample was characterized by DRX showing that there is tin oxide in the form of cassiterite, its unit cell parameters are $a = 4.7382$ Å and $c = 3.1871$ Å. Samples were characterized by SEM and nanoparticles of SnO_2 in size were obtained between 23 and 67.6 nm. The samples were characterized by FTIR-ATR to confirm the presence of the tin oxide bond. It is required to wash the material to remove the most amount of organic material that have since the synthesis, however, the proposed method has effectiveness, since particles of nanometric sizes are obtained and the morphology is spherical.

References

1. Subramaniam MP, Arunachalam G, Kandasamy R, Veluswamy P, Hiroya I (2017) Effect of pH and annealing temperature on the properties of tin oxide nanoparticles prepared by sol–gel method. J Mater Sci Mater Electron 29(1):658–666. https://doi.org/10.1007/S10854-017-7959-2
2. Yang H, Hu Y, Tang A, Jin S, Qiu G (2004) Synthesis of tin oxide nanoparticles by mechanochemical reaction. J Alloy Compd 363(1–2):276–279. https://doi.org/10.1016/S0925-8388(03)00473-0
3. Tazikeh S, Akbari A, Talebi A, Talebi E (2014) Synthesis and characterization of tin oxide nanoparticles via the Co-precipitation method. Mater Sci Poland 32(1):98–101. https://doi.org/10.2478/S13536-013-0164-Y
4. Guo X, Kang Y, Wang L, Liu X, Zhang J, Yang T, Wu S, Wang S (2011) Mesoporous tin dioxide nanopowders based sensors to selectively detect ethanol vapor. Mater Sci Eng, C 31(7):1369–1373. https://doi.org/10.1016/J.MSEC.2011.05.002

5. Parthibavarman M, Sathishkumar S, Prabhakaran S (2017) Enhanced visible light photocatalytic activity of tin oxide nanoparticles synthesized by different microwave optimum conditions. J Mater Sci Mater Electron 29(3):2341–2350. https://doi.org/10.1007/S10854-017-8152-3
6. Nejati-Moghadam L, Esmaeili Bafghi-Karimabad A, Salavati-Niasari HS (2015) Synthesis and characterization of SnO_2 nanostructures prepared by a facile precipitation method. Nanostructures 9–25
7. He JH, Wu TH, Hsin CL, Li KM, Chen LJ, Chueh YL, Chou LJ, Wang ZL (2006) Beaklike SnO2 nanorods with strong photoluminescent and field-emission properties. Small 2(1):116–120. https://doi.org/10.1002/smll.200500210
8. Carreño NLV, Fajardo HV, Maciel AP, Valentini A, Pontes FM, Probst LFD, Leite ER, Longo E (2004) Selective synthesis of vinyl ketone over SnO_2 nanoparticle catalysts doped with rare earths. J Mol Catal A Chem 207(2):91–96. https://doi.org/10.1016/S1381-1169(03)00496-5
9. Snaith HJ, Ducati C (2010) SnO2-Based dye-sensitized hybrid solar cells exhibiting near unity absorbed photon-to-electron conversion efficiency. Nano Lett 10(4):1259–1265. https://doi.org/10.1021/nl903809r
10. Sudhaparimala S (2014) Green synthesis of tin based nano medicine: assessment of microstructure and surface property. Am J Nanosci Nanotechnol 2(4):75. https://doi.org/10.11648/j.nano.20140204.13
11. Zhao Q, Ma L, Zhang Q, Wang C, Xu X (2015) SnO_2-based nanomaterials: synthesis and application in lithium-ion batteries and supercapacitors. J Nanomater 2015(1). https://doi.org/10.1155/2015/850147
12. Zhang J, Gao L (2004) Synthesis and characterization of nanocrystalline tin oxide by sol-gel method. J Solid State Chem 177(4–5):1425–1430

Synthesis and Structural Characterization of Eu_2TiO_5 Using Atomic Substitution with Eu^{+3} in $BaTiO_3$

R. Martínez López, M. Pérez Labra, F. R. Barrientos Hernández, J. A. Romero Serrano, A. Hernández Ramírez, M. I. Valenzuela Carrillo, M. Reyes Pérez, J. C. Juárez Tapia, and V. E. Reyes Cruz

Abstract $BaTiO_3$ is a ceramic compound of ABO_3 perovskite-type where Ba occupies the A site and Ti the B site. The saturation of the $BaTiO_3$ lattice with Eu^{3+} allows the formation of secondary phases with specific applications. In this work, the Eu_2TiO_5 phase was synthesized using the solid-state reaction method and sintering at 1300 °C for 6 h through the $Ba_{1-x}Eu_xTi_{1-x/4}O_3$ electronic compensation mechanism with $x = 0$, 10, and 15 Eu^{3+} (wt.%). The X-ray diffraction spectra of the analyzed samples indicate the presence of the crystalline phase Eu_2TiO_5 (The Joint Committee on Powder Diffraction Standards (JCPDS) 96-200-2716). Rietvel refinement analysis of the orthorhombic Eu_2TiO_5 structure indicated an increase in the lattice parameters "a", "b", and "c" and in the cell volume attributed to the increase in Eu^{+3} concentration. Additionally, the presence of Eu_2TiO_5 was verified by Raman spectroscopy studies in the band at 778 cm^{-1}. The Eu_2TiO_5 phase finds electrical, optical, magnetic, and nuclear applications.

Keywords Ceramics · Characterization · Process technology · Eu_2TiO_5 · Structural evolution

R. Martínez López (✉) · M. Pérez Labra · F. R. Barrientos Hernández · M. I. Valenzuela Carrillo · M. Reyes Pérez · J. C. Juárez Tapia · V. E. Reyes Cruz
Area Académica de Ciencias de la Tierra y Materiales, Universidad Autónoma del Estado de Hidalgo, Mineral de la Reforma 42184, Hidalgo, Mexico
e-mail: richi_3489@hotmail.com

J. A. Romero Serrano · A. Hernández Ramírez
Metallurgy and Materials Department, ESIQIE-IPN, UPALM, Zacatenco, Ciudad de México 07738, Mexico

M. Zhang et al. (eds.), *Characterization of Minerals, Metals, and Materials 2023*, The Minerals, Metals & Materials Series
https://doi.org/10.1007/978-3-031-22576-5_62

Introduction

Ferroelectric materials such as $BaTiO_3$ are of great interest due to their wide range of dielectric, magnetic, thermal, and piezoelectric properties, among others. $BaTiO_3$ has a rhombohedral to orthorhombic phase transition at − 90 °C, orthorhombic to tetragonal at 0 °C, tetragonal to cubic at 120 °C, and cubic to hexagonal at high temperatures. The stoichiometric form of the $BaTiO_3$ phases is of the ABO_3 type. The saturation of the tetragonal perovskite structure of $BaTiO_3$ at room temperature, using not isovalent doping with rare earth elements [1], such as Eu^{3+}, allows obtaining and stabilizing the cubic phase [2, 3], in addition, new phases are generated such as Eu_2OTiO_5 [4–6], $BaTi_2O_5$ [7, 8], TiO_2 [9] and $Ba_2Ti_{13}O_{22}$ [10–13]. The generated phases are of interest because tetragonal $BaTiO_3$ and $BaTi_2O_5$ have high dielectric constant and piezoelectricity properties, making them candidates for applications such as lead-free capacitors, multilayer capacitors, piezoelectric devices, etc. The Eu_2TiO_5 phase has thermal neutron absorption cross-sections and applications in nuclear reactors, the TiO_2 phase has application as an anode in lithium batteries, as a receiving structure for rare earth elements, mechanical, chemic, and thermal resistance, the $Ba_2Ti_{13}O_{22}$ phase has electronic and magnetic properties such as those of a superconducting oxide ($LiTi_2O_4$) and those of a transition semiconductor (Ti_2O_3) and the characteristics of its structure [12, 13].

Experimental Development

High purity precursors (99.9%), $BaCO_3$ (CAS 513-77-9), TiO_2 (CAS 13463-67-7) and Eu_2O_3 (CAS 1308-96-9) were mixed, according to the charge compensation mechanism $Ba_{1-x}Eu_xTi_{1-x/4}O_3$ with $x = 0$, 10 and 15% Eu^{3+} (wt.%) means of the solid-state reaction method. The mixtures were dried at 200 °C for 8 h in a LINDERBERG muffle oven. Subsequently, they were ground in an agate mortar for 50 min with acetone as a control medium. The samples obtained were decarbonated in an alumina crucible inside a FURNACE/THERMOLYNE oven for 12 h at 900 °C using a heating rate of 4 °C/min. Finally, the samples were placed inside a platinum crucible and sintered using a FURNACE/THERMOLYNE furnace at 1300 °C for 6 h using a heating ramp of 4 °C/minute. The structural evolution of the sintered samples was studied by X-ray diffraction using an Equinox 2000 diffractometer with Cobalt Kα1 radiation. The phases present in the samples were identified using the software Match! 3, Rietveld refinement was performed with the FullProf software with the Pseudo-Voigt profile shape function (5th of Fullprof). The Raman spectrum of the samples was analyzed in a PERKIN ELMER NIR Spectrum GX FT-Raman instrument. The studies were performed at room temperature in the wave region of 200–1400 cm^{-1}, with 250 scans at a power of 300 mW, at intervals of 1 cm^{-1}, and at a resolution of 64 cm^{-1}.

Results and Discussion

In the composition $x = 0$ Eu^{3+} (wt.%), shown in Fig. 1, the tetragonal $BaTiO_3$ phase (JCPDS 96-150-7757) was identified, with lattice parameters; $a = 3.9787$ Å, $b = 3.9787$ Å and $c = 4.0093$ Å, a volume of 63.46 Å^3, a theoretical density of 6.102 g/cm^3 and bands in the Raman spectrum at 265, 521 and 725 cm^{-1}. The phases present in the composition $x = 10\%$ Eu^{3+} (wt.%), shown in Fig. 2, were; Cubic $BaTiO_3$ (JCPDS 96-155-9964), with lattice parameters a, b, and $c = 4.0463$ Å, a volume of 62.2502 Å^3, a theoretical density of 6.175 g/cm^3 and bands in the Raman spectrum at 265 and 541 cm^{-1}. Tetragonal TiO_2 (JCPDS 96-900-4143), with lattice parameters $a = 4.5963$ Å, $b = 4.5963$ Å and $c = 2.9695$ Å, a volume of 62.7325 Å^3, a theoretical density of 4.228 g/cm^3 and bands in the Raman spectrum at 123, 144, 200 and 250 cm^{-1}. Finally, orthorhombic Eu_2TiO_5 (JCPDS 96-200-2716) with lattice parameters $a = 10.6493$ Å, $b = 11.2674$, Å, and $c = 3.7132$ Å, a volume of 445.5430 Å^3, a theoretical density of 6.225 g/cm^3 and a band in the Raman spectrum at 790 cm^{-1}. In this composition ($x = 10$ Eu^{3+} (wt.%)) the saturation, with the dopant element (Eu^{3+}), of the tetragonal $BaTiO_3$ structure caused a phase change to cubic by increasing the lattice parameters "a" of 3.9787–4.0463 Å, "c" from 4.0093 to 4.0463 Å and a volume change of 63.46–62.2502 Å^3 was obtained. The Eu_2TiO_5 species was obtained from (1) $BaCO_3 \longrightarrow BaO + CO_2$, (2) $Eu_2O_3 + TiO_2 \longrightarrow Eu_2TiO_5$ [14]. TiO_2 was obtained by not reacting with BaO or with the doping element [14]. Obtaining these phases was attributed to an excess of Eu^{+3}. In the composition 15 Eu^{3+} (wt.%), shown in Fig. 3, the presence of the phases was determined: monoclinic $BaTi_2O_5$ (JCPDS 96-201-3674), obtained in (1) $BaCO_3 \longrightarrow BaO + CO_2$ (2) $BaO + TiO_2 \longrightarrow BaTiO_3$, (3) $BaTiO_3 + TiO_2 \longrightarrow BaTi_2O_5$ [14], with lattice parameters $a = 16.899$ Å, $b = 4.1525$ Å and $c = 9.6705$ Å, a volume of 660.94 Å^3, a density of 5.188 g/ cm^3, and bands in the Raman spectrum at 246, 300 and 550 cm^{-1}. The orthorhombic $Ba_2Ti_{13}O_{22}$ phase (JCPDS 96-200-262was 8), obtained with the reaction of the intermediate phases ($BaTiO_3$, Ti_2, O_3, and TiO) [10–13] in the empirical process of reaction in solid state at high temperatures between $BaCO_3$ and TiO_2 [14], with lattice parameters $a = 10.0183$ Å, $b =$,11.5747 Å, and $c = 14.0940$ Å, a volume of 1634.3236 Å^3, and a density of 5.076 g/cm^3. Finally, orthorhombic Eu_2TiO_5 (JCPDS 96-200-2716), with lattice parameters $a = 10.5338$ Å, $b = 11.2957$ Å, and $c = 3.7409$ Å, a volume of 445.2029 Å^3, a theoretical density of 6.442 g/cm^3 and a band in the Raman spectrum at 790 cm^{-1}. In this composition, the Eu_2TiO_5 phase is maintained, however, it is reduced from 81 to 8.1% according to the data obtained by Rietveld refinement. As it was observed in the composition $x = 10$ Eu^{3+} (wt.%), the obtaining of the Eu_2TiO_5 phase was achieved by reacting excess dopant (Eu_2O_3) and precursor compound (TiO_2), on the other hand, in the composition $x = 15$ Eu^{3+} (wt.%)the presence of this phase decreased and phases

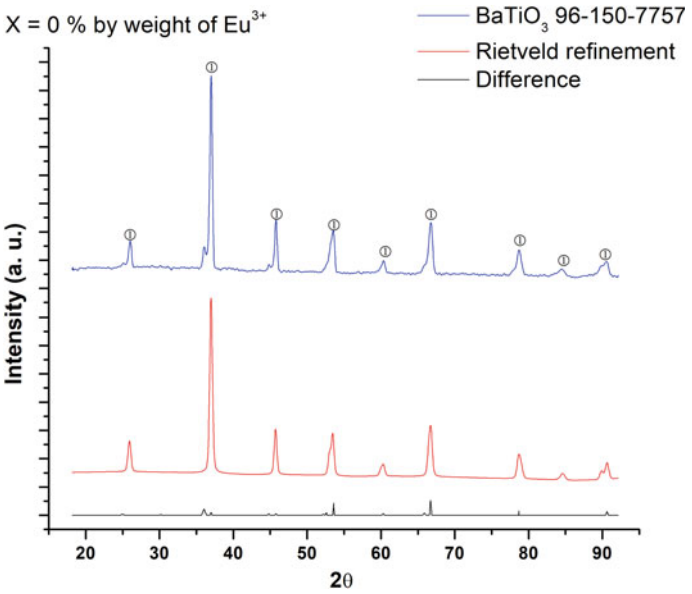

Fig. 1 Composition 0 Eu^{3+} (wt.%), blue line diffraction spectrum of the composition, red line reference standard for Rietveld refinement, black line difference between standards

rich in titanium were present when reacting intermediate phases ($BaTiO_3 + TiO_2$ for $BaTi_2O_5$ and $BaTiO_3$, Ti_2O_3, TiO for $Ba_2Ti_{13}O_{22}$) in the empirical process of formation for $BaTiO_3$. Figure 4 shows the Raman spectra that verify the presence of the phases in the compositions $x = 0$, 10, 15 Eu^{3+} (wt.%), Table 1 shows the data obtained by Rietveld refinement.

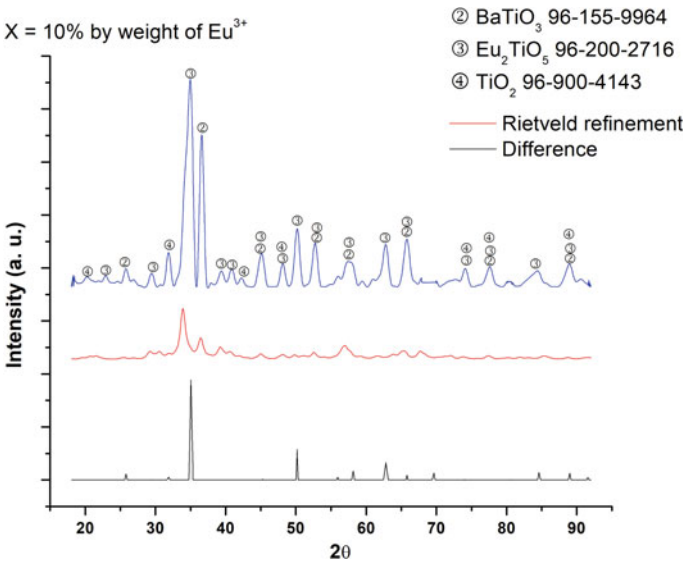

Fig. 2 Composition 10 Eu^{3+} (wt.%), blue line diffraction spectrum of the composition, red line reference standard for Rietveld refinement, black line difference between standards

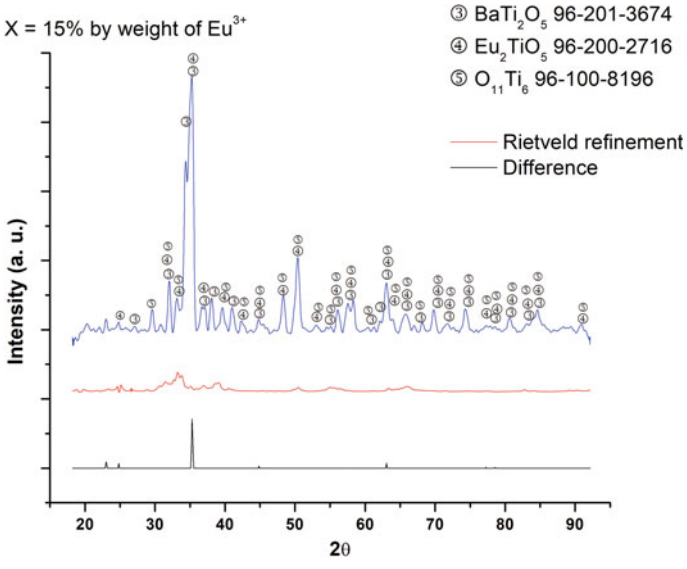

Fig. 3 Composition 15 Eu^{3+} (wt.%), blue line diffraction spectrum of the composition, red line reference standard for Rietveld refinement, black line difference between standards

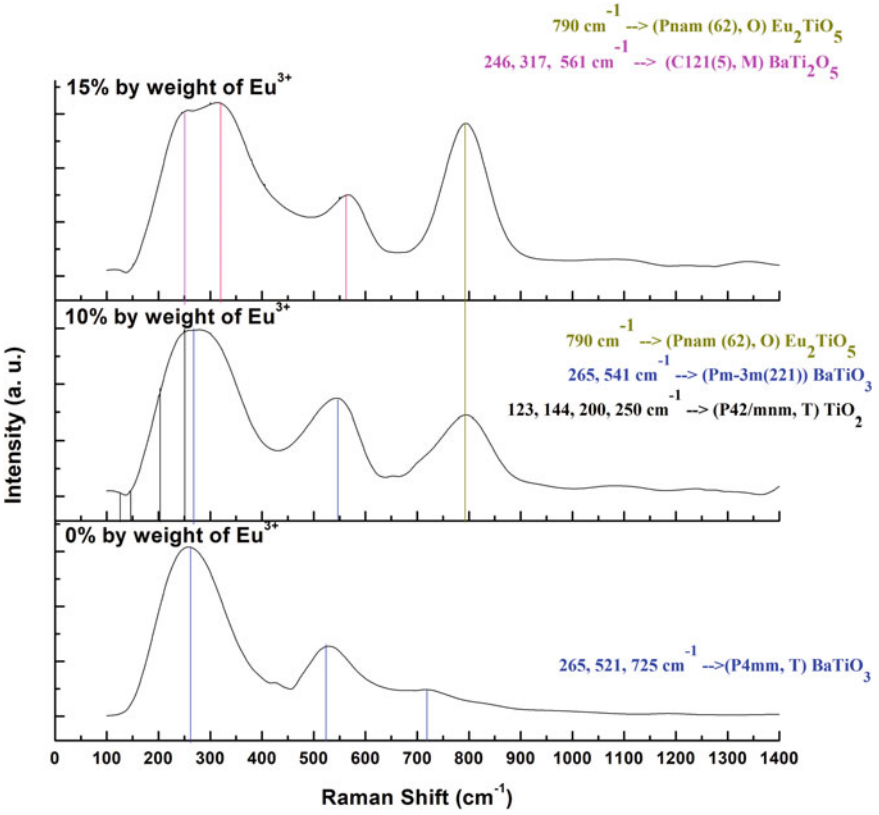

Fig. 4 Raman spectrum of the compositions $x = 0$, 10 and 15 Eu^{3+} (wt.%)

Table 1 Lattice parameters, volume, and theoretical density of the phases, data obtained by Rietveld refinement

Phase/parameters	a (Å)	b (Å)	c (Å)	Volume (Å^3)	Density (g/cm^3)
$BaTiO_3$ tetragonal (0%)	3.9787	3.9787	4.0093	63.4674	6.102
$BaTiO_3$ cubic (10%)	4.0463	4.0463	4.0463	62.2502	6.175
TiO_2 (10%)	4.5963	4.5963	2.9695	62.7325	6.175
$BaTi_2O_5$ (15%)	17.8134	3.8975	9.4105	636.3342	4.902
Eu_2TiO_5 (10%)	10.6493	11.2674	3.7132	445.5430	6.225
Eu_2TiO_5 (15%)	10.5358	11.2957	3.7409	445.2029	6.442
$Ba_2Ti_{13}O_{22}$ (15%)	10.0183	11.5747	14.0940	1634.3236	5.076

Conclusions

The Tetragonal $BaTiO_3$ phase can be obtained by the solid-state reaction method of $BaCO_3$ and TiO_2. By saturating the tetragonal $BaTiO_3$ structure through not isovalent doping with Eu^{3+} rare earth ions, it is possible to sinter structures of interest such as EU_2TiO_5 that have applications in nuclear reactors. The importance structural evolution of the phases is of great interest since it is directly related to the material's thermal expansion that determines the application of EU_2TiO_5 in nuclear reactors. In addition, microstructure and chemical composition are primary factors in determining the properties of materials.

References

1. Liu Q, Liu J, Lu D, Zheng W, Hu C (2018) Structural evolution and dielectric properties of Nd and Mn co-doped $BaTiO_3$ ceramics. J Alloys Compd
2. Caballero AC, Fernandez JF, Duran P, Moure C (1994) Titanato de bario cerámico. Boletin de la Sociedad Española de Ceramica y Vidrio 33:5
3. Hayashi H, Kakamura T, Ebina T (2013) In-situ Raman spectroscopy of BaTiO3 particles dor tetragonal-cubic transformation. J Phys Chem Solids 74:957
4. Muller HK, Werner JP (1994) Zur Kenntnis von Eu_2TiO_5. Letter 206:11
5. McCarthy GJ, White WB, Roy R (1969) The system Eu-Ti-O: phase relations in a portion of the 1400°C Isotherm. J Nucl Chem 31:329
6. Syamala KV, Panneerselvam G, Subramanian GGS, Antony MP (2008) Synthesis, characterization, and thermal expansion studies on europium titanate (Eu_2TiO_5). Thermochim Acta 475:76
7. Miyazaki H, Yamashita Y, Yamata K, Kubota T, Omata K, Tsukada S (2021) Lowering $BaTi_2O_5$ Curie temper temperature facile hydrothermal ion-exion exchange retaining the original particle morphology. Mater Chem Phys 272:125037
8. Falmbingl M, Golovina IS, Hawley CJ, Plokhikh AV, Shafir O, Grinberg I, Spanier JE (2021) Ultrahigh anharmonicity low-permittivity tunable nanocrystalline thin-film $BaTi_2O_5$. Acta Mater 208:116712
9. Ran J, Liu H, Dong H, Gao P, Cheng H, Xu J, Wang H, Wang Z, Fu Q, Yan J, Liu J (2022) Accurate quantification of TiO_2(B)'s phase purity via Raman spectroscopy. Green Ener Environ
10. Akimono J, Gotoh Y, Sohma M, Kawaguchi K, Oosawa Y (1994) Synthesis and crystal structure of $Ba_2Ti_{13}O_{22}$: a reduced form of $BaTi_5O_{11}$by the titanium insertion. J Solid State Chem 113:384
11. Mohr S, Muller-Buschbaum HK (1993) Ein Beitrag zur Synthese und Kristalstruktur eines gemischvalenten Bariumoxotitanats: $Ba_2Ti_{12}{}^{3+}Ti^{4+}O_{22}$. J Alloys Compd 199:203
12. Kataoka K, Kijima N, Hayakawa H, Iyo A, Ohshima K, Akimoto J (2011) Synthesis, structure and physical properties of reduced barium titanate $Ba_2Ti_{13}O_{22}$. J Solid State Chem 184:3117
13. Yamaguchi N, Furuhashi A, Nishihara H, Murata R, Takayama K, Katsufuji T (2016) Photoinduced dynamics in doped Mott insulators with polaronic conduction: $Ba_2Ti_{13}O_{22}$ and $Ba_xTi_8O_{16}$. Phys Rev 94:045199
14. Beauger A, Mutin JC, Niepce JC (1984) Role and, behavior or orthotitanate Ba_2TiO_4 during the processing of $BaTiO_3$ based ferroelectric ceramics. J Mater Sci 19:195

Author Index

M. Zhang et al. (eds.), *Characterization of Minerals, Metals, and Materials 2023*, The Minerals, Metals & Materials Series
https://doi.org/10.1007/978-3-031-22576-5

Subject Index

M. Zhang et al. (eds.), *Characterization of Minerals, Metals, and Materials 2023*, The Minerals, Metals & Materials Series
https://doi.org/10.1007/978-3-031-22576-5

D

E